Investigating Altered Metabolism as a Potential Therapeutic Target in Antimicrobial Resistance

KYOUNG EUN LEE

SOMERVILLE COLLEGE

DEPARTMENT OF CHEMISTRY

UNIVERSITY OF OXFORD

SUBMISSION HILARY 2025

A Thesis Submitted to the Board of the Mathematical, Physical and Life Sciences Division at the University of Oxford in Partial Fulfilment of the Requirements for the Degree of Doctoral of Philosophy

I. Abstract

Antimicrobial resistance poses a critical threat to global health, demanding innovative approaches to mitigate its impact. This study investigates metabolic adaptations underlying antibiotic resistance, focusing on the New Delhi metallo-β-lactamase enzyme, which hydrolyses carbapenems and confers high-level resistance. The primary objective was to identify metabolic vulnerabilities in resistant *Escherichia coli* strains that could be exploited as therapeutic targets to mitigate resistance. By characterising strain-specific metabolic changes under both basal and meropenem exposure, this study aims to inform the development of combination therapies pairing antibiotics with metabolic inhibitors.

Using genetically engineered bacterial strains – wild-type, meropenem-susceptible, and meropenem-resistant – untargeted metabolomics was performed, employing an optimised anion exchange chromatography-mass spectrometry method. Comprehensive analysis revealed significant metabolic reprogramming associated with plasmid carriage and New Delhi metallo-β-lactamase-7 gene expression. Key pathways impacted included nucleotide metabolism, central carbon metabolism, and amino acid biosynthesis, highlighting critical differences between resistant and non-resistant strains.

These findings demonstrate that metabolic changes associated with resistance impose unique vulnerabilities in resistant strains, presenting promising target for disruption. This work highlights the utility of metabolomics in uncovering strain-specific metabolic dependencies, advancing efforts to combat antimicrobial resistance through innovative therapeutic strategies that enhance antibiotic efficacy.

II. Declaration

I declare that the work presented in this thesis was conducted under the supervision of Professor James S. O. McCullagh and Dr Karina Calvopina Tapia. All work described herein is entirely my own unless stated otherwise. Material sourced from other authors or publications, including quoted or paraphrased text, diagrams, charts, tables, and graphs has been clearly indicated and appropriately referenced.

I confirm that no part of this thesis has been submitted, either partially or in full, for any qualification at this University or any other institution. Any assistance I have received, beyond the guidance provided by my supervisor, has been fully acknowledged.

III. Acknowledgements

I would like to begin by expressing my gratitude to my supervisor, James, for giving me the opportunity to embark on this research. His support and encouragement have been invaluable throughout this process.

My heartfelt thanks go to Dr. Karina Calvopina Tapia, who supervised and taught me everything about bacteria and laboratory work. Her generosity in sharing space and lab equipment, especially during the challenging times of COVID-19, was deeply appreciated. I also extend my gratitude to Dr. John Walsby-Tickle, whose expertise and patience in teaching me mass spectrometry techniques, including the use of AEC-MS, were invaluable. His willingness to help, answer my questions, and guide me in the mass spectrometry facility made a significant impact on my work.

I am grateful to the members of the McCullagh group for their unwavering support and inspiration, and day-to-day positivity, as well as the fun chats that kept the spirit alive in the lab. Special thanks to Rachel Williams, Ingvild Comfort Hvinden, and John Sidda for their invaluable proof-reading and insightful suggestions that significantly improved my work.

To my friends who kept me sane during this journey - Abi, Alex, Dani, Emily, Libby, and Zoë - thank you for caring for me and dealing with me since 2014. Karolina and Stefano, thank you for being the reason and root of the courage to come back to Oxford to do a DPhil, and matching my crazy. Hanson, thank you for sending memes to get me through hard times- and Lara, Shruti, Razanne, Ash, Oana, and Andriana- I know I am terrible at keeping in touch, but I do love you all. To my friends from Korea, thank you for being there and providing the balance I needed.

I also extend my deepest appreciation to my family, who had been my rock and supported me from wherever they are in the world. Your belief in me has been a constant source of strength.

I would like to acknowledge all the teaching I have receive over the years, especially from Dr. Gerry Gallacher, whose guidance laid the foundation for my academic pursuits.

III. Acknowledgements

To all the past connections who have shaped me into the person I am today- Riddlesworth Hall, Woldingham, University of Brighton, and University of Oxford- thank you for your influence and contributions to my growth.

Finally, I am endlessly grateful to Klem for standing by me through good and bad times, sharing in my tears, laughter, and moments of craziness and difficulty. Thank you for being everything I needed – a partner, family, teacher, and source of comfort. From a hug to proof-reading, you were always there for me, whenever I needed, and I couldn't have done this without you.

본 논문이 완성되기까지 많은 분들의 도움과 지지가 있었습니다. 이 자리를 빌려 감사의 마음을 전하고자 합니다.

먼저, 언제나 든든한 기둥이 되어주신 부모님과 하나밖에 없는 동생 건우에게 깊은 감사를 드립니다. 또한, 저를 사랑으로 키워주시고 아낌없는 응원과 격려를 보내주신 김옥경 엄마엄마, 한영철 아저씨, 윤아 이모께도 진심으로 감사드립니다. 세상 어디에 있든 늘 저를 지지해 주시는 가족들, 큰고모, 작은고모, 외삼촌, 정주 이모, 로키 삼촌, 수잔 이모을 비롯한 모든 가족분들께 감사의 인사를 전합니다. 친동생처럼 아껴준 소중한 사촌들, 특히 선주 언니, 현화 언니, 규만 오빠, 진희 언니, 원석 오빠 그리고 존재 만으로도 저에게 큰 행복과 위로가 되어주는 사랑스러운 조카들, 지인, 은우, 세아, 채아, 오름 지안에게도 고마움을 전합니다.

몸은 멀리 떨어져 있지만 마음만은 언제나 가까이 있어 준 소중한 친구들 유나, 유림, 소의. 늘 든든한 동생 균학, 예원과 언제든 연락하면 반겨주는 수민 언니를 비롯해 항상 응원과 따뜻한 격려를 보내준 모든 동생, 언니, 오빠들에게도 감사의 마음을 전합니다. 가르침을 주신 모든 선생님들, 그리고 신부님들께도 이 자리를 빌려 깊이 감사드립니다.

이 외에도 제 삶에 소중한 영향을 주신 모든 분들께 진심으로 감사드립니다.

마지막으로, 언제나 저의 믿음이자 힘이 되어 주신 하느님과, 그 곁에서 저를 지켜보고 계실 할머니, 할아버지들께 깊은 감사의 마음을 올립니다.

감사합니다.

IV. Abbreviations

2-DG	2-deoxy-D-glucose
2TY broth	2 × Yeast Extract Tryptone medium
a.u.	Arbitrary units
AB	Antibiotic
AB+INH	Combination therapy; antibiotic with inhibitor
ACN	Acetonitrile
AEC-MS	Anion exchange chromatography coupled with mass spectrometry
AGC	Automatic gain control
AMR	Antimicrobial resistance
ANOVA	Analysis of variance
ATP	Adenosine 5'-triphosphate
BDQ	Bedaquiline
BF	Buffer Factor
bp	Base pairs
BSA	Bovine Serum Albumin
CAAs	Casamino acids
cAMP	Cyclic adenosine monophosphate
CFUs	Colony forming units
$CHCl_3$	Chloroform
CLSI	Clinical and laboratory standards institute
CR-ATC	Continuously regenerated trap column
CRE	Carbapenem-resistant Enterobacteriaceae
CV	Coefficient of variation
dADP	Adenosine diphosphate
dCTP	Deoxycytidine triphosphate
dd	Data-directed
DDA	Data-dependent acquisition
DMEM	Dulbecco's Modified Eagle Medium
dGDP	Deoxyguanosine diphosphate
DHEA	Dehydroepiandrosterone
DMSO	Dimethyl sulphoxide
DNA	Deoxyribonucleic acid
ds	Double-stranded
E	Wild-type *E. coli* strain
ECAR	Extracellular acidification rate
ECMDB	*E. coli* metabolome database
EGC	Eluent generator cartridge
ESBLs	Extended-spectrum β-lactamases
ETC	Electron transport chain
FC	Fold change
FCCP	Carbonyl cyanide 4-(trifluoromethoxy) phenylhydrazone
FDA	USA Food and Drug Administration
FDR	False discovery rate
g	Force of gravity
GC	Gas Chromatography
GC-MS	Gas chromatography-mass spectrometry
GDP	Guanosine diphosphate
GSH	Glutathione

glycoATP	Glycolytic ATP production
glycoPER	Glycolytic proton efflux rate
H_2O_2	Hydrogen peroxide
HCD	High-energy collision dissociation
HCl	Hydrochloric acid
HESI	Heated electrospray ionisation
HGT	Horizontal gene transfer
HILIC	Hydrophilic interaction liquid chromatography
HMDB	Human Metabolome Database
HPIC	High-Pressure Ion Chromatography
HPLC	High-performance liquid chromatography
IC	Ion exchange chromatography
IC-MS	Ion exchange chromatography coupled mass spectrometry
IDH	Isocitrate dehydrogenase
IMS	Imaging mass spectrometry
INH	Inhibitor
IQR	Interquartile range
IT	Injection time
Kat	Catalase
KEGG	Kyoto Encyclopaedia of Genes and Genomes
KOH	Potassium hydroxide
KPC	*klebsiella pneumoniae* carbapenemase
LC	Liquid chromatography
LCGC	Liquid chromatography and gas chromatography
LU	Luminescence unit
m/z	Mass-to-charge ratio
MBL	Metallo-β-lactamase
MCS	Multiple cloning site
MDR	Multidrug-resistant
MDROs	Multidrug-resistant organisms
MDR-TB	Multidrug-resistant tuberculosis
MeCN	Acetonitrile
MeOH	Methanol
MEP	Methylerythritol phosphate
mero	Meropenem
MHA	Meropenem hydrolysis assay
MIC	Minimum inhibitory concentration
MQ	Milli-Q®
MRSA	Methicillin-resistant *Staphylococcus aureus*
MS	Mass spectrometry
MS/MS	Tandem mass spectrometry
mut	Mutant
MWCO	Molecular weight cut-off
NAAG	*N*-Acetylaspartylglutamic acid
NaCl	Sodium chloride
NADH	Nicotinamide adenine dinucleotide
NDM	New Delhi Metallo-β-lactamase
NMR	Nuclear magnetic resonance
OCR	Oxygen consumption rate

OD	Optical density
OD600	Optical density at a wave length of 600 nm
OPLS-DA	Orthogonal PLS-DA
OXPHOS	Oxidative phosphorylation
oxyATP	Oxidative ATP production
PBPs	Penicillin-binding proteins
PBS	Phosphate-buffered saline
PCA	Principal Component Analysis
PCR	Polymer chain reaction
PER	Proton Efflux Rate
PLL	Poly-L-lysine
PLS-DA	Partial Least Squares Discriminant Analysis
ppb	Parts per billion
Prx	Peroxiredoxins
PS	Polystyrene
PTFE	Polytetrafluoroethylene
PTS	Phosphotransferase system
QC	Quality control
R	Meropenem-resistant *E. coli* strain
RC	Regenerated cellulose
redox	Reduction-oxidation
ROS	Reactive oxygen species
Rot/AA	Rotenone/antimycin A
rpm	Revolutions per minute
RT	Retention time
S	Meropenem-susceptible *E. coli* strain
S/B	Signal-to-blank ratio
SD	Standard deviation
SOC	Super Optimal broth with Catabolite repression
SOD	Superoxide dismutases
TA	Taq Polymerase-Added
TAE	Tris Acetate EDTA
TB	Tuberculosis
TCA	Tricarboxylic acid
TIC	Total ion chromatogram
TIC	Total ion current
TOC	Total organic carbon
Trx	Thioredoxins
UTIs	Urinary tract infections
VIP	Variable importance in projection
vs.	Versus
WHO	World Health Organisation
wt	Wild type

V. Table of contents

VI. List of figures

VII. List of tables

Chapter 1 Introduction

1.1 Antimicrobial resistance

Antimicrobial resistance (AMR) is one of the most urgent contemporary challenges for global healthcare, posing a major threat to public health and modern medicine.[1,2] AMR occurs when microorganisms, including bacteria, fungi, viruses, and parasites, evolve mechanisms to withstand the effects of antimicrobial agents, rendering these treatments ineffective.[3] The phenomenon leads to increased morbidity, mortality, and healthcare costs.[4-6] Antibiotic-resistant infections are particularly concerning, as they compromise the treatment of common bacterial diseases, such as pneumonia, urinary tract infections, and sepsis.[7] Alarmingly, the rate at which AMR is developing far exceeds the pace of new antibiotic discovery and development, exacerbating the challenge.[2,8] It is estimated that, by 2050, AMR could lead to 10 million deaths annually and a cumulative economic cost of $100 trillion if left unaddressed.[9-11]

The mechanisms by which microbial pathogens evolve resistance to antibiotics are diverse and interconnected, often involving genetic mutations, horizontal gene transfer (HGT), and biofilm formation.[12-15] HGT in particular, enables the rapid dissemination of resistance genes across bacterial populations, often via plasmids and transposons.[16] As a result, the spread of multidrug-resistant organisms (MDROs) in clinical and environmental settings has been accelerated.[17] The emergence of carbapenem-resistant *Enterobacteriaceae* (CRE), which includes resistant *Escherichia coli* (*E. coli*) strains, exemplifies the critical challenges posed by AMR.[18] These pathogens not only limit therapeutic options but also increase the likelihood of treatment failures, further exacerbating the public health burden.

The global implications of AMR extend beyond healthcare. In agriculture, the widespread use of antibiotics as growth promoters has contributed to the selection of resistant strains, which can transfer to humans through the food chain.[1] In the environment, improper disposal of antibiotics has created reservoirs of resistance genes in soil and water systems.[19] Addressing

AMR, therefore, requires a multifaceted approach that encompasses healthcare, agriculture, and environmental stewardship.

To combat AMR effectively, it is imperative to understand the biological mechanisms driving resistance. While genetic adaptations have been extensively studied, the role of bacterial metabolism in facilitating resistance is less well understood.[20] Metabolic pathways not only sustain cell growth and survival but also mediate stress responses under antibiotic pressure.[21,22] By investigating the metabolic adaptations associated with resistance, there is potential to reveal novel therapeutic targets. In order to explore this potential, the following thesis adopts a metabolic perspective to uncover the interplay between antibiotic exposure and bacterial metabolism, with a specific focus on *E. coli* as a model organism.

1.1.1 Metallo-β-lactamase

β-Lactams, including penicillins, cephalosporins, and carbapenems, represent a cornerstone of current antimicrobial therapy and are among the most widely used and clinically important classes of antibiotics, constituting over 60% of global antibiotic prescription due to their ability to inhibit bacterial cell wall synthesis.[23-25] Carbapenems, in particular, are often considered the last-resort antibiotics treatment for infections caused by multidrug-resistant bacteria.[26,27] However, the increasing prevalence of metallo-β-lactamases (MBLs), a class of enzymes that confer resistance to nearly all β-lactam antibiotics, has substantially undermined their therapeutic value.[28,29]

MBLs function by hydrolysing the β-lactam ring, a structural feature critical for the bactericidal activity of β-lactam, rendering these antibiotics ineffective.[30] The hydrolysis of the β-lactam ring prevents β-lactams from effectively inhibiting penicillin-binding proteins (PBPs), which are essential for bacterial cell wall synthesis.[31] The catalytic activity of MBLs depends on divalent metal ions, typically zinc, at their active site, which facilitate the nucleophilic attack on the β-lactam ring, leading to its cleavage.[32] Unlike serine β-lactamases, which use a serine residue in their active site, MBLs rely exclusively on these metal ions, making them distinct in their mechanism of action.[33]

The broad substrate specificity of MBLs allows them to target a wide range of β-lactam antibiotics, including carbapenems, cephalosporins, and penicillins.[34] Alarmingly, MBL-producing bacteria exhibit resistance to most commercially available β-lactamase inhibitors, such as clavulanic acid, which are designed to target serine β-lactamases.[32] Such resistance drastically limits therapeutic options and poses a serious clinical challenge, particularly as it is estimated that carbapenem resistance rates exceed 50% in certain regions.[35,36] The dissemination of MBLs has been facilitated by their frequent localization on plasmids, which can be horizontally transferred between bacterial populations.[37] The rise of MBL-mediated resistance draws attention to the urgent need for alternative therapeutic strategies to counteract its escalating impact.

1.1.1.1 Role of Plasmids in antimicrobial resistance study

The rapid expansion of MBLs is largely driven by plasmids, which are mobile genetic elements capable of HGT between bacteria, including those from different species and genera.[38] Plasmids play a pivotal role in spreading resistance genes, often carry multiple resistance determinants, enabling bacteria to withstand diverse classes of antibiotics.[39] HGT via conjugation, transformation, or transduction facilitates the rapid acquisition of resistance traits, even among phylogenetically distant bacterial species.[40]

In addition to promoting dissemination, plasmids enhance bacterial adaptability by introducing genetic variability. The adaptability allows bacteria to thrive in diverse and challenging environments, such as those with high antibiotic pressure.[39] Hence, plasmids not only confer antibiotic resistance traits, but also have the potential to influence bacterial metabolism. Understanding these metabolic effects is critical, as they must be accounted for in biological models to ensure accurate interpretation of metabolic changes and resistance mechanisms.

Beyond their natural role in antimicrobial resistance, plasmids are invaluable tools in molecular biology and genetic engineering. Their ability to carry and replicate genetic material makes them essential for cloning, gene modification, and the study of resistance mechanisms.

Leveraging plasmids provides crucial insights into antimicrobial resistance and supports the development of innovative therapeutic strategies.

1.1.1.2 Clinical significance of NDM-7

Among the diverse MBLs, the New Delhi Metallo-β-lactamase (NDM) family has emerged as a critical focus of global AMR research due to its rapid spread, broad substrate specificity, and substantial clinical impact.[41] First identified in 2008, NDM enzyme production as a resistance mechanism has rapidly spread worldwide, with outbreaks reported in healthcare settings across multiple continents.[37] NDM-7, a clinically meaningful variant of the NDM family, exhibits enhanced hydrolytic activity and broader resistance profile compared to earlier variants.[42,43] The mobility of NDM-7 exacerbates its clinical impact, as it allows for the rapid acquisition of resistance traits within bacterial populations. Understanding the metabolic consequences of NDM-7 expression and its role in AMR is crucial for informing the development of novel therapeutic approaches aimed at mitigating its threat.

1.2 The role of metabolism in antibiotic resistance

Bacterial metabolism plays an important role in survival under antibiotic stress by supplying ATP and metabolic precursors necessary for maintaining cellular functions and counteracting antibiotic-induced damage.[44,45] Antibiotics have been shown to exert general and selective pressure by targeting essential molecular processes, disrupting cellular homeostasis and triggering metabolic adaptations aimed at restoring balance and maintaining viability.[46]

Antibiotic treatment has been shown to induce cellular stress by disrupting normal bacterial physiology leading to oxidative damage, impaired energy production, or inhibition of essential biosynthetic pathways.[47-49] The effects of antibiotic treatment have been shown to include oxidative stress due to increased levels of reactive oxygen species (ROS). ROS formation, including hydrogen peroxide (H_2O_2) and superoxide anions, can damage proteins, lipids, and nucleic acids.[50,51] To counteract oxidative damage, bacteria activate stress-response pathways that rely on metabolic reprogramming.[52] For example, glycolysis and oxidative phosphorylation may be upregulated to generate ATP required for detoxification pathways,

such as those mediated by catalases and superoxide dismutases.[53-56] Glycolysis supplies ATP and biosynthetic precursors, while oxidative phosphorylation generates ATP through the electron transport chain found in the plasma membrane of bacteria.[57] These pathways are particularly important under antibiotic stress, as they supply the energy required to repair damaged cellular components and maintain redox homeostasis.[58-60]

In addition to general stress responses, it has been shown that bacteria have developed specific genetic adaptations in response to particular antibiotics. These adaptations often include the expression of enzymes that degrade or modify efflux pumps to expel the drug, or biofilm formation to reduce drug penetration.[61-64] These adaptations involve mechanisms that are intrinsically tied to bacterial metabolism. For instance, efflux pumps require substantial energy in the form of ATP or proton motive force, while the production of antibiotic-degrading enzymes, such as β-lactamases, depends on biosynthetic precursors derived from central carbon metabolism.[59,65]

The interplay between antibiotic mechanisms of action and bacterial resistance strategies is summarised in **Figure 1.1**, which highlights the targets of antibiotics and the corresponding resistance mechanisms employed by bacteria.[66-69]

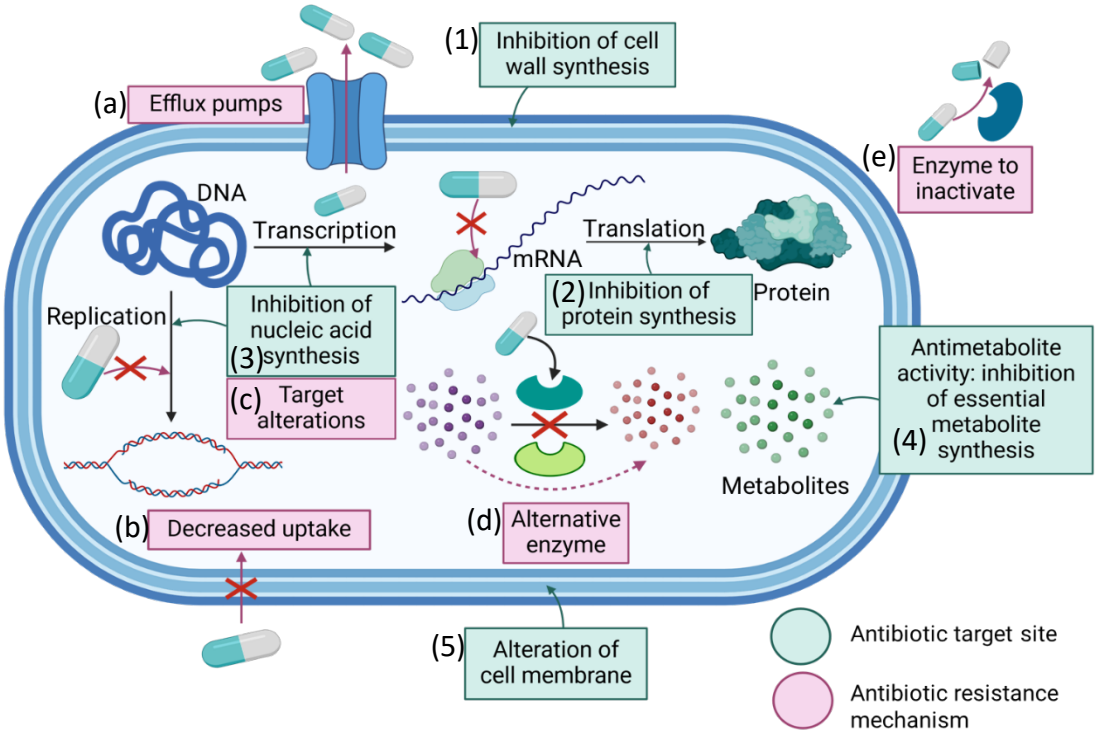

Figure 1.1 Antibiotic mechanisms of action and bacterial resistance strategies. *This diagram depicts the dual aspect of antibiotic activity and bacterial resistance. The antibiotic target sites include (1) Inhibition of cell wall synthesis, which disrupts structural integrity; (2) Inhibition of protein synthesis, interfering with essential protein production; (3) Inhibition of nucleic acid synthesis, preventing DNA replication or transcription; (4) Antimetabolite activity, targeting pathways essential for synthesising key metabolites; and (5) Alteration of the cell membrane, compromising membrane integrity. In response, bacteria employ resistance mechanisms such as (a) Efflux pumps to expel antibiotics; (b) Decreased uptake by altering membrane permeability; (c)Target alterations to reduce antibiotic binding efficacy; (d) Production of alternative enzymes to sustain essential functions; and (e)Enzymes to inactivate antibiotics.*

Antibiotic-specific responses also intersect with broader metabolic processes.[70] For example, exposure to aminoglycosides such as kanamycin has been shown to increase ROS production, necessitating heightened activation of antioxidant pathways.[71,72] Similarly, antibiotics targeting peptidoglycan biosynthesis, such as β-lactams, may redirect metabolic fluxes to compensate for impaired cell wall construction.[22,73,74] These metabolic adaptations highlight the relationship between genetic and metabolic responses which are utilised to enabling bacterial survival under antibiotic pressure.

Bacterial metabolism serves as the central hub that orchestrates both general and specific responses to antibiotic exposure.[58,59] The flexibility of metabolic networks allows bacteria to reallocate resources to pathways that mitigate stress, maintain energy production, and neutralise antibiotic effects.[59,75] These metabolically driven processes are not mutually exclusive but synergise to promote survival. [52,76,77] Understanding how metabolism supports

and integrates these adaptive strategies is therefore critical to understanding how bacteria respond to antibiotic treatment as well as identifying potential vulnerabilities that could be exploited therapeutically.[60,74] Insights into these metabolic changes may also inform the development of interventions that disrupt bacterial metabolic resilience in ways that can enhance the efficacy of existing antibiotics.

1.2.1 Stress response and metabolic adaptation in bacteria

ROS production is a common consequence of antibiotic treatment, particularly with agents that disrupt electron transport chain (ETC) or generate redox imbalance.[58,60,74] Oxidative stress poses a challenge to bacterial survival, leading to upregulation of antioxidant systems such as glutathione, catalase, peroxidases, and superoxide dismutases (SOD).[50,78,79] **Figure 1.2** illustrates the pathways involved in ROS generation and detoxification, highlighting the role of antioxidant enzymes in mitigating oxidative damage.[80-84] The glutathione (GSH) system reduces hydrogen peroxide, while SOD convert superoxide radicals into less reactive molecules.[59,73] Additionally, enzymes such as thioredoxins (Trx) and peroxiredoxins (Prx) play critical roles in repairing oxidised proteins and further support redox stability.

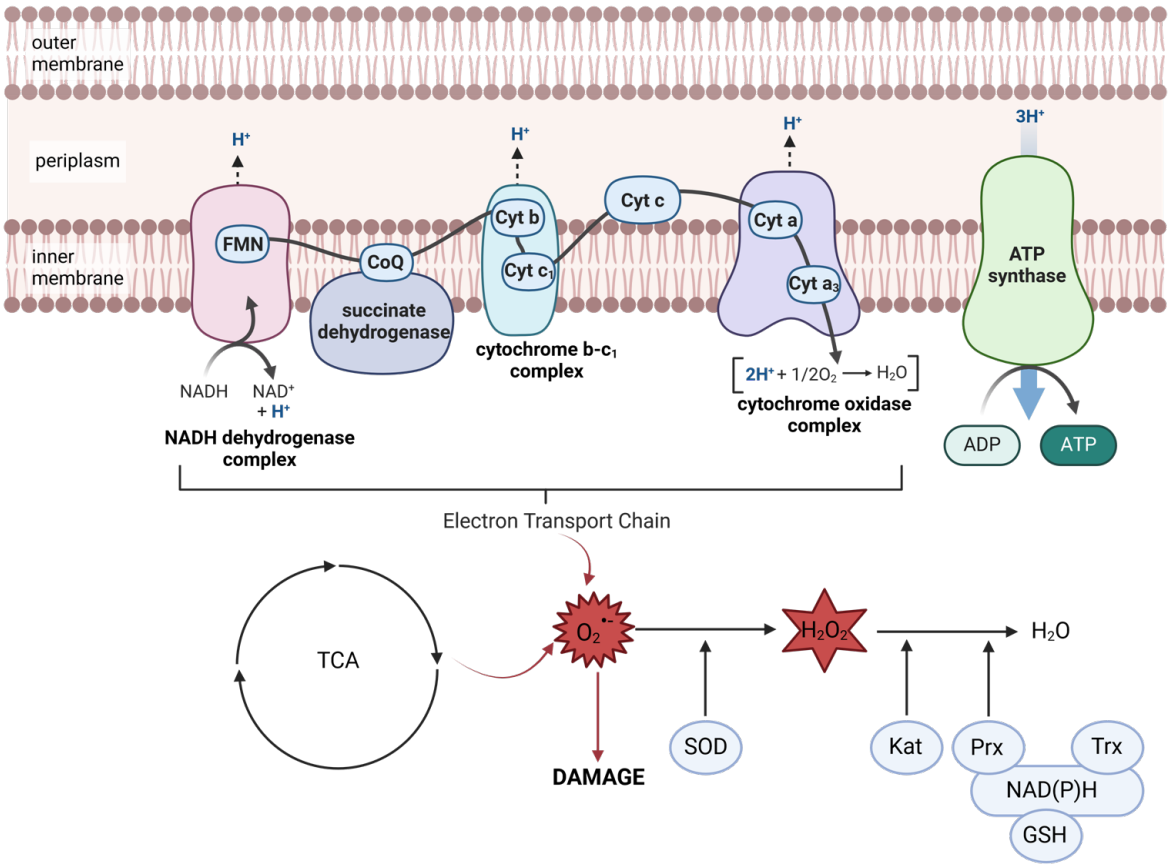

Figure 1.2 ROS generation and detoxification pathways in bacterial metabolism. *Antibiotic-induced disruption of the ETC or TCA cycle leads to ROS production, such as superoxide (O_2^-), which is further converted into hydrogen peroxide (H_2O_2). To counteract oxidative stress, bacteria upregulate antioxidant defence systems, including superoxide dismutases (SOD), which convert superoxide into less reactive molecules, and catalases (Kat), peroxiredoxins (Prx), thioredoxins (Trx), and glutathione (GSH) system reduce hydrogen peroxide. These detoxification mechanisms are crucial for bacterial survival under antibiotic stress, preventing oxidative damage to essential cellular components.*

Antibiotic pressure also induces metabolic changes that can confer specific advantages.[59,85] In resistant strains, metabolic reprogramming often involves the activation of alternative energy production pathways, such as anaerobic respiration or fermentation, which minimizes reliance on pathways targeted by antibiotics.[86] Additionally, the modulation of lipid and nucleotide biosynthesis supports membrane integrity and genetic replication, both of which are critical for survival under stress.[87-89] These adaptive strategies highlight the importance of metabolism as a central determinant of bacterial resilience.

Despite these insights, considerable gaps remain in understanding how different energy substrates influence antibiotic responses. For instance, it is not fully elucidated how bacteria prioritise specific metabolic pathways under stress or how variations in carbon source availability modulate these responses.[59,73] Understanding these dynamics could provide a

foundation for targeting bacterial metabolism therapeutically, disrupting resilience mechanisms, and enhancing the efficacy of antibiotic treatments.[58,74] A comprehensive perspective on central carbon metabolism and its response to antibiotics will serve as a fundamental framework throughout this thesis.

1.2.2 Metabolic pathways as antibiotic targets

Targeting bacterial metabolism offers a promising antimicrobial strategy, either as a standalone approach or to enhance existing antibiotic treatment efficacy.[45,90] Metabolic pathways essential for survival under antibiotic exposure can be disrupted to impair bacterial viability.[91] Sulphonamides and trimethoprim, which inhibit folate biosynthesis, exemplify the success of this approach by targeting critical steps in nucleotide synthesis, thereby halting bacterial replication.[92-94] Sulphonamides act as competitive inhibitors of dihydropteroate synthase, while trimethoprim targets dihydrofolate reductase, both of which are indispensable for folate production.

More recently, bedaquiline, an anti-tuberculosis drug, has been shown to specifically inhibit ATP synthase, thereby impairing oxidative phosphorylation and depleting cellular energy stores.[95] Bedaquiline is now used for the treatment of multidrug-resistant tuberculosis (MDR-TB), where its ability to disrupt energy metabolism has substantially improved patient outcomes.[96] Currently, its application is limited to tuberculosis treatment, as it targets ATP synthase specifically in *Mycobacterium tuberculosis*. The specificity highlights the opportunity for developing similar drugs to target energy metabolism in other pathogenic bacteria. While bacterial energy metabolism offers an attractive therapeutic target, identifying universal or strain-specific vulnerabilities across diverse pathogens remains a major hurdle.

Elucidating metabolic pathway dependencies in bacterial responses to antibiotic exposure, whether in resistant or susceptible strains, has the potential to uncover vulnerabilities that could be exploited therapeutically.[97] One of the aims of this thesis is to elucidate such vulnerabilities by analysing metabolic adaptations in *E. coli* strains with and without resistance traits and their responses to antibiotic treatment. It is intended that by characterising these

metabolic responses, a deeper understanding of bacterial survival mechanisms could inform the development of novel interventions to combat AMR.

1.2.2.1 Targeting ATP synthesis and isoprenoid biosynthesis

The use of bedaquiline represented a paradigm shift in the treatment of tuberculosis by targeting bacterial energy metabolism instead of the traditional biosynthetic targets such as cell wall synthesis, protein synthesis, or nucleic acid synthesis.[98] By specifically inhibiting ATP synthase, bedaquiline disrupts oxidative phosphorylation, leading to ATP depletion and eventual bacterial cell death.[99] Its selective action against *Mycobacterium tuberculosis* was particularly important for treating MDR-TB, where therapeutic options had become limited.[100,101]

The specificity of bedaquiline lies in its ability to target the F_0F_1-ATP synthase in *M. tuberculosis*, which is structurally distinct from the ATP synthase in eukaryotic cells.[102] Such distinction minimises off-target effects and prevents interference with host ATP production, making bedaquiline highly effective with limited host toxicity. The prokaryotic-specific nature of this target exemplifies a major advantage of drugs designed to inhibit bacterial metabolic pathways, as they exploit fundamental differences between bacterial and host cell physiology.

Bedaquiline therefore illustrates the potential of exploiting bacterial energy metabolism as a therapeutic strategy, especially for pathogens with limited treatment options. The specificity of bedaquiline serves as an important reminder of the advantages of targeting prokaryotic-specific pathways, a theme that will be further explored in Chapter 5, stressing the importance of this specificity.

Another example of metabolic targeting is fosmidomycin, an antibiotic primarily investigated for the treatment of malaria and bacterial infections caused by *E. coli*, *Salmonella*, and *Haemophilus influenzae*.[103,104] Fosmidomycin inhibits the non-mevalonate pathway of isoprenoid biosynthesis, also known as the methylerythritol phosphate (MEP) pathway, which is critical for the production of isoprenoids, essential components of bacterial cell membranes and metabolic functions.[105] MEP pathway is present in many eubacteria, including the major

human pathogen, *M. tuberculosis*, as well as apicomplexan protozoa like *Plasmodium* species that cause malaria, but it is absent in human and livestock.[106] Such unique specificity makes fosmidomycin particularly attractive, as it targets a pathway distinct from host metabolic processes, thereby minimising off-target effects.

Fosmidomycin has demonstrated effectiveness against certain Gram-negative bacteria and *Plasmodium falciparum*, the causative agent of malaria.[107] However, its antibacterial activity is limited, particularly ineffective against most Gram-positive bacteria due to lack of the MEP pathway target and poor uptake mechanisms.[108,109] Despite its specificity, resistance to fosmidomycin can develop through mutations in genes encoding enzymes of the MEP pathway or alterations in transport systems required for its uptake.[110] The absence of the MEP pathway in eukaryotes, including humans and livestock, highlights the potential for fosmidomycin to be used selectively to target bacterial pathogens in agriculture without affecting host cells. These examples emphasise the important potential of targeting metabolic processes that are essential for bacterial survival yet distinct from those in host cells. While application of fosmidomycin in AMR settings has been limited, its specificity demonstrates the broader viability of metabolic targeting as an approach to address antimicrobial resistance.

1.2.2.2 Universal and specific metabolic effects of antibiotics

Antibiotics have been shown to elicit both universal and specific effects on bacterial metabolism.[111-113] Universal effects include disruption of central metabolic pathways, such as glycolysis, the TCA cycle, and oxidative phosphorylation, which are critical for energy production and biosynthesis.[50,114] These pathways are commonly affected regardless of the antibiotic class, as they underpin the core metabolic processes required for growth and adaptation under stress.

In contrast, specific metabolic effects have been associated with the mechanism of action for individual classes of antibiotics. For example, β-lactams primarily target peptidoglycan biosynthesis, a process critical for maintaining bacterial cell wall integrity. Although this is a specific target, the inhibition of cell wall synthesis can indirectly disrupt energy production and

central metabolic pathways due to the energetic demands of cell wall repair and maintenance under antibiotic exposure.[69] Similarly, aminoglycosides, by binding to bacterial ribosomes, impair protein synthesis and disrupt processes reliant on accurate gene translation, such as the synthesis of enzymes involved in central metabolism.[115] The effects on metabolism at multiple levels, from general to specific antibiotic mechanisms, highlight the strong interconnection between bacterial metabolism and antibiotic efficacy and susceptibility.

The work in this thesis explores how antibiotics influence bacterial metabolism by analysing the metabolic responses of different strains of *E. coli* with and without resistance mechanisms. The aim is to delineate both universal metabolic changes, including those specific to resistance phenotypes, providing insights into potential vulnerabilities to inform the development of novel therapeutic strategies.

1.3 *E. coli* as a model in antimicrobial resistance research

E. coli is a Gram-negative bacterium belonging to the *Enterobacteriaceae* family, widely used as a model organism in molecular biology, genetics, and microbiology due to its well-characterized genome, rapid growth rate, and ease of genetic manipulation.[116-119] It has contributed to key discoveries in gene regulation, the development of recombinant deoxyribonucleic acid (DNA), and synthetic biology, making it a fundamental tool in laboratory research.[120-122]

Beyond its role as a research model, *E. coli* is a clinically significant pathogen responsible for a wide range of infections, including urinary tract infections (UTIs), bloodstream infections, and sepsis.[123-125] It is also a major cause of hospital-acquired infections, particularly those associated with catheters and invasive medical procedures.[126-128] The emergence of multidrug-resistant (MDR) *E. coli*, has complicated treatments, leading to higher mortality, prolonged hospital stays, and increased healthcare costs.[129-131]

Due to its genetic plasticity and ability to acquire resistance genes via HGT, *E. coli* is a key system for studying AMR evolution, plasmid-mediated resistance, and antibiotic-induced metabolic changes.[132-134] Investigating metabolic adaptations provides insight into fitness costs,

compensatory mechanisms, and potential metabolic vulnerabilities that could be exploited for novel therapeutic strategies. Given its dual role as both a model organism and a clinically relevant AMR pathogen, *E. coli* is an essential system for studying physiology, antibiotic resistance, and novel antimicrobial interventions.[135,136]

1.3.1 Plasmid-mediated resistance in *E. coli*

Plasmids play a central role in the evolution and dissemination of AMR in *E. coli*.[137] Plasmids are extrachromosomal genetic elements which carry genes that confer resistance to multiple classes of antibiotics, including β-lactams, aminoglycosides, and fluoroquinolones.[138] HGT facilitated by conjugation, allows plasmids to transfer resistance genes within and across bacterial populations, accelerating the spread of resistance.[139]

In laboratory settings, plasmids can be engineered to carry genes encoding resistance enzymes, such as metallo-β-lactamases like NDM-7, which hydrolyse carbapenems and render them ineffective.[140] By introducing such plasmids into *E. coli*, researchers can create resistant strains to study genetic, metabolic, and phenotypic impacts of AMR. Beyond conferring resistance, plasmids impose a metabolic burden on their host bacterium, influencing its fitness, growth rate, and pathogenic potential.[141] Despite these costs, resistant strains frequently thrive due to compensatory mutations and adaptive metabolic changes that mitigate the fitness costs associated with plasmid carriage.[142]

Plasmids have been integral in the emergence of MDR *E. coli* strains, particularly those producing extended spectrum β-lactamases (ESBLs) and carbapenemases. For example, the plasmids carrying $bla_{CTX\text{-}M}$ genes, encoding ESBLs, are widespread in clinical *E. coli* isolates and are associated with resistance to third-generation cephalosporins.[143,144] Similarly, plasmids encoding carbapenemases such as *klebsiella pneumoniae* carbapenemase (KPC) and NDM have been linked to global outbreaks of carbapenem-resistant *E. coli*.[145,146] These plasmids often carry additional resistance determinants, enabling resistance to multiple antibiotic classes and limiting therapeutic options.

The study of plasmid-mediated resistance in *E. coli* has been pivotal for understanding the genetic and metabolic factors that drive the evolution and persistence of multidrug-resistant strains. Researchers use *E. coli* as a model to investigate plasmid dynamics, including the conditions under which plasmid-mediated resistance evolves and persists.[147,148] These insights have informed strategies to combat AMR, such as targeting plasmid transfer mechanisms, disrupting plasmid stability, or identifying metabolic vulnerabilities in plasmid-bearing strains.[149]

By using plasmid-mediated resistance models, this thesis aims to elucidate the metabolic adaptations associated with plasmid carriage in *E. coli* and the interplay between resistance mechanisms and bacterial fitness. Understanding these interactions is essential for identifying novel therapeutic targets to combat the spread of multidrug-resistant *E. coli*.

1.4 Metabolomics

Metabolomics is the comprehensive and systematic study of small-molecule metabolites - the chemical end products of cellular processes - within a biological system, has emerged as a transformative tool for investigating bacterial metabolism and how it responds to genetic and environmental perturbations.[150-153] By analysing the chemical fingerprints left by cellular processes, metabolomics can provide a direct snapshot of the complexities of metabolic activity and reveals changes resulting from environmental changes or stressors such as antibiotic treatments.[154,155] Metabolomics, particularly in AMR studies, has advanced substantially with technical developments in high-throughput technologies, such as mass spectrometry (MS) and nuclear magnetic resonance (NMR) spectroscopy, which enable measurement, identification and quantification of hundreds to thousands of metabolites in a single experiment.[156,157] Ahmed et al. (2024) utilised a metabolomics approach to study the metabolic response of *Klebsiella oxytoca* to ciprofloxacin exposure, demonstrating the power of these technologies in elucidating bacterial adaptation mechanisms.[158]

In the context of bacterial systems, metabolomics has facilitated the exploration of metabolic pathways involved in growth, stress adaptation, and survival.[22,152,159-162] By capturing the

global metabolic state of bacteria, metabolomics can provide insights into how cells reprogram their metabolism in response to antibiotics treatments.[45] For instance, metabolomics has revealed changes in central carbon metabolism, redox metabolism, antioxidant responses, and nucleotide biosynthesis in resistant strains compared to their susceptible counterparts.[163-165] Such studies highlight potential metabolic vulnerabilities that could be exploited by therapeutic interventions, that may offer new avenues for combating AMR.[89,154,155]

Metabolomics has also provided unique insights into resistance mechanisms by linking metabolic alterations to specific genetic and biochemical changes.[22,166] In bacteria expressing resistance genes, such as those encoding β-lactamases or efflux pumps, metabolomic analysis has uncovered the downstream metabolic consequences of these adaptations.[167] For example, the increased energy demands of efflux pump activity or the metabolic cost of resistance plasmid maintenance can be quantified and analysed.[168] Such information not only deepens our understanding of resistance mechanisms but also identifies potential metabolic choke points that could serve as targets for combination therapies.[169]

1.4.1 Strengths and limitations of metabolomics

One of the main strengths of metabolomics lies in its ability to provide a holistic view of the metabolic state of an organism under specific conditions and how this state changes in response to genetic or environmental influences.[170] Unlike transcriptomics or proteomics, which infer cellular activity indirectly, metabolomics measures the end products of biochemical reactions, offering a more direct representation of physiological states.[171] Such capability is particularly valuable for studying bacterial responses to antibiotics, as it captures the metabolic changes that occur at a given moment during exposure, providing insight into how bacterial cells adapt or succumb to stress.

The two primary approaches to metabolomics are targeted and untargeted analyses.[172] Targeted metabolomics focuses on specific pathways or metabolites of interest, allowing for precise investigation of known metabolic processes under experimental conditions. In contrast, untargeted metabolomics explores the broader metabolome, enabling the discovery of novel

biomarkers or pathways that may be implicated in AMR or metabolic response to antibiotics.[151,173] While targeted approaches offer higher sensitivity and accuracy for predefined metabolites, untargeted methods provide a more exploratory view, capturing unexpected metabolic adaptations. The distinction is crucial when selecting an approach, as it determines the depth and scope of the metabolic insights obtained.

Despite its strengths, metabolomics faces several challenges. The complexity of metabolomic data, arising from the sheer diversity and abundance of metabolites, poses significant analytical and interpretative hurdles.[174] Standardization of experimental protocols, from sample preparation to data processing, remains a critical issue, as variations can lead to discrepancies in results.[175] Additionally, the identification of metabolites often requires extensive databases and computational resources, and some metabolites may remain unidentified due to limitations in spectral libraries and annotation workflows.[176]

Quantifying metabolites accurately is another challenge, particularly for compounds present at low abundance or those with similar chemical structures to other metabolites within the sample.[177] Many metabolites share closely related mass-to-charge ratios (*m/z*), retention times, or fragmentation patterns, which can complicate their detection and differentiation during mass spectrometry or chromatography-based analyses. The structural similarity increases the likelihood of interference or misidentification, particularly in untargeted metabolomics, where the broad scope of analysis captures a wide array of compounds simultaneously.

In targeted metabolomics, the use of specific standards and optimized methods for predefined metabolites enhances quantification accuracy and resolution, making it more reliable for analysing compounds with overlapping chemical profiles. In contrast, untargeted metabolomics, while offering a comprehensive exploration of the metabolome, often sacrifices precision in quantification due to the challenges of resolving closely related metabolites. Addressing these limitations through advancements in database completeness, analytical technologies, and standardized workflows is essential for improving the reproducibility and reliability of metabolomic studies.

Despite these challenges, metabolomics remains a powerful tool for AMR research, providing unique insights into bacterial metabolism that are not accessible through other omics approaches. By capturing metabolic changes, metabolomics facilitates a deeper understanding of bacterial responses to antibiotics, potentially identifying novel therapeutic targets to combat resistance.

1.4.2 Applications of metabolomics in antimicrobial resistance research

Metabolomics has emerged as a transformative tool in AMR research, offering unique insights into bacterial metabolism and its role in resistance.[22] By capturing the entire complement of metabolites within a system, metabolomics provides a holistic perspective on how bacteria respond to antibiotics and adapt to resistance. Both targeted and untargeted metabolomics approaches have been applied to address key challenges in AMR, including biomarker discovery, therapeutic target identification, and functional analysis of resistance mechanisms.[155]

The targeted metabolomics approach has been used to explore known metabolic changes associated with resistance, providing precise and reproducible data.[178] In contrast, untargeted metabolomics examines the broader metabolome to identify novel biomarkers and pathways implicated in resistance, often leading to the discovery of unexpected metabolic adaptations.[155] For example, a study by Zampieri et al. (2017) demonstrated that exposure to β-lactam antibiotics caused alterations in *E. coli* central carbon metabolism, including pathways involved in purine biosynthesis, and these metabolic adjustments were linked to the adaptive responses of bacteria, contributing to the development of antibiotic resistance.[73] Such findings show the potential of untargeted metabolomics to uncover new dimensions of bacterial adaptation.[111]

An important application of metabolomics in AMR research is biomarker discovery.[170] Unique metabolic signatures associated with resistant and susceptible strains have been identified, offering diagnostic potential for distinguishing resistance phenotypes.[179] For instance, specific metabolites, such as amino acids or nucleotide precursors, have been linked to

carbapenem-resistant strains of *Klebsiella pneumoniae*, facilitating the development of rapid diagnostic assays to detect resistance.[180] These biomarkers provide a critical resource for monitoring resistance in clinical settings and could enhance early detection of resistant infections.

Another important contribution of metabolomics is its ability to study the metabolic effects of antibiotic treatment. Comparative analyses of susceptible and resistant bacterial strains have revealed differential metabolic responses, highlighting the metabolic costs of resistance.[181] These studies suggest that targeting the metabolic burden associated with resistance could improve antibiotic efficacy. For instance, recent work has demonstrated that resistant bacteria often rely on compensatory metabolic pathways to mitigate the fitness costs of resistance, which could be exploited therapeutically.[182,183]

The integration of metabolomics with other omics approaches, such as transcriptomics and proteomics, has further enriched our understanding of AMR. Multi-omics studies provide a comprehensive view of how bacteria adapt to antibiotics at multiple levels by linking metabolic changes to gene expression and protein activity.[184] For example, a multi-omics study on the Costa Rican *Pseudomonas aeruginosa* AG1 strain combined genomics, transcriptomics, and proteomics to investigate its resistance mechanisms to multiple antibiotics, including carbapenems.[185] The analysis revealed the presence of metallo-β-lactamase genes (VIM-2 and IMP-18), overexpression of efflux pump systems such as MexAB-OprM, and mutations in regulatory genes like AmpR, which are critical for β-lactam resistance. Proteomic profiling showed further upregulation of proteins involved in oxidative stress responses and central metabolic pathways, including amino acid and energy metabolism, enabling the bacteria to thrive under antibiotic pressure.[185] Such integrative studies provide a systems-level view of bacterial adaptation, facilitating the identification of novel therapeutic targets and informing combination therapies that exploit metabolic vulnerabilities.

Overall, metabolomics has become a powerful tool for advancing AMR research.[58,154] Its ability to identify metabolic vulnerabilities, uncover biomarkers, and integrate insights with other

omics disciplines, offers substantial potential for developing new diagnostics and treatments to address the growing challenge of antibiotic resistance.[113,166]

1.5 Metabolomics methods and emerging technologies

Over the past two decades, advancements in analytical technologies have revolutionized the field of metabolomics, enabling researchers to unravel intricate metabolic networks underlying bacterial physiology.[170,186] These advancements have positioned metabolomic profiling and pathway analysis as a powerful tool in bacterial research, offering insights into metabolic differences among strains and revealing how these differences contribute to AMR.[152,187]

Metabolomic profiling provides a detailed overview of metabolites across a biological sample, offering a comprehensive snapshot of the metabolome under specific experimental conditions.[188] Pathway analysis complements profiling by integrating metabolic data with known biochemical pathways, identifying metabolic processes that are perturbed under specific conditions, such as antibiotic stress or genetic mutations.[189] **Figure 1.3** (reproduced from Xavier et al. 2021) illustrates how metabolomics data has been used to reconstruct complex metabolic networks, categorising metabolic nodes into functional groups such as energy metabolism, hydride transfer, and carbon metabolism. Such data underscore the power of metabolomics to integrate the complexity of metabolic networks and the interrelationship between pathway in bacterial metabolism.[190] Although conventional metabolomics excels at highlighting altered pathways, it does not measure reaction rates or metabolic flux directly. Flux analysis requires isotope tracers, to track the movement of metabolites through pathways and quantify the rates of biochemical reactions.[191]

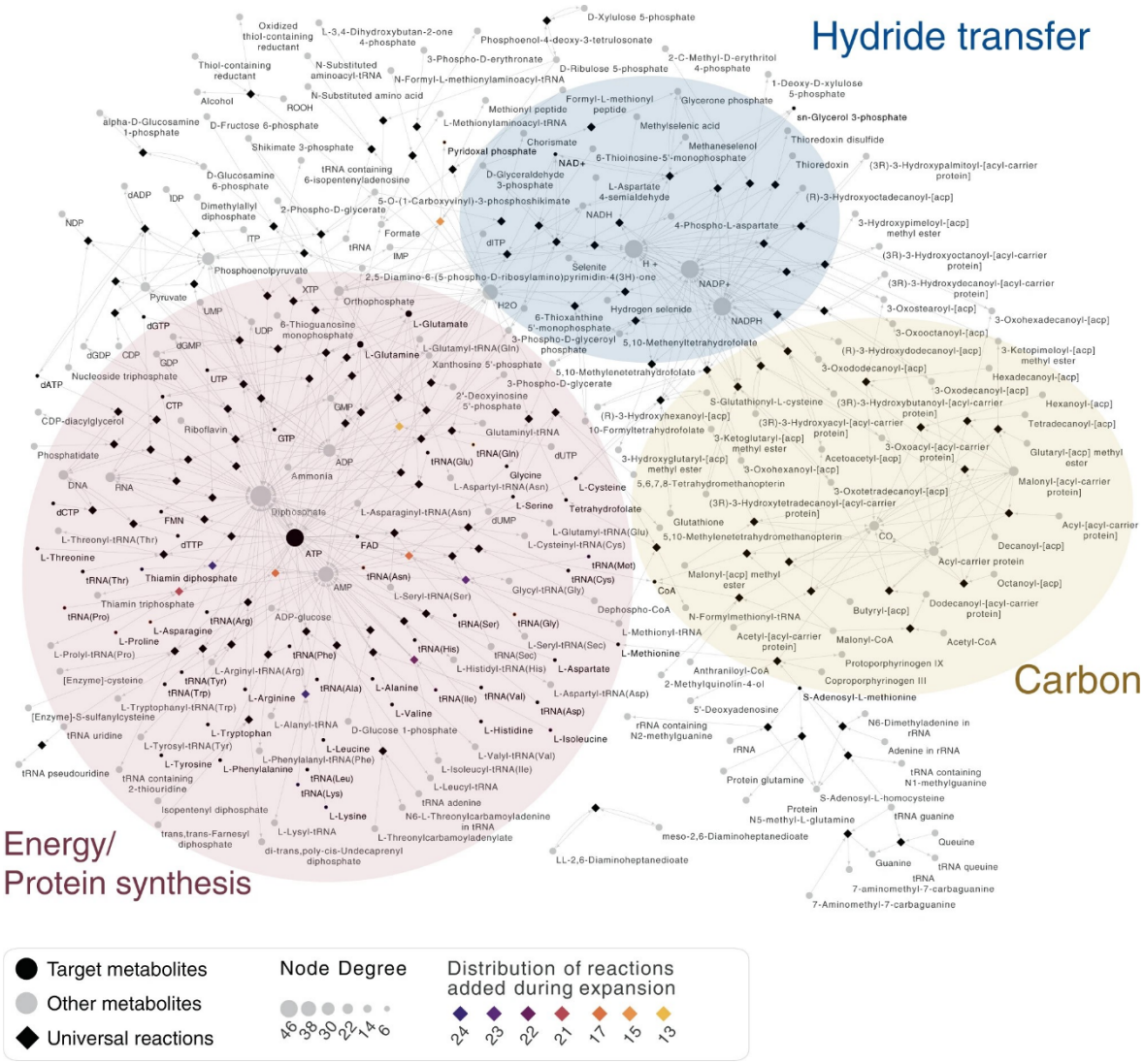

Figure 1.3 A comprehensive network representation of bacterial metabolism, illustrating key processes such as hydride transfer, carbon metabolism, and energy/protein synthesis*. Metabolites (nodes) are categorised into target metabolites, other metabolites, and universal reactions, while node degree indicates the importance of metabolites within the network. This figure highlights how advanced metabolomic profiling enables the elucidation of intricate metabolic networks underlying bacterial physiology. Reproduced from Xavier, J.C., et al., Communications Biology (2021)4:413, Doi: https://doi.org/10.1038/s42003-021-01918-4.*

Analytical techniques such as NMR spectroscopy and MS have been pivotal in metabolomics, providing detailed insights into bacterial metabolism and AMR.[58] NMR offers high reproducibility and requires minimal sample preparation, making it ideal for untargeted studies and structural elucidation of metabolites, though its sensitivity is generally lower compared to MS.[192] MS, on the other hand, provides exceptional sensitivity and a broad dynamic range, enabling the detection and quantification of low-abundance metabolites.[193] Techniques such as gas chromatography-MS (GC-MS) and liquid chromatography-MS (LC-MS)

further enhance metabolomic profiling by separating complex mixtures before analysis, though they require extensive sample preparation and method optimization.[194-196]

Emerging technologies have expanded the scope of metabolomics, offering new avenues for exploring bacterial metabolism with unprecedented detail.[197] Imaging mass spectrometry (IMS) has enabled the spatial mapping of metabolites directly within bacterial colonies or tissues.[198] The technique combines high-resolution mass spectrometry with imaging capabilities, providing localized metabolic information that complements traditional bulk analysis. IMS has been particularly useful for studying biofilm formation and the metabolic interactions within microbial communities, revealing spatially distinct metabolic zones that contribute to bacterial survival and virulence.[199,200]

Despite these advancements, metabolomics still faces challenges in characterising certain classes of metabolites central to primary metabolism. Highly polar and ionic metabolites, including nucleic acids, phosphorylated sugars, and their structural isomers, often elude sensitive and reproducible detection and quantification using conventional LC-MS methods. These metabolites are critical intermediates in pathways such as glycolysis, the pentose phosphate pathway, and nucleotide biosynthesis, yet their acidic and negatively charged nature makes them difficult to analyse with traditional approaches. Hydrophilic interaction liquid chromatography (HILIC)-MS, ion-pairing chromatography-MS and GC-MS using derivatisation are often employed to address these challenges, but each has limitations. HILIC-MS is commonly used for such metabolites due to its ability to retain polar compounds, but reproducibility issues and variable retention times limit its effectiveness. Ion-pairing chromatography-MS improves the retention of anionic metabolites by incorporating ion-pairing reagents, though non-volatile reagents can cause contamination of the MS system, requiring extensive cleaning and re-optimization of methods. GC-MS with derivatization enhances the volatility and detectability of polar metabolites, but derivatization steps can be time-consuming and introduce variability in metabolite stability.[201]

A notable advancement in analysing highly polar and ionic metabolites is the integration of ion chromatography coupled with mass spectrometry (IC-MS). IC-MS offers improved separation efficiency and sensitivity for charged and polar compounds.[202] The technique has been particularly effective in analysing small polar compounds such as organic acids and amines, which are challenging to detect with traditional LC-MS methods.[201] By incorporating IC-MS into metabolomic workflows, researchers can achieve more comprehensive coverage of the metabolome, particularly for metabolites that are difficult to analyse using conventional techniques. These approaches are not only relevant for basic research but also have critical applications in diagnostics and drug development, offering opportunities to identify metabolic vulnerabilities that could be exploited therapeutically.[203]

1.5.1 Anion exchange chromatography-mass spectrometry

Anion exchange chromatography coupled with mass spectrometry (AEC-MS) has emerged as a valuable technology for metabolomics applications focussing on the analysis of ionic and highly-polar metabolites.[204] The technique employs anion exchange chromatography to separate metabolites based on their charge, followed by high-resolution mass spectrometry for identification with high sensitivity and specificity.[205] These capabilities make AEC-MS uniquely suited for resolving complex metabolic profiles, including metabolites such as sugar phosphates, organic acids, and nucleotides, key molecules in primary metabolism and energy transduction.[206,207]

AEC-MS addresses an important need in metabolomics by providing characterisation of structural isomers, such as sugar phosphates and phosphorylated intermediates, which are often difficult to resolve using other LC-MS methods.[205] The ability to resolve these compounds enables a more comprehensive coverage of primary metabolites, with the potential to reveal (or not miss) metabolic changes in associated with cellular function under varied conditions.[208] The reproducibility, robustness, and sensitivity of AEC-MS further enhances its utility.

In contrast to conventional methods such as HILIC-MS or ion-pairing-MS, AEC-MS offers superior reproducibility, metabolic coverage, and scalability.[209] These advantages are critical

for high-throughput studies, especially when working with complex biological matrices such as bacterial extracts, tissues, or biofluids.[210,211] Advancements in automation and data analysis software have streamlined AEC-MS workflow, minimising variability and enhancing the reliability of results.[212]

Through its detailed coverage of metabolites found in primary metabolism, including central carbon pathways and energy transduction, AEC-MS provides an attractive tool for mapping the metabolic landscape in bacterial systems and addressing challenges in antimicrobial resistance research.[206,213]

1.6 Research gaps and limitations in metabolic profiling of resistant strains

Despite important advances in AMR research, critical gaps remain in our understanding of the metabolic adaptations that underpin resistance.[58,154] While considerable attention has been devoted to using genomic, transcriptomic, and proteomic approaches to elucidate potential mechanisms that underly resistance, the metabolic landscape of resistance has been comparatively underexplored.[169,214] However, it is clear that metabolism plays an important role in the responses to, and effectiveness of, antibiotics and in resistance mechanisms, yet metabolomics, uniquely capable of uncovering functional outcomes of genetic and proteomic changes, remains underutilized in studies to understand resistant strains, particularly in the context of antibiotic-induced stress. As a result, key questions remain about how resistant strains reconfigure their metabolism to survive and thrive under therapeutic pressure.

Most investigations have focused on isolated resistant strains, often neglecting to contextualize their findings against susceptible counterparts and there is a general lack of comprehensive and comparative studies between susceptible and resistant strains under identical antibiotic exposure conditions. The gap limits the ability to discern whether observed metabolic alterations are unique to resistance or represent general bacterial stress responses. Furthermore, existing studies often rely on endpoint data, which fail to capture the dynamic metabolic changes occurring during antibiotic exposure. Temporal studies, which have the potential to reveal the evolution of metabolic adaptations in response to antibiotics, are

notably scarce. Such fragmented understanding of metabolic reprogramming has hindered efforts to fully elucidate the sequence of events leading to resistance.

Another underexplored area is the metabolic cost of resistance mechanisms, such as plasmid carriage or the overexpression of efflux pumps. Resistance is often associated with a fitness cost in bacteria, yet the metabolic pathways compensating for this burden remain poorly understood.[215] Investigating these compensatory mechanisms could reveal vulnerabilities unique to resistant strains, providing novel targets for therapeutic intervention.

Finally, the absence of standardized methodologies in bacterial metabolomics research contributes to variability and inconsistency across studies.[216] Differences in sample preparation, extraction protocols, and data analysis approaches make it challenging to compare results or draw definitive conclusions. Addressing these methodological challenges is critical for advancing the field and enabling reproducible, high-quality research.

1.6.1 Opportunities for future investigations

Critical gaps remain in understanding the metabolic adaptations that underpin antibiotic resistance, presenting important opportunities for future research. One key area of investigation involves the metabolic differences between resistant and non-resistant strains, particularly in relation to plasmid carriage and resistance gene expression. Resistance often imposes a fitness cost, yet the compensatory pathways that mitigate this burden remain poorly understood. Exploring these metabolic adaptations may reveal vulnerabilities unique to resistant strains, offering insights into potential therapeutic targets.

Another opportunity lies in understanding how antibiotics influence bacterial metabolism and induce stress responses. Antibiotic exposure disrupts metabolic pathways, including energy metabolism and biosynthesis, yet the dynamic nature of these responses is underexplored. Temporal studies that capture the progression of metabolic changes under antibiotic pressure can provide valuable insights into the sequence of events that lead to survival or cell death. These findings could help identify critical intervention points to enhance antibiotic efficacy.

Advances in live-cell metabolic analysis present additional opportunities to investigate bioenergetic adaptations in bacterial strains. Energy metabolism, particularly in central carbon pathways, plays a pivotal role in bacterial survival under stress and by employing real-time analytical techniques, deeper insights can be gained into the bioenergetic demands of resistant strains and how these pathways contribute to their persistence.

Finally, targeting bacterial metabolism as part of combination therapies holds great promise for overcoming resistance.[217,218] Metabolic modulators that disrupt energy production or biosynthesis can potentiate the effects of existing antibiotics, offering an innovative strategy to combat resistant pathogens. By integrating metabolomics with functional assays, future studies can evaluate the feasibility and efficacy of such combination therapies, paving the way for novel approaches to address antimicrobial resistance.

By addressing the research opportunities outlined above, this thesis seeks to advance our understanding of bacterial metabolism and its role in resistance by uncovering pathways and metabolic vulnerabilities that can inform therapeutic developments in the future.

1.7 Aims of this study

Antibiotic resistance represents a complex and multifaceted therapeutic challenge, influenced by genetic, biochemical, and environmental factors.[219] While considerable progress has been made in understanding the genetic and proteomic basis of resistance, the metabolic dimension in AMR remains underexplored.[220] The underlying concept of the thesis is that metabolic processes may differ between wild-type, susceptible, and resistant *E. coli* strains, both in the presence and absence of antibiotic treatment, and that these differences could reveal metabolic vulnerabilities associated with resistance. It aims to investigate what metabolites and functional pathways are altered. In order to test the potential of altered pathways for therapeutic potential, it will also explore pharmacological treatment of bacterial strains targeting metabolism specifically. A comparative metabolomics approach will be used to analyse metabolic changes across genetically engineered bacterial strains, both with and

without antibiotic exposure, to determine how these responses differ and whether they are linked to resistance mechanisms.

Comparative analyses under standardized experimental conditions will investigate differences between resistant and non-resistant strains, with the goal of providing a detailed understanding of how metabolic adaptations contribute to resistance.[221] AEC-MS will be used to analyse highly polar metabolites, particularly those involved in nucleotide metabolism, glycolysis, and the pentose phosphate pathway, which are critical for bacterial adaptation to antibiotic pressure. Additionally, Seahorse extracellular flux analysis will provide unique insights into live-cell metabolism by measuring real-time oxygen consumption and extracellular acidification rates, complementing microbiology assays that assess bacterial viability, growth dynamics and stress responses.

The research will further examine whether metabolic adaptations associated with resistance impose fitness costs, such as those linked to plasmid carriage or resistance gene expression. Pharmacological treatments targeting key metabolic pathways will be applied to determine whether specific metabolic adaptations are essential for maintaining resistance. By selectively inhibiting or modulating metabolic processes, this approach will identify potential metabolic vulnerabilities that could be exploited therapeutically to weaken resistant strains. Understanding how bacteria compensate for these costs could provide further insights into their survival strategies.

1.7.1 Hypothesis and specific objectives

The central hypothesis of this study is that antibiotic resistance in *E. coli* is accompanied by distinct metabolic adaptations that can be characterized and potentially exploited by targeted therapeutic interventions. The hypothesis serves as a guiding framework for the research, shaping the objectives and experiments.

The specific research objectives of this study are:

1. Develop genetically modified *E. coli* strains carrying specific resistance mechanisms, including plasmid-encoded carbapenem resistance (NDM-7) for direct comparison with isogenic control strains.
2. Develop and validate a workflow for bacterial metabolomics using AEC-MS and use it to identify the metabolic differences between wild-type, susceptible, and resistant *E. coli* strains.
3. Investigate the metabolic impact of antibiotic treatments across the different strains and impact on cell proliferation, highlighting universal and resistance-specific responses.
4. Investigate metabolic vulnerabilities associated with resistance, identifying pathways that could serve as therapeutic targets.
5. Explore the potential of bacterial live cell analysis to explore changes in energy metabolism using a Seahorse analyser.
6. Test drug and metabolic potentiators and their effects on metabolism (including energy metabolism) across bacterial strains.

Chapter 2 Materials and methods

2.1 Materials and reagents

2.1.1 Chemicals

2.1.1.1 General use chemicals

All methanol (MeOH), acetonitrile (MeCN), and formic acid used throughout this study were High-performance liquid chromatography (HPLC)-grade solvents purchased from Sigma-Aldrich (Gillingham, Dorset, UK). Hydrochloric acid (HCl) was obtained from Merck (Gillingham, Dorset, UK), and sodium chloride (NaCl) was sourced from Sigma Aldrich (Saint Louis, MO, USA).

Water used in all experiments was purified either using a Milli-Q® (MQ) Direct 8 system equipped with a Millipak® Express 40 filter (0.22 µm pore size) from Merck Millipore (Burlington, MA, USA) or a Purelab® Chorus system from Elga Veolia (Veolia Water Technologies, Windsor Court, UK). Both systems are designed to produce Type 1 ultrapure water, characterised by a resistivity of 18.2 MΩ·cm and a total organic carbon (TOC) content of less than 2 parts per billion (ppb). Unless otherwise specified, Type 1 water was used throughout all experiments.

Additionally, any chemicals added to media, buffer, or cells were sterile filtered in-house using Sartorius Minisart™ regenerated cellulose (RC) syringe filters.

2.1.1.2 Cell culture chemicals

2.1.1.2.1 Culture media and reagents

2 × Yeast Extract Tryptone medium (2TY broth) granules were purchased from MELFORD (Ipswich, Suffolk, UK) and were used to grow bacterial cells in liquid media. For the preparation of solid media to form bacterial colonies, the following components were used: agar bacteriological obtained from OXOID LTD (Hampshire, UK), yeast extract granulated, and molecular biology grade Tryptone, both obtained from MELFORD (Ipswich, Suffolk, UK). Super Optimal broth with Catabolite repression (SOC) Outgrowth medium was obtained from New England BioLabs®$_{Inc}$ (Ipswich, MA, USA).

Monosodium phosphate, potassium dihydrogen phosphate, ammonium chloride, magnesium sulphate, calcium chloride dihydrate, vitamin B1, potassium nitrate, and dipotassium hydrogen phosphate, glucose, Trizma® base, all from Sigma Aldrich (Saint Louis, MO, USA), were used to prepare either M9 minimal media, phosphate-buffered saline (PBS), or 30 mM tris buffer.

2.1.1.2.2 Other chemicals and reagents

Rely+On™ Virkon® high level surface disinfectant from DuPont™ (Suffolk, UK) was used to disinfect and eliminate any trace of cells. Molecular grade agarose from bioline (London,UK), SYBR® Safe DNA gel stain from Invitrogen (Carlsbad, CA, USA), GeneRuler 1 kb DNA Ladder from Thermo Scientific (Vilnius, Lithuania), and Bradford reagent from Sigma Aldrich (Saint Louis, MO, USA) were used for various experimental needs.

2.1.1.3 Antibiotics and solvents

Based on their solubility, meropenem trihydrate from Glentham life sciences Ltd (Corsham, UK) was prepared using dimethyl sulphoxide (DMSO) from Sigma-Aldrich (Saint Louis, MO, USA) to various concentrations. Kanamycin sulphate and ampicillin sodium, both from Apollo Scientific Ltd (Bredbury, Stockport, UK), were prepared in autoclaved Type 1 water to the desired concentrations. DMSO (molecular biology grade, 99.9% unless stated otherwise) was used as a vehicle control against meropenem.

2.1.1.4 Metabolite extraction chemicals

For metabolic extraction, chloroform ($CHCl_3$) from Fisher Scientific (Loughborough, Leicestershire, UK), methanol, acetonitrile, and Type 1 water was used.

2.1.1.5 Seahorse real time metabolic analysis chemicals

A 0.01% Poly-L-Lysine solution (PLL) from Merck Life Science UK Limited (Gillingham, Dorset, UK) was used to coat the wells of cell culture microplates for cell adhesion before the measurements. XF Seahorse materials and consumables were supplied by Agilent Technologies LDA UK Limited (Cheadle, UK) unless stated otherwise. These include XF Dulbecco's Modified Eagle Medium (DMEM) medium pH 7.4, XF 1.0 M Glucose Solution XF 100 mM pyruvate solution XF 200 mM glutamine solution, and Seahorse XF Calibrant Solution.

Chemicals such as glucose, 2-deoxy-D-glucose (2-DG), oligomycin and rotenone/antimycin A (Rot/AA), carbonyl cyanide 4-(trifluoromethoxy) phenylhydrazone (FCCP) for assay experiments were also purchased from Agilent Technologies LDA UK Limited (Cheadle, UK). Hoechst 33342 solution for normalisation was obtained from Life Technologies Ltd (Paisley, UK).

2.1.1.6 Co-therapeutic agents

To explore the effect of β-lactamase inhibitor, taniborbactam hydrochloride was purchased from Cambridge Bioscience Ltd (Cambridge, UK). Adenosine 5'-triphosphate (ATP) disodium salt hydrate, used to obtain standard curves, was purchased from Sigma Aldrich (Saint Louis, MO, USA). The ATP synthase inhibitor bedaquiline (BDQ) was purchased from Stratech Scientific Ltd (Cambridgeshire, UK).

Additional drugs aimed to interfere with bacterial energy metabolism included 2-DG purchased from Sigma Aldrich (Gillingham, Dorset, UK), heptelidic acid (koning acid) inhibitor from abcam (Cambridge, UK), 2-ketobutyric acid from Santa Cruz Biotechnology (Dallas, TX, USA), dehydroepiandrosterone (DHEA) from APE BIO (Houston, TX, USA), resveratrol and piceatannol from Fluorochem (Hadfield, UK). These compounds were obtained for combination therapy screening.

2.1.2 Consumables

2.1.2.1 Laboratory tools and consumables

Sterile 10 µL inoculating loops were obtained from Scientific Laboratory Supplies Limited (Nottingham, UK), and sterile Fisherbrand™ L-shaped cell spreaders from Fisher Scientific (Loughborough, Leicestershire, UK) were used to handle bacterial cells on agar plates. Gas Permeable Adhesive Seals from Fisher Scientific UK Ltd (Loughborough, Leicestershire, UK) and Advanced Polyolefin Self-Adhesive StarSeal from STARLAB UK Ltd (Milton Keynes, UK) were used to cover 96-well plates during incubation, drug treatment, or growth curve measurement. Sartorius Minisart™ RC syringe filters with 0.2 µm pore size and 15 mm filter diameter were purchased from Fisher Scientific (Loughborough, Leicestershire, UK) for

in-house filtration of chemicals and drugs for cells. Amicon® Ultra 0.5 mL RC filters with 10 kDa molecular weight cut-off (MWCO) were purchased from Merck (Darmstadt, Germany) for sample preparation for anion exchange chromatography-mass spectrometry (AEC-MS). Liquid chromatography and gas chromatography (LCGC) certified clear glass screw neck total recovery vials (1 mL) with caps with pre-slit polytetrafluoroethylene (PTFE)/silicone septa were acquired from Waters (Milford, MA, USA) for AEC-MS analysis. 2 mL VK05 Glass beads micro-organism tubes for bead beating cells were acquired from Stretton Scientific (Alfreton, UK). Sterile pipette tips (20 µL, 200 µL, 1000 µL) were purchased from SARSTEDT (Numbrecht, Germany), and 1250 µL tips were purchased from INTEGRA (Thatcham, Berkshire, UK). Sterile Costar® Stripette® 10 mL pipettes were sourced from Scientific Laboratory Supplies Limited (Nottingham, UK) and sterile 25 mL StarTub polystyrene (PS) Reagent Reservoirs from STARLAB UK Ltd (Milton Keynes, UK). Falcon® tubes (50 mL and 15 mL) were purchased from SARSTEDT AG & Co (Numbrecht, Germany), certified DNA, DNase, and RNase-free. Pipettes (1000 µL, 200 µL, 20 µL, and 10 µL) were Gilson® brand, made in France. Microcentrifuge tubes (0.5 mL and 1.5 mL) were sourced from Eppendorf®, and from SARSTEDT AG & Co (Numbrecht, Germany). A multichannel pipette (1250 µL) was sourced from INTEGRA.

2.1.2.2 Petri dishes and multi-well plates

60 mm and 100 mm sterile PS petri dishes with lids were purchased from Greiner Bio-One Ltd (Stonehouse, UK). Sterile Corning® 96-well clear flat-bottom microplates with low evaporation lids were purchased from Corning Inc (Corning, NY, USA). Sterile V-bottom 96-well MASTERBLOCK® (2 mL) plates for drug treatment were sourced from Greiner bio-one Ltd (Stonehouse, UK). Sterile Corning 384-Well Low Flange White Flat Bottom Microplates with Lids for luminescent assay (BacTiter-Glo™) were purchased from Scientific Laboratory Supplies Limited (Nottingham, UK). XFe24 sensor cartridges and XF24 cell culture microplates for use with a Seahorse XFe24 Analyzer were purchased from Agilent Technologies LDA UK Limited (Cheadle, UK).

2.1.3 Biological models

For the biological model used throughout this study, Library Efficiency® DH5α™ Chemically Competent Cells and The Original TA Cloning® Kit pCR®2.1 vector was purchased from Invitrogen (Carlsbad, CA, USA). The DH5α cell line were employed for the transformation and propagation of plasmids, while the pCR®2.1 vector served as the carrier plasmid for resistant gene NDM-7. Hence, empty pCR®2.1 vector was used to produce the susceptible strain for subsequent analysis. The GeneJET plasmid Miniprep Kit from Thermo Scientific (Vilnius, Lithuania), was used for plasmid isolation when needed. The resistant plasmid (pCR2.1 containing NDM-7) was gifted by Dr. David Wareham.[222]

Additionally, for various assays, LigaFast™ Rapid DNA Ligation System and BacTiter-Glo™ Microbial Cell Viability Assay were procured from Promega UK Ltd (Chilworth, Southampton, UK).

2.1.4 Laboratory equipment and techniques

2.1.4.1 Sterilisation

Sterilisation of media, consumables, and specific water preparations was with high-pressure saturated stem at high temperature was performed using an autoclave machine from LTE Scientific LTD (Greenfield, Oldham, UK). Water intended for use in the preparation of drugs, media, or buffers for cellular application was sterilised by autoclaving prior to use to ensure the elimination of any potential biological contaminants.

2.1.4.2 Water bath

A Fisherbrand® water bath from Fisher Scientific (Loughborough, Leicestershire, UK) was used for precise temperature regulation required for various biological and chemical reactions.

2.1.4.3 PCR thermal cycler

Polymer chain reaction (PCR) amplification was performed using a Thermal cycler from Bio-Rad Laboratories Ltd (Watford, UK). The thermal cycler provided accurate temperature cycling essential for the successful amplification of DNA samples.

2.1.4.4 Electroporation of plasmid DNA

Electroporation of plasmid DNA into electrocompetent bacterial strains was performed using the Eppendorf Eporator® purchased from Eppendorf SE (Hamburg, Germany). The device is specifically designed for efficient and reproducible transformation of plasmid DNA into bacterial cells through an electrical pulse that temporarily permeabilises the cell membrane, allowing the plasmid DNA to enter the cells.

2.1.4.5 Gel imaging and documentation

DNA bands were visualised using the Molecular Imager® Gel Doc™ XR System from Bio-Rad Laboratories (Hercules, CA, USA). The system is designed for imaging and documenting agarose gels stained with fluorescent dye such as SYBR® safe. The Gel Doc™ XR system features a 16-bit CCD camera for high-resolution imaging, coupled with a blue light transilluminator to safely excite SYBR® Safe-stained DNA, minimising UV-induced DNA damage. Images were captured using the Image Lab™ software (version 5.2.1), with the appropriate settings for SYBR® Safe selected to ensure optimal visualisation and analysis.

2.1.4.6 Cell incubation

Cell incubation on agar plates was conducted using a Heraeus B6030 incubator from Thermo Scientific (Hanau, Germany). For overnight culture and drug treatments done in liquid media, an Excella® E25 incubator shaker was used for smaller volumes (10-30 mL), while innova®44 incubator shaker was used for larger volumes (above 100 mL), both from New Brunswick™ Eppendorf AG (Hamburg, Germany).

2.1.4.7 Spectroscopic measurements

Spectroscopic measurements, including optical density at 600 nm (OD_{600}), were taken with either a WPA biowave CO8000 Cell density meter from Biochrom Ltd (Cambridge, UK) or a CLARIOStar® Plus Multi-Mode Plate Reader from BMG Labtech (Ortenburg, Germany). DNA concentrations were measured using a NanoDrop One microvolume UV-VIS spectrophotometer from Thermo Fisher Scientific (Waltham, MA, USA). For double-stranded (ds) DNA quantification, 2 µL sample volumes were used, and absorbance was measured at

260 nm to determine nucleic acid concentration.

2.1.4.8 Centrifugation

Sample centrifugation was performed using a Megafuge 8R Small Benchtop Centrifuge from Thermo Fisher Scientific (Waltham, MA, USA), equipped with 30-sample or 48-sample insert. For processing larger sample volumes or 96-well MASTERBLOCK®, Allegra® X-12R Centrifuge from Beckman Coulter (High Wycombe, UK) was used.

2.1.4.9 Sonication

Sonication for cell disruption and sample homogenisation was carried out using a micro-tipped SONICS® Vibra Cell™ Ultrasonic Homogenizer from Sonics & Materials, INC. (Newtown, CT, USA).

2.1.4.10 Real-time metabolic analysis

Real time metabolic changes, such as oxygen consumption rate (OCR) and extracellular acidification rate (ECAR), were measured using a Seahorse XFe24 Analyzer from Agilent (Santa Clara, CA, USA). The analyser provided crucial insights into the metabolic activities of cells under various experimental conditions.

2.2 Bacterial culturing

2.2.1 Media preparation

2.2.1.1 Agar gel preparation

Agar gel was prepared with the following composition: 1.5% agar, 1% bactotryptone, 0.5% yeast extract, and 1% NaCl. Specifically, 3 g agar, 2 g bactotryptone, 1 g yeast extract, and 2 g NaCl were dissolved in 200 mL of Type 1 water. The prepared media were dispensed into glass bottles, filled to no more than two-thirds of their volume, and capped loosely to allow pressure equilibration. Sterilisation was performed using a full autoclave cycle following the conditions: 121-125 ℃ for at least 15 minutes, 126-130 ℃ for at least 10 minutes, or 134-138 ℃ for at least 3 minutes.

2.2.1.2 2TY liquid medium (broth) preparation

The liquid 2TY medium, often referred as broth, consists of 1.6% tryptone, 0.5% NaCl, and 1%

yeast extract. Specifically, 16 g tryptone, 10 g yeast, and 5 g NaCl were dissolved in 1 litre of Milli-Q water. The pH was adjusted to 7.0 using NaOH if necessary, and the solution was then autoclaved.

2.2.1.3 M9 medium preparation

The preparation of M9 medium involved first creating a concentrated M9 salt solution. To prepare 500 mL of this solution, 17 g of NaH_2PO_4, 7.5 g of KH_2PO_4, 5 g of NH_4Cl, and 2.5 g of NaCl were dissolved in water and autoclaved to ensure sterility.

To prepare 1 litre of M9 medium, 200 mL of the autoclaved concentrated M9 salt solution was combined with 10 mL of 20% (w/v) glucose, 100 µL of 1M Mg SO_4, 100 µL of 1 M $CaCl_2$, and 10 µL of 0.5% w/v vitamin B1. The mixture was then brought up to a final volume of 1 litre with autoclaved Type 1 water.[223]

2.2.2 Plasmid ligation

To circularise the linear pCR2.1 plasmid, a ligation reaction was performed using the LigaFast™ Rapid DNA Ligation System. The reaction was prepared in a total volume of 10 µL, containing 2 µL of linear pCR2.1 plasmid DNA, 2 µL of 2X LigaFast™ ligation buffer, 1 µL of T4 DNA ligase, and 5 µL of sterile water. The reaction was incubated at room temperature for 5 minutes to facilitate ligation, followed by incubation on ice. The ligation mixture was then used for transformation into competent *E. coli* cells.

2.2.3 Plasmid isolation

Plasmid DNA was isolated using the GeneJET Plasmid Miniprep Kit from Thermo Scientific (Waltham, MA, USA). Bacterial cells were harvested from an overnight culture by centrifugation at 12,000 × *g* (force of gravity) for 1 minute to obtain a pellet. The bacterial pellet was resuspended in 250 µL of the resuspension solution, followed by the addition of 250 µL of the lysis solution. The mixture was gently inverted several times and incubated for 2 minutes to ensure complete lysis of the cells. Subsequently, 350 µL of the neutralisation solution was added, and the solution was mixed thoroughly.

Following centrifugation at 12,000 × *g* for 10 minutes, the supernatant containing the plasmid

DNA was transferred to a GeneJET spin column. The column was centrifuged for 1 minute at 12,000 × *g* to bind the plasmid DNA to the silica membrane. The column was then washed twice with 500 µL of wash solution (diluted with ethanol), with centrifugation at 12,000 × *g* for 1 minute and then for 2 minutes to remove contaminants and residual ethanol.

Finally, the plasmid DNA was eluted by adding 50 µL of autoclaved Mili-Q water directly to the centre of the column membrane, incubating for 2 minutes, and centrifuging at 12,000 × *g* for 1 minute. The purified plasmid DNA was then quantified by measuring its concentration using a NanoDrop One spectrophotometer, and was subsequently used for downstream applications.

2.2.4 Plasmid transformation

2.2.4.1 Chemical transformation

Chemically competent *E. coli* DH5α cells were transformed using the heat shock method.[224,225] For plasmid preparation, 3 µL of each plasmid (pCR2.1 with NDM-7 or pCR2.1) was mixed with 3 µL of water and heated at 85 °C for 7 minutes to removed potential contaminants such as viruses, followed by cooling on ice.

For transformation, 1 µL of plasmid was added to 30 µL of DH5α cells and incubated on ice for 30 minutes. Cells were heat shocked at 42 °C for 45 seconds and immediately cooled on ice for 2 minutes. The heat shock creates transient pores in the bacterial cell membranes, allowing the negatively charged plasmid DNA to enter the cells.

Following heat shock, 300 µL of SOC medium was added, and the mixture was incubated at 37 °C for 1 hour with shaking to allow cell recovery. The cells were centrifuged at 5,370 × *g* for 2 minutes, the supernatant was mostly removed, and the pellet was resuspended in 50 µL of the remaining supernatant.

To select for transformants, 50 µL aliquot of the bacterial suspension was plated onto kanamycin agar plates and incubated at 37 °C overnight. Since the pCR2.1 plasmid carries a kanamycin resistance gene, only bacteria that successfully incorporated the plasmid would survive. The plates were incubated at 37 °C overnight to allow colony formation.

2.2.4.2 Electroporation

The plasmid was introduced into electrocompetent cell line by electroporation. In total, 2 µL of plasmid DNA was added to 30 µL of electrocompetent *E. coli* cells, and the mixture was incubated on ice for 10 minutes. Following incubation, 32 µL of the plasmid-cell mixture was transferred into an electroporation cuvette. Additional volumes of electroporation buffer added to reach a final volume of 60 µL.

The cuvette was placed into the electroporation apparatus, and electroporation was performed by delivering an electrical pulse. Immediately after electroporation, the contents of the cuvette were transferred into a sterile tube, and 250 µL of SOC medium was added. The cells were incubated in a shaking incubator at 37 °C for 1 hour to allow recovery and expression of the plasmid.

Following incubation, the cells were centrifuged at 5,370 × *g* for 2 minutes, and the supernatant was removed. The cell pellet was resuspended in 20 µL of the remaining broth, and the suspension was streaked onto kanamycin agar plate. The plates were incubated at 37 °C overnight to allow colony formation.

2.2.5 PCR amplification of plasmid DNA

PCR amplification was performed to analyse plasmid DNA samples. Plasmid DNA was isolated from bacterial cultures using the GeneJET Plasmid Miniprep Kit (ThermoScientific, Waltham, MA, USA) as described previously (2.2.3 Plasmid Isolation). Each PCR reaction was prepared in a total volume of 25 µL. The reaction mixture contained 1 µL of plasmid DNA, 0.2 µM each of M13 forward primer (5'-GTAAAACGACGGCCAG-3') and M13 reverse primer (5'-CAGGAAACAGCTATGAC-3') and 12.5 µL of DreamTag™ Green PCR Master Mix (Thermo Fisher Scientific), which includes loading dye. Autoclaved Type 1 water was added to reach the final volume.

PCR amplification was carried out using a thermal cycler under the following conditions: an initial denaturation at 95 °C for 3 minutes, followed by 35 cycles of denaturation at 95 °C for 30 seconds, annealing at 55 °C for 30 seconds, and extension at 72 °C for 1 minute. A final

extension was performed at 72 °C for 5 minutes, and the reaction were then held at 4 °C until further analysis.

After amplification, the PCR products were analysed by agarose gel electrophoresis as described in 2.2.6 Gel Electrophoresis. The expected PCR product sizes corresponded to the plasmid with and without the insert, allowing for comparison between samples.

2.2.6 Gel electrophoresis

Agarose gel electrophoresis was performed to analyse plasmid DNA. A 1% agarose gel was prepared in 1X Tris Acetate EDTA (TAE) buffer. The mixture was heated in a microwave at high power for 2-3 minutes until fully dissolved. The solution was cooled until it could be comfortably handled. A gel tray with a comb was set up, and approximately 5% of the gel volume of SYBR Safe DNA gel stain (Thermo Fisher Scientific) was added to the cooled agarose solution, which was gently swirled to mix. The mixture was poured into the gel tray to a sufficient depth (approximately 10 mm) and left to solidify at room temperature.

Once the gel had solidified, the comb and separator were removed, and the gel was placed in the electrophoresis chamber, with the wells positioned near the negative (black) electrode. The chamber was filled with 1XTAE buffer until the gel was completely submerged.

5 µL of a 1 kb GeneRuler DNA ladder (Thermo Fisher Scientific) was loaded into one of the wells as a molecular weight marker. The remaining wells were loaded with 10 µL each of the DNA samples; control (PCR chemicals), *E. coli* (E, DH5α), susceptible strain (S, DH5α pCR2.1), and resistant strain (R, DH5α pCR2.1NDM-7).

Electrophoresis was run at 100 V for 35 minutes. Voltage was monitored throughout the run, ensuring adequate buffer coverage and the presence of bubbles as an indication of proper operation. After electrophoresis, the DNA bands were visualised using a blue-light transilluminator in the Molecular Imager® Gel Doc™ XR System, and an image of the gel was captured for analysis.

2.2.7 Glycerol stock preparation

Protect Micro-organism Preservation Beads in cryovial, used for long term storage of bacterial

strains, were purchased from Technical Service Consultants (Lancashire, UK). Glycerol stocks for preservation of the bacterial strains were prepared by adding colonies from agar plates into cryovial containing Protect Micro-organism preservation beads. The bacteria were evenly distributed among the beads, each vial was labelled with the strain and date, then stored at -80 °C.

2.2.8 Agar plate culture preparation

To culture *E. coli* DH5α, a 10 µL inoculation loop was used to streak a small amount of glycerol stocks onto agar plates to form colonies. Antibiotics were added to the agar, when necessary, typically at a ratio of 1:1000 (e.g., 20 µL of antibiotic to 20 mL of agar). Plates were incubated at 37 °C for 16-18 hours until colonies formed.

2.2.9 Overnight culture

A single colony of *E. coli* (DH5α) was inoculated into 20 mL of 2TY medium in a Falcon tube and placed in a 37 °C shaker at 200 rpm (revolutions per minute) overnight. When antibiotics were needed, a ratio of 20 µL antibiotic to 20 mL of broth was used.

2.2.9.1 Colony count: Time kill assay

The bacterial culture was sampled at specific time points during the assay. For the 0-hour time point, a small aliquot of the treated sample was removed immediately after the addition of meropenem for analyses. For subsequent time points, treated cultures were incubated at 37 °C in a shaking incubator, and aliquots were removed for analyses at each specific time point. To preserve metabolic states, samples were cooled to 4 °C right after sampling. Each sample was serially diluted up to a 10^{-5} dilution using 2TY broth. A 50 µL aliquot from the 10^{-5} dilution was spread evenly onto a 6 cm agar plate using a sterile spreader. The plates were then incubated at 37°C for 24 hours, after which the bacterial colonies were counted to determine the colony-forming units (CFU).

2.2.10 Subculture

A 200 µL aliquot of the overnight culture was sub-cultured into 20 mL fresh 2TY medium and grown in a shaker at 37 °C until the OD_{600} reached 0.3-0.4.

2.2.11 Antibiotic exposure

A subculture of *E. coli* was grown in 2TY medium at 37 °C in a shaking incubator (200 rpm) for 4 hours until the OD_{600} reached 0.4, corresponding to the log phase of the growth.[226,227] The cell density was then normalised by diluting the cultures to an OD_{600} of 0.4 using fresh 2TY medium.[227] Antibiotic stock solutions were prepared in DMSO at 1000 times the desired final concentration. To achieve the desired antibiotic concentrations, 2 µL of the 1000× stock solution was added to 2 mL of bacterial culture at OD_{600} 0.4, resulting in a 1:100 dilution. Treated cultures were incubated at 37 °C in a shaking incubator (200 rpm) for specific durations based on the experiment.

2.2.11.1 Meropenem hydrolysis assay

E. coli strains were subcultured from overnight cultures in 2TY broth. When the optical density at 600 nm (OD_{600}) reached 0.4, bacterial cells were harvested by centrifugation at 4°C for 15 minutes at 16,000 × g. The supernatant was discarded, and the resulting pellet was retained for further analysis.

The metallo-β-lactamase (MBL) buffer used in the assay contained 50 mM HEPES (pH 7.2), 1 µM $ZnCl_2$, 1 µg/mL bovine serum albumin (BSA), and 0.01% (v/v) Triton X-100 to facilitate cell lysis. The buffer was sterilized by filtration using a 0.2 µM filter, and the filter was pre-washed with sterile water before use.

The bacterial pellet was resuspended in 500 µL of MBL buffer. Cell lysis was achieved through sonication for a total of 3 minutes, using cycles of 10 seconds on and 10 seconds off, while keeping the sample on ice to preserve lysate integrity.

Protein concentrations in the lysates were measured using the Bradford assay. In a 96-well microplate, 5 µL of the lysate or a standard solution, 5 µL of buffer, and 250 µL of Bradford reagent were combined in each well. Absorbance was measured at 595 nm using a microplate reader. Protein concentrations were determined based on a standard curve generated from known protein concentrations ranging from 125 µg/mL to 2000 µg/mL.

Meropenem was prepared at a concentration of 200 µM in MBL buffer. For the assay, 5 µL of

the bacterial lysate was incubated with 200 µL of the meropenem solution. Hydrolysis of meropenem was monitored by measuring the decrease in absorbance at 300 nm, the wavelength at which meropenem exhibits its highest absorbance. The reaction was conducted at 37°C, and measurements were taken at 2-minute intervals to track the rate of hydrolysis.

The rate of meropenem hydrolysis was calculated by normalizing the absorbance values to the protein concentration of each lysate sample. Absorbance measurements from the buffer control were subtracted to account for any background activity. Protein concentrations were calculated using the standard curve generated during the Bradford assay. The hydrolysis rates were compared among wild-type (E), meropenem-susceptible (S), and meropenem-resistant (R) *E. coli* strains.

2.2.11.2 Checkerboard assay

Checkerboard assays were performed to evaluate the combined antimicrobial effects of meropenem with various compounds against *E. coli* strains. Meropenem was prepared as a stock solution and serially diluted 2-fold across the horizontal axis of a 96-well plate to achieve final concentrations of 256, 128, 64, 32, 16, 8, 4, 2, 1, 0.5, 0.25, and 0 µg/mL. The test compounds were also serially diluted 2-fold along the vertical axis.

Each well contained 180 µL of 2TY broth supplemented with the appropriate concentrations of meropenem and the test compound, and 20 µL of bacterial inoculum. The inoculum was prepared either by diluting OD_{600} of 0.4 subculture to a final OD_{600} of 0.01, or by suspending a single colony in 3 mL of PBS and diluting to a final OD_{600} of 0.01.

Plates were incubated at 37 °C for 24 hours, and bacterial growth was monitored by measuring optical density (OD_{600}) using a CLARIOstar microplate reader.

2.2.12 Growth curve

Bacterial cultures were initiated with an inoculum adjusted to an initial OD_{600} of 0.01. The inoculum was prepared either from a single bacterial colony or a subculture grown in 2TY broth. The cultures were incubated at 37°C with continuous shaking to ensure aeration.

The OD_{600} was measured every 10 minutes over a 24-hour period in CLARIOstar.

Measurements were recorded in real-time to monitor bacterial growth kinetics. Data were used to construct growth curves, which provided insights into lag, exponential, and stationary growth phases under the specified experimental conditions.

2.3 Metabolite extraction

2.3.1 Method A

For each sample, 100 µL of whole-cell broth were directly transferred to 240 µL of an extraction solution containing 50% (v/v) methanol and 50% (v/v) acetonitrile at -20 °C. The extraction process involved incubating the samples for 1 hour at -20 °C, followed by centrifugation at 14,000 × *g* for 5 minutes.[228] Sample normalisation and filtration were performed as needed for AEC-MS sample preparation. Refer to **Section2.3.6** for detailed sample preparation methods for AEC-MS analysis.

2.3.2 Method B

Samples were rapidly quenched in a dry ice/ethanol bath and kept on ice for all following steps. The samples were centrifuged for 10 minutes at 3,220 × *g* at 4 °C. The supernatant was collected for extracellular metabolites. Aliquots of the supernatant were filtered through Millipore Amicon Ultra centrifugal filters, and 30 µL of the filtered supernatant was mixed with 250 µL chloroform:methanol:water (1:3:1, v/v, -80 °C).[229] The mixture was then centrifuged at 14,000 × *g* for 10 minutes at 4 °C, and the supernatant was collected into injector vials for AEC-MS analysis.

For intracellular metabolites, the cell pellets were washed three times with 200 µL cold sterile phosphate-buffered saline (PBS) and centrifuged for 3 minutes at 3,220 × *g* at 4 °C. Cellular metabolites were extracted with 200 µL chloroform:methanol:water (1:3:1, v/v, -80 °C). The samples were immediately frozen in liquid nitrogen, thawed on ice, and this freeze-thaw process was repeated three times to lyse the cells and release intercellular metabolites. The extracted samples were centrifuged for 10 minutes at 3,220 × *g* at 4 °C, and the supernatant was further centrifuged at 14,000 × *g* for 10 minutes at 4 °C.[229] After the centrifugation, the samples were normalised and filtered as described in **Section 2.3.6** for AEC-MS analysis.

2.3.3 Method C: Adaptation of mammalian protocol

A single colony from each strain (E, S, and R) were grown overnight in broth. The susceptible and resistant strains were grown in the presence of kanamycin. Subculture were grown until OD_{600} reached 0.4, and the cultures were normalised to OD_{600} 0.4 if necessary. Three replicates of 6 mL of cells from each condition (E, S, R) were prepared. The cells were centrifuged at 14,000 × *g* for 10 minutes, and the supernatant was filtered and kept separately. The cell pellet was washed with 5 mL PBS buffer, resuspended, and centrifuged at 14,000 × *g* for 10 minutes; this wash step was repeated twice. The washed cell pellets were snap-frozen in liquid nitrogen. The frozen cells were resuspended in 500 µL of cold 80% methanol and placed on an ice bath. The samples were centrifuged at maximum speed (>16,000 × *g*) for 30 minutes. DNA was measured and normalised before filtering the supernatant and broth (500 µL each) for subsequent analysis as described in **Section 2.3.6** for AEC-MS analysis.[210]

2.3.4 Mechanical cell lysis method

The efficacy of cell disruption for intracellular metabolite extraction was evaluated using sonication and bead beating methods. For sonication, 1 mL of subculture (OD_{600} 0.4) was centrifuged at 8,385 × *g* for 5 minutes, the supernatant was removed, and the pellet was washed twice in 1 mL of 30 mM Tris buffer. After the wash and removal of the supernatant, finally, the pellet was resuspended in 350 ul of buffer. Sonication was performed in an ice bath using a microtip sonicator set to 40% amplitude, with 3 minutes of pulsed treatment (10 seconds on, 10 seconds off).[230] The sonicator probe was cleaned with ethanol and water between samples. Protein concentration was measured using Bradford assay, where 50 µL of the sample was mixed with 250 µL Bradford reagent and absorbance was read at 595 nm, with controls showing minimal protein detection.[231] DNA concentration was also measured using a NanoDrop spectrophotometer to normalise the samples before proceeding with the 50:50 extraction method. For extraction, the sonicated subculture equivalent to 100 µL of the original subculture was mixed with 240 µL of 50:50 (methanol:acetonitrile) and incubated at -20 °C for 1 hour, followed by centrifugation at 8,385 × *g* for 5 minutes. The sample was then normalised

to DNA concentration of 8 ng, filtered as described in **Section 2.3.6** and 180 µL was transferred to a sample vial for storage at -80 °C until AEC-MS analysis.

For bead beating, a subculture was grown to an OD_{600} of 0.4, and 1 mL of cells was incubated with 1 µL (4 µg) of meropenem, shaken for 1 hour, and washed twice with PBS, centrifuging at 1,900 × *g* for 10 minutes each time. The pellet was resuspended in 500 µL of 50:50 methanol:acetonitrile and incubated for 1 hour at -20 °C. Bead beating involved pre-chilling the samples at -80°C, followed by vortexing for 3 minutes at 500 rpm, or alternatively, vortexing for 30 seconds with 2 minute intervals on ice, repeated five times.[232] After bead beating, samples were centrifuged at 8,385 × *g* for 10 minutes, filtered through a MWCO filter, and centrifuged again at 8,385 × *g* for 15 minutes. DNA concentration was measured using a NanoDrop spectrophotometer, and samples were normalised accordingly.

2.3.5 Optimised bacterial metabolite extraction protocol

Following the drug treatment, 1 mL of bacterial culture were pelleted by centrifugation at 3,220 × *g* for 10 minutes at 4 °C. The supernatant was discarded, and the pellet was washed twice with ice-cold PBS to remove any residual medium or drug compounds. The washing process involved resuspending the pellet in 1 mL ice-cold PBS, followed by centrifugation at 3,220 × *g* for 5 minutes at 4 °C. The supernatant was carefully removed, and the pellet was resuspended in fresh ice-cold PBS for a second wash. After the final centrifugation, the supernatant was discarded. The washed cell pellets were resuspended in 300 µl of a 50:50 methanol/acetonitrile (MeOH/ACN) mixture, which was pre-cooled to -20 °C. The samples were incubated at -20 °C for 1 hour to facilitate metabolite extraction. After incubation, the samples were centrifuged at 14,000 × *g* for 5 minutes at 4 °C, and the supernatant containing metabolites was collected. Then followed DNA normalisation and filtration as described in **Section 2.3.6** for AEC-MS analysis.

2.3.6 Sample preparation for anion exchange chromatography-mass spectrometry analysis

After extraction, DNA concentration (ng/µL) of the final supernatants were measured with

NanoDrop™.[233] Then, samples were normalised by relative DNA concentration with the appropriate extraction solvent (methanol:acetonitrile 50:50 or chloroform:methanol:water (1:3:1, v/v)) up to 200 µL, then filtered with an Amicon® Ultra-0.5 centrifugal 10 kDa cut-off filter. After filtration, the samples were collected into total recovery vials (1.0 mL) with screw neck and cap with pre-slit PTFE/silicone septa (Waters, Milford, USA) for AEC-MS analysis. Quality control (QC) samples were made by collecting equal aliquots from all samples into one vial.[210]

2.4 Anion exchange chromatography-mass spectrometry method

2.4.1 Instrumentation and column setup

Samples were analysed on a Q Exactive™ HF hybrid quadrupole-Orbitrap™ mass spectrometer (Thermo Scientific, Bremen, Germany), coupled to a Dionex™ ICS-5000$^+$ Capillary High-Pressure Ion Chromatography (HPIC) system. The system was equipped with a Dionex™ IonPac™ AS11-HC column (2×250 mm, 4 µm particle size), and eluent generation was achieved using an eluent generator cartridge (EGC 500 KOH) for automated online hydroxide gradient production. A sample volume of 5 µL was injected using partial loop injection. To maintain sample purity, a continuously regenerated trap column (CR-ATC) was used to remove contaminants from the eluent, while ion suppression was achieved using a Dionex™ ERS 500e electrochemical suppressor (AERS 500e 2 mm) operating in external water mode with the water regenerant flow rate of 500 µL/min. Unless otherwise specified, all products were purchased from Thermo Scientific, Sunnyvale, CA, USA.

2.4.2 Chromatography conditions

The autosampler was maintained at 4 °C, and the column was kept at a constant temperature of 30 °C. The mobile phase flow rate was set to 250 µL/min. The hydroxide gradient applied was as follows; 0.0 min at 5 mM, 1.0 min at 5 mM, 15.0 min at 60 mM, 25.0 min at 100 mM, 30.0 min at 100 mM, 30.1 min at 5 mM, and 37.0 min at 5 mM. A curve setting of 5 was applied for all gradient steps. The ion suppressor current was set to 62 mA.

2.4.3 Mass spectrometry parameters

The mass spectrometer was equipped with a heated electrospray ionisation (HESI II) probe operating in negative ion mode. The spray voltage was set to -3.6 kV (negative polarity), the capillary temperature to 320 °C, and the probe heater temperature to 350 °C. Other key parameters included the S-Lens RF Level of 70%, the auxiliary gas flow rate at 20 arbitrary units (a.u.), the sheath gas rate at 60 a.u., and the spare gas at 0 a.u.

The Q-Exactive method involved full scan MS data collection, followed by automatic (Top 10) data-directed (dd) high-energy collision dissociation (HCD) fragmentation. Known as Full MS-ddMS^2 approach, it provided comprehensive analysis of the samples. For Full MS settings, the microscans were set to 2, with a resolution of 70,000, a scan range of 60 to 900 *m/z*. an automatic gain control (AGC) target of 1e6, and a maximum injection time (IT) of 120 ms. For dd-MS/MS settings, the microscans were set to 1, with a resolution of 17,500, an AGC target of 1e5, and maximum IT of 250 ms.

2.5 Data processing and analysis

2.5.1 Raw data acquisition

The raw mass spectrometry data files obtained from AEC-MS analysis were imported and processed using Progenesis QI, a software from Nonlinear Dynamics (a Waters Company, Newcastle upon Tyne, UK). The instrument type was set as a 'High resolution mass spectrometer' and the data format was set to 'Profile data'. The ionisation polarity was set to negative, with the adducts $[M-H]^-$ and $[M-H_2O-H]^-$ selected for analysis.

2.5.2 Peak detection and chromatographic peak alignment

Progenesis QI automatically selected the most suitable sample, often QC sample, to serve as the reference for chromatographic peak alignment across all samples. The alignment process ensured consistent detection and retention time alignment, correcting for any potential shifts that may occur during the run. Accurate alignment is critical for consistent comparisons between samples, with an alignment score of ≥ 90% generally accepted as reliable. After alignment, peak picking was conducted with the software identifying and integrating

chromatographic peaks based on retention time and *m/z* pairs. The default peak picking sensitivity and noise estimation algorithms were applied, without imposing minimum peak width or retention time limits, which effectively reduced data complexity by consolidating detected ions into compound features across all samples, aiding in accurate compound identification. The detected peaks were then deconvoluted into compound features, which were used for identification process.

2.5.3 Metabolite identification

Detected features were matched against an in-house metabolite database specifically designed for AEC-MS analysis (details provided in **Table Appendix I.I** in **Appendix I**)Identification was performed using parameters such as accurate mass, retention time, isotopic patterns, and MS/MS fragmentation data. The identification process was guided by set parameters, including a retention time deviation of ≤ 3 minutes, precursor tolerance of ≤ 5 ppm, and fragment tolerance of ≤ 12 ppm to ensure accuracy.

Progenesis QI generated a robust identification score by aggregating mass accuracy, retention time alignment, isotopic pattern matching, and fragmentation data. The score was critical for prioritising and validating potential compound identification. Retention time error, mass error, fragmentation score (calculated using the Progenesis QI algorithm)[234], isotope similarity, minimum coefficient of variation (CV) and maximum abundance were crucial for differentiating between potential identifications.

Noise was filtered out using minimum CV and maximum abundance criteria, where a CV > 50% and/or abundance < 50 were considered highly likely to be noise. Only high-confidence identifications, with strong evidence from mass accuracy, retention time, isotopic pattern, and fragmentation data, was prioritised and accepted.

2.5.4 Data export and further analysis

The Progenesis QI output (peak intensity table of compound ions) was formatted as required for further analysis in MetaboAnalyst (www.metaboanalyst.ca). Although samples were normalised by OD_{600} and DNA concentration prior to AEC-MS, additional computational

normalisation was applied during analysis to account for systematic variations and ensure data reliability.

2.5.5 Data filtering and pre-processing

To ensure high-quality and reliable data analysis, data filtering was implemented to remove noise, irrelevant, or redundant data that could potentially mask true biological signals. The process included assessments for missing values, duplicate features, and data inconsistencies. Features with low variance across samples were filtered using the interquartile range (IQR) variance filter with a threshold of 40%, which removed non-informative noise.

2.5.6 Data normalisation, transformation, and scaling

Data normalisation was applied to minimise any technical variability across samples. Sample-specific normalisation, based on DNA content, was conducted during sample preparation to standardise sample inputs. Further computational normalisation was performed during data processing to account for any technical variations and ensure accurate comparisons of metabolite intensities across samples. Median normalisation was applied to adjust metabolite intensities by dividing each feature by the median intensity of all features within a sample, which is robust to outliers and provides a consistent baseline for analysis.

Following normalisation, logarithmic transformation was used to stabilise variance and compress the dynamic range, particularly effective in reducing the influence of high-intensity metabolites that could otherwise dominate the analysis. The transformation made the data distribution more symmetrical, a requirement for many statistical analyses.

After transformation, Pareto scaling was applied, dividing each feature by the square root of its standard deviation. The scaling method balanced the contribution of larger signals while minimising noise, making it effective for highlighting biologically relevant differences without allowing any feature to disproportionately affect the results.

Median normalisation, logarithmic transformation, and Pareto scaling were applied consistently throughout the analysis to ensure that the processed data were optimally prepared for statistical evaluation in MetaboAnalyst, as these methods were best suited for the

dataset and the specific objectives of the analysis, highlighting biologically relevant differences while minimising technical variability.

2.5.7 Statistical analysis

The data were processed using a range of statistical techniques within MetaboAnalyst. Within uploaded data, different sample datasets can be selected to undergo any statistical analyses. The processed data were visualised through methods such as heatmaps, which allowed for the observation of general patterns in metabolite abundance across samples. Principal Component Analysis (PCA) to visualise underlying trends, patterns, and clustering within the data, allowing for the separation of samples based on their metabolomic profiles, while also reducing dimensionality and identifying potential outliers. Volcano plots were generated to combine fold-change and statistical significance, providing a clear visualisation of significant metabolite changes.

Univariate analysis, including t-tests, fold-change analysis, and analysis of variance (ANOVA), was used to assess individual metabolites and identify statistically significant differences between groups. It is important to note that ANOVA detects statistically significant differences between any two groups within a dataset; therefore, not all compound features identified as significant will necessarily exhibit differences across all treatment and control conditions. These methods offered insights into specific metabolite changes across conditions helping to validate hypotheses and draw conclusions from the data.

Multivariate analysis was applied to explore broader patterns in the dataset. Partial Least Squares Discriminant Analysis (PLS-DA) and Orthogonal PLS-DA (OPLS-DA) were used for supervised classification, aiding the prediction of sample groupings based on their metabolomic profiles. Variable importance in projection (VIP) scores were used to rank metabolites based on their contribution to group separation, enhancing the understanding of metabolic differences and helped classify the groups.

Additionally, hierarchical clustering using the Ward method was applied to identify groups and metabolites with similar profiles, providing further insights into the metabolic relationships

and variance within the dataset. The Ward algorithm minimises the variance within clusters, ensuring that grouped features share high similarity, which enhances the interpretability of complex metabolomic data.[235]

2.5.8 Pathway analysis

Untargeted pathway analysis, also referred as functional analysis, was conducted on the AEC-MS data using MetaboAnalyst to explore the biological context of the identified metabolites by investigate metabolic pathways associated with those metabolites. Binary comparisons, such as those between resistant and susceptible strains, were used highlight relevant biological differences. The data were formatted as .csv files specifically tailored for functional analysis as specified by MetaboAnalyst.

For functional analysis, Mummichog was applied. The tool processes mass spectrometry data to predict pathway activities independently from manual metabolite identification, reducing the impact of potential errors in identification from tools like Progenesis QI. Pathways were mapped based on the mass features present, allowing for an unbiased analysis of metabolic changes.

Pathway and network visualisations were generated to identify affected metabolic pathways and explore potential interactions between metabolites. These analyses provide a basis for understanding the functional implications and the biological significance of the observed metabolic differences between strains.

2.5.9 Further statistical analysis and visualisation

MetaboAnalyst was used to generate a variety of visualisations, including scatter plots, volcano plots, heatmaps, pathway maps, and boxplots, to aid the interpretation and presentation of the results. Visualisations and results were saved and downloaded for inclusion in reports or publications. MetaboAnalyst also allows the export of process data for further analysis.

Additional statistical analyses were conducted using Prim 9.4.0 from GraphPad (San Diego, USA). Visual representations of the data, including figures and charts, were created using Biorender.com under a student license. The comprehensive approach ensured accurate data

processing and facilitated meaningful interpretation, supporting the validation of hypotheses and the formulation of conclusions.

SnapGene Viewer 7.2.1, developed by GSL Biotech LLC (Chicago, IL, USA), was utilized for the visualization of plasmid constructs, genes, and protein sequences. Chromatogram analysis was conducted using Freestyle 1.6, developed by Thermo Fisher Scientific (Waltham, MA, USA), to review sequencing results and ensure data quality.

2.6 Seahorse XFe24 Analyzer

2.6.1 Sensor cartridge preparation

The XF sensor cartridge was hydrated one day prior to the assay by submerging it into the utility plate containing 1 mL of XF Calibrant per well. The plate was incubated overnight at 37 °C in a non-CO_2 incubator. On the day of the experiment, the hydro booster was removed, and injected ports were loaded with the appropriate reagents, as specified for the assay.

2.6.2 Plate coating

Seahorse XFe24 cell culture microplates were coated with PLL to enhance bacterial cell adhesion during Seahorse assays. A 0.01% (0.1 mg/mL) PLL stock solution was prepared and diluted 1:10 using autoclaved Type 1 water.

To coat the plate, 50 µL of the diluted PLL solution was added to each well of the microplate. The plate was incubated at room temperature for 30 minutes to allow sufficient adherence of the PLL to the well surface. After incubation, the wells were washed with an equal volume of sterile water to remove any excess PLL. The plate was then allowed to air-dry completely in a laminar-flow hood.

If not used immediately, the coated plates were stored at 4°C for up to one week. Prior to cell seeding, the plates were brought to room temperature to ensure optimal adherence conditions. Bacterial cells were added to the wells, centrifuged to enhance adhesion, and the growth medium was carefully removed. Fresh medium was added, and the plates were prepared for Seahorse assay analysis.

2.6.3 Agilent Seahorse XF assay media preparation

2.6.3.1 Glycolysis stress test

Seahorse XF DMEM Medium (99 mL, pH 7.4) was supplemented with 1 mL of 200 mM L-glutamine to prepare the glycolysis stress assay medium. The medium was freshly prepared on the day of the assay.

2.6.3.2 Real-time ATP rate assay, glycolytic rate assay, and cell energy phenotype test

Seahorse XF DMEM Medium (97 mL, pH 7.4) was supplemented with 1 mL of 1 M glucose, 1 mL of 100 mM pyruvate, and 1 mL of 200 mM L-glutamine to prepare the assay medium. The medium was also freshly prepared on the day of the experiment.

All prepared media were heated and kept at 37 °C in a non-CO_2 incubator, where they were maintained throughout the assay day. Any leftover media were discarded after the experiment.

2.6.4 Loading injection ports

The preparation of reagents for Seahorse XF assays involved diluting compounds to appropriate concentrations in pre-warmed assay medium, ensuring consistency and accuracy in experimental conditions. Injection port volumes were standardised across all assays to facilitate consistent reagent delivery and experimental reproducibility. Specifically, the following volumes were loaded into the respective ports of the sensor cartridge: 56 µL for port A, 62 µL for port B, 69 µL for port C, and 75 µL for port D.

These injection volumes were calibrated for a basal starting volume of 500 µL assay medium in each well of the Seahorse XF24 plate. The final well concentrations of the injected solutions were achieved through precise dilution upon mixing with the basal medium during the Seahorse XFe 24 Analyser operation. Standardisation of port volumes ensured uniformity in reagent addition, allowing for accurate interpretation of the metabolic parameters measured, such as OCR and ECAR.

After reagent loading, the sensor cartridge, which had been hydrated overnight in XF Calibrant, was inserted into the Seahorse XFe 24 Analyser for calibration. The calibration step ensured the accurate integration of injected reagents into the assay workflow, maintaining the

precision of the resulting metabolic measurements. By maintaining consistent injection volumes across assays, the methodology provided a reliable framework for assessing metabolic activity in bacterial cells.

2.6.4.1 XF Glycolytic stress test

XF Glycolysis Stress Test reagents were diluted in warmed Glycolytic Stress Test assay medium for a final concentration as follows; glucose 100 mM, oligomycin 10 µM, and 2-DG 500 mM. Solutions were vortexed thoroughly to ensure dissociation. Diluted reagents were loaded into the sensor cartridge as follows; 56 µL glucose in injection port A, 62 µL oligomycin in injection port B, and 69 µL 2-DG in injection port C. Reagent concentration and loading volume were used to make a final well concentration of 10 mM glucose, 1 µM oligomycin, and 50 mM 2-DG. After loading the sensor cartridge submerged in XF calibrant was loaded into the Seahorse XFe24 Analyser for calibration.

2.6.4.2 XF Glycolysis rate test

Reagents for the XF Glycolysis Rate Test were prepared to achieve final well concentrations of 10 mM glucose, 1 µM oligomycin, and 50mM 2-DG. Stock solutions were prepared at concentrations of 100 mM glucose, 10 µM oligomycin, and 500 mM 2-DG. The reagents were diluted in pre-warmed Seahorse XF assay medium to ensure consistency and accuracy.

The sensor cartridge was loaded with 56 µL of the glucose solution into port A, 62 µL of the oligomycin solution into port B, and 69 µL of the 2-DG solution into port C. These volumes were calculated to achieve the desired final well concentrations upon injection into the assay wells containing 500 µL of Seahorse XF assay medium.

Following reagent loading, the sensor cartridge, which had been hydrated overnight in XF Calibrant, was calibrated in the Seahorse XFe24 Analyser before initiating the assay. The setup allowed for precise measurement of glycolysis by differentiating between glycolytic and non-glycolytic acidification rates, facilitating a comprehensive understanding of the metabolic activity of the bacterial cells under investigation.

2.6.4.3 XF Real-time ATP rate assay

For the XF Real-Time ATP Rate Assay, the sensor cartridge was prepared with reagents specifically designed to assess ATP production through glycolysis and the ETC. Oligomycin, an ATP synthase inhibitor, and a mixture of Rot/AA, which inhibit the ETC, were used as injection solutions. These reagents were diluted in pre-warmed Seahorse XF assay medium to achieve final well concentrations of 1 μM oligomycin and 0.5 μM Rot/AA.

Reagents were prepared as follows: oligomycin stock solution was diluted to 10 μM, and Rot/AA was diluted to 5 μM. The sensor cartridge was loaded with 62 μL of oligomycin in port A and 69 μL of Rot/AA in port B, ensuring consistent delivery of reagents during the assay. The assay workflow involved measuring basal OCR and ECAR values, followed by sequential injections of oligomycin and Rot/AA to assess ATP production rates from glycolysis and oxidative phosphorylation.

After loading, the cartridge underwent calibration in the Seahorse XFe24 Analyser before initiating the experiment. The assay quantified ATP production rates by measuring changes in OCR and ECAR, distinguishing glycolytic ATP production (glycoATP) from oxidative ATP production (oxyATP), and providing a comprehensive view of energy metabolism.

2.6.4.4 Buffer factor

The Buffer Factor (BF) assay was conducted to determine the relationship between ECAR and the actual proton flux in the assay medium. The assay was necessary for accurately converting qualitative ECAR measurements into quantitative Proton Efflux Rate (PER) values, ensuring precise analysis of extracellular acidification.

For the BF assay, the assay plate was prepared with Seahorse XF assay medium, identical to the medium used in other Seahorse assays but without cells. A 5mM HCl solution was prepared in the same assay medium and loaded into port A of the sensor cartridge at 56 μL per well. Control wells containing only assay medium were included to measure baseline pH changes.

During the assay, incremental injections of HCl were performed, and the resulting pH changes were recorded in real time using the Seahorse XFe24 Analyser. The Seahorse XF Buffer Factor

Calculator was used to calculate the BF, expressed as millimolar per pH unit (mM/pH). The value accounted for system-specific properties, such as the buffer capacity of the medium and the materials used in the Seahorse system, and was critical for accurately interpreting ECAR data in terms of proton flux.

2.6.4.5 XF Cell phenotype

The XF Cell Energy Phenotype Test was designed to evaluate the basal and maximal metabolic capacities of the cells by measuring OCR and ECAR under baseline conditions and following metabolic perturbations. The assay was performed using the Agilent Seahorse XFe24 Extracellular Flux Analyser to characterise the bioenergetic profile of *E. coli*. Key assay parameters, including cell seeding density and the optimal concentration of FCCP, were optimized prior to experimentation.

Cell seeding density was empirically determined to ensure that OCR and ECAR values remained within the dynamic range of the Seahorse Analyser. Overnight bacterial cultures were diluted to the desired density, and seeded onto the assay plate. For mammalian cells, densities corresponding to 50-90% confluency were targeted, as recommended by the manufacturer, to ensure optimal metabolic activity and reproducibility. Cells were seeded into prewarmed to 37 °C XF Assay medium (as detailed in **Section 2.6.3.2**). Wells containing assay medium without cells were included as controls for baseline correction.

A five-point FCCP titration was performed to identify the concentration that yielded maximal OCR. Two groups were prepared on the assay plate. The first range included low concentrations of 0.125, 0.25, and 0.5 µM while the second range tested higher concentrations of 0.5, 1.0, and 2.0 µM. All grounds were pre-treated with 1 µM oligomycin, an ATP synthase inhibitor, to block oxidative phosphorylation and stimulate maximal uncoupled respiration. FCCP was injected sequentially using the XFe24 cartridge injection ports, with each group receiving three injections corresponding to the designated concentrations. These injections were performed in triplicate for reproducibility, and the resulting OCR values were used to generate a concentration-response curve.

The Seahorse Analyser measured OCR and ECAR under basal and stress conditions following each injection. Basal rates provided insights into the native metabolic activity of the cells, while FCCP-induced uncoupling revealed the maximal respiratory capacity. ECAR data captured extracellular acidification changes associated with proton extrusion and metabolic by-products.

The data were analysed using the Seahorse XF Report Generator, which calculated basal and maximal OCR and ECAR values. FCCP concentrations that elicited the highest OCR without compromising reproducibility were identified as optimal for subsequent assays. The results provided an initial assessment of the bioenergetic capacity of *E. coli*, forming the foundation for more detailed metabolic studies. The method ensured robust characterisation of bacterial energy metabolism, enabling a comprehensive understanding of how meropenem-susceptible and meropenem-resistant *E. coli* strains modulate their bioenergetics under stress.

Chapter 3 Investigating metabolic differences between resistant and nonresistant strains of *E. coli*

3.1 Introduction

Understanding metabolic adaptations that occur in association with antibiotic resistance could reveal potential new therapeutic targets.[59,60] It has been shown that changes in metabolism are associated with bacterial dormancy and biofilm formation that can affect bacterial susceptibility to antibiotics.[58,236-240] The development of antibiotic resistance has been shown to impose a fitness cost, which may have a direct metabolic impact.[241-244] Carbapenem resistance, due to the expression of MBL enzymes, has been associated with major metabolic reprogramming for example.[59] These changes include disruptions in central carbon metabolism, such as alterations to the function of the TCA cycle and glycolysis, which help bacteria adapt to the metabolic burden of resistance.[59,245,246] Additionally, the inactivation or redirection of enzymes in central carbon metabolism has been proposed as a mechanism contributing to resistance development, linking antibiotic resistance to broader metabolic changes.[247,248] Understanding the metabolic changes associated with carrying and expressing resistance genes in more detail therefore has the potential to not only provide insight into how these organisms overcome antibiotic pressure and adapt to survive but may also provide potential new therapeutic targets.[60,249] The overall aim of this chapter was therefore to investigate whether differences in bacterial metabolism could be identified in *E. coli* with and without expression of resistant genes.

In order to explore these aims, the first objective was to create biological models to study consisting of three *E. coli* strains: wild-type (E), a meropenem-susceptible strain (S) containing a pCR2.1 plasmid (empty vector), and a meropenem-resistant strain (R) carrying the NDM-7 gene within the pCR2.1 plasmid (**Section 3.2**). These models would be designed to be able to investigate the metabolic differences between meropenem resistant and non-resistant strains, while controlling for the presence of the pCR2.1 carrier plasmid.

Before conducting metabolomics experiments, a suitable metabolomics method also needed to be developed, and validated, along with an effective sample preparation protocol that was compatible with bacterial metabolomics experiments. The process of method selection, development and validation is described in **Section 3.3**. Finally, comparative metabolomics analysis of the three bacterial strains was performed to determine whether the presence of resistance to altered bacterial metabolism. Finally, any metabolic changes were evaluated to see if they represent potential metabolic vulnerabilities that could be pharmacologically exploited (**Section 3.4**).

In summary this chapter reports the development of a suitable biological model using genetically engineered bacterial strains, optimisation of a metabolomics protocol suitable for metabolite extraction and analysis of bacterial samples and explores how the presence of pCR2.1 plasmid and the NDM-7 gene affects metabolism in these strains. **Figure 3.1** summarises the overall experimental workflow developed and optimised in this chapter for these comparative analyses of bacterial strains.

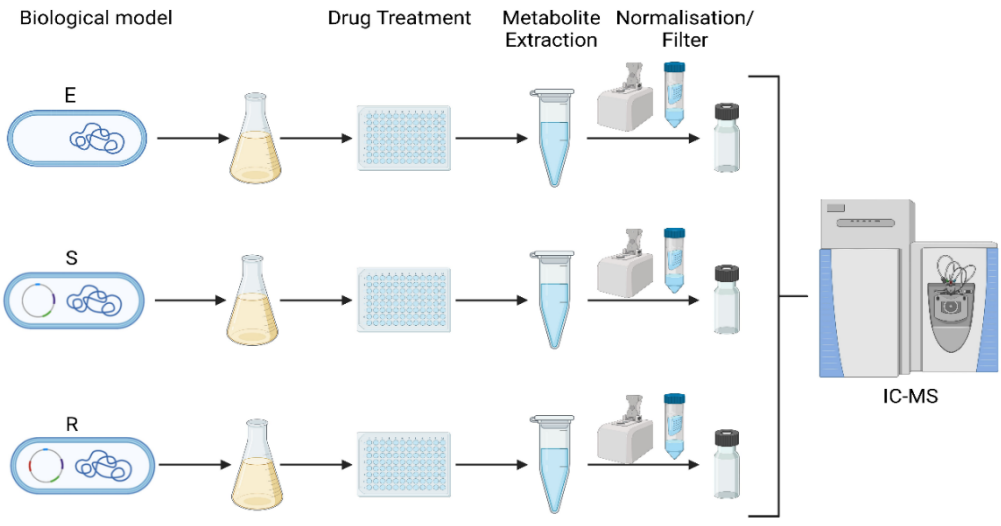

Figure 3.1 Experimental workflow for comparative metabolic profiling of* E. coli *strains. *Step-by-step workflow used to analyse metabolic changes across three* E. coli *strains: wild-type (E), susceptible (S) carrying the pCR2.1 plasmid, and resistant (R) with the NDM-7 gene in pCR2.1 plasmid. The process includes bacterial culture preparation and drug treatment, metabolite extraction, filtration and normalisation, and analysis using AEC-MS.*

3.2 Genetic modification of *E. coli* strains

The use of *E. coli* as a model organism has proven instrumental in microbiology, particularly in understanding bacterial physiology and metabolic pathways.[250,251] In this study, genetic modifications were introduced into *E. coli* strains in order to investigate the metabolic consequences of meropenem resistance. The primary goal was to create a bacterial model system that enabled the investigation and comparison of any metabolic changes between wild-type, meropenem-susceptible, and meropenem-resistant strains (**Table 3.1**).

***Table 3.1 Overview of the genetic characteristics of the* E. coli *strains developed for the study**. The table summarises the key genetic and phenotypic differences among the three* E. coli *strains: the wild-type strain (E), the meropenem-susceptible stain (S) carrying the pCR2.1 plasmid, and the meropenem-resistant strain (R) carrying the pCR2.1 plasmid with the NDM-7 gene.*

Strains	 E	 S	 R
Bacterial strain: *E. coli* DH5α	✓	✓	✓
Plasmid: pCR2.1 (carrier)	✗	✓	✓
Resistance gene: NDM-7 (metallo-β-lactamase producing)	✗	✗	✓
Resistant to meropenem	✗	✗	✓

The pCR2.1 plasmid was chosen as an expression vector due to its compatibility with cloning techniques and its ability to maintain plasmid stability within *E. coli* through the inclusion of kanamycin and ampicillin resistance markers.[252-254] These markers ensure the plasmid remains inside the bacteria by providing selective pressure, preventing plasmid loss. However, it is important to acknowledge that the metabolic comparison between the wild-type strain (E) and the meropenem-susceptible strain (S) also includes the presence of antibiotic resistance markers inherent to the pCR2.1 plasmid. The comparison between the meropenem-susceptible strain (S) and meropenem-resistant strain (R) therefore enables identification of metabolic changes specifically associated with NDM-7 gene mediated carbapenem resistance. The DH5α strain was selected for its genetic tractability, capability to stably express plasmid-borne genes, and resistance to bacteriophages.[255]

Initial experiments also tested NDM-1 and NDM-5 genes; however, these proved unstable, with only the NDM-7 gene providing consistent expression.[222] NDM-7 enzyme is a variant of NDM-1 enzyme with a specific amino acid substitution at position 130 (asparagine to glycine) and at position 154 (methionine to leucine).[256] The modification alters the structure of the enzyme, improving the stability and efficiency in binding and hydrolysing carbapenems like meropenem.[256,257] While NDM-5 also has substitutions (valine at position 88 and leucine at 153), these do not confer the same stability or broad spectrum activity as NDM-7.[258] Studies suggest that NDM-7 has a higher catalytic efficiency for carbapenem hydrolysis, allowing it to maintain the bacterial resistance phenotype under selective pressure longer than NDM-1 and NDM-5.[259]

Additionally, NDM-7 enzyme demonstrates improved thermal stability, allowing it to function at higher temperatures or under more stressful conditions.[260] The enhanced stability of NDM-7 compared to NDM-1 and NDM-5 may be due to specific structural variations that increase its resilience under environmental stress.[140,261] The stability makes the NDM-7 gene more resilient in clinical isolates, contributing to its geographic spread and posing a greater challenge in combating antimicrobial resistance.[262] Understanding NDM-7 gene and its metabolic impact is critical for developing targeted inhibitors, as it represents a more pressing concern for treatment failures due to its robust activity against a wide range of β-lactam antibiotics, including meropenem.[259] This study therefore focused on the metabolic impact of the NDM-7 genes specifically.

Verification of the presence of the active genetic modifications was confirmed through antibiotic susceptibility testing, plasmid sequencing, and application of a meropenem hydrolysis assay.[263] These steps ensured the strains were appropriately characterised and validated for downstream metabolic analysis.

3.2.1 Plasmids for antibiotic resistance studies

The meropenem-resistant plasmid containing the NDM-7 gene responsible for carbapenem resistance, which was used to modify the *E. coli* to create resistance and susceptible strains for

this study, was provided by David Wareham.[222] The integration of the resistance gene is depicted in **Figure 3.2**. The pCR2.1 plasmid is commonly used for Taq Polymerase-Added (TA) cloning, a technique that allows the direct insertion of PCR products (desired gene) into vectors.[264] The method relies on complementary overhangs where the PCR product and the vector can efficiently ligate due to the complementary adenine (A) and thymine (T) overhangs.[264] Taq polymerase adds a single adenine (A) overhang to the 3' ends of the PCR product, generating 'sticky' ends crucial for the ligation process into the pCR2.1 vector.[264] The plasmid is linearised at its multiple cloning site (MCS) located within the lacZα gene region, with complementary thymine (T) overhangs at the 3' ends, allowing efficient ligation.[265] Once the PCR product (a gene of interest, such as NDM-7) is prepared with complementary overhangs, it is combined with the linearised pCR2.1 vector. T4 DNA ligase is then added to catalyse ligation, by forming phosphodiester bonds between the complementary overhangs, sealing the gaps in the DNA backbone, and completing the insertion of the gene into the plasmid.[266] Thus, the PCR product (gene) will be inserted in the lacZα gene region in the vector.[267] Disruption of lacZα gene serves as a common marker for successful cloning.

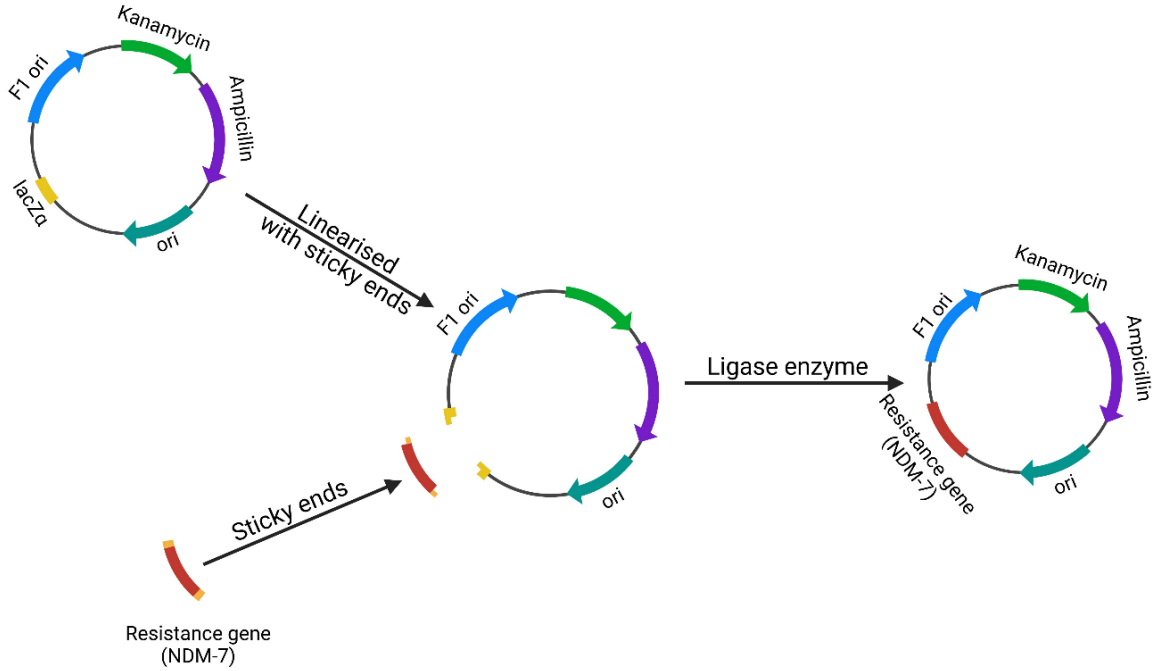

Figure 3.2 Illustration of plasmid modification via gene insertion. *Theoretical process of modifying a plasmid to include the gene (NDM-7 resistance gene). Plasmid pCR2.1 initially carrying resistance genes for kanamycin and ampicillin, along with origins of replication (F1 ori and pUC ori), is linearised using restriction enzymes. The NDM-7 gene, which confers resistance to carbapenems, is then inserted into the plasmid at the site created by the restriction enzyme. The result is a recombinant plasmid containing a carbapenem resistance gene, which can then be used to study meropenem resistance mechanisms.*

To verify the metabolic impact of the NDM-7 gene, a control strain (meropenem-susceptible strain) carrying the pCR2.1 plasmid without the NDM-7 gene was constructed by introducing the pCR2.1 plasmid into the *E. coli* DH5α strain via heat shock transformation. Meropenem-susceptible control allowed a comparison between any metabolic changes specifically associated with presence of the NDM-7 gene and those caused by the presence of the pCR2.1 plasmid with its associated mutations. The meropenem-susceptible strain (S) without the NDM-7 served as a reference for distinguishing the metabolic effects related to carbapenem resistant versus the impact of plasmid.

3.2.1.1 Stabilisation and verification of plasmid integration

Transformation was performed in this study to introduce the desired plasmid and gene into bacterial cells.[268] Due to DNA being negatively charged it cannot cross the cell membrane under normal conditions and a heat shock process was used to facilitate DNA uptake.[269] During the heat shock process, the rapid increase in temperature created transient pores in the bacterial cell membrane.[270] The increased permeability of the cell membrane allows plasmid DNA to enter the bacterial cells.

During transformation, not all bacteria would have taken up the plasmid. To ensure that only bacteria containing the pCR2.1 plasmid were selected, the transformed cells (both meropenem-susceptible and meropenem-resistant strains) were grown on selective agar containing the antibiotic kanamycin.[271] Kanamycin agar ensured that only cells retaining the plasmid grew because the plasmid carries a kanamycin resistance gene, allowing transformed bacteria to survive in the presence of this antibiotic.

Next, verification of successful plasmid integration was performed and involved several stages. First, plasmid DNA was isolated using a plasmid miniprep kit.[272] A portion of the isolated plasmids was sent to Eurofins Genomics for Sanger sequencing using their TubeSeq Supreme service. Sanger sequencing involves the amplification of the target DNA region followed by the incorporation of labelled dideoxynucleotides, which terminate the DNA chain at specific points.[273] These fragments are then separated by capillary electrophoresis, and the DNA

sequence determined by reading the labelled nucleotide at each position.[274] The sequencing targets the region containing the NDM-7 gene, and confirmed the identity of the NDM-7 gene inserted in the meropenem-resistant bacterial strain. **Table 3.2** presents the sequencing results for both meropenem- susceptible (S) and meropenem-resistant (R) strain, confirming the presence of the NDM-7 gene in the resistant strain.

Table 3.2 Sequencing results of meropenem-susceptible plasmid (pCR2.10) and meropenem-resistant plasmid (pCR2.1 NDM-7). *Yellow highlight indicates* EcoRI *site. Red letters indicate NDM-7 gene.*

Meropenem-Susceptible (pCR2.1)	Meropenem-Resistant (pCR2.1 NDM-7)
TTAGGGCGAATGGGCCCTCTAGATGCATGCTCGAGCGG CCGCCAGTGTGATGGATATCTGCAGAATTCCAGCACAC TGGCGGCCGTTACTAGTGGATCCGAGCTCGGTACCAAG CTTGGCGTAATCATGGTCATAGCTGTTTCCTGTGTGAA ATTGTTATCCGCTCACAATTCCACACAACATACGAGCC GGAAGCATAAAGTGTAAAGCCTGGGGTGCCTAATGAGT GAGCTAACTCACATTAATTGCGTTGCGCTCACTGCCCGC TTTCCAGTCGGGAAACCTGTCGTGCCAGCTGCATTAAT GAATCGGCCAACGCGCGGGGAGAGGCGGTTTGCGTATT GGGCGCTCTTCCGCTTCCTCGCTCACTGACTCGCTGCGC TCGGTCGTTCGGCTGCGGCGAGCGGTATCAGCTCACTCA AAGGCGGTAATACGGTTATCCACAGAATCAGGGGATAA CGCAGGAAAGAACATGTGAGCAAAAGGCCAGCAAAAGG CCAGGAACCGTAAAAAGGCCGCGTTGCTGGCGTTTTTC CATAGGCTCCGCCCCCCTGACGAGCATCACAAAAATCGA CGCTCAAGTCAGAGGTGGCGAAACCCGACAGGACTATA AAGATACCAGGCGTTTCCCCCTGGAAGCTCCCTCGTGCG CTCTCCTGTTCCGACCCTGCCGCTTACCGGATACCTGTC CGCCTTTCTCCCTTCGGGAAGCGTGGCGCTTTCTCATAG CTCACGCTGTAGGTATCTCAGTTCGGTGTAGGTCGTTC GCTCCAAGCTGGGCTGTGTGCACGAACCCCCCGTTCAGC CCGACCGCTGCGCCTTATCCGGTAACTATCGTCTTGAGT CCAACCCGGTAAGACACGACTTATCGCCACTGGCAGCA GCCACTGGTAACAGGATTAGCAGAGCGAGGTATGTAGG CGGTGCTACAGAGTTCTTGAAGTGGTGGCCTAACTACG GCTACACTAGAAGAACAGTATTTGGTATCTGCGCTCTG CTGAAGCCAGTTACCTTCGGAAAAAGAGTTGGTAGCTC TTGATCCGGCAAACAAACCACCGCTGGTAGCGGTGGTT TTTTTGTTTGCAAGCAGCAGATTACGCGCAGAAAAAAA GGATCTCAGAAAGATCCTTTGATCTTTTCTACGGGGTC TGACGCTCAGTG	TTGGGGCGAATTGGGGCCCTCTAGATGCATGCTCGAGC GGCCGCCAGTGTGATGGATATCTGCAGAATTCGCCCTT CACCTCATGTTTGAATTCGCCCCATATTTTTGCTACAGT GAACCAAATTAAGATCATCTATTTACTAGGCCTCGCAT TTGCGGGGTTTTTAATGCTGAATAAAAGGAAAACTTGA TGGAATTGCCCAATATTATGCACCCGGTCGCGAAGCTG AGCACCGCATTAGCCGCTGCATTGATGCTGAGCGGGTG CATGCCCGGTGAAATCCGCCCGACGATTGGCCAGCAAA TGGAAACTGGCGACCAACGGTTTGGCGATCTGGTTTTC CGCCAGCTCGCACCGAATGTCTGGCAGCACACTTCCTAT CTCGACATGCCGGGTTTCGGGGCAGTCGCTTCCAACGGT TTGATCGTCAGGGATGGCGGCCGCGTGCTGGTGGTCGA TACCGCCTGGACCGATGACCAGACCGCCCAGATCCTCAA CTGGATCAAGCAGGAGATCAACCTGCCGGTCGCGCTGG CGGTGGTGACTCACGCGCATCAGGACAAGATGGGCGGT ATGAACGCGCTGCATGCGGCGGGGATTGCGACTTATGC CAATGCGTTGTCGAACCAGCTTGCCCCGCAAGAGGGGC TGGTTGCGGCGCAACACAGCCTGACTTTCGCCGCCAATG GCTGGGTCGAACCAGCAACCGCGCCCAACTTTGGCCCGC TCAAGGTATTTTACCCCGGCCCCGGCCACACCAGTGACA ATATCACCGTTGGGATCGACGGCACCGACATCGCTTTT GGTGGCTGCCTGATCAAGGACAGCAAGGCCAAGTCGCT CGGCAATCTCGGTGATGCCGACACTGAGCACTACGCCGC GTCAGCGCGCGCGTTTGGTGCGGCGTTCCCCAAGGCCAG CATGATCGTGATGAGCCATTCCGCCCCCGATAGCCGCGC CGCAATCACTCATACGGCCCGCATGGCCGACAAGCTGCG CTGAGCCATGGCTGACCACGTCACCCCAATCTGCCATCG CGCGATTTCGATGTGACAGAGAAGGGCGAATTCCAGCA CACTGGCGGCCGTTACTAGTGGATCCGAGCTCGGTACC AGCTTGATGCAAAGCTTGAGTATTCTATAGTGTCACTA AATAGCTGGCGAATCAGGGCATAGCTGTTTCCGGGTGA AATGTATCCG

Figure 3.3 shows the map of the meropenem-susceptible pCR2.1 plasmid, while **Figure 3.4** displays the map of the meropenem-resistant plasmid, where the NDM-7 gene was inserted in pCR2.1 plasmid to confer carbapenem resistance.

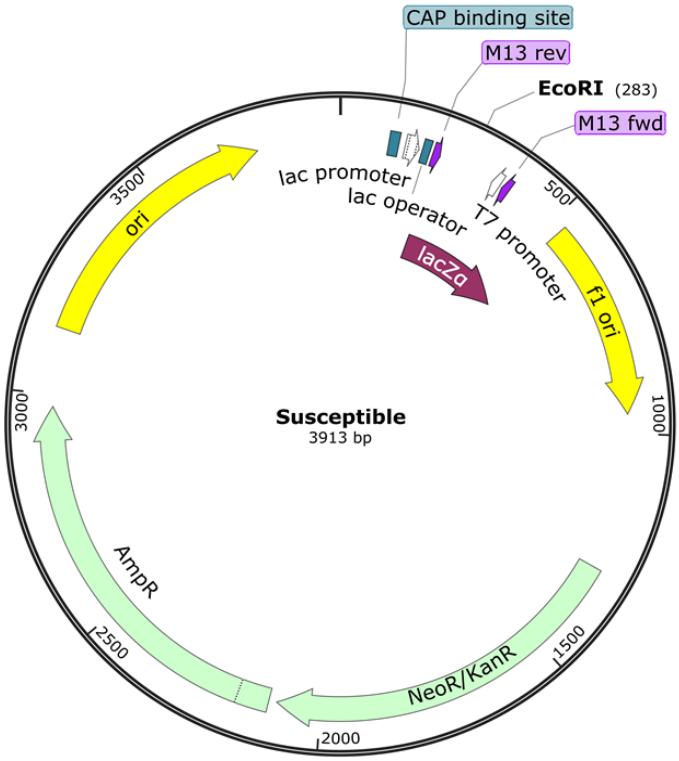

Figure 3.3 Plasmid map of meropenem-susceptible strain (pCR2.1). *The plasmid includes the lacZα gene region, used for blue-white screening, and the kanamycin resistance gene (Neo/KanR). The origins of replication (ori) include F1 ori and the pUC ori. Multiple restriction sites, such as* EcoRI*, are available for cloning and manipulation. Plasmid map created using SnapGene Viewer (version 7.2.1 GSL Biotech LLC).*

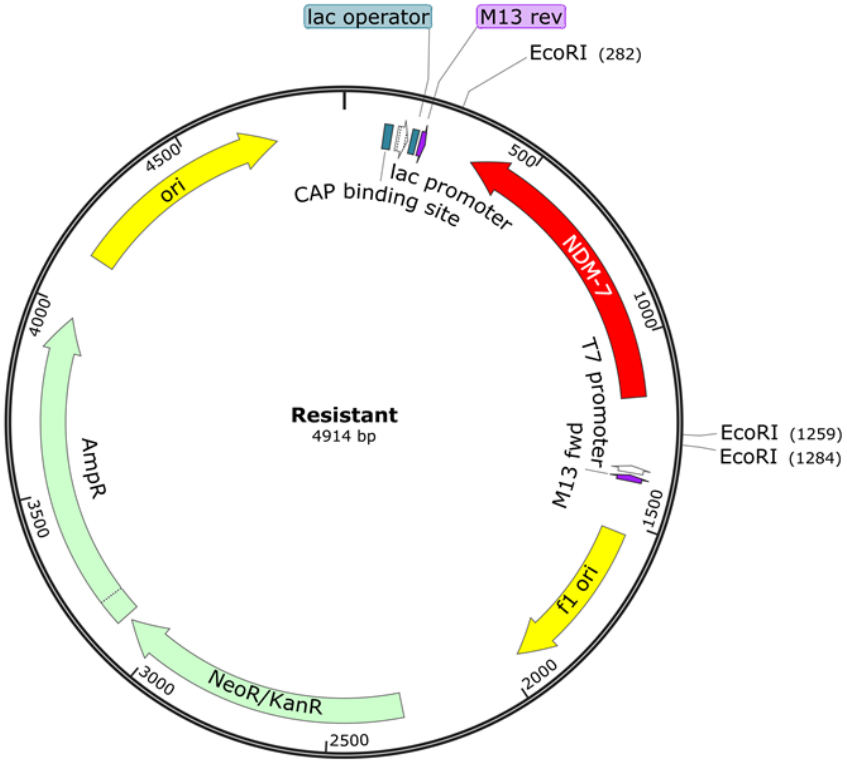

Figure 3.4 Plasmid map of meropenem-resistant strain (pCR2.1 NDM-7). *The NDM-7 gene responsible for carbapenem resistance is inserted into the plasmid. The insertion disrupts the lacZα gene, allowing for blue-white screening if needed. The plasmid retains kanamycin resistance and origins of replication (F1 ori and pUC ori). The map includes several restriction sites used for cloning and verification. Plasmid map created using SnapGene Viewer (version 7.2.1 GSL Biotech LLC).*

Following plasmid sequencing, the meropenem-susceptible plasmid sequence was analysed and compared to the commercial pCR2.1 sequence (purchased from Thermo Fisher) within the M13 forward and reverse primer regions. Using the alignment tools (SnapGene Viewer Version 7.2.1; GSL Biotech LLC) missing regions consistent with a restriction enzyme cut site were identified. Plasmid sequence alignment confirmed that *Eco*RI was used for linearisation of the pCR2.1 plasmid, consistent with the pCR2.1 preparation protocol. The analysis ensured that the cloning strategy has successfully followed the standard procedure for pCR2.1 plasmid preparation.

Next, the same analysis was conducted on the meropenem-resistant plasmid sequence to confirm the insertion of the NDM-7 gene. A search for *Eco*RI restriction sites within the meropenem-resistant plasmid sequence identified matching *Eco*RI cut sites, indicating that the NDM-7 gene was also restricted with *Eco*RI prior to its insertion. The full fragment of NDM-7, including the *Eco*RI cut site, was identified and found to match the expected sequence. The fragment was then incorporated into the commercial pCR2.1 backbone to construct the complete plasmid map for the resistant strain.

Following the construction of the plasmid map, the nucleotide sequence of the NDM-7 insert was translated into its corresponding protein sequence. The predicted protein sequence was then aligned with the literature reported sequence for NDM-7 metallo-β-lactamase.[256] The alignment revealed 100% similarity, confirming that the resistant plasmid encodes the correct NDM-7 protein, further verifying the integrity of the gene insert and its function in conferring antibiotic resistance.

The multi-step process of sequence verification, restriction site analysis, and protein sequence alignment ensured that the resistant plasmid not only contained the correct gene but also encoded a functional metallo- β-lactamase protein, which was essential for the experimental investigation into carbapenem resistance.

Next, PCR amplification was performed on the remaining isolated plasmid samples to further verify the presence of the inserted gene. Amplification targeted the lacZα region using M13

forward and reverse primers, where the NDM-7 was expected to be inserted, confirming both the presence and exact location of the gene within the plasmid.[275] To visualise the PCR product, gel electrophoresis (**Figure 3.5**) was conducted to assess the size of the amplified fragments, verifying the successful integration of the NDM-7 gene at the expected region.[276]

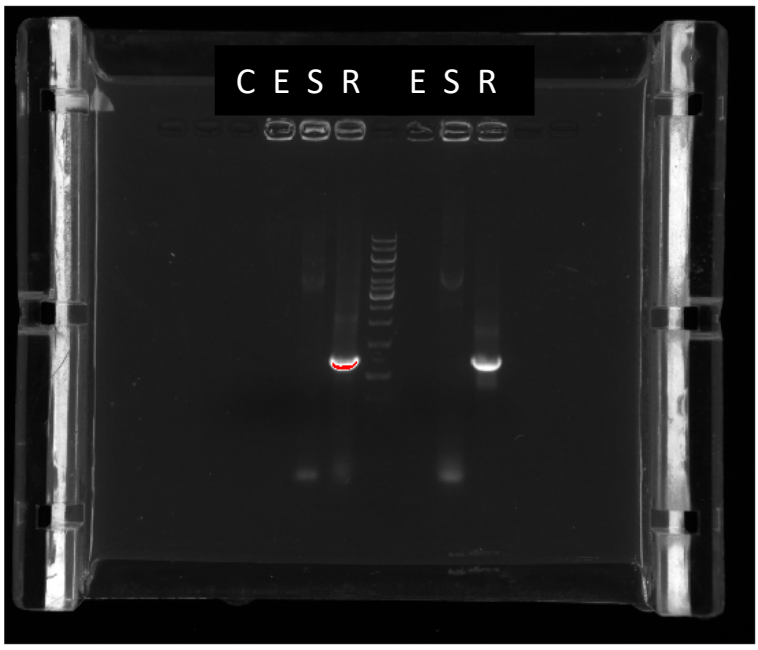

Figure 3.5 Agarose gel electrophoresis of plasmid PCR products. *Gel electrophoresis testing for the presence of an insert in the lacZα region in three* E. coli *strains: E (wild type), S (meropenem-susceptible), and R (meropenem-resistant). Lane C is control where no bacterial sample was added. Lanes E and S show no PCR product bands; conversely, lane R exhibits a prominent band between the DNA ladder bands of size 1000 and 750, confirming the desired presence of the resistance gene (NDM-7).*

The band in the 'R' lane in **Figure 3.5**, estimated to be around 800 base pairs (bp), represents the PCR product corresponding to the NDM-7 gene. The PCR product matches the expected size for the NDM-7 insert[140,256,277], providing evidence of its presence in the resistant strain. Conversely, no bands at similar sizes were observed in PCR products from E or S. However, faint smearing was also observed in both 'S' and 'R' lanes, which may have been the result of non-specific binding during PCR amplification or sample overloading.[278] The presence of a clear, distinct band in the resistant strain sample verified the successful insertion of the NDM-7 gene into the plasmid.

3.2.2 Validation of the biological model

The experimental bacterial models developed consisted of wild-type (E), meropenem-susceptible (S), and meropenem-resistant (R) *E. coli* strains. Next, these required careful validation to ensure suitability for investigating the metabolic consequences of carbapenem resistance mediated by NDM-7. The primary objective of developing these models was to be able to differentiate metabolic changes that could be specifically attributed to the presence of the NDM-7 gene and carbapenem resistance, while accounting for the presence of the pCR2.1 plasmid in both S and R strains.

A critical aspect of this model was the use of the pCR2.1 plasmid as a vector for the NDM-7 gene. Plasmids are essential for introducing foreign genes into bacterial systems, as bacteria do not readily take up foreign DNA without a carrier.[279,280] In this study, the pCR2.1 plasmid was used to carry the NDM-7 gene into the *E. coli* system, enabling the expression of carbapenem resistance. The plasmid also provided kanamycin and ampicillin resistance genes, which were crucial for selecting bacteria that successfully retained the plasmid throughout the study.[281,282]

It is important to acknowledge that the meropenem-susceptible strain (S) also therefore contains resistance genes for kanamycin and ampicillin, encoded within the pCR2.1 plasmid. These resistance markers served the critical function of maintaining selective pressure to ensure that the plasmid remained within the bacterial population.[283] Without this selective pressure, the bacteria would be liable to lose the plasmid over time, making it impossible to study the effects of the NDM-7 gene.[284]

While both kanamycin and ampicillin resistance genes are present in both the meropenem susceptible and resistant strains, they should not interfere with the specific function of NDM-7.[285,286] Kanamycin resistance is mediated by phosphorylation of the aminoglycoside antibiotic, and ampicillin resistance is provided through β-lactam hydrolysis.[287-289] Neither mechanism affects carbapenems such as meropenem, which are targeted specifically by NDM-7.[246,290]

To confirm the selective resistance conferred by NDM-7, antibiotic susceptibility tests were conducted. As expected, both the S and R strains demonstrated resistance to kanamycin, verifying the functionality of the pCR2.1 plasmid in both strains.[291] Only the R strain was capable of hydrolysing meropenem (**Figure 3.6**), confirmed by a meropenem hydrolysis assay (MHA). The assay measured the degradation of meropenem over time by monitoring absorbance at 300 nm, a wavelength corresponding to meropenem. A decrease in absorbance indicated enzymatic hydrolysis of meropenem, confirming R strain actively degraded the antibiotic. MHA demonstrated that the meropenem resistance phenotype, observed in the R strain, was specifically due to the presence of the NDM-7 gene, encoding a metallo-β-lactamase capable of hydrolysing carbapenems, including meropenem. In contrast, the susceptible (E and S) strains showed no significant changes in absorbance, indicating an inability to hydrolyse meropenem and, consequently, their susceptibility to the antibiotic.

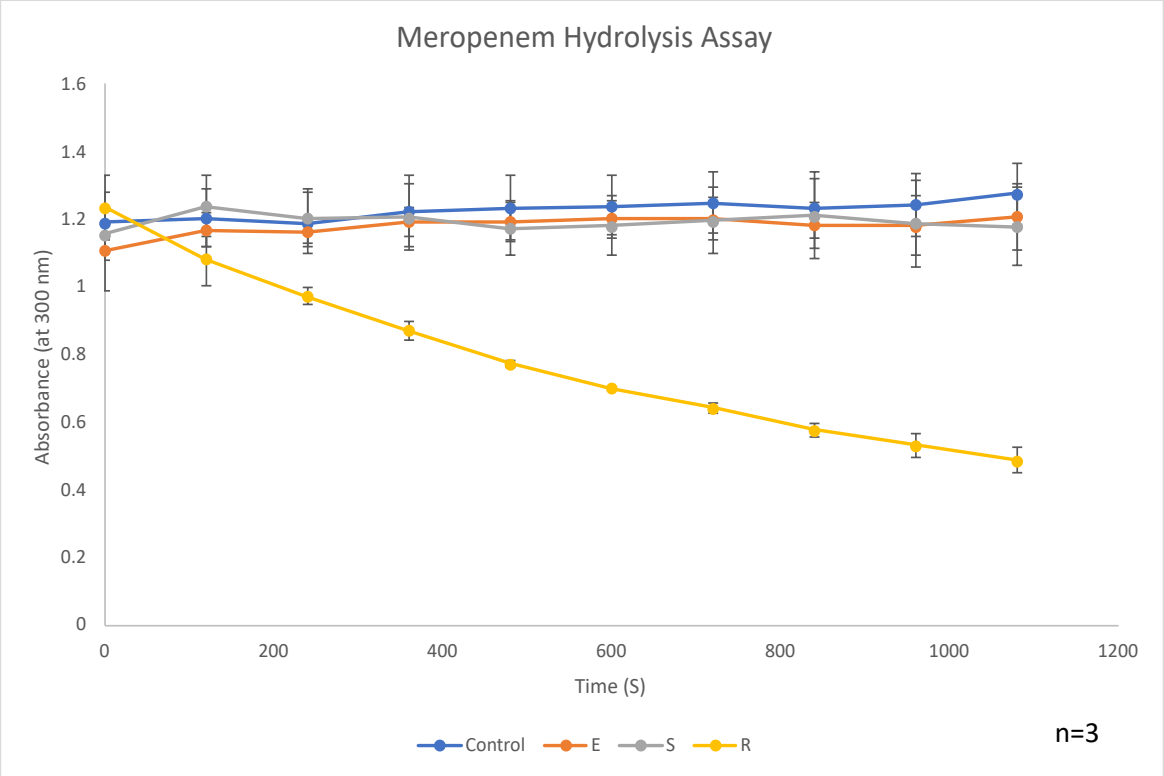

Figure 3.6 Meropenem hydrolysis assay. *The graph displays the results of a meropenem hydrolysis assay, comparing the absorbance over time for a control, a resistant strain (R), and susceptible strains (E and S). The resistant strain (R) demonstrates a decrease in absorbance, indicating its ability to hydrolyse meropenem, thus conferring resistance to the antibiotic. In contrast, the susceptible strains (E and S) and the control show little to no change in absorbance, indicating the inability to hydrolyse meropenem and thus, susceptibility to the antibiotic.*

By employing the same strain background for the wild-type, meropenem-susceptible, and meropenem-resistant conditions, any observed metabolic differences could be directly attributed to the presence or absence of the pCR2.1 plasmid and the NDM-7 gene, rather than to variations in the genetic background. The validation of the biological models confirmed that the metabolic changes observed in the R strain were specifically due to NDM-7 expression allowing a selective investigation of its metabolic impact under controlled conditions.[279,280,281,282]

3.2.3 Summary and discussion of *E. coli* model development and validation

The successful genetic modification of *E. coli* strains, specifically the introduction of the NDM-7 gene via the pCR2.1 plasmid, was confirmed through plasmid sequencing and gel electrophoresis of the PCR product. Kanamycin resistance, encoded by the pCR2.1 plasmid, were used as selection marker to verify plasmid uptake in both the meropenem-susceptible (S) and meropenem resistant (R) strains. Meropenem resistance, observed only in the R strain, was directly linked to the presence and functional expression of the NDM-7 gene, as demonstrated by the ability of the strain to hydrolyse meropenem. The functional validation of the NDM-7 gene confirmed its role as a metallo-β-lactamase conferring carbapenem resistance. Plasmid sequencing also confirmed the complete and correct insertion of the NDM-7 gene in the R strain, ensuring the genetic integrity of the construct. The resistant strain contained the full NDM-7 gene sequence, confirming that the metabolic changes in the R strain could be directly attributed to NDM-7 expression. The specificity was critical for isolating the influence of carbapenem resistance from other plasmid components.

Antibiotic susceptibility testing, meropenem hydrolysis assay, and plasmid sequencing provided robust validation of the biological model used. Kanamycin and ampicillin resistance markers confirmed stable plasmid retention in both S and R strains, while meropenem resistance confirmed NDM-7 activity. A clear differentiation between metabolic effects from general plasmid carriage (S) and those specifically due to NDM-7 expression (in R) could therefore be achieved.

The comparative metabolic analysis of the wild-type (E), meropenem-susceptible (S), and meropenem-resistant (R) strains will be used reported later in the chapter to provide insights into whether genetic modifications, particularly the acquisition of antibiotic resistance genes, impacted bacterial metabolism. The S strain, carrying the pCR2.1 plasmid alone, allows for the assessment of metabolic changes related to plasmid carriage and resistance to kanamycin and ampicillin. By comparing S and R strains, the additional metabolic adaptations imposed by NDM-7 expression will be investigated.

3.2.4 Conclusion

A model for investigating metabolic changes associated with antibiotic resistance, particularly meropenem resistance mediated by the NDM-7 gene was successfully developed. The resistant strain demonstrated functional expression of metallo-β-lactamase. The results from meropenem hydrolysis assay, support the conclusion that NDM-7 is solely responsible for conferring meropenem resistance in this strain.

The models enable subsequent metabolomic studies aimed at identifying metabolic vulnerabilities in resistant bacteria. In this section the validation of the genetic modifications introduced to create meropenem-susceptible and resistant strains were established.

The validity of the biological model used in this work was confirmed by the distinct mechanisms through which the resistance genes operate. The ampicillin resistance gene present in the pCR2.1 plasmid encodes a β-lactamase enzyme that hydrolyses the β-lactam ring of ampicillin, while the NDM-7 gene encodes a metallo-β-lactamase that hydrolysis the β-lactam ring of carbapenems.

3.3 Development of a sample preparation protocol for bacterial metabolomics using anion exchange chromatography-mass spectrometry

In order to accurately profile metabolic changes across the *E. coli* strains developed in the previous section, a robust metabolite extraction and analysis protocol needed to be developed and validated. Bacterial systems present unique challenges for metabolomics experiments due to their complex cell structure, distinct metabolome and metabolic pathways compared to

mammalian metabolism, and diverse responses to environmental stress, including antibiotic exposure. Therefore, it was important to find an appropriate and effective metabolomics approach and validate it for this study.

Although a number of specific methods for bacterial metabolomics have been published, they differ markedly in their coverage and, in particular, sample preparation approaches.[292-294] The aim of the current project was to be able to perform both discovery metabolomics (untargeted analysis) and functional analysis.[295] In addition, it was deemed important that coverage of metabolites found in central carbon metabolism (which tend to be highly polar or anionic) was robust and comprehensive to be able to report on changes to energy metabolism.[296] To meet these needs anion-exchange chromatography tandem mass spectrometry (AEC-MS/MS) was selected based on previous publications and experience in the group.[205,210] A method developed for mammalian cell metabolomics using AEC-MS had previously been published and shown to provide broad, reproducible quantitative coverage of metabolites and pathways found in primary metabolism.[205] It was therefore decided to test this analytical method and optimise the protocol for bacterial metabolomics prior to performing a comparative analysis of the three bacterial strains.

Sample preparation was deemed one of the most important aspects to investigate in the workflow. The metabolic and biochemical diversity of *E. coli* required a metabolite extraction approach which could efficiently capture a wide range of metabolites and the sample preparation published with the AEC-MS method was for adherent mammalian cells. Therefore, it was necessary for the development of an optimised extraction protocol to capture the true metabolic state of bacterial cells with minimum degradation or loss of key metabolites during the process. Differences in cell structure, growth environment, and metabolic response to stress, such as antibiotic exposure, were deemed important parameters to consider.

3.3.1 Exploration of metabolite extraction protocols

Three extraction protocols (labelled ‘Method A’, ‘Method B’, and ‘Method C’) were compared for their ability to recover metabolites with high reproducibility and efficiency, aiming to

determine the most effective method for the analysis of *E. coli*. These methods differed in their extraction solvent, and whether they collected intracellular vs. extracellular metabolites. The extracts were analysed using the untargeted AEC-MS method described in **Section 2.4**.[205]

Table 3.3 summarises the three different extraction protocols. Method A (see **Chapter 2 Section 2.3.1** for details) was selected due to its established efficiency in bacterial metabolomics. Campos and Zampieri (2019) highlighted its high extraction efficiency for small polar metabolites, compatibility with LC-MS, simplicity, and reproducibility. Method A extracts metabolites from the whole cell culture, including both intracellular and extracellular components.[228] Method B (see **Chapter 2 Section 2.3.2** for details) was chosen for its ability to separate intracellular and extracellular metabolites, allowing for a selective analysis of endogenous metabolism. Based on the protocol by Maifiah et al. (2017), bacterial cultures were centrifuged to isolate spent medium for extracellular metabolite analysis, while intracellular metabolites were extracted from the cell pellet separately.[229] Method C (see **Chapter 2 Section 2.3.3** for details) was adapted from mammalian cell metabolomics and tested for its applicability to bacterial samples. Similar to method B, Method C isolated intracellular metabolites.[210]

Table 3.3 Overview of the key differences between the three tested extraction protocols. Methods were evaluated using* E. coli *strains (E, S, and R).

	Method A	Method B	Method C
Quenching	Direct extraction	Dry ice/ethanol bath	Liquid nitrogen
Extraction solvent	50:50 methanol:acetonitrile (-20 °C)	1:3:1 chloroform:methanol: water (-80 °C)	80% methanol (cold, 4 °C)
Extraction	Incubation at -20 °C for 1 h, followed by centrifugation	Freeze-thaw lysis (liquid nitrogen and ice) followed by centrifugation	Ice bath incubation, centrifugation
PBS wash	No	Yes	Yes
Sample type	Whole-cell broth	Intracellular & extracellular metabolites isolated separately	Intracellular & extracellular metabolites isolated separately

Table 3.4 provides a comparative overview of the AEC-MS analysis of samples prepared using the three different extraction methods, including the number of compounds meeting the criteria for coefficient of variation (CV < 30%) and raw abundance (> 100).

Table 3.4 Comparison of metabolite detection and evaluation metrics between Method A, Method B and Method C. *The table compares the three methods based on various analytical metrics for metabolite detection, including the number of compounds meeting criteria for coefficient of variation (CV < 30%), abundance (> 100).*

	Method A	Method B		Method C	
		Intracellular	Extracellular	Intracellular	Extracellular
Total ion intensity	1.1×10^{9}	3.2×10^{8}	3.5×10^{8}	6.1×10^{7}	8.3×10^{8}
Peak Alignment score	98.7-99.3%	95.6-98.9%	90.8-98.9%	87.6-98.9%	74.4-98.7%
Total compound-features	23878	10398	11587	30970	13707
Abundance > 100	23144 (96.9%)†	9866 (94.9%)†	10905 (94.1%)†	26015 (84%)†	13570 (99%)†
Features with a CV < 30%	17945 (75%)‡	485 (4.7%)‡	4690 (40.4%)‡	12233 (39.5%)‡	11966 (87.3%)‡
Features with abundance > 100 and CV < 30%	17852 (192 identified)	309 (14 identified)	4675 (132 identified)	1574 (95 identified)	11268 (113 identified)

† Proportion of compounds with abundance > 100, indicating general metabolite abundance.
‡ Proportion of compounds with CV < 30%, indicating general metabolite reproducibility in the dataset.

Method B exhibited high variability in intracellular compound-feature recovery, with only 4.7% (485 compounds) meeting the CV < 30% threshold and 309 compounds also meeting abundance > 100. Indicating that compound-features were either present at low levels or displayed high variability. The high %CV and limited metabolite recovery potentially suggested incomplete cell lysis may have led to less efficient intracellular metabolite extraction.

Method C recovered a substantially higher number of intracellular compounds compared to Method B. Specifically, 39.5% of intracellular features met CV < 30% and 1,574 intracellular compounds met both CV < 30% and abundance > 100, indicating improved metabolite reproducibility compared to Method B, but still lower than Method A.

Overall, results indicated that Method A provided superior metabolite recovery and reproducibility, with 75% of detected compounds meeting the CV < 30% threshold, and 17852

meeting CV < 30% and abundance > 100 threshold but its ability to report on intracellular metabolic changes remained constrained by being mixed with extracellular metabolites.

To enhance intracellular metabolite recovery, mechanical cell lysis techniques were tested using Method A, which employed sonication and bead beating. Sonication was performed in an ice bath using a microtip sonicator at 40% amplitude, while bead beating involved vortexing pre-chilled samples at 500 rpm with glass beads. These methods were evaluated to determine whether additional mechanical disruption improved the reproducibility or extraction efficiency.

While these methods aimed to enhance cell lysis and improve metabolite recovery, they introduced several challenges. Both methods were associated with increased variability, as indicated by a lower percentage of metabolites meeting the CV < 30% threshold (**Table 3.5**). Heat generation was a shared potential issue. Both sonication and bead beating produced heat during the mechanical disruption process, which could accelerate metabolite degradation reactions such as oxidation.[297,298] Additionally, not all samples could be processed simultaneously using the sonicator, substantially reducing throughput. The variability in processing time and potential risk of overheating further complicated the use of these methods. Given these limitations, mechanical disruption was not pursued further for bacterial metabolite extraction.

Table 3.5 Comparison of mechanical cell lysis techniques for metabolite recovery*. The table compares the effectiveness of different mechanism cell lysis techniques, including sonication and bead beating, for enhancing metabolite recovery from bacterial samples. The evaluation criteria include general metabolite abundance (percentage of total compound-features with an abundance > 100) and general metabolite reproducibility (percentage of total compound-features with a CV < 30%). The results indicate the relative performance of each method in achieving consistent lysis and metabolite extraction.*

	Sonication	Bead beating
Total compound features	1607	52347
Compound-feature abundance (Percentage of total compound features with an abundance greater than 100)	72.6%	89.6%
Compound-features reproducibility (Percentage of total compound features with a CV less than 30%)	32.6%	4.9%

The metabolite signals from Method A reflected both bacterial metabolism and contributions from the culture medium.[299,300] 2TY broth, which contains yeast extract, introduced additional

metabolic signals that can interfere with metabolite detection. As shown in **Figure 3.7**, the total ion chromatogram (TIC) of the broth alone (without bacterial culture) exhibited substantial signal intensity compared to the blank (extraction solvent only), demonstrating that the medium itself contained extractable metabolites which would presumably obscure endogenous bacterial metabolic signatures. The signal from the medium may contribute lower variability in extracellular compound measurements, which was misleading since the dominant components originated from the broth rather than bacterial metabolic activity. As a result, changes in bacterial metabolism may have been masked, complicating data interpretation.

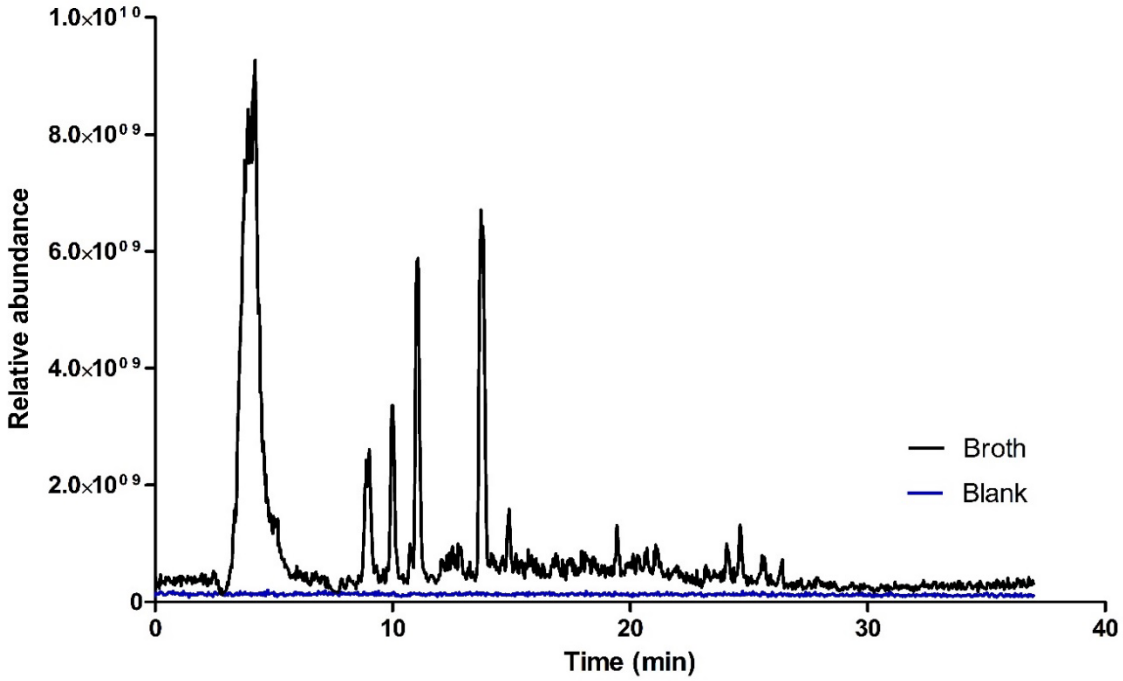

Figure 3.7 Chromatographic comparison of 2TY broth and blank (Solvent Control) in AEC-MS analysis. *The total ion chromatogram (TIC) chromatograph compares the relative metabolite abundance detected from 2TY broth (black line) and a blank sample (extracted solvent control, 50:50 MeOH:ACN, blue line) using AEC-MS. This demonstrates the substantial background noise contributed by the broth, highlighting the challenge of distinguishing bacterial metabolites of interest from broth-derived signals in metabolomics analysis.*

To reduce background interference from 2TY broth in extracellular metabolite analysis, an alternative growth medium, M9 minimal medium, was tested.[223] Unlike complex media such as 2TY, M9 minimal medium contains only essential nutrients, thereby eliminating extraneous metabolites from yeast extract or other rich components that could interfere with metabolite

detection. The use of M9 medium was expected to reduce background signal interference, enabling more accurate detection and identification of extracellular metabolites. However,

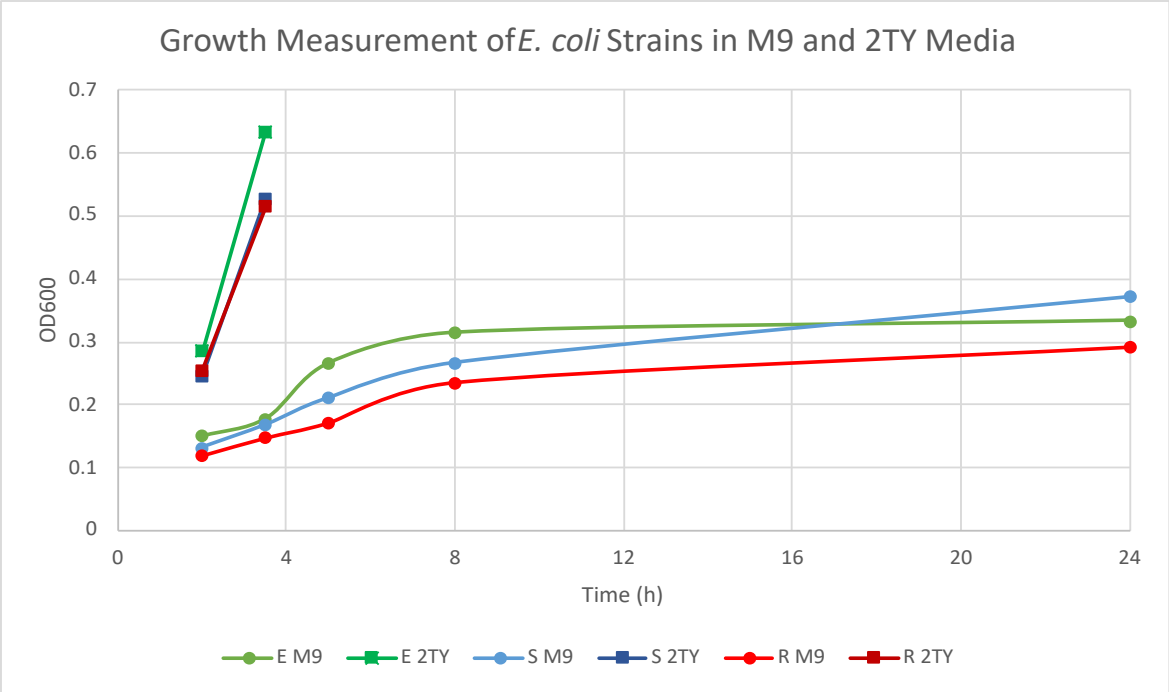

Figure 3.8 Growth measurement of* E. coli *Strains in M9 and 2TY media. *Optical density (OD_{600}) was measured to assess the growth of* E. coli *strains E, S, and R in M9 minimal media and 2TY rich media. Cells were initially grown overnight in 2TY, then subculture into the appropriate media (1 mL overnight culture in 19 mL M9 broth or 2TY broth). The cultures in M9 media showed insufficient growth (OD_{600} < 0.4) even after extended incubation, making them unsuitable for metabolomic experiments. In contrast, cultures in 2TY media achieved sufficient growth for further metabolomic analysis.*

E. coli cultures in M9 exhibited slower growth (OD_{600} < 0.4; **Figure 3.8**), leading to lower metabolite yields. Since nutrient availability also influences bacterial metabolism, M9 medium was deemed unsuitable. The reduced growth resulted in lower biomass, which directly impacted metabolite yields. Since metabolomic analysis relies on capturing metabolic activity at biologically relevant stages, such as the exponential growth phase, the inability of *E. coli* to reach this phase in M9 medium posed a substantial limitation.[301,302] Given this limitation, the use of supplemented M9 was ultimately rejected, as it would not provide a meaningful improvement over 2TY in terms of reducing media-derived metabolite signals.

Given these challenges, 2TY broth was retained for bacterial growth due to its ability to support rapid proliferation and achieve sufficient cell density. However, to minimise interference from broth-derived signals in metabolomics analyses, a PBS washing step was introduced. Cell washing involved resuspending the bacterial pellet in ice-cold PBS, followed by centrifugation

to separate the cells from any remaining broth or extracellular substances. Introducing this step helped to reduce media contamination without compromising bacterial cell integrity.

In addition to removing extracellular metabolites, washing bacterial pellets with ice-cold PBS also slowed down enzymatic activity and hence metabolic reactions, thereby preserving the intracellular metabolic profiles.[303] While organic solvents are commonly used for quenching metabolic activity, their simultaneous role in metabolite extraction poses challenges.[67,304,305] Solvent-based quenching can lead to metabolite leakage, particularly in bacteria exposed to antibiotics, as stress-induced membrane damage increases permeability.[306-308] To mitigate metabolite leakage an alternative approach was adopted. Samples were centrifuged at 4 °C to rapidly cool and separate cells from the medium, followed by gentle washing with ice-cold PBS. The method aimed to preserve bacterial cell integrity while minimising metabolite loss, ensuring a more reliable metabolomic analysis.

Initial efforts using Method A, with bacterial cultures washed and resuspended in PBS to maintain sample concentration, followed by 100 µL of the cell resuspension added to 240 µL of extraction solvent initially appeared promising. However, the protocol resulted in reduced metabolite abundance. To improve intracellular metabolite recovery, bacterial cultures were sampled at a higher density (OD_{600}=0.7). **Table 3.6** presents a comparison of metabolite recovery metrics at OD_{600} = 0.4 and OD_{600} = 0.7, including total ion intensity, alignment score, total compound-features, and reproducibility. Citrate abundance was specifically examined as a representative intracellular metabolite, given its well-documented role in central carbon metabolism. While a higher OD_{600} produced higher yield of intracellular metabolites, such density represented the middle of the log phase, where nutrient depletion begins, and cells may initiate stress responses.[227,309] Consequently, this phase was not ideal for capturing representative metabolic profiles, as nutrient scarcity and increased cell density could cause stress-related changes in metabolism. Thus, an OD_{600} of 0.4, representing the early log phase where nutrient availability is abundant and cells are in their optimal growth state, was chosen to avoid stress-induced variability in metabolite profiles.

Table 3.6 Comparison of metabolite recovery metrics at different bacterial cell densities (OD_{600}=0.4 vs. OD_{600}=0.7) using Method A with washing step. *The table summarises the key quality metrics for metabolite extraction, including total ion intensity, alignment score, total compound features, and citrate abundance, along with compound-feature abundance and reproducibility.*

	Method A_OD0.4_wash	Method A_OD0.7_wash
Total ion intensity	5.424e+007	2.145e+008
Alignment score	96.7-98.5	98.7-99.1
Total compound features	7083	6864
Citrate Max abundance	2368	28550
Compound-feature abundance (% total compound-features with an abundance >100)	23.6	90.4
Compound-feature reproducibility (% total compound-features with a CV < 30%)	34.8	34.25

Additionally, the PBS resuspension step introduced further complications and reduced the maximum theoretical yield of the extraction process. Recognising that the dilution of the cell pellet was unnecessary, the protocol was revised to enhance efficiency and recovery. Instead of resuspending the pellet after washing with ice-cold PBS, the PBS was removed, and 300 µL of extraction solvent was added directly on the cell pellet (**Figure 3.9**). The modification eliminated an unnecessary dilution step, allowing the extraction solvent to come into direct contact with a higher concentration of cellular material. As a result, this adjustment substantially improved the metabolite recovery and enhanced the overall efficiency of the extraction process, ensuring the preservation of intracellular metabolites for subsequent analysis.

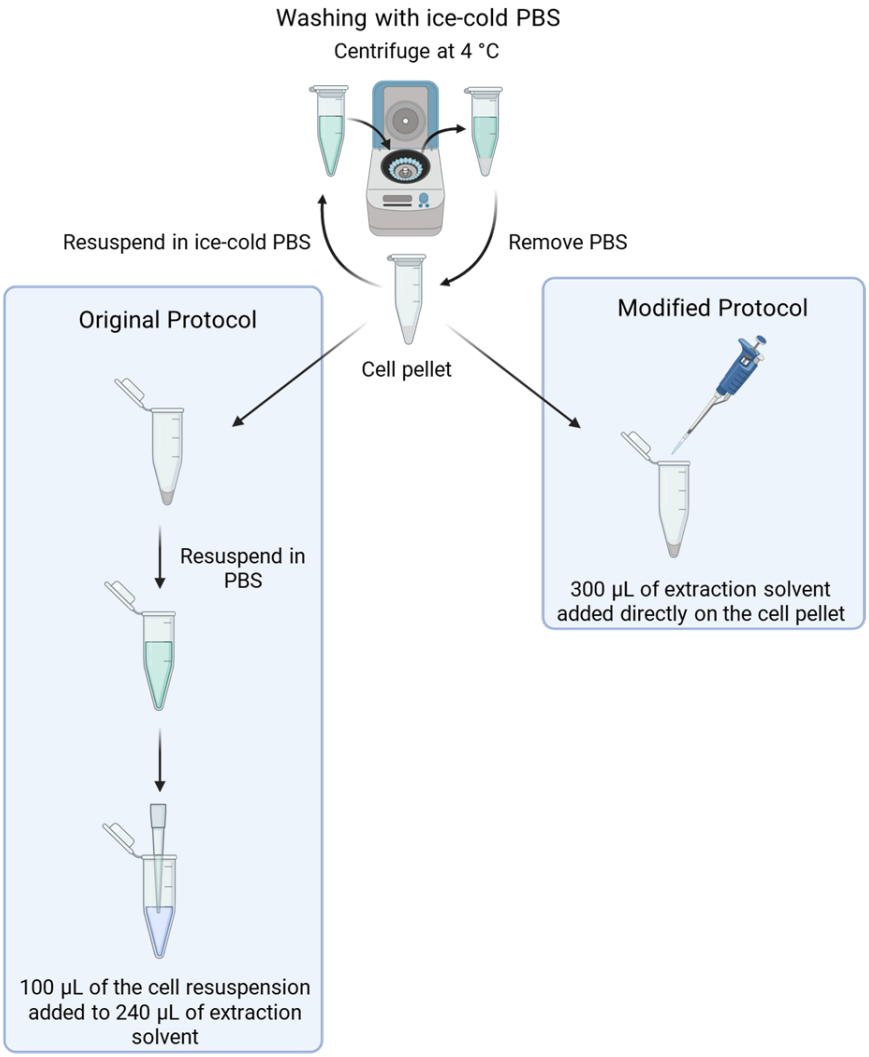

Figure 3.9 Illustration of the original and modified extraction protocols. *The original protocol involves resuspending the cell pellet in PBS before adding the extraction solvent, introducing an unnecessary dilution step. The modified protocol eliminates this step by directly adding the extraction solvent to the cell pellet, optimising metabolite recovery and enhancing extraction efficiency.*

3.3.2 Assessing the impact of PBS washing on intracellular metabolite integrity

The integrity of intracellular metabolite extraction was crucial for accurately assessing the metabolic state of *E. coli* cells. In this study, intracellular metabolites were extracted following a PBS washing step. However, the potential for metabolite leakage during this washing step, due to osmotic stress or mechanical forces such as centrifugation, need to be investigated.

To evaluate the impact of the PBS washing step on intracellular metabolite leakage, samples were collected from different stages of the protocol, including: (i) the broth medium, (ii) PBS washes, and (iii) intracellular extracts (Pilot_E_control; bacterial group). Additionally, controls consisting of PBS only, as well as broth samples added to PBS, and a full protocol using only

broth (negative control), were included to control for any potential contamination or baseline metabolites that could arise from the buffer itself. For the negative control (broth wash and broth extraction), broth was spun down to remove the supernatant (media), and the remaining residue was washed and processed using the same protocol applied to the cell samples. The PBS wash ensured that any contribution from the broth medium itself, and not from cells, could be accounted for.

To further analyse potential metabolite leakage, compounds with an average signal intensity of less than 100 were removed from the dataset for each sample group. The threshold was selected to minimise the inclusion of low-abundance features, which are more likely to represent background signals or have higher experimental variability. While there was a possibility that leaked metabolites could be removed using this filter, prioritising compounds with higher signal intensities would provide a more reliable assessment. The filtered lists, comprising both identified and unidentified compound-features, were used to evaluate shared and unique metabolites between sample groups, providing a comprehensive evaluation of the integrity of intracellular metabolite extraction.

A PCA plot (**Figure 3.10**) was employed to compare the metabolic profiles across the different sample groups, including the intracellular extracts, the PBS washes and the control samples. The PCA score plot demonstrated distinct clustering between intracellular metabolites (Pilot E control extracted) and those found in the PBS wash and broth controls. The observed clustering patterns suggests that the PBS washing step did not lead to substantial leakage of intracellular metabolites into the wash buffer. The intracellular samples exhibited a metabolite profile that was largely preserved, reinforcing the effectiveness of the washing step in maintaining cell integrity.

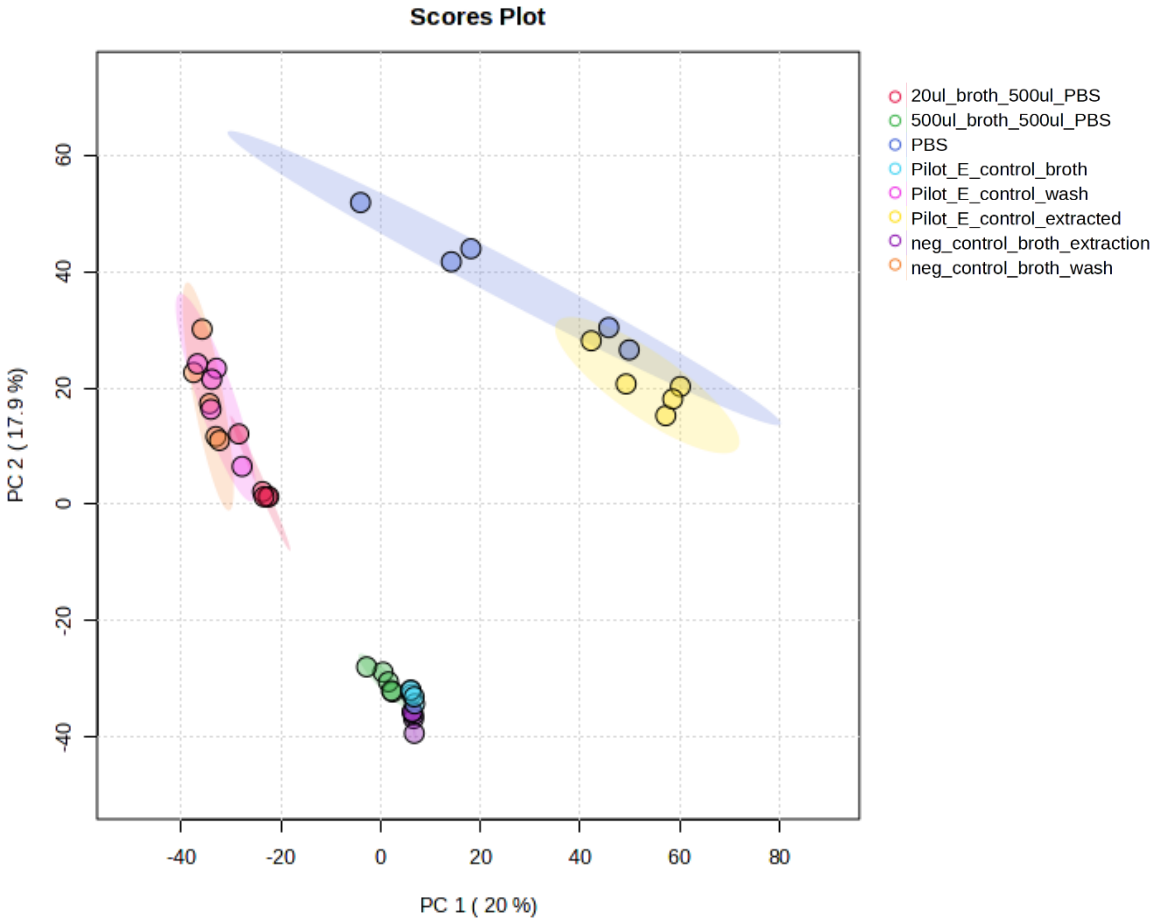

Figure 3.10 PCA score plot of metabolite profiles from intracellular extracts, PBS washes, and control groups. *PCA plot highlighting the separation of metabolite profiles across various sample groups: 20 µL broth with 500 µL PBS, 500 µL broth with 500 µL PBS, PBS only, Pilot E control broth, Pilot E control wash, Pilot E control intracellular extract, and negative controls (broth and broth wash). PC1 and PC2 explain 20% and 17.9% of the variance, respectively.*

Interestingly, the plot also shows that the 500 µL Broth 500 µL PBS group, Pilot E control broth, and the negative control broth cluster closely together, suggesting metabolite profiles of these groups are primarily broth (media). Whereas the 20 µL Broth 500 µL PBS group, Pilot E control wash, and the negative control broth wash cluster together, indicating a different metabolite profile for these groups, potentially mixture of PBS and residual broth. The clear separation across groups further supports the conclusion that the washing process successfully removed extracellular components without compromising intracellular metabolite integrity.

To quantify potential metabolite overlap between sample types, Venn diagrams (**Figure 3.11** and **Figure 3.12**) were created to highlight the shared and unique metabolites among the broth, PBS wash, and intracellular extracts. In **Figure 3.11**, it is evident that only a small fraction (approximately 1%) of metabolites are shared between the intracellular fraction and the PBS wash (0% overlap when only identified metabolites were considered), supporting the conclusion that the PBS wash step did not considerably compromise the integrity of the intracellular metabolite pool. Similarly, the Venn diagram comparing PBS, wash, and intracellular samples (**Figure 3.12**) indicated that intracellular metabolites remain distinct from those present in the PBS wash and broth samples.

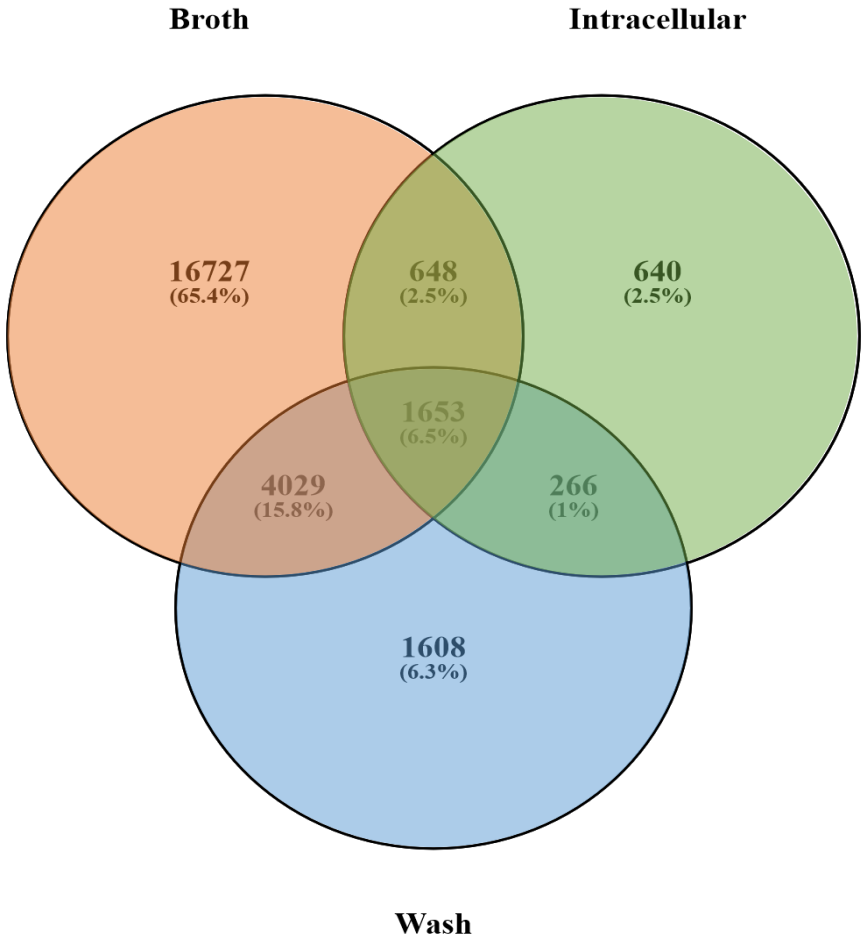

Figure 3.11 Venn diagram comparing unique and shared metabolites across broth, wash, and intracellular samples*. Metabolites were filtered to include only those with an average abundance greater than 100 across samples. The majority of metabolites were unique to the broth sample (65.4%), while the intracellular and wash fractions had fewer unique metabolites (2.5% and 6.3%, respectively). A small fraction of metabolites (6.5%) was shared among all three groups.*

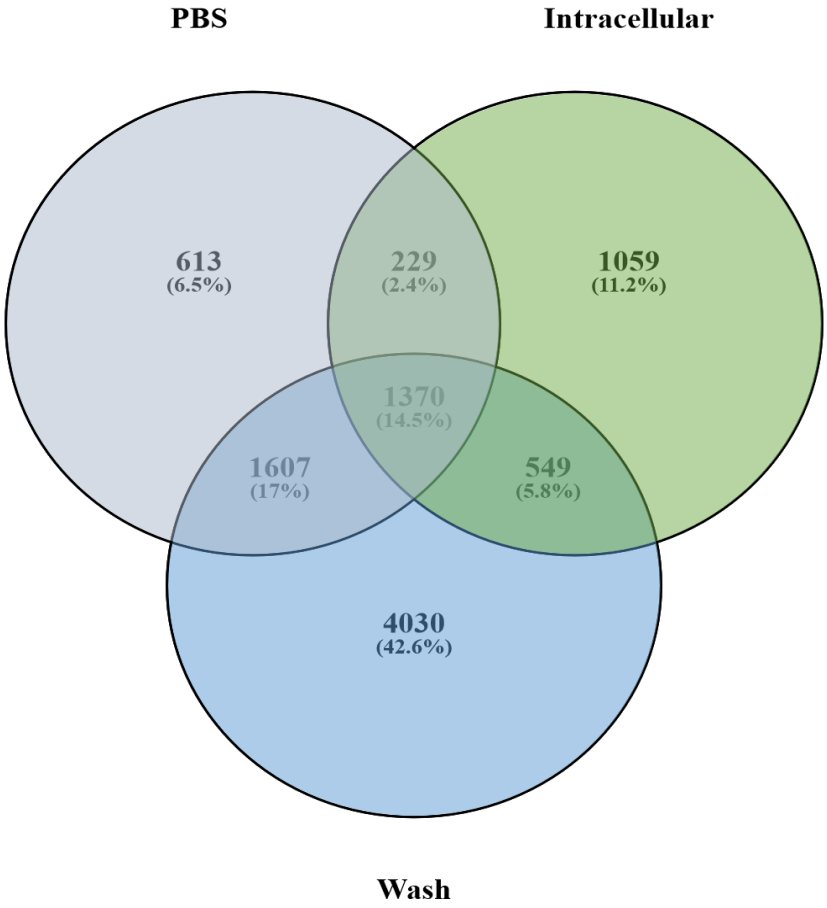

Figure 3.12 Venn diagram of metabolite distribution across PBS, wash, and intracellular extracts. *Metabolites were filtered to include only those with an average abundance greater than 100 across samples. Each circle represents a unique list of metabolites from one sample type: PBS (grey), wash (blue), and intracellular extracts (green). The overlapping sections represent metabolites shared between sample types. Notably, only a small fraction (14.5%) of metabolites are shared between all three groups, with the majority of intracellular metabolites being distinct from those found in PBS and wash samples. This indicates that the PBS washing step does not lead to substantial leakage of intracellular metabolites.*

These results suggest that the washing process with PBS, conducted at 4 °C, did not induce substantial metabolite leakage from the bacterial cells. Moreover, the controls, including the broth-PBS mix, demonstrated that residual media components were effectively removed through washing, without introducing extraneous metabolites into the intracellular extracts. Therefore, the PBS washing step was considered a useful and reliable component of the sample preparation workflow, preserving intracellular metabolites for selective endogenous metabolomic analysis. The inclusion of negative controls such as the PBS-only control and broth-wash control helped confirm the absence of contamination and background metabolites within the washing buffer.

3.3.3 Optimisation and validation of the metabolite extraction protocol

Metabolite extraction protocol optimisation led to the development of a robust method for intracellular metabolite extraction from *E. coli*. Validation of the protocol was performed using general reference points for assessing the quality of the metabolomics data based on multiple criteria (**Table 3.7**). In addition to untargeted metrics to compare the extraction protocols including the number of compound-features, the proportion and number with a %CV < 30, compound-feature intensity etc, a targeted approach was simultaneously employed focussing on citrate. To assess extraction efficiency and compare data quality across the extraction approaches investigated, citrate was selected as a target metabolite due to its role as a representative carboxylic acid measured by the AEC-MS method. Citrate is a key intermediate in the TCA cycle, making it relevant for bacterial metabolism studies, and its well-defined retention time and ionisation properties facilitate reliable detection and quantification. The 'optimised protocol' demonstrated superior performance in terms of total ion intensity, alignment score, and general metabolite abundance and reproducibility.

Table 3.7 Comparison of metabolomics data quality and citrate detection across different extraction protocol. *The table summarises the performance of various intracellular metabolite extraction protocols, including Method A, Method B, Method C, sonication modification of Method A, and bead beating on Method A. Key indicators such as total ion intensity, alignment score, compound features, and citrate-related metrics are compared to evaluate the efficiency and reproducibility of each method. The optimised protocol demonstrates superior metabolite recovery and data quality.*

	Method A	Method B	Method C	Sonication (Method A)	Bead beatings (Method A)	Optimised protocol
Total ion intensity	5.4×10^{7}	3.2×10^{8}	6.3×10^{7}	6.6×10^{7}	2.3×10^{9}	4.9×10^{8}
Alignment score	96.7-98.5%	95.6-98.8%	87.6-98.9%	98.8-99.5%	93.1-97.7%	98.1-99.0%
Total compound features	7083	11587	3970	1607	52347	6818
Citrate max abundance	2368	9192	6001	2705	47330	102895
Retention time for citrate	15.28 min	15.27 min	15.23 min	15.28 min	14.93 min	15.26 min
Peak width for citrate	0.62 min	0.75 min	0.59 min	0.68 min	0.41 min	0.47 min
Citrate ppm mass accuracy	-1.63 ppm	1.54 ppm	-0.82 ppm	-1.62 ppm	1.18 ppm	0.65 ppm
Citrate isotope accuracy	98.77%	99.17%	81.4%	97.83%	96.94%	99.12%
Citrate CV%	16.97%	48.04%	22.42%	12.78%	47.1%	14.07%
General metabolite abundance	90.4%	94.9%	84%	72.6%	89.6%	97.8%
General metabolite reproducibility	34.8%	4.7%	39.5%	32.6%	4.9%	41.5%

The results indicated that Method A performed the best overall compared to Method B, the mammalian cell extraction adaptation (Method C), sonication (on Method A), and bead beating (modification of Method A). Method A consistently demonstrated superior metabolite recovery, reproducibility, and data quality. In contrast, Method B exhibited low reproducibility, as reflected in the high variability.[310] The variability suggested that intracellular metabolites were not being efficiently extracted, leading to lower quality metabolite recovery.[311] Sonication and bead beating, while improving cell disruption, introduced variability, leading to decreased reproducibility and metabolite integrity.

Method C demonstrated lower compatibility with bacterial systems, as evidence by lower general metabolite abundance, a greater range in alignment scores, and fewer total compound-features. A wider alignment score range indicates variability in peak detection between samples, which could indicate inconsistent metabolite recovery and lower reproducibility. However, alignment scores must be interpreted carefully, as a lower score within an experimental group suggests technical inconsistency, whereas a lower score between experimental groups may reflect true metabolic differences. Fewer detected features suggest that Method C was less efficient at extracting intracellular metabolites. The findings highlighted a limitation of Method C (adapted from the mammalian extraction protocol) for bacterial metabolomics.

Based on these comparisons, the final protocol was developed by streamlining the extraction process and focusing on direct extraction from the cell pellet, eliminating a dilution step. The approach maximised metabolite recovery while minimising loss and contamination.

The optimised protocol is illustrated in **Figure 3.13**. The protocol was then used in all subsequent metabolomic investigation reported (unless otherwise stated) for comprehensive analysis of bacterial metabolites.

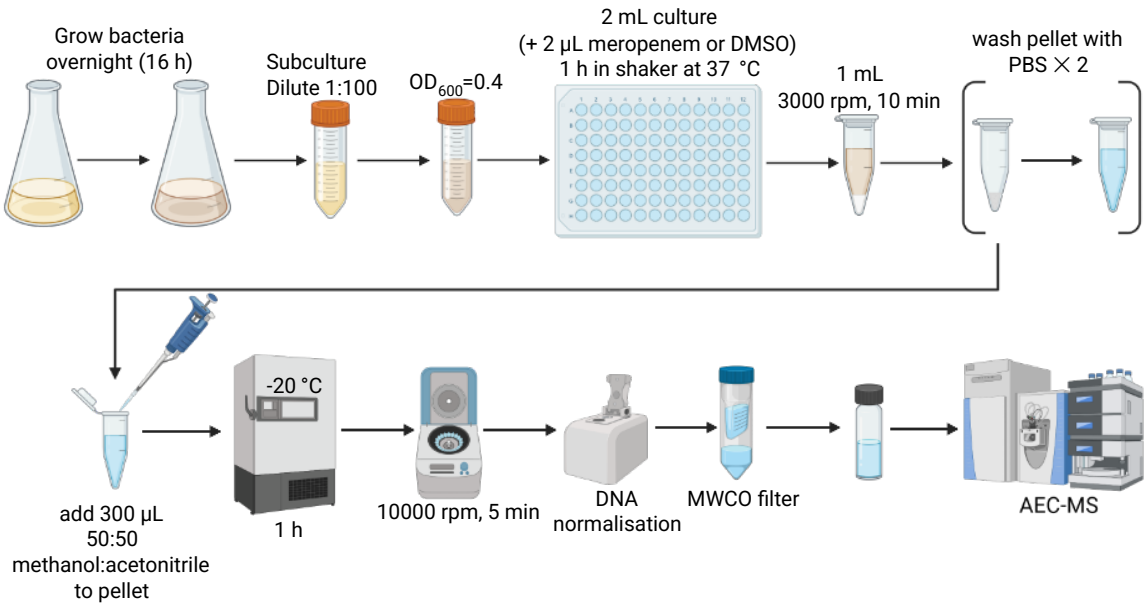

Figure 3.13 Final protocol for bacterial metabolite extraction and sample preparation for AEC-MS analysis. *Final protocol used for the extraction and analysis of intracellular metabolites from* E. coli *strains. Bacterial were grown overnight, followed by a 1:100 subculture and incubation to an* OD_{600} *of 0.4. Cultures were then treated with meropenem for 1 hour at 37 °C. After treatment, the cultures were centrifuged at 3000 rpm for 10 minutes at 4 °C, and the resulting cell pellet was washed twice with ice-cold PBS to remove residual medium and drug compounds. The pellet was resuspended in 300 µL of 50:50 MeOH:ACN, pre-cooled to -20 °C, and incubated for 1 hour at -20 °C for metabolite extraction. The sample was centrifuged at 10,000 rpm for 5 minutes at 4 °C, and the DNA concentration of the supernatant was normalised. The sample was processed through MWCO filters prior to AEC-MS analysis.*

3.3.4 Discussion

A number of different extraction protocols and their variables were evaluated to identify the most suitable approach for bacterial metabolomics by AEC-MS. Currently, the extraction of polar metabolites from bacteria for AEC-MS remains under-reported in the literature, with no standardised method widely adopted, making this optimisation an important contribution to the field.[312,313] Method A, selected for its simplicity and compatibility with downstream analysis techniques, initially provided consistent results with relatively low noise and high reproducibility, but was limited to extracellular metabolites including those derived from the media.

In contrast, Method B, which had capability to distinguish between intracellular and extracellular metabolites, revealed shortcomings in intracellular metabolite recovery. The rigidity of the bacterial cell wall likely hindered efficient lysis, as reflected by the lower number of metabolites meeting reproducibility and abundance criteria. The lysis inefficiency ultimately

limited its utility for bacterial metabolomics, despite the initial appeal of fractionating the intracellular and extracellular metabolomes.

The attempt to improve cell lysis using mechanical disruption techniques, such as sonication and bead beating, introduced new challenges, including heat generation, increased sample variability, and risk of cross-contamination. While these methods improved lysis, the inconsistency they introduced rendered them unsuitable for the precise and reproducible extraction required for comprehensive metabolomic analysis.

A persistent challenge was the interference caused by the nutrient-rich 2TY broth. Background signals from the broth overshadowed bacterial metabolites, complicating the analysis. Control samples confirmed that substantial interference originated from the broth, which prompted an exploration of M9 minimal medium. However, slower growth rates and lower cell densities in M9 medium raised concerns about insufficient metabolite yields for analysis, as cells did not consistently reach the log phase required for optimal extraction.

To mitigate broth interference, a key adaptation was the introduction of a PBS washing step. The modification successfully removed extracellular components without compromising cell integrity, allowing intracellular metabolites to be preserved. The quenching effect of ice-cold PBS washing slowed enzymatic activity, ensuring that metabolic reactions were halted effectively.

Efforts to optimise the protocol also led to the removal of an unnecessary resuspension step, which had previously diluted the sample and reduced metabolite recovery. By directly adding extraction solvent to the washed cell pellet, the revised protocol substantially improved metabolite yields and reduced variability, particularly in the intracellular fraction.

Finally, the PBS washing step was validated through Venn diagrams, and PCA analyses, all of which confirmed minimal overlap between intracellular metabolites and PBS-washed or broth fractions. The result demonstrated that the PBS washing did not lead to considerable leakage of intracellular metabolites, reinforcing the robustness of the protocol.

3.3.5 Conclusions

A reproducible and robust protocol for intracellular metabolite extraction from bacteria was developed which was compatible with untargeted AEC-MS analysis. Among the methods evaluated, Method A, using the 50:50 methanol/acetonitrile as extraction solvent, demonstrated clear superiority in metabolite recovery and reproducibility. With the added benefit of minimal background noise when combined with a PBS washing step to remove extracellular components, further enhanced the clarity and reliability of the extracted metabolite profiles.

The systematic optimisation of the protocol, including the direct extraction from cell pellets and elimination of unnecessary resuspension steps, has resulted in a streamlined workflow that maximises the integrity and yield of intracellular metabolites. The workflow was further validated through comprehensive analyses, demonstrating minimal cross-contamination between intracellular and extracellular fractions, and preserving the metabolic state of *E. coli* cells without inducing stress-related artifacts.

The optimised metabolomics workflow not only ensured the reliable profiling of intracellular metabolic changes but also provided a protocol for future studies, including the exploration of metabolic changes in drug-resistant bacterial strains. The development work in this section highlighted the critical role of tailored metabolite extraction protocols for the analysis of bacterial systems, where both cell structure and media interference present major challenges. Ultimately, this comparative study contributes to the development of standardised approaches for bacterial metabolomics, offering valuable insights into the important variables associated with highly polar and ionic metabolites extractions.

3.4 Comparative metabolic profiling of *E. coli* strains

Metabolism plays a central role in how bacteria adapt to new environments and proliferate.[314,315] Investigating whether the presence of AMR affects metabolic processes therefore has the potential to reveal key insights into how resistant strains function and potentially expose new targets for therapeutic intervention.[58,154,316,317]

To investigate whether altered metabolic processes were associated with NDM-7 expression in *E. coli*, the three bacterial strains (wild-type (E), the susceptible strain carrying the pCR2.1 plasmid (susceptible to meropenem, S), and the resistant strain carrying the pCR2.1 plasmid containing the metallo-β-lactamase gene NDM-7 (resistant to meropenem, R)) were compared using the adapted protocol for untargeted metabolic profiling developed and reported previously in this chapter. Specifically, it was hypothesised that comparison of the three strains would show how the presence of the pCR2.1 plasmid (ampicillin and kanamycin resistant) and the NDM-7 gene impacted metabolite abundances profiled by AEC-MS, if at all, in the absence of antibiotics. It was assumed that any differences would be due to the expression of the NDM-7 gene conferring resistance. Any such differences could potentially be exploited by targeted therapeutic approaches in resistant bacteria.

Untargeted metabolomics was applied to provide a comprehensive analysis of metabolite profiles across the three different *E. coli* strains, providing the potential for hypothesis-generating observations at the metabolome level. Statistical analyses, including univariate tests (such as t tests and ANOVA) and multivariate analyses (including PCA and PLS-DA), were used to identify significantly altered metabolites and metabolite abundance patterns associated with resistance.

3.4.1 Metabolic profiling of wild-type, susceptible, and resistant *E. coli* strains

The three *E. coli* strains – wild-type (E), meropenem-susceptible (S), and meropenem-resistant (R) – were grown in parallel under identical bacterial culture conditions to minimise variability. Five biological replicates for each strain were prepared, and cultures were harvested using the adapted sampling protocol optimised for intracellular metabolite extraction. Metabolite extraction was performed with the 50:50 methanol/acetonitrile solvent, and samples were normalised based on total cell biomass (measured as OD_{600} before treatment) and DNA concentration during AEC-MS sample preparation. The prepared samples were subjected to untargeted metabolic profiling AEC-MS as described in the Methods section (**2.4 Anion exchange chromatography-mass spectrometry method**). Individual raw data files were

processed (See **Sections 2.5.1-2.5.3**) to generate a data table of compound features and chromatographic peak areas for downstream statistical analysis.

Metabolites were identified based on established criteria for metabolomics. Using authentic standards and an in-house database containing retention times and MS/MS spectra, 136 metabolites were identified, including those confirmed to Level 1 (high confidence with authentic standards) and Level 2 (putative annotation based on spectral similarity to database entries).[318,319]

To evaluate data quality, data processing involved median normalisation, log transformation, and Pareto scaling, minimising technical variability while preserving biological differences. After scaling and transformation, the data followed a more normal distribution, making it suitable for multivariate analysis such as PCA and PLS-DA. A Kernel plot (**Appendix II Figure II.**) was used to confirm and illustrate the change in distribution.

A PCA scores plot was generated to visualise metabolic variance between the strains and to check for sample outliers (**Figure 3.14**). The PCA plot revealed a distinct separation between the three strains, with no major sample outliers. Wild-type (E) samples formed a distinct cluster, separate from the susceptible (S) and resistant (R) strains, which suggest a strong metabolic differences between the wild-type and modified strains. Notably, the metabolic profiles of the meropenem-susceptible (S) and meropenem-resistant (R) strains are more closely aligned, indicating that their metabolic profiles are more similar than to the wild-type (E). The clustering pattern is consistent with the introduction of the pCR2.1 plasmid in both the S and R strains, reflecting metabolic changes are associated with these genetic modifications in the absence of antibiotic pressure.

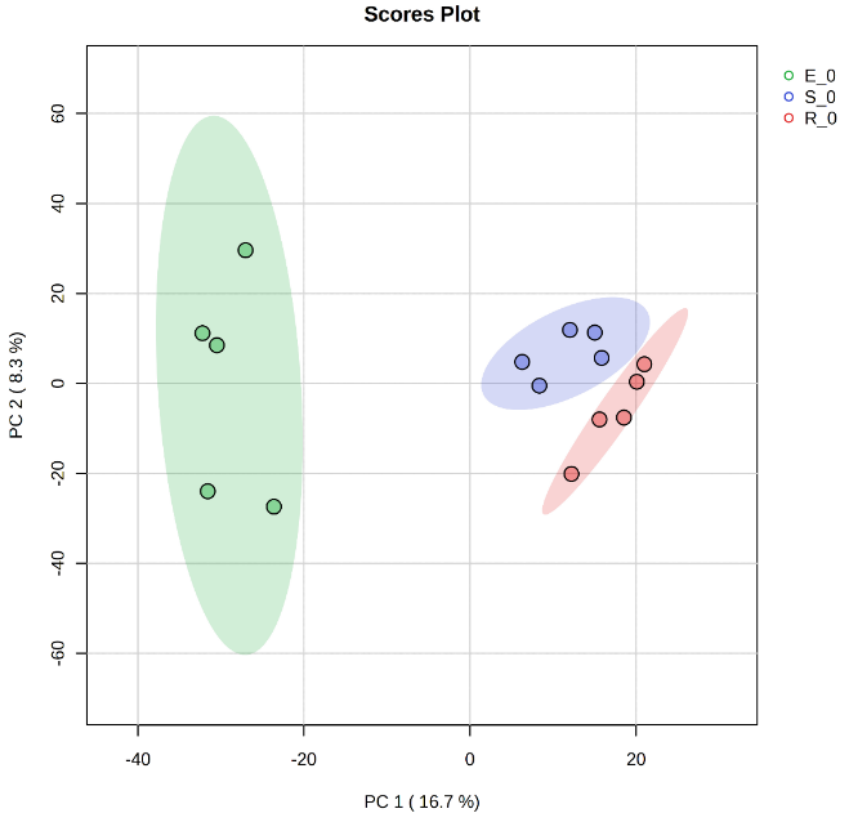

Figure 3.14 PCA scores plot illustrating metabolic distinctions among wild-type (E), meropenem-susceptible (S), and meropenem-resistant (R)* E. coli *strains. *The plot shows the separation of metabolic profiles across the three strains. Wild-type (E) samples (green) form a distinct cluster, while meropenem-susceptible (S) samples (blue) and meropenem-resistant (R)samples (red) show some overlap, indicating similar metabolic profiles. Five biological replicates are shown for each sample group (n=5). PC1 and PC2 explain 16.7% and 8.3% of the variance, respectively.*

In order to test whether samples were well-normalised and the differences indicated by the PCA plot were the result of endogenous metabolic changes and not class bias resulting from sample handling or analysis, an un-clustered heatmap was created from the full dataset (**Figure 3.15**). It was assumed that endogenous changes in metabolism would be manifest in a minority of metabolite abundance changes and that most metabolite abundances would not be altered, and this was confirmed by the heatmap. No significant inter or intra-class variation was visible in the heatmap confirming samples and groups were effectively normalised.

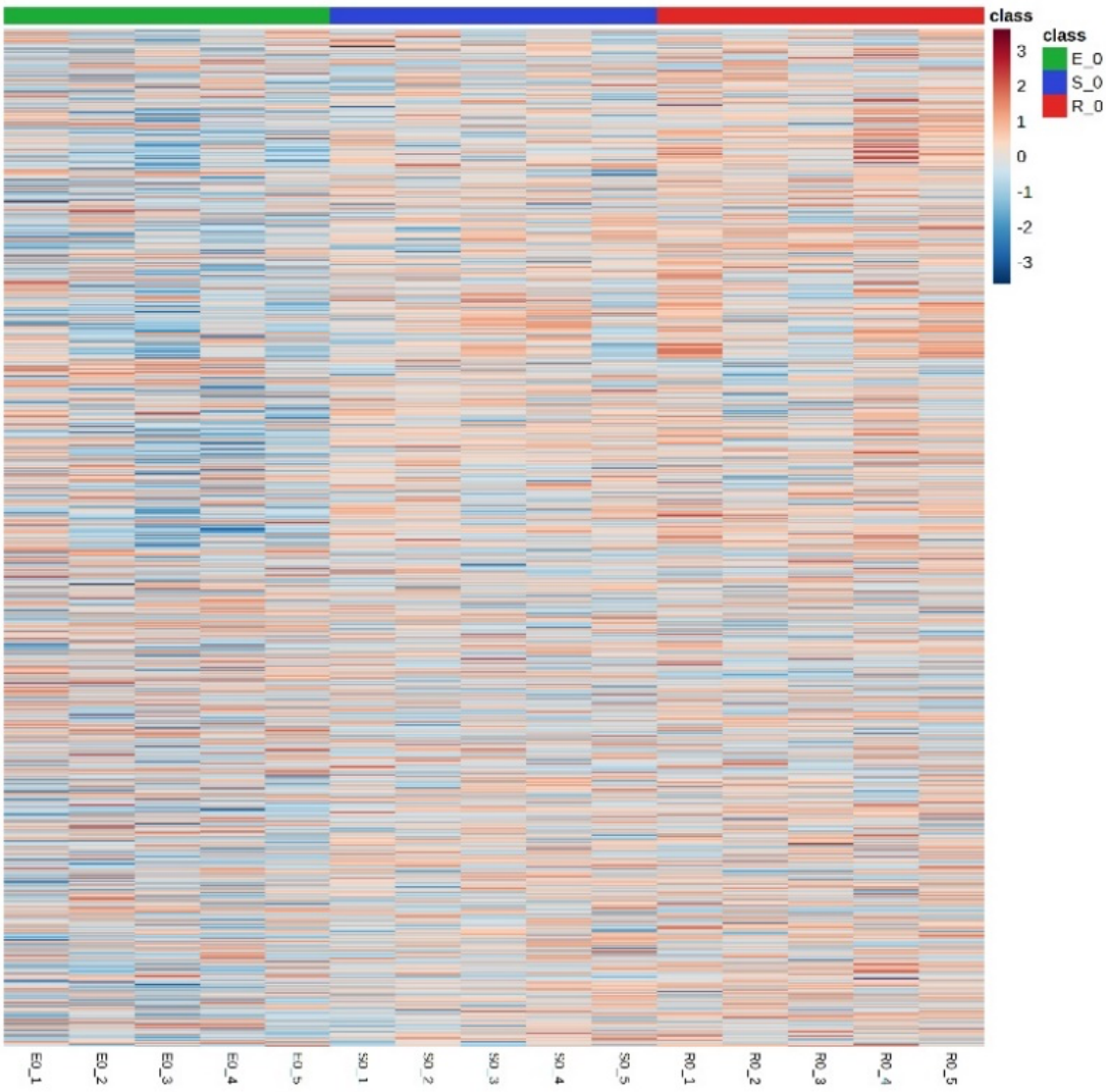

Figure 3.15 Heatmap of untargeted metabolomics data for wild-type (E), meropenem-susceptible (S), and meropenem-resistant (R)* E. coli *strains*. The heatmap shows the global metabolic profiles of the three strains. Each row represents a metabolite, and each column corresponds to an individual biological replicate (n=5 per strain). The colour gradient represents abundance of metabolites, with blue indicating lower levels and red indicating higher levels. The heatmap confirms high data quality, with no major class differences and well-normalised distribution across samples.*

3.4.2 Identification of significantly altered metabolites in *E. coli* strains

To identify whether any metabolites were significantly altered in abundance between the three experimental groups (wild-type, meropenem-susceptible, and meropenem-resistant *E. coli*), an ANOVA was performed on the metabolomics dataset. The analysis revealed several metabolites with significant changes in abundance ($p < 0.05$, false discovery rate (FDR) corrected). The ANOVA plot (**Figure 3.16**) visualised this, which highlighted a subset of metabolites that were significantly altered in abundance between the strains. A total of 81 identified metabolites were significantly altered (**Appendix II Table Appendix II.I**). The significantly altered metabolites included nucleic acids, modified amino acids, and carboxylic acids. Nucleotide-related metabolites, such as deoxycytidine triphosphate (dCTP), cytidine monophosphate, and uridine 5'-disphosphate, were significantly elevated in the S and R strains. Conversely, uracil was elevated in the wild-type (E) strain compared to the modified strains.

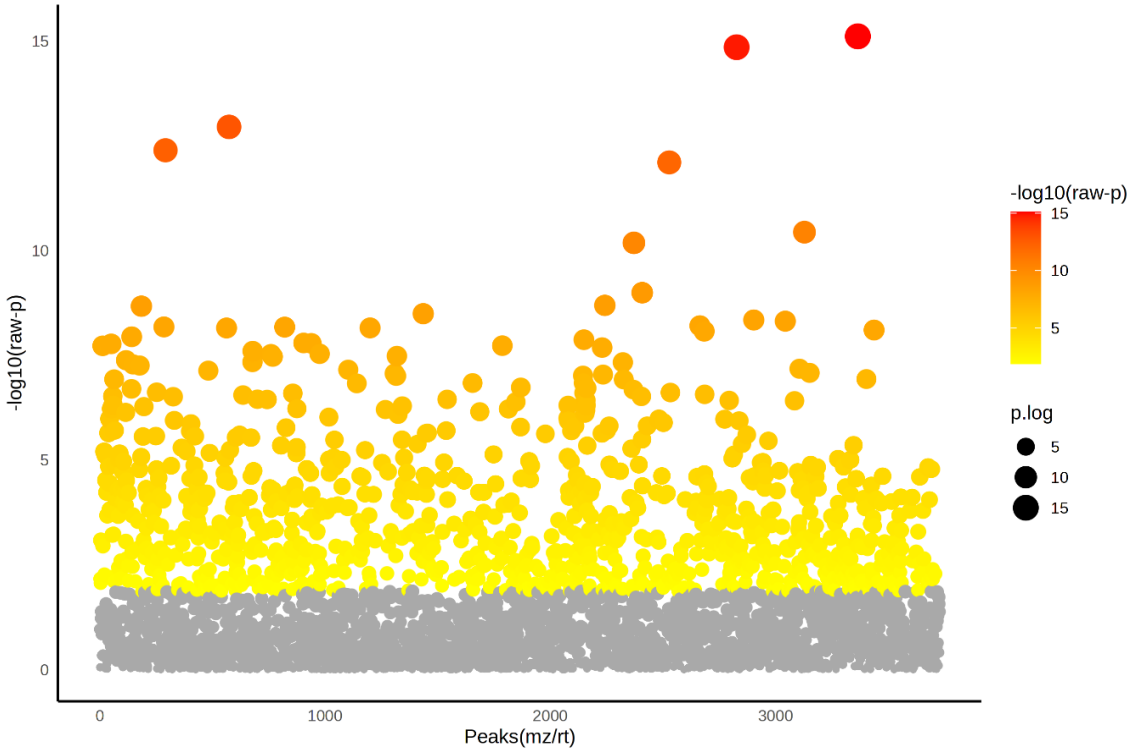

Figure 3.16 Scatter plot of ANOVA significance for metabolites across wild-type (E), meropenem-susceptible (S), and meropenem-resistant (R)* E. coli *strains. *The plot illustrates the significance (-log 10 raw p-value) of metabolite abundance differences across the three strains, plotted against peaks (m/z and retention time). Each point represents a detected metabolite and the colour gradient indicates the p-value significance (yellow to red presenting increasing significance). Grey points represent non-significant metabolites ($p > 0.05$ after FDR correction). Larger point size corresponds to higher log p-values. The red circles highlight the most significantly altered metabolites, with p-values < 0.001, suggesting key metabolic differences between the strains.*

Significant changes were also observed related to amino acid metabolism, with modified amino acids such as *N*-Acetyl-L-phenylalanine and *N*-Acetyl tryptophan exhibited reduced levels in both the S and R strains, with more pronounced decreases in the meropenem-resistant strain. Additionally, central carbon metabolites such as fructose 6-phosphate and sorbitol-6-phosphate showed elevated levels in both the S and R strains, while sedoheptulose 1-phosphate and glucose 1-phosphate were even higher in the R strain. Furthermore, intermediates of the TCA cycle, including 3-isopropylmalic acid and isocitrate, displayed notable changes, particularly in the R strain. These observations highlight substantial differences in metabolite abundance associated with the introduction of the pCR2.1 plasmid and the NDM-7 gene.

Box plots (**Figure 3.17**) were produced to illustrate the relative abundance changes of the significantly altered metabolites and the direction of these changes. The S strain, which carries the pCR2.1 plasmid, often showed intermediate metabolic levels (blue in **Figure 3.17**). The resistant strain, carrying both the plasmid and the NDM-7 gene, showed more pronounced alterations in nucleotides and amino acids, indicating further metabolic reprogramming linked to carbapenem resistance.

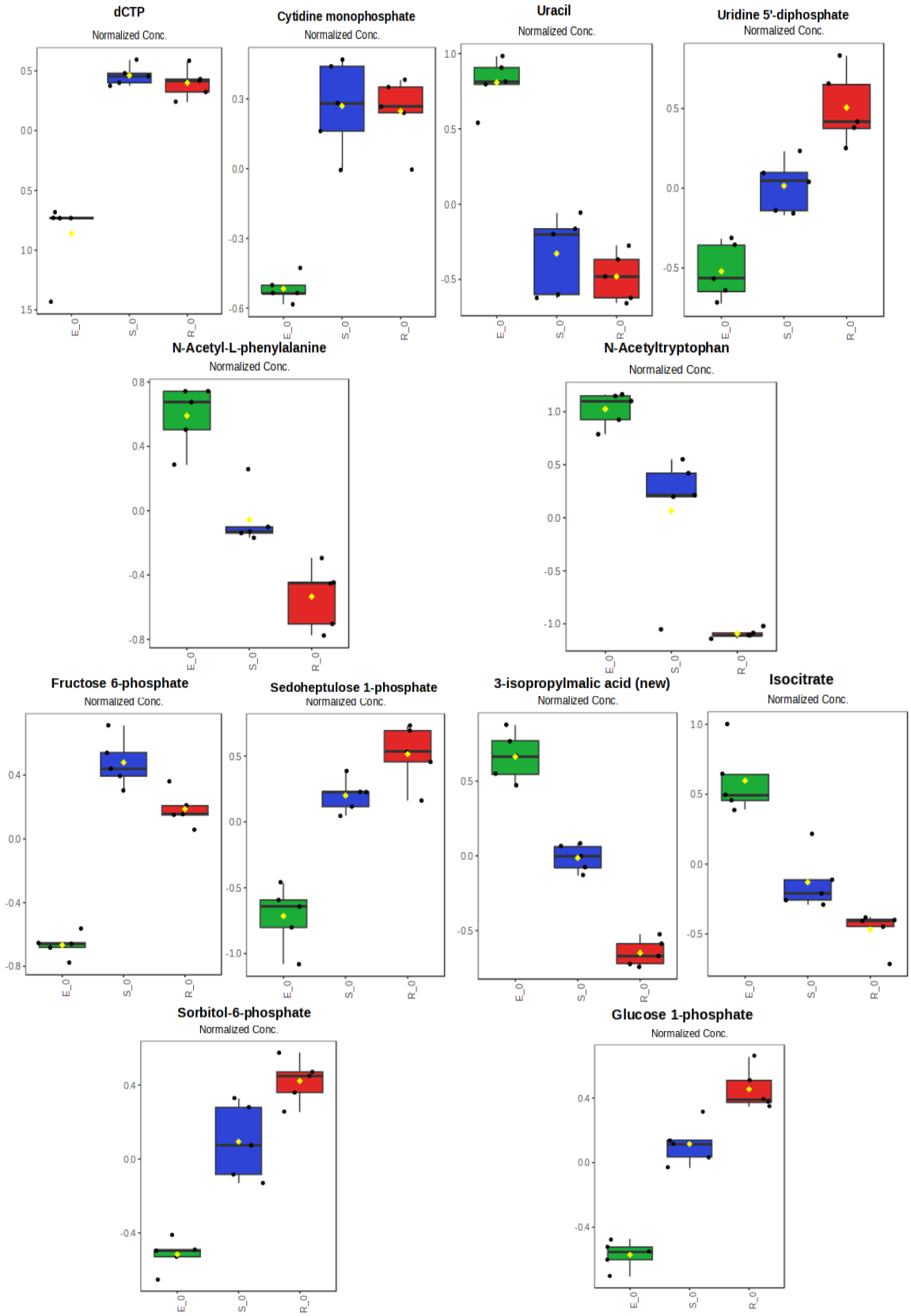

Figure 3.17 Box plots of significantly altered metabolites between wild-type (E), meropenem-susceptible (S), and meropenem-resistant (R)* E. coli *strains. *The box plots show the relative abundance (normalised) of the top 12 significantly altered metabolites across the E (green), S (blue), and R (red) strains. The metabolites were identified through ANOVA analysis ($p < 0.05$, FDR corrected) and include a variety of metabolic classes such as nucleotides, amino acids, and central carbon metabolism intermediates.*

While changes in identified metabolites offer valuable insights, the relatively small number of metabolites actually identified, means they provide a somewhat biased view of altered metabolism or the extent to which changes have occurred. Unidentified compounds (compound-features) measured by untargeted metabolomics are of interest, as they collectively provide greater metabolome coverage and may therefore represent broader insights into changes at the whole metabolome level.

In this study, several unidentified compound-features showed significantly altered abundances across the wild-type (E), meropenem-susceptible (S), and meropenem-resistant (R) strains. The top 10 most significantly altered unidentified compounds (**Figure 3.18**) were visualised using box plots, highlighting distinct abundance profiles between the strains. For example, 9.48_729.6900 *m/z* and 12.53_319.0960 *m/z* displayed significantly lower abundance only in the S strain, possibly related to the insertion of NDM-7 gene into pCR2.1 plasmid. Since the wild-type (E) strain lacks this plasmid, and in the resistant strain, the NDM-7 gene is inserted into the lacZ region of the plasmid, any compound linked to the region disrupted by the insertion of gene could be unique to the S strain. Differences between the S and R strains may be due to presence of NDM-7 or specific insertion sites, while variations between the wild-type and modified strains may reflect the metabolic impact of plasmid carriage. Notably, some compound-features, such as 20.99_319.0960 *m/z*, showed significant differences in abundance in both the S and R strains compared to the E strain, but more pronounced changes in the resistant strain, this may be attributed to the increasing number of resistance factors, possibly linked to the number of resistance genes.

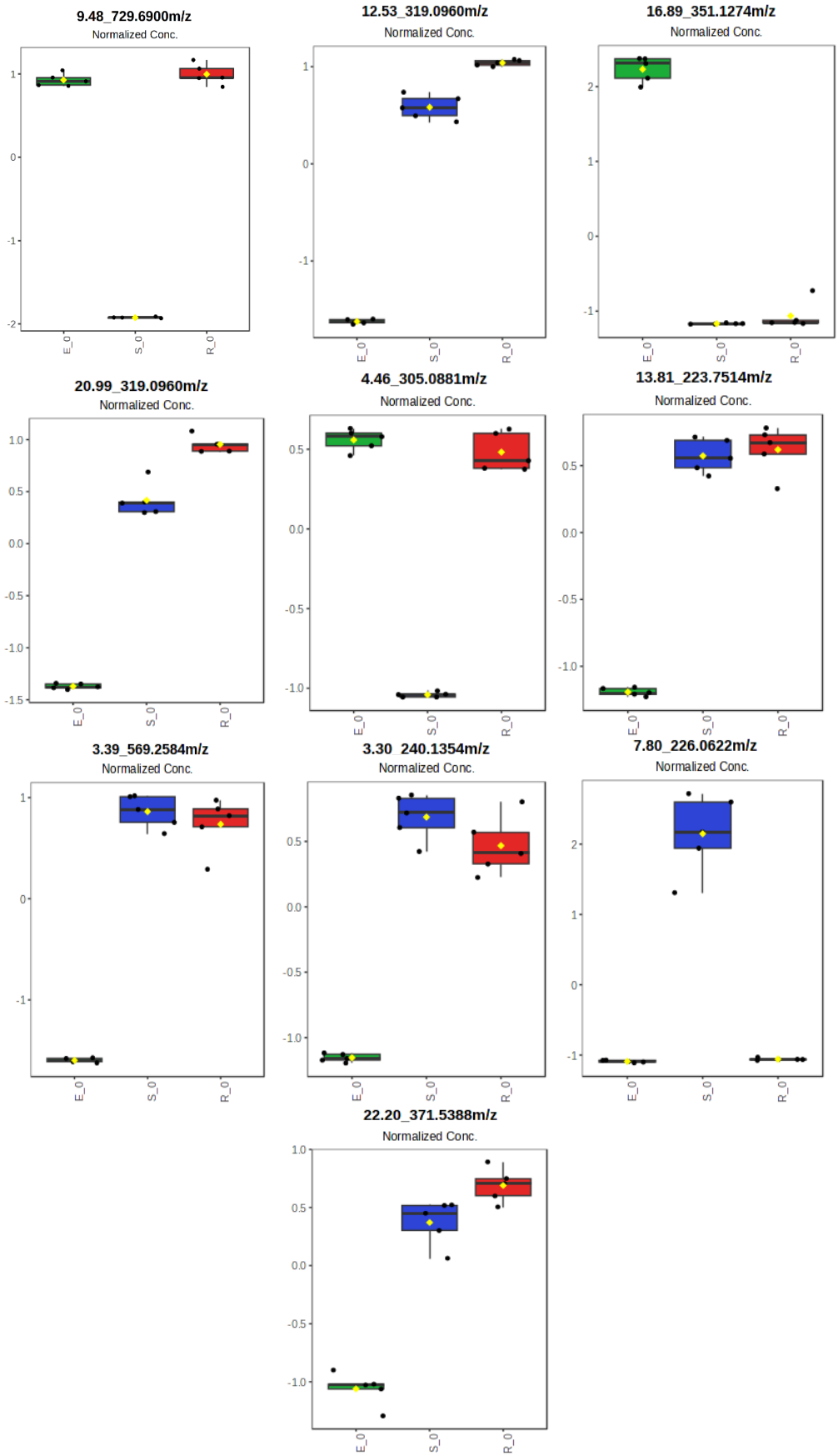

Figure 3.18 Box plots of the top 10 most significantly altered unidentified compounds between wild-type (E), susceptible (S), and resistant (R) E. coli strains. *The box plots show the relative abundance (normalised concentration) of the unidentified metabolites across the E (green), S (blue), and R (red) strains.*

To explore the potential identities of the most significantly altered unidentified compounds, their *m/z* values were cross-referenced with the Human Metabolome Database (HMDB) and the *E. coli* Metabolome Database (ECMDB). Although they do not contain direct retention time (RT) information, attempts were made to validate putative identifications through the literature and by predicting where candidate metabolites would be likely to elute by anion-exchange chromatography. Notably, approximate retention times for different chemical structures can often be predicted more reliably in anion-exchange chromatography compared to other approaches, such as HILIC due to the simpler retention and elution mechanism which is based on strength of ionic charge interactions.[201]

For compounds measured with associated MS/MS spectra via data-dependent acquisition (DDA), fragmentation patterns were compared to reference spectra in these databases to support identifications. However, the low abundance of many compounds often limited the clarity of the fragmentation patterns. Despite these limitations, one potential identification was for compound-feature 16.89_351.1274 *m/z*, which corresponded to Amylose (or a sugar structural isomer of amylose), based on ECMDB data, although this could not be confirmed due to the low abundance in the complex datasets.

In cases where corroborating evidence from retention time and fragmentation patterns was available, putative identifications were proposed (**Appendix II Table Appendix II.II**). Though level 1 identifications were not attempted. The analysis lays the groundwork for future investigation into the roles these metabolites play in the metabolic landscape of antibiotic resistance.

3.4.3 Exploring the metabolic phenotypes of the wild-type (E), meropenem-susceptible (S), and meropenem-resistant (R) *E. coli* strains

Univariate statistical analysis treats each metabolite as a separate variable and hence as independent to one another. Whilst in some cases this may be true, in the majority of cases metabolites changes are linked to others in metabolism. We know that metabolites are linked together in metabolic pathways and highly dependent on each other.[320] In order to look at how

metabolites may be linked and to assess whether the metabolic profiles of the wild-type (E), meropenem-susceptible (S), and meropenem-resistant (R) *E. coli* strains represent distinct metabolic phenotypes, multivariate statistical approaches were applied, including hierarchical clustering, PLS-DA, and OPLS-DA modelling. These methods were used to explore the separation of metabolic profiles and to identify key metabolites driving the differences between strains.

First, hierarchical clustering was performed to examine how samples and compound-features/identified metabolites were clustered. The dendrogram (**Figure 3.19**) shows that samples in all three groups cluster closer to others within the same strain rather than with those of another strain. Interestingly, the S and R strains, both containing the pCR2.1 plasmid, are a sub-cluster to the wild-type (E) strain, suggesting that the introduction of the plasmid and subsequent gene expression impacts the metabolic landscape in those bacteria more similarly than to the wild-type.

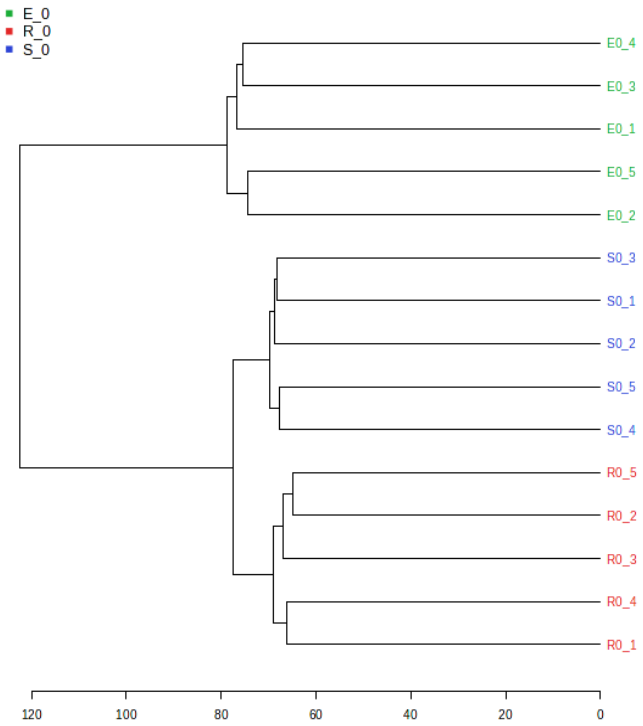

Figure 3.19 Dendrogram of hierarchical clustering analysis using Euclidean distance and Ward's linkage. *The dendrogram shows distinct clustering of the wild-type (E), meropenem-susceptible (S), and meropenem-resistant (R)* E. coli *strains based on their metabolomic profiles. The close clustering of the meropenem-susceptible and meropenem-resistant strains suggests similar metabolic reprogramming between the two, likely driven by the genetic modifications (insertion of pCR2.1 plasmid). n=5*

The top 50 most significantly altered compounds (ANOVA, FDR-corrected p-values <0.05) were hierarchically clustered and visualised in a heatmap (**Figure 3.20**). The heatmap highlights a trend of increased abundance of several metabolites in the meropenem-susceptible and meropenem-resistant strains compared to the wild-type strain. Notably, metabolites involved in central carbon metabolism, such as fructose 6-phosphate and guanosine diphosphate (GDP), show elevated levels in both modified strains, reflecting substantial metabolic reprogramming in response to the introduction of the plasmid with resistance genes (resistant to ampicillin and kanamycin). Additionally, several compounds displayed strain-specific changes, suggesting unique metabolic adaptations in that strain only.

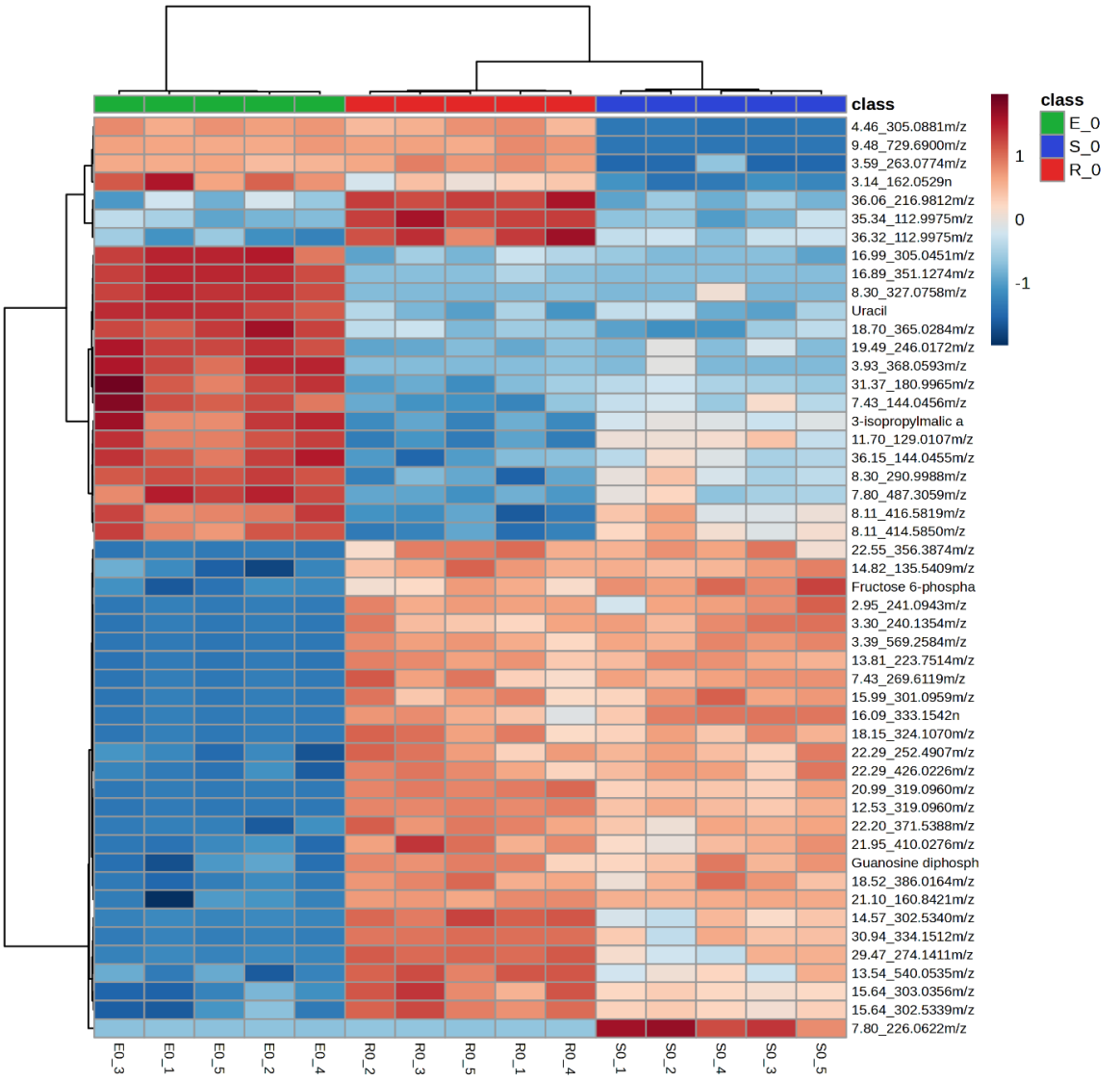

Figure 3.20 Hierarchically clustered heatmap of the top 50 most significantly altered metabolites across the wild-type (E), susceptible (S), and resistant (R)* E. coli *strains. *Warmer colours (red) indicate increased metabolite abundance, while cooler colours (blue) represent reduced abundance.*

To further investigate the metabolic distinctions between the strains, PLS-DA modelling was performed. The scores plot (**Figure 3.21**) displays clear separation between the wild-type (E), S, and R groups, highlighting the model can generate distinct metabolic phenotypes.

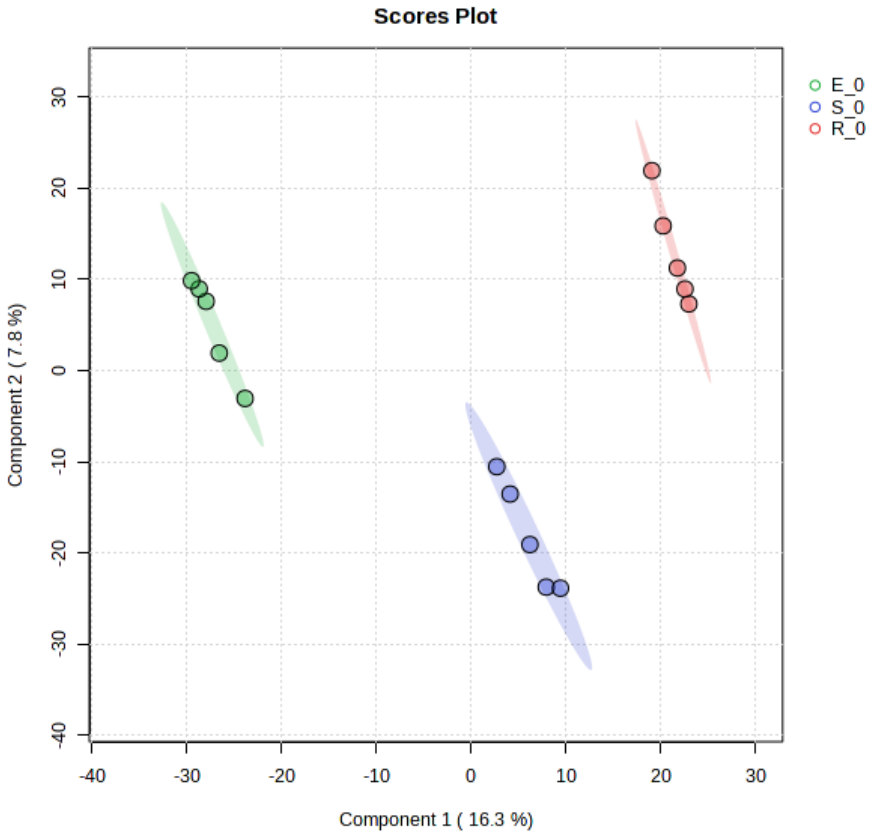

Figure 3.21 PLS-DA scores plot for wild-type (E), meropenem-susceptible (S), meropenem-resistant (R) strains. *Component 1 explains 16.3% of the variance, while Component 2 accounts for 7.8%. n=5 for each experimental group.*

Despite the strong visual separation, concerns about model robustness were raised based on validation metrics of the model. While the R2 values were high across models with multiple components (R2 > 0.9), indicating a good fit, the Q2 values were lower (ranging from 0.65 to 0.69) and more than 0.2 away from the R2 values. The gap between R2 and Q2 suggests the potential for overfitting of the data, where the model captures noise or variance specific to this dataset rather than generalisable trends.

Additionally, cross-validation accuracy was high (up to 0.93 for models with more than two components), supporting a good fit to the current dataset. However, the limited predictive power, reflected in the Q2 values, suggests that the model may struggle to generalise beyond

this dataset. One potential reason for this overfitting could be the relatively low number of biological replicates, which may not be sufficient to capture the variability of metabolic responses across the strains. **Figure 3.22** presents performance metrics of the model, indicating consistent accuracy, R2, and Q2 values across models with different component numbers. Despite this consistency, the lower Q2 values highlight the need for caution when interpreting the results.

PLS-DA cross validation details:

Measure	1 comps	2 comps	3 comps	4 comps	5 comps
Accuracy	0.66667	0.93333	0.93333	0.93333	0.93333
R2	0.94651	0.9993	0.99999	1.0	1.0
Q2	0.6348	0.64077	0.64106	0.64118	0.6412

Figure 3.22 PLS-DA cross-validation details for the wild-type (E), meropenem-susceptible (S), and meropenem-resistant (R) strains. *The table shows performance metrics for models with different numbers of components. While the accuracy and R2 values remain high across all models, the Q2 values indicate a lower predictive ability, suggesting the potential for overfitting. The highest Q2 value observed is 0.68621, with the accuracy stabilising at 0.93333 for models with two or more components.*

The Variable Importance in Projection (VIP) scores (**Figure 3.23**) were used to identify the most influential metabolites contributing to the separation observed in the PLS-DA model. The top-ranked compounds were critical in driving the separation between strains, underscoring the substantial metabolic changes associated with the introduction of the pCR2.1 plasmid and NDM-7 gene. However, it is important to note that both identified and unidentified compounds contributed to the differentiation, reinforcing the complexity of the metabolic changes in response to genetic modification.

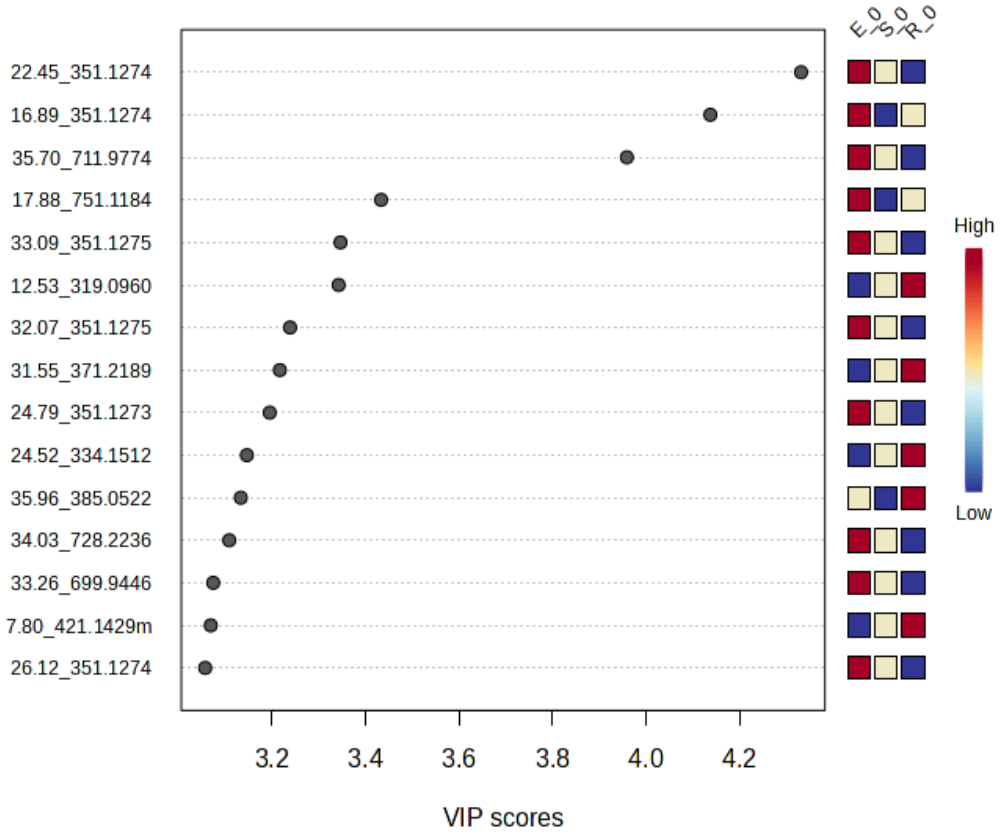

Figure 3.23 VIP scores from the PLS-DA model, showing the top-ranking metabolites contributing to the separation between wild-type (E), meropenem-susceptible (S), and meropenem-resistant (R) strains. *Higher VIP score indicate a stronger contribution of these metabolites to the observed group separation. The heatmap adjacent to the VIP score represents the relative abundance of these metabolites across the three strains, with colour (red high, white middle, blue low) reflecting the metabolite levels in each strain.*

OPLS-DA was also performed, a very similar vector-based multivariate modelling approach, to see if it could perform more effectively. The rationale for this approach lies in the inherent ability of OPLS-DA to differentiate between class-related variation (predictive variation) and unrelated variance (orthogonal variation), making it particularly useful in untargeted metabolomics where subtle metabolic changes might be present in amongst substantial 'noise' in the data. In the comparison of the wild-type stains (E) against either the S or R strains, OPLS-DA helped to better isolate the effect of the pCR2.1 plasmid (present in both S and R) and the additional NDM-7 gene (only in R). The OPLS-DA comparison between S and R was not included due to their relatively similar metabolic profiles, both being plasmid-bearing strains. The primary metabolic differences are likely between the wild-type strain and the modified strains, with the introduction of the plasmid and NDM-7 gene representing the most significant variables. OPLS-DA provided a clearer visualisation of metabolite differences by focusing on the variance directly associated with those factors.

The scores plot for both E vs. S (**Figure 3.24 A**) and E. vs. R (**Figure 3.24 B**) shows clear group separation, reflecting significant metabolic differences between these strains. The validation metrics showed that the OPLS-DA model passed the permutation tests (**Appendix II Figure II.** and **Figure II.**), indicating that the model separation of groups was statistically significant. Specifically, for E vs. S, the R2Y value was 0.999 ($p < 0.05$, 0/20 permutations) and the Q2 value was 0.91 ($p < 0.05$, 0/20 permutations), while for E vs. R, the R2Y value was 0.999 ($p < 0.05$, 0/20 permutations) and the Q2 value was 0.872 ($p < 0.05$, 0/20 permutations). These results indicated that the observed group separations were not due to random chance and provide confidence in the robustness of the OPLS-DA models. However, as with the PLS-DA, the validation metrics for the OPLS-DA models also indicated concerns about overfitting. Although the R2 values were high, the Q2 values were notable lower again (shown in **Appendix II Figure II.**), suggesting that predictive power of the model was limited. The overfitting could again be attributed to the low number of biological replicates, which may not be sufficient basis for building a robust and generalisable multivariate model. Therefore, while these results are valuable, further experiments with a larger sample size are needed to strengthen the validity of the findings.

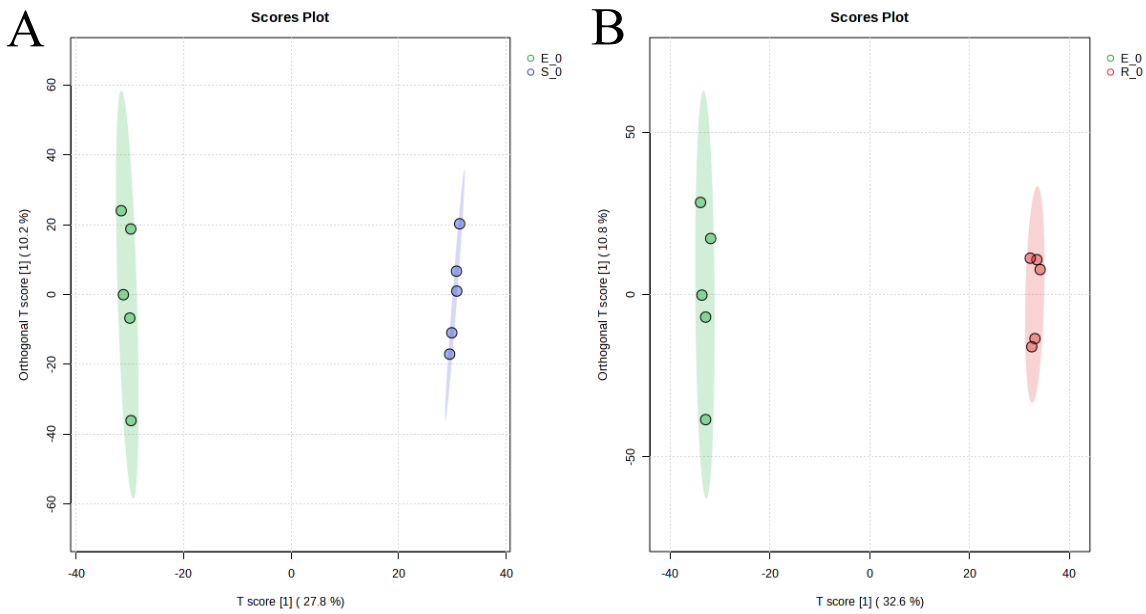

Figure 3.24 OPLS-DA scores plots showing the separation between A) wild-type (E) and susceptible (S) strains, and B) wild-type (E) and resistant (R) strains. *Each point represents an individual sample. n=5 for each group.*

Both the PLS-DA and OPLS-DA were performed to explore the potential metabolic shifts between the wild-type, meropenem-susceptible, and meropenem-resistant strains. While these multivariate analyses provided interesting insights into metabolic changes that support differences between the strains, the results must be interpreted with caution due to potential for overfitting and limited model validation. These data were therefore not included in interpreting metabolic differences between the strains, avoiding overinterpretation of potentially overfitted models. The relevant PLS-DA and OPLS-DA data, including cross-validation metric, VIP scores, and feature importance plots, are included in the Supplementary Information (**Appendix II Figure II. - Figure II.**).

3.4.4 Comparing metabolic profiles independently between meropenem-susceptible and meropenem-resistant strains with wild-type *E. coli* control

Having considered the metabolic changes associated with the introduction of the pCR2.1 plasmid in the meropenem-susceptible strain (S) and additional NDM-7 gene in the meropenem-resistant strain (R) together, they were next analysed separately. Volcano plots were used to identify significantly altered metabolites and compound-features between the E and S strains, as well as between the E and R strains. An FDR-corrected p-value threshold (< 0.05) and a fold change ($FC > 2$) was applied to identify significant altered compound-features of interest.

Volcano plots, presented in **Figure 3.25** and **Figure 3.26**, visually illustrate the differentially regulated metabolites and compound-features. Significant up-regulated and down-regulated metabolites are highlighted, providing insight into shared and distinct metabolic adaptations in the S and R strains. The strain R exhibited more extensive metabolic reprogramming compared to the strain S, as evidenced by the higher number of significantly altered features.

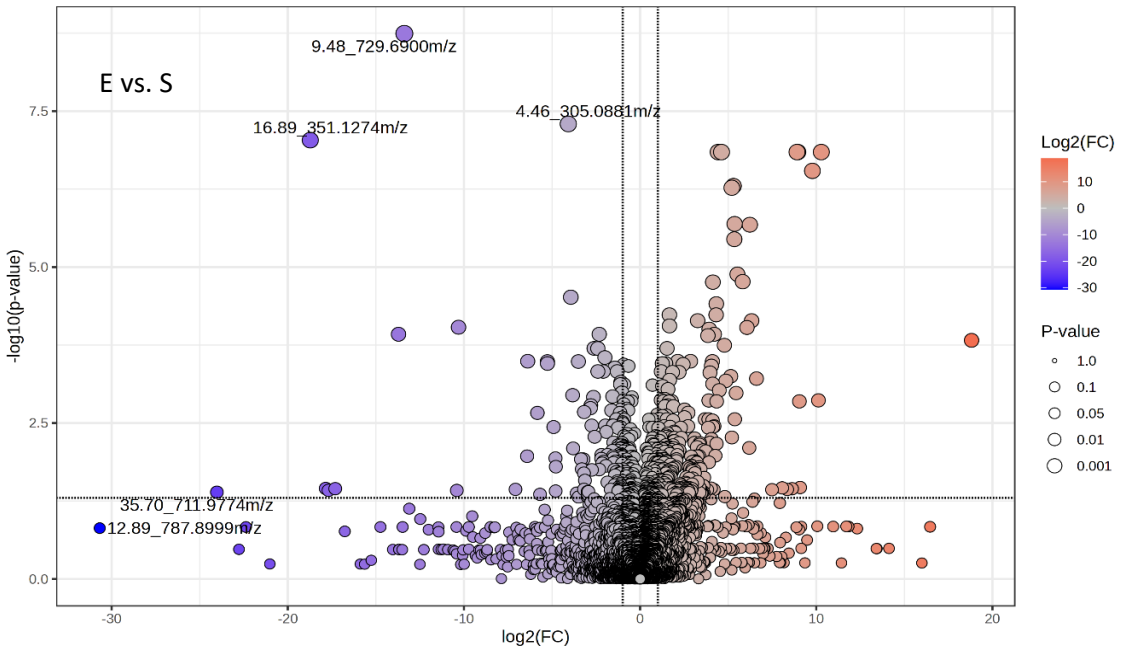

Figure 3.25 Volcano plot comparing the metabolic profiles between the wild-type (E) and susceptible (S) strains. *The x-axis represents the log2 FC of metabolite abundance, while y-axis shows the -log10 (p-values) for significance. Significantly up-regulated metabolites (positive log2FC) are displayed in red, and down-regulated metabolites (negative log2FC) in blue. The size of the points corresponds to the p-value, with larger points representing more significant changes. Identified metabolites are labelled by their mass-to-charge ratio (m/z). FDR-corrected p-value threshold of < 0.05 and FC > 2 was applied.*

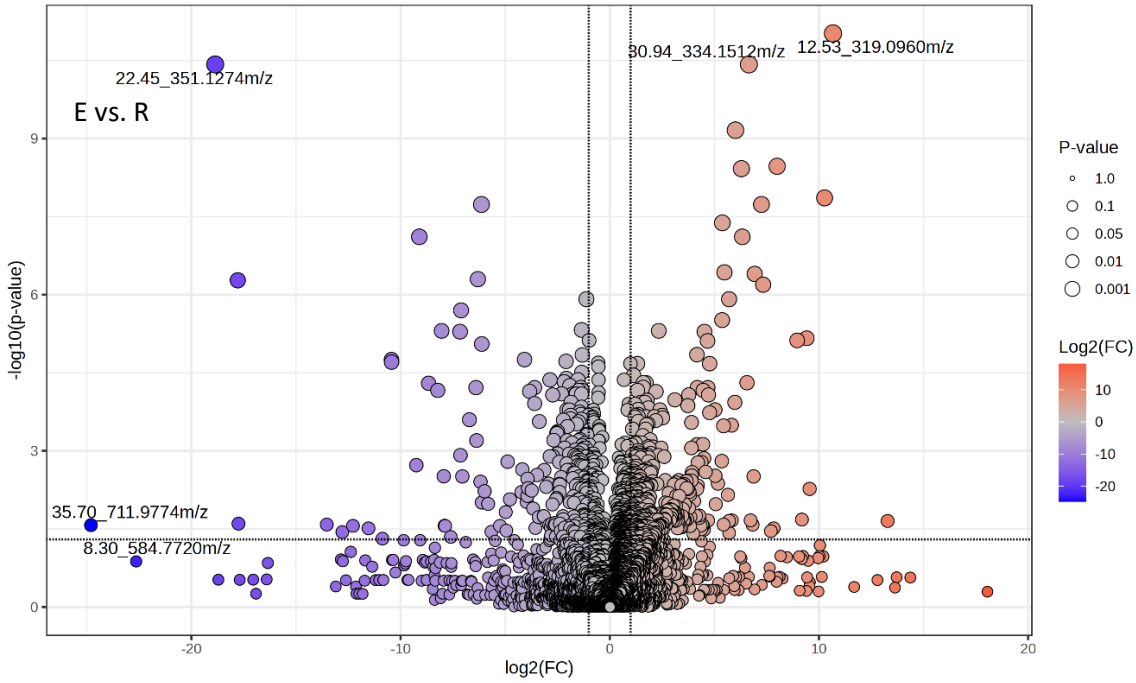

Figure 3.26 Volcano plot comparing the metabolic profiles between the wild-type (E) and resistant (R) strains. *The x-axis represents the log2 FC of metabolite abundance, while y-axis shows the -log10 (p-values) for significance. Significantly up-regulated metabolites (positive log2FC) are displayed in red, and down-regulated metabolites (negative log2FC) in blue. The size of the points corresponds to the p-value, with larger points representing more significant changes. Identified metabolites are labelled by their mass-to-charge ratio (m/z). FDR-corrected p-value threshold of < 0.05 and FC > 2 was applied.*

The overall comparison between the strains revealed substantial metabolic reprogramming in both the S and R strains compared to the wild-type. In the E vs. S comparison. 118 compound-features were down-regulated 248 were up-regulated, and 3355 were non-significant. In the E vs. R comparison, 207 compound-features were down-regulated, 370 were up-regulated, and 3146 were non-significant.

Analysis of the identified metabolites across both comparisons, revealed significant differences in metabolic profile. In the E vs. S comparison, 12 metabolites were down-regulated, 18 were up-regulated, while 99 metabolites showed no significant changes. Similarly, in the E vs. R comparison, 13 metabolites were down-regulated and 22 were up-regulated, with 94 non-significant.

To further explore these metabolic differences, a comparative table (**Table 3.8**) was generated summarising the key identified metabolites, including their fold changes and p-values. These results indicate both common metabolic changes related to plasmid introduction and additional unique changes associated with the presence of the NDM-7 gene in the resistant strain. Metabolites such as fructose 6-phosphate, ribulose 5-phosphate, and isocitrate were significantly altered in both comparisons, indicating broad disruption of energy and biosynthesis pathways. Conversely, some metabolites showed unique responses in one comparison but not the other, reflecting some distinct metabolic effects of the NDM-7 gene in the resistant strain.

For example, acetylphosphate, showed significant changes in the E vs. S comparison but not in E vs. R, suggesting that the introduction of NDM-7 gene may introduce further metabolic demands. The lack of significant changes in acetylphosphate levels in the E vs. R comparison could be associated with shared metabolic features or disruptions between these strains, potentially linked to the insertion of the NDM-7 gene into the *lacZ* region in the pCR2.1 plasmid of the resistant strain. As the *lacZ* region is absent in E (no plasmid) and disrupted in R (NDM-7 inserted in *lacZ*), this shared feature could reduce the differential metabolic impact compared to the S strain, where the *lacZ* region remains intact. Additionally, acetylphosphate is a

high-energy intermediate involved in central metabolism, linking energy production, signal transduction, and the regulation of acetyl-CoA levels.[321]

Table 3.8 Comparative analysis of key identified metabolites significantly altered between the wild-type (E), meropenem susceptible (S), and meropenem resistant (R) strains. *The table includes FC and p-values for E vs. S and E vs. R comparisons, highlighting shared and distinct metabolic changes. Metabolites are grouped based on their related metabolic pathways.*

	FC E vs S	p value E vs S	FC E vs R	p value E vs R	Related Pathway
Fructose 6-phosphate	3.9378	5.70E-05	2.764	1.22E-05	Central Carbon Metabolism - glycolysis
Fructose 2,6 diphosphate	2.8691	0.004123	N/A	N/A	Central Carbon Metabolism - glycolysis
2,3-Diphosphoglyceric acid	4.5785	0.0042776	N/A	N/A	Central Carbon Metabolism - glycolysis
Glucose 1-phosphate	2.0587	0.0004829	2.9346	1.20E-05	Central Carbon Metabolism - glycolysis/glycogen metabolism
Ribulose 5-phosphate	0.42157	0.0032098	N/A	N/A	Central Carbon Metabolism - pentose phosphate pathway
Sedoheptulose 1-phosphate	3.2591	0.00095223	5.0431	0.00024345	Central Carbon Metabolism - pentose phosphate pathway
6-phosphonoglucono-lactone	N/A	N/A	2.0653	0.038516	Central Carbon Metabolism - pentose phosphate pathway
Isocitrate	0.43137	0.0045208	0.2889	0.00024074	Central Carbon Metabolism - TCA Cycle
Acetylphosphate	5.8192	0.033068	N/A	N/A	Central Carbon Metabolism - glycolysis/TCA Cycle
N-acetylneuraminic acid (new)	4.7629	0.0015593	4.0714	0.00084623	Sugar Metabolism
Sorbitol-6-phosphate	N/A	N/A	2.5115	1.22E-05	Sugar Metabolism
Glucuronic acid	0.41763	0.0023267	0.46451	0.0017748	Carbohydrate Metabolism
UDP-galactose	2.4444	0.029271	3.5008	0.0027389	Carbohydrate Metabolism
Guanosine diphosphate (GDP)	5.6375	0.0002676	6.0426	3.56E-05	Nucleotide Metabolism
Cytidine triphosphate	3.7902	0.001073	3.675	0.00024074	Nucleotide Metabolism
Thymidine triphosphate	N/A	N/A	2.4874	0.00066048	Nucleotide Metabolism
Uridine 5'-diphosphate	N/A	N/A	3.0705	0.00030634	Nucleotide Metabolism
Adenosine 2',3'-cyclic phosphate	N/A	N/A	0.44342	0.00084623	Nucleotide Metabolism
dCTP	6.9388	0.00059528	6.3773	0.00026363	Nucleotide Metabolism - pyrimidine metabolism
Uracil	0.20173	0.00069417	0.15686	2.82E-05	Nucleotide Metabolism - pyrimidine metabolism
Cytidine monophosphate	2.0982	0.00059528	2.0442	6.96E-05	Nucleotide Metabolism - pyrimidine metabolism
Thymine	0.31742	0.00059528	0.37241	0.00011788	Nucleotide Metabolism - pyrimidine metabolism
Uridine 5'-monophosphate	N/A	N/A	2.1043	0.0020321	Nucleotide Metabolism - pyrimidine metabolism
dGDP	2.7047	0.0037618	3.0831	0.0008255	Nucleotide Metabolism - purine metabolism
Succinyl-Homoserine	11.341	0.039965	59.912	5.42E-07	Amino Acid Metabolism - TCA cycle

Maleamate	9.2516	0.0033655	8.3938	0.0024679	Amino Acid Metabolisms - nitrogen metabolism
N-Acetyl-L-phenylalanine	0.46809	0.0035397	0.26783	0.0001847 5	Amino Acid Metabolism
N-Acetyl-L-methionine	0.49878	0.010588	0.38919	0.0008462 3	Amino Acid Metabolism
N-Acetyltryptophan	0.18029	0.029271	0.008700 2	3.74E-07	Amino Acid Metabolism
N-Acetylaspartylglutamic acid	0.31997	0.0058516	0.016677	0.0043883	Amino Acid Metabolism
N-Acetylvaline	N/A	N/A	0.4273	0.0003063 4	Amino Acid Metabolism
3-Methyl-2-oxovaleric acid	2.3712	0.011295	2.6072	0.0074134	Amino Acid Metabolism
Pyroglutamic acid	2.4165	0.0033252	2.2536	0.0086263	Amino Acid Metabolism
Hippuric acid	0.27403	0.0032098	0.11714	4.44E-05	Miscellaneous Organic Acids - detox
Galactaric acid (mucic acid)	0.26702	0.004123	0.07052	2.08E-06	Miscellaneous Organic Acids - carbohydrate metabolism
Ureidopropionic acid	N/A	N/A	3.8186	0.040431	Miscellaneous Organic Acids - purine and pyrimidine metabolism
AICAR	10.63	0.0044929	16.88	0.0020321	Miscellaneous Organic Acids - purine and energy metabolism
3-isopropylmalic acid	0.40842	0.0006941 7	0.17848	9.25E-06	Miscellaneous Organic Acids - Leucine Biosynthesis

The table summarises the identified metabolites that were identified as consistently disrupted across both comparisons, reflecting changes in their abundance. For example, GDP is markedly elevated in the resistant strain, which may indicate enhanced nucleotide turnover to support increased cellular repair or replication mechanisms. Similarly, significant increases in dCTP and deoxyguanosine diphosphate (dGDP) align with the heightened need for DNA synthesis and repair activities, likely contributing to the resistance phenotype. These changes underline the central role of nucleotide metabolism in the metabolic adaptations observed in the resistant strain.

Other metabolites, such as fructose 6-phosphate and fructose 2,6-diphosphate, show substantial changes in abundance, pointing to disruptions in glycolytic flux. These changes likely reflect metabolic adjustments needed to maintain energy production under stress. The dramatic elevation of succinyl-homoserine in the meropenem-resistant strain suggests its potential involvement in amino acid metabolism and its connection to the TCA cycle, suggesting a possible role in supporting biosynthetic demands.

These observations focus on specific metabolite changes rather than general pathways, providing insights into how individual metabolites changes contribute to the metabolic landscape of NDM-7 mediated antibiotic resistance in *E. coli*. The emphasis on specific features such as fold changes and strain differences help to unravel the intricate roles these metabolites play in mediating resistance mechanisms.

In conclusion, the combination of volcano plots and the comparative table offers a comprehensive overview of the significant metabolic changes between the strains. These findings illustrated both common and strain-specific metabolic adaptations following plasmid introduction and antibiotic resistance gene acquisition.

3.4.5 Functional analysis of altered metabolism in meropenem susceptible and resistant *E. coli* strains

Altered metabolite abundances (information from univariate statistical analysis) and correlations and patterns between these abundance changes (derived from multivariate statistical models) described so far suggest changes in metabolism but do not reveal how this may be occurring at a functional level. To explore the functional differences between in the meropenem-susceptible and meropenem-resistant strains, untargeted pathway analysis was performed. The analysis compared the S and R strains to the *E. coli* control (E). The goal was to identify which metabolic pathways were significantly impacted due to the introduction of the pCR2.1 plasmid in the S strain and the additional presence of the NDM-7 gene in the R strain.

There are number of different approaches that can be used for metabolic pathway analysis (also known as 'functional analysis'). Functional analysis maps the identified (or in some cases unidentified) metabolites to known metabolic pathways in the organism of interest and provides a statistical framework to determine the significance of pathway alterations. The significance is calculated based on the magnitude of change and the statistical relevance of the individual mapped metabolites.[320,322]

Untargeted functional pathway analysis, such as that implemented by the mummichog algorithm in MetaboAnalyst, enables pathway-level insights without requiring comprehensive

metabolite identification. Instead, it uses *m/z* values directly to generate putative metabolite IDs, incorporating retention time information to refine adduct assignments.[323] The algorithm identifies pathways by evaluating how well the putative metabolite matches cohere within known metabolic networks.[324,325] Metabolites that map sensibly to a single pathway and show significant enrichment are given higher weighting, while matches that are randomly distributed across multiple pathways are deprioritized. As a result, the algorithm to infer functional changes in metabolic pathways even when the exact metabolite identity remains uncertain.

By integrating statistical models with pathway topology, mummichog provides a robust framework for functional analysis, identifying biologically relevant pathways that may be disrupted under experimental conditions. The approach enables researchers to gain insights into the broader functional implications of metabolite changes, linking observed alterations to specific metabolic processes. The results can be visualised through bubble plots which provide an estimate of the enrichment and significance of individual Kyoto Encyclopedia of Genes and Genomes (KEGG) pathways.[326,327]

Untargeted Pathways Analysis (using MetaboAnalyst) was performed using the untargeted datasets to compare the wild-type (E) vs. meropenem-susceptible (S) and wild-type vs. meropenem-resistant (R) separately. These analyses identified four significantly altered pathways (pFisher < 0.05) in the E vs. S comparison and six in the E vs. R comparison. The results are presented as ranked list of predicted altered pathways (**Table 3.9** and **Table 3.10**) and visualised using bubble plots **Figure 3.27** and **Figure 3.28**.

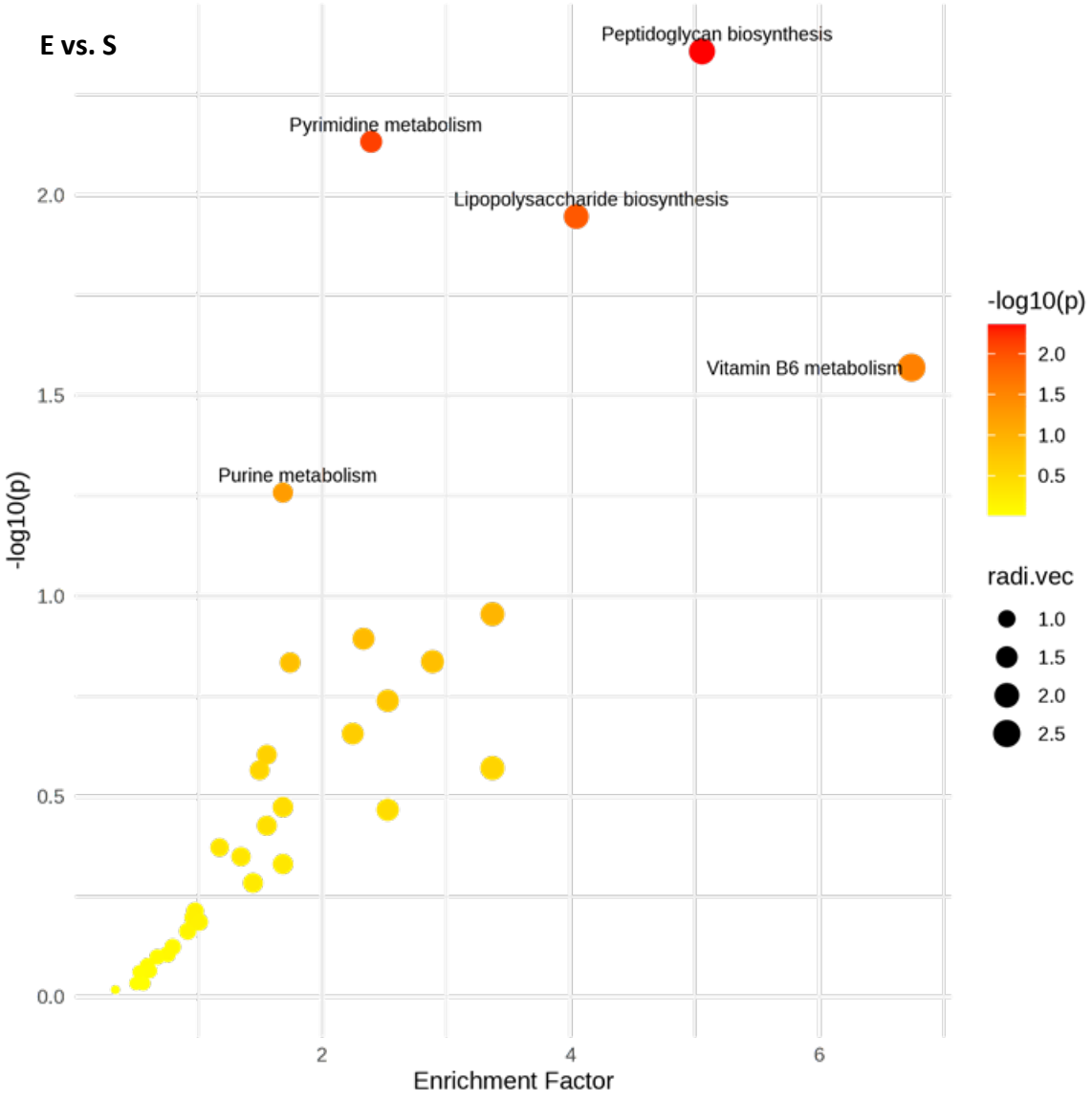

Figure 3.27 Pathway enrichment analysis for metabolic changes between the wild-type (E) and meropenem-susceptible strain (S). *The plot highlights the most significantly altered metabolic pathways between the wild-type (E) and susceptible strain (S). The y-axis represents pathway impact based on topology analysis, while the x-axis indicates pathway enrichment. Bubble colour intensity reflects the significance of the pathways (red indicating higher statistical significance), and bubble size indicates the pathway impact. This visualisation provides insight into the pathways most affected by the introduction of the pCR2.1 plasmid.*

Table 3.9 Functional analysis of metabolic pathways between wild-type (E) and meropenem susceptible strain (S). *This table presents the results of functional analysis, highlighting most significantly altered metabolic pathways affected by the presence of pCR2.1 plasmid. The columns include the total number of compounds in each pathway (Total), the number of all detected hits (Hits (all)), the number of significant hits (Hits (sig.)), the expected number of hits based on random distribution (Expected), and statistical significance values from Fisher's exact test (*P(Fisher)*) and gamma distribution-based analysis (*P(Gamma)*).*

Pathway Name	Total↑↓	Hits(all)↑↓	Hits(sig.)↑↓	Expected↑↓	P(Fisher)↑↓	P(Gamma)↑↓
Peptidoglycan biosynthesis	18	7	3	0.79121	0.0043784	0.0020969
Pyrimidine metabolism	51	25	9	3.7582	0.0073562	0.0021191
Lipopolysaccharide biosynthesis	46	11	8	0.98901	0.011307	0.0021489
Vitamin B6 metabolism	13	1	1	0.2967	0.026936	0.0022712
Purine metabolism	76	33	12	5.9341	0.055223	0.0025115
Beta-Alanine metabolism	13	4	1	0.59341	0.11101	0.0030673
O-Antigen nucleotide sugar biosynthesis	21	14	6	1.2857	0.1279	0.0032602
Riboflavin metabolism	17	6	2	0.69231	0.14585	0.0034795
Folate biosynthesis	38	9	5	2.8681	0.14664	0.0034895
Glutathione metabolism	22	6	2	0.79121	0.18261	0.0039787
D-Amino acid metabolism	25	9	2	0.89011	0.22057	0.0045753
Pantothenate and CoA biosynthesis	24	13	3	2.5714	0.24901	0.0050847
Ubiquinone and other terpenoid-quinone biosynthesis	23	2	1	0.2967	0.26886	0.0054762
Biotin metabolism	20	2	1	0.2967	0. 26886	0.0054762
Amino sugar and nucleotide sugar metabolism	44	29	13	2.6703	0.27217	0.0055446
Streptomycin biosynthesis	9	7	5	1.1868	0.33638	0.0070709
Inositol phosphate metabolism	8	6	4	1.1868	0.33638	0.0070709
Lysine biosynthesis	13	4	1	0.3956	0.34165	0.0072152
Biosynthesis of various plant secondary metabolites	6	3	2	1.2857	0.37428	0.0081822
Pentose phosphate pathway	26	21	10	4.2527	0.42434	0.0099531

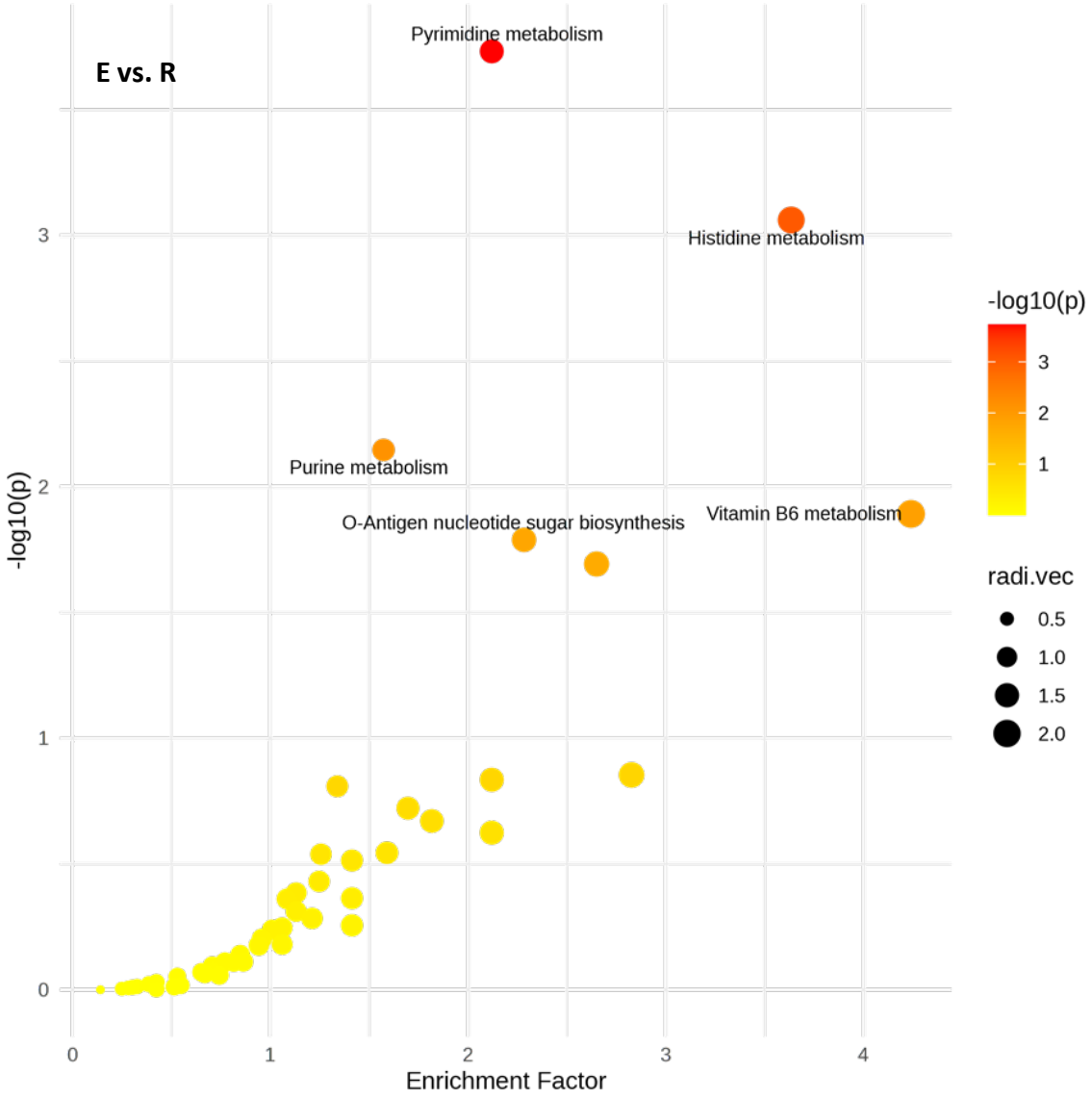

Figure 3.28 Pathway enrichment analysis for metabolic changes between the wild-type (E) and meropenem-resistant strains (R). *The plot highlights the most significantly altered metabolic pathways between the wild-type (E) and resistant strain (R). The y-axis represents pathway impact based on topology analysis, while the x-axis indicates pathway enrichment. Bubble colour intensity reflects the significance of the pathways (red indicating higher statistical significance), and bubble size indicates the pathway impact. This representation highlights the key metabolic pathways altered due to the expression of the NDM-7 gene in the resistant strain.*

Table 3.10 Functional analysis of metabolic pathways between wild-type (E) and meropenem-resistant (R) strains*. This table summarizes the pathway enrichment analysis results, highlighting the metabolic pathways impacted by the presence of the pCR2.1 plasmid and NDM-7 gene in* E. coli*. The columns include the total number of compounds in each pathway (Total), the number of all detected hits (Hits (all)), the number of significant hits (Hits (sig.)), the expected number of hits based on random distribution (Expected), and statistical significance values from Fisher's exact test (*P(Fisher)*) and gamma distribution-based analysis (*P(Gamma)*).*

Pathway Name	Total↑↓	Hits(all)↑↓	Hits(sig.)↑↓	Expected↑↓	P(Fisher)↑↓	P(Gamma)↑↓
Pyrimidine metabolism	51	25	20	8.9607	1.8595E-4	0.010179
Histidine metabolism	12	4	4	1.6507	8.7097E-4	0.010195
Purine metabolism	76	33	18	14.62	0.0071464	0.010366
Vitamin B6 metabolism	13	1	1	0.70742	0.012834	0.010522
O-Antigen nucleotide sugar biosynthesis	21	14	10	3.0665	0.016273	0.010618
Peptidoglycan biosynthesis	18	7	4	1.8865	0.020301	0.010731
Ubiquinone and other terpenoid-quinone biosynthesis	23	2	1	0.70742	0.13996	0.01477
Acarbose and validamycin biosynthesis	3	2	1	1.4148	0.14629	0.015025
Galactose metabolism	39	36	14	8.9607	0.1553	0.015397
Lipopolysaccharide biosynthesis	46	11	7	2.3581	0.18982	0.016919
Arginine biosynthesis	16	6	2	1.6507	0.21342	0.018055
Polyketide sugar unit biosynthesis	5	3	1	1.6507	0.21342	0.018055
Riboflavin metabolism	17	6	2	1.6507	0.21342	0.018055
Lysine biosynthesis	13	4	2	0.94323	0.23748	0.0193
Glutathione metabolism	22	6	3	1.8865	0.28553	0.022082
Amino sugar and nucleotide sugar metabolism	44	29	12	6.3668	0.28943	0.022327
Inositol phosphate metabolism	8	6	5	2.8297	0.3064	0.023427
Methane metabolism	26	11	4	4.0087	0.37096	0.028212
Folate biosynthesis	38	9	6	7.0742	0.41207	0.031836
Beta-Alanine metabolism	13	4	2	1.4148	0.43257	0.033842

In the comparison between the wild-type and meropenem-susceptible strain (E vs. S), the most significantly altered pathway was peptidoglycan biosynthesis. Altered peptidoglycan biosynthesis aligns with the presence of plasmid pCR2.1, which confers resistance to ampicillin (a β-lactam antibiotic known to target cell wall synthesis). The observation could suggest that the metabolic shifts in the meropenem-susceptible strain may be partly driven by adaptations related to resistance mechanism of the plasmid. Additionally, multiple pathways involved in nucleotide biosynthesis (purine and pyrimidine metabolism), were also significantly altered, which may reflect broader metabolic demands introduced by plasmid expression.

In the comparison between the wild-type and meropenem-resistant strain (E vs. R), we see some similar but also additional changes in metabolic pathways. Pyrimidine and purine metabolism were again altered, along with unique changes in histidine metabolism and O-antigen nucleotide sugar biosynthesis. The inclusion of the NDM-7 gene likely induced additional metabolic demands on the R strain, particularly in energy metabolism and

nucleotide turnover. Changes in pathways such as nucleotide biosynthesis and nucleotide sugar metabolism suggest potential metabolic adaptations. These adaptations may reflect the efforts of the strain to meet the increased demand for precursors required for plasmid maintenance and resistance gene expression. Such metabolic shifts may be critical for the ability of the strain to survive and function under antibiotic pressure. However, it is also important to consider the limitations of this model, as the observed changes may not solely reflect adaptive responses to resistance but could also arise due to the artificial introduction of a foreign plasmid. The metabolic burden associated with plasmid carriage, rather than meropenem resistance alone, may have contributed to some of the observed differences.

3.4.6 Metabolic impact of NDM-7 expression in *E. coli*; comparison between meropenem susceptible (S) and meropenem-resistant (R) strains

Understanding the specific metabolic demands of the NDM-7 gene is best achieved without the added complexity of plasmid expression effects. In **Sections 3.4.1** to **3.4.5** it was demonstrated that the introduction of the pCR2.1 plasmid alone imposes metabolic demands on the cells, including changes in nucleotide metabolism. To isolate the effects of the NDM-7 gene specifically, a metabolic comparison between the meropenem-susceptible (S) and meropenem-resistant (R) strains was performed. While both strains harboured the pCR2.1 plasmid, only the resistant strain (R) carried the additional NDM-7 gene responsible for carbapenem resistance. The design controlled for the metabolic impact of plasmid insertion in order to highlight the specific effects that may have been introduced by the NDM-7 gene alone. The clustered heatmap of the top 50 all features (**Figure 3.29**) showed clear differential compound-feature and identified metabolite expression between S and R strains, with distinct upregulation and downregulation patterns observed in the meropenem resistant strain. These shifts suggest a pattern of metabolite changes in the presence of the NDM-7 resistance gene, which accompany the antibiotic resistance mechanism. Notably, metabolites such as cyclic AMP and 3-isopropylmalate showed significant alterations.

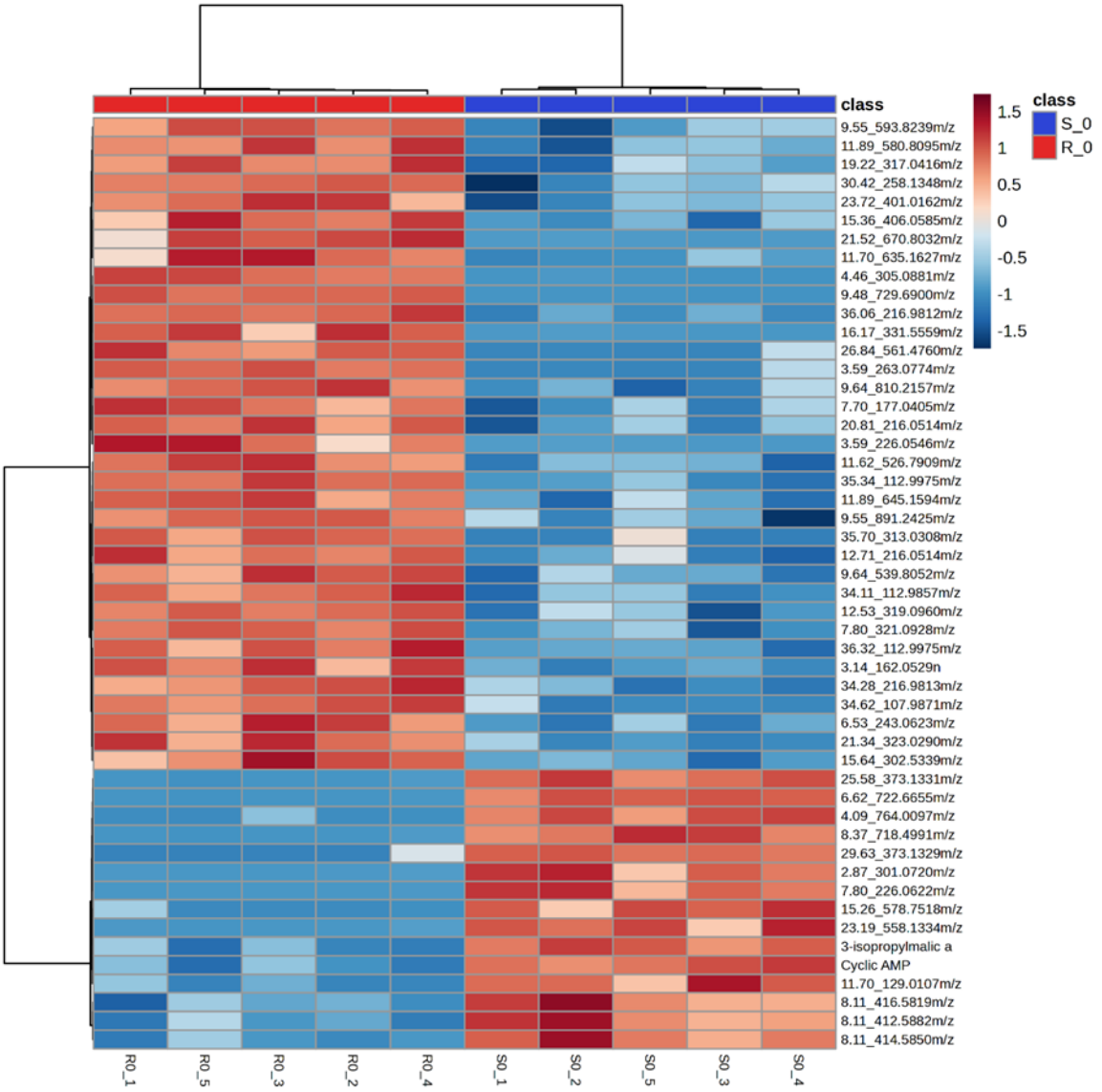

Figure 3.29 Clustered heatmap of differential metabolite expression between meropenem-susceptible (S) and meropenem-resistant (R)* E. coli *strains. *The heatmap displays the relative abundance of the top 50 most differential compound-features in susceptible (S_0) and resistant (R_0)* E. coli *strains. Rows represent individual metabolites, while columns represent biological replicates of each strain type. Red and blue colours indicate higher and lower relative metabolite abundance, respectively. The clear contrast between S_0 and R_0 samples illustrate significant metabolic reprogramming due to NDM-7 expression.*

The volcano plot (**Figure 3.30**) provided a detailed overview of the differentially expressed metabolites between the S and R strains. A total of 25 compound-features were downregulated, 49 were upregulated, and 3642 were non-significant. The comparison revealed fewer significant changes in comparison to the comparisons with wild-type (E) strain, likely due to the genetic similarities between S and R strains, including shared resistance to kanamycin and ampicillin. Nevertheless, the data indicated specific metabolite shifts driven by NDM-7

expression, highlighting metabolic changes that were associated with NDM-7 mediated resistance.

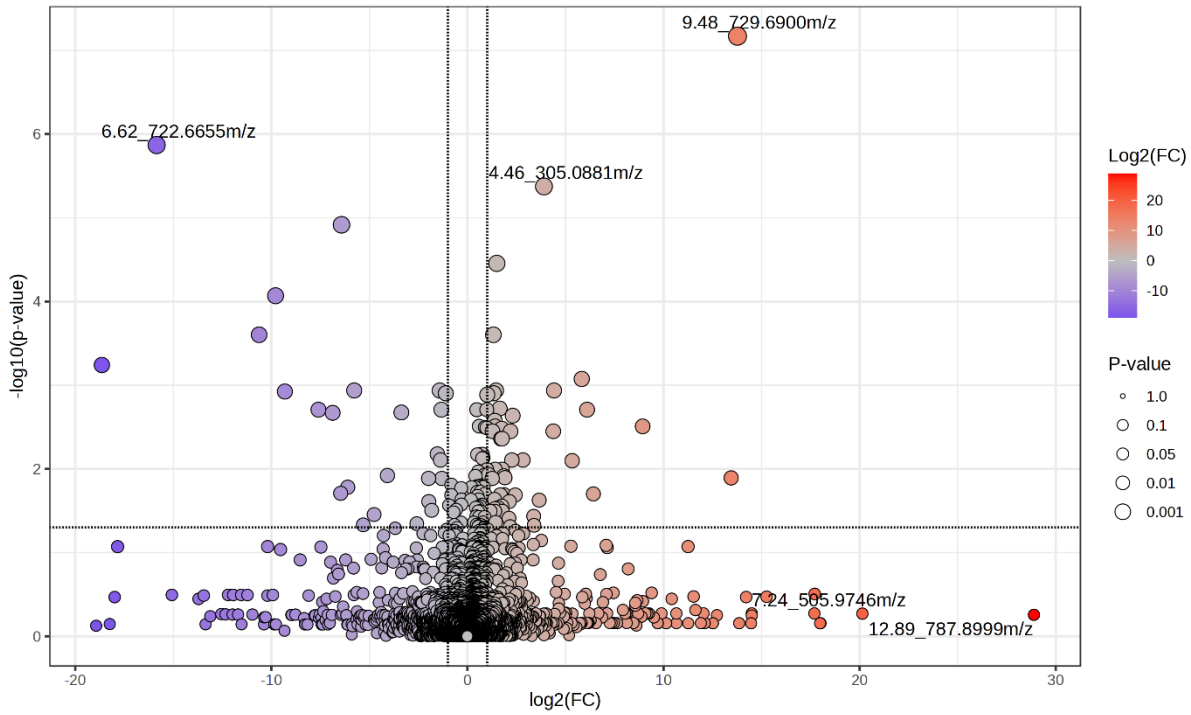

Figure 3.30 Volcano Plot Showing Differentially Expressed Metabolites Between Susceptible (S) and Resistant (R)* E. coli *Strains. *The volcano plot depicts the log2 fold change in metabolite abundance versus the -log p-value between S_0 and R_0 strains. Metabolites with significant changes (p < 0.05) are highlighted, with upregulated metabolites in R_0 shown on the right and downregulated metabolites on the left.*

The boxplots (**Figure 3.31**) illustrate significantly altered-identified metabolites. For instance, cyclic AMP, a critical signalling molecule, was markedly decreased in the R strain, a trend consistent across replicates. However, cyclic AMP was not found to be significantly altered in the comparisons of the susceptible and resistant with wild type (E) strain, suggesting that the difference observed here may be closely tied to the expression of NDM-7 gene. Another key metabolite, 3-isopropylmalic acid, was identified as significantly altered across both the S and R strains compared to E strain, indicating that it is not likely to be a direct consequence of NDM-7 expression but perhaps more reflective of shared resistance mechanisms present in both S and R strains. Such metabolite plays a role in leucine biosynthesis, which could be linked to resistance adaptation.[328,329]

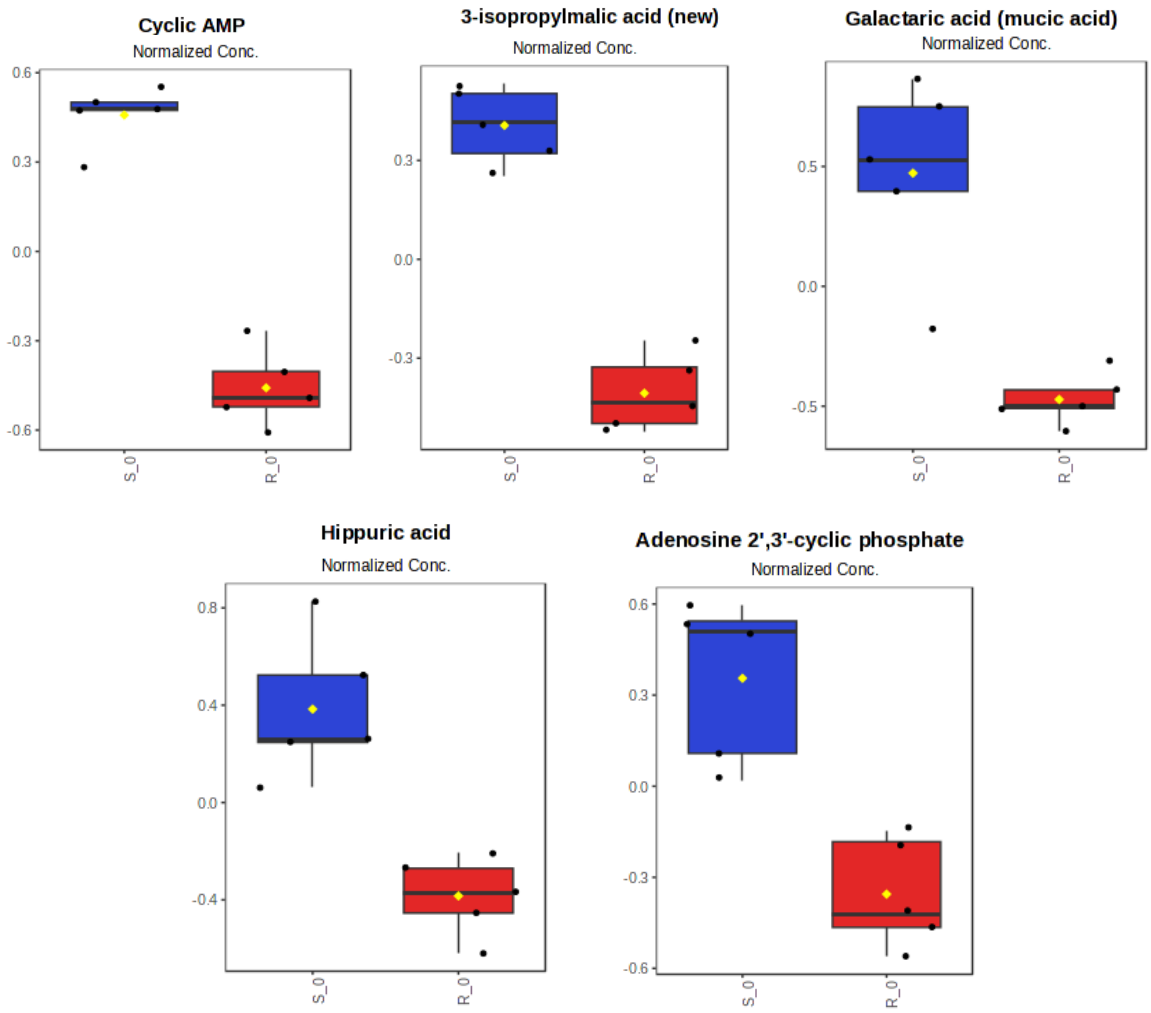

Figure 3.31 Boxplots of Normalised compound in meropenem-Susceptible (S) and Resistant (R)* E. coli *Strains. *Top 5 most significantly altered identified metabolites.*

Functional pathways analysis (**Figure 3.32**) revealed several metabolic pathways that were significantly altered between the meropenem-susceptible (S) and meropenem-resistant (R) strains. Interestingly, the R strain exhibited changes in pyrimidine metabolism, galactose metabolism, pentose phosphate pathway, amino sugar and nucleotide sugar metabolism, and fructose and mannose metabolism (**Table 3.11**). These pathways imply a metabolic reprogramming in response to the expression of the NDM-7 gene and focus more heavily on pathways involved in energy metabolism. For example, the alteration in the pentose phosphate pathway indicates shifts in cellular redox balance and biosynthesis of nucleotides and amino acids, further supporting the adaptation to oxidative stress. Alterations in the galactose and fructose/mannose metabolism point to changes in sugar metabolism, possibly compensating

for the energy and biosynthetic demands associated with carbapenem resistance. Pyrimidine metabolism was significantly altered (as observed in other comparisons), suggested an additional effect on nucleotide synthesis associated with the expression of the NDM-7 gene. The alteration may reflect increased demands for DNA repair and replication, potentially driven by the metabolic requirements of carbapenem resistance.

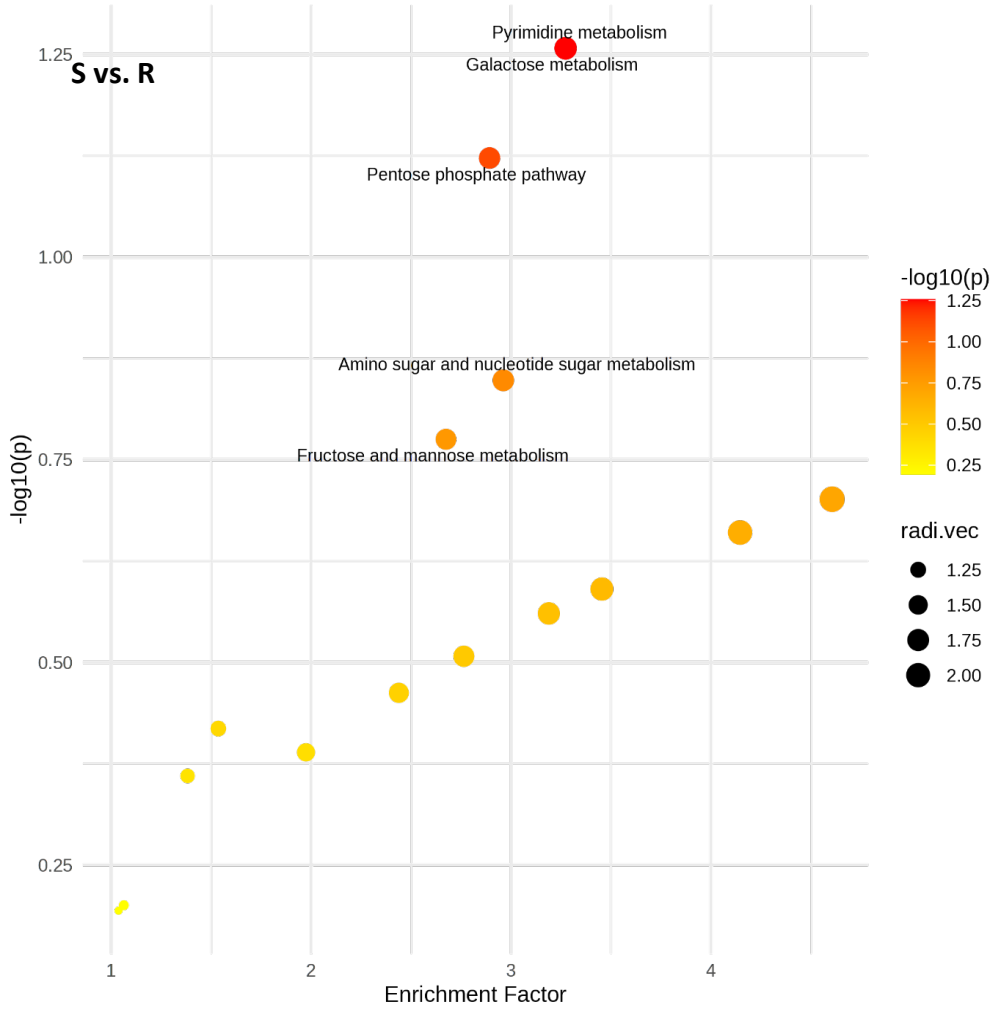

Figure 3.32 Functional analysis for metabolic changes between the meropenem-susceptible strain (S) and meropenem-resistant strain (R). *The plot highlights the most significantly altered metabolic pathways between the meropenem-susceptible (S) and meropenem-resistant (R) strains. The y-axis represents pathway impact based on topology analysis, while the x-axis indicates pathway enrichment. Bubble colour intensity reflects the statistical significance of the pathways (red indicating higher significance), and bubble size represents the pathway impact. This analysis provides insights into the metabolic pathways most affected by the expression of the NDM-7 gene in the resistant strain.*

Table 3.11 Results of functional analysis of metabolic pathways between meropenem-susceptible (S) and meropenem-resistant (R) strain. *The table summarises the functional analysis, listing the total number of compounds in each pathway, the number of hits (both all compounds and significant compounds), and the expected number of hits based on random distribution. The statistical significance of pathway enrichment is represented by p-values derives from Fisher's exact test (P(fisher)) and gamma distribution-based analysis (P(Gamma)). Pathways with notable changes include pyrimidine metabolism, pentose phosphate pathway, and galactose metabolism, suggesting metabolic reprogramming associated with carbapenem resistance.*

Pathway Name	Total↑↓	Hits(all)↑↓	Hits(sig.)↑↓	Expected↑↓	P(Fisher)↑↓	P(Gamma)↑↓
Galactose metabolism	39	36	9	0.91667	0.055238	8.5065E-4
Pyrimidine metabolism	51	25	6	0.91667	0.055238	8.5065E-4
Pentose phosphate pathway	26	21	4	1.0373	0.075451	9.2494E-4
Amino sugar and nucleotide sugar metabolism	44	29	7	0.67544	0.14188	0.0012207
Fructose and mannose metabolism	33	28	6	0.74781	0.166775	0.0013613
Peptidoglycan biosynthesis	18	7	1	0.21711	0.19888	0.0015535
Lipopolysaccharide biosynthesis	46	11	1	0.24123	0.21859	0.0016899
Streptomycin biosynthesis	9	7	2	0.28947	0.2567	0.0019906
Inositol phosphate metabolism	8	6	1	0.28947	0.2567	0.0019906
O-Antigen nucleotide sugar biosynthesis	21	14	2	0.3136	0.27512	0.0021558
Starch and sucrose metabolism	22	15	2	0.36184	0.31071	0.0025178
Pyruvate metabolism	27	12	1	0.41009	0.34471	0.0029247
Pentose and glucuronate interconversions	38	32	4	1.3026	0.38154	0.0034465
Glycolysis/Gluconeogenesis	29	16	3	0.50658	0.40817	0.0038858
Purine metabolism	76	33	4	1.4474	0.43648	0.0044204
Valine, leucine and isoleucine biosynthesis	22	20	2	0.94079	0.63025	0.011212
Ascorbate and aldarate metabolism	20	16	1	0.96491	0.64001	0.011785

The observed changes in individual metabolite abundances and metabolic pathways provide evidence that NDM-7 expression may impact not only antibiotic resistance but also impacts fundamental cellular processes, including energy metabolism. These metabolic adaptations could enable the meropenem-resistant strain to better manage stress and maintain cellular function in the presence of carbapenem antibiotics, such as meropenem. Additionally, the significant shifts in energy-related metabolites may suggest that the resistant strain experiences increased energy demands, potentially reflecting the metabolic cost of maintaining resistance mechanisms and adaptive responses under antibiotic pressure.

3.4.7 Discussion of the untargeted metabolomics results

Untargeted metabolomics has provided evidence that the introduction of the pCR2.1 plasmid and the NDM-7 gene reprogram the metabolic landscape in *E. coli* strains in the absence of antibiotic pressure. Untargeted metabolomics allowed for comprehensive view of how plasmid acquisition and carbapenem resistance influence core metabolic pathways.

The PCA and hierarchical clustering revealed distinct metabolic phenotypes between the wild-type (E), meropenem-susceptible (S), and meropenem-resistant (R) strains. The E strain exhibited a unique metabolic profile compared to the plasmid-bearing strains (S and R), as evidenced by the clustering pattern that separated the E strain from the other two strains. The finding indicates that the introduction of the pCR2.1 plasmid was sufficient to induce significant metabolic shifts. The S and R strains exhibited more similarity to each other, largely because they both harboured the plasmid, but the meropenem-resistant strain (R), containing the additional NDM-7 gene, displayed further metabolic divergence.

The metabolic shifts observed in the S strain compared to the E strain were primarily linked to the presence of the pCR2.1 plasmid, which confers resistance to ampicillin and kanamycin. These changes included significant alterations in peptidoglycan biosynthesis, reflecting adaptations to the β-lactam antibiotic resistance mechanism of ampicillin. Additionally, pyrimidine metabolism, lipopolysaccharide biosynthesis, vitamin B6 metabolism, and purine metabolism were significantly impacted in the S strain compared to E strain. These alterations suggest that the introduction of the plasmid alone imposes metabolic demands related to nucleotide biosynthesis, cell wall structure, and cofactor metabolism, even in the absence of antibiotic stress.

In the comparison between the wild-type (E) and meropenem-resistant (R) strains, which harboured both the pCR2.1 plasmid and the NDM-7 gene, more profound metabolic reprogramming was evident. Altered pathways in the R strain included pyrimidine metabolism, histidine metabolism, purine metabolism, O-antigen nucleotide sugar biosynthesis, and vitamin B6 metabolism. The presence of the NDM-7 gene appeared to further disrupt nucleotide metabolism and amino acid biosynthesis, reflecting the additional biosynthetic and stress adaptation requirements imposed by carbapenem resistance.

Significantly altered metabolites in both the S and R strains compared to the E strain indicated disruptions in nucleotide metabolism, amino acid metabolism, and central carbon metabolism. These include key pathways such as glycolysis and the pentose phosphate pathway, which are

critical for energy production and redox balance.[330]These findings suggest that the metabolic burden of carrying the plasmid and expressing resistance genes leads to fundamental shifts in energy metabolism, likely reflecting the need for increased resources to support plasmid replication, resistance gene expression, and survival under antibiotic pressure.

The comparison between the S and R strains revealed fewer significant metabolic differences, which was not surprising given their genetic similarities. However, the R strain showed specific metabolic changes, driven by NDM-7 expression, that were not present in the S strain. Notably in pathways involved in nucleotide synthesis (pyrimidine metabolism), sugar metabolism (galactose metabolism, fructose/mannose metabolism), and the pentose phosphate pathway. These pathways are essential for energy production, redox balance, and biosynthesis, suggesting that NDM-7 expression increases the cellular burden, necessitating further metabolic adaptations.[331,332] Such metabolic changes align with the role of the NDM-7 gene in conferring resistance to carbapenems, antibiotic that place significant stress on bacterial cells.

3.4.8 Comparative metabolic profiling conclusions

The comparative metabolic profiling of *E. coli* strains revealed that both the introduction of the pCR2.1 plasmid and the NDM-7 gene significantly altered the metabolic landscape of the bacteria. The wild-type strain, lacking the plasmid and the NDM-7 gene, exhibited a distinct metabolic profile, while the meropenem-susceptible and meropenem-resistant strains showed similar, yet distinct, metabolic reprogramming due to the plasmid and additional gene expression. The metabolic shifts observed in the meropenem-susceptible and meropenem-resistant strains were primarily driven by the metabolic demands of plasmid maintenance and resistance gene expression.

Key pathways affected by the introduction of the pCR2.1 plasmid included nucleotide metabolism, central carbon metabolism, and amino acid biosynthesis. These findings suggest that the metabolic cost of harbouring plasmid with resistance genes are high, even in the absence of antibiotic pressure. Additionally, the expression of the NDM-7 gene in the resistant strain introduced further metabolic burdens, particularly in pathways related to nucleotide

synthesis, sugar metabolism, and energy production, underscoring the complexity of metabolic adaptations required for carbapenem resistance.

These findings have important implications for understanding the metabolic consequences of antibiotic resistance in bacteria. By uncovering how resistance genes reshaped core metabolic pathways, this study highlights potential metabolic vulnerabilities that could be targeted to overcome resistance. Future work should focus on validating these findings and exploring how these metabolic adaptations impact bacterial fitness in the presence of antibiotics, potentially paving the way for novel therapeutic strategies aimed at disrupting metabolic processes critical to the survival of resistant strains.

3.5 Chapter 3 summary and conclusions

This chapter presented a detailed investigation into the metabolic consequences of antibiotic resistance in *E. coli* strains through a comparative metabolomic analysis. The study was designed to explore the metabolic shifts induced by the presence of the pCR2.1 plasmid and the NDM-7 gene which is responsible for resistance to carbapenem antibiotics like meropenem. Using three *E. coli* strains (wild-type, meropenem-susceptible, and meropenem resistant), comprehensive analysis of the metabolic changes associate with antibiotic resistance in these isogenic *E. coli* models using untargeted AEC-MS in addition to optimisation of metabolite extraction protocol was performed.

Genetically engineered *E. coli* strains were successfully developed to carry the pCR2.1 plasmid with and without the NDM-7 gene. The incorporation of these genetic elements was confirmed through sequencing, antibiotic susceptibility testing, and meropenem hydrolysis assays. The study demonstrated that the pCR2.1 plasmid conferred resistance to kanamycin and ampicillin, while the NDM-7 gene specifically conferred resistance to meropenem.

The metabolomics metabolite extraction and sample preparation workflow were carefully optimised and validated to ensure reliable extraction of intracellular metabolites from *E. coli* cells. Method A, which used a 50:50 methanol/acetonitrile extraction solvent, was identified as the most effective for bacterial metabolomics, yielding high-quality data with high

reproducibility. To reduce interference from the growth media and preserve metabolite integrity, a PBS washing step was introduced.

Comparative metabolomic profiling revealed distinct metabolic differences between the three strains. The meropenem-susceptible strain, carrying only the pCR2.1 plasmid, exhibited significant alterations in nucleotide metabolism, amino acid biosynthesis, and central carbon metabolism, reflecting the metabolic cost of plasmid carriage. The meropenem-resistant strain, which expressed the NDM-7 gene in addition to the pCR2.1 plasmid, showed further metabolic reprogramming, particularly in pathways related to nucleotide synthesis, energy metabolism, and redox balance. These findings suggest that both plasmid carriage and NDM-7 expression impose significant metabolic demands on *E. coli.*

In summary, a biological model was successfully established and validated for investigating the metabolic consequences of antibiotic resistance in *E. coli*. The findings demonstrate the metabolic cost of maintaining plasmid-borne resistance genes and provide insights into the specific pathways affected by NDM-7 expression. Several limitations should be acknowledged. First, the study used a single wild-type *E. coli* strain adapted to laboratory conditions, which may not fully represent the regulatory or stress responses of clinical or environmental isolates. Second, the use of the high-copy-number plasmid pCR2.1, while convenient for cloning, likely introduces metabolic burden on the host cell, potentially complicating interpretation of plasmid-specific effects. Lastly, while the NDM-7 expression was confirmed phenotypically, the promoter context was not investigated, leaving it unclear whether expression is constitutive or regulated under promotor control.

Despite these limitations, the findings provide a foundation for subsequent investigations, particularly in Chapter 4, which will explore how these metabolic changes evolve under antibiotic pressure. By identifying key metabolic vulnerabilities, this research supports the develop of novel strategies to combat carbapenem-resistant bacterial infections by leveraging the metabolic consequences of resistance mechanisms and targeting these pathways therapeutically to weaken meropenem-resistant strains and restore antibiotic susceptibility.

Chapter 4 Metabolic changes in resistant and non-resistant *E. coli* strains treated with the antibiotic meropenem

4.1 Introduction

Antibiotics are essential tools in combating bacterial infections, yet their impact on bacterial metabolism extends beyond their primary targets. Meropenem, a β-lactam antibiotic within the carbapenem class, disrupts bacterial cell wall synthesis by targeting penicillin-binding proteins.[333] Recent studies have shown that antibiotics, including meropenem, can also perturb central metabolic pathways, such as glycolysis, nucleotide biosynthesis, and energy production.[45,334] These disruptions create physiological stress within bacteria, manifesting as imbalances in metabolite levels and energy depletion, and which ultimately contribute to cell death.[154,316,333] The interconnectedness of bacterial metabolic networks are underscored by these disruptions, emphasizing the importance of understanding how antimicrobial agents influence cellular processes.

This chapter analyses the metabolic consequences of meropenem exposure with two primary objectives: (i) to investigate strain-specific metabolic changes associated with antibiotic-induced stress and (ii) to identify any pathways uniquely altered in resistant strains that could represent metabolic vulnerabilities. By examining the interplay between genetic background, antibiotic pressure, and metabolic alterations, experiments explored how meropenem, disrupts bacterial metabolic pathways, inducing physiological stress such as energy depletion and imbalances in biosynthetic processes.[21,335] Metabolic profiling, introduced in Chapter 3, offers a powerful approach to uncover the dynamic responses and elucidate adaptive metabolic mechanisms that underpin resistance and susceptibility. Resistant and non-resistant strains were studied with and without antibiotic challenge in order to identify strain-specific metabolic vulnerabilities that could act as therapeutic targets or markers to monitor antibiotic treatment efficacy.

Untargeted metabolomics was used to investigate changes in metabolite abundances across wild-type, meropenem-susceptible, and meropenem-resistant *E. coli* strains exposed to

varying concentrations of meropenem. The analysis highlighted differences between strains in the presence of the antibiotic and revealed pathway-level changes associated with meropenem exposure. These metabolic changes may rise from physiological stress caused by disrupted cell wall synthesis and potential off-target effects of meropenem on specific metabolic reactions. Understanding how *E. coli* strains reconfigure their metabolism under meropenem pressure has relevance for advancing our knowledge of antibiotic action and resistance and potentially elucidating new drug targets. By investigating both global metabolome and pathway-specific changes, this chapter seeks to provide a holistic view of the metabolic responses that support bacteria survival under antibiotic challenge and therefore has the potential to reveal areas of metabolic vulnerability that could be exploited to target carbapenem-resistance.

4.2 Antibiotic response analysis

4.2.1 Determination of minimum inhibitory concentration

In order to evaluate the efficacy of the broad-spectrum carbapenem antibiotic meropenem against the meropenem-resistant *E. coli* strain, a minimum inhibitory concentration (MIC) experiment was performed.[336] While non-resistant strains of *E. coli* are inherently susceptible to meropenem and were determined to not survive even at low concentrations, determining the MIC was crucial for validating the resistance phenotype and for establishing the appropriate antibiotic concentration that would stress bacterial cells sufficiently to induce metabolic changes without causing complete cell death, therefore establishing a treatment concentration suitable for enabling subsequent metabolomic analyses.

To achieve this, the resistant *E. coli* strain (R) was grown in the presence of various concentrations of meropenem, ranging from 0 μg/mL up to 256 μg/mL. The drug concentrations were prepared using a 1 in 2 serial dilution method. For the 0 μg/mL condition, DMSO was used as the vehicle control, since the meropenem was initially dissolved in DMSO for all other conditions. Each well in the 96 well plate contained 20 μL of bacterial subculture (at an OD_{600} of 0.01) and 180 μL of fresh media with meropenem at the corresponding concentration or DMSO. The bacterial growth was continuously monitored using a CLARIOstar

plate reader (BMG Labtech), by measuring optical density at 600 nm every 10 minutes over a 24-hour period. Previous studies have shown that DMSO at low concentrations (≤ 5%) does not inhibit *E. coli* growth under standard laboratory conditions, but its inclusion as a control ensures any solvent-related effects are accounted for in the experimental design.[337]

The growth curves, see **Figure 4.1**, demonstrated a clear concentration-dependent inhibition of the resistant strain growth by meropenem. In the absence of meropenem (0 µg/mL), *E. coli* exhibited robust growth, reaching OD_{600} of approximately > 3. At lower concentrations of meropenem (0.25, 0.5, and 1 µg/mL), bacterial growth was moderately inhibited, with the cultures displaying delayed exponential phases and reduced maximum OD_{600} values compared to the control. Growth curves for the wild-type and meropenem-susceptible strains (E and S, **Appendix II Figure II. and Figure II.**) were not included, as these strains did not produce detectable growth in the presence of meropenem, apart from the control condition.

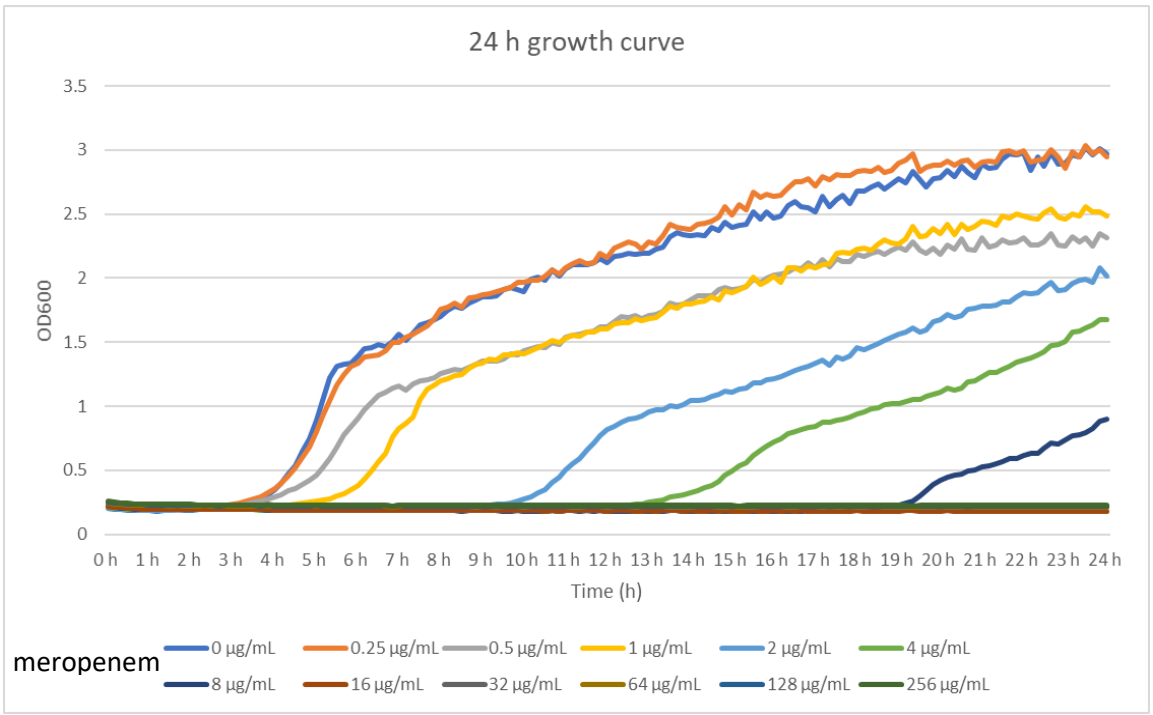

Figure 4.1 24-hour growth curve of* E. coli *resistant strain in the presence of various concentration of meropenem. *The OD600 was measured every 10 minutes for over a 24-hour period. The concentrations of meropenem tested were 0, 0.25, 0.5, 1, 2, 4, 8, 16, 32, 64, 128, 256 µg/mL, as indicated in the legend. The growth curves show a clear concentration-dependent inhibition of* E. coli *by meropenem, with higher concentrations leading to greater suppression of bacterial growth.*

As the concentration of meropenem increased, the inhibitory effects on bacterial growth became more pronounced. At lower concentrations (0.25 – 8 µg/mL), bacterial growth was

delayed, with the lag phase extending in a concentration-dependent manner and bacterial growth was markedly reduced. The observed delay in growth at sub-inhibitory concentrations suggests that meropenem exerts metabolic stress on the resistance strain before the cells either adapt or succumb to the antibiotics. The observation indicated that despite resistance, exposure to meropenem still imposes a metabolic change on the bacteria, potentially affecting key pathways required for growth. The concentration-dependent inhibition highlights that while the resistant strain can tolerate lower concentrations, increasing antibiotic pressure progressively limits bacterial survival. Cultures exposed to 16 μg/mL meropenem or higher exhibited no growth. The MIC of meropenem for the meropenem-resistant strain is therefore approximately 16 μg/mL, as this is the lowest concentration at which there was no observable growth over the 24-hour period. The MIC value establishes the concentration at which meropenem effectively inhibits growth in the resistant strain, providing a reference point for designing future metabolomic experiments to explore the metabolic response of the meropenem-resistant strain under antibiotic exposure.

4.2.2 Determining optimal meropenem concentrations and exposure times for metabolomic analysis

The meropenem concentrations chosen for this study were strategically selected to cover the susceptibility and resistance thresholds defined by both the Food and Drug Administration (FDA) and the 2010 Clinical and Laboratory Standards Institute (CLSI) guidelines. According to the FDA, bacterial isolates are classified as susceptible to meropenem when the MIC is ≤ 2 μg/mL, intermediate at a MIC of 4 μg/mL, and resistant at a MIC ≥ 8 μg/mL.[338] The CLSI defines susceptibility at a MIC ≤1 μg/mL, intermediate at 2 μg/mL, and resistance at MIC ≥ 4 μg/mL.[339,340]

To understand how the *E. coli* strains respond to varying levels of meropenem exposure over time, a time-kill assay was designed to assess bacterial survival responses at critical thresholds of inhibition and resistance. The experiment was used to determine the optimal meropenem exposure duration to ensure bacteria were under stress but still viable. Based on the results of

the 24-hour growth curve and the established guidelines for meropenem resistance, meropenem concentrations of 0 μg/mL, 1 μg/mL, 4 μg/mL, and 16 μg/mL were selected for a time-kill assay. The approach aimed to evaluate whether different exposure times to selected concentrations of meropenem could sufficiently induce metabolic changes in the bacterial cells without causing immediate lysis or complete population death.

For the time kill assay, the subculture was grown, and OD_{600} was normalised to 0.1. Four concentrations of meropenem, 0 μg/mL, 1 μg/mL, 4 μg/mL, and 16 μg/mL, were tested at five different time points: 0 min, 30 min, 60 min, 4 hours, and 24 hours. For each concentration and time point, 200 μL of the sample was collected in duplicate. Each sample was then diluted in broth by a factor of 10^5. Subsequently, 50 μL of the diluted samples were plated on agar for colony growth. After 24 hours of incubation, colonies were counted.

The colony-count (**Figure 4.2** and **Figure 4.3**) demonstrate distinct responses between the susceptible (S) and resistant (R) *E. coli* strains. For the susceptible strain (**Figure 4.2**), colony counts decreased rapidly with increasing concentrations of meropenem and duration of exposure. No colonies were detectable at 1 μg/mL, 4 μg/mL, and 16 μg/mL after 4 hours of exposure, indicating complete inhibition of growth at these concentrations within this timeframe. However, at the 24-hour time point, colony counts increased in cultures previously exposed to 1 μg/mL and 4 μg/mL, suggesting that a subpopulation of cells survived and was able to regrow once the antibiotic pressure diminished. The revival was not observed at 16 μg/mL, indicating that at this concentration, bacterial survival was completely suppressed. The regrowth at lower concentrations suggests a potential transient inhibition rather than complete eradication, possibly due to adaptive responses or the degradation of meropenem over time. The observation aligns with expectations for bactericidal antibiotics, where a fraction of cells may persist and resume growth once the antibiotic concentration decreased or tolerance mechanism can overcome the antibiotic effect. However, the lack of regrowth at 16 μg/mL supports the conclusion that this concentration is sufficient to eliminate the susceptible population completely within the tested timeframe.

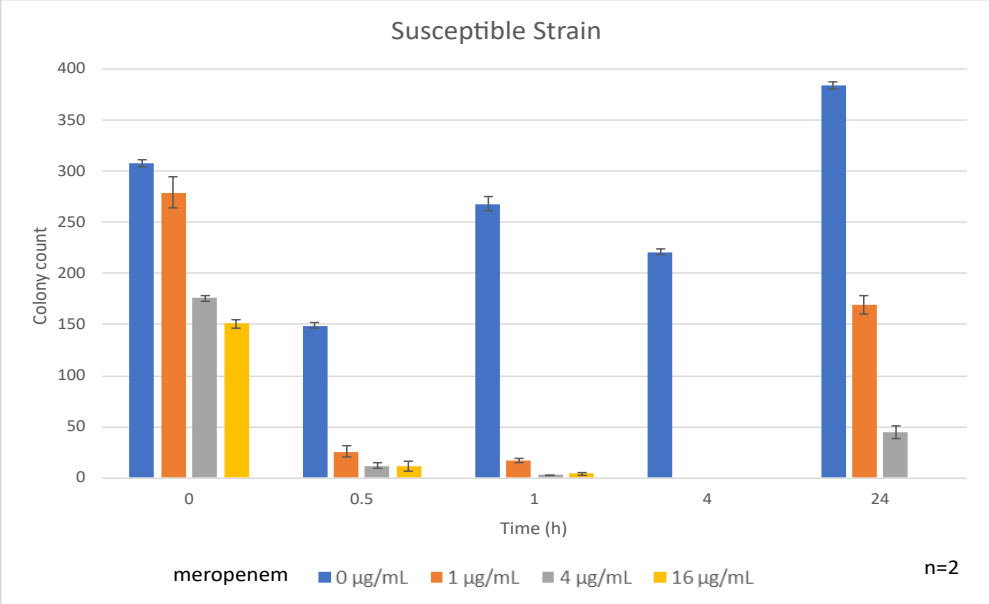

Figure 4.2 Colony counts of susceptible* E. coli *strain at varying time points and meropenem concentrations. *CFUs were measured at 0 min, 30 min, 60 min, 4 h, and 24 h for each concentration of meropenem (0 µg/mL, 1 µg/mL, 4 µg/mL, and 16 µg/mL). Bars represent the mean of two experimental replicates (n=2); vertical lines indicate the range.*

In contrast, the resistant strain (**Figure 4.3**) maintained higher colony counts across all concentrations. At 16 µg/mL, colony counts were greatly reduced by 4 hours, but partial recovery observed by 24 hours. The ability of the resistant strain to tolerate higher concentrations of meropenem compared to the susceptible strain is evident from these observations.

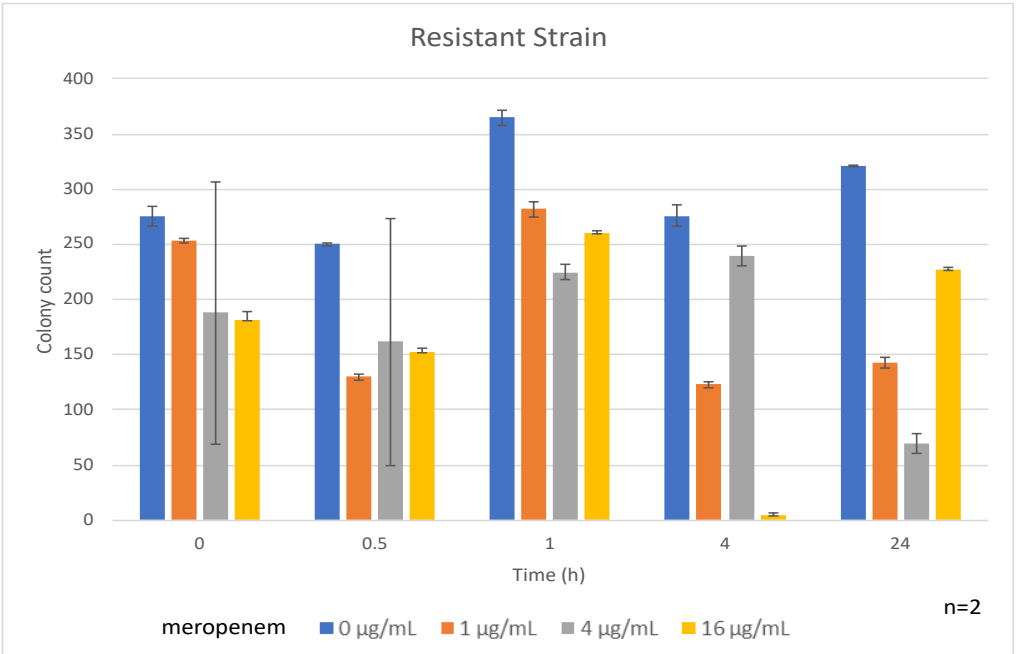

Figure 4.3 Colony counts of resistant* E. coli *strain at varying time points and meropenem concentrations. *CFUs were measured at 0 min, 30 min, 60 min, 4 h, and 24 h for each concentration of meropenem (0 µg/mL, 1 µg/mL, 4 µg/mL, and 16 µg/mL). Bars represent the mean of two experimental replicates (n=2); vertical lines indicate the range.*

These findings suggest that extending the drug exposure time beyond 4 hours is unnecessary for effective evaluation of meropenem impact, as the most critical effects of meropenem had already occurred within this period. Therefore, an exposure time shorter than 4 hours was sufficient to capture the key effects of meropenem on both susceptible and resistant *E. coli* strains. These results guided the selection of antibiotic concentrations for subsequent metabolomic experiments, ensuring that the chosen concentrations effectively challenge both resistant and susceptible strains without completely eradicating them. The strategy was used to establish a framework for investigating the effect of meropenem treatment on metabolic mechanisms underlying antibiotic resistance in future studies.

4.2.3 Antibiotic treatment

To investigate the metabolic responses of *E. coli* strains to meropenem, subcultures of wild-type (E), meropenem-susceptible (S), and meropenem-resistant (R) strains were grown to the log phase of growth (OD_{600} 0.4). Antibiotic exposure was carried out as described in Section **2.2.11 Antibiotic exposure**, ensuring consistency in treatment conditions.

The treatment was performed to evaluate how varying durations and concentrations of meropenem impacted cellular metabolism, enabling the identification of strain-specific metabolic adaptations under antibiotic influence.

4.2.4 Viability of *E. coli* strains following meropenem exposure

Next it was decided to investigate the effect of antibiotic concentration on cell viability to assess the metabolic response to antibiotic-induced stress. To evaluate the viability of *E. coli* strains after exposure to meropenem, wild-type (E), susceptible (S), and resistant (R) strains were subjected to a 1-hour treatment with varying concentration of meropenem (0 μg/mL, 1 μg/mL, 4 μg/mL, and 16 μg/mL). After exposure, the cells were transferred to fresh medium, and their growth recovery was monitored over a 3-hour period by measuring optical density at 600 nm (OD_{600}). Monitoring recovery dynamics under antibiotic stress provided insights into the suitability of each condition for further metabolic analysis (**Figure 4.4**).

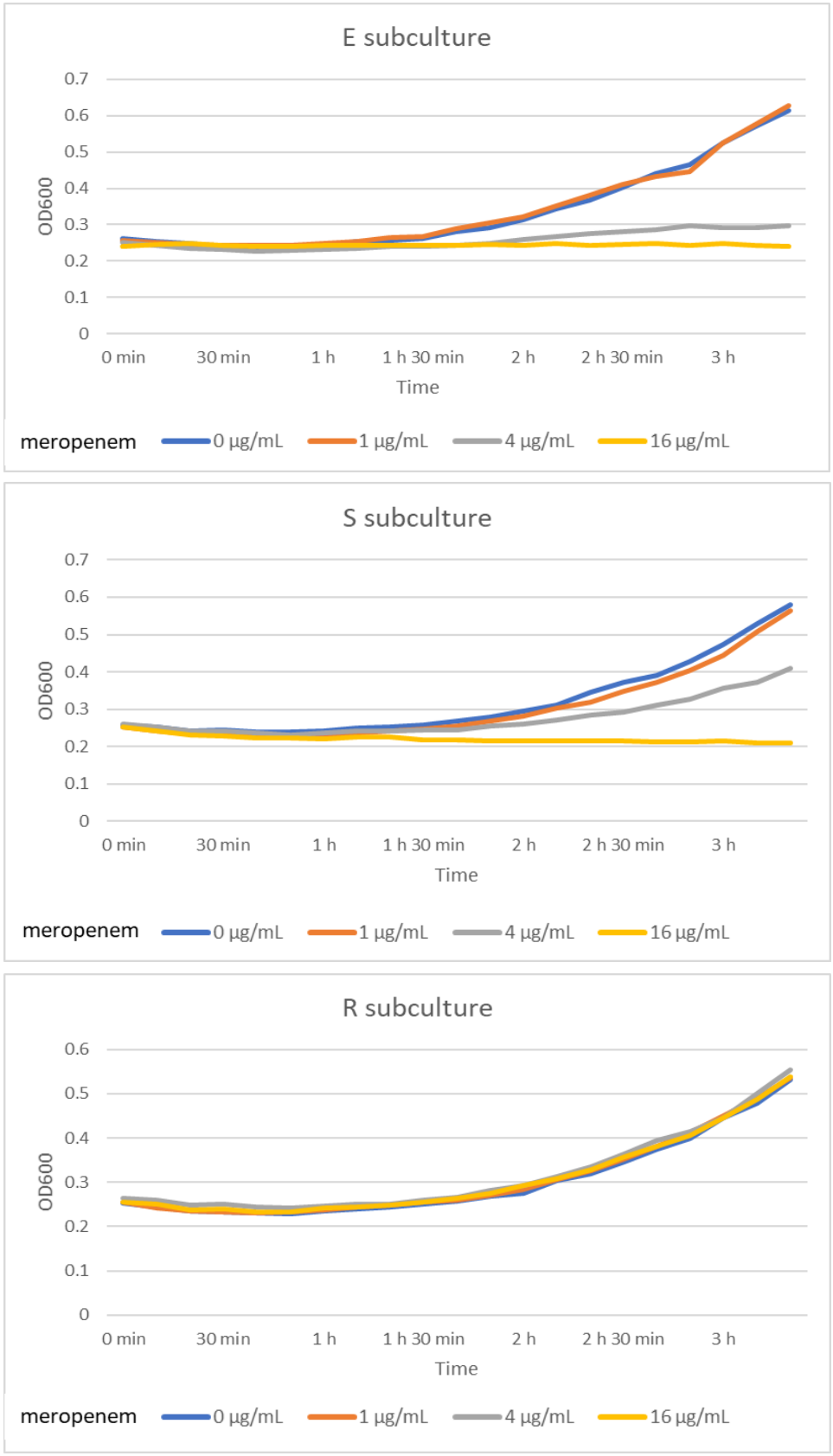

Figure 4.4 Growth Recovery of Wil-type (E), Susceptible (S), and Resistant (R)* E. coli *Strains After 1-hour Exposure to Meropenem Followed by Subculturing. *Each strain was exposed to varying concentrations of meropenem (0,1, 4, and 16 µg/mL) for 1 hour, followed by recovery in fresh medium. OD_{600} was measured over 3 hours post-subculturing to assess recovery. Both the wild-type and susceptible strains showed significant growth inhibition at 16 µg/mL, while the resistant strain exhibited consistent growth across all concentration.*

The growth recovery results indicated that a 1-hour exposure to meropenem was sufficient to apply selective pressure on the bacteria without completely killing off the population, except at the highest concentration (16 μg/mL) for the wild-type and susceptible strains. At 16 μg/mL, wild-type and susceptible strains exhibited minimal recovery, with substantial inhibition of growth. As a result, this concentration was excluded from further metabolic analysis, since the lack of viable cells would interfere with downstream profiling.

At 4 μg/mL, both wild-type and susceptible strains demonstrated clear signs of stress, with delayed growth compared to lower concentrations. However, recovery was still evident, suggesting that while 4 μg/mL caused substantial metabolic stress but was not entirely lethal, thus indicating a 1-hour exposure was sufficient to exert pressure while preserving cell viability for further analysis depending on concentration.

In contrast, the resistant (R) strain displayed consistent growth across all concentrations, including 16 μg/mL, which represents the MIC for this strain. After 1-hour exposure, the resistant strain was able to recover and continue growing, showing that while 16 μg/mL exerted substantial stress, it was not entirely lethal. Growth at all meropenem concentrations in the resistant strain was similar to the control (0 μg/mL, DMSO), indicating strong resistance to the antibiotic.

4.2.5 Conclusion

In determining the optimal concentrations of meropenem for metabolic studies, the MIC of 16 μg/mL was identified as the threshold beyond which bacteria growth was completely inhibited. Identification of the MIC was crucial for allowing us to stress bacterial cells while still maintaining viability, which is critical for metabolomic analysis. The chosen concentrations of 1 μg/mL, 4 μg/mL, and 16 μg/mL effectively spanned the susceptibility and resistance threshold defined by both FDA and CLSI guidelines, ensuring that the bacterial strains were adequately challenged in subsequent experiments.

The results of colony count analysis showed that a 4-hour exposure to meropenem was sufficient to capture key effects on bacterial viability, providing a suitable window for conducting further experiments without inducing complete cell death in susceptible strains.

The viability assessment reveals important insights into the differential responses of wild-type, susceptible, and resistant *E. coli* strains to meropenem. The wild-type and susceptible strains exhibited substantial growth inhibition at 16 μg/mL, suggesting that this concentration is nearly lethal for these strains. Consequently, metabolomic results at this concentration are likely to reflect metabolites associated with cell death or maximum defence mechanisms in a last attempt at survival.

At 4 μg/mL, both wild-type and susceptible strains showed delayed but evident recovery, making this concentration suitable for studying metabolic stress without completely impairing viability. In contrast, the resistant strain demonstrated strong growth across all concentrations, including 16 μg/mL, indicating a robust resistance mechanism.

These findings validate that 1-hour exposure to meropenem is sufficient to induce metabolic stress in the meropenem-susceptible (S) and wild-type (E) strains, while still preserving enough cell viability for subsequent metabolomic analysis, particularly at lower concentration. To ensure direct comparison across all strains, a consistent 1-hour exposure was chosen. Establishing this standardised exposure period provides an ideal framework for investigating metabolic adaptations and immune responses under antibiotic pressure, offering opportunities for comparisons between strains to uncover potential metabolic vulnerabilities. These insights may ultimately inform the development of future strategies targeting AMR.

4.3 Metabolic responses to sub-lethal meropenem treatment of *E. coli* strains

Understanding how bacteria adapt their metabolism under antibiotic exposure is critical for developing strategies to combat resistance. Next it was decided to examine the metabolic responses of three *E. coli* strains following exposure to meropenem using untargeted metabolomics. Building upon baseline metabolic characterisation discussed in Chapter 3, the aim was to investigate how antibiotic treatment affects bacterial metabolism. By analysing

metabolic changes in wild-type, meropenem-susceptible, and meropenem-resistant strains, this experiment sought to identify metabolites altered in abundance by exposure to meropenem and investigate their impact on functional metabolic processes.

Each of the three strains (the wild-type strain (E), the meropenem-susceptible strain harbouring the pCR2.1 plasmid (S), and the meropenem-resistant strain carrying the pCR2.1 plasmid along with the NDM-7 resistance gene (R)) were exposed to a sub-lethal concentration of meropenem (1 μg/mL and 4 μg/mL) for 1-hour. The concentration and exposure time were determined based on results from the viability assays (Section 4.2.2), which demonstrated that 1-hour exposure of 4 μg/mL meropenem induced cellular response in all strain without causing death in wild-type (E) and meropenem-susceptible (S) strains. Although the meropenem-resistant (R) strain exhibited minimal growth inhibition at this concentration and duration, maintaining a consistent exposure time and concentration across all strains was essential for direct comparison. The approach allows for investigating early metabolic responses under antibiotic pressure, even in the resistant strain, where metabolic effects may be more subtle or require longer exposure to become pronounced.

Following antibiotic treatment, untargeted metabolomics was employed to comprehensively analyse the metabolic changes of each strain in response to meropenem exposure. Metabolites were extracted using a cold methanol/acetonitrile-based protocol optimised for bacterial cultures in Chapter 3 (**Section 2.3.5**). After extraction, DNA normalisation and filtration were performed as described in **Section 2.3.6** to ensure sample consistency prior to AEC-MS/MS analysis.

Samples were analysed using the AEC-MS/MS (**Section 2.4**)workflow validated in Chapter 3. Full MS-ddMS2 was employed to enable comprehensive metabolite identification, operating in negative ion mode. Data processing and analysis was performed as described previously in **Section 3.3** for the comparison between strains. Briefly, metabolites were identified by matching accurate mass, isotope pattern, chromatographic retention time and MS2 fragments to in-house database enabling Level 1 (high confidence with authentic standards) and Level 2

(putative annotation based on spectral similarity to database entries). Data processing was performed using median normalisation, log transformation and Pareto scaling.

4.3.1 Data quality and overview of metabolic profiles

Data quality was assessed using an unclustered heatmap and PCA plot to visualise the absence of significant inter or intra-class biases or outliers. During quality control, sample R1_2 was identified as an outlier due to substantial deviations in metabolite abundances compared to other R_1 replicates in the non-normalised dataset (**Appendix II Figure II.** heatmap)**.** The sample also fell outside the confidence ellipse of the R_1 group in the PCA (**Appendix II Figure II.** PCA plot), indicating a lack of alignment with the metabolic profiles of other R_1 samples. Such deviation suggests potential technical artifacts, experimental error, or biological anomaly. Excluding this sample ensured that downstream analyses accurately reflected biological differences rather than confounding technical variability.

The unclustered heatmap (**Figure 4.5**), illustrated the overall consistency and reliability of the dataset. The analysis confirmed the absence of any systematic intra- or inter-class differences introduced during sample preparation or data acquisition. Establishing dataset consistency is essential to ensure that any observed metabolite changes in subsequent analyses were driven by biological differences rather than technical artifacts. Normalised metabolite abundances from wild-type (E, green), meropenem-susceptible (S, blue), and meropenem-resistant (R, red) *E. coli* strains were visualised, including both vehicle control (0 µg/mL) and meropenem-treated (1 and 4 µg/mL) conditions.

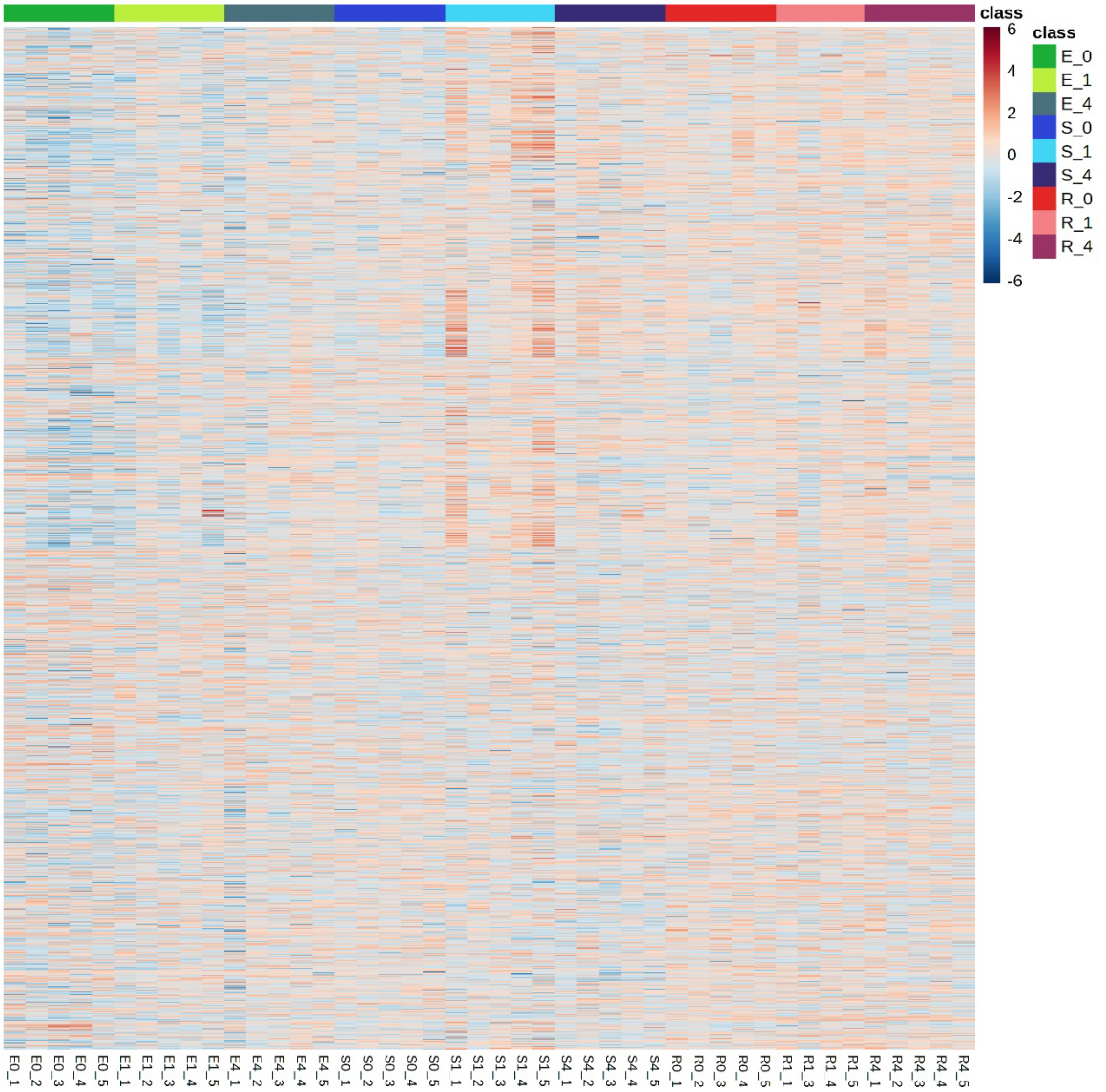

Figure 4.5 Heatmap of* E. coli *strains exposed to 0, 1, and 4 µg/mL meropenem. *This heatmap displays normalised abundances of metabolites in wild-type (E), meropenem-susceptible (S), and meropenem-resistant (R)* E. coli *strains, comparing DMSO control (0 µg/mL) and meropenem-treated (1 or 4 µg/mL) conditions. Rows represent individual metabolites, with colour intensity indicating relative abundance levels (blue for lower and red for higher abundance).*

The PCA plot (**Figure 4.6**) provided an overview of the variance in metabolite profiles across all three strains (wild-type (E), meropenem-susceptible (S), and meropenem-resistant (R)) and treatment conditions (0, 1, and 4 µg/mL of meropenem). By integrating all groups in a single PCA plot, the analysis enables a direct comparison of metabolic changes under meropenem exposure and revealed distinct clustering patterns indicative of strain-specific and dose-dependent metabolic responses. No major outliers were observed beyond sample R1_2.

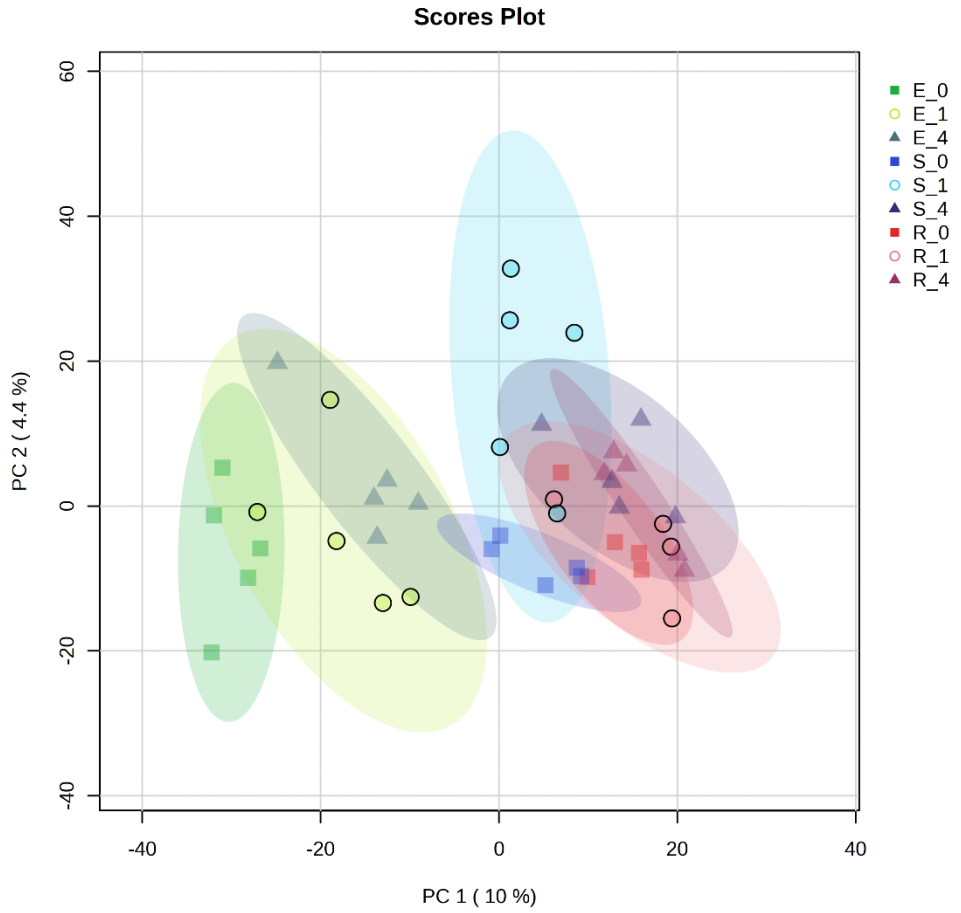

Figure 4.6 PCA plot showing the metabolic profiles of* E. coli *strains under vehicle control (0 µg/mL) and meropenem treated (1 or 4 µg/mL) conditions. *The plot includes data for wild-type (E)-green, meropenem-susceptible (S)-blue, and meropenem-resistant (R)-red strains. Each point represents a biological replicate, and confidence ellipses indicate group clustering. PC1 accounts for 10% of the variance, and PC2 accounts for 4.4% of the variance in the dataset.*

For the wild-type (E) strain, clear separation was observed between vehicle control (E_0) and 4 µg/mL meropenem-treated samples (E_4), reflecting significant metabolic changes at this concentration. The 1 µg/mL treated samples (E_1) overlapped with both E_0 and E_4, indicating a dose-dependent metabolic response. The meropenem treated samples (E_1 and E_4) exhibited greater variability compared to vehicle control, suggesting a broader range of metabolic states under antibiotic exposure, while more tightly clustered E_0 samples reflected a more stable baseline metabolic profile.

The meropenem-susceptible strain (S), also showed distinct separations between vehicle control (S_0) and 4 µg/mL meropenem-treated (S_4) condition, indicating significant changes in the metabolic profiles at 4 µg/mL meropenem. Samples treated with 1 µg/mL (S_1) clustered

between 0 and 4 μg/mL, demonstrating more pronounced changes in S_4, suggesting that exposure to 4 μg/mL meropenem imposes a stronger impact in cellular metabolism than 1 μg/mL. The tighter clustering observed in the untreated condition (S_0) indicated a relatively more consistent baseline metabolic state in the absence of antibiotic pressure. In contrast, the broader dispersion observed in S_1 and S_4 reflects increased metabolic variability under meropenem exposure with S_1 exhibiting greater variability than S_4. Exposure to 1 μg/mL may induce a wider range of adaptive responses, while 4 μg/mL might result in more uniform stress-induced metabolic changes due to higher antibiotic pressure. While the plasmid present in the S strain does not confer resistance to meropenem, its presence may influence the adaptive response of the strain to antibiotic pressure, distinguishing it from the wild-type (E) strain. These findings emphasise the measurable impact of meropenem-induced stress on the metabolic state of meropenem-susceptible strain and the interplay between plasmid carriage and antibiotic-induced metabolic changes.

In contrast, the meropenem-resistant strain (R) displayed overlapping confidence ellipses across vehicle control (R_0) and meropenem-treated samples (R_1 and R_4), indicating limited metabolic perturbation under antibiotic exposure. The relatively similar metabolic profile suggests that the R strain is less affected by meropenem, likely due to its ability to enzymatically degrade the antibiotic via NDM-7. Consequently, the metabolic disruptions observed in the E and S strains are likely mitigated in the R strain.

4.3.1.1 Summary of data quality and consistency

The unclustered heatmap analysis (**Figure 4.5**) confirmed internally consistency across the dataset, with biological groups showing no evidence of systematic inter or intra- group differences in overall metabolite abundances. Normalised metabolite abundances across experimental conditions were consistent, with an absence of batch effects or technical biases.

The PCA (**Figure 4.6**) demonstrated that experimental groups reflected a distinct metabolic profile, with samples forming well-defined clusters across all strains and conditions, indicating minimal variability within groups and confirming the high reproducibility of the data. The

analysis revealed an apparent strain-specific metabolic response to meropenem exposure, with clear metabolic changes observed in the wild-type (E) and meropenem-susceptible (S) strains, while the meropenem-resistant (R) strain displayed relatively stable metabolic profiles.

4.3.2 Metabolic responses to meropenem exposure in wild-type, meropenem-susceptible, and meropenem-resistant *E. coli* strains

This section focuses on the metabolic differences between the wild-type (E), meropenem-susceptible (S) and meropenem-resistant (R) *E. coli* strains upon exposure to 0, 1, or 4 μg/mL meropenem. By analysing the response of all three strain to antibiotic exposure at the same concentration, strain specific effect can be compared.

4.3.2.1 Identifying significantly altered metabolites upon exposure to sub-lethal concentrations of meropenem

ANOVA was performed to identify metabolites with significant changes in abundance across experimental groups, providing initial insights into metabolic differences between wild-type (E), meropenem-susceptible (S), and meropenem-resistant (R) strains under vehicle control (DMSO) or meropenem treatment (mero). By applying ANOVA with post hoc test, the analysis captured strain-specific metabolic responses to meropenem in order to assess the broader metabolic impact of antibiotic treatment.

Initially compound-feature data from the untargeted analysis across all groups (E, S, and R strains, under DMSO or mero) were analysed using ANOVA, with significance threshold and FDR-corrected p-value < 0.05 (**Figure 4.7**). The analysis identified 1,548 compound-features significantly altered in abundance between one or more experimental groups, with the remaining 2,179 compound-features showing no significant differences. Given the number of different groups the absolute number was less relevant than the fact that changes were observed and the trends inherent in those changes.

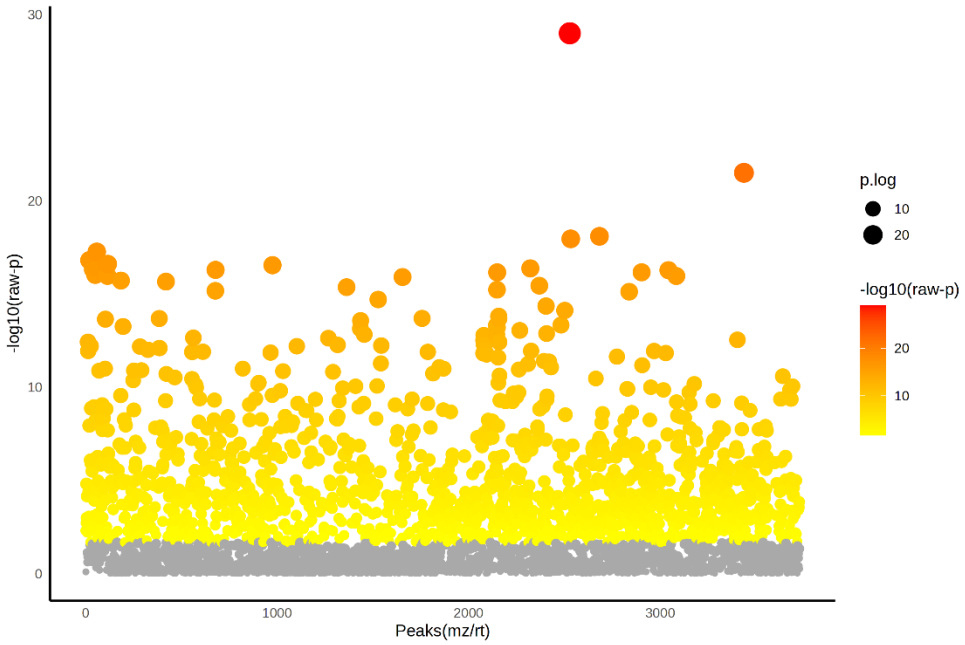

Figure 4.7 ANOVA results showing the distribution of significant and non-significant features across all detected compounds in wild-type (E), meropenem-susceptible (S), and meropenem-resistant (R) **E. coli** ***strains under DMSO (vehicle control, E_0, S_0, R_0) and meropenem treatment (E_1, E_4, S_1, S_4, R_1, R_4).*** *The x-axis represents peaks (*m/z *or retention time), and the y-axis represents -log10 of the raw p-value. Significant features (adjusted p-value < 0.05) are shown in orange and red, with nonsignificant features in grey. Larger points represent higher statistical significance.*

Boxplots were generated across all experimental groups for significantly altered compound-features and identified metabolites. These provided insights into the metabolic responses of wild-type (E), meropenem-susceptible (S), and meropenem-resistant (R) strains under 0, 1, and 4 μg/mL meropenem exposure. Interestingly these clearly showed both strain-specific and concentration-dependent effects of antibiotic treatment.

Strain-specific differences in compound-feature and identified metabolite levels are highlighted in **Figure 4.8**. For example, 4-methyl-2-oxovaleric acid (ketoleucine), thymine, and uracil were elevated in the E strain in comparison to S and R strains, suggesting a metabolic profile mainly influenced by plasmid carriage although interestingly some evidence of a dose dependent effect for the R strain for ketoluecine and uracil.

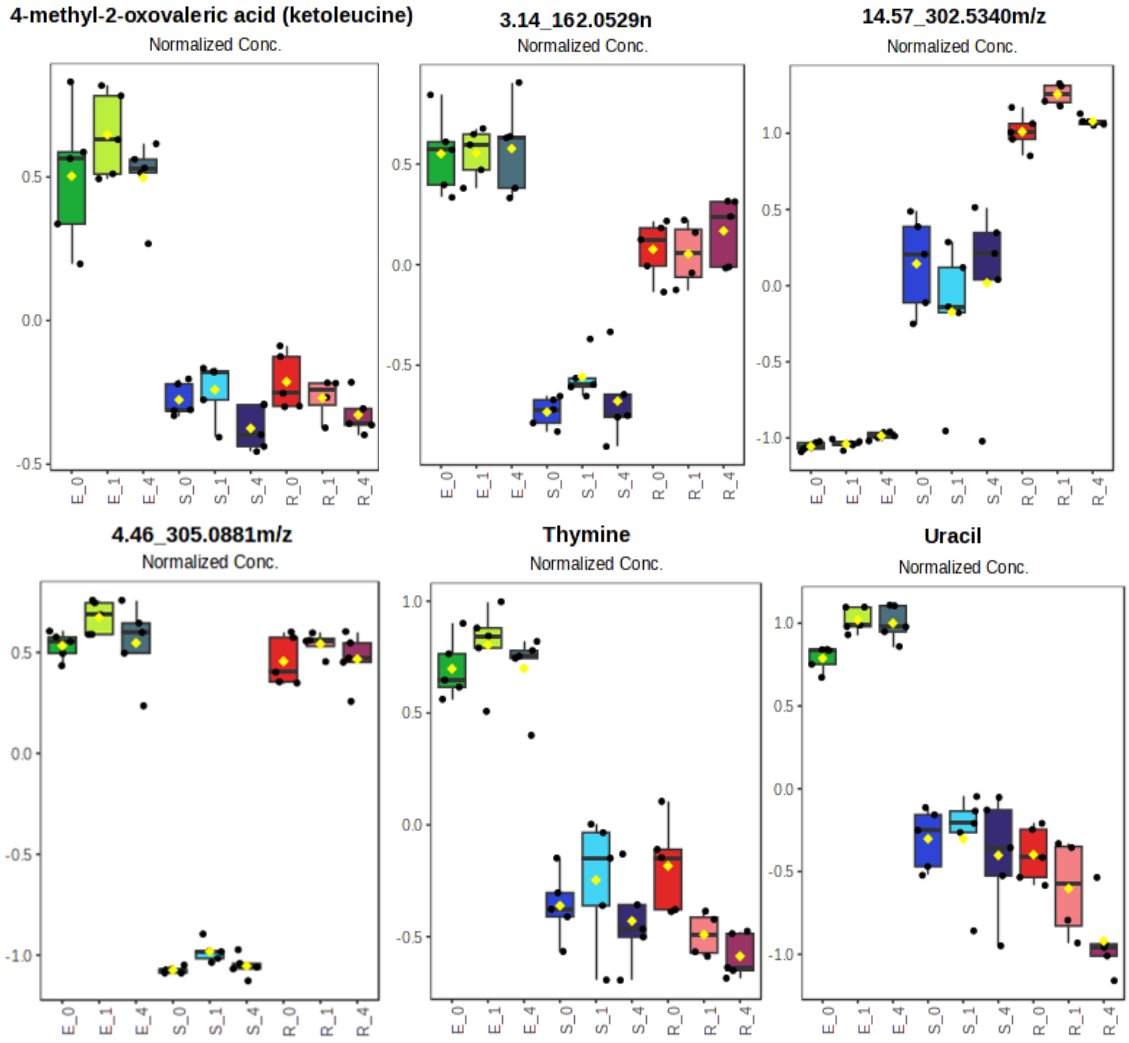

Figure 4.8 Boxplots illustrating strain-specific changes compound abundance across wild-type (E), meropenem-susceptible (S), and meropenem-resistant (R) **E. coli** ***strains under meropenem exposure (0, 1, and 4 µg/mL).*** *The boxplots display the normalized concentrations of selected metabolites, highlighting strain-specific metabolic differences. Each box represents the IQR with the median indicated, and dots represent individual biological replicates.*

Other metabolites and compound-features displayed a clearer concentration-dependent effect as illustrated in **Figure 4.9**. Cyclic AMP (cAMP) levels decreased progressively with increasing meropenem concentrations in E strain, but had opposite effect in S and R strain, where the levels decreased as meropenem concentration increased. Glucose 1-phosphate levels

increased as concentration of meropenem across all strains. Glucuronic acid levels decreased in R stain as meropenem concentration increased, while the dose-dependent effect was less pronounced in the E and S strains. Compound-feature such as 18.70_365.0284 *m/z* displayed decreases in both the S and R strains with increasing meropenem concentration.

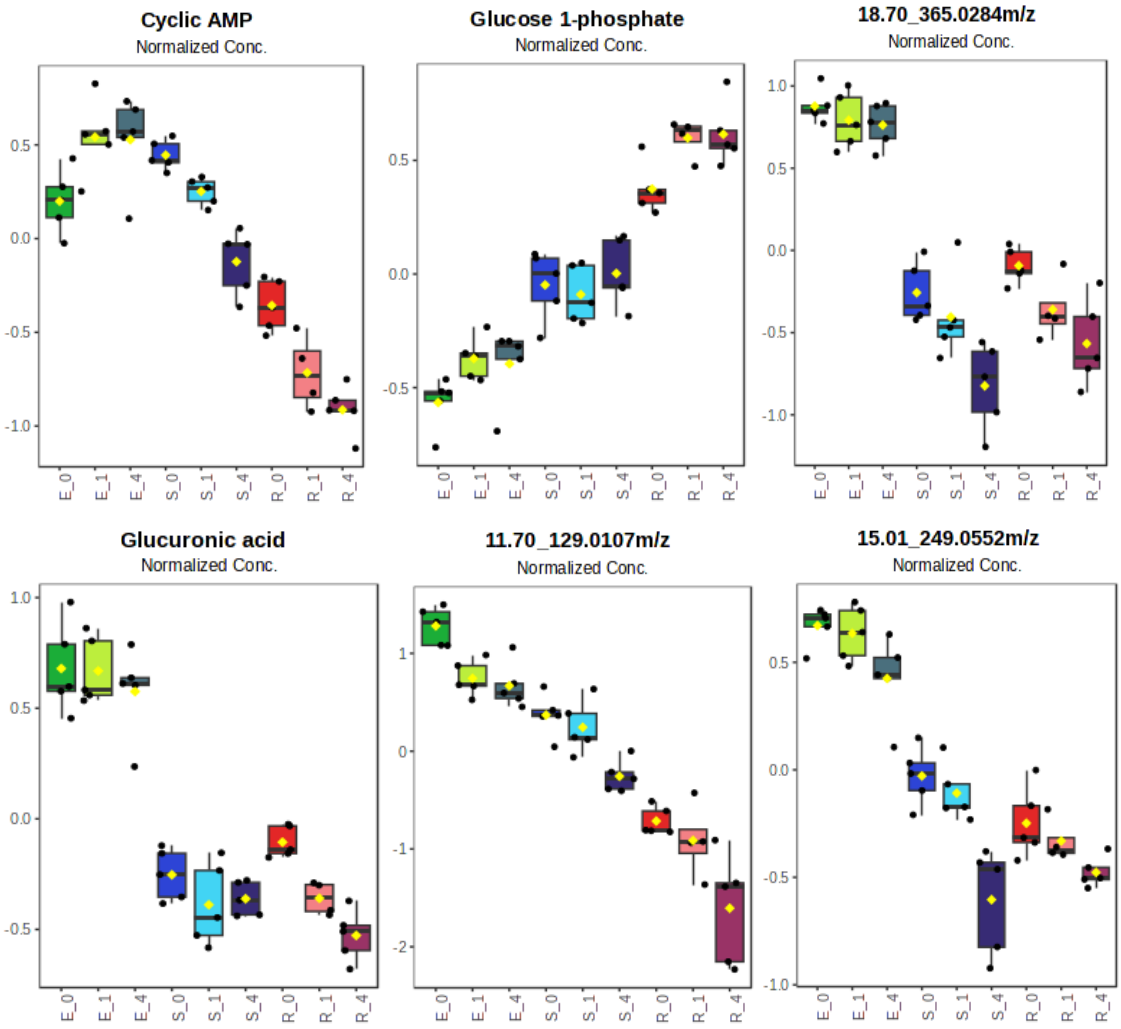

Figure 4.9 Boxplots illustrating concentration-dependent changes in metabolite abundance across wild-type (E), meropenem-susceptible (S), and meropenem-resistant (R)* E. coli *strains under meropenem exposure (0, 1, and 4 µg/mL). *The boxplots display the normalized concentrations of selected metabolites, highlighting dose-dependent metabolic changes at 0, 1, and 4 µg/mL. Each box represents the IQR with the median indicated, and dots represent individual biological replicates.*

In overview the results showed clearer a mixture of metabolic differences between strains and in response to meropenem treatment, with often with a dose-depended effect. Compound-features such as 18.70_365.0284 *m/z*, and uracil demonstrate how strain type and antibiotic dose interact to shape metabolic responses. These patterns highlight the utility of combining multiple treatment concentrations with ANOVA for differentiating metabolic

changes, providing insights into the interplay between strain-specific traits and meropenem-induced metabolic changes.

By identifying statistically significant compound-features and visualising their variability, the univariate analysis provided a foundation for subsequent multivariate and functional pathway analyses. The results demonstrated the importance of considering both strain-specific traits and the influence of meropenem treatment when interpreting metabolic data.

4.3.2.2 Multivariate statistical analysis of metabolic differentiation in wild-type, meropenem-susceptible, and meropenem-resistant E. coli *strains under meropenem exposure*

Univariate statistical analysis provided useful information about which compound-features and identified metabolites were significantly altered in abundance. In order to investigate the patterns inherent in these changes in more detail multivariate statistical analysis was used to evaluate the metabolic differentiation between wild-type (E), meropenem-susceptible (S), and meropenem-resistant (R) *E. coli* strains under 0, 1, and 4 μg/mL meropenem exposure. The analysis aimed to identify the patterns inherent in strain-specific metabolic differences and highlight metabolic changes driven by antibiotic treatment.

The clustered heatmap of the top 50 altered compound-features (**Figure 4.10**) revealed distinct groupings based on strain type (E, S, R) and treatment condition (0, 1, 4 μg/mL meropenem), emphasising the strain-specific biology and antibiotic-induced metabolic changes observed from the univariate analysis. Metabolites such as cyclic AMP (cAMP) were more abundant in the E and S strains, possibly reflecting their activation as part of stress-response processes.[341] These metabolites can play roles in oxidative stress management, nucleotide metabolism, and transcriptional regulation to counteract the disruptions induced by meropenem.[342] Unique metabolic differences in meropenem-resistant strain (R) included elevated levels of sedoheptulose 1-phosphate and glucose-1-phosphate, potentially supporting energy metabolism and cell wall biosynthesis pathways that contribute to membrane stability under stress.[343,344] Such adaptations may confer an advantage to the R strain in maintaining

cellular integrity and function under antibiotic exposure. Additionally, fructose 6-phsophate was elevated in both S and R suggesting potential role in relation to plasmid.

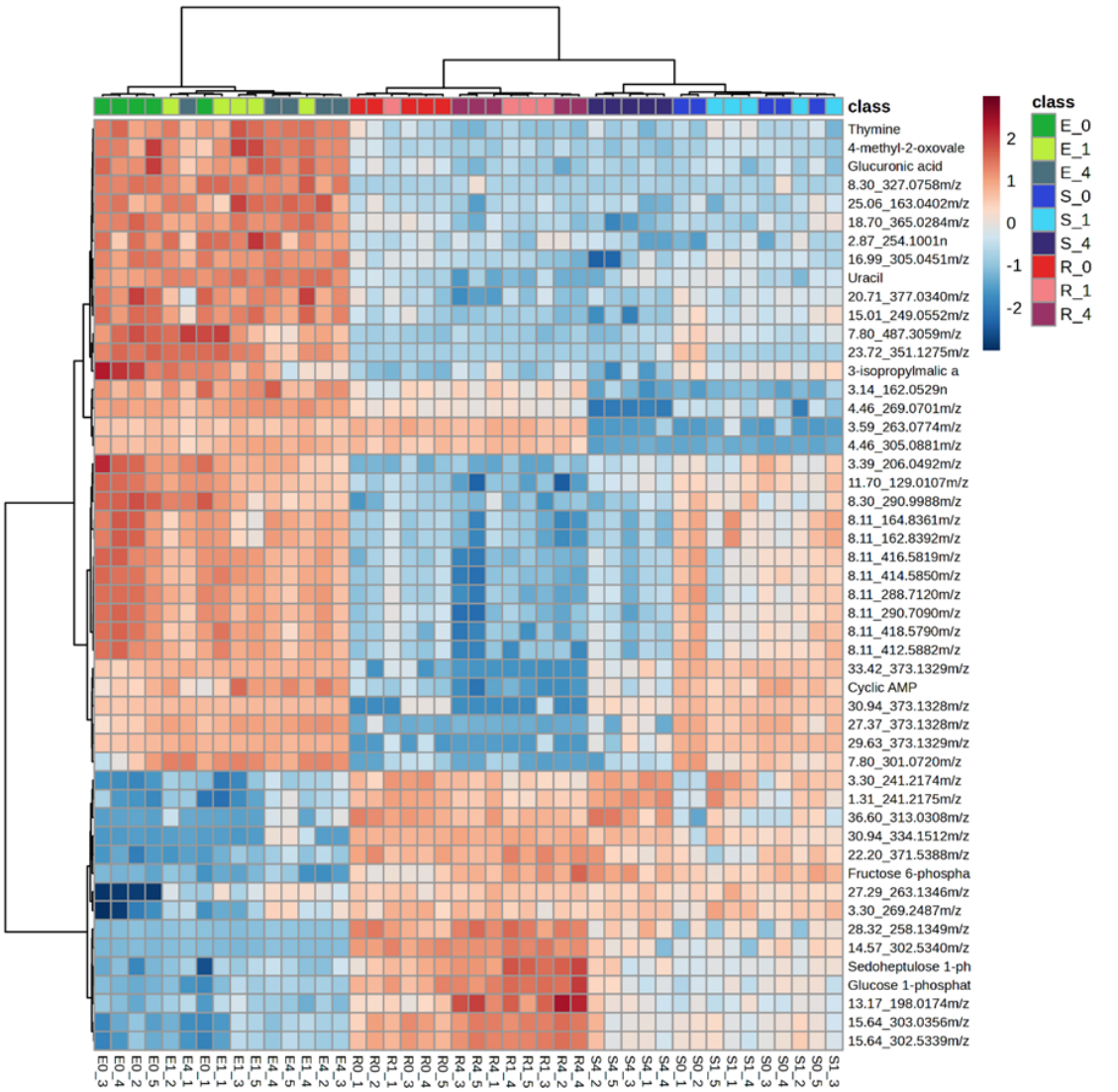

Figure 4.10 Heatmap of differential metabolite abundance across strains under meropenem exposure. *This heatmap highlights the top 50 altered metabolites among wild-type (E), meropenem-susceptible (S), and meropenem-resistant (R) strains exposed to 4 µg/mL meropenem. Rows represent metabolites, while columns represent experimental groups: treated (E_0, E_1, E_4, S_0, S_1, S_4, R_0, R_1, R_4). Red indicates higher relative metabolite abundance, and blue indicates lower relative abundance, normalized across all samples.*

Overall, the heatmap highlight mainly strain-specific differences but also some drug-induced metabolic changes (for example cyclic AMP and Fructose-6 phosphate). These findings highlight the distinct adaptive strategies of *E. coli* strains, shaped by their genetic and phenotypic differences, in responding to meropenem exposure.

4.3.3 Strain-specific metabolic responses to meropenem exposure: Comparative analysis of vehicle control (0 μg/mL) and meropenem (1 or 4 μg/mL) treatments

In order to investigate the metabolic responses triggered by meropenem exposure in more detail, significance testing and functional analyses were conducted on the metabolomics datasets for the wild-type (E), meropenem-susceptible (S), and meropenem-resistant (R) strains separately. Comparison between vehicle controls (0 μg/mL) and samples exposed to 1 μg/mL and 4 μg/mL meropenem were performed.

The aim of this data analysis was to identify metabolic changes that accompany non-lethal exposure to meropenem specifically (as distinct from strain-specific differences) and investigate the functional metabolic changes that company susceptibility and resistance across the three strains.

4.3.3.1 Metabolic changes in the wild-type strain exposed to meropenem

The wild-type (E) strain serves as a baseline model to understand how exposure to meropenem influences metabolic processes. The comparison between vehicle control (E_0, bright green) and meropenem treated (E_1 and E_4, light green and dark green) groups enabled the identification of specific metabolic adjustments, providing insights into the broader metabolic responses triggered by meropenem exposure in a strain without inherent resistance.

The PCA scores plot (**Figure 4.11**) provided an initial visualisation of the overall metabolic differences between the vehicle control (E_0) and samples exposed to 1 μg/mL (E_1), and 4 μg/mL (E_4) meropenem. The PCA plot revealed distinct clustering of metabolic profiles between E_0 and E_4, with E_1 positioned between these two groups. The positioning suggests a dose-dependent impact of meropenem on the metabolic profile of the wild-type (E) strain. The higher the concentration of meropenem, the greater the observed metabolic divergence from the control. These results indicated that increasing concentrations of meropenem induced progressively greater alterations in the metabolic state of the strain.

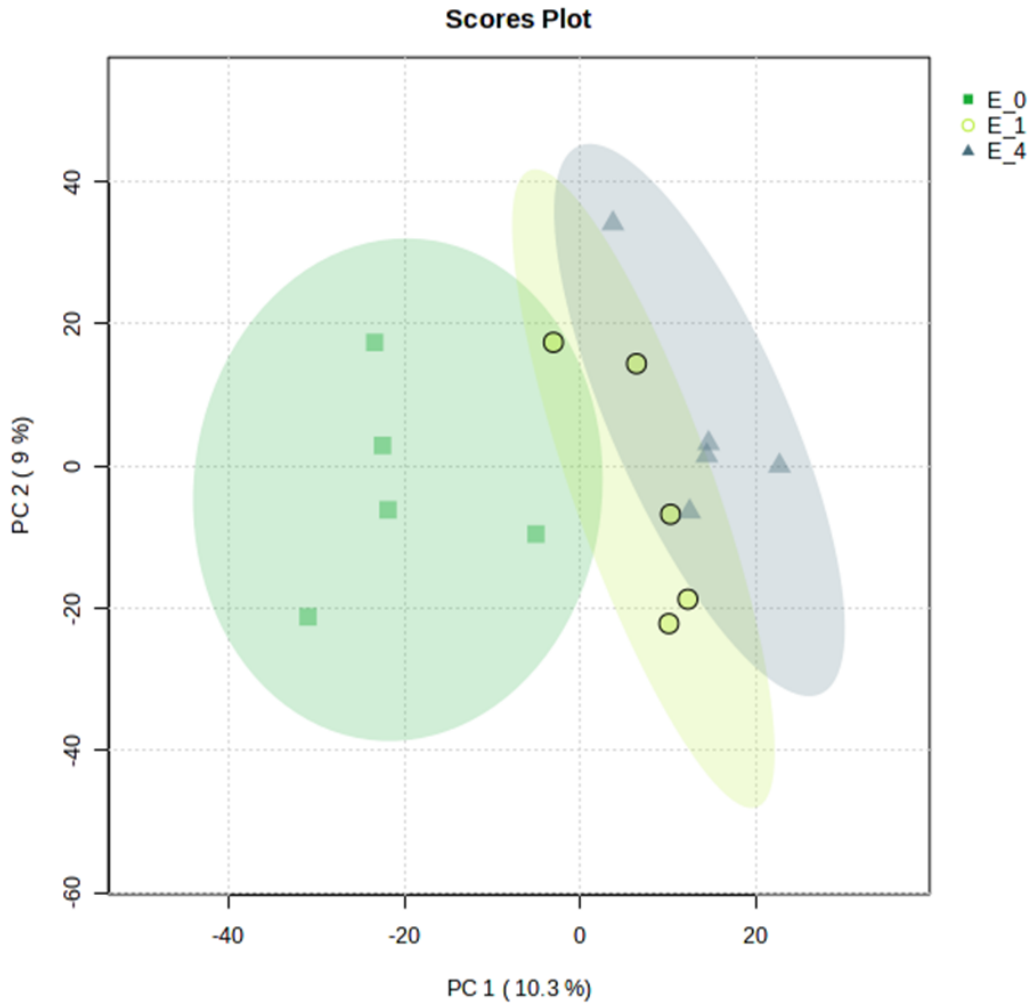

Figure 4.11 PCA scores plot showing metabolic profiles of wild-type (E)* E. coli *strain across different concentrations of meropenem (E_0, E_1, and E_4). *The plot shows the first two principal components (PC1 and PC2), explaining 10.3% and 9% of the variance, respectively. Ellipses represent 95% confidence intervals for each group. Symbols indicate the following conditions: squares for E_0 (untreated), circles for E_1, and triangles for E_4.*

The clustered heatmap (**Figure 4.12**) of the top 50 altered compound-features, illustrated the global metabolic changes associated with meropenem exposure. The main differences were between vehicle control group (E_0) and meropenem treated groups (E_1 and E_4) with compound-features and metabolites both elevated and depleted in association with meropenem treatment. Notably, E_1 and E_4 demonstrated progressively distinct profiles, corresponding to the increasing intensity of meropenem treatment. Interestingly, there was also a small group of features which were elevated in the E_1 group compared to both vehicle control and E_4.

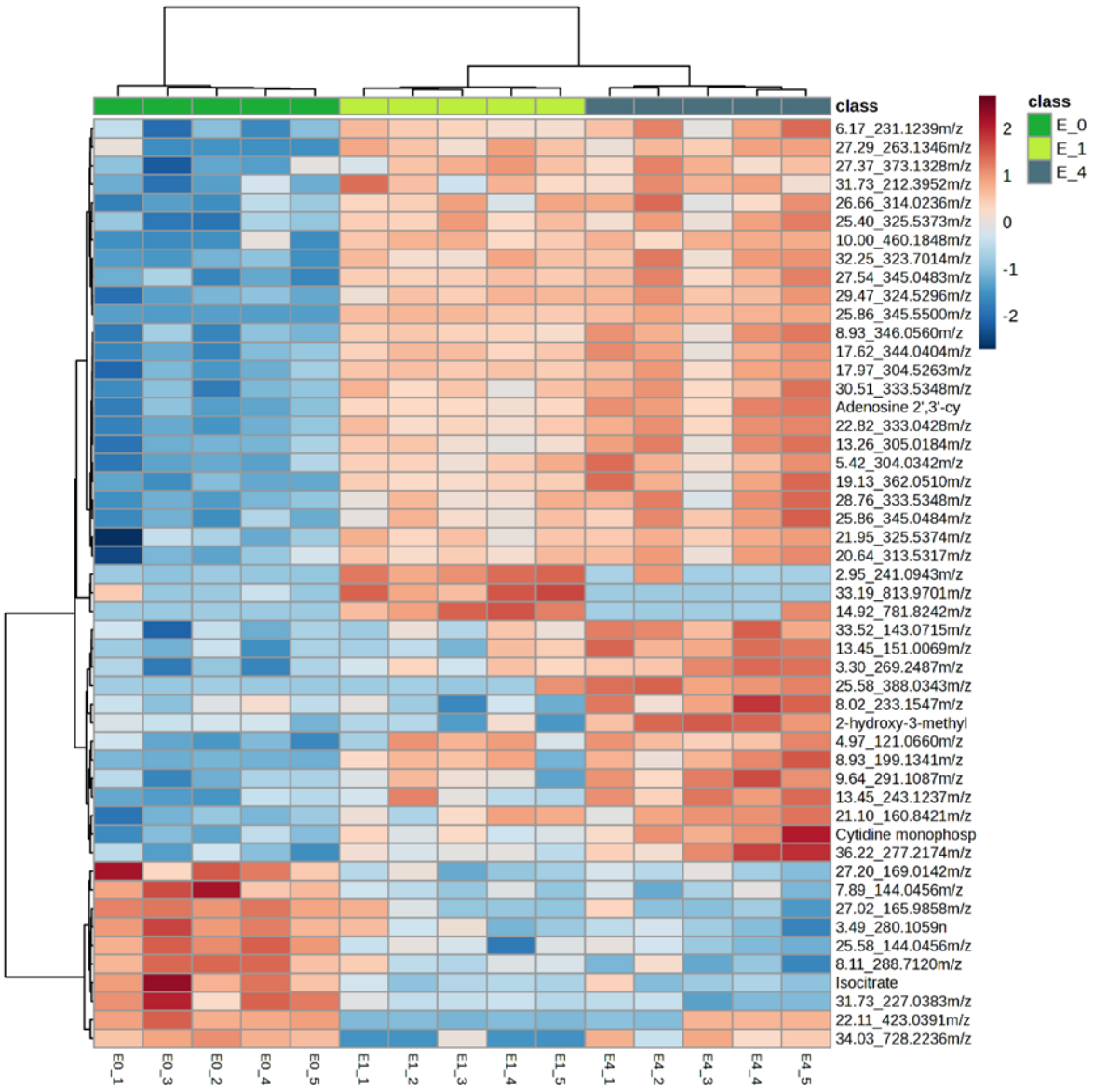

Figure 4.12 Clustered heatmap illustrating the top 50 compound-feature variation across wild-type (E)* E. coli *strain across different concentrations of meropenem (E_0, E_1, and E_4). *The top 50 metabolites were selected based on their variance across conditions. Metabolite abundance was normalized, and hierarchical clustering was performed using Ward's method with Euclidean distance as the distance measure. Rows correspond to compound-features (annotated by* m/z *values and names where available), and columns represent replicates for each condition. The colour scale indicates relative abundance, with red representing higher abundance and blue representing lower abundance. Class labels on the top (green: E_0, light green: E_1, dark green: E_4) correspond to untreated, intermediate, and treated conditions, respectively.*

Several compound-features showed a trend of either increasing or decreasing abundance correlating with meropenem concentration, suggesting dose-dependent metabolic adjustments in the E strain. These trends highlight the gradual and cumulative impact of meropenem on bacterial metabolome.

Boxplots (**Figure 4.13**) highlighted distinct changes in the abundance of specific compound-features in response to increasing concentrations of meropenem in the E strain. Adenosine 2',3'-cyclic phosphate and cytidine monophosphate displayed a dose-dependent increase in abundance, suggesting their potential involvement in pathways activated under antibiotic stress. Conversely, isocitrate exhibited a decreasing trend with increased meropenem concentration. Interestingly, compound-feature 27.29_263.1346 *m/z* was elevated in both meropenem treated groups (E_1 and E_4), suggesting that its abundance was independent of the meropenem concentration but still associated with exposure. In contrast, 25.58_388.0343 *m/z* was higher only in the E_4 group, indicating a response specific only to the higher antibiotic concentration. These patterns reveal dose-dependent metabolic changes in the wild-type strain under meropenem treatment.

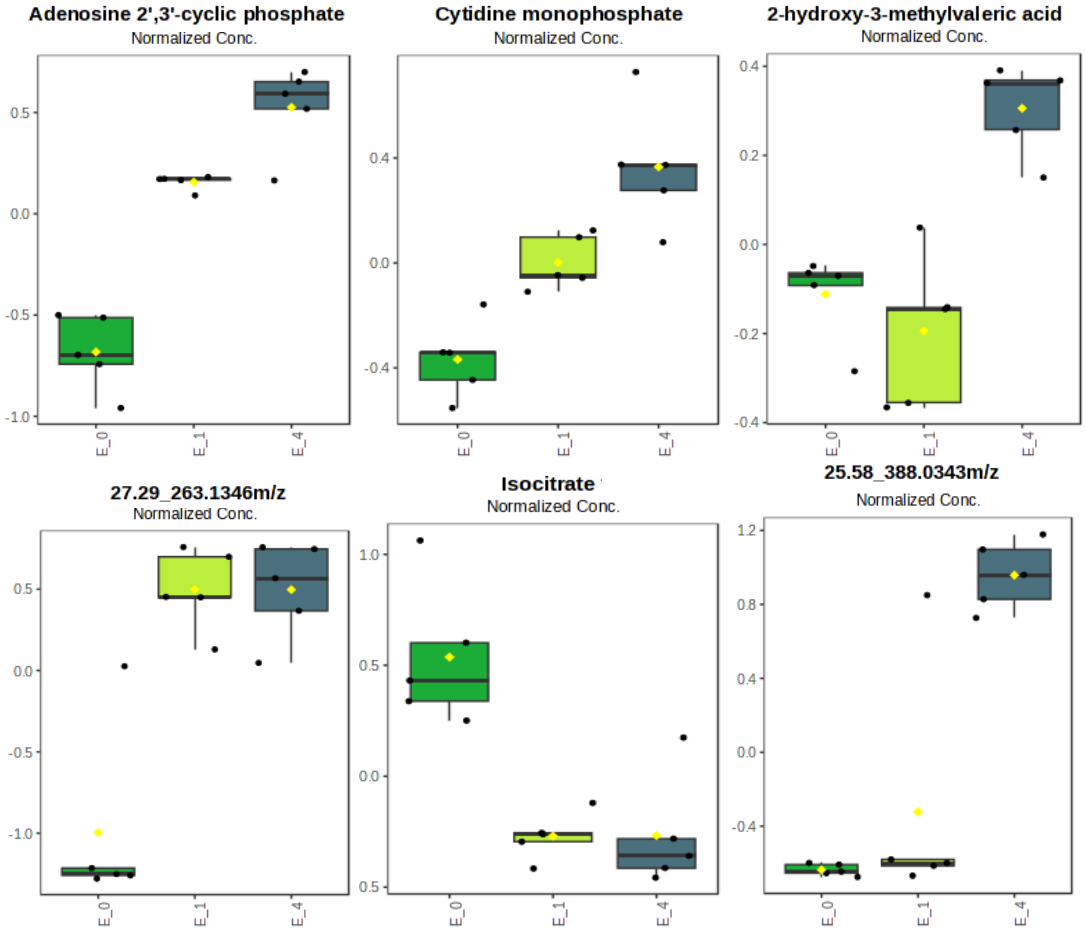

Figure 4.13 Boxplots of compound-features highlighting significant variations across wild-type (E)* E. coli *strain under different concentrations of meropenem (E_0, E_1, and E_4). *Each boxplot represents the normalized abundance of individual compound-features. Data are shown for untreated (E_0, green), 1 µg/mL (E_1, light green), and 4 µg/mL treated (E_4, blue) conditions. Boxes indicate the interquartile range (IQR), with the median represented by a horizontal line, whiskers showing 1.5 × IQR, and individual data points represented by black dots. Yellow diamonds represent the group mean.*

The volcano plot (**Figure 4.14**) illustrates the differential abundance of all measured compound features in the wild-type (E) strain comparing the vehicle control (E_0) and exposure to 4 µg/mL meropenem (E_4). The comparison enables a clearer distinction between the basal and stress-induced metabolic states. Significance thresholds, including a fold-change cut-off of 2 and a FDR-adjusted p-value < 0.05, were applied to identify compound features with statistically significant changes in abundance. The analysis revealed 9 significantly downregulated, and 30 significantly upregulated compound features, while 3674 features remaining unchanged. By considering all measured compound features, the analysis provides a broad overview of the metabolic impact of meropenem exposure.

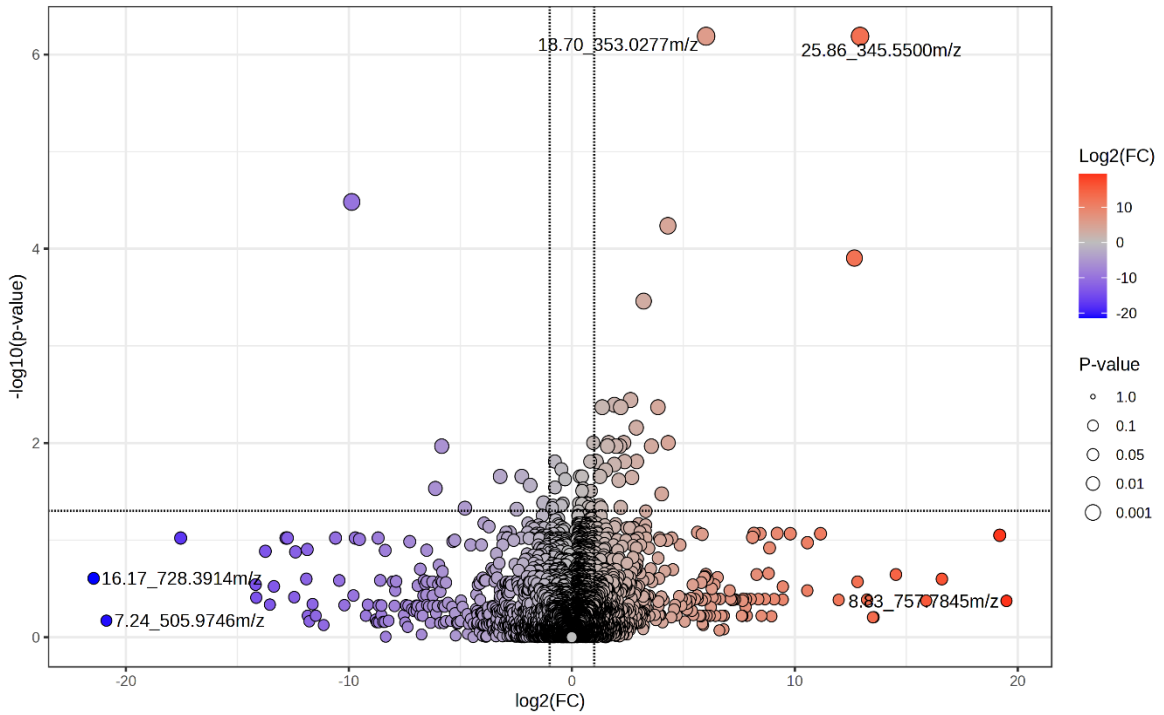

Figure 4.14 Volcano plot illustrating the differential abundance of metabolite features in the wild-type* E. coli *strain after exposure to meropenem at 4 µg/mL compared to untreated control (0 µg/mL). *The x-axis represents the log2 fold change (FC) in metabolite abundance, with positive values indicating upregulation and negative values indicating downregulation in response to meropenem. The y-axis shows the -log10 of the adjusted p-value, indicating the statistical significance of the changes. Each point represents a metabolite feature, with size indicating p-value significance and colour corresponding to the magnitude of the fold change. Metabolite features with significant changes (adjusted p-value < 0.05) are highlighted.*

The volcano plot in **Figure 4.15** provides a similar volcano plot for only the identified metabolites. This revealed one significantly upregulated metabolite, adenosine 2', 3'-cyclic phosphate (related to RNA metabolism and stress response).[345] Conversely, eight metabolites were significantly downregulated in the treated group, including *N*-acetyltryptophan,

N-Acetyl-L-phenylalanine, hippuric acid, NAAG, galactaric acid (mucic acid), 3-isopropylmalic acid, isocitrate (a key intermediate in the TCA cycle), and *N*-acetyl-L-methionine.[73] These observed changes revealed metabolic adjustments by *E. coli* in response to sub-lethal meropenem treatment.

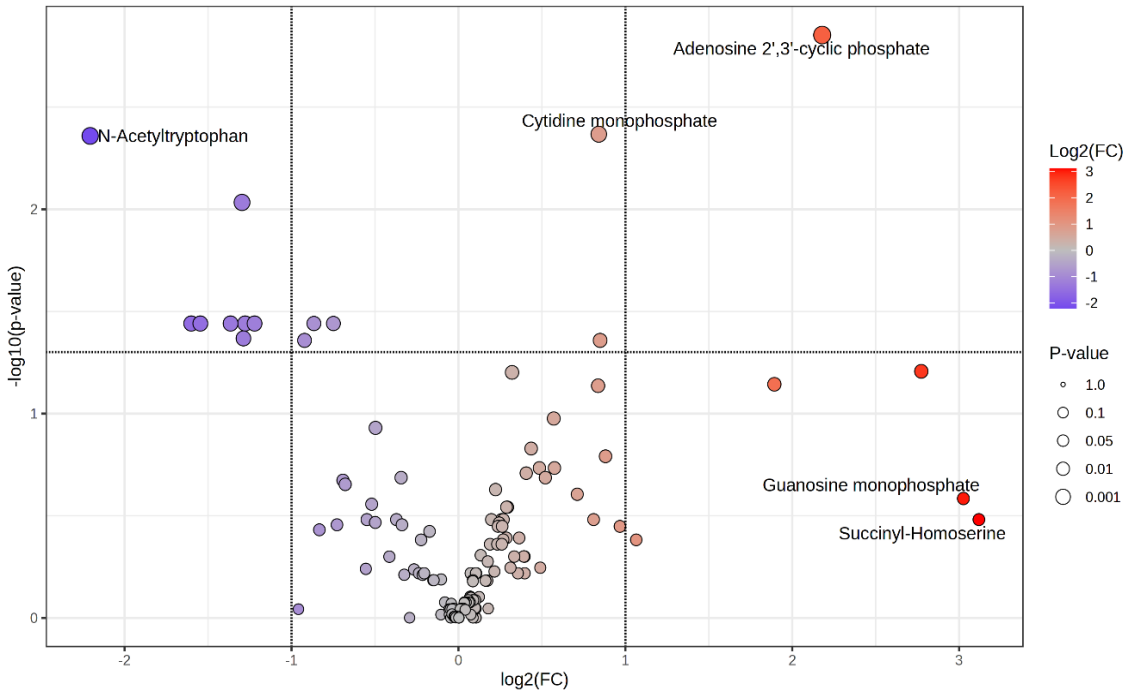

Name	log2(FC)	p.adjusted
Adenosine 2',3'-cyclic phosphate	2.1819	0.0015368
N-Acetyltryptophan	-2.194	0.0032389
N-Acetyl-L-phenylalanine	-1.2868	0.0052287
Hippuric acid	-1.5886	0.034174
N-Acetylaspartylglutamic acid	-1.5413	0.034174
Galactaric acid (mucic acid)	-1.3669	0.034174
3-isopropylmalic acid	-1.2689	0.034174
Isocitrate	-1.215	0.034174
N-Acetyl-L-methionine	-1.2791	0.035842

Figure 4.15 Volcano plot and table illustrating the differential abundance of metabolites in the wild-type (E) E. coli strain after exposure to meropenem at 4 µg/mL compared to vehicle control (0 µg/mL). *The x-axis represents the log2 FC in metabolite abundance, with positive values indicating upregulation and negative values indicating downregulation in response to meropenem. The y-axis shows the -log10 of the p-value, indicating the statistical significance of the changes. Metabolites with significant changes (FDR-adjusted p-value < 0.05) are highlighted, with coloured circles indicating the magnitude and direction of the change. The size of the points represents the p-value significance, with larger points denoting higher confidence in differential abundance. The table provides details of the significantly altered metabolites, including log2(FC), and adjusted p-value.*

These data collectively demonstrate that meropenem exposure induced dose-dependent metabolic changes in the wild-type strain, impacting metabolites that are found in pathways such as nucleotide metabolism, amino acid metabolism, and central carbon metabolism. The insights gained from these analyses provide a foundation for understanding how meropenem effects *E. coli* metabolism.

4.3.3.2 Metabolic changes in the meropenem-susceptible strain exposed to meropenem

The meropenem-susceptible (S) strain, harbouring the pCR2.1 plasmid, provides a unique perspective on how plasmid carriage influences metabolic responses to meropenem. Comparing vehicle control (S_0), 1 μg/mL meropenem treated (S_1), and 4 μg/mL -treated (S_4) offers insights into the adaptive mechanisms of the strain and its vulnerabilities under antibiotic exposure.

The PCA scores plot (**Figure 4.16**) demonstrated the metabolic differentiation across the vehicle control (S_0) and the treated groups (S_1 and S_4), reflecting the dose-dependent effects of meropenem on the meropenem-susceptible (S) strain. The distinct clustering of S_0 from S_4 highlights the significant metabolic perturbation induced by meropenem. The intermediate positioning of S_1 between S_0 and S_4 suggested a progressive alteration in the metabolic landscape with increasing concentrations of meropenem, emphasising the systematic and concentration-dependent metabolic response of the strain.

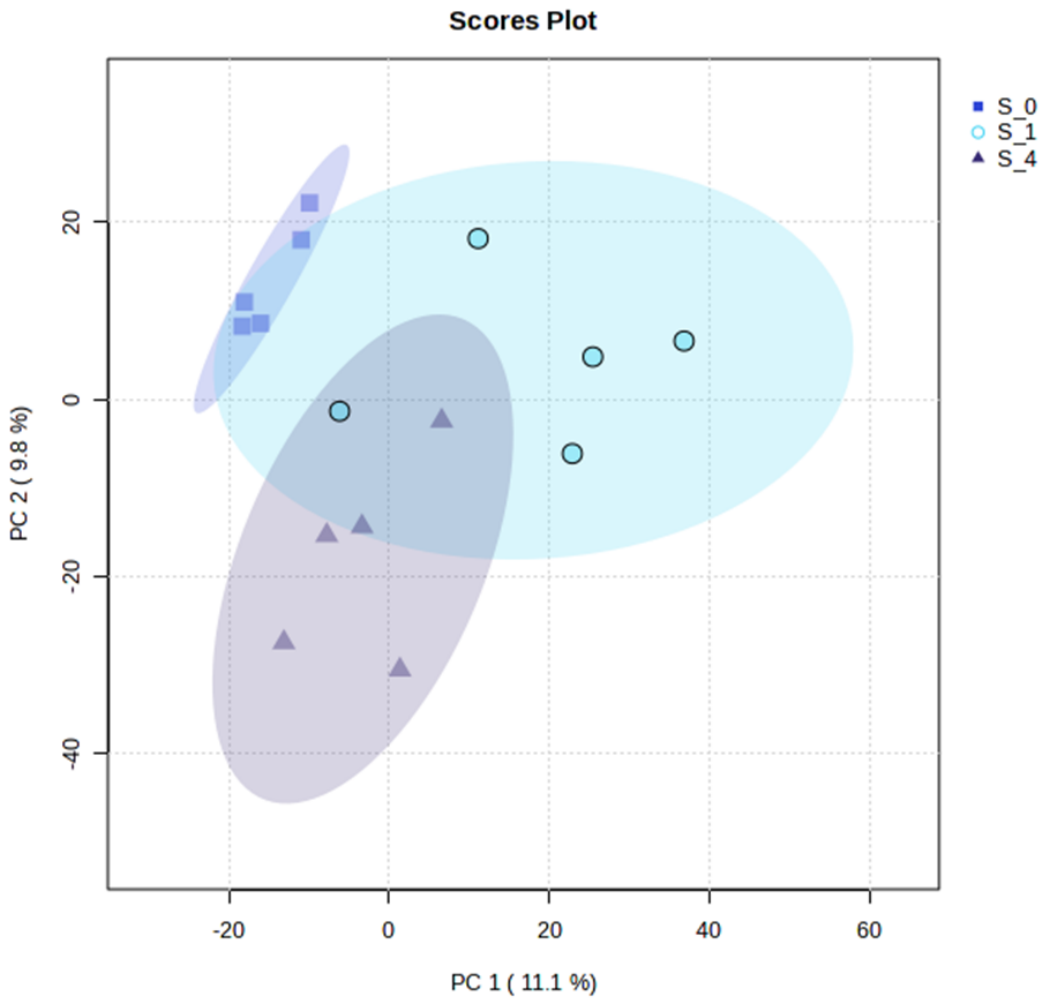

Figure 4.16 PCA scores plot showing metabolic profiles of the meropenem-susceptible* E. coli *strain (S) across different concentrations of meropenem (S_0, S_1, and S_4). *Principal component analysis (PCA) was performed to visualize the metabolic differences between untreated (S_0, blue squares), 1 µg/mL-treated (S_1, light blue circles), and 4 µg/mL-treated (S_4, dark blue triangles) groups. The first two principal components (PC1 and PC2) explained 11.1% and 9.8% of the total variance, respectively. Ellipses represent the 95% confidence intervals for each group.*

The clustered heatmap (**Figure 4.17**) provided a detailed visualisation of the top 50 altered compound-features, offering an overview of the metabolic reprogramming in response to meropenem exposure. The heatmap captures dose-dependent metabolic changes in the meropenem-susceptible strain, with distinct metabolic profiles observed across S_0, S_1 and S_4. Compound-features such as cAMP, exhibited higher abundance in vehicle control progressively diminished as meropenem concentrations increased. While compound-features such as 18.52_378.0326 *m/z* were selectively upregulated in treated conditions. These trends illustrate the metabolic adjustments undertaken by the meropenem-susceptible strain to adapt to the stress imposed by increasing concentrations of meropenem, highlighting the systematic alterations of the metabolome.

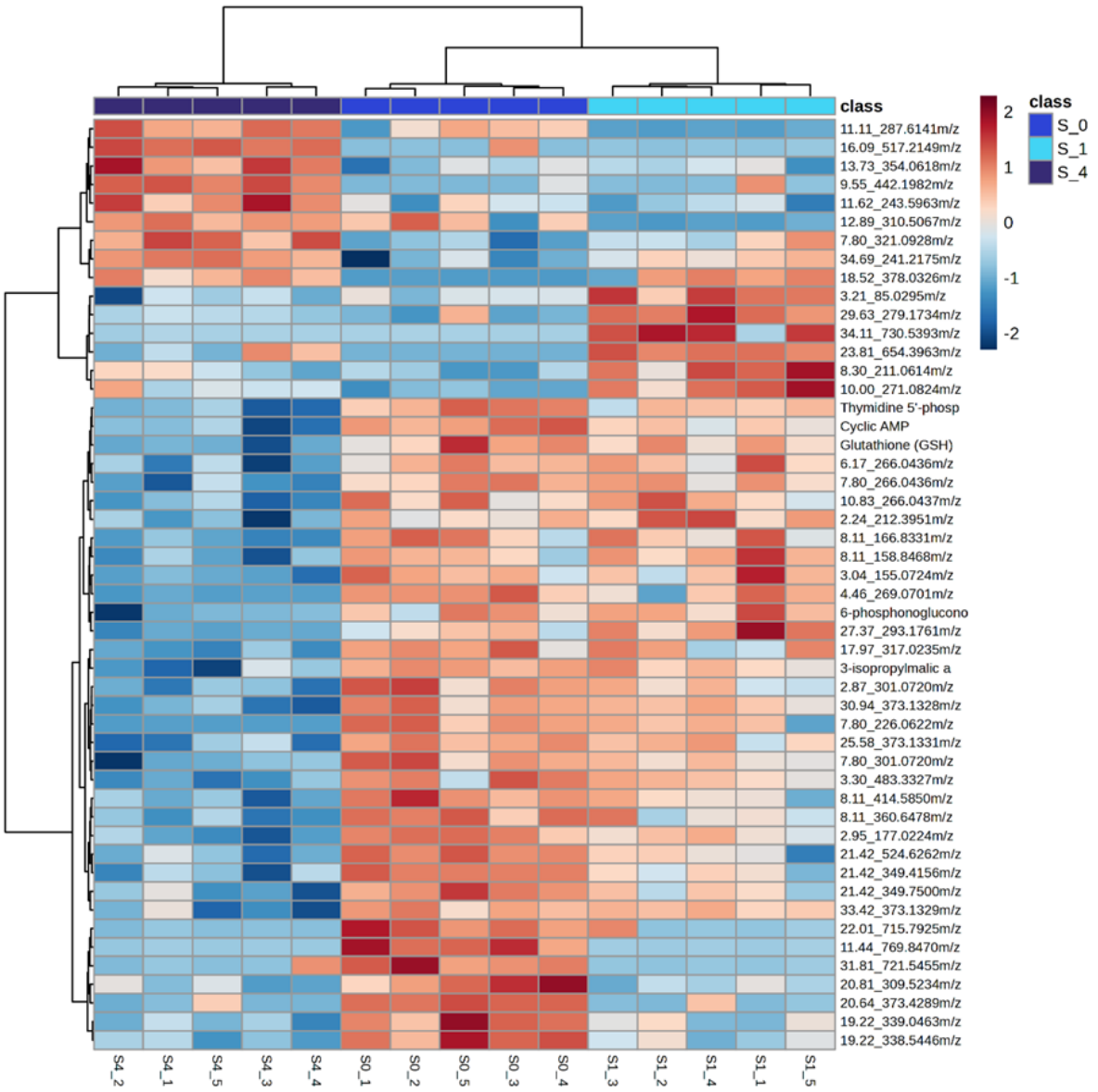

Figure 4.17 Clustered heatmap illustrating the top 40 most significantly altered compound features in the meropenem-susceptible* E. coli *strain (S) across different meropenem concentrations (S_0, S_1, and S_4). *Metabolite abundance data were normalized, and hierarchical clustering was performed using Ward's method with Euclidean distance as the distance measure. Rows represent individual metabolite features (annotated by* m/z *values and names where available), while columns correspond to replicates for untreated (S_0, blue), 1 µg/mL-treated (S_1, light blue), and 4 µg/mL-treated (S_4, dark blue) samples. The colour scale indicates relative metabolite abundance, with red denoting higher abundance and blue denoting lower abundance.*

The boxplots (**Figure 4.18**) illustrated dose-dependent changes in compound-feature abundance in the S strain across S_0, S_1, and S_4 conditions. Notable depletions were observed in metabolites such as cAMP and thymidine 5'-phosphate at the highest meropenem concentration (S_4). The reduction in cAMP abundance, in particular, suggests a potential disruption in nucleotide metabolism or signalling pathways, reflecting the metabolic stress induced by increasing concentrations of meropenem. The results highlight the systematic metabolic adaptations undertaken by the S strain in response to antibiotic exposure. These

findings align with the metabolic changes observed in the E strain, where alterations in nucleotide metabolism were also detected, including the upregulation of adenosine 2',3'-cyclic phosphate in response to meropenem exposure.

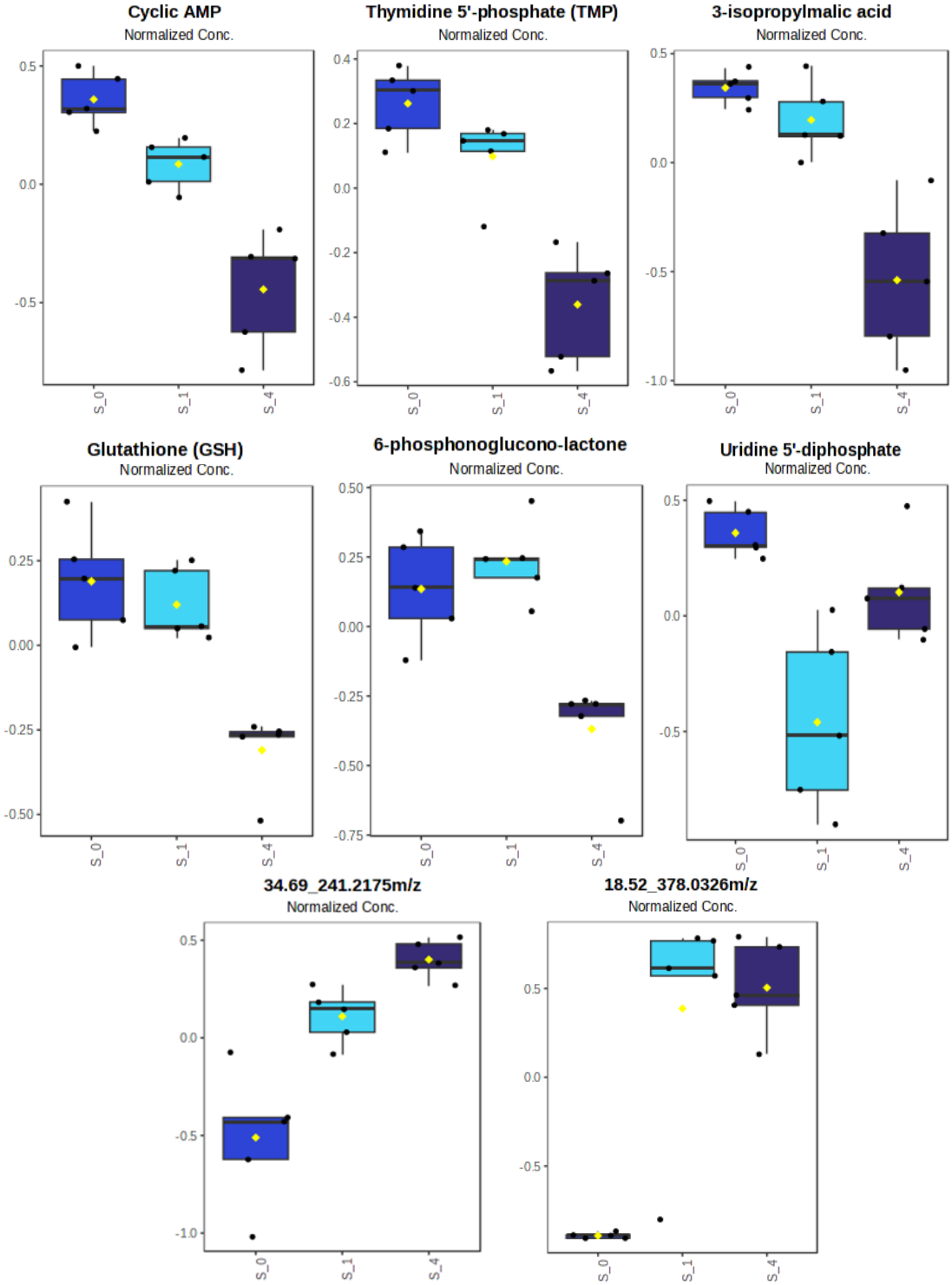

Figure 4.18 Boxplots of selected metabolites showing significant variations in the meropenem-susceptible* E. coli *strain (S) across different concentrations of meropenem (S_0, S_1, and S_4). *Each boxplot illustrates the normalized abundance of individual metabolites. Data are shown for untreated (S_0, blue), 1 µg/mL-treated (S_1, light blue), and 4 µg/mL-treated (S_4, dark blue) conditions. The box indicates the interquartile range (IQR), with the median represented by a horizontal line and whiskers extending to 1.5 × IQR. Black dots represent individual data points, and yellow diamonds indicate group means.*

The volcano plot (**Figure 4.19**) highlighted statistically significant changes in compound-feature abundance between S_0 and S_4. Using the threshold of fold change > 2 and FDR adjusted p-value < 0.05, the analysis identified 10 significantly upregulated and 29 significantly downregulated compound-features, while 3682 features remained statistically unchanged.

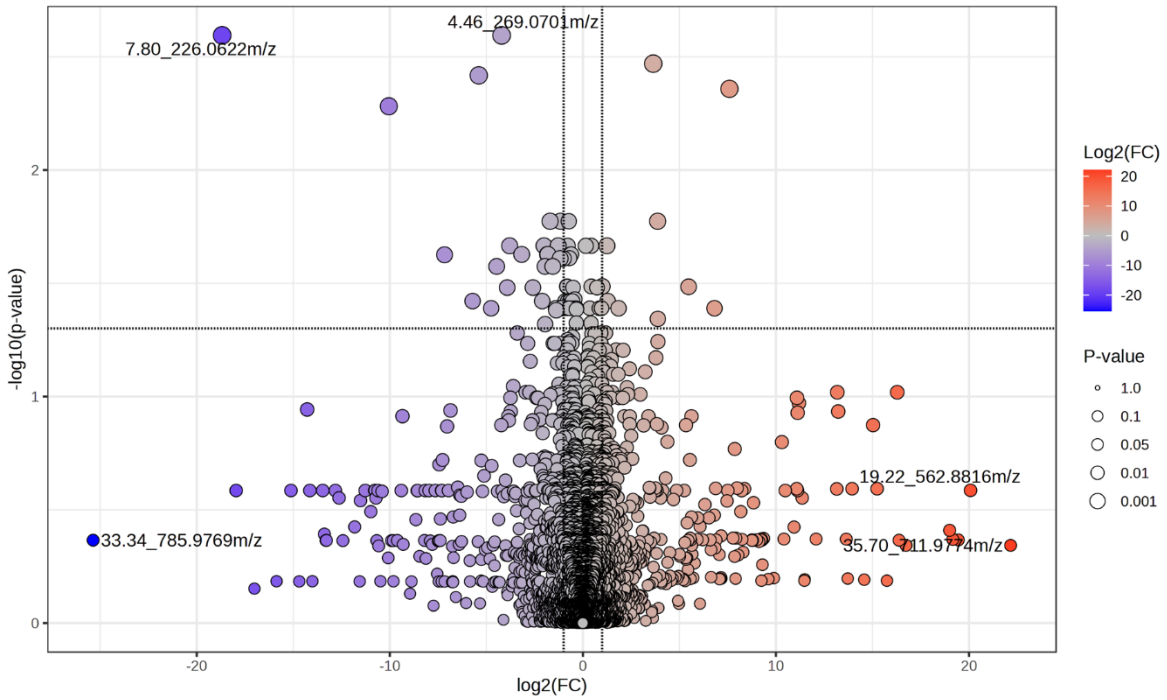

Figure 4.19 Volcano plot illustrating the differential abundance of metabolite features in the meropenem-susceptible* E. coli *strain (S) after exposure to meropenem at 4 µg/mL compared to untreated control (0 µg/mL). *The x-axis represents the log2 fold change (FC) in metabolite abundance, with positive values indicating upregulation and negative values indicating downregulation. The y-axis displays the -log10 of the adjusted p-value, reflecting the statistical significance of changes. Each point represents a metabolite feature, with point size indicating p-value significance and colour reflecting the magnitude of the fold change. Significant metabolite features (adjusted p-value < 0.05) are highlighted*

The volcano plot (**Figure 4.20**) focuses exclusively on identified metabolites, providing a more targeted analysis of metabolic perturbations in the meropenem-susceptible (S) strain following 4 µg/mL meropenem exposure. Among the identified metabolites, three were significantly downregulated in the treated group (S_4) compared to the vehicle control (S_0). These include NAAG, cAMP, and 3-isopropylmalic acid. These alterations suggest that pathways associated with these metabolites may be affected by meropenem exposure.[346,347] The analysis emphasises specific metabolic alterations induced by meropenem exposure, offering insights into metabolic adjustments of the S strain.

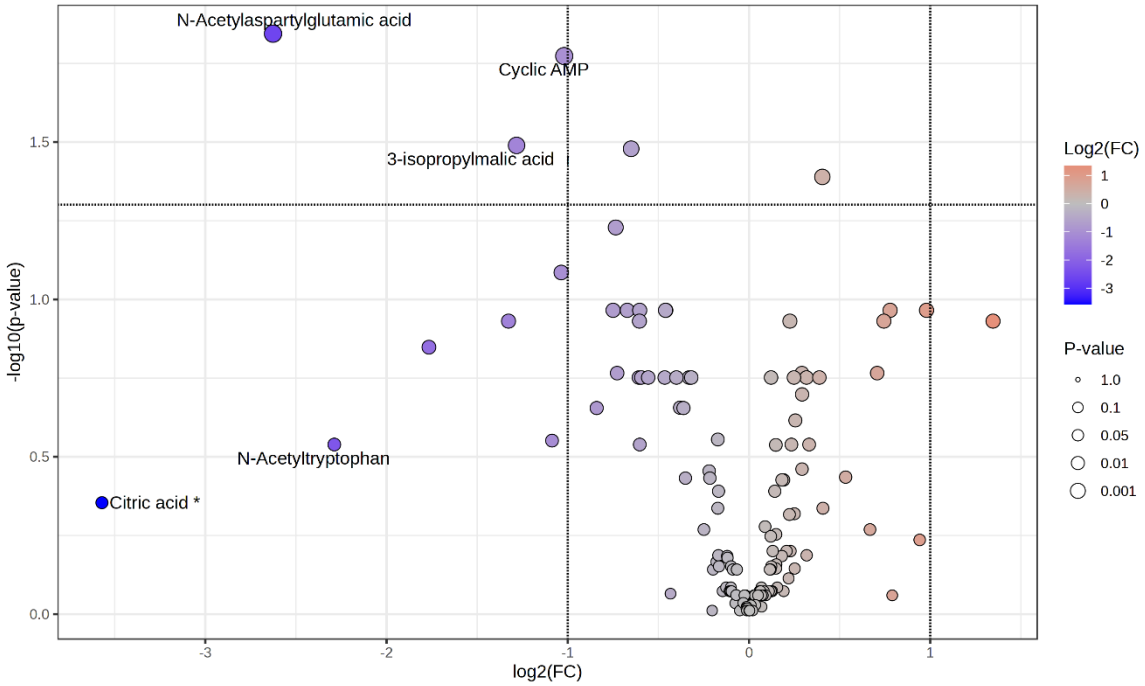

Name	log2(FC)	p.adjusted
N-Acetylaspartylglutamic acid	-2.6211	0.015215
Cyclic AMP	-1.014	0.016394
3-isopropylmalic acid	-1.2785	0.027714

Figure 4.20 Volcano plot and table showing the differential abundance of metabolites in the meropenem-susceptible (S)* E. coli *strain following exposure to 4 µg/mL meropenem compared to the untreated control (0 µg/mL). *The x-axis represents the log2 FC in metabolite abundance, with positive values indicating upregulation and negative values indicating downregulation due to meropenem treatment. The y-axis indicates the -log10 of the p=value, representing the significance of the changes. Significant metabolites (FDR-adjusted p-value < 0.05) are highlighted. The size of each point corresponds to the p-value significance, with larger points indicating higher confidence in the differential abundance. The table provides details of the significantly altered metabolites, including log2(FC), and adjusted p-value.*

Overall, the observed metabolic changes highlight a metabolic reprogramming in response to meropenem exposure in the meropenem-susceptible strain. Broad metabolic changes evident in the PCA and heatmap analyses underscore reliance of the strain on adaptive metabolic pathways to survive under increasing drug exposure. Further pathway-specific investigations are necessary to elucidate the functional significance of these metabolic changes.

4.3.3.3 Metabolic changes in the meropenem-resistant (R) strain exposed to meropenem

The resistance mechanism associated with the meropenem-resistant (R) strain, mediated by expression of the NDM-7 gene, offers an opportunity to study metabolic stability under meropenem exposure. To do this vehicle control (R_0) was compared to meropenem-treated

(R_1 and R_4) to investigate how the presence of the meropenem resistance gene impacted the metabolic response of the strain to sub-lethal antibiotic exposure.

The PCA scores plot (**Figure 4.21**) revealed more overlapping metabolic profiles across the conditions (R_0, R_1, and R_4) compared to the E and S strains. The overlap between clusters indicated a degree of metabolic similarity between the groups, even under increasing antibiotic concentration. These findings highlight the ability of R strain to maintain metabolic homeostasis despite meropenem exposure, which may indicate that the resistance mechanism protected against the metabolic perturbations seen in the E and S strains.

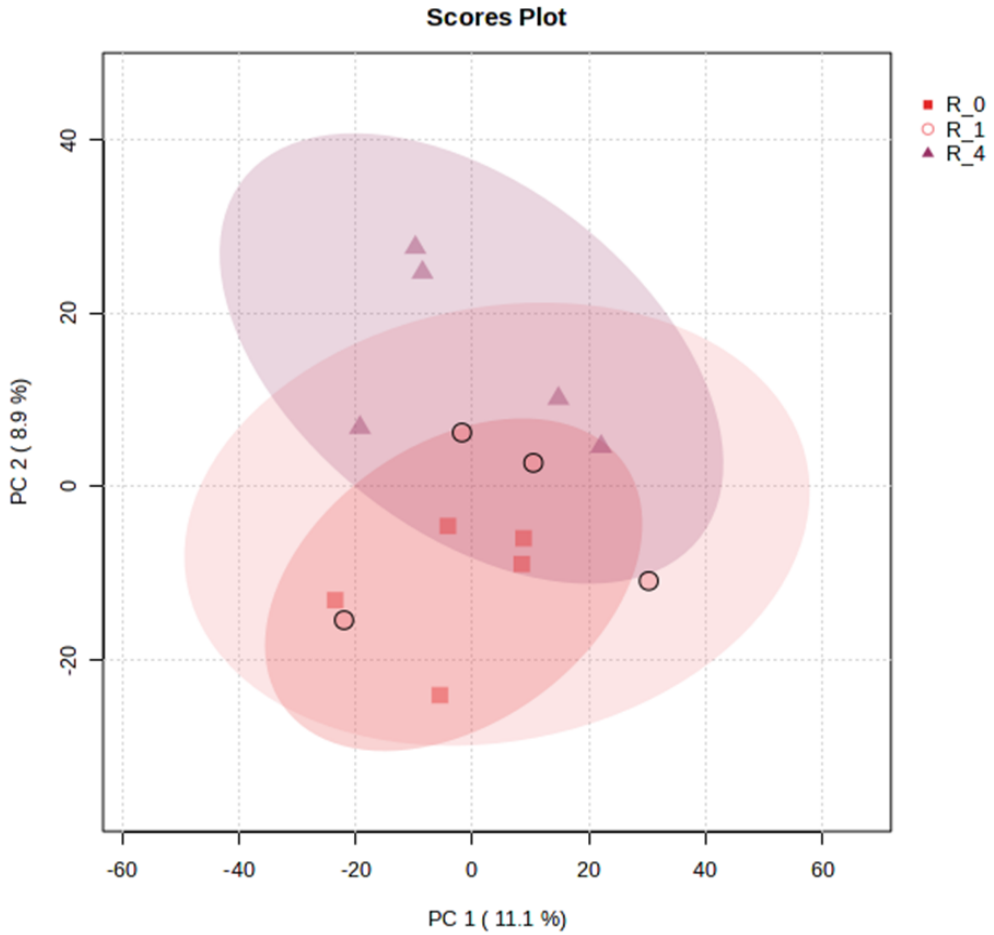

Figure 4.21 PCA scores plot showing metabolic profiles of the meropenem-resistant* E. coli *strain (R) across different concentrations of meropenem (R_0, R_1, and R_4). *Principal component analysis (PCA) was performed to assess the overall metabolic differences between untreated (R_0, red squares), 1 µg/mL-treated (R_1, light red circles), and 4 µg/mL-treated (R_4, dark red triangles) conditions. The first two principal components (PC1 and PC2) accounted for 11.1% and 8.9% of the total variance, respectively. Ellipses represent the 95% confidence intervals for each group.*

The clustered heatmap (**Figure 4.22**) visualised the top 50 most altered compound-features capturing the metabolic response of the meropenem-resistant (R) strain to increasing concentrations of meropenem. While some changes in metabolites abundance were observed

between groups, these generally appeared to be more subtle than for the E and S strains. The metabolic stability contrasted with the more dynamic responses observed in susceptible strains. However, it was observed that Cyclic AMP and glucuronic acid were both elevated at the highest meropenem concentration suggesting some meropenem-mediated effects in the meropenem-resistant strain.

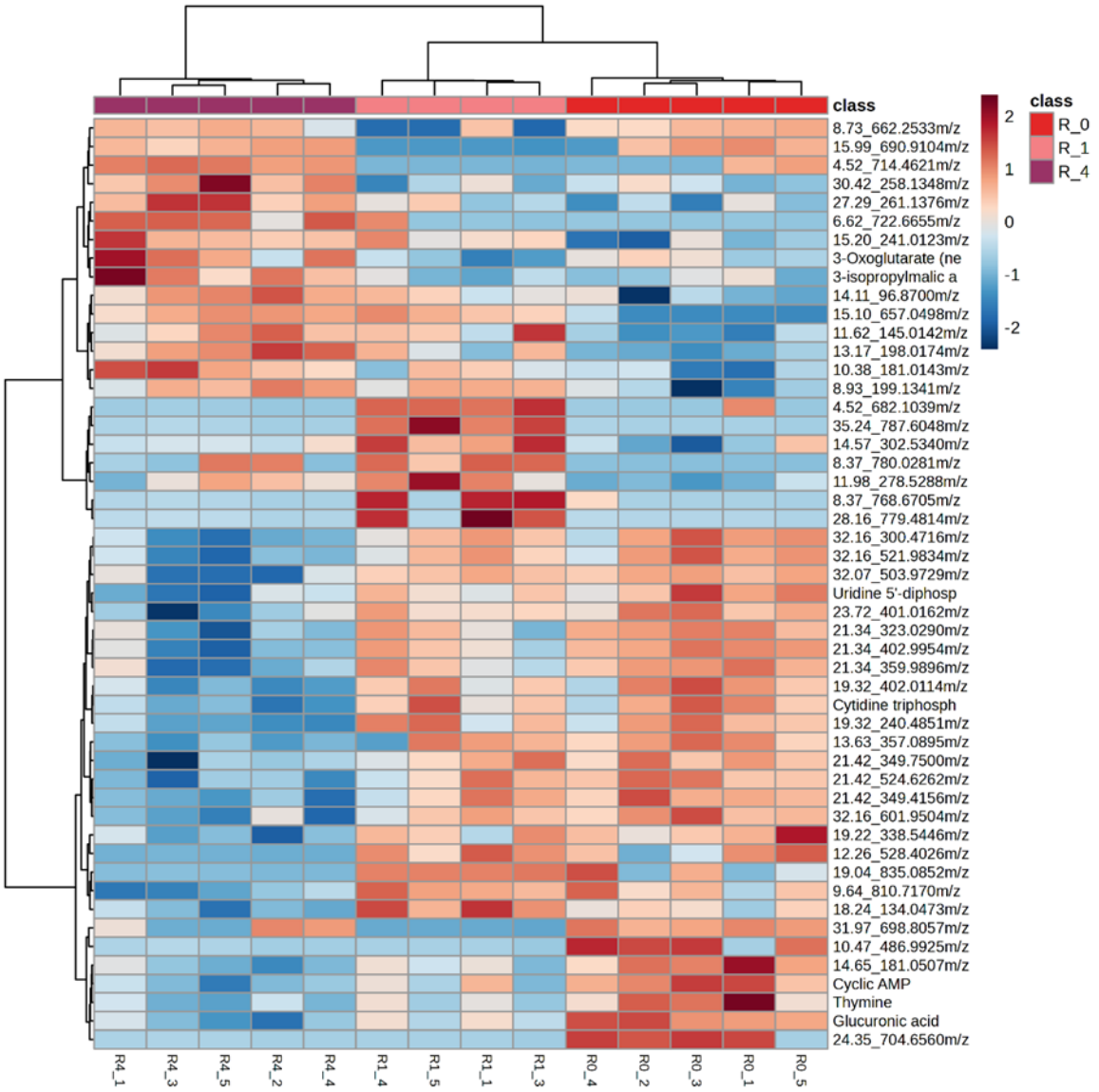

Figure 4.22 Clustered heatmap illustrating the top 50 most significantly altered compound features in the meropenem-resistant* E. coli *strain (R) across different meropenem concentrations (R_0, R_1, and R_4). *Metabolite abundance data were normalized, and hierarchical clustering was performed using Ward's method with Euclidean distance as the distance measure. Rows represent individual metabolite features (annotated by* m/z *values and names where available), while columns correspond to replicates for untreated (R_0, red), 1 µg/mL-treated (R_1, light red), and 4 µg/mL-treated (R_4, dark red) conditions. The colour scale indicates relative metabolite abundance, with red denoting higher abundance and blue indicating lower abundance.*

Boxplots (**Figure 4.23**) illustrate dose-dependent changes in the abundance of two significantly altered compound-features, 35.24_787.6048 *m/z* and 15.10_657.0498 *m/z*, in the R strain under increasing meropenem concentration. The feature 35.24_787.6048 *m/z* exhibited significant elevation specifically at 1 µg/mL (R_1), while 15.10_657.0498 *m/z* demonstrated increased abundance in both treated groups (R_1 and R_4), with a slight further elevation at 4 µg/mL (R_4). These patterns reflect some metabolic adaptations in the R strain under meropenem exposure, with distinct responses observed for the two compound-features.

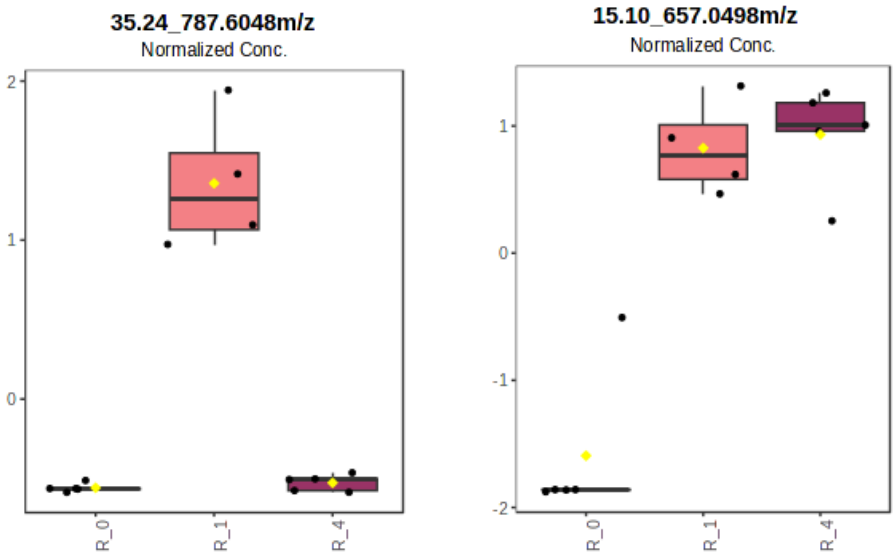

Figure 4.23 Boxplots of compound-features showing significant changes in the meropenem-resistant* E. coli *strain (R) across different concentrations of meropenem (R_0, R_1, and R_4). *The boxplots depict the normalized abundance of two significantly altered metabolites: 35.24_787.6048* m/z *and 15.10_657.0498* m/z*. Data are shown for untreated (R_0, red), 1 µg/mL-treated (R_1, light red), and 4 µg/mL-treated (R_4, dark red) conditions. Boxes represent the interquartile range (IQR), with the median indicated by a horizontal line, whiskers extending to 1.5 × IQR, and black dots representing individual data points. Yellow diamonds denote group means.*

The analysis of metabolic responses in the meropenem-resistant strain (R) was conducted using volcano plots to assess the abundance of compound-features between vehicle control (R_0) and 4 µg/mL meropenem treated (R_4) conditions (**Figure 4.24**). When evaluating all measured compound-features, despite exposure to meropenem, the volcano plot revealed no statistically significant difference in abundance, highlighting the absence of significant perturbations in the overall metabolome.

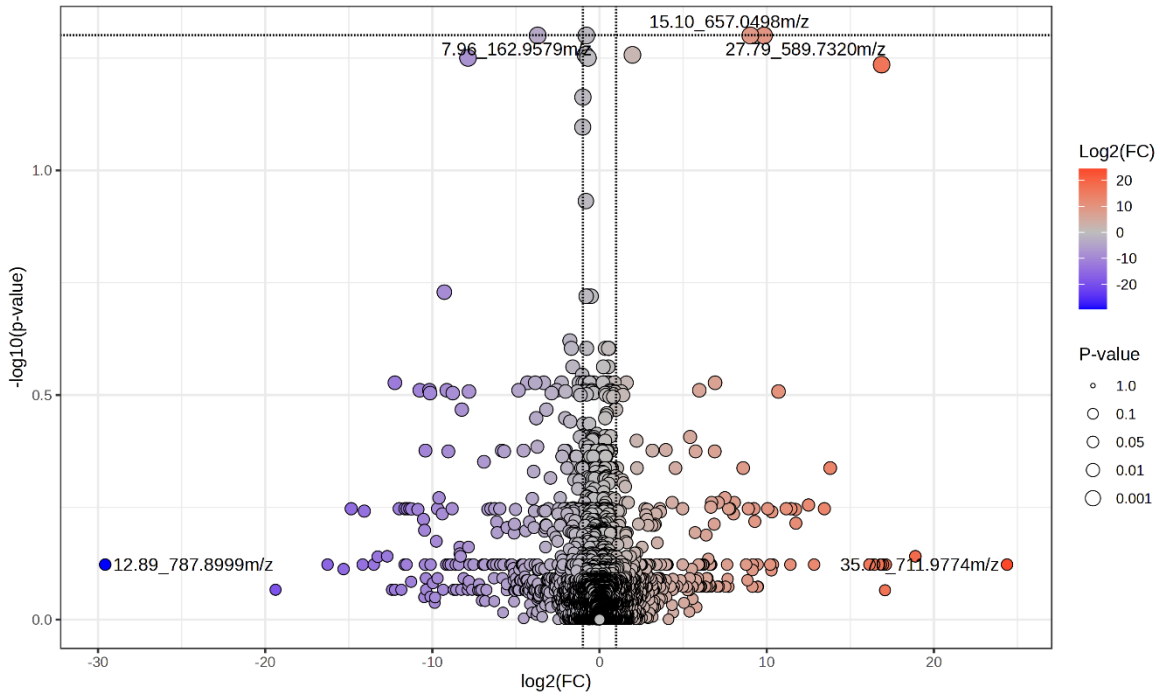

Figure 4.24 Volcano plot comparing metabolic features in meropenem-resistant (R) strain treated with vehicle control (R_0) and 4 µg/mL meropenem (R_4). *Each point represents a metabolite feature, with the x-axis showing log2 fold change (log2FC) and the y-axis displaying -log10(p-value).*

When the analysis was restricted to identified metabolites (**Figure 4.25**) significant changes were detected in cAMP and glucuronic acid, which were borderline significantly downregulated in response to meropenem exposure. As a signalling molecule often associated with stress responses, the downregulation of cAMP may be a more targeted response to a xenobiotic compound.[342] The limited number of significantly altered metabolites revealed the metabolic stability of the meropenem-resistant strain under carbapenem exposure.

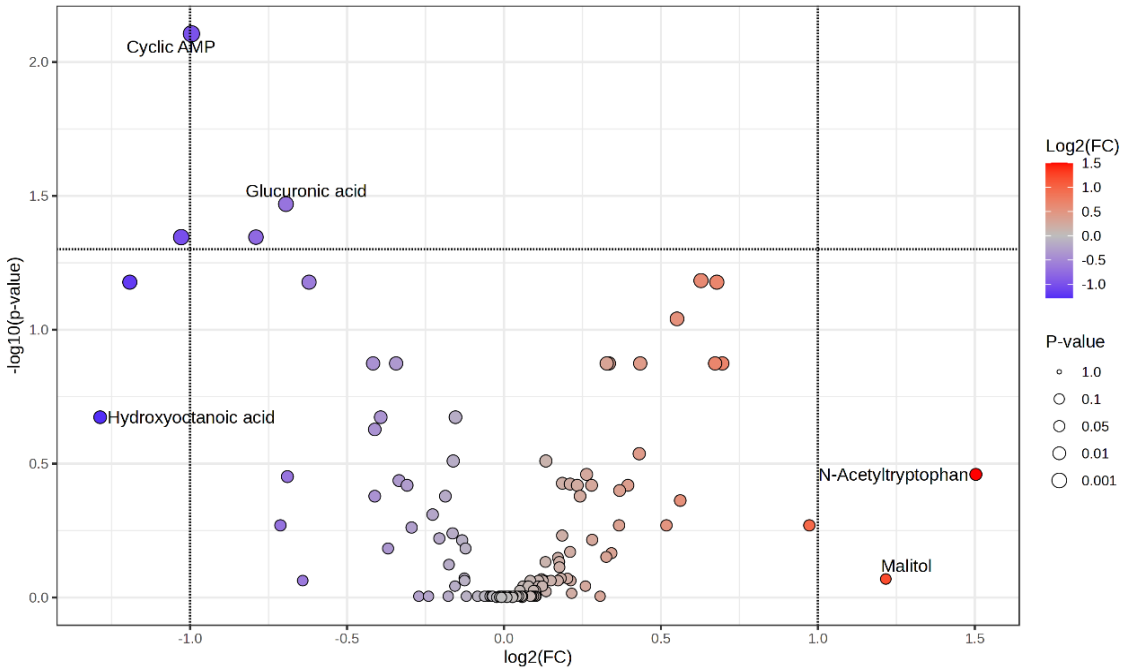

Name	log2(FC)	p.adjusted
Cyclic AMP	-1.034	0.010209
Uridine 5'-diphosphate	-1.0732	0.032155

Figure 4.25 Volcano plot illustrating differential metabolite abundance in the meropenem-resistant (R) E. coli strain following treatment with 4 µg/mL meropenem, compared to the vehicle control (0 µg/mL). *The x-axis represents the log2 FC in metabolite abundance, where positive values indicate upregulation and negative values indicate downregulation due to meropenem treatment. The y-axis displays the -log10(p-value), reflecting the statistical significance of observed changes. Larger points indicate metabolites with lower p-values, denoting higher statistical confidence. FDA < 0.05 thresholds are applied to identify significant changes.*

The results indicated markable metabolic stability under sub-lethal meropenem exposure, with only limited number of metabolites exhibiting significant changes. The stability observed in the clustered heatmap supports the hypothesis that enzymatic degradation of meropenem via NDM-7 mitigates metabolic stress, preserving core metabolic functions.[256] While cAMP downregulation may reflect reduced activation of stress-response, further pathway-level analysis is needed to confirm the functional roles of the altered metabolites and their contributions to resistance mechanisms.

4.3.3.4 Summary

The comparative analysis across strains revealed distinct metabolic strategies employed by *E. coli* strains in response to meropenem exposure at sub-lethal concentrations of meropenem. These observations underscore the strain specific metabolic adaptation or stability under antibiotic exposure, reflecting their genetic and physiological differences.

The wild-type (E) strain demonstrated substantial metabolic changes in response to meropenem, with progressive dose-dependent changes in metabolite abundance. These changes likely reflect reallocation of metabolic resources toward processes that support survival under stress, such as pathways involved in nucleotide synthesis, amino acid metabolism, and oxidative stress management.[348-350] These findings underscore the dynamic responses of the wild-type strain to external stressors, reflecting its ability to adjust metabolism under meropenem exposure.

The meropenem-susceptible (S) strain exhibited extensive metabolic changes. These changes reflected a robust and dose-dependent metabolic response to meropenem exposure. The observed metabolic adjustments may be influenced not only by the direct effects of meropenem but also by the metabolic demands of plasmid carriage.[351]

In contrast to the E and S strains, the meropenem-resistant (R) strain showed fewer changes in metabolite abundance under meropenem exposure, indicating a higher degree of metabolic stability. The stability likely reflects the efficacy of resistance mechanisms which mitigate metabolic disruptions and reduce the need for broad reprogramming. By neutralising the antibiotic effects, the meropenem-resistant strain preserved core metabolic functions, maintained a relatively unchanged metabolic state despite external stressors.

Collectively, these findings illustrate the differing response of *E. coli* strains to meropenem at metabolome-wide scale. The wild-type and meropenem susceptible strains actively engaged in metabolic adjustments consistent with efforts to manage meropenem-induced stress, reallocating resources toward nucleotide synthesis, amino acid metabolism, and oxidative stress management.[346,347,352-355] In contrast, the metabolic profile of the meropenem-resistant strain remained largely unaltered, reflecting its reliance on robust defence mechanisms to buffer against metabolic disruptions, avoiding the need for extensive metabolic changes. The comparative analysis underscores the complex interplay between genetic factors, plasmid burden, and resistance mechanisms in shaping bacterial metabolic responses. However, what

these metabolome-wide changes mean in the context of bacterial cell function remains unclear. In order to pursue this in more detail metabolic pathways analysis was performed next.

4.3.4 Functional analysis: Pathway insights into metabolic response

4.3.4.1 Membrane integrity and stress management pathway altered in wild-type strain

The wild-type (E) strain was analysed under vehicle control (E_0) and meropenem-treated (E_4) conditions to predict metabolic pathway adaptations during exposure to sub-lethal meropenem concentrations. The comparison aimed to identify enriched pathways impacted by the antibiotic and explore how these changes contribute to metabolic flexibility of the strain. Functional pathways analysis was performed as described in Chapter 3. **Figure 4.26** illustrates the pathways identified as significantly altered along with the predicted degree of enrichment and calculated significance. The main significantly altered pathways were glycerophospholipid metabolism, porphyrin metabolism, ubiquinone and other terpenoid-quinone biosynthesis, vitamin B6 metabolism, and siderophore group non-ribosomal peptide biosynthesis. Glycerophospholipid metabolism exhibited the highest impact, suggesting substantial membrane remodelling.[356,357] Pathways related to oxidative stress management, such as vitamin B6 metabolism and siderophore biosynthesis, were also prominently affected.[358-360] Ubiquinone biosynthesis showed alterations linked to electron transport and energy production.[361,362]

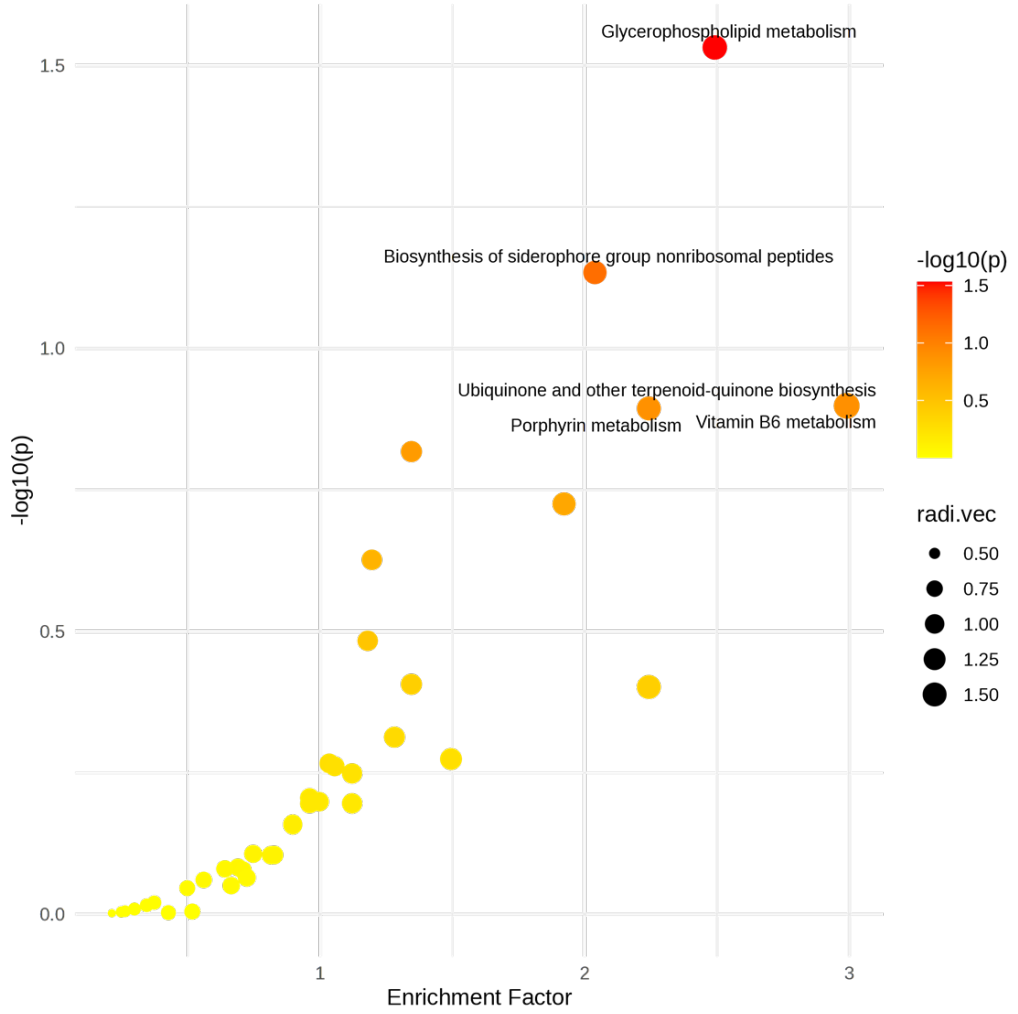

Pathway Name	Total↑↓	Hits(all)↑↓	Hits(sig.)↑↓	Expected↑↓	P(Fisher)↑↓	P(Gamma)↑↓
Glycerophospholipid metabolism	22	4	2	2.006	0.029399	0.022659
Biosynthesis of siderophore group nonribosomal peptides	5	2	2	2.4525	0.073442	0.025042
Ubiquinone and other terpenoid-quinone biosynthesis	23	2	1	0.66887	0.12633	0.028276
Vitamin B6 metabolism	13	1	1	0.66887	0.12633	0.028276
Porphyrin metabolism	35	7	4	1.3377	0.12769	0.028366
Valine, leucine and isoleucine biosynthesis	22	20	10	8.9183	0.15219	0.030025
Aminobenzoate degradation	8	3	2	1.5607	0.18827	0.03267
Purine metabolism	76	33	12	13.377	0.2364	0.036614
Pyrimidine metabolism	51	25	8	8.4724	0.32861	0.04578
Valine, leucine and isoleucine degradation	22	6	3	2.2296	0.39219	0.053649
Carbapenem biosynthesis	3	2	1	0.44592	0.39659	0.05425
Histidine metabolism	12	4	3	1.5607	0.4864	0.068446
Peptidoglycan biosynthesis	18	6	2	1.5607	0.4864	0.068446

Figure 4.26 Functional analysis and pathway enrichment for the wild-type (E) E. coli strain comparing 0 µg/mL and 4 µg/mL meropenem conditions. *The plot displays enriched metabolic pathways based on significantly altered metabolites, with pathway impact (x -axis) plotted against the -log10(p-value) of enrichment significance (y-axis). Each point represents a pathway, where the size of the point indicates the number of significantly altered metabolites associated with the pathway, and the colour intensity reflects the p-value significance (larger, redder points indicate higher significance).*
The accompanying table lists the enriched pathways, showing the total number of metabolites mapped to each pathway (Total), the number of detected metabolite (Hits [all]), the number of statistically significant metabolites (Hits [sig.]), the expected number of metabolites in each pathway based on the background dataset (Expected), and statistical significance evaluated using Fisher's exact test (PFisher) and gamma-adjusted p-values (P[Gamma]). These data provide insights into the relevance and impact of specific pathways under antibiotic stress.

The significant enrichment of glycerophospholipid metabolism suggested the critical role of membrane remodelling in maintaining structural integrity and functional integrity and functionality during antibiotic stress.[356,357] Such modifications are essential for preserving the barrier and transport roles of the cell membrane.[363] Additionally, alterations in the biosynthesis of siderophore group non-ribosomal peptides suggest a potential adjustment in iron acquisition processes, which is vital for managing oxidative stress and maintaining redox balance under stress conditions.[364-366] Similarly, the impact on vitamin B6 metabolism highlighted its essential role in amino acid metabolism and as a cofactor in enzymatic reactions critical for oxidative stress management.[358-360] These pathways reflect the prioritisations by the strain of processes that enhance cellular resilience against stressors.

Ubiquinone and other terpenoid-quinone biosynthesis pathways were also significantly impacted, indicating adjustments in energy production and electron transport mechanisms, which are fundamental to meeting the elevated energy demands of stressed cells.[361,362]

Furthermore, significant changes in porphyrin metabolism, potentially including processes such as heme biosynthesis, indicate possible adjustments related to respiratory activity or stress mitigation mechanisms under meropenem exposure.[367-370]

Collectively, these findings showed that the wild-type strain exhibited significant metabolic flexibility in response to meropenem. These metabolic adjustments reflect the adaptability of the strain, highlighting its ability to deprioritise non-essential processes in favour of mechanisms that enhance its survival under antibiotic pressure.[76,371] These findings underscore capacity of the strain to engage in extensive metabolic reprogramming when faced with antibiotic pressure, a strategy that may enhance its survival in hostile environments.[45]

4.3.4.2 Pathways related to stress management and cellular repair observed in the meropenem-susceptible strain treated with meropenem

The meropenem-susceptible (S) strain was analysed to identify pathway-level adaptations and metabolic vulnerabilities during meropenem exposure. The analysis also allowed comparison with metabolic responses observed for the control and meropenem-resistant (E and R) strain.

Functional analysis was conducted using untargeted pathways analysis in the same way as for the E strain. Key pathways were ranked by their statistical significance and biological impact, providing insights into the metabolic processes most affected by antibiotic exposure.

Interestingly, functional analysis (**Figure 4.27**) identified significant changes in pyrimidine metabolism, histidine metabolism, arginine and proline metabolism, glutathione metabolism, and peptidoglycan biosynthesis. These pathways reflect critical processes impacted in the meropenem-susceptible strain (S) upon exposure to meropenem.

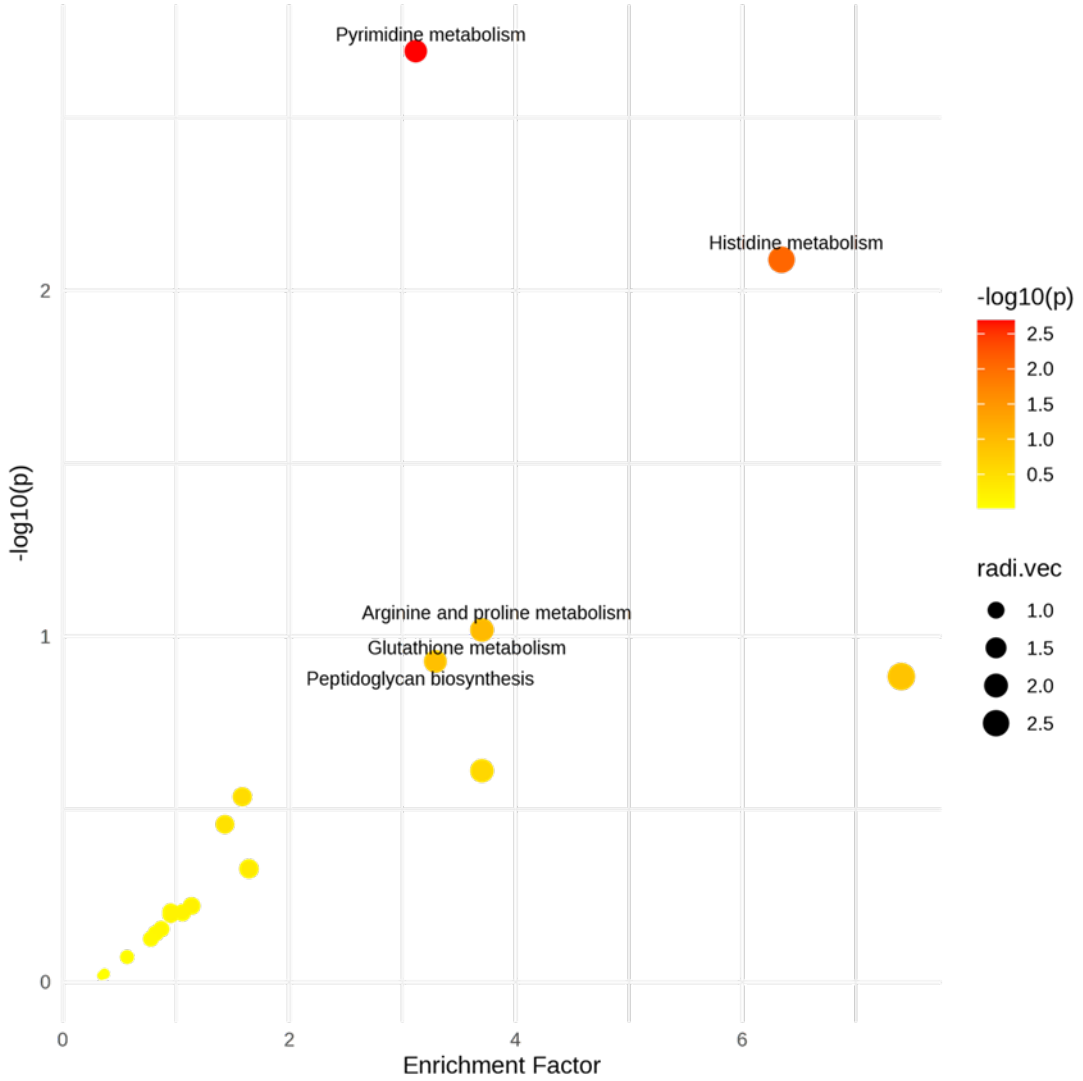

Pathway Name	Total↑↓	Hits(all)↑↓	Hits(sig.)↑↓	Expected↑↓	P(Fisher)↑↓	P(Gamma)↑↓
Pyrimidine metabolism	51	25	10	2.5664	0.0020297	0.0023936
Histidine metabolism	12	4	3	0.47277	0.0081404	0.0024447
Arginine and proline metabolism	29	8	2	0.54031	0.095826	0.0033195
Glutathione metabolism	22	6	2	0.54031	0.095826	0.0033195
Peptidoglycan biosynthesis	18	7	2	0.60784	0.11812	0.0035911
Fatty acid degradation	41	1	1	0.13508	0.13065	0.0037539
Lysine biosynthesis	13	4	1	0.27015	0.24471	0.0056558
Amino sugar and nucleotide sugar metabolism	44	29	3	1.8911	0.29105	0.01327
Fructose and mannose metabolism	33	28	7	2.0937	0.34962	0.022788
Glycerophospholipid metabolism	22	4	1	0.60784	0.47012	0.025224
O-Antigen nucleotide sugar biosynthesis	21	14	1	0.878	0.60212	0.025673
Purine metabolism	76	33	5	4.1874	0.62571	0.026634
Alanine, aspartate and glutamate metabolism	22	9	1	0.94553	0.62977	0.035531

Figure 4.27 Functional analysis for the meropenem-susceptible (S)* E. coli *strain comparing 0 µg/mL and 4 µg/mL meropenem conditions. *The scatter plot shows enriched pathways based on significantly altered metabolites, with pathway impact scores on the x-axis and -log10(p=value) of enrichment significance on the y-axis. Each point represents a pathway, with its size and colour denoting the p-value (larger, redder points indicate higher significance). The accompanying table provides detailed pathway enrichment statistics, including the total number of pathway metabolites (Total), detected hits (Hits), significant hits (Hits (sig.)), expected hits (Expected), p-value (PFisher), and pathway impact score (P[Gamma]).*

Alterations in pyrimidine metabolism suggest a heightened demand for nucleotide synthesis, possibly to support DNA repair mechanisms under meropenem exposure.[332] Such pathway, essential for maintaining cellular homeostasis, may be activated to counteract damage to the nucleic acid structure caused by antibiotic-induced stress.[372] Similarly, changes in histidine metabolism and arginine and proline metabolism potentially point toward altered amino acid biosynthesis.[373,374] These pathways likely support the production of proteins involved in stress responses and cellular repair, indicating a reallocation of metabolic resources to sustain survival under stress conditions.[348,375]

Enrichment in glutathione metabolism underscores the role of antioxidant defence mechanisms in managing oxidative stress.[376,377] Glutathione plays a central role in detoxifying ROS, which are typically elevated under antibiotic pressure.[378] The observed changes suggest an increased need for oxidative stress management in the meropenem-susceptible strain, a common bacterial response to antibiotic-induced stress.[379]

Significant changes in peptidoglycan biosynthesis highlight the effort of the strain to maintain cell wall integrity during meropenem exposure.[380] As a major structural component of the bacterial cell wall, peptidoglycan biosynthesis is critical for preserving cell morphology and preventing lysis under osmotic and antibiotic stress.[381] The presence of pCR2.1 plasmid, which contains an ampicillin resistance gene against β-lactam antibiotic, may further influence changes in peptidoglycan biosynthesis.[382] While meropenem disrupts cell wall synthesis as part of its mechanism, these observations suggest an adaptive attempt by the strain to counteract such effects.

The results indicate that the S strain reallocates metabolic resources toward critical pathways involved in nucleotide synthesis, amino acid metabolism, and oxidative stress management. The activation of glutathione metabolism underscores the effort of the strain to mitigate ROS-induced damage, while changes in peptidoglycan biosynthesis reflect its attempts to counteract cell wall-disrupting effects of the antibiotic. These findings highlight the metabolic reprogramming of the strain under meropenem pressure, albeit within the constraints

imposed by its plasmid-mediated susceptibility.

The S and E strains exhibited both shared and distinct metabolic pathway enrichments in response to meropenem exposure. Both strains showed enrichment in pyrimidine metabolism, purine metabolism, and peptidoglycan biosynthesis, suggesting that meropenem exposure induced increased nucleotide turnover and cell wall remodelling. In the S strain, glutathione metabolism was significantly enriched, indicating an oxidative stress response, whereas this pathway was not significantly altered in the E strain.[376] Additionally, fatty acid degradation and lysine biosynthesis were enriched in the S strain but not in the E strain. The E strain exhibited significant enrichment in amino sugar and nucleotide sugar metabolism, which was absent in the S strain, indicating potential differences in sugar utilisation or modifications affecting bacterial surface structures under meropenem exposure.

In contrast to the E and S strains, the R strain exhibited no significant metabolic pathway enrichment when exposed to meropenem. With insufficient statistical significance to generate a pathway enrichment map. The finding indicates a lack of substantial metabolic alterations in response to meropenem. The result is critical, as it suggests that the R strain maintains metabolic homeostasis even under antibiotic stress, likely due to its efficient hydrolysis of meropenem via NDM-7 activity. The absence of detectable metabolic perturbations highlights the metabolic stability of the resistant strain, reinforcing the idea that meropenem exerts minimal selective pressure at the metabolic level when resistance is already established.

4.3.4.3 Functional analysis comparing meropenem-susceptible and meropenem-resistant strains

Finally, comparing metabolic adaptations between the meropenem-susceptible (S) and meropenem-resistant (R) strains was performed to identify whether significantly altered metabolic pathways were present. Controlling for presence of the plasmid and other strain specific criteria, this comparison would reveal metabolic pathways linked directly to the presence of the resistant gene that had been inserted. Functional analysis (**Figure 4.28** pathway enrichment map) was performed to compare significantly altered pathways between S and R strains under 4 μg/mL meropenem exposure.

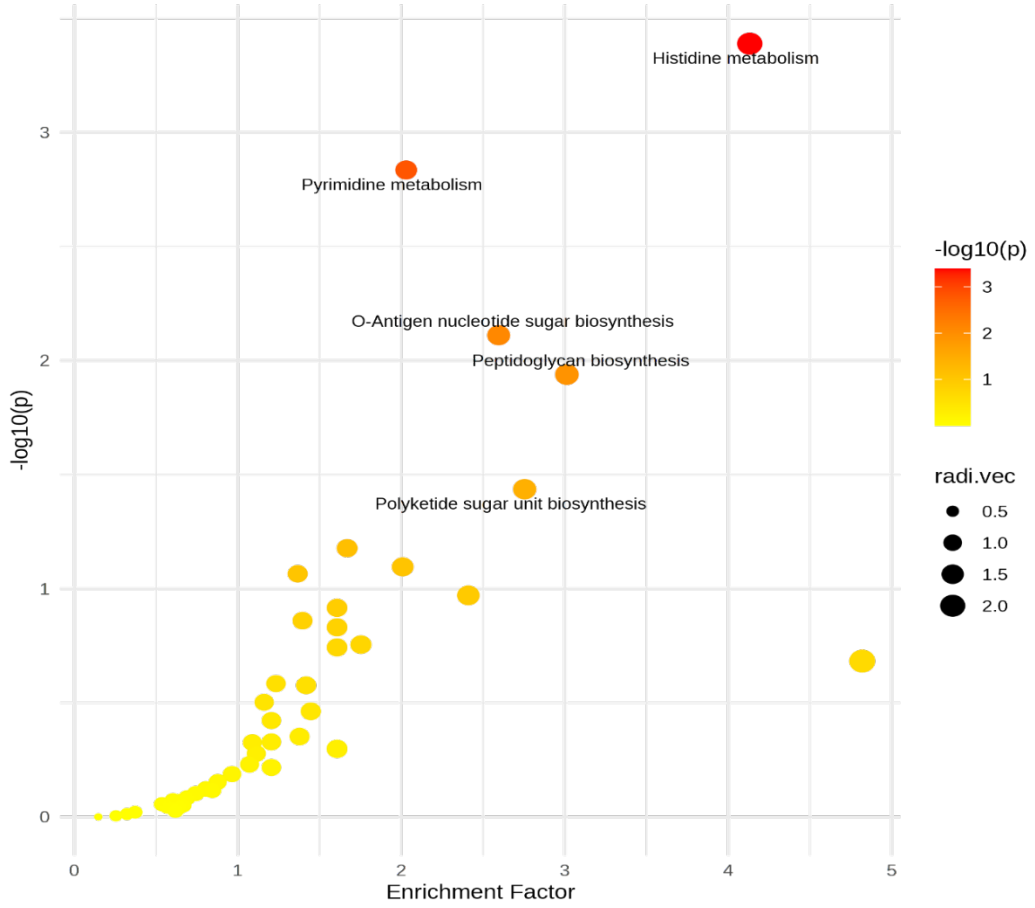

Pathway Name	Total↑↓	Hits(all)↑↓	Hits(sig.)↑↓	Expected↑↓	P(Fisher)↑↓	P(Gamma)↑↓
Histidine metabolism	12	4	4	1.4525	4.0809E-4	0.0099531
Pyrimidine metabolism	51	25	16	7.8852	0.0014605	0.0099808
O-Antigen nucleotide sugar biosynthesis	21	14	11	2.6976	0.0077442	0.010148
Peptidoglycan biosynthesis	18	7	4	1.66	0.011514	0.01025
Polyketide sugar unit biosynthesis	5	3	3	1.4525	0.036622	0.010957
Amino sugar and nucleotide sugar metabolism	44	28	19	5.3951	0.066406	0.011865
Streptomycin biosynthesis	9	7	7	2.4901	0.080183	0.012312
Purine metabolism	76	33	14	12.45	0.085965	0.012505
Acarbose and validamycin biosynthesis	3	2	2	1.245	0.10694	0.013234
Glycolysis/Gluconeogenesis	29	16	11	4.3576	0.12126	0.013758
Galactose metabolism	39	36	20	7.8852	0.13807	0.014402
Cysteine and methionine metabolism	41	12	4	3.7351	0.14759	0.014402
Glycerolipid metabolism	15	7	3	2.2826	0.17573	0.014781
Starch and sucrose metabolism	22	15	8	3.1126	0.18076	0.01619
Fatty acid degradation	41	1	1	0.20751	0.20751	0.017434
Pentose phosphate pathway	26	21	11	8.9227	0.26037	0.020216

Figure 4.28 Functional analysis of metabolic profiles comparing meropenem-susceptible (S) and meropenem-resistant (R) strains under 4 µg/mL meropenem exposure. *The scatter plot highlights pathways significantly altered in the S vs. R comparison, with pathway impact scores on the x-axis and -log10(p-value) of enrichment significance on the y-axis. Each point represents a pathway, with its size and colour denoting the p-value (larger, redder points indicate higher significance). The accompanying table provides detailed pathway enrichment statistics, including the total number of pathway metabolites (Total), detected hits (Hits), significant hits (Hits (sig.)), expected hits (Expected), p-value (PFisher), and pathway impact score (P[Gamma]).*

The analysis identified significant differences in key pathways, including histidine metabolism, pyrimidine metabolism, O-antigen nucleotide sugar biosynthesis, peptidoglycan biosynthesis, and polyketide sugar unit biosynthesis. These pathways reflected critical cellular processes, particularly in the context of membrane integrity, nucleotide synthesis, and stress response.[383-388]

Alterations in histidine metabolism may indicate changes in amino acid biosynthesis pathways, potentially linked to the metabolic demands imposed by antibiotic exposure.[389] Similarly, the enrichment of pyrimidine metabolism, which plays a critical role in nucleotide synthesis, showed significant involvement, potentially reflecting a higher demand for nucleotide precursors under meropenem exposure.[390] Such observation could be related to processes such as DNA repair or RNA synthesis.

Pathways associated with cell wall integrity, such as O-antigen nucleotide sugar biosynthesis and peptidoglycan biosynthesis, were significantly impacted.[386,387] The involvement of polyketide sugar unit biosynthesis suggests differences in secondary metabolite production between the strains.[391,392] The meropenem-susceptible strain may divert resources to the production of stress-response metabolites, reflecting its vulnerability to meropenem. Meanwhile, efficient resistance mechanisms of the R strain likely reduce the need for such compensatory metabolic responses. These findings provide insights into the metabolic trade-offs associated with susceptibility and resistance in *E. coli*. The metabolic instability of and adaptive reprogramming of S strain highlight its vulnerability to meropenem, while the R resilience of R strain highlights the metabolic advantages conferred by NDM-7 expression. The contrasting functional profiles between the S and R strains not only enhanced our understanding of metabolic consequences of resistance mechanisms but also offer potential targets for therapeutic interventions aimed at disrupting adaptive pathways or enhancing the efficacy of antibiotics.[393]

4.3.5 Discussion and conclusion

The chapter 4 results sections highlighted distinct metabolic responses of the wild-type (E), meropenem-susceptible (S), and meropenem-resistant (R) strains of *E. coli* to meropenem exposure. These responses were shaped by differences in genetic background, resistance mechanisms, and metabolic capacity, revealing how bacterial strains adapt to antibiotic exposure through metabolic changes.

The wild-type strain (E) demonstrated substantial metabolic reprogramming in response to meropenem. Functional analyses indicated the involvement of pathways associated with nucleotide metabolism, oxidative stress management, and central carbon metabolism. These findings suggest that the wild-type strain reallocates metabolic resources to processes critical for maintaining cellular homeostasis and mitigating oxidative damage. For example, increased activity in pathways like glycerophospholipid metabolism suggests membrane remodelling as an essential mechanism for preserving structural integrity during antibiotic exposure. The absence of intrinsic resistance mechanisms in the wild-type strain necessitates these extensive metabolic adjustments, which are energetically demanding.

The meropenem-susceptible strain exhibited a more constrained metabolic responses compared to the wild-type strain. Functional analyses highlighted the involvement of pathways such as nucleotide biosynthesis, oxidative stress management, and membrane integrity. However, the metabolic burden imposed by the pCR2.1 plasmid, may limit its adaptive capacity but further studies would be required to investigate this. The dual burden – plasmid-associated metabolic costs and the lack of specific resistance to meropenem – may influence metabolic response of the strain to meropenem.

In contrast, the meropenem-resistant strain demonstrated remarkable metabolic stability, with minimal changes in its metabolic profile under meropenem exposure.[342] The metabolic stability is likely to be due to the presence of NDM-7 carbapenemase, which hydrolyses the meropenem antibiotic, consequently reducing the need for widespread of metabolic adjustments. Functional analysis could not identify enriched pathways for the comparison

between vehicle control and meropenem treatment of meropenem-resistant strain (R) due to insufficient significant differences between conditions. The lack of metabolic change suggests that the pre-existing enzymatic resistance mechanisms of the strain mitigate the need to alter core biosynthetic processes to maintain homeostasis under antibiotic stress.

In addition to pathway-level insights, key metabolites driving the observed metabolic changes across strains were identified. **Table 4.1** summarizes these metabolites, their changes under meropenem exposure, and potential roles in cellular processes, with a significance threshold of FC > 1.5 and p value < 0.05. The metabolic responses to meropenem exposure varied across *E. coli* strains, with distinct changes observed in nucleotide metabolism, stress signalling, and central carbon pathways. Cytidine diphosphate, involved in membrane phospholipid synthesis, increased in wild-type strains but decreased in susceptible strains, suggesting strain-specific differences in membrane remodelling. [394] Stress-related metabolites, including 2',3'-cAMP and cAMP, showed differential regulation, indicating antibiotic-induced stress responses, while glutathione was upregulated in resistant strains, highlighting an adaptive oxidative stress response. [342,395] [341,396,397] Changes in TCA cycle intermediates, such as isocitrate, and glycolytic metabolites, including fructose-6-phosphate and 2-phosphoglycerate, suggest metabolic rewiring under antibiotic pressure.[398-400] Amino acid metabolism was also affected, with decreases in isopropyl malate and multiple N-acetylated amino acids, reflecting disruptions in biosynthetic pathways.[401-404] Additionally, sedoheptulose-1-phosphate, linked to the pentose phosphate pathway, showed strain-dependent changes, suggesting altered carbon flux and membrane adaptation. [330,405] Overall, wild-type and susceptible strains exhibited greater metabolic perturbations, while resistant strains showed more stable metabolic profiles, with specific adaptations to oxidative stress and altered carbon metabolism.

Table 4.1 Summary of key metabolite changes driving metabolic responses to meropenem across wild-type, susceptible, and resistant* E. coli *strains. Increase and decreases indicated by up and down arrows, arow to right indicates no change *(FC cut off value = 1.5 p-value < 0.05, *FDR corrected).*

Metabolite	E0 vs E4	S0 vs S4	R0 vs R4	R0 vs R16	Potential Role /Refs
Cytidine diphosphate	↑*	↓*	→	↓*	Membrane phospholipid [394]
Thymidine phosphate	→	↑*	→	→	Thymidine salvage [406]
2',3'-cAMP	↑*	↑	→	→	Antibiotic related stress[395]
Isocitrate	↓	↓	→	↑*	TCA cycle [398]
Galactaric acid	↓	↓	→	→	Galactarate catabolism[407]
Isopropylmalate	↓	↓*	↑	→	Leucine biosynthesis [401]
N-Acetyl-methionine	↓	→	→	→	Methionine biosynthesis [402]
N-Acetyl-tryptophan	↓*	→	→	→	Protein synthesis [403]
N-Acetyl-valine	↓	→	→	→	
N-Acetylaspartyl-glutamate	↓	↓*	→	→	Nucleotide synthesis, oxidative stress [408, 409,410]
N-Acetyl Phenylalanine	↓	→	→	→	Protein synthesis [404]
Hippurate	↓	→	→	→	
Glutathione	→	→	→	↑*	Protection against oxidative stress [397]
6-Phosphogluconate	→	→	→	→	Pentose phosphate pathway [411]
Oxoadipate	↓	→	→	↑	Aromatic compound catabolism [412]
Sorbitol	↑	→	→	→	
Sedoheptulose-1-phosphate	↑	→	↑	↓	Pentose phosphate pathway, counteracting oxidative stress [330,405]
cAMP	↑	↓*	↓	↑	Stress signalling [342 341,396]
Fructose 2,6-biphosphate	↓	→	→	→	
Frucose-6-phosphate	→	→	↑	↓	Glycolysis [399]
Pyroglutamate	→	↑	→	↓	Inhibition of glutamate uptake [413]
2,3-Diphosphsphoglycerate	→	↓	→	→	
2-Phosphoglycerate	→	↓	→	↓*	Central carbon metabolism [400]
3-Phosphoglycerate	→	↓	→	→	[400]
Glucoronate	→	→	↓	→	Carbon source [414]
UDP	→	→	↓	↓*	Lipopolysaccharide biosynthesis [415]
Uracil	→	→	↓	↑*	Nucleotide metabolism [416]
Thymine	→	→	↓	→	DNA repair [417]
Total up/down/no change	**5/11/12**	**3/9/16**	**3/5/20**	**6/5/17**	

Comparing the metabolic responses of the three strains highlights key differences in their adaptive strategies. The wild-type and meropenem-susceptible strains exhibited greater metabolic reprogramming, consistent with their need to activate pathways involved in survival under antibiotic pressure. These responses come at an energetic cost, requiring resource allocation to stress management processes. In contrast, the metabolic stability observed in the meropenem-resistant strain underscores the efficiency of its resistance mechanisms, which mitigate disruptions to core metabolic functions by neutralizing the antibiotic before broader cellular effects occur.

To provide a comparative overview of the metabolic changes across strains, **Table 4.2** summarizes the predicted pathway changes in response to meropenem exposure. The data highlight key pathways that were significantly altered in the wild-type (E) and susceptible (S) strains**,** while the resistant (R) strain showed no substantial metabolic changes. Notably, glycerophospholipid metabolism was enriched in both the E and S strains but not in R**,** suggesting that membrane remodelling plays a role in susceptible strains under antibiotic stress. Peptidoglycan metabolism and histidine metabolism were significantly enriched in the S strain but not in the E strain, indicating a strain-specific response to cell wall and amino acid metabolism. In contrast, the resistant strain (R) exhibited no significant metabolic pathway enrichment upon meropenem exposure (R0 vs R4), further reinforcing the minimal metabolic impact of meropenem on this strain.

Table 4.2 Predicted pathway change comparison.

Pathways	E0 vs E4	S0 vs S4	R0 vs R4	S4 vs R4	R0 vs R16
Glycerophospholipid metabolism	YES	YES	N/A	YES	NO
Siderophore metabolism	YES	NO	N/A	NO	YES
Ubiquinone metabolism	YES	NO	N/A	NO	NO
Vit B6 metabolism	YES	NO	N/A	NO	NO
Porphyrin metabolism	YES	NO	N/A	NO	NO
Amino acid metabolism	YES	YES	N/A	YES	YES
Pyrimidine and purine	YES	YES	N/A	YES	YES
Aminobenzoate metabolism	YES	NO	N/A	NO	YES
Glutathione metabolism	NO	YES	N/A	NO	NO
Peptidoglycan metabolism	NO	YES	N/A	YES	NO
Histidine metabolism	NO	YES	N/A	YES	NO
Glycolysis	NO	NO	N/A	YES	NO
Pentose phosphate pathway	NO	NO	N/A	YES	NO
Fatty acid degradation	NO	NO	N/A	YES	YES

These results have broader implication for understanding the metabolic dynamics of antibiotic resistance and susceptibility. The reliance of the meropenem-resistant strain on NDM-7 mediated resistance and associated pathways present opportunities for intervention by disrupting these systems or enhancing metabolic stress to overcome resistance. By characterising strain-specific metabolic adaptations, this study provides valuable insights into the interplay between antibiotic stress and bacterial metabolism. These findings offer promising avenues for the development of targeted therapies aimed at combating carbapenem-resistant pathogens.

In conclusion, the metabolic adaptations observed in response to meropenem exposure reflect the interplay between genetic and resistance factors in shaping bacterial survival strategies. The wild-type strain relies on extensive metabolic reprogramming to adapt to meropenem-induced stress. The meropenem-susceptible strain shows constrained metabolic adjustments, potentially influence by the dual burden of plasmid-associated resistance and meropenem stress, and the meropenem-resistant strain maintain metabolic stability through efficient resistance mechanism. These findings contribute to a broader understanding of the metabolic strategies underpinning antibiotic susceptibility and resistance, providing critical insights for the development of targeted therapeutic interventions against carbapenem-resistant pathogens.

4.4 Metabolic responses of resistant *E. coli* (DH5α pCR2.1 NDM-7) to minimum inhibitory concentration (16 μg/mL) meropenem exposure

The exposure of the meropenem-resistant strain (R) to 16 μg/mL meropenem represents an important step in understanding the metabolic and adaptive strategies employed by this strain under extreme antibiotic pressure. The concentration of meropenem, established as the MIC in **Section 4.2.1**, was shown to be the threshold at which bacterial growth was inhibited by the antibiotic. While 4 μg/mL meropenem induced some metabolic changes in the meropenem-resistant strain compared to the wild-type (E) and meropenem-susceptible (S) strains, it remained to be understood what the metabolic effects were at higher antibiotic concentrations, specifically at MIC.

Moreover, identifying metabolic vulnerabilities at MIC could inform therapeutic strategies aimed at disrupting pathways that are working to maintain homeostasis in resistant strains under critical antibiotic load. Understanding how the R strain achieves metabolic stability, despite heightened antibiotic stress, could reveal critical pathways or metabolites that represent potential targets for intervention, paving the way for novel approaches to combatting antibiotic resistance. Therefore, next the R strain was treated with 16 μg/mL for 1-hour and compared to the vehicle control. Untargeted metabolomics by AEC-MS/MS was performed on metabolite extracts.

4.4.1 Data quality assessment and metabolic responses in meropenem-resistant *E. coli* at minimum inhibitory concentration

The data quality assessment for the meropenem-resistant (R) strain under vehicle control (R_0) and MIC-treated conditions (R_16) was conducted. By evaluating the clustering of replicates and the global variance in metabolic profiles, this step aimed to confirm that the observed differences were consistent and reflective of biological effects rather than technical variation.

The unclustered heatmap (**Figure 4.29**) shows the abundances of metabolites across the R_0 (untreated) and R_16 (MIC-treated) conditions, providing a detailed overview of the dataset. It

shows no major intra-class variability indicating not bias in sample experimental or technical bias in the data.

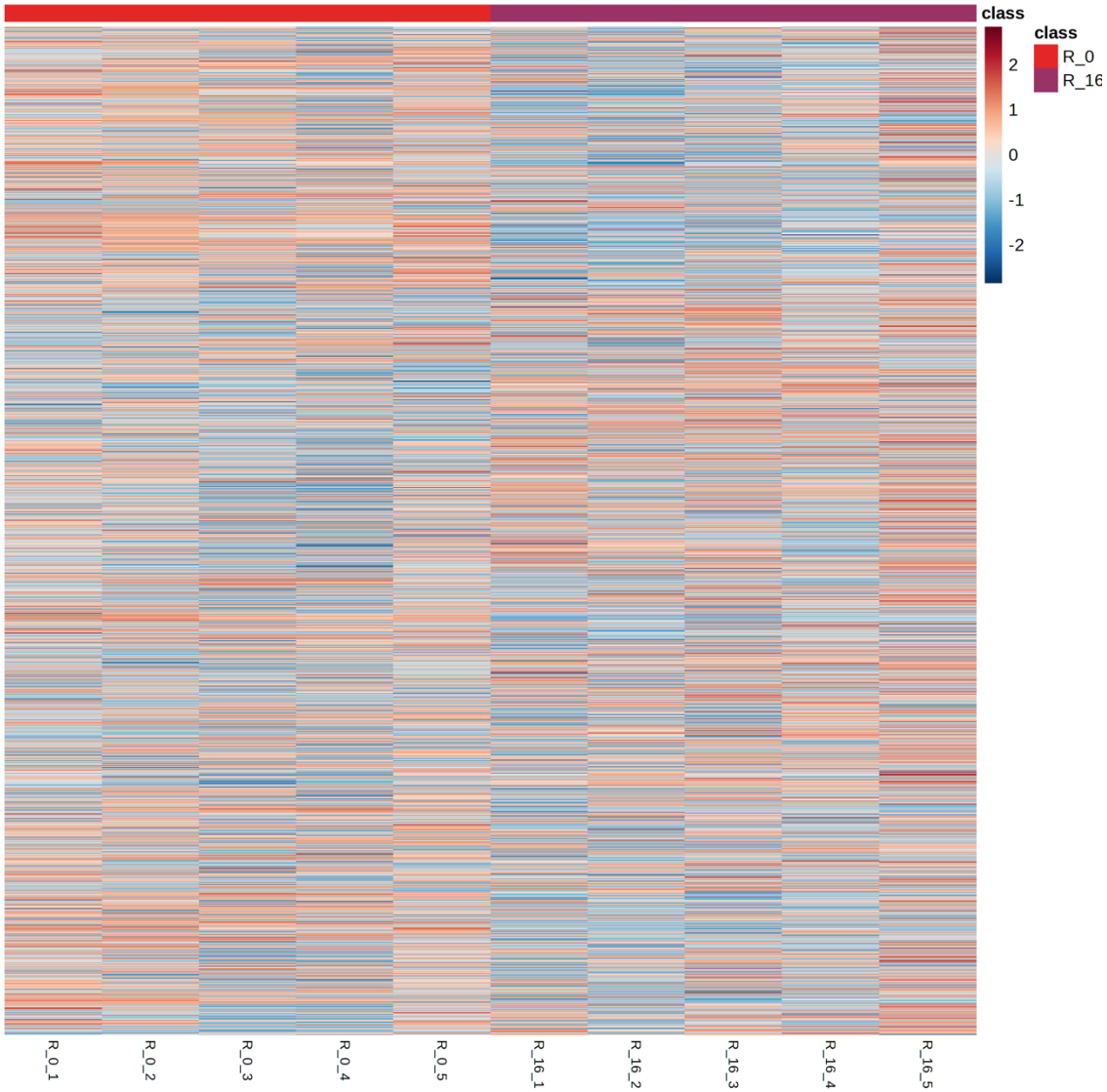

Figure 4.29 Unclustered heatmap showing metabolite abundance profiles of the meropenem-resistant* E. coli *strain (R) under vehicle control (R_0, red) and MIC-treated conditions (R_16, magenta). *Each column represents a biological replicate, and each row corresponds to a detected compound feature. Normalized abundances are represented, with red indicating higher abundance and blue indicating lower abundance.*

The PCA plot (**Figure 4.30**) shows clear separation between the metabolic profiles of R_0 and R_16 samples, with distinct clustering of biological replicates in each condition. The separation along the primary components highlights the impact of meropenem on metabolic landscape of the R strain at MIC. The clustering of R_16 replicates indicate a uniform metabolic adaptation to meropenem-induced stress, whereas the separation from R_0 highlights a distinct reprogramming of metabolic pathways in response to the antibiotic.

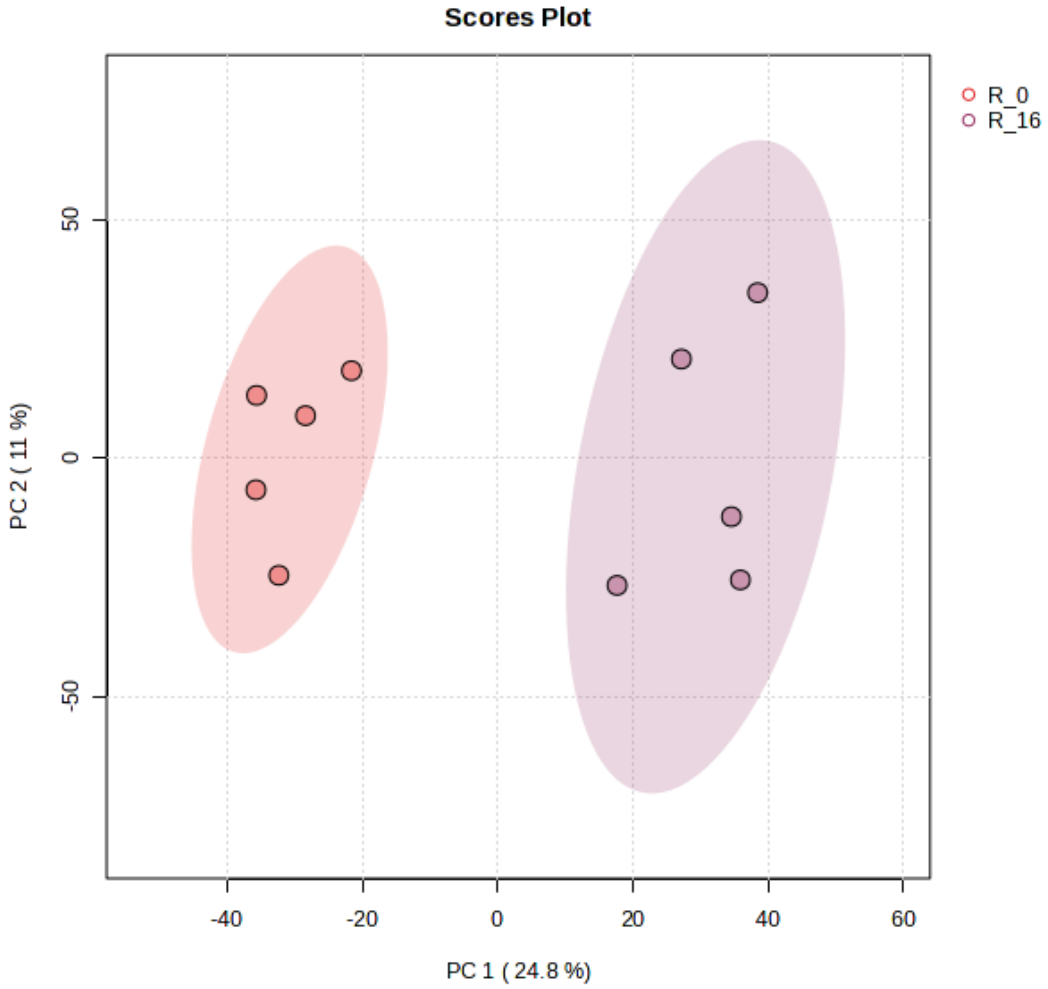

Figure 4.30 Principal Component Analysis (PCA) plot comparing the metabolic profiles of R_0 (DMSO) and R_16 (16 µg/mL meropenem-treated) samples. *The PCA plot highlights clear separation between the metabolic profiles of the untreated (R_0) and MIC-treated (R_16) samples, with distinct clustering of replicates for each condition. The first two components account for 24.8% and 18.1% of the variance, respectively, underscoring significant shifts in the global metabolic landscape upon meropenem exposure at MIC.*

4.4.2 Metabolites altered under minimum inhibitory concentration conditions

The metabolic profile of the meropenem-resistant strain (R) exposed to the MIC of meropenem (16 µg/mL) were further investigated to better understand the biochemical adjustments under high antibiotic concentration. The analysis specifically aimed to identify significantly altered metabolites that reflect the interplay between resistance mechanisms and broader metabolic responses, highlighting pathways that are activated or suppressed in response to antibiotic stress. The findings provide insights into resistance-associated metabolic changes.

Univariate analysis was employed to compare the metabolite abundances between the vehicle control (R_0, bright red) and MIC-treated (R_16, magenta) conditions. A volcano plot (**Figure 4.31**) was generated to visualize compound features with statistically significant changes,

based on log2 FC and adjusted p-values (FDR correction < 0.05). Box plots (**Figure 4.32**) were used to highlight the top 10 significantly altered metabolites, providing a detailed view of changes in their normalized concentrations across biological replicates.

The volcano plot (**Figure 4.31**) revealed a total of 195 significantly upregulated compound-features and 605 significantly downregulated compound-features in R_16 condition compared to R_0. These changes emphasise the ability of the strain to adjust its metabolic network under meropenem exposure. A substantial proportion of the compounds (3289) showed no significant change, indicating a level of metabolic stability.

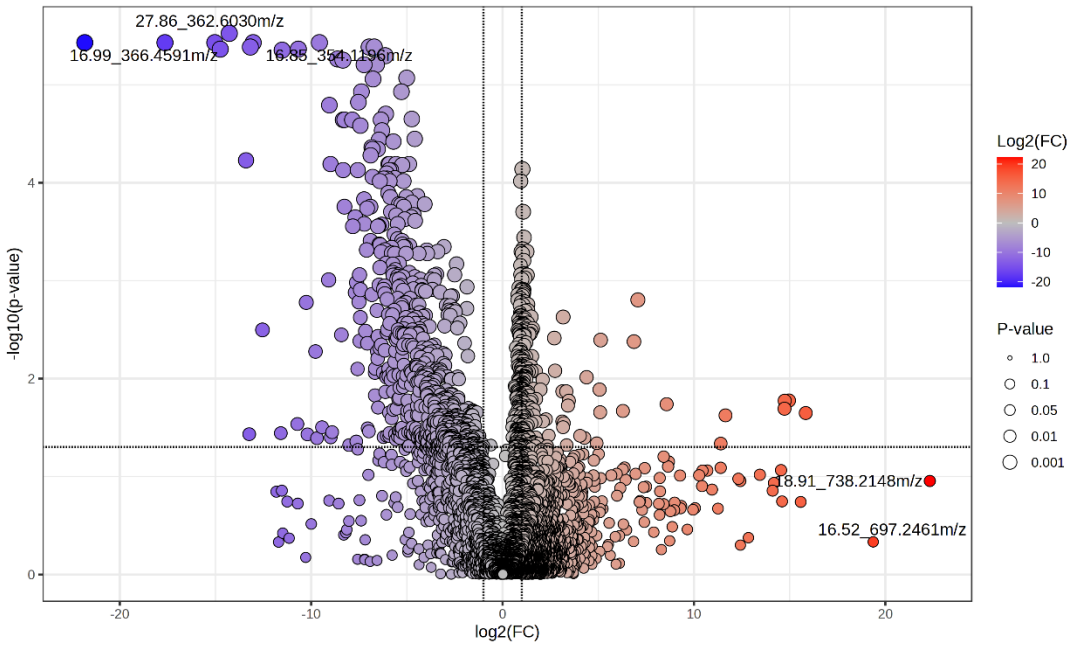

Figure 4.31 Volcano plot comparing significantly altered metabolites between R_0 (DMSO vehicle control) and R_16 (16 µg/mL meropenem-treated) conditions. *The x-axis represents the log2 FC in metabolite abundance, while the y-axis displays -log10(p-value), reflecting the statistical significance. Red points indicate significantly upregulated metabolites, blue points indicate significantly downregulated metabolites, and larger points represent metabolites with higher statistical confidence (FDR corrected p-value < 0.05).*

The box plots (**Figure 4.32**) highlight key metabolites altered under MIC conditions. Glucosamine-6-phosphate, a key component in peptidoglycan biosynthesis, was notably downregulated, while 2-hydroxyglutarate was significantly upregulated, suggesting activation of oxidative stress pathways to mitigate ROS accumulation and help to preserve cellular integrity.[418,419] Additionally, the upregulation of 4-hydroxybutyric acid indicates a shift toward alternative energy generation, reflecting an increased reliance on non-glycolytic mechanisms.[420] Conversely, several metabolites, including uridine 5'-diphosphate and

adenosine diphosphate (dADP), were downregulated, suggesting resource reallocation, with energy and precursors diverted away from routine biosynthetic activities and towards pathways supporting immediate stress adaptation.[421,422]

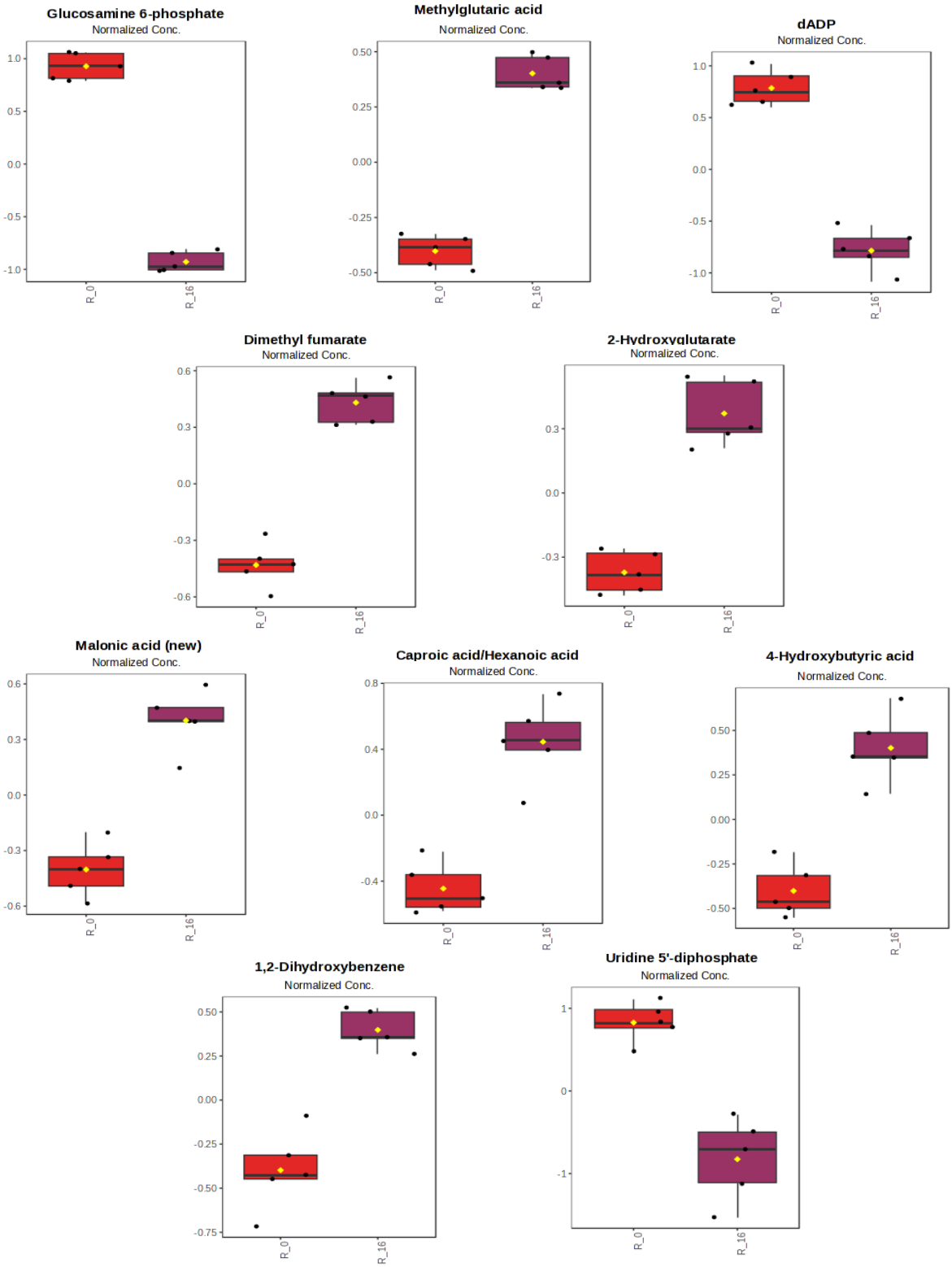

Figure 4.32 Box plots of the top 10 significantly altered metabolites comparing DMSO (R_0) and MIC meropenem-treated (R_16) conditionds fo the meropenem-resistant (R) strain exposed to 16 µg/mL meropenem. *The box plots represent normalised concentrations for each metabolite across biological replicates. FDR-adjusted p-value < 0.05*

The altered metabolic profile of the meropenem-resistant strain highlights its capacity to reallocate metabolic resources under antibiotic exposure. The observed downregulation of metabolites such as uridine 5'-diphosphate may indicate a reduced demand for certain biosynthetic pathways, potentially as part of a broader strategy to reallocate resources. Concurrently, the upregulation of metabolites associates with oxidative stress and energy metabolism suggests possible roles in mitigation of the damaging effects of meropenem exposure while maintaining cellular homeostasis.

4.4.3 Multivariate analysis of metabolic profiles under minimum inhibitory concentration conditions

Multivariate statistical analysis was performed to evaluate the global metabolic changes in the meropenem-resistant strain (R) under MIC-treated (R_16) and vehicle control (R_0) conditions. The approach captured the overarching metabolic phenotype and detect complex patterns of metabolite changes across the two conditions. By integrating multiple metabolites into a vector-based model, the analysis aimed to identify key discriminatory metabolites and metabolic trends that define the response of the resistant strain to meropenem exposure at MIC.

The analysis employed hierarchical clustering of the top 50 metabolites with the highest variance to generate a heatmap. The method grouped metabolites by similarity in abundance patterns, enabling visualization of metabolic regulation differences between R_0 and R_16 conditions. VIP scores from the PLS-DA model identified metabolites contributing most significantly to the separation between conditions. The quality of the PLS-DA model was evaluated using cross-validation metrics, including accuracy, R^2, and Q^2 values.

The hierarchical clustering heatmap (**Figure 4.33**) revealed distinct metabolite abundance profiles between the vehicle control (R_0) and MIC-treated (R_16) conditions with biological replicates from each condition grouping closely together, validating data reproducibility. Considerable differences were observed in metabolite clusters, indicating substantial regulation in response to meropenem exposure.

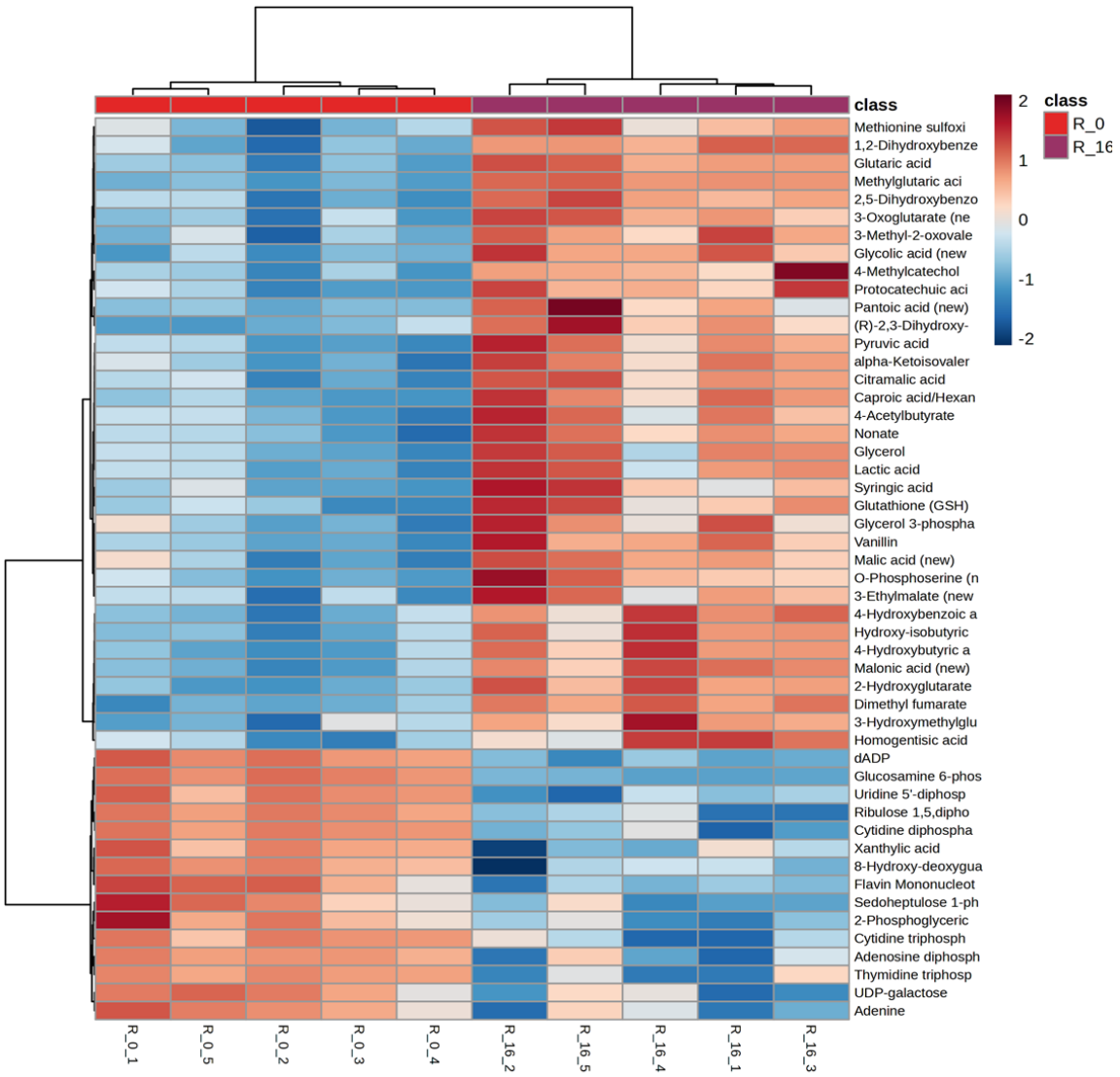

Figure 4.33 Hierarchical clustering heatmap of the top 50 identified metabolites showing differential abundance patterns between R_0 (DMSO vehicle control, red) and R_16 (16 µg/mL meropenem-treated, magenta) conditions. *The heatmap visualizes normalized metabolite abundances across biological replicates for both conditions. Red indicates higher abundance, blue indicates lower abundance, and clustering reflects similarities in metabolite abundance profiles between samples.*

These clusters highlight patterns of upregulation and downregulation of metabolites under MIC conditions, reflecting pronounced metabolic adjustments aimed at countering meropenem exposure. Several metabolite clusters exhibited strong upregulation in R_16, potentially pointing to critical adaptive processes required to mitigate the antibiotic effects.

VIP scores (**Figure 4.34**) from the PLS-DA model identified metabolites contributing most significantly to the separation between conditions, including thymidine triphosphate, cytidine diphosphate, and glucosamine-6-phosphate as key discriminatory metabolites. These metabolites were linked to nucleotide metabolism, cell wall biosynthesis, and oxidative stress response, reflecting adaptive mechanisms employed by the resistant strain.[356,418,423]

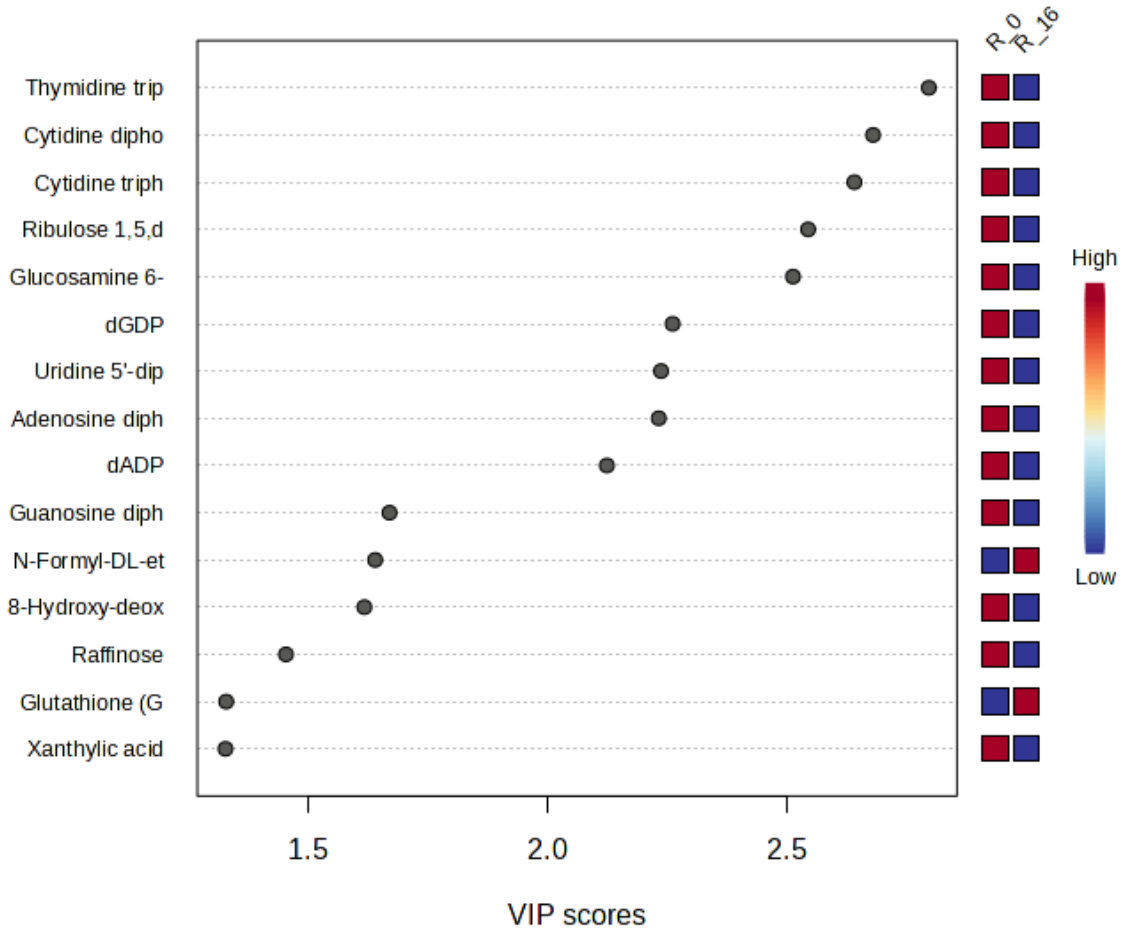

Figure 4.34 VIP (Variable Importance in Projection) scores plot highlighting key metabolites contributing to the differentiation between R_0 (DMSO, vehicle control) and R_16 (16 µg/mL meropenem-treated) conditions. *The x-axis displays the VIP scores, while the y-axis lists the identified metabolites. The heatmap on the right visualizes normalized abundance patterns for each metabolite across the two conditions, with red indicating higher abundance and blue indicating lower abundance.*

The hierarchical clustering heatmap provided a comprehensive overview of the metabolic reprogramming in response to MIC exposure, with clear evidence of upregulated pathways linked to stress response and energy metabolism. The separation of metabolite clusters between R_0 and R_16 underscores the metabolic flexibility and targeted responses of the meropenem-resistant strain. Complementing these observations, the PLS-DA model (**Figure 4.35**) demonstrated robust classification between treated and untreated conditions, with the one-component model achieving optimal performance metrics (accuracy = 1.0, R^2 = 0.94916, and Q^2 = 0.87123). The result highlights the discriminatory power of the selected metabolites in capturing the metabolic shifts induced by meropenem.

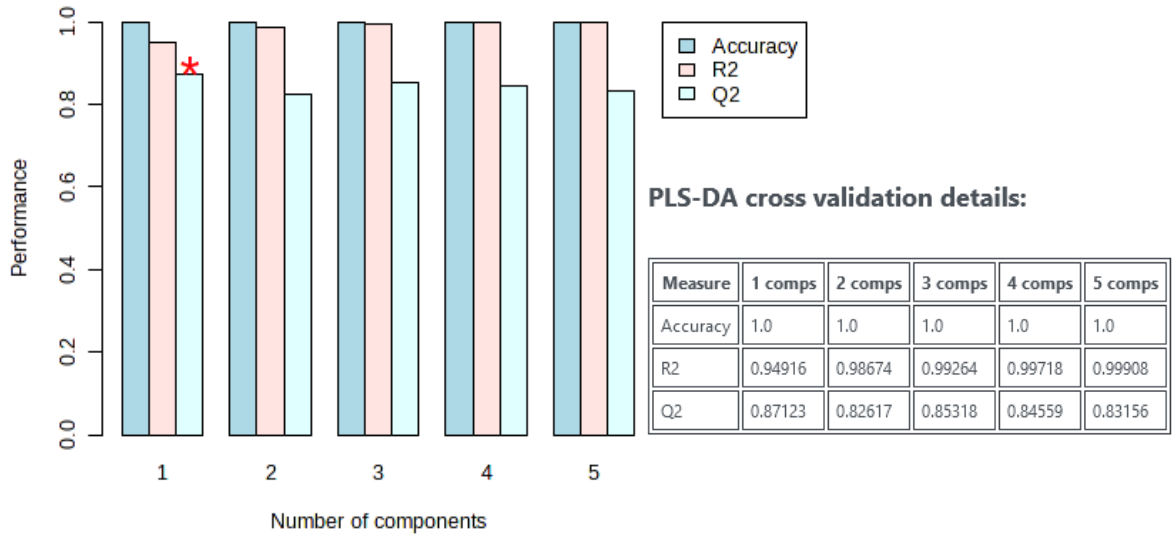

Measure	1 comps	2 comps	3 comps	4 comps	5 comps
Accuracy	1.0	1.0	1.0	1.0	1.0
R2	0.94916	0.98674	0.99264	0.99718	0.99908
Q2	0.87123	0.82617	0.85318	0.84559	0.83156

Figure 4.35 Performance metrics for the PLS-DA cross validation. *The bar plot represents the performance of models with varying numbers of components based on three metrics: accuracy, R^2, and Q^2. The table on the right provides detailed values for these metrics for 1 to 5 components. The model with one component is highlighted with a red asterisk, indicating its optimal performance with accuracy = 1.0, R^2 = 0.94916, and Q^2 = 0.87123. This analysis demonstrates the robustness and predictive ability of the PLS-DA model across components.*

VIP scores complemented the heatmap analysis by quantitatively ranking metabolites that are most critical in differentiating treated and untreated conditions. High VIP scores for nucleotides and stress-related metabolites indicate significant metabolic perturbations between these conditions. However, these metabolites were found higher levels in R_0 than in R_16, suggesting that nucleotide depletion occurred following meropenem exposure. Decrease in nucleotide pools in R_16 likely indicates a reduced capacity for DNA synthesis and repair, potentially due to cell cycle arrest or impaired replication. The metabolic profile of R_16 appears to reflect bacteria experiencing severe stress and struggling to counteract meropenem-induced damage.

Together, these findings reveal the metabolic responses of the meropenem-resistant strain under MIC conditions. The results suggest a state of metabolic distress, where bacteria attempt to mitigate damage but may experience declining viability. These insights emphasise the complexity of metabolic responses under antibiotic exposure and could inform targeted therapeutic interventions aimed at disrupting these adaptive metabolic processes to combat resistance.

4.4.4 Functional analysis in meropenem-resistant *E. coli* under minimum inhibitory concentration conditions

Understanding how meropenem-resistant *E. coli* strains adapt their metabolic pathways when exposed to the MIC of meropenem is crucial for identifying metabolic vulnerabilities. This study aimed to evaluate pathway-level changes induced by meropenem exposure, providing insights into the biochemical strategies employed by the strain to mitigate antibiotic stress and maintain cellular homeostasis. Functional analysis was used to assess the enriched pathways and their biological relevance, revealing key metabolic adaptations.

Functional analysis was conducted using significantly altered metabolites identified between the vehicle control (R_0) and MIC-treated (R_16) conditions. The enrichment analysis applied pathway-level statistical evaluations, integrating metabolite abundance data with known biochemical networks to identify pathways significantly affected by meropenem exposure. Metrics such as pathway impact scores and adjusted p-values quantified the significance and biological importance of these pathways. A comprehensive table detailed the pathways impacted, along with the number of hits and statistical significance.

The functional analysis (**Figure 4.36**) revealed significant pathway-level changes induced by exposure to the MIC of meropenem (16 μg/mL). Key enriched pathways included purine metabolism, phenylalanine, tyrosine, and tryptophan biosynthesis, and biosynthesis of siderophore group nonribosomal peptides, and novobiocin biosynthesis. These pathways underscore the metabolic flexibility of the strain and highlight its ability to support critical cellular functions under stress.

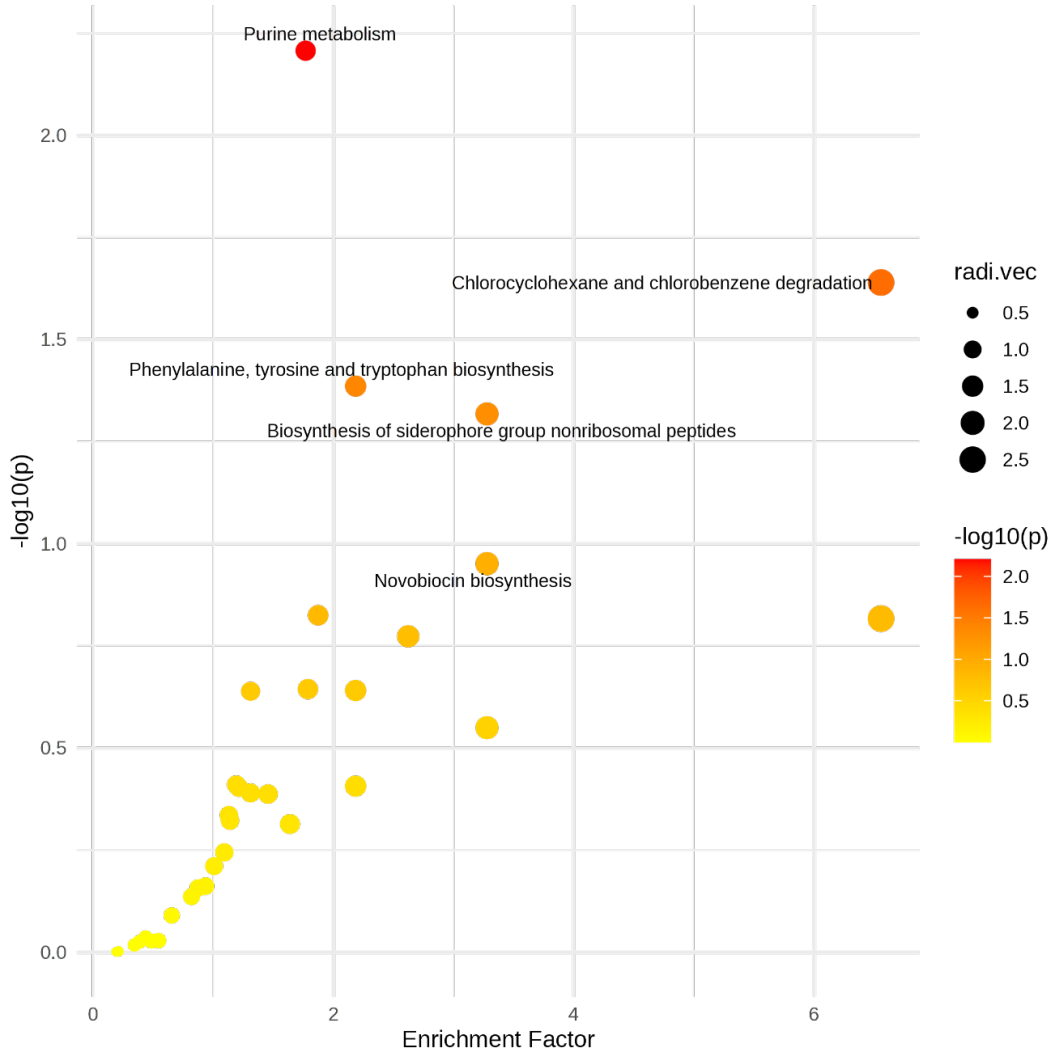

Pathway Name	Total↑↓	Hits(all)↑↓	Hits(sig.)↑↓	Expected↑↓	P(Fisher)↑↓	P(Gamma)↑↓
Purine metabolism	76	35	17	9.6075	0.0062082	0.0024275
Chlorocyclohexane and chlorobenzene degradation	11	3	3	0.305	0.022932	0.0025729
Phenylalanine, tyrosine and tryptophan biosynthesis	23	10	4	2.745	0.041139	0.0027416
Biosynthesis of siderophore group nonribosomal peptides	5	2	2	0.915	0.048113	0.0028093
Novobiocin biosynthesis	3	2	1	0.61	0.11189	0.0035169
Phosphonate and phosphinate metabolism	8	3	2	0.61	0.11189	0.0035169
Tyrosine metabolism	13	10	4	2.135	0.14968	0.0040234
Fluorobenzoate degradation	3	1	1	0.1525	0.1525	0.0040642
Benzoate degradation	15	4	3	0.7625	0.1685	0.004304
Dioxin degradation	7	4	3	0.7625	0.1685	0.004304
Aminobenzoate degradation	8	2	2	0.7625	0.1685	0.004304
C5-Branched dibasic and metabolism	8	7	5	1.6775	0.22694	0.0053169
Xylene degradation	7	4	3	0.915	0.22869	0.0053508
Pyrimidine metabolism	51	26	10	6.8625	0.22969	0.0053704
Fatty acid degradation	41	2	1	0.305	0.28207	0.0065093

Figure 4.36 Functional analysis of enriched pathways comparing R_0 (DMSO, vehicle control) and R_16 (16 µg/mL meropenem-treated) metabolic profiles. *The x-axis represents the pathway impact score, and the y-axis denotes -log10(p-value) of enrichment. Larger, redder points indicate pathways with higher significance and impact. The table below summarizes key pathways, including the number of hits, expected values, and statistical significance metrics.*

Purine metabolism, a key pathway in nucleotide biosynthesis, was significantly impacted. The enrichment aligns with the increased demand for nucleotides to support DNA repair and replication, which are essential for survival under stress conditions.[424] The activation of this pathway underscores the ability of the strain to prioritise fundamental cellular processes necessary for adaptation to antibiotic exposure.

The enrichment of the biosynthesis of siderophore group nonribosomal peptides suggests an adaptive strategy to scavenge iron, a vital resource under stress-induced environments.[425] Siderophores play a crucial role in iron acquisition, helping to mitigate the effects of oxidative stress and maintain cellular function. Such response highlights the importance of iron homeostasis as a key component of bacterial survival mechanisms under meropenem-induced stress.

Pathways involved in phenylalanine, tyrosine, and tryptophan biosynthesis also showed significant enrichment, indicating the need for aromatic amino acids.[426] These amino acids are essential for protein synthesis and may also support the production of secondary metabolite involved in stress responses.[427]

Interestingly, the activation of novobiocin biosynthesis and chlorocyclohexane and chlorobenzene degradation pathways suggests potential strategies for counteracting stress.[428] These pathways may contribute to the survival of the strain by supporting detoxification harmful by-products or mitigating oxidative stress generated during antibiotic exposure.[429]

The functional analysis highlighted the metabolic adaptability of the meropenem-resistant strain under MIC conditions. Enrichment in purine metabolism reflects the prioritisation of the strain such as nucleotide biosynthesis, critical for cellular repair and replication under stress. Similarly, the activation of siderophore biosynthesis demonstrates the importance of iron acquisition in mitigating oxidative stress and supporting cellular functions. The enhanced activity in aromatic amino acid biosynthesis pathways suggests their dual role in protein synthesis and stress adaptation.

Interestingly, the involvement of novobiocin biosynthesis and degradation pathways for chlorocyclohexane and chlorobenzene suggests additional stress-mitigating strategies, such as neutralising toxic by-products. These coordinated metabolic adaptations highlight the ability of the strain to reallocate resources efficiently, ensuring survival under meropenem-induced stress.

4.4.5 Summary

The metabolic response of the meropenem-resistant (R) *E. coli* strain to MIC-level meropenem exposure highlights the precision of NDM-7 mediated resistance. While substantial metabolic reprogramming was observed, these changes were targeted and efficient, underscoring the robustness of adaptive mechanisms of the R strain under antibiotic stress. The distinct clustering of treated and untreated samples indicates that meropenem at 16 μg/mL elicits a focused metabolic response to maintain cellular function under stress.

Functional analysis revealed that pathways such as purine metabolism and phenylalanine biosynthesis are critical for sustaining resistance, while suppressed basal activity in other pathways suggested a strategic reallocation of resource to essential functions. These findings contribute to our understanding of how carbapenemase-producing strains, such as those carrying NDM-7 gene, mitigate high antibiotic stress.

From a therapeutic perspective, the metabolic dependencies observed in the R strain at MIC may represent exploitable vulnerabilities. Pathways activated during antibiotic exposure, particularly those linked to detoxification, oxidative stress management and energy homeostasis, could serve as potential targets for disrupting resistance mechanisms. As summarised in **Table 4.3**, several metabolic pathways and their respective enzymes or proteins have been identified as promising targets for intervention. This study underscores the value of combining metabolic profiling with pathway-focused analyses to inform the development of novel intervention strategies for combating antibiotic resistance.

Table 4.3 Overview of potential metabolic and enzymatic targets for therapeutic intervention in bacterial systems. *The table highlights key pathways, target enzymes or proteins, possible inhibitors, and associated previous studies.*

Metabolic Pathway	Target Enzyme/Protein	Inhibitor	Study/reference
Glycolysis	Enolase	SF2312	[430]
Glycolysis	GAPDH and aerobic glycolysis	Dimethyl fumarate	[110]
Oxidative Stress Response	TrxR	Ebselen	[431]
Energy Metabolism	ATP Synthase	Bedaquiline	[99]
Lipid A Biosynthesis	LpxC	CHIR-090	[432]
Peptidoglycan Biosynthesis	MurA	Fosfomycin	[433]

In conclusion, the metabolic response of the resistant strain at MIC reflects a delicate balance between targeted pathway activation and metabolic efficiency. While these findings highlight the evolutionary success of NDM-7 mediated resistance, they also expose specific metabolic dependencies that could serve as potential targets for therapeutic intervention. This study underscores the importance of integrating metabolic profiling and functional pathway analyses to uncover actionable strategies for combating carbapenem-resistant pathogens.

4.5 Conclusion

This chapter investigated the metabolic responses of wild-type (E), meropenem-susceptible (S), and meropenem-resistant (R) *E. coli* strains under exposure, to sub-lethal meropenem concentrations (1 and 4 μg/mL) and explored the response of meropenem-resistant strain to the MIC concentration (16 μg/mL). Strains were grown until early exponential phase (OD_{600} = 0.4), and meropenem was added. An exposure duration of 1 hour was selected to allow sufficient time for measurable metabolic response, while minimising extensive cell death. These analyses illuminated the strain-specific adaptive strategies employed to mitigate antibiotic exposure.

At 4 μg/mL meropenem, the wild-type exhibited metabolic reprogramming, activating pathways such as nucleotide metabolism, oxidative stress management, and glycerophospholipid metabolism. Metabolites such as adenosine 2', 3'-cyclic phosphate and

glucosamine-6-phosphate were significantly altered, reflecting efforts to repair damaged cellular components and maintain homeostasis. These changes demonstrate the reliance of the strain on energetically expensive reprogramming to combat antibiotic exposure, despite lacking intrinsic resistance mechanisms.

The meropenem-susceptible strain also responded to 1 and 4 μg/mL meropenem. Key pathways, such as pyrimidine metabolism and peptidoglycan biosynthesis, were impacted, with significant downregulation of metabolites like cAMP and *N*-acetylaspartylglutamic acid. These findings highlight vulnerability of the strain under antibiotic exposure and its plasmid-related metabolic demands.

The meropenem-resistant strain exhibited minimal metabolic changes at 4 μg/mL meropenem, underscoring the effectiveness of NDM-7-mediated resistance in hydrolysing the antibiotic. Such metabolic stability reflects its ability to avoid widespread reprogramming and maintain core biosynthetic functions under moderate antibiotic concentration. However, exposure to MIC (16 μg/mL) imposed a more substantial metabolic burden, prompting targeted reprogramming to sustain resistance and cellular homeostasis.

At MIC, the resistant strain exhibited distinct clustering and pathway-level changes, indicating a focused but efficient metabolic response. Functional analysis revealed the alterations in purine metabolism, phenylalanine, tyrosine, and tryptophan biosynthesis, and siderophore biosynthesis, reflecting the strain's prioritization of nucleotide production, protein synthesis, and iron acquisition under high antibiotic pressure. Metabolites such as thymidine triphosphate, cytidine diphosphate, and 4-hydroxybutyric acid were upregulated, suggesting their roles in supporting oxidative stress management and alternative energy production. In contrast, the suppression of basal activities, such as those involving UDP-galactose, highlighted a strategic resource reallocation to essential survival processes.

These findings emphasize the metabolic efficiency and precision of the resistant strain under MIC exposure. While NDM-7-mediated resistance allows the strain to hydrolyse meropenem, the associated metabolic demands expose vulnerabilities, particularly in pathways linked to

oxidative stress management, nucleotide metabolism, and energy homeostasis. These vulnerabilities represent potential targets for therapeutic intervention to disrupt resistance mechanisms.

As shown in Chapter 3, no evidence of metabolite leakage was observed due to washing or centrifugation steps. However, the specific impact of meropenem on cell membrane integrity prior to PBS washing was not directly assessed. Thus, while the observed metabolic changes are consistent with intracellular adaptation, the possibility of limited leakage in response to antibiotic exposure cannot be entirely excluded.

In conclusion, this chapter revealed distinct metabolic strategies employed by *E. coli* strains in response to meropenem. The wild-type and susceptible strains engaged in extensive reprogramming to counteract sub-lethal antibiotic exposure, with substantial energetic costs. In contrast, the resistant strain maintained metabolic stability at sub-lethal concentrations but exhibited significant metabolic adjustments at MIC, reflecting its adaptive limits. By identifying specific pathways and metabolites involved in these responses, this study provides valuable insights into the metabolic dynamics underpinning antibiotic resistance and susceptibility, offering potential avenues for therapeutic interventions to combat carbapenem-resistant pathogens.

Chapter 5 Live cell analysis of bacterial metabolism: Challenges and opportunities for AMR studies

5.1 Introduction

Antibiotic resistance remains a major global health challenge, with new therapeutic approaches holding the potential to have a major impact on public health. All bacteria respond metabolically to xenobiotic exposures, irrespective of their antibiotic susceptibility, necessitating highlighting the need for deeper insights into the metabolic adaptations that enable bacteria to withstand antibiotic pressures.[46,58] Understanding bacterial metabolic responses therefore has the potential to identify vulnerabilities and possible new treatment targets in resistant pathogens or to enhance efficacy and longevity of antibiotic efficacy in non-resistant pathogens with novel therapeutic strategies.[154]

In Chapter 3 and 4 untargeted metabolomics revealed significant alterations in central carbon metabolism in resistant strains of *E. coli*, indicating a metabolic reprogramming linked to survival under antibiotic pressure [**Section 3.4.6** and **4.3.5**]. In order to investigate this further using orthogonal techniques, this chapter reports an investigation into attempts to measure energy metabolism and bioenergetic adaptations using a Seahorse XF metabolic analyser and independently a BacTiter-Glo™ ATP assay.[434,435] Together, these methodologies were evaluated as ways to report on *E. coli* metabolism and its adaptations, from the perspective of energy metabolism under antibiotic stress, that would offer insights into energy production pathways in resistant and non-resistant strains.[344] As almost all published methods using Seahorse technologies have used mammalian cells, the aim was to establish a proof of principle for its application to bacterial cultures. This chapter aims to contribute to advancing methodological approaches for studying bacterial bioenergetics and provides a foundation for incorporating these into future investigations to understand the metabolic basis of antibiotic resistance.

5.2 Seahorse real time cell metabolic analysis

The Seahorse XF Analyser measures oxygen consumption rate (OCR) and extracellular acidification rate (ECAR), providing real-time analysis of oxidative and glycolytic metabolism

in live cells.[436,437] The technique was originally developed for mammalian systems, where glycolysis and mitochondrial oxidative phosphorylation (OXPHOS) are the primary ATP-producing pathways.[438] However, prior studies have indicated that key bioenergetic pathways targeted by Seahorse inhibitors, such as ATP synthase and the electron transport chain (ETC), are conserved between mitochondria and bacterial plasma membranes.[439-441] Given that bacterial ETC components share structural and functional similarities with their eukaryotic counterparts, particularly in oxidative phosphorylation, it was decided to investigate whether Seahorse experiments could provide insights into bacterial metabolism as well.[442] This study explored the feasibility of repurposing Seahorse technology for prokaryotic systems, focussing on *Escherichia coli* to investigate bioenergetic processes and bacterial metabolism with high temporal resolution.

Despite similarities mentioned, some metabolic pathways of *E. coli* differ fundamentally from those of eukaryotic cells, presenting potentially unique challenges when applying Seahorse technology for bacterial studies.[443] Unlike mammalian cells, which rely on mitochondrial oxidative phosphorylation, *E. coli* performs oxidative metabolism via a cytoplasmic ETC embedded in the inner membrane of the bacterial cell wall.[444,445] The bacterial ETC functions analogously to mitochondrial OXPHOS, coupling the TCA cycle with ATP production via oxidative processes. [446] OCR measurements in *E. coli* therefore should reflect ETC activity, while ECAR should capture proton export and metabolic by-products.[447] The application of Seahorse experiments to *E. coli* also required consideration of the pharmacological interventions used in the various mammalian seahorse experiments. Stressor drugs are commonly used in Seahorse application on mammalian systems to challenge energy production processes. Examples include oligomycin (a complex V inhibitor), carbonyl cyanide 4-(trifluoromethoxy) phenylhydrazone (FCCP, which depolarises the mitochondrial membrane) and rotenone (an ETC inhibitor).[448,449] Although bacteria lack mitochondria, they do possess a similar energy production process mediated via electron transport chain embedded in the bacterial cell

membrane. Additionally, *E. coli* exhibits metabolic flexibility, including glycolysis, oxidative phosphorylation, and fermentation under different environmental conditions.[443,450,451]

The primary aim of employing Seahorse analysis was to assess its suitability for measuring differences in bacterial energy metabolism. Seahorse experiments rely on two fundamental measurements OCR and ECAR so the first experimental aim was to determine whether these measurements could be reliably made with bacteria. Second, whether application of the same pharmacological agents to stress energy metabolism in mammalian systems, could be used with *E. coli*. The overall aim was to see whether reproducible differences in energy metabolism could be identified between meropenem-susceptible and meropenem-resistant *E. coli* strains using Seahorse measurments.[45] By comparing their glycolytic and oxidative profiles under antibiotic exposure, metabolic adaptations associated with resistance and its impact on live cell metabolism could be investigated with and without antibiotic pressure. Seahorse analysis provides a novel platform for bacterial studies, offering real-time metabolic measurements that traditional endpoint assays cannot achieve.[452]

5.2.1 Baseline analysis: application of Seahorse XFe24 analyser using a mammalian cell line

Initially the Seahorse XF Analyzer was used to analyse mammalian LN18 glioblastoma cells in order to validate functionality of the assay in a system aligned with its original design for eukaryotic metabolism. The experiment was undertaken to demonstrate the performance of the Seahorse Glycolysis Rate Assay in measuring glycolytic and oxidative metabolic pathways under well-established conditions and provide a benchmark for comparing subsequent results from bacterial studies.

5.2.1.1 Normalisation of Seahorse assay data using Hoechst dye fluorescence curve

To ensure accurate normalization, a Hoechst dye fluorescence curve was generated for LN18 cells. Cells were seeded at an initial density of 1.5×10^5 cells per well, followed by serial dilutions halving the concentration down to 9.38×10^3 cells per well, with a well with no cells serving as the control. After 48 hours of incubation to allow cell attachment and growth, Hoechst dye was

added.[210] Fluorescence intensity was measured using a BMG CLARIOstar PLUS microplate reader, with the excitation and emission wavelengths set to 355 nm and 455 nm, respectively (**Table 5.1**). Measurements were taken as endpoint readings, with an automatic gain and focus adjustment and plotted against cell density to generate a standard curve (**Figure 5.1**). Data within the linear range were used to derive an equation correlating fluorescence with cell number, which was subsequently used to normalize Seahorse assay data (**Figure 5.2**).

Table 5.1 CLARIOstar microplate reader setting for Hoechst dye fluorescence measurement used for DNA normalisation of Seahorse assay data.

Read mode		Endpoint – top read
Monochromator settings	Excitation	355 nm (bandwidth 20 nm)
	Emission	455 nm (bandwidth 30 nm)
Gain and focus		auto
Number of flashes		2
Matrix scan		15 × 15 (3 mm)

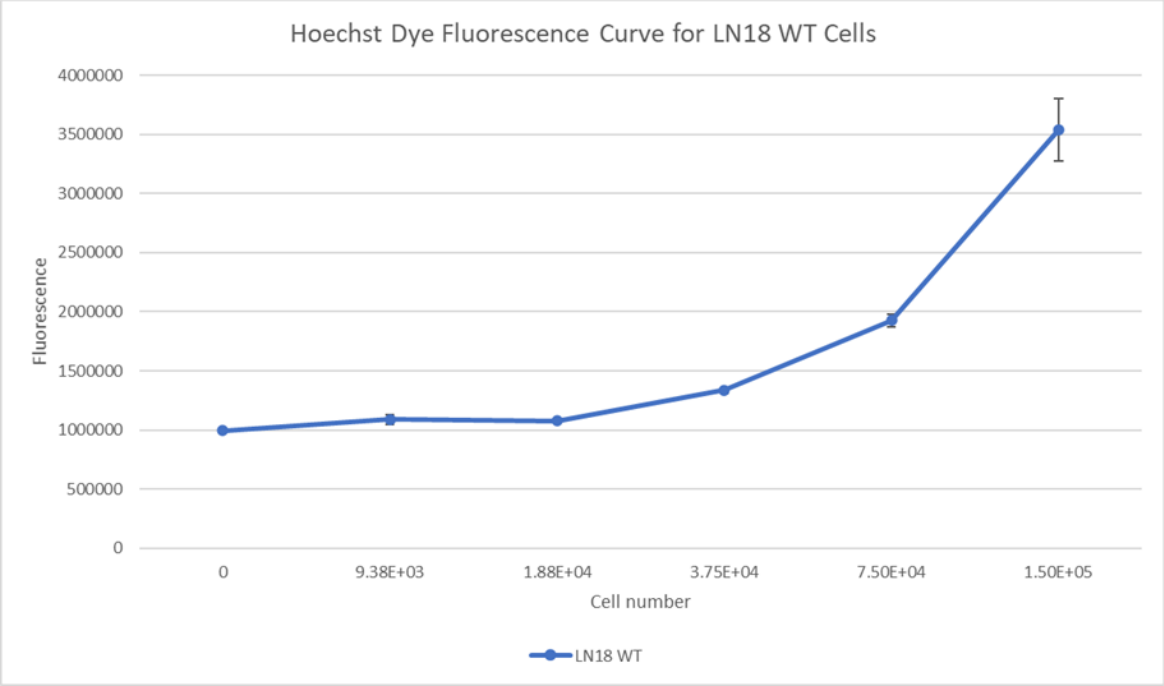

Figure 5.1 Hoechst dye fluorescence curve for LN18 wild-type mammalian cells at varying seeding densities. *Fluorescence intensity of Hoechst dye in LN18 wild-type mammalian cells plated at initial density of 5 × 10^4 cells and serially diluted by half to a minimum of 9.38 × 10^3 cells, including an empty well as a control (final dye concentration: 30 mM). The assay was performed in duplicate (n = 2), and error bars represent standard deviations.*

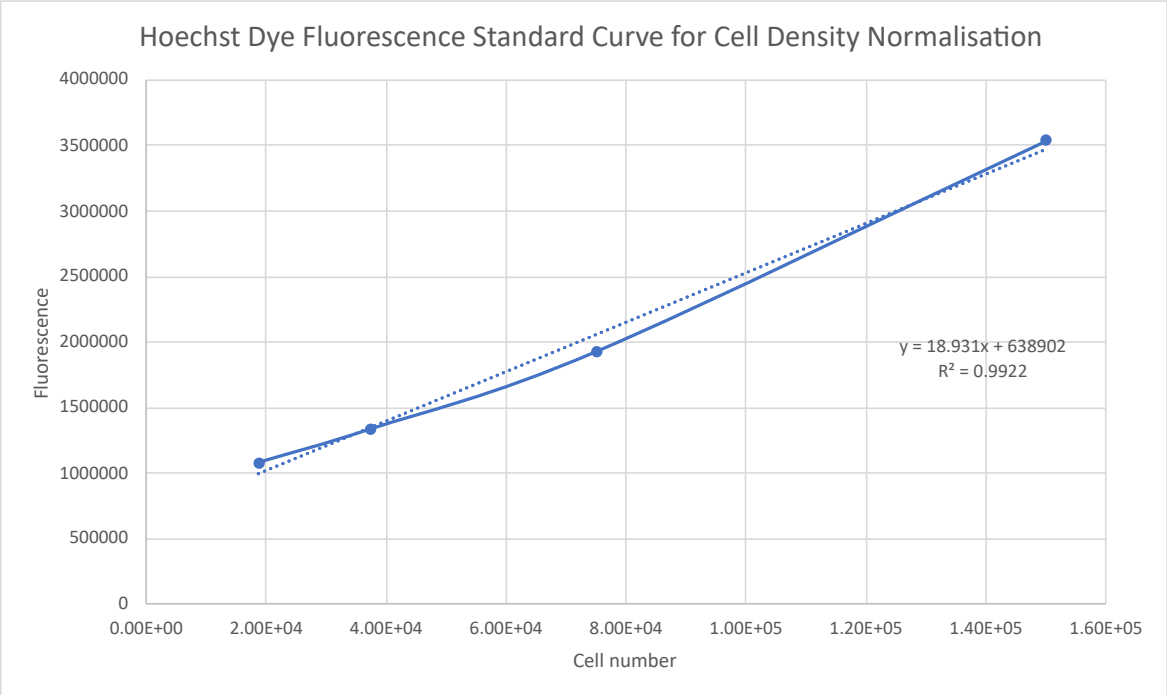

Figure 5.2 Hoechst Dye Fluorescence Standard Curve for Cell Density Normalization. *The linear range of Hoechst dye fluorescence intensity was plotted against the estimated cell number per well for LN18 wild-type mammalian cells. The initial seeding densities were halved serially, and the cell numbers were assumed to double after 48 hours. The equation derived from the standard curve (y = 18.931x + 638902, R^2 = 0.9922) was used to normalize Seahorse assay data based on cell density. Error bars represent standard deviations from duplicate measurements (n = 2).*

5.2.1.2 Validation of Seahorse glycolysis rate assay in LN18 mammalian cells

The Seahorse Glycolysis Rate Assay is designed to measure the glycolytic activity of live cells by quantifying the proton efflux rate (PER), a parameter reflecting extracellular acidification primarily driven by lactate production during glycolysis.[453] The assay uses sequential injections of metabolic inhibitors to distinguish glycolytic and non-glycolytic contributions to PER. Injection of rotenone and antimycin A (Rot/AA) inhibits mitochondrial oxidative phosphorylation, forcing cells to rely on glycolysis for ATP production, which is accompanied by an increase in PER. Subsequent injection of 2-deoxy-D-glucose (2-DG), a glucose analogue that inhibits glycolysis, substantially reduces PER, confirming the glycolytic contribution to extracellular acidification.[436]

For the Seahorse Glycolysis Rate Assay, LN18 glioblastoma wild-type (WT) and isocitrate dehydrogenase 1 (IDH1) R132H mutant (Mut) cells were seeded at 2.5×10^4 cells per well and allowed to attach and grow for 48 hours. The IDH1 R132H mutation is a gain-of-function alteration that leads to the production of the oncometabolite D-2-hydroxyglutarate (D-2HG). The mutant cell line was selected to assess its impact on glycolytic flux, as IDH1 mutations are known to alter metabolic pathways, potentially influencing glycolytic rates. [210] The assay results are summarised in **Figure 5.3**, demonstrating that injection of Rot/AA increased PER, reflecting a metabolic shift to glycolysis upon inhibition of oxidative phosphorylation. A subsequent decrease in PER after 2-DG injection confirmed the glycolytic contribution to proton efflux.

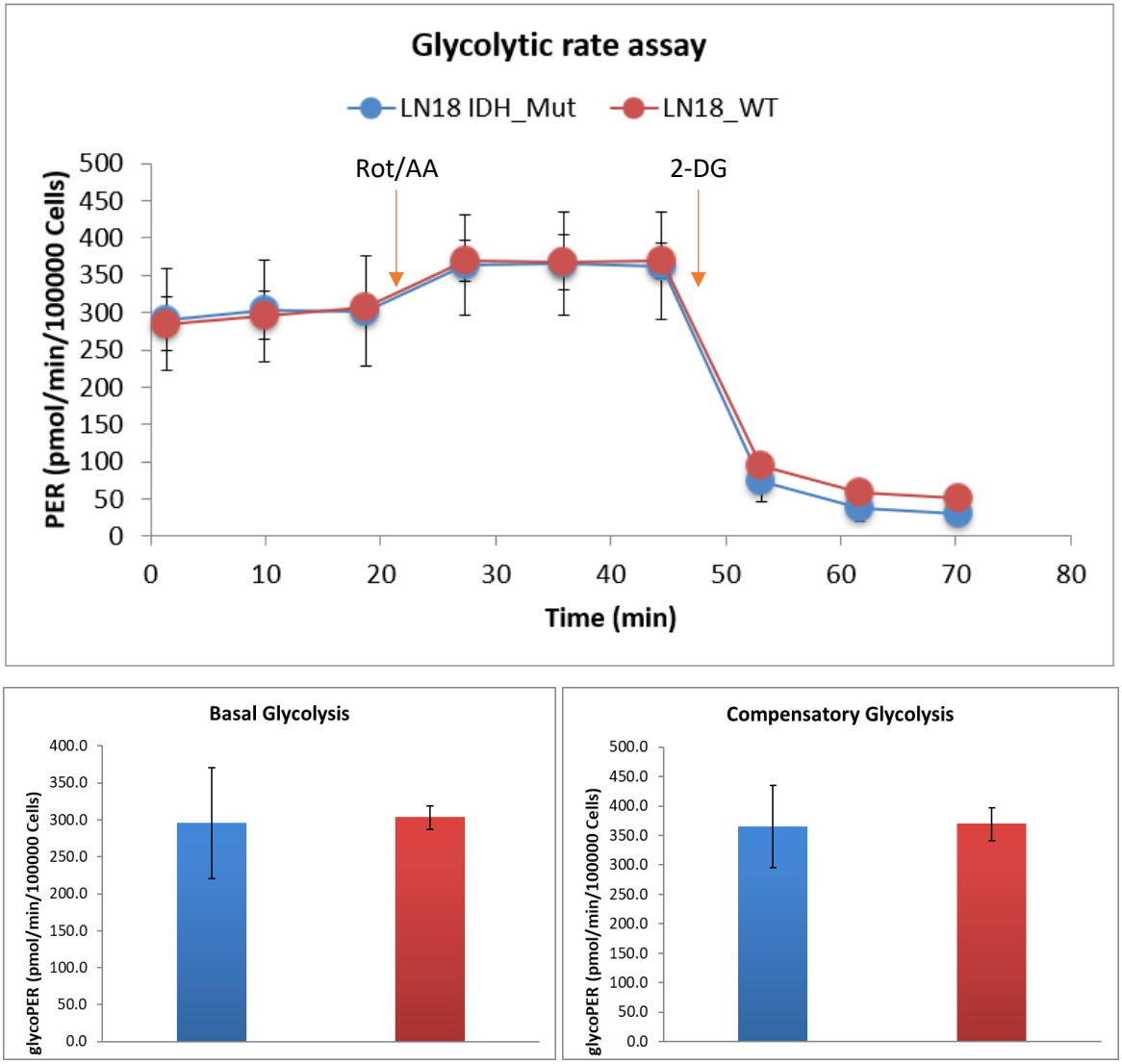

Figure 5.3 PER and Glycolysis Rates in LN18 Wild-Type (WT) and Mutant (Mut) Mammalian Cells*. The upper panel shows the Proton Efflux Rate (PER) measured over time for WT and Mutant cells, normalized to cell density (per 100,000 cells). Basal PER was recorded initially, followed by the injection of Rotenone/Antimycin A (Rot/AA) at 20 minutes to inhibit oxidative phosphorylation, causing an increase in PER. At 47 minutes, 2-Deoxy-D-Glucose (2-DG) was injected to inhibit glycolysis, resulting in a sharp decline in PER. The lower panels compare basal glycolysis (left) and compensatory glycolysis (right) rates between WT and Mutant cells, normalized per 100,000 cells. Error bars represent standard deviations from biological replicates (n = 5).*

No significant differences were observed between WT LN18 cells and IDH mutant cells under basal or stressed conditions. Given that IDH1 mutations typically lead to altered metabolic flux, including increased D-2HG production and potential shifts in glycolysis and oxidative metabolism, the lack of observed differences was unexpected.[454,455] However, it was subsequently suspected that the overexpression of the mutant IDH enzyme has been lost in the mutant cells (which had been introduced by lentiviral vector and cell passaged a number of times previously) and was subsequently demonstrated by other researchers in the group using

the same cell line. The observation likely explains the strong similarity between the mutant and wild-type results from the Seahorse assay as the cells were otherwise isogenic.

Irrespective of the lack of difference between the mutant and wild-type cells, the results confirmed that the Seahorse XF Glycolysis Rate Assay functions as intended in mammalian cell lines, yielding reliable data on glycolytic and oxidative metabolic pathways.

5.2.1.3 Conclusion

The Seahorse XF Analyzer demonstrated robust functionality in LN18 mammalian cells, producing reliable and reproducible results consistent with known metabolic responses. The Hoechst dye fluorescence curve provided a reliable normalization method by correlating fluorescence intensity to cell density. Cells were only counted at the time of plating, the use of a standard curve enabled a more accurate estimation of cell numbers at the time of the assay, accounting for variability in cell doubling over the 48-hour incubation period. Therefore, Hoechst dye normalisation helps minimise artifacts in cell counting, thereby improving the accuracy of normalising metabolic data relative to cell density.

The Glycolysis Rate Assay produced results consistent with expectations. The increase in PER following Rot/AA injection highlighted the metabolic shift toward glycolysis upon inhibition of oxidative phosphorylation. The subsequent decrease in PER after 2-DG injection confirmed the specificity of glycolysis as the primary contributor to proton efflux. These findings validated sensitivity of the assay to glycolytic and oxidative ATP production and highlight its reliability in detecting metabolic shifts. By confirming the efficacy of Seahorse XF Analyzer in eukaryotic systems, these results provide a benchmark for evaluating its application to bacterial models.

5.2.2 Investigating Seahorse analysis of bacterial systems

5.2.2.1 Cell adhesion optimisation

During initial experiments using the Seahorse XFe24 Extracellular Flux Analyser, it became apparent that bacterial cells, such as *E coli*, did not adhere effectively to the uncoated microplate surface. Despite centrifugation to settle cells onto the plate, substantial cell detachment occurred, particularly during the mixing step of the assay. Such detachment

subsequently disrupted OCR and ECAR measurements, and introduced substantial variability between replicates.

To address this issue, microplate wells were coated with poly-L-lysine (PLL), a positively charged polymer known to enhance bacterial adherence by interacting with the negatively charged surface of *E. coli* cells.[456] Studies have demonstrated the utility of PLL coating to ensure consistent cell attachment, minimised detachment during OCR and ECAR measurements, and reduced variability between replicates.[457,458] However, the metabolic consequences of using PLL on bacterial cells to enhance adhesion to plates are not known. Further investigation would be warranted (albeit complicated) to ensure that the coating does not introduce artifacts into bioenergetic measurements; such analysis was beyond the scope of the current study and it was assumed this was not a major issue for the experiments reported in this chapter.

5.2.2.2 Oxygen consumption rate and extracellular acidification rate measurement

Baseline measurements of OCR and ECAR were performed to assess the reproducibility of metabolic activity data in *E. coli* using the Seahorse XF Analyser. Biological replicates (R_1 and R_2) were used, with each condition measured in five replicates to capture variability. Measurements were recorded over three consecutive measurement cycles.

The OCR values, as illustrated in **Figure 5.4**, showed consistent OCR across biological replicates, with technical variability remaining low as indicated by the error bars (approximately 10% error), providing confidence in the ability of the Seahorse platform to reliably monitor oxidative metabolic activity under unstimulated conditions. Similarly, ECAR measurements exhibited reproducible acidification rates across the biological replicates. The trends observed across all three measurements were consistent, with low variability within technical replicates, confirming the robustness of ECAR data acquisition.

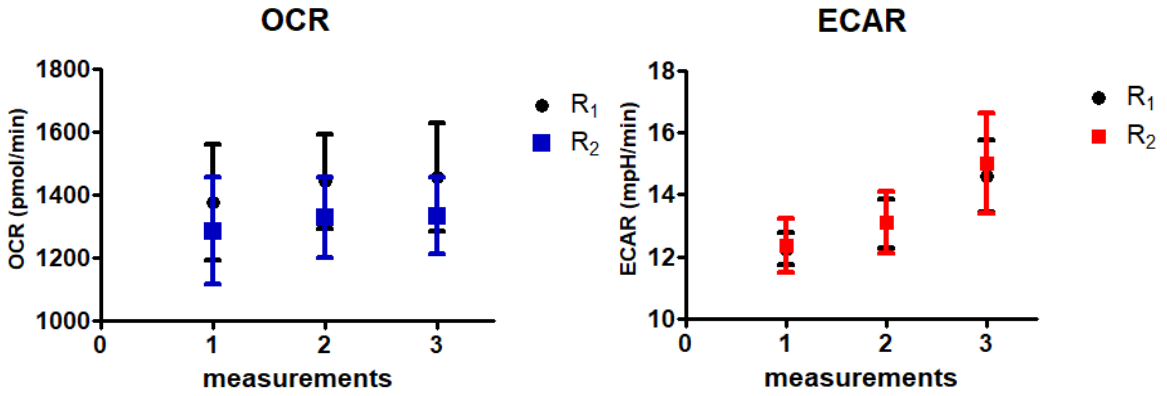

Figure 5.4 OCR and ECAR measurements for* E. coli *using the Seahorse XF Analyzer. *OCR and ECAR were measured across three consecutive cycles for two biological replicates (R1 and R2). Error bars represent variability from five technical replicates per condition. (Left) OCR values for biological replicates R1 (black circles) and R2 (blue squares) remained consistent across measurement cycles, with approximately 10% variability between technical replicates. (Right) ECAR values for biological replicates R1 (black circles) and R2 (red squares) showed reproducible trends, with minimal variation observed between technical replicates.*

The reproducibility of these OCR and ECAR measurements highlighted the reliability of the Seahorse XF Analyser for capturing fundamental metabolic activity in *E. coli*. The consistency across biological and technical replicates demonstrated robustness of the system for application to study dynamic bioenergetic responses in bacterial cells.

5.2.2.3 Cell seeding density optimisation

Achieving an appropriate cell density would ensure that metabolic activity measurements reflected genuine biological phenomena without technical interference. An experiment was conducted using *E. coli* strains plated at varying optical densities (OD_{600} 0.01, 0.05, 0.1, 0.2 and 0.4). For each OD_{600}, cells were seeded in wells with 500 µL of Seahorse assay medium. Measurements of OCR and ECAR were captured using the Seahorse XFe24 Analyser. Measurements were conducted in cycles with the following parameters: a mixing phase for 3 minutes, a waiting phase for 2 minutes, and a measurement phase of 3 minutes. The cycle was repeated eight times to monitor metabolic activity over time.

The results were analysed to evaluate whether metabolic activity remained within the recommended dynamic range, with basal OCR expected between 50-400 pmol/min and ECAR between 20-120 mpH/min.[459] Densities leading to hypoxia reflected by low oxygen levels below 35 mmHg were flagged as unsuitable.

Figure 5.5 illustrates the OCR measurements for meropenem-susceptible (S) and meropenem-resistant (R) *E. coli* strains seeded at varying densities. At OD_{600} of 0.01, the S strain (dark blue) exhibited minimal changes in oxygen consumption throughout the assay, suggesting that this density might have been too dilute to generate a detectable metabolic response. In contrast, the R strain (light blue) showed fluctuations in OCR but remained well within the acceptable range, indicating metabolic activity at this density. At OD_{600} 0.05, represented by green (S) and pink (R), OCR values began within the acceptable dynamic range. However, pronounced fluctuations were observed during the mixing phases, potentially due to localized oxygen depletion or uneven oxygen distribution or detachment of some cells. While O_2 level recovered partially after each mix, the variability among replicates suggested inconsistent oxygen availability. Despite this, OD_{600} 0.05 maintained an oxygen level above the hypoxia threshold on average, indicating its potential suitability for Seahorse analysis. At OD_{600} 0.1, represented by purple (S) and light green (R), O_2 values dropped below the hypoxia threshold of 35 mmHg immediately after the first measurement. The rapid decline in oxygen availability indicated this density led to substantial oxygen depletion as cells consumed oxygen faster than it could diffuse into the medium. For higher densities (OD_{600} 0.2 – yellow for S and brown for R, and 0.4 – red for S and magenta R), OCR values fell below the hypoxia threshold early in the assay, making them unsuitable for Seahorse analysis.

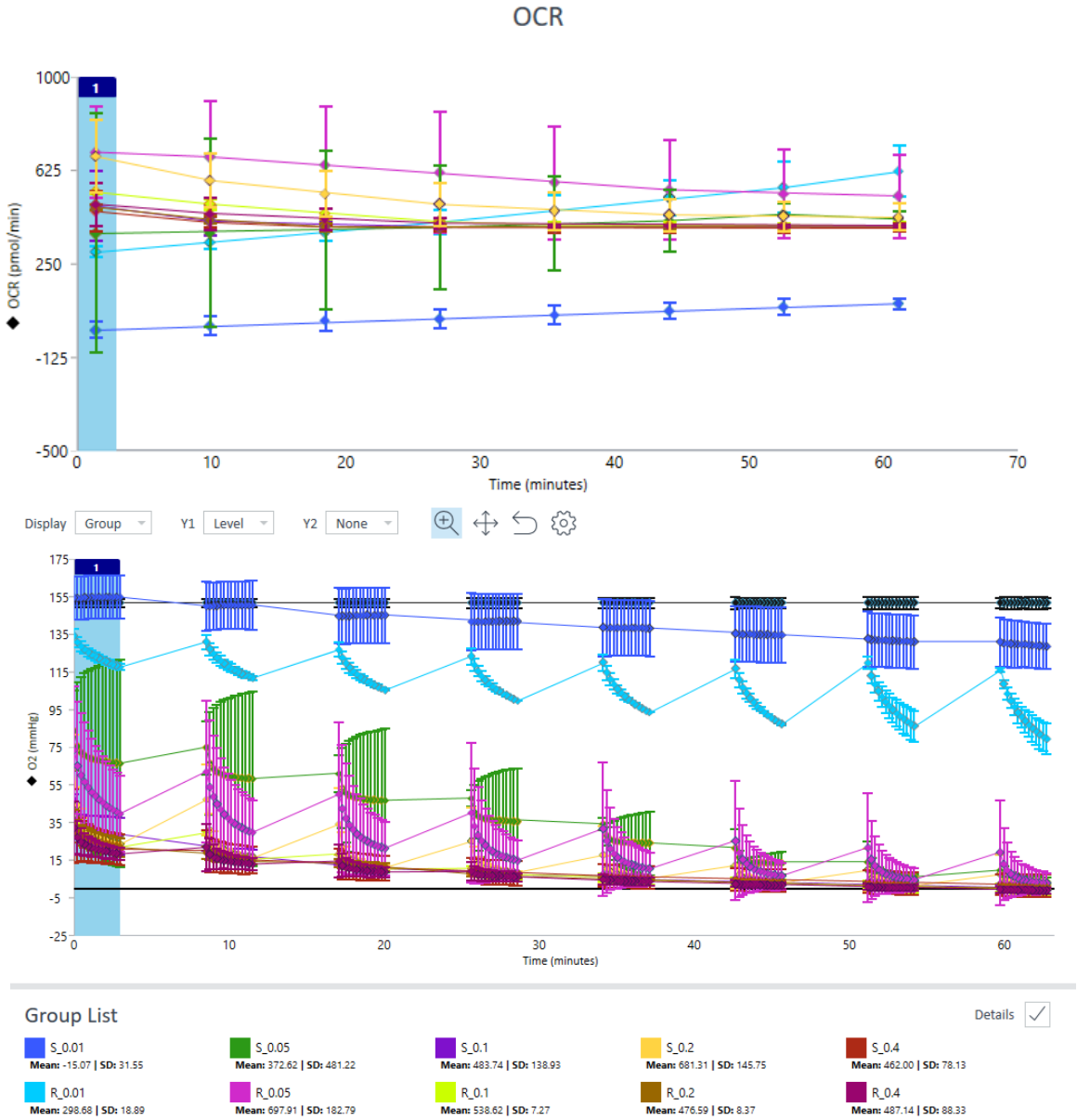

Figure 5.5 OCR measurements for meropenem-susceptible (S) and meropenem-resistant (R)* E. coli *strains seeded at varying optical densities (OD_{600} 0.01, 0.05, 0.1, 0.2, and 0.4). *The top panel shows the oxygen consumption rate (OCR) over time for S and R strains seeded at different optical densities (OD_{600} 0.01, 0.05, 0.1, 0.2, and 0.4). The bottom panel represents the oxygen level time course, illustrating dynamic changes in O_2 levels throughout the assay. Dark blue and light blue indicate S and R strains at OD_{600} 0.01, green and pink at OD_{600} 0.05, purple and light green at OD_{600} 0.1, yellow and brown at OD_{600} 0.2, and red and magenta at OD_{600} 0.4. Error bars represent standard deviation from biological replicates of n=2.*

The results demonstrated that cell seeding density played a critical role in ensuring reliable and interpretable OCR measurements. At OD_{600} 0.01, the minimal change in OCR observed for the *S* strain suggested that this density was too low to generate a detectable metabolic response, potentially due to insufficient cellular respiration. In contrast, the *R* strain at OD_{600} 0.01 showed OCR fluctuations within the acceptable range, highlighting metabolic activity despite the low

density. These differences between the strains may reflect successful cell seeding, or inherent variations in metabolic activity or oxygen consumption rates under low-density conditions.

At OD_{600} 0.05, while the OCR values remained within the dynamic range of the Seahorse instrument, the transient dips during the mixing phases indicated localized oxygen depletion or uneven oxygen distribution. These disruptions could have arisen due to the rapid oxygen consumption by cells, coupled with the limitations of oxygen diffusion within the medium, or mechanical effects introduced during mixing. However, the overall performance of OD_{600} 0.05 supported its suitability as a seeding density for Seahorse assays, provided that variability during mixing is carefully considered.

Densities at OD_{600} 0.1, 0.2, and 0.4 resulted in O_2 concentration values falling below the hypoxia threshold early in the assay, particularly for the higher densities reflecting substantial oxygen depletion. The hypoxic conditions and increased variability in OCR across replicates at these densities highlighted the challenges of using higher cell densities for Seahorse analysis, as they may compromise the reliability and consistency of metabolic measurements.

5.2.2.3.1 Discussion

The findings emphasize the importance of selecting an appropriate cell seeding density to ensure reliable and interpretable results in Seahorse assays. Low densities, such as OD_{600} 0.01, were insufficient to produce detectable metabolic activity for the S strain, likely because the total respiration signal was near or below the limit of detection of instrument. Additionally, low cell density could render cells more susceptible to errors during preparation and handling, further contributing to variability. In contrast, the R strain maintained metabolic activity even at low density, possibly reflecting differences in strain-specific respiration rates or metabolic flexibility. These strain-specific differences, could provide insights into the physiological mechanisms underlying antibiotic resistance.

OD_{600} 0.05 emerged as a suitable seeding density for Seahorse analysis of *E. coli* strains under the tested conditions, as it maintained OCR values within the dynamic range while avoiding

hypoxic conditions. Based on this initial results, additional densities closer to OD 0.05 were subsequently investigated to further optimise assay reproducibility and sensitivity.

5.2.3 XF Cell energy phenotype test

The XF Cell Energy Phenotype Test was applied next to assess its capability for characterizing the bioenergetic profile of meropenem-susceptible (S) and meropenem-resistant (R) *E. coli* strains. The assay measures OCR and ECAR, providing insights into oxidative and glycolytic metabolism, respectively. By assessing basal and stressed metabolic activities, it categorises metabolic phenotypes into aerobic, glycolytic, energetic, or quiescent states, enabling a visual representation of cellular energy utilisation through energy maps. The maps provide a framework to compare metabolic states across conditions, illustrating how cells shift their energy production strategies in response to stress.

The assay was applied to bacterial cells, which lack mitochondria but instead rely on a highly efficient ETC embedded in the plasma membrane.[460,461] The test involved injections of oligomycin, an ATP synthase inhibitor, and FCCP, a protonophore that uncouples oxidative phosphorylation by uncoupling the ETC from ATP synthesis. Although these pharmacological compounds were originally designed for eukaryotic systems, their use in bacterial cells was based on their potential to target conserved components of oxidative metabolism, such as the ETC. Following oligomycin injection, OCR is expected to decrease as ATP-linked respiration is inhibited, reducing oxygen consumption associated with oxidative phosphorylation. In contrast, ECAR may increase due to a compensatory shift towards glycolysis-driven acidification. After FCCP injection, OCR is expected to increase, as the uncoupling effect maximises electron flow through the ETC, driving oxygen consumption to its maximal respiratory capacity. ECAR may also increase as metabolic demand rises under stressed conditions. The experiment aimed to determine ATP-linked respiration, maximal respiratory capacity, and bioenergetic reserve, shedding light on the metabolic flexibility of the strains under basal and stressed conditions.

Next a FCCP titration was performed at concentrations of 0.25 µM, 0.5 µM, 1.0 µM, and 2.0 µM. Basal OCR and ECAR were recorded initially, followed by oligomycin (1 µM) with FCCP to drive maximal respiration, allowing assessment of respiratory reserve capacity. These steps were designed to identify the FCCP concentration that elicited maximal OCR while minimizing variability across replicates.

All experiments were conducted in five replicates and the results were analysed using Wave software. The OCR and ECAR profiles were used to categorize the metabolic states of the strains and evaluate differences in bioenergetic flexibility between susceptible and resistant *E. coli* under basal and stressed conditions.

5.2.3.1 Cell seeding density for XF Cell energy phenotype test

To evaluate the impact of cell seeding density on OCR and ECAR measurements, meropenem-susceptible (S) and meropenem-resistant (R) *E. coli* strains were plated at OD_{600} of 0.01, 0.02, 0.04, and 0.08. While OD_{600} 0.05 was identified in earlier experiments as a reasonable baseline for Seahorse use, this test explored a broader range of densities to refine conditions for future experiments and ensure robust metabolic measurements.

Basal OCR and ECAR were recorded to establish baseline oxidative and acidification activity before introducing pharmacological stressors (oligomycin and FCCP). Oligomycin (1 µM final concentration) was injected to inhibit ATP synthesis, providing a measure of basal non-ATP-linked respiration and FCCP (1 µM final concentration) was added to uncouple the ETC, driving maximal electron transport activity and oxygen consumption. The data collected included time-resolved OCR and ECAR measurements, energy maps categorising metabolic states, and bioenergetic parameters analysed using the Seahorse XF Cell Energy Phenotype Test Report Generator.

Figure 5.6 displays the OCR and ECAR, and energy phenotype profiles of the S strain seeded at a range of seeding densities. The OCR trends showed that cells seeded at OD_{600} 0.01 exhibited minimal signal in oxygen consumption throughout the assay, suggesting insufficient cell density to generate detectable metabolic activity. At OD_{600} 0.02, oxygen consumption increased

steadily following the addition of oligomycin and FCCP, reflecting a measurable metabolic response, with oxygen levels remaining within the acceptable range (> 35 mmHg) throughout the assay. Cells seeded at OD_{600} 0.04 demonstrated the highest OCR and ECAR values, however, the O_2 level dipped below 35 mmHg during mixing phases after 40 min indicated localised oxygen depletion. At OD_{600} 0.08, OCR plateaued after the first measurement, likely indicating oxygen depletion due to high cell density, while ECAR values disproportionately increased, possibly reflecting a compensatory metabolic shift. The energy phenotype map generated from Seahorse XF Cell Energy Phenotype Test Report confirmed that OD_{600} 0.02 provided consistent OCR and ECAR profiles, with minimal variability across replicates. The energy map highlighted metabolic flexibility at this density, with cells transitioning from a quiescent towards an energetic state upon FCCP injection. OD_{600} 0.01 and 0.08 were deemed unsuitable due to insufficient metabolic signals and hypoxia, respectively.

These findings build on earlier results and support OD_{600} 0.02 as the most reliable seeding density of *E. coli* for Seahorse assays. While OD_{600} 0.05 was previously identified as a strong candidate, these results highlight how slight adjustments in density can influence metabolic responses, guiding protocol optimisation based on assay requirements and bacterial physiology.

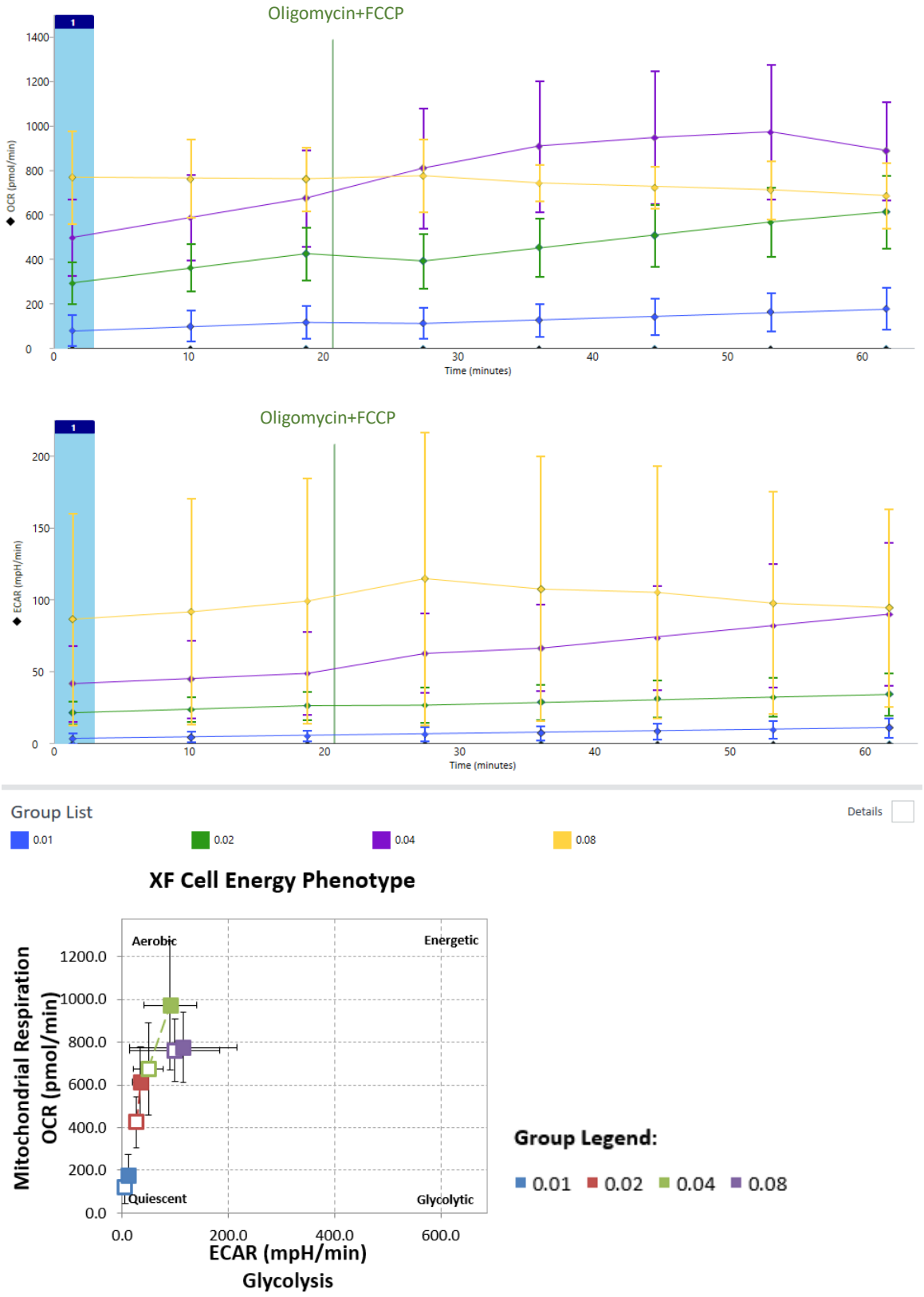

Figure 5.6 OCR and ECAR profiles of the meropenem-susceptible (S)* E. coli *strain seeded at varying seeding densities (OD 0.01, 0.02, 0.04, and 0.08). *The OCR (top) and ECAR (middle) graphs depict trends in oxygen consumption and media acidification rates overtime, respectively, while the XF Cell energy phenotype energy map (bottom) categorizes metabolic states at different seeding densities. Error bars representing standard deviations from five replicates.*

The OCR, ECAR, cell energy phenotype profiles for the R strain are shown in **Figure 5.7**. At OD_{600} 0.01, the R strain displayed a fluctuating OCR pattern but remained within the acceptable range, demonstrating sufficient metabolic activity even at low cell density. At OD_{600} 0.02 OCR increased consistently after the injection of oligomycin and FCCP, maintaining robust metabolic activity. At 0.04, OCR and ECAR values were the highest among the tested densities. However, oxygen levels fell below 35 mmHg during mixing phase after 30 min, and after 50 min did not fully recovery above the threshold even during the measurement phase. Cells seeded at OD_{600} 0.08 showed signs of oxygen depletion, with OCR plateauing and ECAR increasing disproportionately, reflecting potential metabolic shifts due to hypoxic conditions. The Seahorse XF Cell Energy Phenotype Test Report for the R strain supported OD_{600} 0.02 as the most reliable density based on the balance between metabolic activity (measured by OCR and ECAR) and oxygen availability (oxygen level). The energy map at 0.02 showed metabolic flexibility, with cells transitioning from a quiescent towards an energetic state upon FCCP injection. Although OD_{600} 0.04 demonstrated higher OCR and ECAR values, oxygen depletion during prolonged measurements raised concerns about reproducibility. OD_{600} 0.08 exhibited severe oxygen depletion, while OD_{600} 0.01 produced inconsistent metabolic signals.

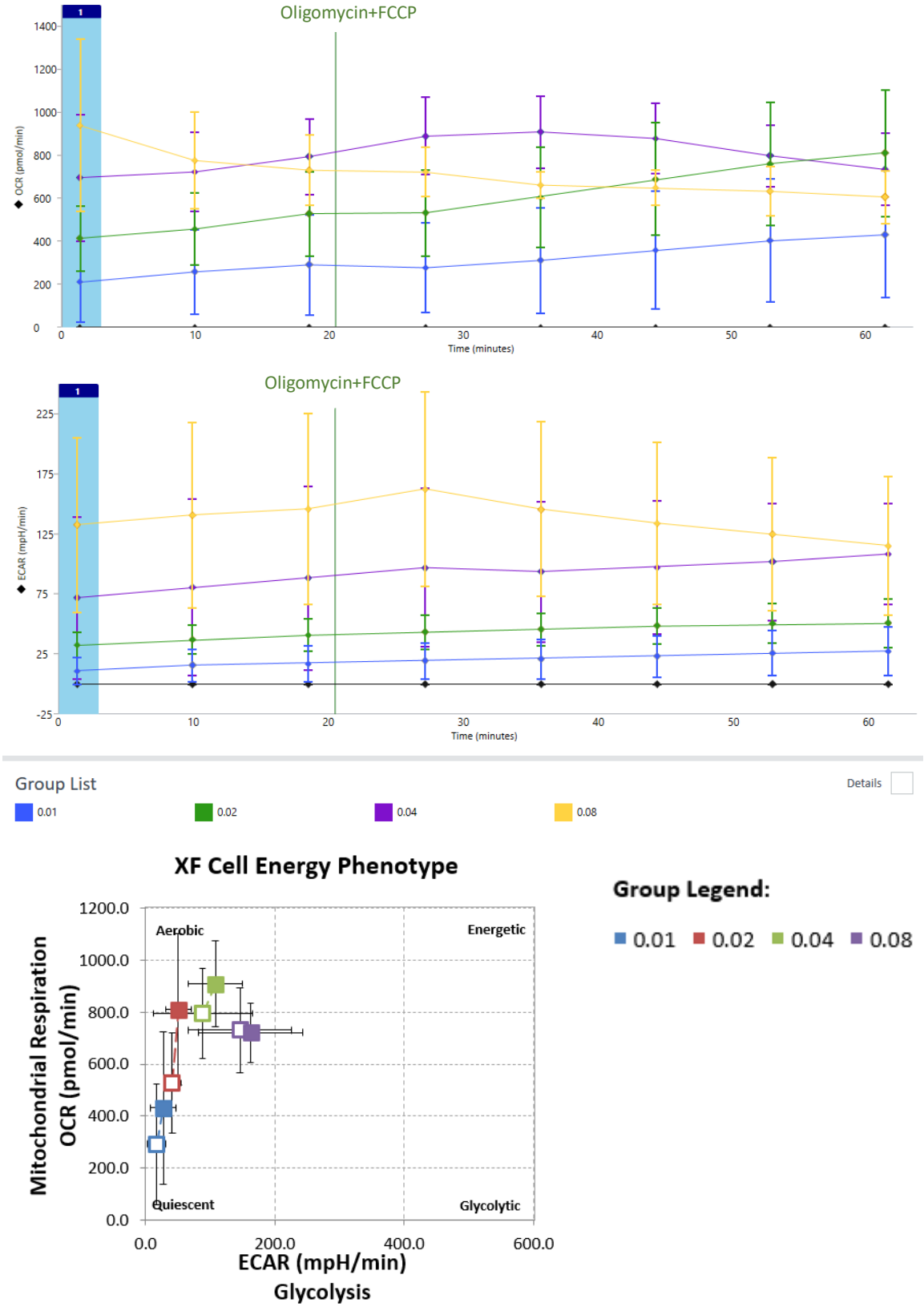

Figure 5.7 OCR and ECAR profiles of the meropenem-resistant (R)* E. coli *strain seeded at varying densities (OD 0.01, 0.02, 0.04, and 0.08). *The OCR (top left) and ECAR (bottom left) graphs illustrate trends in oxygen consumption and acidification rates during the assay. The energy map (top right) categorizes metabolic states. Data were collected using the Seahorse XFe24 Analyzer, with error bars representing standard deviations from five replicates.*

The results underscore the importance and challenges of optimizing cell seeding density for bacterial samples to ensure reliable and interpretable metabolic comparisons in Seahorse XF Cell Energy Phenotype Tests. For both S and R strains, OD_{600} 0.02 was identified as the optimal seeding density. The density provided robust OCR and ECAR values while minimizing the risk of oxygen depletion or signal variability.

While OD_{600} 0.04 yielded the highest OCR and ECAR values, transient oxygen depletion during mixing phases reduced its reliability for long-term measurements. In contrast, OD_{600} 0.01 was insufficient to generate detectable metabolic activity for the S strain, and while the R strain maintained some metabolic activity, the low density raised concerns about reproducibility. OD_{600} 0.08 led to severe oxygen depletion and metabolic shifts, rendering it unsuitable for Seahorse assays.

By identifying OD_{600} 0.02 as the optimal seeding density, these experiments established a balance between detectable metabolic activity and consistent oxygen availability, ensuring reproducible and robust bioenergetic profiling of *E. coli* strains. Therefore, seeding density of OD_{600} 0.02 was used for subsequent Seahorse analyses.

5.2.3.2 FCCP titration in the XF Cell energy phenotype test

To further characterize the metabolic profiles of meropenem-susceptible (S) and meropenem-resistant (R) *E. coli* strains, FCCP titration was conducted using the Seahorse XF Cell Energy Phenotype Test. FCCP, drives maximal oxygen consumption by allowing electrons to flow freely through the ETC, bypassing ATP production. The process provides insights into the maximal respiratory capacity and reserve respiratory capacity of the strains, which are critical parameters for allocating energy phenotypes. FCCP titration facilitates this allocation by identifying the maximal OCR, revealing reserve capacity, and assessing changes in ECAR, which collectively reflect the metabolic flexibility of cells. FCCP titration also enables mapping these metabolic states in the energy map, highlighting how cells shift between oxidative phosphorylation and glycolysis under stress.

The experiment was conducted using *E. coli* cells seeded at OD_{600} 0.02, as this density provided consistent metabolic activity while avoiding oxygen depletion. Final FCCP concentrations of 0.25 μM, 0.5 μM, 1.0 μM, and 2.0 μM were tested, with basal OCR and ECAR measured before sequential injections of oligomycin (1.0 μM) and FCCP.

Figure 5.8 illustrates the OCR and ECAR profiles for the S strain at varying FCCP concentrations (0.25, 0.5, 1.0, and 2.0 μM). Basal OCR values were measured before the injection of oligomycin and FCCP. Following FCCP injection, OCR increased proportionally with FCCP concentration, peaking at 1.0 μM. At this concentration, maximal respiratory activity was achieved, reflecting maximal ETC activity. However, OCR plateaued at 2.0 μM FCCP, suggesting that further increases in FCCP concentration did not enhance respiratory activity, potentially due to proton gradient depletion or toxicity effects. The Seahorse XF Cell Energy Phenotype Report categorized the metabolic states based on OCR and ECAR values. At 1.0 μM FCCP, the S strain shifted to an energetic phenotype with enhanced OCR and moderate ECAR values. Lower FCCP concentrations (0.25 and 0.5 μM) and higher FCCP concentration (2.0 μM) maintained a more quiescent state.

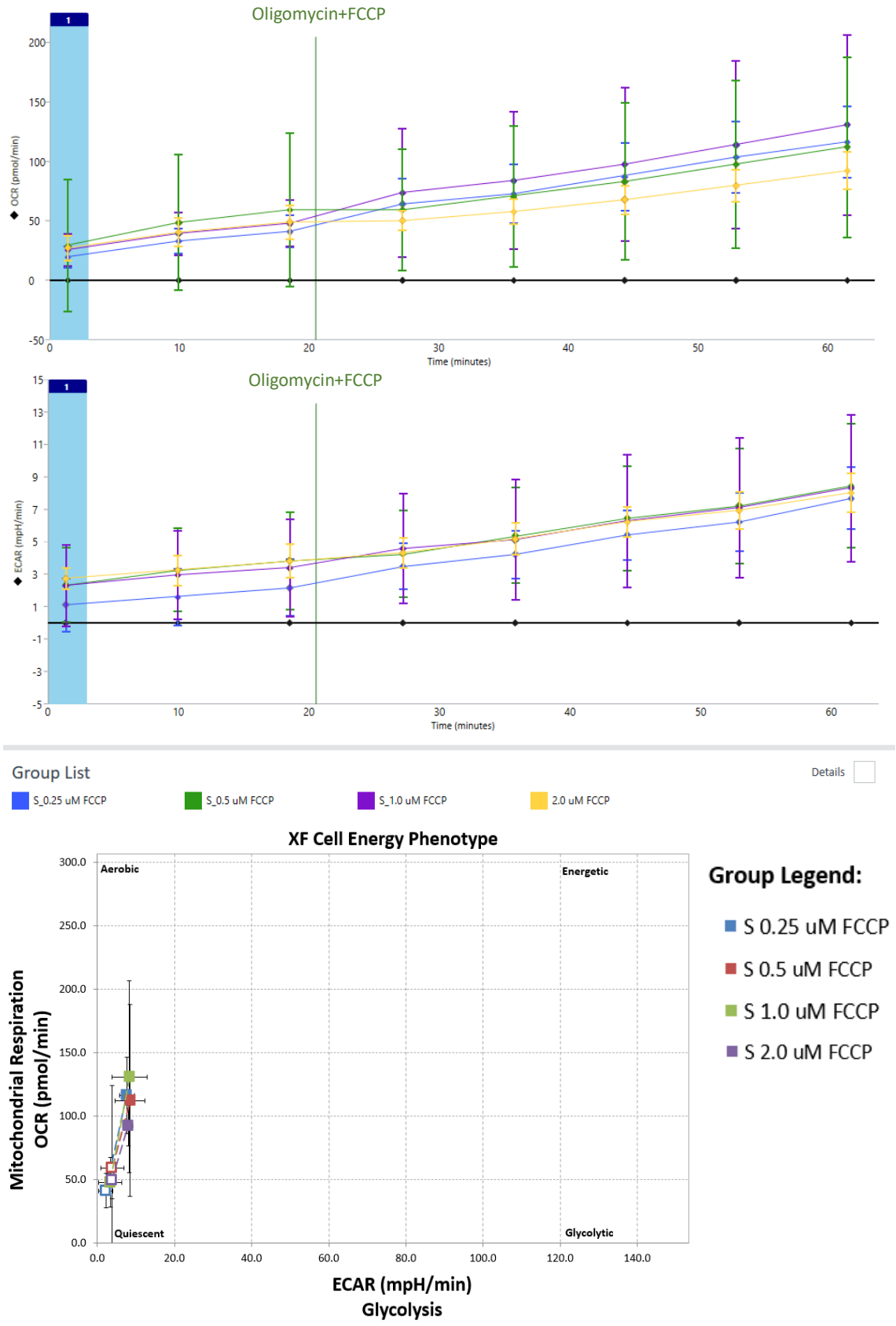

Figure 5.8 OCR and ECAR profiles for meropenem-susceptible (S)* E. coli *strains at varying FCCP concentrations (0.25 µM, 0.5 µM, 1.0 µM, 2.0 µM). *The OCR (top panel) and ECAR (bottom panel) graphs depict trends in oxygen consumption and acidification rates across the assay, following injections of oligomycin and FCCP. The energy map (bottom panel) categorises metabolic phenotype into aerobic, energetic, glycolytic, and quiescent states based on OCR and ECAR measurements. Error bars representing standard deviation from five replicates.*

Figure 5.9 depicts the OCR and ECAR profiles for the R strain at varying FCCP concentrations, oligomycin and FCCP given simultaneously. Basal OCR was higher in the R strain compared to the S strain, suggesting increased oxidative metabolism. However, contrary to expectations of FCCP-mediated uncoupling, no significant increases in OCR were observed after FCCP injections across any concentrations. Instead, a gradual decline in OCR occurred at 2.0 μM FCCP, suggesting potential toxicity at higher FCCP concentrations. ECAR trends for the R strain revealed fluctuations with FCCP titration. At 0.5 μM FCCP, ECAR values initially dipped after injection, followed by stabilization. Similarly, a noticeable decline in ECAR occurred at 2.0 μM FCCP, indicating potential metabolic stress or inefficiency in compensatory glycolysis under these conditions. The Seahorse XF Cell Energy Phenotype Report highlighted metabolic flexibility of the R strain. At 1.0 μM and 0.25 μM FCCP, the R strain displayed slightly increased OCR compared to baseline, reflecting its energetic potential, but this was not sustained across other FCCP concentrations. The R strain did not consistently exhibit an energetic phenotype, as OCR enhancements were not proportional to FCCP doses. While the ECAR values showed moderate increases, the variability in response suggested metabolic instability rather than flexibility. The metabolic potential of the R strain remained comparable across FCCP concentrations, indicating that reserve capacity of the strain did not increase substantially beyond baseline, contradicting initial assumptions of superior bioenergetic reserves. Potential concern regarding initial OCR and ECAR values observed. The difference in OCR and ECAR at t=0 requires clarification. While consistent seeding density (OD_{600}=0.02) were used, baseline metabolic variability, or technical factors in the assay setup could have influenced the starting metabolic parameters. Further investigation is needed to determine whether these differences stem from metabolic behaviour, or experimental variation such as cell detachment.

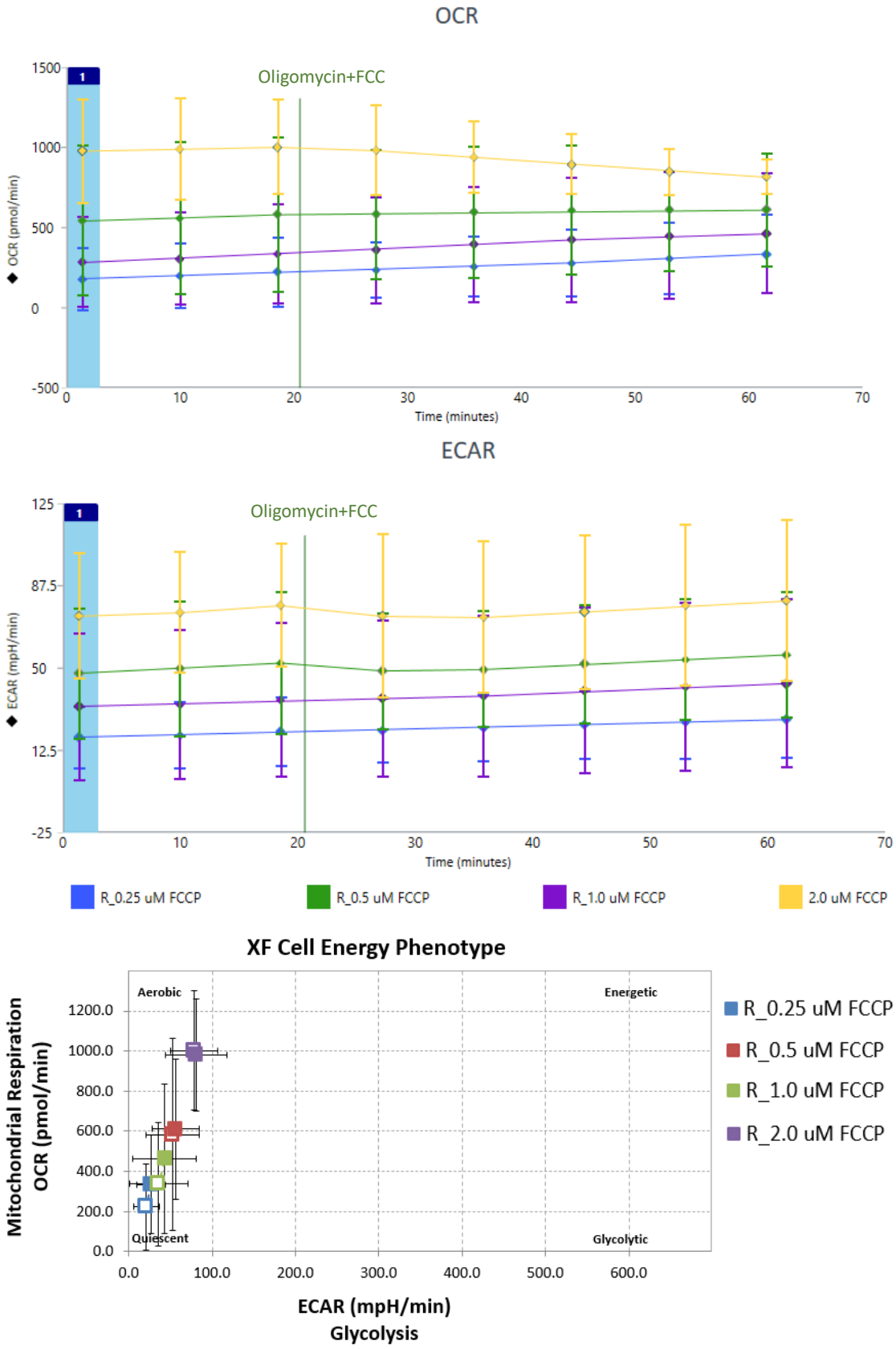

Figure 5.9 OCR and ECAR profiles for meropenem-resistant (R)* E. coli *strains at varying FCCP concentrations (0.25 µM, 0.5 µM, 1.0 µM, 2.0 µM). *The OCR (top panel) and ECAR (middle panel) graphs depict trends in oxygen consumption and acidification rates across the assay, while the energy map (bottom panel) categorizes metabolic phenotype into aerobic, energetic, glycolytic, and quiescent states based on OCR and ECAR measurements. Error bars representing standard deviation from five replicates.*

The FCCP titration experiments for both the meropenem-susceptible (S) and meropenem-resistant (R) *E. coli* strains revealed distinct metabolic responses to increasing FCCP concentrations. FCCP, as a protonophore, uncouples oxidative phosphorylation, forcing maximal respiration by disrupting the proton gradient across the electron transport chain (ETC). The assay allows an assessment of the strains' bioenergetic reserve capacity and metabolic flexibility.

In the S strain, OCR increased steadily across FCCP concentrations, with the highest OCR observed at 1.0 μM FCCP (**Figure 5.8**). However, at 2.0 μM FCCP, OCR began to plateau, suggesting a threshold beyond which the ETC could no longer compensate for the uncoupling effect. ECAR increased moderately in response to FCCP but remained within the dynamic range, reflecting a balanced contribution of oxidative and glycolytic metabolism. The Seahorse XF Cell Energy Phenotype analysis categorized the S strain primarily as quiescent at baseline but shifted towards an energetic phenotype under FCCP-induced stress. The result indicated that the S strain was capable of engaging its reserve capacity when challenged, though its response was dose-dependent and peaked at intermediate FCCP concentrations.

In the R strain, baseline OCR was consistently higher than in the S strain, reflecting elevated oxidative metabolism even under unstressed conditions (**Figure 5.9**). However, upon FCCP injection, OCR did not increase in a dose-dependent manner, displaying considerable variability across replicates. While 1.0 μM FCCP elicited the highest OCR, the response was less consistent across replicates, and at 2.0 μM FCCP, OCR began to decrease progressively over time. The result suggested potential toxicity at higher FCCP doses, which may induce over-uncoupling proton leak rather than enhanced respiration. The variability observed likely due to difference in seeding density or inconsistencies in FCCP addition between wells. ECAR trends showed dips immediately after FCCP injections at 0.5 μM and 2.0 μM, indicating transient disruptions in acidification rates potentially linked to altered proton export. The Seahorse XF Cell Energy Phenotype analysis placed the R strain in the aerobic and energetic quadrants under FCCP stress, suggesting a capacity for metabolic adaptation. However, the lack

of a clear dose-dependent OCR response and greater variability compared to the S strain suggests reduced metabolic efficiency or instability in maintaining optimal uncoupled respiration.

Overall, these results demonstrated that FCCP titration effectively distinguished the metabolic phenotypes of the S and R strains. The S strain displayed a more predictable and consistent shift towards energetic metabolism, whereas the R strain exhibited a higher basal metabolism but inconsistent OCR responses under stress. These differences highlight the potential metabolic differences in the R strain that could be targeted to overcome resistance mechanisms.

5.2.4 Buffer factor assay

The Buffer Factor (BF) assay was conducted to evaluate whether 2TY medium was suitable for use in Seahorse XF assays. Accurate interpretation of ECAR data requires converting qualitative proton extrusion measurements, reported in milli-pH per minute (mpH/min), into quantitative PER values. The conversion depends on determining the BF of the assay system, which accounts for both the buffer capacity of the medium and the specific properties of the Seahorse XF Analyser setup.

The BF is defined as the amount of H^+ ions (in millimoles) required to change the pH of the assay medium by one unit within the Seahorse XF Analyser system. Unlike intrinsic buffer capacity, which is solely a property of the medium, BF accounts for system-specific factors such as the material composition of the instrument and labware. Determining the BF allows ECAR data to be converted into absolute proton flux values, facilitating for quantitative metabolic studies.

The suitability of 2TY medium for Seahorse XF assays was evaluated because its buffering capacity could influence ECAR measurements. While Seahorse XF Assay Medium is typically recommended due to its optimised properties for detecting proton flux, 2TY medium was assessed as a potential alternative to support bacterial metabolism in experiments involving *E. coli*. By determining the BF of 2TY, the compatibility of this medium with Seahorse XF measurements was examined.

The BF was determined empirically by titrating a known concentration of acid (5 mM HCl) into the assay medium and measuring the corresponding pH changes within the Seahorse XF Analyser. The approach accounted for system-specific effects on acidification and allowed for the calculation of BF values specific to the experimental setup.

An assay plate was prepared with the 2TY medium under the same conditions as a typical Seahorse experiment but without cells. Sequential injections of 5mM HCl or 2TY medium were performed, and the resulting pH changes were measured. Control wells containing medium without acid injections were included to establish baseline effects. The Seahorse XF Buffer Factor Calculator processed the data to calculate the BF, expressed in millimoles of H^+ ions per pH unit (mM/pH). The value enabled the conversion of ECAR into PER.

Figure 5.10 illustrates the pH changes over time in 2TY medium after sequential HCl injections. In the control condition, where medium was injected into medium, minimal pH fluctuations were observed, confirming no external acidification. In contrast, HCl injections into 2TY medium produced steeper and more pronounced pH decreases.

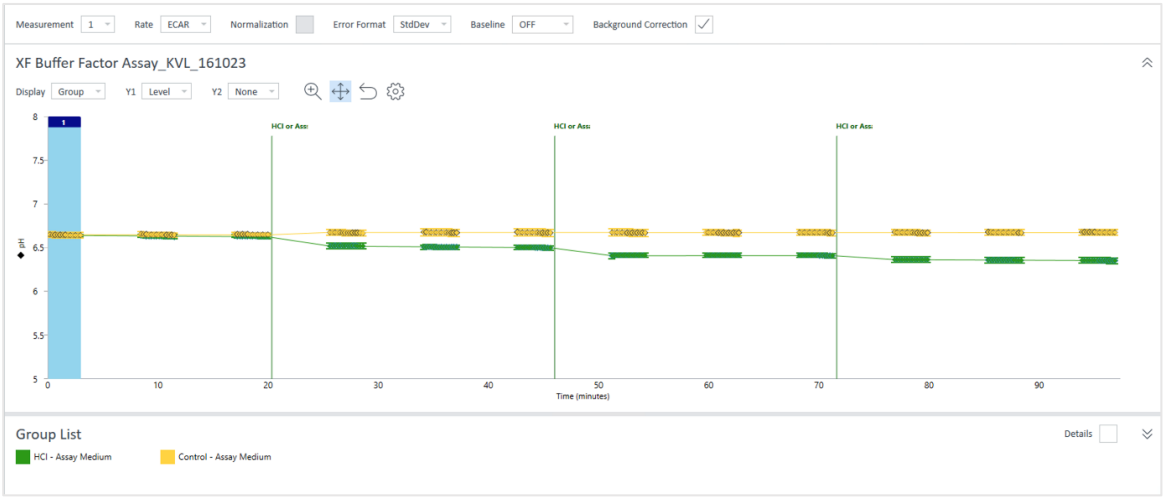

Figure 5.10 pH changes in 2TY medium after HCl titration. *The graph illustrates the pH changes induced by sequential HCl injections (green) and 2TY medium injections (yellow) in 2TY medium. Error bars represent standard deviation from five independent measurements.*

Figure 5.11 shows the change in pH as a function of HCl concentration, with a linear regression performed to calculate the BF of 2TY medium. The slope of the regression line indicates that 2TY medium has a high buffering capacity. Based on Seahorse Buffer Factor calculation, 2TY medium had a BF of 5.0 mM/pH, exceeding acceptable range of the Seahorse system (0-4 mM/pH). The high buffering capacity reduces the sensitivity of ECAR measurements by limiting pH changes in response to extracellular proton flux, making 2TY medium unsuitable for Seahorse XF ECAR analysis.

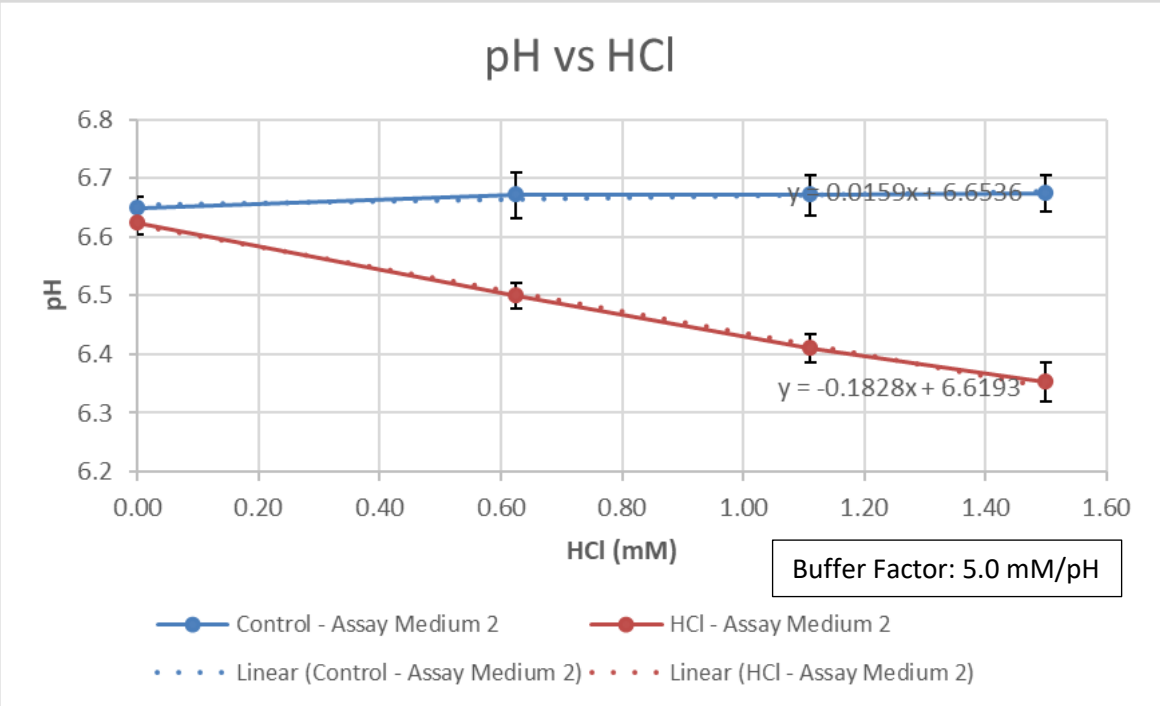

Figure 5.11 Seahorse XF Analyzer pH response to HCl titration in 2TY medium. *pH changes from the Seahorse XF Buffer Factor Calculator used to calculate the buffer factor (BF) for 2TY medium. The BF exceeded the platform's acceptable range (0–4 mM/pH), rendering 2TY unsuitable for ECAR analysis.*

The findings confirmed that the 2TY medium is not suitable for Seahorse XF assays. The results demonstrated the necessity of employing media with appropriate buffering capacities to ensure accurate metabolic profiling. Therefore, for subsequent analyses, Seahorse XF assay medium, specifically designed to support reliable ECAR measurements, will be utilized to enable precise quantification of glycolytic activity and proton dynamics.

5.2.5 Normalisation with Hoechst dye staining

To ensure accurate interpretation of Seahorse assay data, normalisation was essential to account for variability in cell density across wells. In this experiment, Hoechst dye staining was explored as a DNA-based normalisation technique. Hoechst dye binds specifically to DNA, enabling quantification of relative cell numbers through fluorescence intensity. This approach aimed to complement optical density (OD_{600}) measurements used during cell plating, providing an additional layer of normalisation to correct for inconsistencies in cell seeding and attachment. By implementing Hoechst dye staining, the study sought to enhance the reliability and precision of metabolic measurements obtained from bacterial strains.

Literature from the University of Illinois Biotechnology Centre suggested for bacterial cells, the optimal concentration of Hoechst dye ranges between 0.1 and 12 μg/mL (0.178 – 21.37 mM), with an incubation time of 10 to 30 minutes.[462] However, due to the lack of established protocols for Seahorse assays on bacteria, slightly higher concentration (final concentration 27 mM - 30 mM) were tested in this study. These concentrations were selected to ensure adequate fluorescence signal detection given the challenges associated with bacterial cell wall permeability and potential variability in dye uptake. Additionally, the higher concentrations were employed to overcome potential variability in DNA content between bacterial cells, as no established protocols existed for Seahorse assays on bacterial systems. Such an approach aimed to empirically determine a suitable dye concentration for reliable signal detection in this specific experimental context.

5.2.5.1 Experimental procedure

Two independent experiments were conducted to evaluate the suitability of Hoechst dye staining for normalisation. In the first set, subcultures were grown to OD_{600} 0.3, diluted to the desired OD_{600}, and attached to the Seahorse plate in 2TY medium. Hoechst dye stock solutions of 270 mM and 300 mM were diluted 1:10 upon addition to the wells, resulting in final concentrations of 27 mM and 30 mM in the samples. The dye was then incubated, and fluorescence was measured using a BMG CLARIOstar PLUS microplate reader. Fluorescence

readings were averaged across technical replicates. In the second set, to address the potential impact of the medium on fluorescence signal, subcultures were similarly grown and diluted but were washed with Seahorse XF DMEM medium after the attachment to remove residual 2TY medium suspended in Seahorse XF DMEM medium. Hoechst dye stock solution at 300 mM was diluted 1:10 upon addition to the wells, resulting in a final concentration of 30mM in the samples. Fluorescence was measured in biological replicates under the same conditions.

The first experiment, which used cells in 2TY medium, exhibited variability in fluorescence data. While some trends were observed, the fluorescence signal did not consistently correlate with OD_{600} measurements. Similarly, substitution of 2TY medium with Seahorse XF DMEM medium did not improve fluorescence signal variability and signal did not correlate with OD_{600} measurements. **Figure 5.12** presents the fluorescence data for the second experiment, highlighting inconsistent relationships between OD_{600} and fluorescence intensity across biological replicates. The observed fluorescence signal for each well was planned to be normalized by subtracting the blank signal and calculating a signal-to-blank ratio (S/B). The normalisation values were directly imported into Wave 2.6.3 software for Seahorse data analysis.

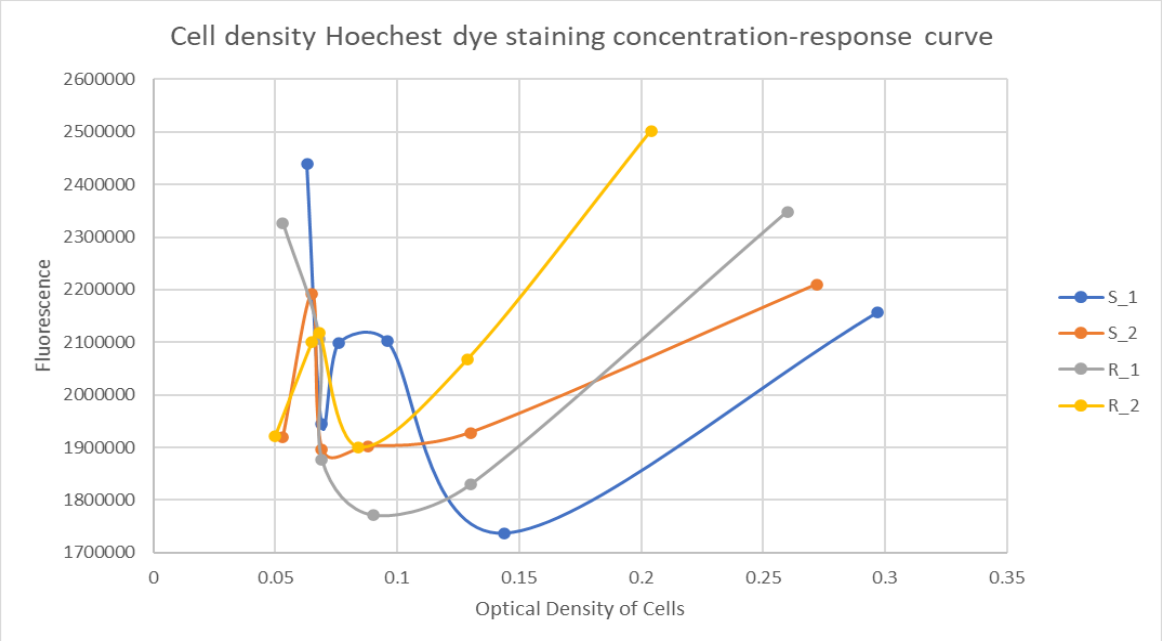

Figure 5.12 Hoechst dye concentration curve. *Fluorescence intensity plotted against optical density at wave length 600 nm (OD_{600}) for washed meropenem-susceptible (S) and meropenem-resistant (R)* E. coli *cells stained with 30 mM Hoechst dye. S_1 and S_2 represent biological replicates for the susceptible strain, while R_1 and R_2 represent replicates for the resistant strain.*

The inconsistencies observed in the Hoechst dye fluorescence data suggested that this approach may not be suitable for bacterial normalisation in Seahorse assays. Washing the cells and using Seahorse assay media, did not reduce this variability to acceptable limits. The result suggested that factors such as variability in dye uptake and bacterial cell properties, such as potential variability in DNA content or membrane permeability, might have played a role in the observed inconsistencies. The lack of a consistent correlation between OD_{600} and fluorescence further undermined the reliability of Hoechst dye normalization under the tested conditions.

5.2.5.2 Discussion

While Hoechst dye staining is a well-established method for normalization in eukaryotic systems, its application to bacterial systems revealed significant challenges. The inconsistent correlation between OD_{600} and fluorescence intensity suggested that bacterial cell properties, such as cell size, membrane permeability, or DNA content, may contribute to the signal variability. Although interactions between 2TY medium components and Hoechst dye were considered as a potential factor, there was no evidence to confirm such interference. The second experiment aimed to address the inconsistent correlation issue by replacing 2TY medium with Seahorse assay media, but the results still showed substantial variability across biological replicates. These experiments revealed that the normalisation approach employing Hoechst dye that is widely used in mammalian culture experiments is not compatible with bacterial cultures. Instead, OD_{600} will remain as the method for normalisation in Seahorse experiments.

5.2.6 XF Glycolysis rate assay

The XF Glycolysis Rate Assay provides a quantitative evaluation of glycolytic activity in meropenem-susceptible (S) and meropenem-resistant (R) *E. coli* strains, addressing limitations of the Glycolysis Stress Test by isolating glycolysis-specific extracellular acidification. The assay distinguishes glycolytic proton efflux rate (glycoPER) from non-glycolytic acidification by integrating OCR measurements to account for CO_2 hydration, enabling more precise calculations of proton flux. The approach was particularly crucial for

E. coli, where the bacterial ETC operates in the inner membrane, and CO_2 from TCA cycle activity contributes to extracellular acidification.

The assay medium was prepared with glucose, pyruvate, glutamine, and HEPES buffer to stabilise pH during the experiment. The basal OCR and ECAR were recorded over three measurement cycles to establish baseline glycolytic and non-glycolytic activity. The first injection introduced Rot/AA, which inhibited the ETC, suppressing oxygen consumption and reducing CO_2-derived acidification.[463] The step isolated the proton efflux attributable to respiration, allowing the calculation of the glycolytic PER. The second injection introduced 2-DG, a glucose analogue which competitively inhibits glucokinase, halting glycolytic activity dependent on ATP-phosphorylation of glucose. The resulting decrease in proton efflux would provide qualitative confirmation that acidification observed prior to 2-DG injection is primarily due to glycolysis. However, in bacteria with glucose uptake mechanisms reliant on the phosphoenolpyruvate-dependent phosphotransferase system (PTS), the effect of 2-DG may be diminished or variable due to alternative pathways for glucose metabolism.[464,465]

5.2.6.1 Results

Figure 5.13 illustrates the PER trends for meropenem-susceptible (S) and meropenem-resistant (R) *E. coli* strains under basal and stressed conditions, highlighting compensatory glycolysis. PER provides a corrected measure of glycolytic acidification by accounting for CO_2 hydration-derived acidification. The correction allows for a more accurate quantification of glycolysis-specific proton production, isolating metabolic acidification from respiration-derived extracellular acidification. Both strains displayed a slight increase in glycoPER following the injection of Rot/AA, which inhibits the electron transport chain, forcing the cells to rely on glycolysis. However, this increase was minimal and fell well below the expected compensatory response typically observed in glycolytic rate assays. After the 2-DG injection, which inhibits glycolysis, glycoPER decreased in both strains, confirming that the proton efflux observed during the earlier phase was primarily glycolysis-driven.

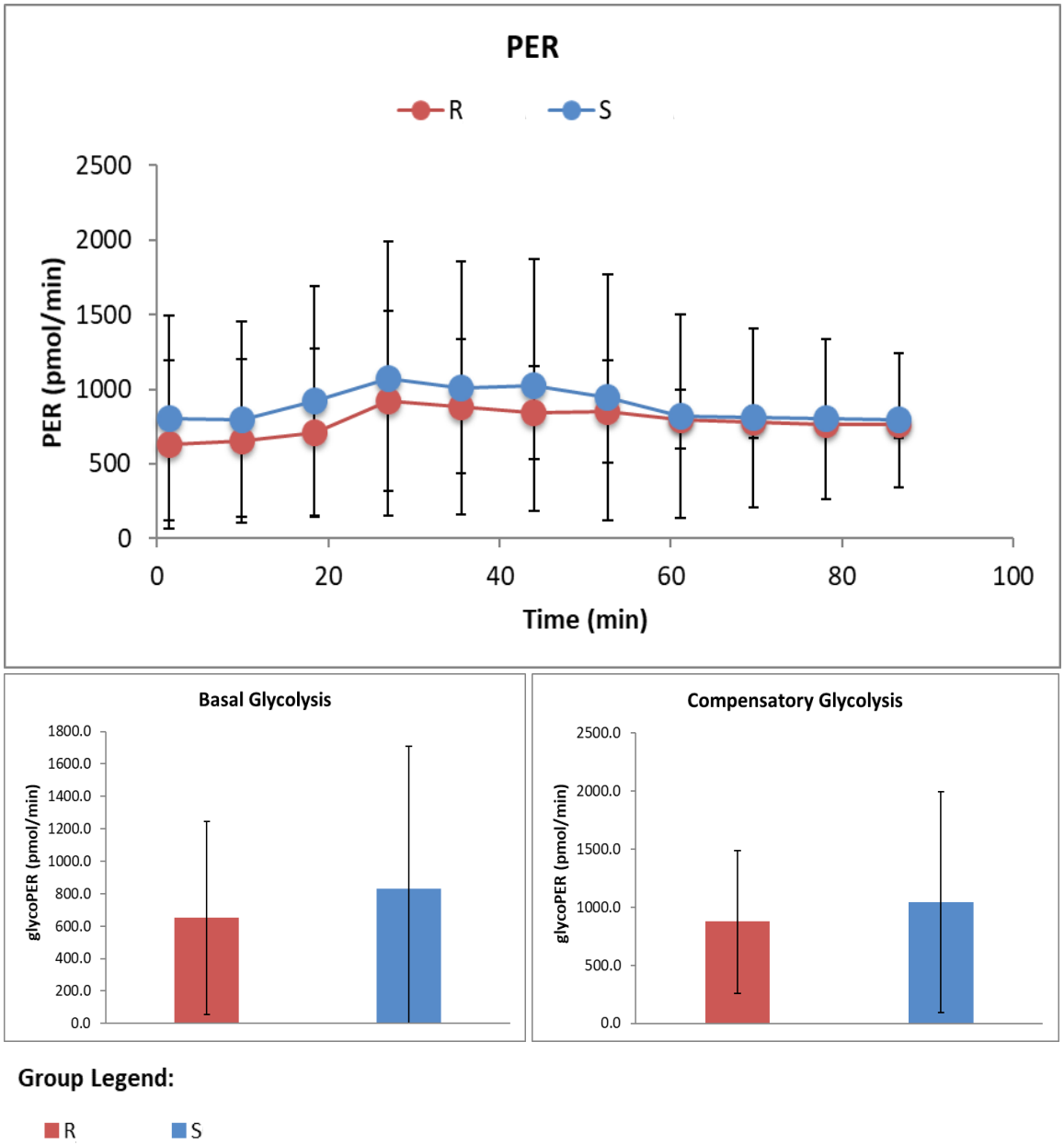

Figure 5.13 PER trends in meropenem-susceptible (S) and meropenem-resistant (R) E. coli ***strains under basal and stressed conditions.*** *Basal glycolysis was measured before any injection, and compensatory glycolysis was calculated as the glycoPER increase after Rot/AA injection. Rot/AA was injected at 20 minutes, and 2-DG was injected at 60 minutes. Error bars represent standard deviation from replicates n=5.*

The basal glycolysis rate, calculated before any injection, showed slight differences between the S and R strains; however, overlapping error bars indicate high variability, making it difficult to conclude statistically significant differences (**Figure 5.13**, bottom left). Similarly, the compensatory glycolysis rate, representing the glycolytic upregulation after Rot/AA injection, was slightly higher in the S strain but remained within the margin of error, demonstrating high

variability, and preventing meaningful distinction between the two strains (**Figure 5.13**, bottom right). Overall, the assay revealed only subtle changes in glycoPER for both strains in response to Rot/AA and 2-DG. The lack of a pronounced compensatory glycolytic response suggests that the bacterial metabolic systems do not behave as expected under these conditions. The discrepancy could be attributed to differences in how Rot/AA inhibits the ETC in bacteria compared to eukaryotic cells. While antimycin A is known to inhibit the bacterial ETC at Complex III (cytochrome bc1 complex), rotenone specifically targets Complex I of the mitochondrial ETC.[449,466] In eukaryotes, Rot/AA effectively halts oxidative phosphorylation and forces a compensatory shift to glycolysis.[467,468] However, in *E. coli*, the ETC is embedded in the plasma membrane and consists of distinct respiratory complexes, including multiple nicotinamide adenine dinucleotide (NADH) dehydrogenases and terminal oxidases operating in parallel, which can provide functional redundancy that can bypass parts of the ETC inhibited by rotenone or antimycin A.[469-472] The redundancy may limit the metabolic shift toward glycolysis typically observed in eukaryotic cells under similar conditions. Furthermore, the slight glycoPER increase following Rot/AA injection suggests that glycolysis is activated to some extent, but not at the levels expected to compensate for the loss of oxidative metabolism. Future experiments could explore alternative inhibitors or combinations of inhibitors that more effectively target bacterial ETC components to induce a robust compensatory glycolytic response.

The Seahorse XF Glycolysis Rate Assay was repeated to investigate the potential impact of meropenem exposure on the metabolic response of meropenem-susceptible (S) and meropenem-resistant (R) *E. coli* strains. The aim of this experiment was to assess whether antibiotic treatment alters glycolytic activity, particularly compensatory glycolysis, which could elucidate metabolic adaptations contributing to resistance mechanisms.

The results are summarised in **Figure 5.14** and indicate minimal changes in ECAR in both S and R strains. In the absence of meropenem, the ECAR trends for both strains remained consistent with earlier observations, displaying slight increases after Rot/AA injection and decreases following 2-DG injection, apart from meropenem-treated susceptible sample which displayed decreased in ECAR after Rot/AA injection. The decrease in ECAR following 2-DG injection confirmed the glycolytic origin of the observed proton efflux, as previously noted. Across all conditions, the ECAR values remained relatively stable, and no significant distinction was observed between the S and R strains.

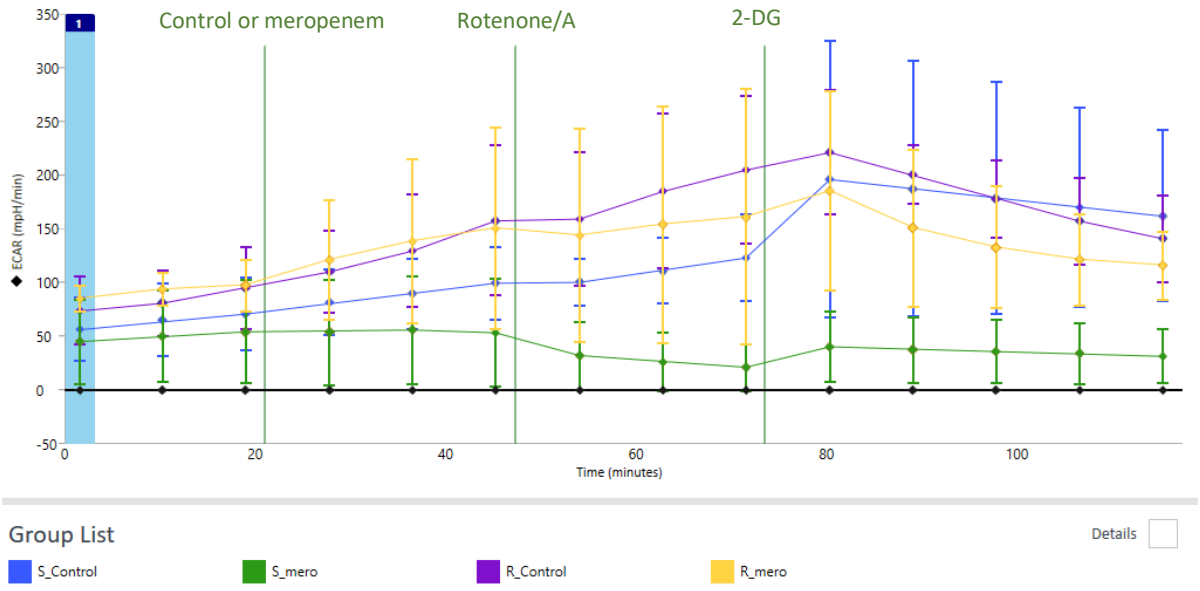

Figure 5.14 ECAR measurements from the Seahorse XF Glycolysis Rate Assay for S and R strains with and without meropenem*. The graph highlights ECAR trends before and after the injections of Rot/AA (20 minutes) and 2-DG (60 minutes). Error bars represent standard deviation from replicates n=5.*

The lack of a distinct metabolic response to meropenem, combined with the absence of a pronounced compensatory glycolytic response, suggests that the assay may not effectively capture the metabolic dynamics of *E. coli* under antibiotic stress. Despite the inclusion of antibiotic-treated samples, the assay failed to provide meaningful insights into glycolytic adaptations, reinforcing concerns regarding its applicability to bacterial systems.

5.2.6.2 Conclusion

The limitations observed in the glycolysis rate assay likely arise from fundamental differences between bacterial and eukaryotic energy metabolisms, including the absence of mitochondria and reliance on membrane-embedded electron transport chains.

Pharmacological treatments such as rotenone and antimycin A are designed to inhibit specific complexes in the eukaryotic ETC—Complex I and Complex III, respectively.[473] While antimycin A has been shown to effectively inhibit the bacterial cytochrome bc1 complex, the impact of rotenone on bacterial NADH dehydrogenases remains unclear.[474] *E. coli*, expresses multiple NADH dehydrogenases, including NDH-1 and NDH-2, that contribute to metabolic flexibility.[475] If rotenone selectively inhibits NDH-1 (functions similar to Complex I in eukaryotic mitochondria), NDH-2 could compensate, mitigating the overall metabolic impact and reducing glycolytic activation. The redundancy, combined with the branched architecture of the bacterial ETC, may explain the minimal compensatory glycolysis observed.

The variability and limited metabolic responses observed in this study highlight a need for a more nuanced understanding of how pharmacological inhibitors interact with bacterial ETC components. Previous studies have demonstrated that the ETC in *E. coli* dynamically adapts to environmental and metabolic conditions, such as oxygen availability and carbon source, which could further mitigate the effects of these inhibitors.[476]

The Seahorse XF Glycolysis Rate Assay**,** while highly effective for evaluating glycolytic activity in eukaryotic cells, was determined to be unsuitable for bacterial cells like *E. coli* under the current experimental conditions. The reliance of the assay on assumptions regarding mitochondrial respiration and extracellular acidification does not fully align with the metabolic architecture of bacterial cells. The minimal and inconsistent changes in glycolytic proton efflux rate (glycoPER) observed across both meropenem-susceptible (S) and meropenem-resistant (R) strains, even under stress conditions such as antibiotic exposure, highlight inability of the assay to capture dynamic metabolic adaptations in bacteria. Compensatory glycolysis, a key

measure of metabolic flexibility, was not distinctly observed in either strain, further challenging applicability of the assay.

Future studies should focus on optimizing assay parameters such as inhibitor concentrations, cell seeding densities, and buffer compositions to align with bacterial physiology. Additionally, methods tailored specifically to bacterial systems—such as employing inhibitors that target bacterial-specific ETC components, using alternative metabolic readouts, or combining Seahorse analysis with complementary techniques like metabolomics—are critical to gaining a comprehensive understanding of bacterial metabolic adaptations.

In conclusion, the Glycolysis Rate Assay in its current form does not provide reliable or biologically relevant data for *E. coli*. While it holds promise as a tool for exploring bacterial glycolysis, its application to bacterial systems requires substantial modifications, such as the use of bacteria-specific compounds, optimization of assay timing, and recalibration of baseline measurements to align with the unique metabolic features of prokaryotic cells.

5.2.7 XF Real time ATP rate assay

The Agilent Seahorse XF Real-Time ATP Rate Assay is used to measure ATP production rates in eukaryotes and was tested next with *E. coli*. The aim was to distinguish contributions from glycolytic and oxidative pathways. The assay integrates OCR and ECAR measurements to determine the rate of ATP production. OCR indicates oxidative activity, whilst ECAR reflects proton efflux associated with glycolysis and other acidification processes. By using metabolic inhibitors such as oligomycin and rotenone/antimycin A, the assay should allow separation of ATP contributions from glycolysis and the ETC, potentially providing dynamic insights into the energy metabolism of *E. coli* under basal and stressed conditions.

Glycolytic ATP production is calculated based on proton efflux rates, while oxidative ATP production is determined from OCR changes after inhibitor injections. In bacterial systems, glycolytic ATP production is associated with proton efflux during glucose metabolism, which contributes to extracellular acidification. Pyruvate, the end product of glycolysis, is metabolised either via the TCA cycle, driving the ETC and oxygen consumption, or through

fermentation pathways, producing acidic by-products.[477,478] These processes mirror the mammalian pathways but occur without mitochondria in bacteria, relying solely on the bacterial cytoplasm and plasma membrane for energy production and redox balance.[479]

The assay began by recording basal OCR and ECAR in cells incubated in Seahorse XF Assay Medium containing glucose, pyruvate, and glutamine. Oligomycin was then injected to inhibit ATP synthase, reducing OCR and reflecting ATP production from the ETC. Subsequently, rotenone, a Complex I inhibitor, and antimycin A, a Complex III inhibitor, were injected to block electron flow through the ETC. In mammalian cells, rotenone prevents the transfer of electrons from NADH to ubiquinone, while antimycin A inhibits the transfer of electrons from ubiquinol to cytochrome c, effectively halting oxidative phosphorylation and isolating the glycolytic contribution to ATP production. These sequential perturbations enabled the calculation of ATP production rates from glycolysis (glycoATP) and oxidative pathways (oxyATP, attributed to the ETC).

ATP production rates were calculated based on established biochemical stoichiometries. Glycolytic ATP production was equated to the glycolytic proton efflux rate (glycoPER, eq. 1), while oxidative ATP production (eq. 2, 3) was calculated by transforming OCR changes after inhibitor injection using a validated P/O ratio (eq. 4). The total ATP production rate was derived by summing the contributions from glycolysis and oxidative pathways (eq. 5).

$$glycoATP\ Production\ Rate\ (pmol\ ATP/min)\ =\ glycoPER\ (pmol\ H^{+}/min) \quad (1)$$

$$oxyATP\ Production\ Rate\ (pmol\ ATP/min) = OCR_{ATP}\ \times 2 \times P/O \quad (2)$$

$$OCR_{ATP} = OCR - OCR_{Oligomycin} \quad (3)$$

$$P/O\ Ratio\ = \frac{ATP\ produced\ (mol)}{Oxygen\ consumed\ (mol)} \quad (4)$$

$$Total\ ATP\ Production\ Rate\ \left(pmol\frac{ATP}{min}\right) = glycoATP\ Production\ Rate\ + oxyATP\ Production\ Rate \quad (5)$$

The assay was selected to evaluate its ability to quantify ATP production rates in *E. coli* and attribute them to specific pathways, while assessing whether it could address some of the challenges previously encountered in bacterial metabolic studies.

5.2.7.1 Results

Figure 5.15 summarises the results from the XF Real-Time ATP Rate Assay, showing minimal changes in OCR and PER throughout the experiment for both meropenem-susceptible (S) and meropenem-resistant (R) *E. coli* strains. At baseline, OCR remained relatively stable, with slightly higher values observed in the R strain compared to the S strain, indicating marginally increased oxidative activity in the resistant strain. However, OCR did not show the expected substantial reduction after oligomycin injection, suggesting that ATP synthase inhibition was incomplete. Similarly, PER increased only slightly, reflecting a limited compensatory glycolytic response. The deviation from expected patterns may indicate reduced sensitivity of bacterial ATP synthase to oligomycin or alternative ATP-generating mechanisms compensating for its inhibition. Following the injection of rotenone and antimycin A, OCR showed only a marginal decrease and failed to drop to near-zero levels, which indicated incomplete ETC inhibition. The observation aligns with previous results suggesting that the branched and redundant architecture of the *E. coli* ETC may mitigate the impact of these inhibitors. PER exhibited minor fluctuations without the substantial rise typically associated with glycolysis-driven ATP production, likely reflecting the metabolic flexibility and alternative pathways available to *E. coli*. The transitions between oxidative and glycolytic ATP production were not well-delineated, deviating substantially from expected assay patterns.

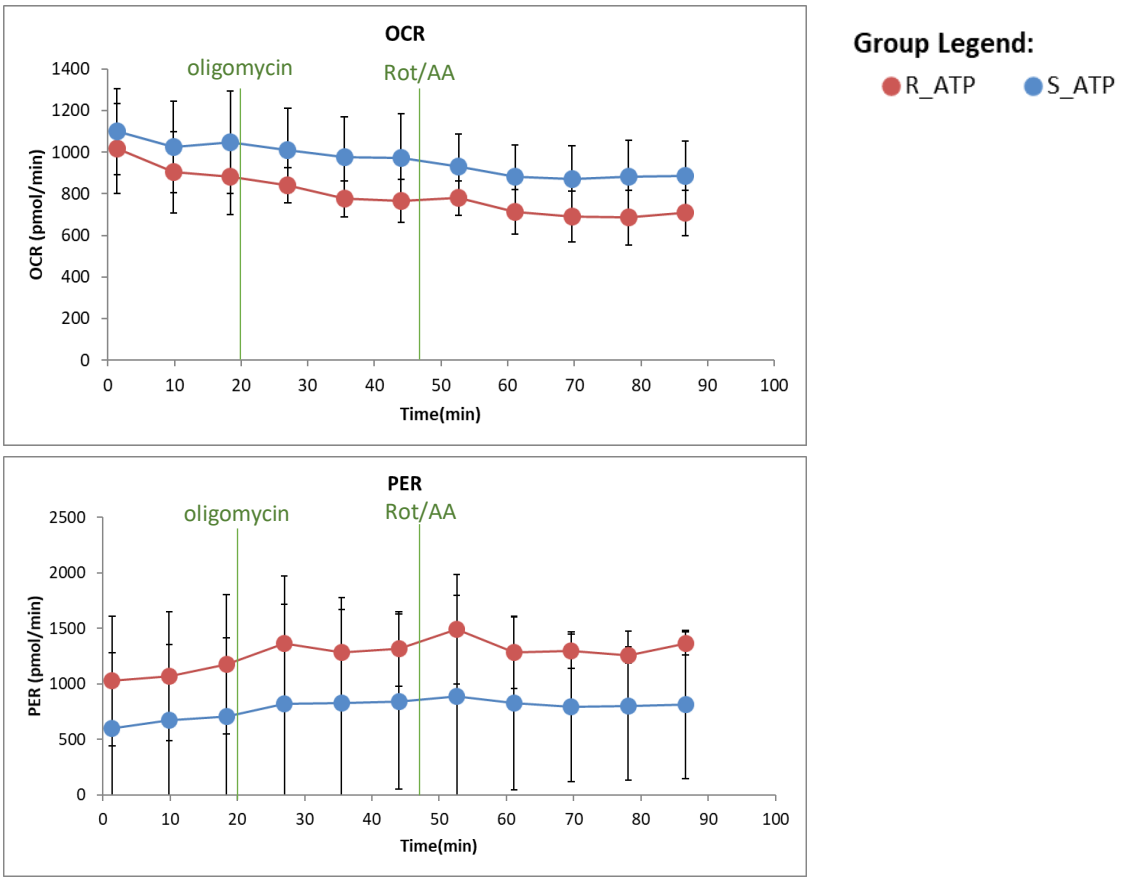

Figure 5.15 OCR and PER profiles for meropenem-susceptible (S) and meropenem-resistant (R)* E. coli *strains during the XF Real-Time ATP Rate Assay. *Basal and stressed OCR and PER were recorded over 90 minutes, following sequential injections of oligomycin and rotenone/antimycin A. Error bars represent standard deviation from replicates (n=5).*

The results demonstrate that *E. coli* cells did not exhibit the changes oxidative phosphorylation and glycolysis as expected for mammalian systems. The bacterial ETC, which is embedded in the plasma membrane rather than mitochondria, may be less responsive to inhibitors like oligomycin, rotenone, and antimycin A. These observations highlight there are major challenges of directly applying eukaryotic bioenergetic assays to bacteria, reinforcing the need for alternative approaches or modified inhibitor strategies to accurately quantify bacterial ATP production.

Despite the elevated baseline oxidative activity, neither strain exhibited the pronounced compensatory glycolytic response typically observed in mammalian cells under similar assay conditions. PER trends were also minimally different between the two strains, indicating that glycolytic contributions to energy production remained low and relatively static under the

tested conditions. These results suggest that the observed metabolic distinctions between the R and S strains are subtle and not fully captured by this assay.

The calculation of ATP production rates using the mammalian P/O ratio may not be directly applicable to bacteria, further complicating the interpretation of OCR-derived ATP production. The assay, in its current form, does not effectively capture the metabolic dynamics of *E. coli*.

5.2.7.2 Discussion and conclusion

The XF Real-Time ATP Rate Assay revealed several limitations in its application to *E. coli* metabolism. The pharmacological stressors used in the assay failed to produce the expected transitions between oxidative and glycolytic ATP production, with OCR and PER measurements showing minimal changes across both meropenem-susceptible (S) and meropenem-resistant (R) strains. Baseline OCR was generally higher in the R strain compared to the S strain, suggesting increased oxidative activity potentially associated with resistance mechanisms, such as enhanced proton pumping or electron flow adaptations. However, this elevated oxidative activity did not translate into distinct metabolic shifts following inhibitor injections. Oligomycin did not significantly reduce OCR, indicating inadequate ATP synthase inhibition, while rotenone and antimycin A injections failed to completely block the bacterial ETC, likely due to its branched and redundant architecture.

PER trends further underscored limitations of the assay, with only minor changes observed following inhibitor injections and no pronounced compensatory glycolysis. The limited glycolytic response suggests that energy metabolism of *E. coli* may rely on alternative pathways or intrinsic metabolic flexibility under these conditions. These findings highlight fundamental differences between bacterial and eukaryotic bioenergetics, including the absence of mitochondria and the unique organization of the bacterial ETC within the plasma membrane.

Although the assay was able to provide some insights into baseline oxidative activity differences between the R and S strains, it did not effectively capture dynamic metabolic changes or glycolytic adaptations under antibiotic stress. Additionally, the reliance on the mammalian P/O ratio for ATP calculations may not be directly applicable to bacterial systems,

further complicating data interpretation. In conclusion, the XF Real-Time ATP Rate Assay, in its current form, is unsuitable for capturing the metabolic dynamics of *E. coli*.

5.2.8 Seahorse XF analyser discussion and conclusions

The experiments using Seahorse metabolic analysis assays to investigate bacterial metabolism highlighted limitations in their current form. Initially developed for mammalian systems, the Seahorse Analyzer has been well-validated for measuring OCR and ECAR as indicators of oxidative and glycolytic metabolism, respectively. Mammalian LN18 glioblastoma cells were used initially to provide a benchmark for its subsequent application using *E. coli*. It was also established that OCR and ECAR measured could be reproducibly made with *E. coli,* demonstrating its fundamental potential.

However, experiments with *E. coli* revealed major challenges in adapting Seahorse assays to bacterial systems when applying pharmacological treatments. Also, initial challenges were encountered in achieving consistent bacterial seeding density due to poor cell adhesion, a problem not typically observed with adherent mammalian cells. PLL was subsequently employed to enhance bacterial attachment to the assay plates. While OCR and ECAR were successfully measured, performing the various Seahorse assays to investigate glycolysis and other energy production pathways, it became clear that the pharmacological inhibitors used to manipulate mammalian energy transduction pathways—such as oligomycin, rotenone, and antimycin A—were largely ineffective in bacterial cells. Although it was not possible to experiment at the enzyme level, it was expected that this limitation reflected fundamental differences in bacterial and eukaryotic enzyme structure, cell architecture and bioenergetics. Unlike eukaryotes, *E. coli* rely on a membrane ETC that features a branched architecture with multiple NADH dehydrogenases and terminal oxidases capable of bypassing inhibited complexes, conferring metabolic redundancy and flexibility. These characteristics likely reduce the sensitivity of bacterial ETC components to inhibitors like rotenone, which selectively targets NDH-1 but does not affect NDH-2. Similarly, effectiveness of oligomycin may be diminished in bacterial ATP synthases due to structural differences. While antimycin A is

known to target the bacterial cytochrome bc1 complex in other bacterial systems, the results in *E. coli* suggest potential variability in sensitivity or incomplete inhibition. These findings underscore the need for further studies to evaluate the effectiveness of specific inhibitors in bacterial ETCs and their impacts on metabolic readouts.

The high proliferation rates of bacterial cells presented additional challenges, particularly in determining appropriate seeding densities. Ensuring that metabolic activity remains within dynamic range of the Seahorse Analyzer without inducing hypoxia or overwhelming the system is critical for accurate measurements. Furthermore, metabolic flexibility of *E. coli*, which allows rapid adaptation to environmental changes, may be an additional factor making them less susceptible to pharmacological interventions, underscoring the challenge in designing universal protocols or inhibitors for bacterial systems. The contrast between bacterial and mammalian results highlights the importance of tailoring Seahorse technology to the unique physiology of bacteria. Inhibitors developed for mammalian ETCs, such as rotenone and oligomycin, target complexes with structural homology to bacterial components but the results presented here suggest they lack sufficient specificity or potency to disrupt bacterial ETC activity effectively. For example, when NDH-1 is inhibited by rotenone, *E. coli* compensates by relying on NDH-2.[471] The redundancy may explain the minimal compensatory glycolytic response and the lack of significant shifts in ATP production rates observed in these experiments.

The XF Analyzer provided some insights into baseline metabolic activity and highlighted strain-specific differences, such as elevated baseline OCR in the resistant strain. However, it failed to capture dynamic transitions between oxidative phosphorylation and glycolysis in *E. coli*. The calculation of ATP production rates using mammalian-derived P/O ratios further complicated the interpretation of OCR-derived ATP production in bacteria, reinforcing the need for recalibration to reflect bacterial physiology.

Future studies should focus on the development of bacterial-specific inhibitors targeting ETC components, as well as the optimization of experimental parameters such as seeding density,

buffer composition, and recalibration of P/O ratios. Complementary approaches, including metabolomics or direct measurement of fermentation by-products, will be essential to validate Seahorse assay findings and provide a more comprehensive understanding of bacterial bioenergetics and its adaptations to antibiotic stress.

In conclusion, experiments presented in this chapter demonstrated that Seahorse technology could reliably measure OCR and ECAR in bacterial cells but assays involving pharmacological treatments require substantial methodological adaptations to improve efficacy for bacterial systems. These findings lay the foundations for refining Seahorse technology to better explore bacterial metabolic adaptations, particularly those associated with antibiotic resistance. After addressing bacterial-specific limitations, this platform has significant potential for monitoring and comparing strain-specific metabolic changes in energy metabolism that could help inform innovative therapeutic strategies that target bacterial energy metabolism.

5.3 Quantitative assessment of ATP levels in *E. coli* using the BacTiter-Glo™ microbial cell viability assay

A BacTiter-Glo™ cell viability assay was employed to quantify ATP levels in *E. coli*, providing a complementary approach to the real-time metabolic measurements performed using the Seahorse XF Analyser. ATP serves as the primary energy currency in all living organisms, including *E. coli*, where it is synthesised through glycolysis, oxidative phosphorylation, and under anaerobic conditions (fermentation).[480] Accurate quantification of bacterial ATP could provide insights into metabolic strategies employed by bacterial strains to sustain energy demands during environmental stress, such as antibiotic exposure. Given the differences in energy metabolism reported by metabolomics experiments and the seahorse OCR and ECAR measurements, it was decided to measure ATP levels directly to compare meropenem-susceptible (S) and meropenem-resistant (R) strains, to evaluate the impact of antibiotic treatment on this bacterial energy currency.

The BacTiter-Glo™ assay is based on a luciferase-catalysed reaction between ATP and luciferin, resulting in luminescence proportional to ATP concentration which is related to metabolic

activity and cellular viability.[481] The assay provides a snapshot of ATP concentration at a given time rather than real-time continuous monitoring. While this limits the ability to track dynamic metabolic changes over time, it offers a reliable and straightforward means to compare ATP levels under defined conditions. By quantifying ATP under both basal and treated conditions, metabolic adaptations influencing ATP production that underpin bacterial response to antibiotic challenges could be investigated.

5.3.1 Results

First, a standard curve was generated using defined ATP concentrations to validate precision of the assay and ensure accurate quantification of luminescence data (**Figure 5.16**). The curve demonstrated a strong linear relationship (R^2 = 0.99) between ATP concentration and luminescence, confirming reliability of the assay for bacterial ATP measurement.

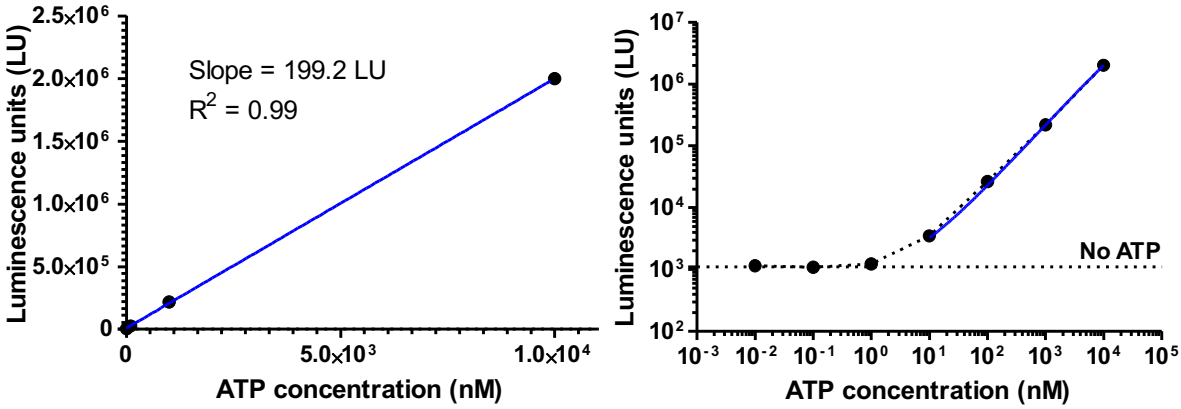

Figure 5.16 Luminescence vs. ATP concentration curve generated using the BacTiter-Glo™ Microbial Cell Viability Assay. *The standard curve was created using ATP disodium salt at concentrations of 0 nM, 0.01 nM, 0.1 nM, 1 nM, 10 nM, 100 nM, 1,000 nM, and 10,000 nM. Each concentration was measured in triplicate, and the luminescence values were recorded as the mean of three replicates, with standard deviation represented as error bars. A strong linear correlation was observed (R^2 = 0.99), validating the assay's precision and sensitivity for ATP quantification. This curve served as a reference for calculating ATP levels in experimental samples. The log-transformed graph showed the detection limit of the assay. Lower concentration (0 nM, 0.01 nM, and 0.1 nM) falling outside of the linear range.*

To test compatibility of the assay with bacterial systems, a concentration curve using bacterial cells was established. *E. coli* strains (E, S, and R) were subcultured from overnight culture, and luminescence and optical density were measured at regular intervals (**Figure 5.17**). At 24 hours, luminescence decreased substantially despite high OD_{600} values indicating that the BacTiter-Glo™ assay detects luminescence only in metabolically active, viable cells, confirming its specificity for ATP measurement within living bacterial populations.

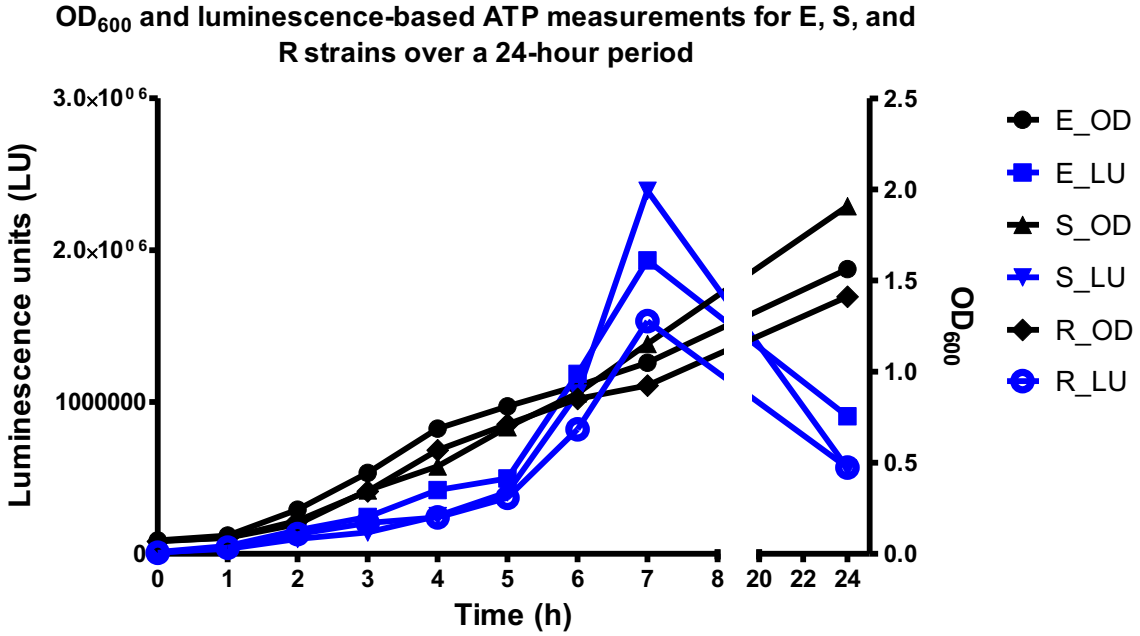

Figure 5.17 Luminescence-based ATP measurements and optical density (OD_{600}) of* E. coli *strains over time. *ATP (luminescence, LU) and bacterial growth (OD_{600}) were measured for wild-type (E), meropenem-susceptible (S), and meropenem-resistant (R)* E. coli *strains over a 24-hour period.*

For the antibiotic-stress test, *E. coli* strain densities were normalized to an OD_{600} of 0.4 and exposed to different concentrations of meropenem and bedaquiline for 1-hour. ATP levels were then measured to evaluate the metabolic impact of these antibiotics on susceptible and resistant strains. The ATP luminescence data (**Figure 5.18**) shows that the E (wild-type) strain produced the highest fluorescence levels, followed by S (meropenem-susceptible) strain, with the R (meropenem-resistant) strain displaying the lowest fluorescence across all tested concentrations of bedaquiline and meropenem. The pattern reflects intrinsic differences in metabolic activity and ATP production capacity between the strains.

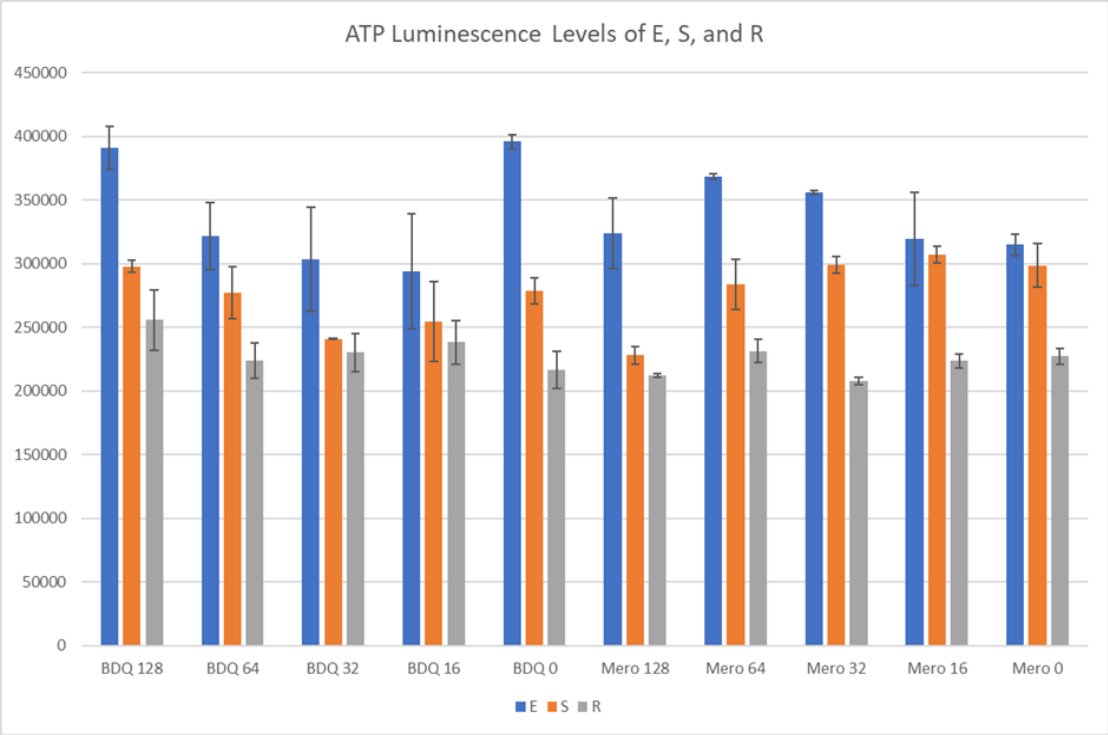

Figure 5.18 ATP luminescence levels of E, S, and R strains after exposure to bedaquiline (BDQ) and meropenem (Mero). *Luminescence measured using BacTiter-Glo ATP assay for E (wild-type; blue), S (meropenem-susceptible; orange), and R (meropenem-resistant; grey) strains after 1-hour exposure to varying concentrations of bedaquiline (BDQ: 128 µg/mL, 64 µg/mL, 32 µg/mL,16 µg/mL, and 0 µg/mL) or meropenem (Mero: 128 µg/mL, 64 µg/mL, 32 µg/mL, 16 µg/mL, and 0 µg/mL). Luminescence levels correspond to ATP concentration, reflecting cellular viability and metabolic activity. Error bars represent standard deviation from biological replicates n=2.*

For bedaquiline, ATP luminescence in the wild-type strain (E) increased with rising bedaquiline concentration; however, the highest concentration of bedaquiline produced luminescence levels comparable to the control condition (no bedaquiline). A similar trend was observed in the S strain, with ATP luminescence increased with bedaquiline concentrations, although the maximum luminescence at the highest bedaquiline concentration was greater than that in the control. In contrast, the resistant strain (R) exhibited consistently lower ATP levels compared to the other strains, regardless of bedaquiline concentration.

When the wild-type (E) train was treated with meropenem, there was an initial increase in ATP luminescence with increasing meropenem concentration, peaking before declining at the highest tested concentration (128 µg/mL). The meropenem-susceptible (S) strain, as expected, showed decreased ATP luminescence with increasing concentrations of meropenem. The resistant strain (R) maintained relatively stable ATP levels across all meropenem concentrations, consistent with its resistance to this antibiotic.

The ATP luminescence data provide insights into ATP production differences between the E (wild-type), S (meropenem-susceptible), and R (meropenem-resistant) *E. coli* strains under exposure to bedaquiline and meropenem. The consistently higher ATP luminescence in the wild-type (E) strain suggests elevated ATP production capacity under both basal and antibiotic-treated conditions. In contrast, the meropenem-resistant (R) strain exhibited the lowest ATP luminescence across all conditions, indicating reduced ATP production, potentially associated with the adaptations related to meropenem resistance. The lower ATP levels in the resistant strain observed here may reflect the metabolic cost of maintaining resistance, further supporting the idea that resistance mechanisms impose energetic trade-offs that can impact bacterial metabolic efficiency and overall fitness.[482]

The response of the E strain to bedaquiline suggests a capacity for metabolic adaptation, with ATP production increasing as drug concentrations rise. However, at the highest bedaquiline concentration (128 μg/mL), ATP luminescence was similar to the control, which is difficult to reconcile with expected metabolic inhibition. Similarly, the S strain showed bedaquiline dose-dependent increase in ATP luminescence, with the highest concentration resulting in ATP levels surpassing the untreated control. In contrast, the consistently low ATP levels in the R strain across all bedaquiline concentrations suggest that resistance mechanisms may fundamentally alter ATP production pathways or reduce reliance on ATP synthase. Such observation aligns with the idea that the metabolic cost of resistance could limit ability of the strain to adapt energetically under antibiotic stress, as seen in resistant strains in other studies.[142,215,241,482] The lack of variability in ATP luminescence across conditions further highlights the metabolic rigidity of the R strain when exposed to bedaquiline.

Under meropenem treatment, the wild-type (E) strain initially exhibited an increase in ATP luminescence with rising concentrations, which may indicate a transient upregulation of energy production pathways. The observation could indicate a compensatory upregulation of metabolic activity, where the cells temporarily increase ATP production in an effort to maintain essential functions and counteract the stress imposed by the antibiotic.[483,484] However, at the

highest concentration of meropenem (128 μg/mL), ATP levels declined, likely reflecting the point at which the antibiotic overwhelmed the cells' metabolic capacity, leading to an inability to sustain energy production. The steady decline in ATP luminescence in S strain with increasing meropenem concentrations aligns with its susceptibility to meropenem. The decrease likely reflects progressive inhibition of essential metabolic pathways, ultimately leading to energy depletion. In contrast, stable ATP levels across all meropenem concentrations in R strain suggest the presence of effective resistance mechanisms. These mechanisms likely enable the resistant strain to mitigate the drug impact on ATP production, maintaining metabolic homeostasis despite antibiotic exposure.

5.3.2 Conclusion

The BacTiter-Glo™ assay was proved a sensitive method for quantifying ATP levels in bacterial cells. Its application to the three *E. coli* strains, provided insights into differences in ATP production when exposed to antibiotics. However, as an endpoint measurement, the assay reflects the cumulative outcome of multiple metabolic pathways (and potentially inputs), making it challenging to isolate specific responses to antibiotics such as bedaquiline and meropenem.

The patterns observed, particularly in the wild-type (E) strain's response to meropenem and the divergent trends under bedaquiline exposure, showed experimental limitations. Factors such as strain-specific metabolic flexibility, or subtle differences in antibiotic susceptibility, could have contribute to this variability. Additionally, certain aspects of the assay, such as potential sensitivity to environmental variables, may have introduced experimental noise, complicating the interpretation of the data.

The findings underscore the need for additional experiments with stricter control of assay parameters and complementary validation methods, such as metabolomics or other direct measurements of metabolic intermediates, to confirm the observed trends and elucidate the mechanisms driving ATP production changes. Furthermore, sensitivity of the assay to factors such as population heterogeneity and partial resistance needs further investigation and

highlights the complexity of interpreting ATP dynamics under stress conditions. Addressing these challenges in future work will be critical to fully leverage this assay for bacterial bioenergetics research.

5.4 Chapter discussion and conclusion

This chapter investigated the application of Seahorse XF Analyzer technology and the BacTiter-Glo™ ATP assay to study energy metabolism in *E. coli* strains under basal and antibiotic conditions. These potentially complementary approaches were employed to evaluate ATP production dynamics and their relationship to antibiotic exposure and provide insights into how resistance mechanisms influence metabolic pathways, particularly focusing on differences between meropenem-susceptible (S) and meropenem-resistant (R) strains.

Seahorse experiments with mammalian cells were used to initially validate the ability of the experimental assay to capture real-time metabolic changes, including potentially transitions between oxidative phosphorylation and glycolysis. The consistent patterns observed in the mammalian system, such as increased PER following Rot/AA injection and reduced glycolytic activity after 2-DG, contrasted sharply with the lack of response observed in bacterial experiments. The observation emphasized the fundamental principles of live-cell analysis are robust, but the methods require substantial adaptation for bacterial applications.

The Seahorse XF Analyzer demonstrated that OCR and ECAR could be reliably measured in *E. coli*, providing a foundation for investigating bacterial bioenergetics. However, the pharmacological inhibitors used in mammalian ETCs, such as oligomycin and rotenone, were largely ineffective in bacterial cells.[452] Such limitation is likely due to the fundamental differences between eukaryotic and prokaryotic energy metabolism and the enzyme architectures involved. Consequently, assumptions underpinning mammalian-based assays are not likely to be directly translatable to bacterial systems.[485]

Interpretation of Seahorse results from the analysis of bacterial systems was further complicated by rapid extracellular acidification and the metabolic diversity of *E. coli*.[486] Bacteria utilize a broader range of carbon sources and metabolic pathways compared to

eukaryotes, including fermentation and alternative oxidases, which are not accounted for in standard Seahorse assay protocols. To better capture bacterial energy metabolism, future Seahorse studies should incorporate bacterial-specific approaches. These include developing inhibitors tailored to target bacterial ETC components, optimizing media compositions to reflect bacterial metabolic preferences, and accounting for rapid bacterial proliferation rates to minimize hypoxia during measurements. Addressing these factors will enhance the sensitivity and relevance of Seahorse technology for bacterial studies.

Technical issues also contributed to the observed variability in Seahorse data. Poor cell adhesion to assay plates, rapid oxygen consumption leading to hypoxia, and inconsistencies in dye-based normalization methods were major obstacles. Although Hoechst dye staining is commonly used as a DNA-based normalization technique, its application to *E. coli* proved less reliable than in mammalian cells, with variability observed in fluorescence signals further complicating data interpretation. Addressing these obstacles, such as optimising plate coating and refining normalisation methods, will be critical for improving assay reproducibility.

Additionally, not all AMR-relevant bacteria exhibit similar energy production pathways. Differences in terminal oxidase usage, fermentation capacity, and preferred carbon sources between bacterial species may necessitate species-specific assay protocols. Exploring interspecies variations in energy metabolism will be essential for establishing robust, generalizable methodologies for studying bacterial bioenergetics under antibiotic stress and resistance.

Despite these challenges, this study established a foundation for adapting Seahorse XF technology to bacterial systems. The reliable measurement of OCR and ECAR in *E. coli* demonstrated the potential of live-cell analysis for investigating bacterial metabolism using OCR and ECAR measurements. By addressing the identified limitations, future research could leverage Seahorse technology to uncover metabolic vulnerabilities associated with antibiotic resistance and inform novel therapeutic strategies targeting bacterial energy production.

The BacTiter-Glo™ ATP assay was applied to complement Seahorse findings by quantifying ATP levels in the context of antibiotic exposure. The results showed that ATP luminescence patterns varied between strains, reflecting intrinsic differences in ATP production capacity. For instance, the wild-type strain (E) consistently exhibited higher ATP levels than the susceptible (S) and resistant (R) strains, underscoring its greater energy production potential. The observed trends under bedaquiline and meropenem exposure highlight the complexity of interpreting ATP dynamics in bacterial systems. For example, the wild-type strain (E) displayed increased ATP levels with rising bedaquiline concentrations, although the highest ATP luminescence level was observed at 0 μg/mL bedaquiline. Similarly, during meropenem treatment, the E strain exhibited an initial increase in ATP production before declining at the highest concentration. Such observation was unexpected, as the E strain is also susceptible to meropenem, albeit lacking the pCR2.1 plasmid present in the S strain. In contrast, the S strain showed a progressive decrease in ATP luminescence as meropenem concentration increased, consistent with its known susceptibility to the drug. These differences in ATP dynamics likely reflect biological phenomena, such as metabolic adaptation to intermediate drug concentrations or thresholds beyond which ATP production is inhibited.

Rather than indicating assay limitations, these results may represent real biological responses to antibiotic stress, highlighting the complexity of bacterial metabolic adaptations. For example, the transient ATP increase in the E strain at lower meropenem concentrations could suggest a compensatory upregulation of metabolic activity to counteract the initial stress. The subsequent decline at higher concentrations likely reflects the point at which the antibiotic overwhelms the cells' ability to sustain energy production. Similarly, the stable ATP levels in the resistant (R) strain across all conditions reflect its metabolic resilience, likely driven by effective resistance mechanisms.

These findings emphasize the need for further investigation to elucidate the mechanisms driving ATP fluctuations under antibiotic exposure. Validation through complementary methods, such as metabolomics or other direct measurements of metabolic intermediates, will

be essential for distinguishing biological phenomena from experimental variability. The approach will help to clarify the dynamic metabolic responses observed in bacterial strains and provide a more comprehensive understanding of their energy metabolism under stress conditions.

As an endpoint assay, BacTiter-Glo™ measures the cumulative outcome of multiple metabolic pathways on ATP production. Despite its sensitivity and specificity for ATP levels, its reliance on end-point luminescence measurements limits the ability to capture dynamic changes over time. Complementing this assay with real-time approaches such as Seahorse technology, or metabolomic profiling, it provides a more comprehensive understanding of bacterial energy metabolism under antibiotic stress.

Future work should focus on optimizing Seahorse assays for bacterial systems, including the development of tailored protocols and media, improved normalization techniques, and the use of bacterial-specific inhibitors. Integrating real-time and endpoint assays, along with complementary metabolomic analyses, will be essential for uncovering the metabolic adaptations underlying antibiotic resistance and bacterial responses to altered conditions. By investigating the application of these technologies to measure bacterial metabolism, using multiple independent assays, this study lays the groundwork for advancing our understanding of bacterial energy metabolism and its role in resistance mechanisms, paving the way for innovative therapeutic strategies targeting metabolic vulnerabilities.

Chapter 6 Investigating combination therapy approaches against anti-microbial resistance

Antibiotic resistance currently poses one of the greatest challenges in modern medicine, with bacterial infections increasingly evading efficacious treatment via genetic mutations and adaptive metabolic mechanisms.[487] The diminishing pipeline of new antibiotics has necessitated alternative strategies to combat resistant bacteria.[488,489] Among these, combination therapy offers a promising approach by combining existing antibiotics with complementary agents to enhance their efficacy.[490] By targeting bacterial vulnerabilities, such as energy metabolism, combination therapy aims to not only maximize the potential of current antimicrobials but also provide a potential means of overcoming resistance.[488]

The aim of the work designed in this chapter is to investigate combination therapy strategies that exploit bacterial metabolism as a target to combat AMR. In Chapter 3 and 4 it was established that bacterial metabolism plays an important role in both resistant mechanisms and in response to antibiotic stress, making it a potentially useful target for combination therapy.[94] While combination therapy has been extensively explored and targeting energy metabolism has shown efficacy in tuberculosis (TB), where it forms the cornerstone of treatment, this approach illustrates promise against other resistant pathogens, particularly in addressing biofilm associated infection, gram-negative MDR bacteria, and methicillin-resistant *Staphylococcus aureus* (MRSA) where it has been less extensive studied.[491-494] By combining antibiotics with metabolic modulators and/or inhibitors, disruption of bacterial homeostasis will be explored in this chapter, to enhance susceptibility to antibiotic treatment.[495]

The research reported in this chapter integrates findings from checkerboard assays, metabolic profiling, and Seahorse live metabolic analyser studies to evaluate the potential of combination therapies to target energy metabolism therapeutically. Checkerboard assays were employed to determine MICs and assess synergistic interactions between antibiotics and metabolic modulators. A Seahorse metabolic analyser method was used to provide insight into how

metabolic modulators influence OCR and ECAR, revealing strain-specific responses that could inform the development of targeted therapies. By combining the results from these assays, novel combination therapies are proposed that integrate metabolic modulators with existing antibiotics.

6.1 Taniborbactam: A novel β-Lactamase inhibitor for combating carbapenem resistance

Carbapenems are among the most potent antibiotics available for the treatment of bacterial infections.[496] However, the rise in carbapenem resistance, largely mediated by MBLs such as NDM, has severely limited their clinical efficacy. NDM enzymes, which require zinc ions for their catalytic activity, have evolved to hydrolyse the beta-lactam ring of carbapenem antibiotics, rendering them ineffective. The widespread dissemination of NDM-producing Enterobacterales poses a critical global health challenge, with limited therapeutic options to combat these infections.

While traditional β-lactamase inhibitors, such as clavulanic acid and tazobactam, have demonstrated effectiveness against serine β-lactamases, their lack of activity against MBLs has inspired research into the development of novel inhibitors capable of targeting MBLs.[497] Taniborbactam, a cyclic boronate β-lactamase inhibitor, has emerged as a promising candidate with potent activity against both serine β-lactamase and MBLs, including NDM.[498] Unlike earlier inhibitors, taniborbactam effectively targets MBL requiring zinc ions for activity, providing a unique mechanism to help overcome carbapenem resistance.[499]

Taniborbactam (**Figure 6.1**), a novel diazabicyclooctane-based β-lactamase inhibitor, had been studied for its ability to restore the efficacy of carbapenems such as meropenem against β-lactamase-producing pathogens.[498] Previous studies have demonstrated the potency of taniborbactam in combination with meropenem against multidrug-resistant Gram-negative bacteria, including clinical isolates of *E. coli*.[500] Checkerboard assays have been conducted on *E. coli* strains to evaluate the ability of taniborbactam to inhibit β-lactamase enzymes effectively and its synergistic potential with meropenem against *E. coli* expressing NDM-7,

while also exploring its dose-dependent activity to optimise a combination therapy strategy. The aim of the experiments reported in this chapter was not only to explore ability of taniborbactam to restore meropenem efficacy but also to investigate potential underlying metabolic changes induced by its use, both in isolation and in combination with meropenem.

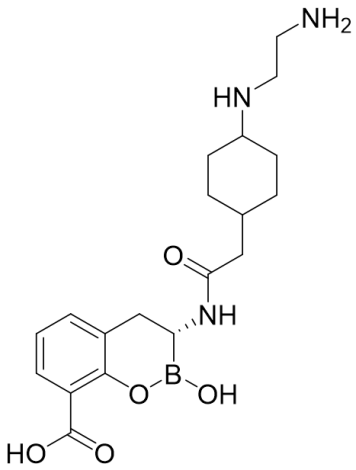

Figure 6.1 Chemical structure of taniborbactam, a novel diazabicyclooctane-based β-lactamase inhibitor. *Drawn in ChemDraw 23.0.1.10*

The efficacy of taniborbactam against the meropenem-resistant strain (R, DH5α pCR2.1 NDM-7) was evaluated initially by focusing on its ability to inhibit resistance mechanisms mediated by NDM-7 carbapenemase and whether it impacts on bacterial metabolism. To investigate this checkerboard assays were performed first to evaluate the MICs of individual and combined treatments, and metabolic profiling was used to explore the impact on bacterial growth. These investigations were performed in order to provide a deeper understanding of how inhibiting resistance mechanisms influenced bacterial metabolism, beyond restoring carbapenem activity.

6.1.1 Evaluating taniborbactam and meropenem combination treatment using checkerboard assays

A checkerboard assay was performed to assess the potential synergistic interactions between taniborbactam, a β-lactamase inhibitor, and meropenem, a carbapenem antibiotic, using meropenem-resistant *E. coli* (R strain) The checkerboard assay systematically varied the concentrations of the two treatment agents in a two-dimensional gradient across a 96-well

microplate, enabling comprehensive assessment of their combined antimicrobial activity.[501] Meropenem was serially diluted along one axis of the microplate, while taniborbactam was diluted along the other, creating a matrix of a wide range of concentration combinations.

Each well was inoculated with a standardised suspension of the meropenem-resistant *E. coli* strain in 2TY and incubated at 37 °C. Bacterial growth was continuously monitored by measuring optical density at 600 nm (OD_{600}) every 10 minutes over a 24-hour period using a plate reader. Endpoint OD_{600} values were recorded after the incubation period to quantify overall bacterial growth in each well.

The assay was conducted exclusively on the meropenem-resistant strain, as the primary objective was to investigate the ability of taniborbactam to potentiate meropenem activity and overcome resistance mechanisms. The targeted approach allowed for a focused exploration of the potential synergy in resistant strains, which represents the most clinically relevant scenario.

The results from the checkerboard assay are provided in **Figure 6.2**. Each well represents the optical density (OD_{600}) of bacterial growth following 24 hours of incubation with varying concentrations of taniborbactam (diluted across rows) and meropenem (diluted across columns). The opacity of each well was directly correlated with the OD_{600} values, reflecting bacterial density and allowing clear visualisation of growth inhibition patterns. Transparency levels were calculated using the equation Transparency (%) = $100 \times (10^{-OD600})$.[502] For example, wells with $OD_{600} = 2$ correspond to 99% light absorbed (1% transparency), indicating maximal bacterial growth. Conversely, wells with lower OD_{600} values exhibit higher transparency levels, reflecting reduced bacterial growth or complete inhibition.

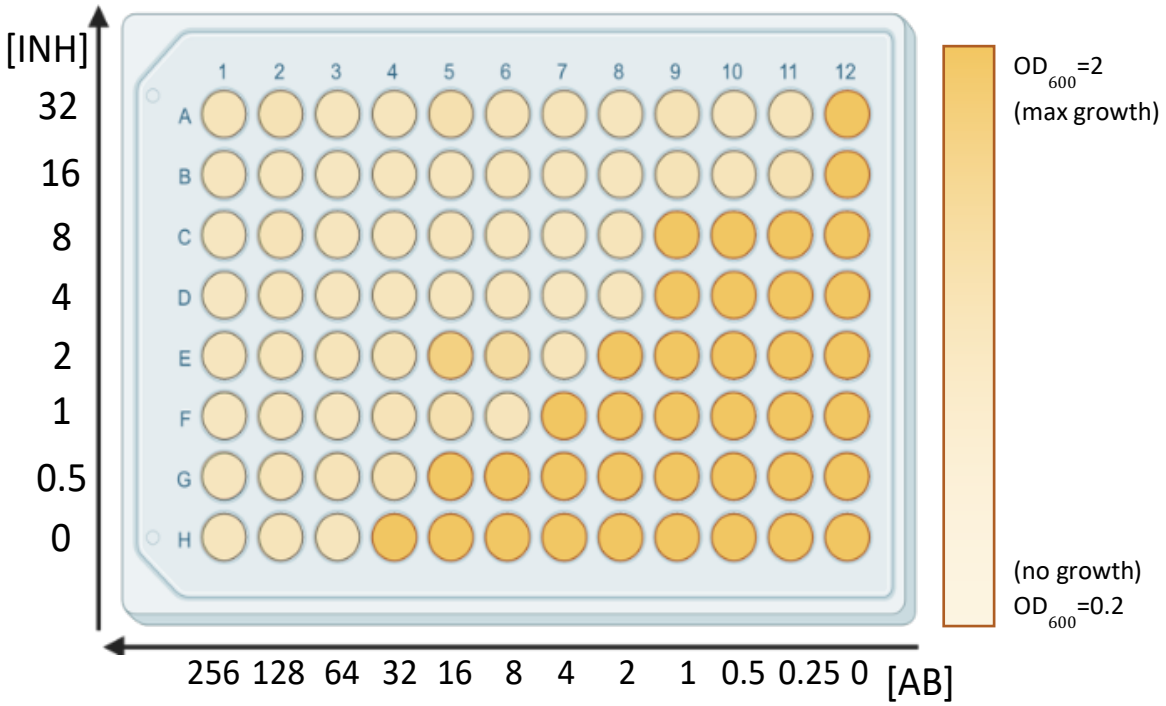

Figure 6.2 Visual representation of bacterial growth from the checkerboard assay evaluating taniborbactam and meropenem synergy. *The 96-well plate illustrates the optical density (OD_{600}) values of* E. coli *growth after 24 hours of incubation under varying concentrations of taniborbactam [INH] (diluted across rows) and meropenem [AB] (diluted across columns). The opacity of each well correlates with the amount of light absorbed: wells with higher OD_{600} values (e.g., OD = 2, indicating 99% light absorbed) are displayed as fully opaque (such as H12, control) indicating maximal bacterial growth, while wells with lower OD_{600} values exhibit reduced opacity (such as H1, maximum concentration of meropenem), reflecting decreased bacterial growth. Clear wells represent no growth (low OD values, where most light passes through). This visualisation highlights areas of inhibited growth, which reflect the potential synergistic effects of the two compounds. Concentrations are reported in µg/mL.*

The results revealed a distinct gradient in bacterial growth inhibition across the plate, with increasing transparency correlating with higher concentrations of either or both agents. Wells treated with taniborbactam alone (column with fixed meropenem concentration of zero) exhibited no indication of bacterial growth inhibition, while wells treated with meropenem alone (row with fixed taniborbactam concentration at zero) show inhibition at concentrations above ≥ 64 µg/mL. Wells at the intersections of moderate to high concentration of both agents exhibit a pronounced reduction in bacterial growth, lowering MIC, suggesting an enhanced inhibitory effect when the two agents are combined.

The assay revealed a dose-dependent effect of the combination treatment, as higher concentrations of both taniborbactam and meropenem resulted in progressively greater bacterial growth inhibition. The observed gradients in growth inhibition across the plate

emphasised the importance of optimised dosing strategies to maximise the efficacy of this combination therapy approach.

The results of the MIC experiment demonstrate that the combination of taniborbactam and meropenem substantially enhanced antimicrobial activity compared to treatment with either agent alone. The observed synergy was likely due to the inhibition of β-lactamase enzymes by taniborbactam, which restored the effectiveness of meropenem against the resistant bacterial strain. However, while the checkerboard assay highlighted the combined efficacy of the two agents, it did not provide any mechanistic insight into how this synergy occurred. Further studies were therefore needed to explore what biochemical processes drove the effect observed.

The checkerboard assay results showed that combining taniborbactam and meropenem for treatment of resistant bacterial strains was effective at reducing bacterial growth. The experiment confirmed that taniborbactam restored the efficacy of meropenem, providing evidence for its efficacy as a β-lactamase inhibitor and potential for combating meropenem-resistant bacteria. Notably, the dose-dependent growth inhibition observed demonstrated the importance of optimising dosing strategies for combination therapy applications. These findings aligned with prior studies on the efficacy of taniborbactam for restoring carbapenem activity but extended prior work by evaluating its effect against *E. coli* strains specifically carrying the NDM-7 gene. The results therefore offer novel insights into the potential application of taniborbactam in addressing carbapenem resistance.

6.1.2 Assessing bactericidal activity of meropenem and taniborbactam combinations on meropenem-resistant *E. coli* strain using a time-kill assay

A time-kill assay was performed to evaluate the bactericidal efficacy of meropenem and taniborbactam combinations and to determine the optimal concentrations for subsequent metabolomics studies. The proposed experiment aimed to identify drug concentrations that induced metabolic stress in treated bacteria but did not kill bacterial cells directly, ensuring the availability of viable cells for downstream metabolomics analysis.

The time-kill assay involved exposing a meropenem-resistant *E. coli* strain to varying concentrations of meropenem and taniborbactam. Time points were taken at T=0, T=1, T=2, T=3, T=4, T=5, and T=6 hours post-exposure. CFUs were determined by plating diluted aliquots on nutrient agar and incubating at 37 °C for 24 hours. The results were recorded as average colony counts from two biological replicates, and the standard deviation was calculated to assess variability.

At higher drug concentrations, specifically 32 μg/mL meropenem combined with either 4 μg/mL or 6 μg/mL taniborbactam, bacterial survival was minimal. A single colony was observed at T=0 in one of the replicates for both conditions, averaging 0.5 colonies, but no colonies were detected at subsequent time points (T=1 to T=6). The combination of 32 μg/mL meropenem with 8 μg/mL taniborbactam was completely bactericidal, with no colonies detected at any time points, including T=0. These findings indicated that the combination was too bactericidal to maintain bacterial viability.

Moderate concentrations, such as 8 μg/mL meropenem combined with 6 μg/mL or 4 μg/mL taniborbactam, allowed for more gradual decline in colony counts, as shown in **Figure 6.3**. Between the two conditions, the combination with 6 μg/mL taniborbactam exhibited slightly faster bacterial clearance. Despite their bactericidal activity, the lack of substantial bacterial death at earlier time points suggests they may not be ideal for inducing detectable metabolic changes for downstream analyses.

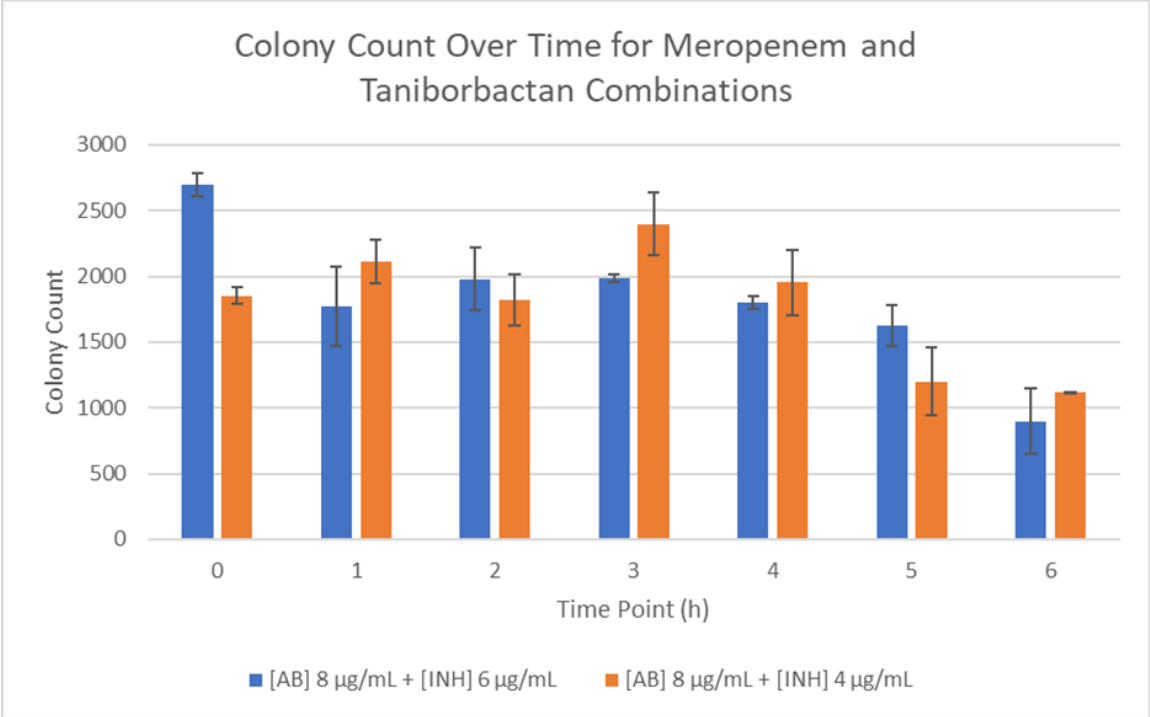

Figure 6.3 Colony count of meropenem-resistant* E. coli *strain at varying time point and concentration of meropenem [AB]+taniborbactam [INH]. *Samples were collected at time points, 0h, 1 h, 2 h, 3 h, 4 h, 5 h, and 6h. Combination of 8 µg/mL AB and 6 µg/mL INH, and 8 µg/mL AB and 4 µg/mL INH was tested. Bars represent the mean of two biological replicates (n=2); vertical lines indicate the range.*

The combination of 2 µg/mL meropenem with 16 µg/mL taniborbactam demonstrated balanced bactericidal activity, as shown in **Figure 6.4**. Colony counts substantially declined by T=3 and T=5, but bacterial survival was evident at earlier time points. Therefore, 2 µg/mL meropenem and 16 µg/mL taniborbactam combination was deemed suitable for subsequent metabolomics experiments, as it ensured sufficient bacterial exposure to antibiotics while maintaining viability for analysis.

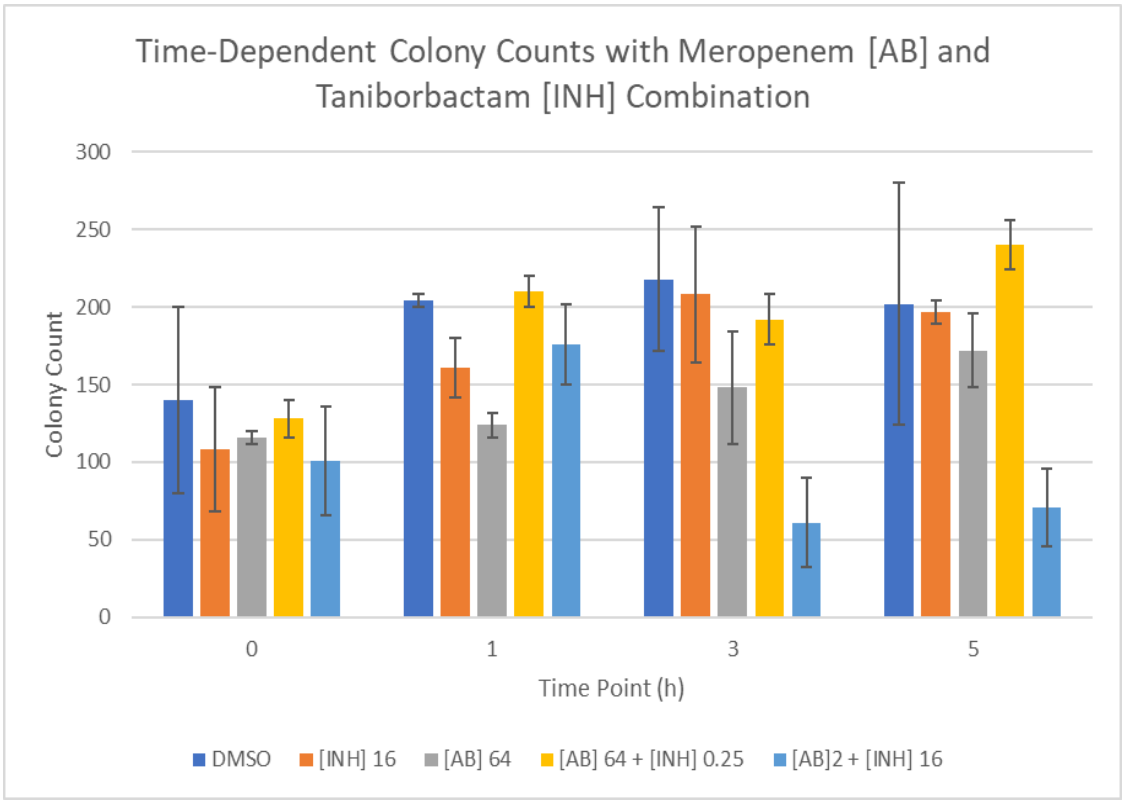

Figure 6.4 colony counts of meropenem-resistant* E. coli *strains at varying time points and DMSO, taniborbactam [INH], meropenem [AB], and combination [AB+INH]. *Samples were taken at 0 h, 1 h, 3 h, and 5 h for each treatment; DMSO, INH 16 µg/mL, AB 64 µg/mL, combination with 64 µg/mL AB and 0.25 µg/mL INH, and combination with 2 µg/mL AB and 16 µg/mL INH. Bars represent the mean of two biological replicates (n=2); vertical lines indicate the range.*

The results from the time-kill assay highlighted the concentration-dependent bactericidal effects of meropenem and taniborbactam combinations on the meropenem-resistant *E. coli* strain. Higher concentrations, such as 32 µg/mL meropenem with 6 µg/mL taniborbactam, were too bactericidal for metabolomics studies, whereas moderate concentrations were less effective at providing the necessary metabolic stress. The combination of 2 µg/mL meropenem with 16 µg/mL taniborbactam provided the optimal balance, exposing bacteria to antibiotic stress while maintaining their viability. The results of the experiment underscored the importance of optimizing drug concentrations to achieve the objectives of exerting sufficient antibiotic effect while maintaining bacterial viability for meaningful metabolic profiling under experimental conditions.

6.1.3 Metabolic effects of taniborbactam treatment

Taniborbactam, a β-lactamase inhibitor (INH) with potent activity against NDM-mediated carbapenem resistance, has been shown to restore the efficacy of carbapenem antibiotics (AB) like meropenem.[498] While its enzymatic role in inhibiting β-lactamase activity is well-established, its potential to alter bacterial metabolism or uncover metabolic vulnerabilities remains unexplored. Understanding whether taniborbactam, either alone or in combination with meropenem (AB+INH), perturbs bacterial metabolic pathways is of relevance as it provides insights into potential combination therapy mechanisms and could inform strategies aimed at enhancing treatment efficacy and helping to overcome antibiotic resistance.

Next, in order to investigate the metabolic effects of taniborbactam treatment, separate batches of OD_{600} 0.4 *E. coli* were treated with either 16 μg/mL taniborbactam, meropenem at 2 μg/mL, or their combination (2 μg/mL meropenem + 16 μg/mL taniborbactam; AB+INH) for 1-hour. Each of the three *E. coli* strains with differing resistance phenotypes: wild-type (E), meropenem-susceptible (S), and meropenem-resistant (R) were treated. Metabolites were extracted using the method developed in Chapter 3 and untargeted metabolomic profiling using AEC-MS was performed to investigate global and pathway-specific metabolic changes associated with treatment.

To identify trends and significant differences, multivariate statistical analyses, including PCA and hierarchical clustering, were applied to assess global metabolic patterns. Univariate analyses were conducted to determine significant alterations in individual metabolite abundances. Comparisons were made between treated and vehicle control samples, as well as between antibiotic-only, and combination treatments, to determine whether taniborbactam treatment induced distinct metabolic changes or highlighted synergistic metabolic effects when combined with meropenem. This investigation aimed to provide a systematic analysis of the metabolic landscape following taniborbactam exposure, in order to provide insights into potential role of the drug in disrupting bacterial metabolism.

6.1.3.1 Data quality and overview of metabolic profiles

AEC-MS data quality was initially assessed. Inter-sample and inter-group variability were visualised using an unclustered heatmap of compound-features and the un-supervised clustering of experimental groups via a PCA scores plot of normalised metabolite abundances. The unclustered heatmap (**Figure 6.5**) provided an overview of normalised metabolite abundances across all samples, showing no substantial sample to sample variability or class bias across biological replicates. Signal intensities were generally uniform across treatment groups, although a slight variability between samples was observed compared to some other experiments. Such variability, while present, was not deemed prohibitive for downstream analysis, as it did not interfere with the ability to detect treatment-specific effects. The balanced colour distribution, indicative of uniform abundances, across conditions suggested appropriate normalisation, ensuring that treatment-specific effects were not masked by excessive variability or bias in the dataset.

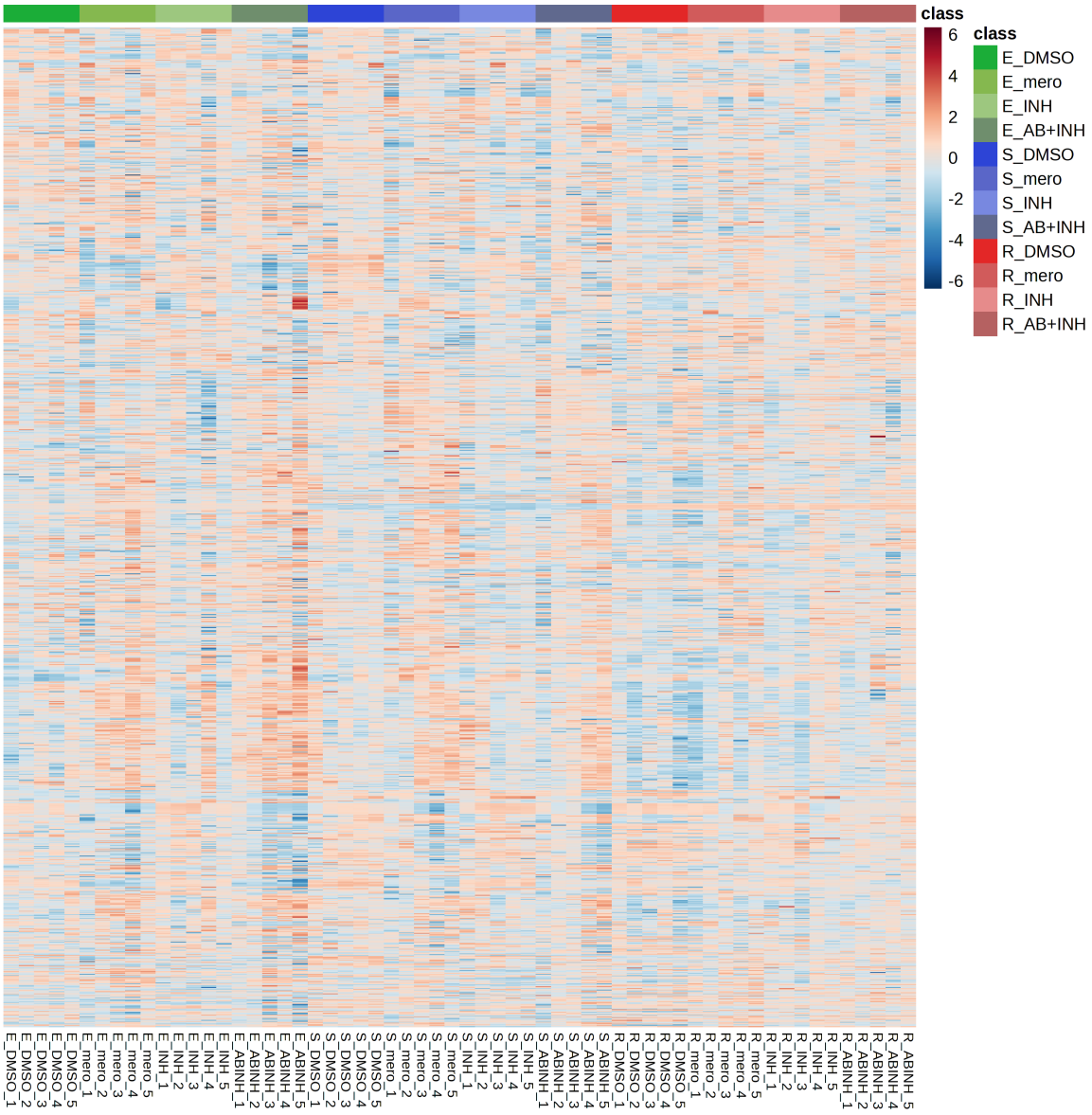

Figure 6.5 Unclustered heatmap of normalised metabolite abundances across* E. coli *strains and treatments. *Rows represent individual metabolites, and columns correspond to biological replicates under each treatment conditions (n=5): DMSO (vehicle control), meropenem (mero), taniborbactam (INH), and combination therapy (AB+INH). Metabolite abundances are scaled (z-scores) and visualised in a gradient from blue (low abundance) to red (high abundance).*

The PCA scores plot (**Figure 6.6**) provided an overview of how experimental groups clustered relative to each other and their similarity and differences in metabolomic profiles across *E. coli* strains (E, S, and R) and treatment conditions (vehicle control, meropenem, taniborbactam, and combination therapy). Consistent with findings in Chapters 3 and 4, the meropenem-resistant strain (R) formed a distinct cluster that separated clearly from the wild-type (E) and meropenem-susceptible (S) strains along PC1, explaining 30.2% of the total variance. In contrast, the E and S strains displayed considerable overlap, indicating similar metabolic profiles.

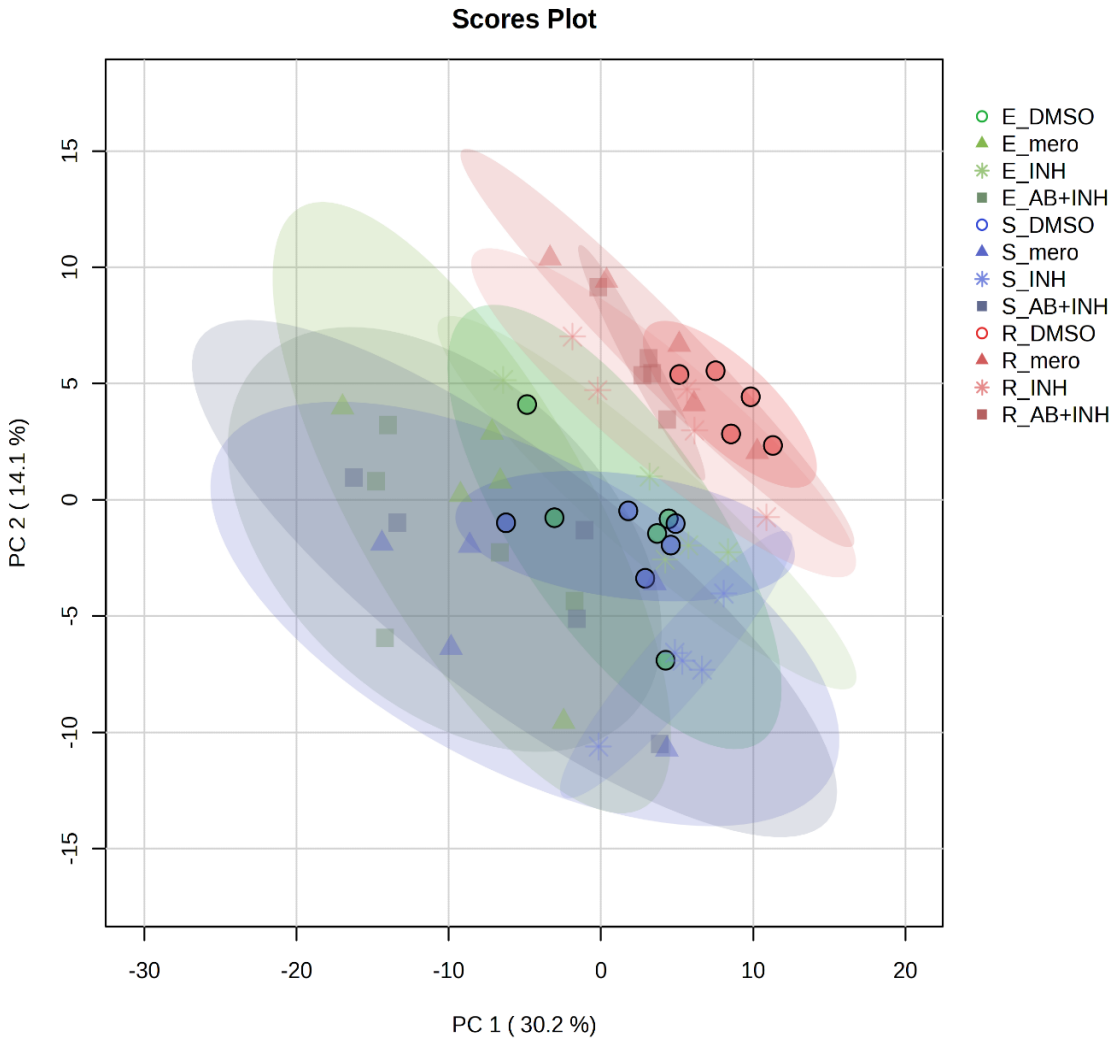

Figure 6.6 PCA scores plot of metabolomic data across* E. coli *strains and treatments. *Points represent biological replicates (n=5) of wild-type (E), meropenem-susceptible (S), and meropenem-resistant (R)* E. coli *strains treated with DMSO (vehicle control), meropenem (mero), taniborbactam (INH), and combination therapy (AB+INH). Ellipses represent 95% confidence intervals.*

To investigate metabolic differences between group in more detail, PCA plots were generated for individual strains for each of the different treatments (**Figure 6.7**-**Figure 6.9**). For the wild-type strain (E) (**Figure 6.7**), the PCA plot showed clustering of treatment groups, with partial overlap observed between taniborbactam (INH) and vehicle control as well as between meropenem (mero) and combination therapy (AB+INH). These results indicated that while the treatments resulted in some degree of separation, the profiles for taniborbactam treated samples were closer to vehicle controls, whereas meropenem and combination therapy exhibited greater similarity to each other as expected.

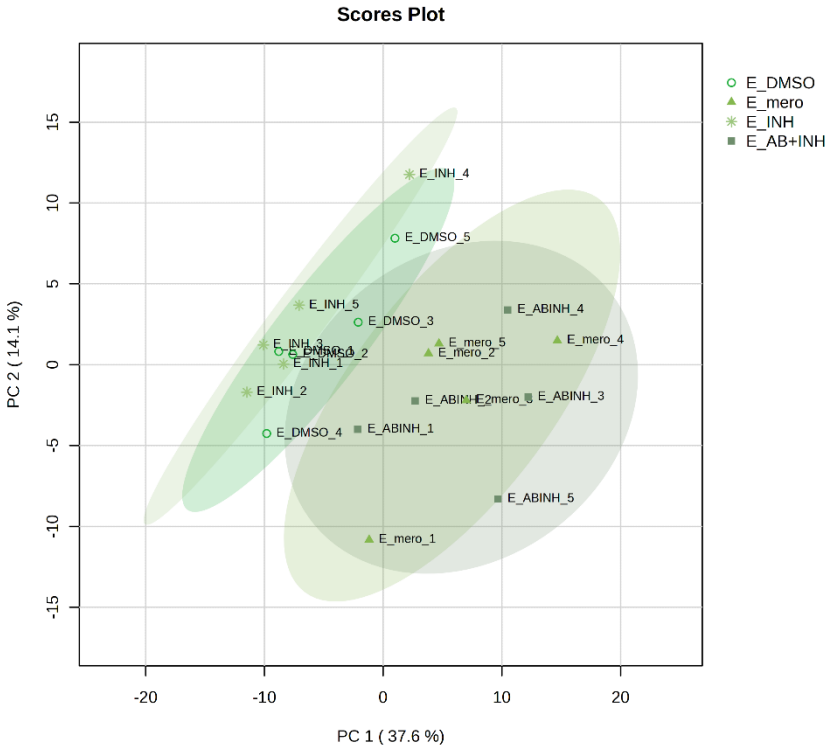

Figure 6.7 PCA scores plot of the wild-type strain (E) under different treatment conditions. *Biological replicates (n=5) of the wild-type strain treated with DMSO (vehicle control), meropenem (mero), taniborbactam (INH), and combination therapy (AB+INH) are shown.*

For experiments with the meropenem-susceptible strain (S) (**Figure 6.8**), the PCA plot showed clustering of treatment groups with partial overlap between vehicle control and taniborbactam (INH) again. The taniborbactam treated samples also displayed slight overlap with both meropenem (mero) and combination therapy (AB+INH), while the meropenem and combination therapy groups exhibited considerable overlap with each other. The vehicle control group remained tightly clustered, indicating lower variability within the vehicle control samples. In contrast, meropenem and combination therapy displayed greater spread, with some degree of separation from vehicle control, suggesting a treatment-associated response within this strain.

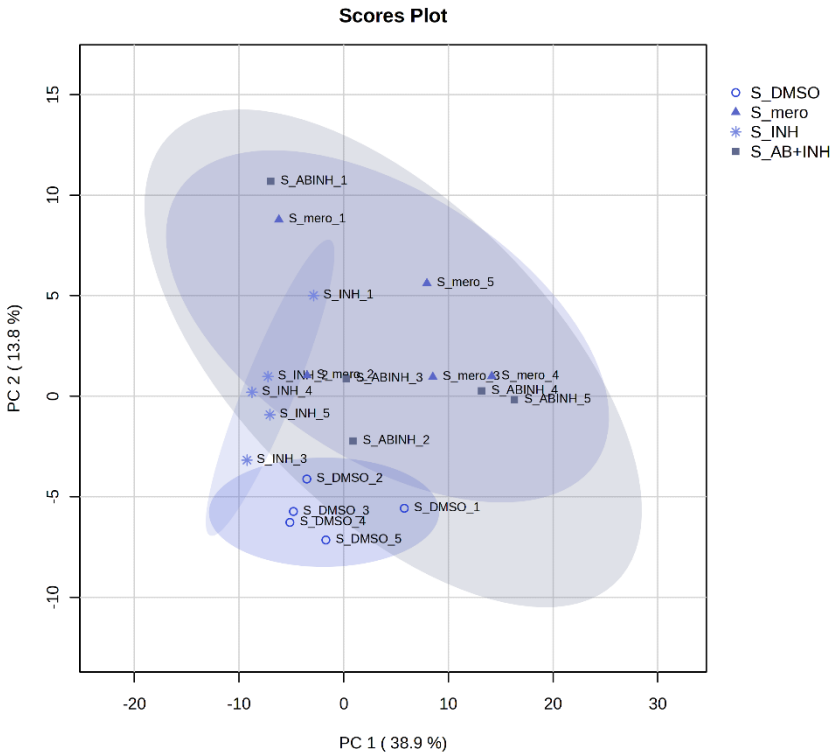

Figure 6.8 PCA scores plot of the meropenem-susceptible strain (S) under different treatment conditions. *Biological replicates (n=5) of the susceptible strain treated with DMSO (vehicle control), meropenem (mero), taniborbactam (INH), and combination therapy (AB+INH) are displayed.*

For the meropenem-resistant strain (R) (**Figure 6.9**), the PCA plot showed substantial overlap among treatment groups. Taniborbactam treated (R_INH) overlapped with the vehicle control (R_DMSO), as well as with the meropenem treated (R_mero) and combination therapy (R_AB_INH). However, the combination therapy displayed separation from vehicle control but remained largely overlapping with meropenem and taniborbactam, indicating minimal distinction in the metabolic profiles among treatments.

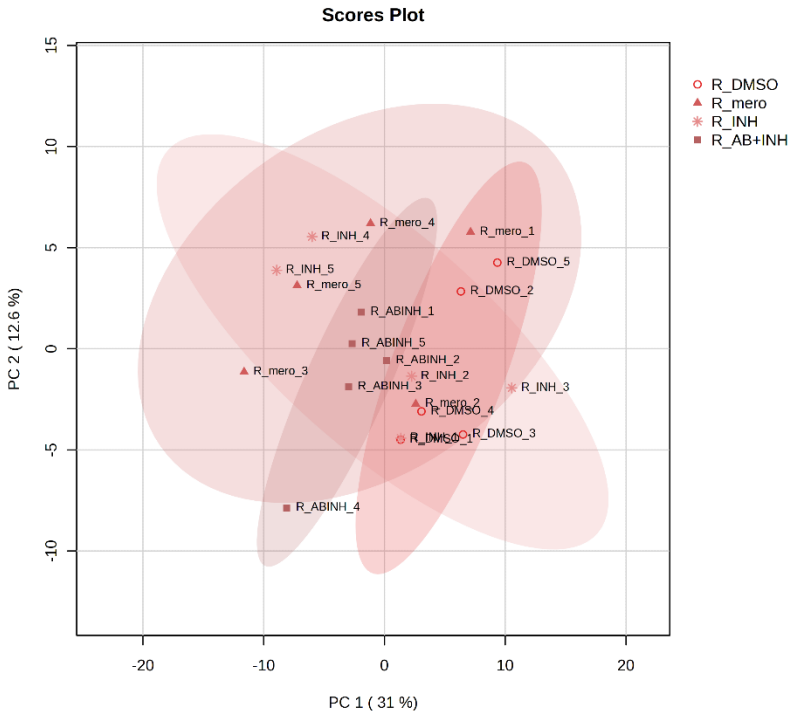

Figure 6.9 PCA scores plot of meropenem-resistant strain (R) under all treatment conditions. *Combination therapy (R_AB+INH) shows partial separation from vehicle controls (R_DMSO) and overlaps with meropenem treatment (R_mero), (suggesting antibiotic-driven metabolic responses). Each conditions had 5 biological replicates.*

6.1.3.1.1 Data quality conclusion

Collectively, unclustered heatmap and the PCA plots provided an overview of metabolic variance and confirmed the quality of the metabolomic data across *E. coli* strains and treatment conditions, as evidenced by the consistent clustering of biological replicates within each treatment group and minimal variability within the vehicle control samples (DMSO). The reproducibility across replicates highlighted suitable data acquisition and normalisation.

The analyses further suggested that taniborbactam did not induce significant metabolic changes. Across all strains, the taniborbactam treated samples closely overlapped with the vehicle controls, indicating a minimal metabolic response to taniborbactam itself. Similarly, meropenem and combination therapy responses appeared similar to one another. These observations indicated that the metabolic effects of taniborbactam were negligible compared to the changes induced by meropenem treatment.

6.1.3.2 Significantly altered metabolites and compound features across treatments

To explore whether taniborbactam induced metabolic changes that could signal increased susceptibility of the meropenem-resistant (R) strain to meropenem by inhibiting the NDM-7 enzyme, univariate statistical analysis (ANOVA) was performed. The vehicle control (DMSO), meropenem (mero), and combination therapy (AB+INH) treatment conditions on the R strain was analysed. A total of 12 significantly altered compound features were identified, as shown in **Table 6.1**. The aim was to investigate metabolic responses specific to these treatment conditions and to determine whether the combination therapy with taniborbactam and meropenem led to distinct metabolic changes compared to meropenem alone. The comparison focused on identifying key metabolites that might reflect increased susceptibility due to inhibition of the NDM-7 enzyme.

Table 6.1 Significantly altered compound features identified by ANOVA in the meropenem-resistant (R) strain under different treatment conditions. *The treatments included vehicle control (DMSO), meropenem (mero), and combination therapy (AB+INH). The table lists the compound names,* m/z *values, f-values, p-values, false discovery rates (FDR), and associated post-hoc tests indicating pairwise comparisons where significant differences were observed.*

Name	f.value	p.value	-log10(p)	FDR	Post-hoc tests
17.82_338.5448m/z	48.274	1.8254E-6	5.7386	0.0071592	R_DMSO - R_AB+INH; R_mero - R_AB+INH
6.19_186.1137m/z	44.345	2.8654E-6	5.5428	0.0071592	R_AB+INH - R_DMSO; R_AB+INH - R_mero; R_DMSO - R_mero
1-Deoxy-D-xylulose 5-phosphate	34.058	1.1291E-5	4.9473	0.017874	R_AB+INH - R_DMSO; R_mero - R_DMSO
17.82_225.3604m/z	32.49	1.4349E-5	4.8432	0.017874	R_DMSO - R_AB+INH; R_mero - R_AB+INH
Beta-Alanine	31.046	1.805E-5	4.7435	0.017874	R_DMSO - R_AB+INH; R_mero - R_AB+INH; R_DMSO - R_mero
9.03_390.0814m/z	29.992	2.1461E-5	4.6683	0.017874	R_AB+INH - R_DMSO; R_mero - R_DMSO
9.76_243.0278m/z	25.545	4.735E-5	4.3247	0.031783	R_AB+INH - R_DMSO; R_mero - R_DMSO
19.36_460.0178m/z	25.169	5.0883E-5	4.2934	0.031783	R_DMSO - R_AB+INH; R_DMSO - R_mero
17.69_319.0136m/z	23.786	6.6804E-5	4.1752	0.037091	R_DMSO - R_AB+INH; R_DMSO - R_mero
5-Hydroxyhexanoic acid	22.823	8.1369E-5	4.0895	0.038621	R_DMSO - R_AB+INH; R_mero - R_AB+INH; R_DMSO - R_mero
2-Aminoisobutyric acid	22.613	8.5018E-5	4.0705	0.038621	R_AB+INH - R_DMSO; R_mero - R_DMSO
N-Acetyl-aspartate	21.927	9.8345E-5	4.0072	0.040953	R_AB+INH - R_DMSO; R_mero - R_AB+INH; R_mero - R_DMSO

Box plots of the significantly altered compound features are shown in **Figure 6.10**. Metabolites such as *N*-acetyl-aspartate, which increased under meropenem treatment, were significantly reduced when taniborbactam was added, suggesting a potential reversal of resistance-associated metabolic perturbations. Similarly, 6.19_186.1137 *m/z* which decreased under meropenem treatment, increased beyond vehicle control levels with combination

therapy, suggesting a distinct metabolic effect of taniborbactam in combination with meropenem. In contrast, metabolites like 1-deoxy-D-xylulose 5-phosphate were elevated in both meropenem and combination treatments compared to vehicle control, suggesting this change was primarily driven by meropenem, with minimal contribution from taniborbactam. The observed trends in beta-alanine and 5-hydroxyhexanoic acid, which progressively decreased across vehicle control, meropenem, and combination treatments, highlighting their potential involvement in pathways modulated by both drugs. Conversely, 2-aminoisobutyric acid exhibited an opposite trend, increasing significantly under the combination therapy.

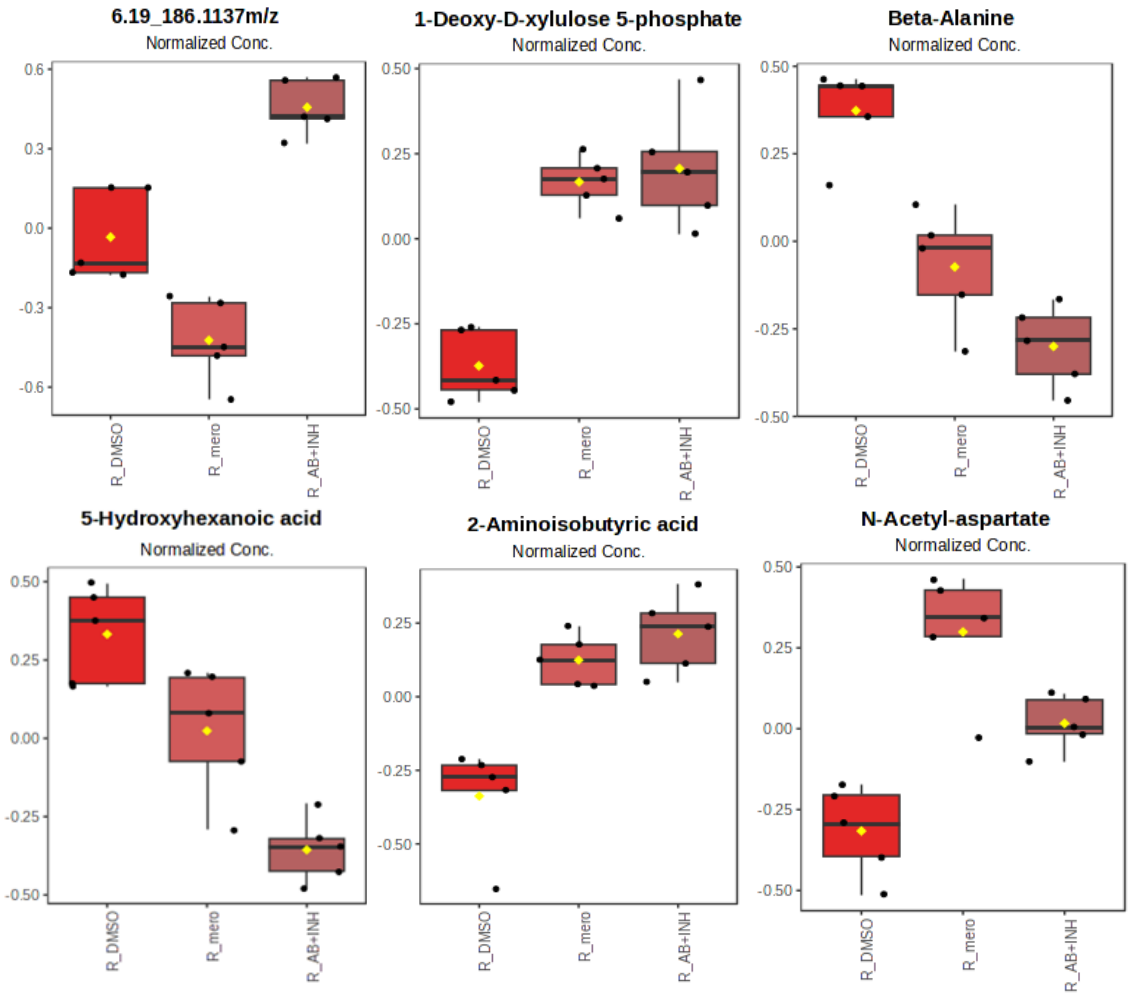

Figure 6.10 Box plots of significantly altered compound features across meropenem-resistant (R) strains treated with vehicle control (DMSO), meropenem (mero), and combination therapy (AB+INH). *Each box plot represents normalized concentrations of individual metabolites, highlighting their relative abundance across treatments. Yellow dots represent the mean values for each treatment group.*

Collectively, these findings suggest that taniborbactam exerts some effects on the metabolic profiles of the meropenem-resistant (R) strain when combined with meropenem, compared to meropenem alone. These effects likely reflect the role of taniborbactam in restoring susceptibility to meropenem by counteracting resistance mechanisms.

To further explore treatment-associated metabolic changes, binary comparisons were performed across all strains. Pairwise comparisons of all detected features revealed no significant differences between vehicle control and taniborbactam (INH) treatments, or between meropenem treatment (mero) and combination therapy (AB+INH) in the susceptible and wild-type strains. As no features met the significance thresholds (fold change > 2 and FDR corrected p value < 0.05), it was evident that the addition of taniborbactam did not result in measurable metabolic changes in these *E. coli* strains. Even when the fold-change threshold was reduced to 1.2, the differenced remained minimal, in the E strain only one feature was upregulated, and in the S strain there were just two upregulated and two downregulated features. The consistency across thresholds further supports the conclusion that taniborbactam did not induce substantial metabolic changes in these strains under these experimental conditions.

Similarly, comparing meropenem-resistant vehicle control (R_DMSO) and the taniborbactam-treated group (R_INH) also did not reveal any significant changes in metabolite abundance at fold change > 2 and FDR corrected p value < 0.05 threshold, nor at FC > 1.2 threshold. Collectively, these observations demonstrate that taniborbactam treatment of *E. coli* in the absence of antibiotic did not elicit a measurable metabolic effect, even in the meropenem-resistant strain.

These findings aligned with expectations, as taniborbactam is a β-lactamase inhibitor, targeting a specific enzyme not known to be involved in metabolic processes. Function of the enzyme is to restore the efficacy of β-lactam antibiotics rather than to directly perturb bacterial metabolism. Its mechanisms of action primarily target enzymatic activity associated with antibiotic breakdown and not endogenous metabolic pathways. Therefore, the lack of

significant metabolic changes under taniborbactam treatment was consistent with its intended pharmacological function and leading to the conclusion that no measurable 'off-target' metabolic effects were identified.

Next a meropenem-resistant strain was compared under meropenem treatment (R_mero) compared to combination therapy (R_AB+INH). A single significantly upregulated compound-feature was identified, as highlighted in the volcano plot (**Figure 6.11**), with the corresponding box plot showing its relative abundance across two conditions. The result remained consistent even when the fold-change threshold was lowered to 1.5, reinforcing the minimal metabolic impact of combination therapy compared to meropenem treatment. Most features (1124 in total) showed no significant differences, suggesting majority of metabolites are not directly affected by treatment and reflect baseline metabolic processes. However, the minimal number of altered features under combination therapy in the meropenem-resistant strain is notable and suggests that taniborbactam, while effective in restoring susceptibility and reducing MIC, did not result in significant metabolic changes under the experimental conditions. The result was somewhat unexpected, as a greater number of metabolic alterations were anticipated given the impact of taniborbactam on bacterial growth and resistance mechanisms.

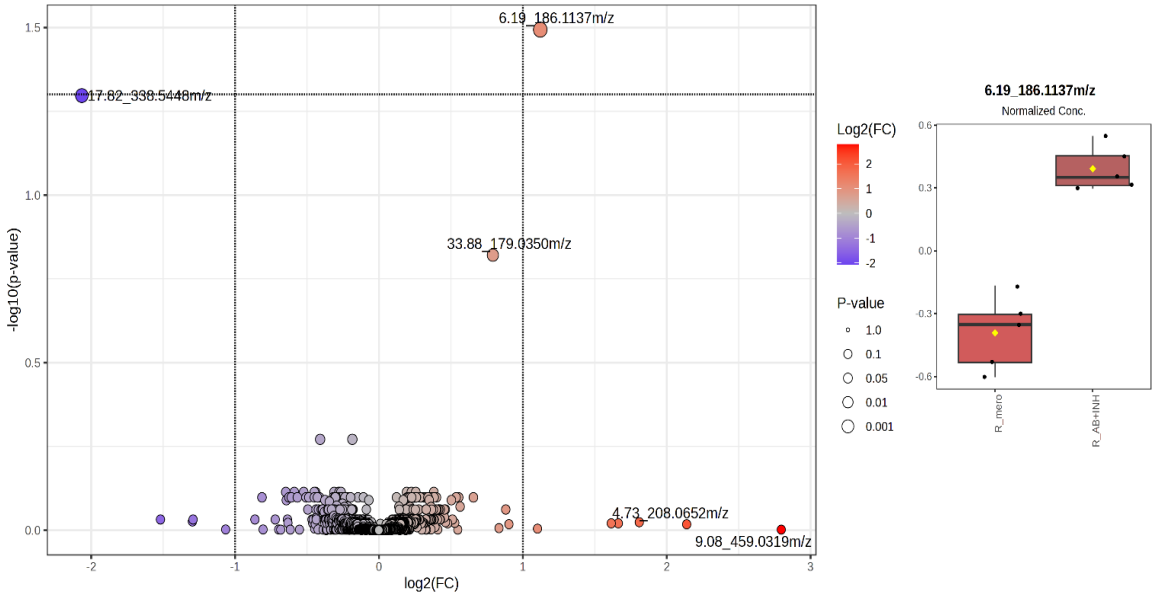

Figure 6.11 Volcano plot of metabolite changes in resistant strains comparing meropenem treatment (R_mero) and combination therapy (R_AB+INH). *The single significantly upregulated metabolite (log2FC > 2, FDR < 0.05) is indicated, with boxplot showing its relative abundance across the two conditions.*

Overall, univariate analysis demonstrated that taniborbactam treatment, either alone or in combination with meropenem, did not induce significant changes in the metabolic profiles of *E. coli* strains. These results suggests that taniborbactam exerted its primary effect through enzymatic inhibition of β-lactamases without widespread metabolic disruption.

It is important to acknowledge that no direct evidence of intracellular drug presence was obtained in this study, as the presence of taniborbactam was administered in a stable form at a known concentration, it remains unverified how effectively it penetrated bacterial cells under the experimental conditions. No evidence of intact taniborbactam was in the AEC-MS/MS data, likely because it did not produce a strong enough anion to be resolved chromatographically. Furthermore, the metabolomic approach employed in this study primarily captures highly polar and ionic metabolites. While no significant metabolic changes were observed, it remains possible that alterations in low-or moderately polar metabolites, which were less effectively detected by AEC-MS/MS, could still occur.

The cells were treated with various conditions (vehicle control, taniborbactam, meropenem, and combination) for 1-hour, a time point selected based on preliminary experiments demonstrating that this duration was sufficient to exert metabolic stress without inducing cell death across the strains (**Section 4.2.2**). The 1-hour treatment window was chosen purposefully to ensured that metabolic changes observed were representative of active physiological responses to the drugs rather than secondary effects of cell lysis or viability loss. Furthermore, results from the time-kill experiments indicated that the combination of 16 μg/mL taniborbactam and 2 μg/mL meropenem was sufficient to reduce colony counts in the resistant strain, showing its potency at higher concentrations.

6.1.3.3 Meropenem-driven metabolic alterations and limited impact of taniborbactam in E. coli *strains*

To investigate the metabolic profiles of *E. coli* strains under different treatment conditions, multivariate analyses were performed initially to assess whether patterns associated with metabolite changes showed treatment-specific trends. While previous results suggested minimal metabolic response to taniborbactam treatments, multivariate approaches may provide insights into more subtle patterns present in the data which were not identified by univariate analysis.

Despite a lack of significantly altered identified metabolites in the univariate analyses described previously, a hierarchically-clustered heatmap of the top 50 compound-features (***Figure 6.12***) revealed distinct trends and correlations in compound-feature abundance changes between experimental groups in the untargeted dataset. In the meropenem-resistant strain (R), samples treated with combination therapy (R_AB+INH) displayed separation from vehicle control (R_DMSO) but overlapped substantially with meropenem-treated samples (R_mero). The clustering suggested that the metabolic response to the combination therapy was primarily driven by meropenem, with taniborbactam contributing minimally to further metabolic change. In contrast, taniborbactam treatment alone (R_INH) did not induce

measurable metabolic changes, as these samples clustered closely with the vehicle control treated group (R_DMSO).

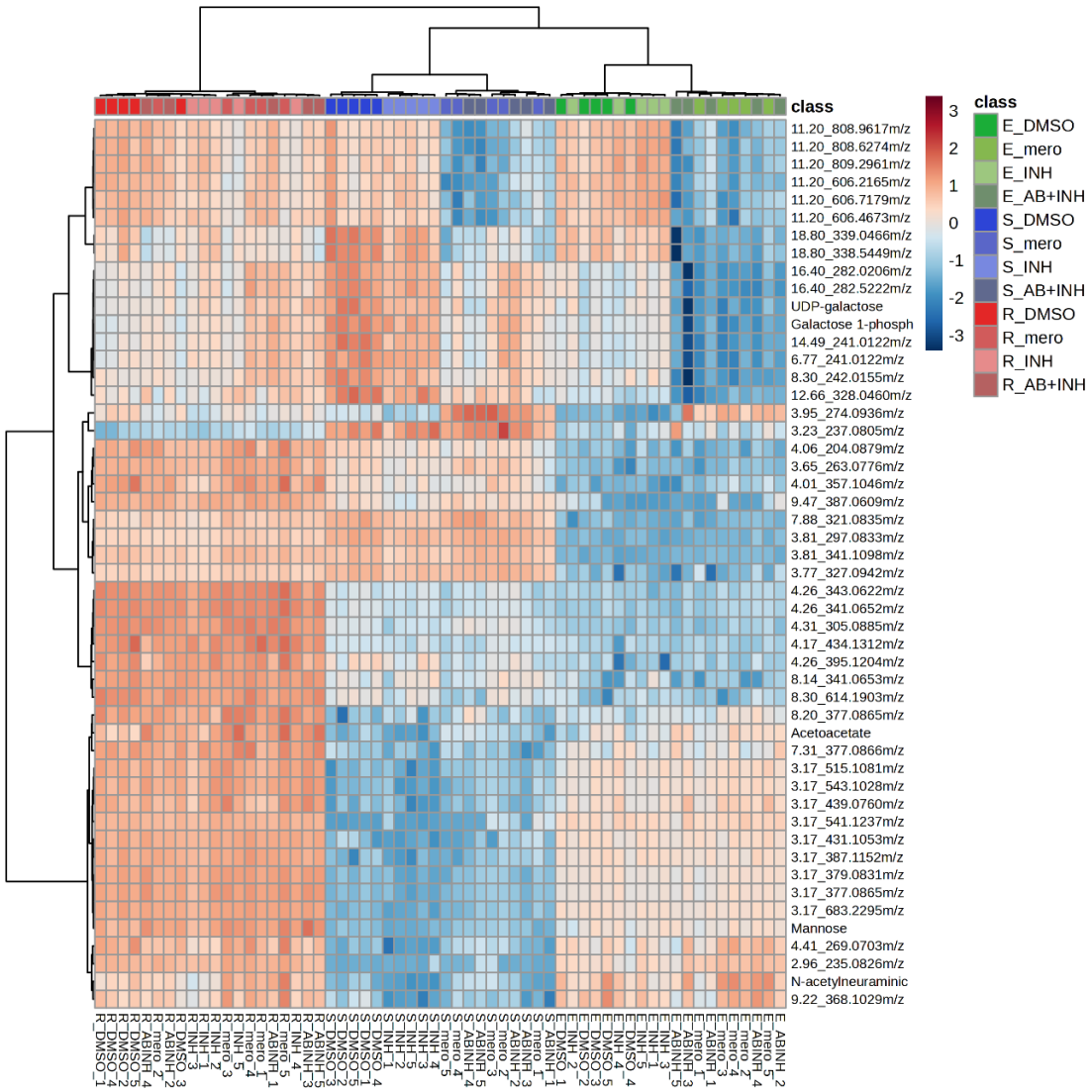

Figure 6.12 Clustered heatmap of Top 50 compound features across* E. coli *strains and treatment conditions. *The heatmap displays the top 50 compound features derived from metabolomic analysis of* E. coli *strains (E: wild type; S: susceptible with pCR2.1; R: resistant with pCR2.1 carrying NDM-7) under different treatment conditions, including DMSO (control), meropenem (mero), taniborbactam (INH), and their combination (AB+INH). Rows represent compound features identified by their* m/z *values, while columns represent individual samples, clustered by hierarchical similarity. The colour scale indicates the relative abundance of each compound feature, ranging from high abundance (red, +3) to low abundance (blue, −3), normalized and auto scaled across all samples. Distinct clustering patterns highlight metabolic differences between strains and treatments, emphasizing the impact of antibiotic and inhibitor combinations on the metabolic profile. Replicates for each condition are labelled for clarity.*

Samples treated with taniborbactam (S_INH and E_INH) clustered closely with their respective vehicle controls, suggesting minimal metabolic perturbation was induced by the inhibitor (taniborbactam). The combination therapy group in these strains also remained indistinguishable from meropenem-treated samples, reinforcing the idea that the observed metabolic effects were primarily driven by meropenem exposure rather than taniborbactam.

Overall, the clustered heatmap highlights subtle but distinct metabolic trends across experimental groups. Taniborbactam treatment alone did not induce notable changes in the metabolic profiles of each *E. coli* strain, regardless of resistance phenotype. Combination therapy resulted in metabolic responses that were largely similar to meropenem treatment, suggesting that any differences between vehicle control/INH-treated and mero/combination-treated groups were driven predominantly by meropenem.

6.1.3.4 Pathway perturbations in the meropenem-resistant strain under combination therapy

Functional pathway analysis was performed to investigate whether any metabolic pathway perturbations resulting from taniborbactam treatment, either alone or in combination with meropenem. Comparisons were focused on the meropenem-resistant (R) strain to determine whether combination therapy (R_AB+INH) induced metabolic effects beyond those caused by meropenem alone (R_mero), as the meropenem-resistant strain harbours the NDM-7 gene and represents the primary target for taniborbactam's β-lactamase inhibition.

Functional analysis comparing the meropenem-treated R strain (R_mero) and the combination therapy group (R_AB+INH) revealed no significant differences in pathway-level perturbations. The observation aligned with the findings from the multivariate and univariate analyses, which demonstrated minimal metabolite-level changes under combination therapy compared to meropenem treatment alone.

In contrast, when comparing the vehicle control group (R_DMSO) to the meropenem treated (R_mero) significant pathway enrichment was observed (**Figure 6.13**), such as pentose phosphate pathway, lipopolysaccharide biosynthesis, galactose metabolism, pentose and glucuronate interconversions, and peptidoglycan biosynthesis.

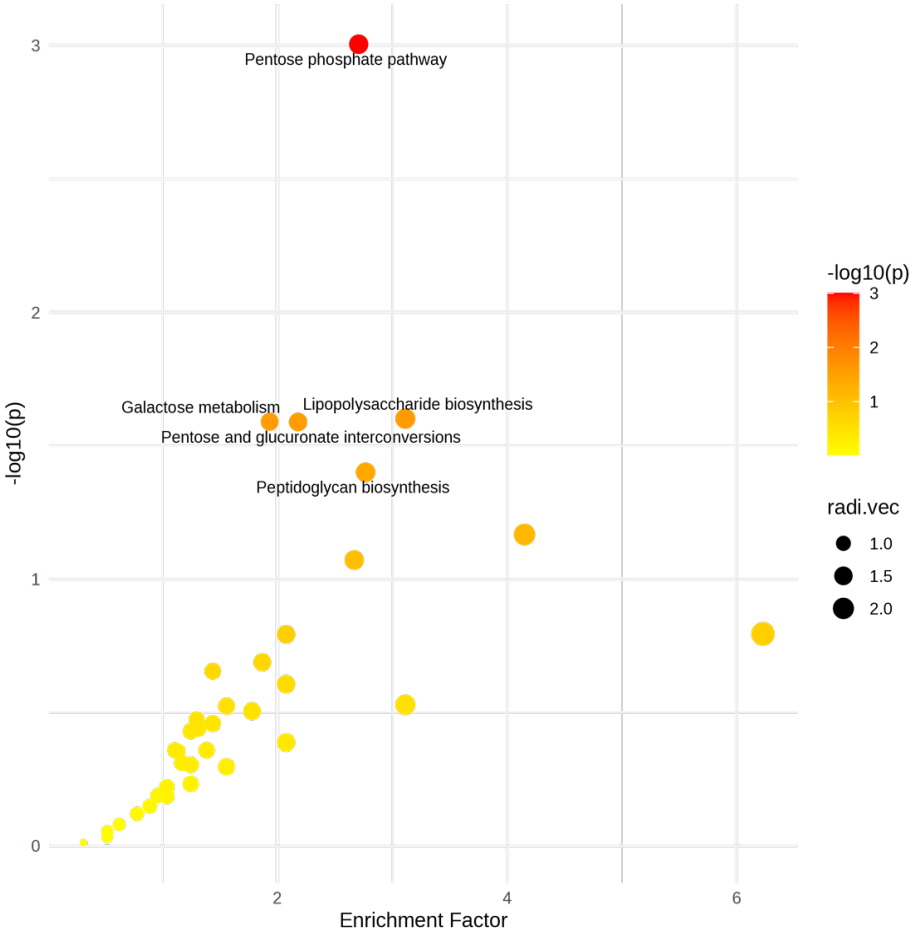

Pathway Name	Total↑↓	Hits(all)↑↓	Hits(sig.)↑↓	Expected↑↓	P(Fisher)↑↓	P(Gamma)↑↓
Pentose phosphate pathway	26	18	14	3.6934	9.8721E-4	0.001039
Lipopolysaccharide biosynthesis	46	9	8	1.2847	0.025028	0.0011379
Galactose metabolism	39	32	8	4.6569	0.025697	0.0011408
Pentose and glucuronate interconversions	38	29	11	3.2117	0.02577	0.0011411
Peptidoglycan biosynthesis	18	7	4	1.4453	0.039774	0.0012034
Phosphate and phosphinate metabolism	8	3	2	0.48175	0.068069	0.0013403
D-Amino acid metabolism	25	10	5	1.1241	0.084822	0.001429
Selenocompound metabolism	15	1	1	0.16058	0.16058	0.0019148
Ascorbate and aldarate metabolism	20	10	4	1.4453	0.16116	0.0019191
beta-Alanine metabolism	13	5	2	1.4453	0.16116	0.0019191
Folate biosynthesis	38	7	3	1.6058	0.20513	0.0022796
Amino sugar and nucleotide sugar metabolism	44	28	12	4.1752	0.22143	0.002431
Acarbose and validamycin biosynthesis	3	2	1	0.9635	0.24773	0.0026982
Novobiocin biosynthesis	3	1	1	0.32117	0.29587	0.0032722

Figure 6.13 Functional analysis comparing meropenem-resistant strains treated with DMSO (R_DMSO) and meropenem (R_mero). *The scatter plot visualizes pathway enrichment analysis results, with each point representing a metabolic pathway. The x-axis denotes the pathway impact score, which measures the contribution of identified metabolites to the pathway, while the y-axis represents -log10(p-value), indicating the statistical significance of pathway enrichment. Larger circles correspond to higher pathway impact scores, and the colour gradient from yellow to red reflects the significance level, with red indicating more significant pathways (lower p-values). The accompanying table provides details about each pathway, including the total number of compounds associated with the pathway, the number of compound features detected in the dataset (Hits all), and the subset of features that are significantly altered (Hits Sig.) with an FDR-corrected p-value < 0.05. The table also includes the expected number of features for each pathway based on random distribution (Expected), the Fisher's exact test p-value for pathway enrichment (pFisher), and the gamma-adjusted p-value to account for multiple testing (pGamma).*

Similarly, the comparison between the vehicle control group (R_DMSO) and the combination therapy group (R_AB+INH) revealed enrichment of a wide range of pathways (**Figure 6.14**), including peptidoglycan biosynthesis, O-antigen nucleotide sugar biosynthesis, glycolysis/gluconeogenesis, and fructose and mannose metabolism. These pathways predicted functional changes in metabolism resulting from combination therapy compared to vehicle control. With peptidoglycan biosynthesis displaying the highest impact and statistical significance. The result was consistent with the known mode of action of meropenem which targets bacterial cell wall synthesis, whilst taniborbactam inhibits metallo-β-lactamase activity, thereby restoring meropenem efficacy.[499,503]

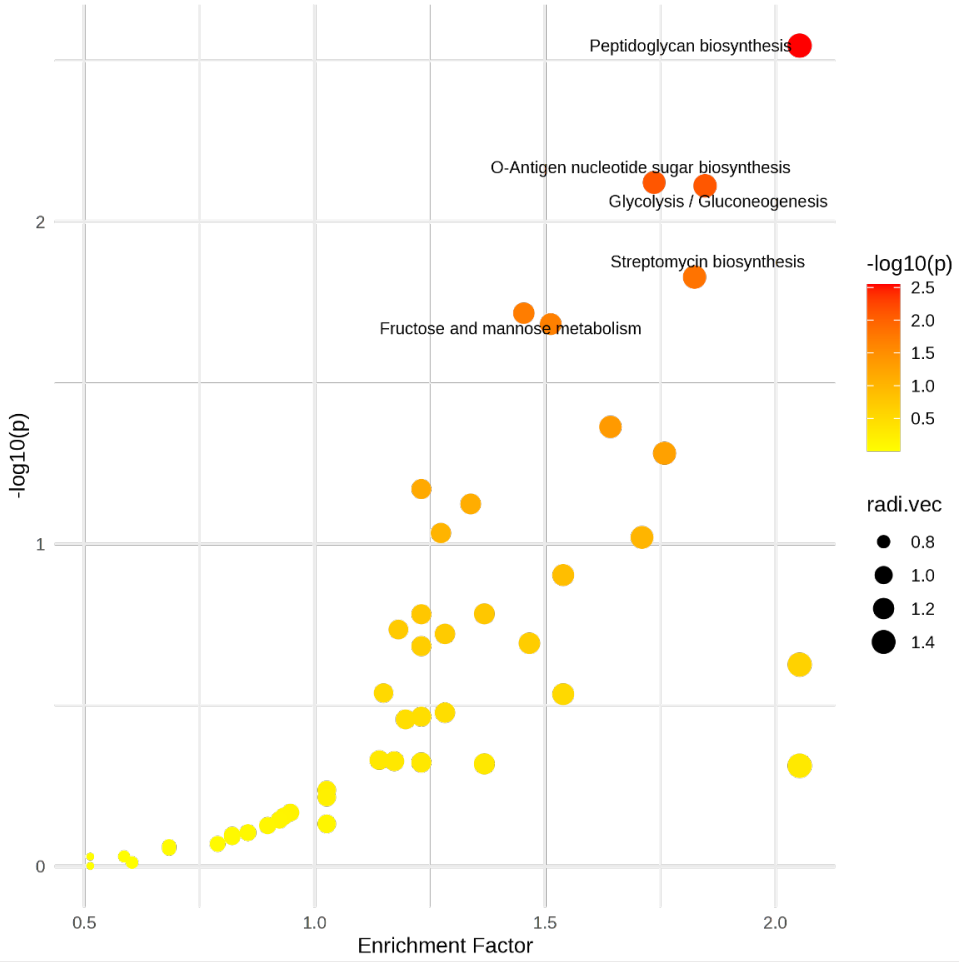

Pathway Name	Total↑↓	Hits(all)↑↓	Hits(sig.)↑↓	Expected↑↓	P(Fisher)↑↓	P(Gamma)↑↓
Peptidoglycan biosynthesis	18	7	7	3.8974	0.0028397	0.0035339
O-Antigen nucleotide sugar biosynthesis	21	13	13	6.333	0.0075502	0.0035873
Glycolysis/Gluconeogenesis	29	10	10	4.8718	0.0077324	0.0035893
Streptomycin biosynthesis	9	7	7	4.3846	0.014841	0.0036715
Fructose and mannose metabolism	33	25	24	11.692	0.019199	0.0037229
Alanine, aspartate and glutamate metabolism	22	10	10	9.2564	0.020765	0.0037415
Methane metabolism	26	6	5	4.8718	0.043277	0.0040208
Polyketide sugar unit biosynthesis	5	3	3	3.4103	0.052255	0.0041383
Inositol phosphate metabolism	8	4	4	3.4103	0.052255	0.0041383
Purine metabolism	76	31	24	21.923	0.067476	0.0043459
Pentose phosphate pathway	26	18	15	11.205	0.075054	0.0044534
Galactose metabolism	39	32	22	14.128	0.092388	0.00471
Acarbose and validamycin biosynthesis	3	2	2	2.9231	0.095313	0.0047548
Lipopolysaccharide biosynthesis	46	9	9	3.8974	0.12477	0.0052326
Starch and sucrose metabolism	22	15	10	5.8462	0.16453	0.0059607

Figure 6.14 Functional analysis comparing meropenem-resistant strains treated with DMSO (R_DMSO) and combination therapy (R_AB+INH). *The scatter plot visualizes pathway enrichment analysis results, with each point representing a metabolic pathway. The x-axis denotes the pathway impact score, which measures the contribution of identified metabolites to the pathway, while the y-axis represents -log10(p-value), indicating the statistical significance of pathway enrichment. Larger circles correspond to higher pathway impact scores, and the colour gradient from yellow to red reflects the significance level, with red indicating more significant pathways (lower p-values). The accompanying table provides details about each pathway, including the total number of compounds associated with the pathway, the number of compound features detected in the dataset (Hits all), and the subset of features that are significantly altered (Hits Sig.) with an FDR-corrected p-value < 0.05. The table also includes the expected number of features for each pathway based on random distribution (Expected), the Fisher's exact test p-value for pathway enrichment (pFisher), and the gamma-adjusted p-value to account for multiple testing (pGamma).*

The overlap in enriched pathways between the DMSO vs. meropenem and DMSO vs. combination therapy comparison, such as peptidoglycan biosynthesis and energy metabolism, indicates that pathway perturbations are primarily driven by meropenem action. Differences between the two comparisons, such as the enrichment of O-antigen nucleotide sugar biosynthesis in combination therapy, suggest a potential contribution from taniborbactam in enabling meropenem activity.

Overall, the functional pathway analysis demonstrated that taniborbactam does not induce additional metabolic disruptions beyond those caused by meropenem in the meropenem-resistant strain. The observed pathway perturbations in combination therapy reflect the metabolic consequences of meropenem treatment, reinforcing role of taniborbactam as a β-lactamase inhibitor that restores antibiotic efficacy without eliciting broader metabolic changes.

6.1.4 Discussion and conclusion: Taniborbactam

The metabolomic analysis revealed that taniborbactam treatment, whether administered alone (INH) or in combination with meropenem (AB+INH), did not result in significant metabolic alterations in *E. coli* strains. Across all analyses, taniborbactam-treated samples closely resembled their respective vehicle controls. Similarly, combination therapy samples showed profiles largely consistent with meropenem treatment, suggesting that taniborbactam induced minimal metabolic perturbation. The observation aligns with trends seen in the PCA plots and functional analysis, supporting the conclusion that taniborbactam alone does not significantly impact bacterial metabolism but instead functions as a complementary agent to enhance meropenem efficacy.

Functional analysis of the meropenem-resistant strain (R) revealed multiple metabolic pathways predicted to be significantly altered upon treatment. The perturbation of O-antigen nucleotide sugar biosynthesis suggests potential alterations in lipopolysaccharide production, which may influence membrane integrity and immune evasion.[504] Changes in glycolysis/gluconeogenesis and fructose and mannose metabolism indicate changes in central

carbon metabolism, possibly reflecting metabolic adaptations to antibiotic stress or compensatory mechanisms to maintain cellular energy homeostasis.[60,163] Additionally, peptidoglycan biosynthesis pathway being perturbed, reflected the action of meropenem.[505] Taniborbactam appeared to have limited additional metabolic impact beyond its role in neutralizing β-lactamase activity.[498] These findings align with previous studies, which show that β-lactamase inhibitors, including taniborbactam, primarily act through enzymatic inhibition and exhibit minimal off-target metabolic effects.[506] However, further studies comparing pathway enrichment with and without β-lactamase inhibitors in resistant strains are needed to clarify their broader metabolic implications.

While these results confirm the known role of taniborbactam in restoring meropenem efficacy, they also highlight the limited impact of the inhibitor on bacterial metabolism. The similarity of taniborbactam-treated samples to vehicle controls emphasizes the specificity of inhibitor for its enzymatic target rather than broader metabolic pathways.

These findings demonstrate the need for complementary strategies targeting metabolic vulnerabilities in resistant strains to enhance combination therapy efficacy. Specifically, pathways altered in response to meropenem or combination therapy, such as peptidoglycan biosynthesis in resistant strains, could serve as targets.

6.2 Potential combination therapy

Bacterial energy metabolism plays a critical role in survival and adaptation under stress, yet it remains an underexplored target in the fight against antibiotic resistance.[94] Disrupting or enhancing energy-related pathways offers an opportunity to develop novel combination therapies that potentiate antibiotic efficacy.[45] The approach has shown potential in previous studies, such as those investigating tuberculosis, where targeting metabolic vulnerabilities has demonstrated therapeutic promise.[491]

Building on the hypothesis that bacterial energy metabolism represents a potential metabolic vulnerability, this section investigates whether modulating energy-related pathways can alter antibiotic activity against resistant strains. By focusing on compounds known to interfere with

or augment bacterial energy metabolism, the aim was to uncover strategies that could disrupt bacterial homeostasis to improve the efficacy of existing antibiotics.

Three compounds were selected to perturb bacterial metabolism in different ways. Bedaquiline, an ATP synthase inhibitor, disrupts oxidative phosphorylation and ATP production, impairing bacterial energy balance.[99] 2-deoxy-D-glucose (2-DG), a glycolysis inhibitor, interferes with ATP synthesis by targeting key enzymes in the glycolytic pathway.[507,508] Glucose supplementation, in contrast, will be used to try to enhance bacterial energy metabolism.[509] These compounds were separately combined with antibiotics and untargeted metabolomics performed to compared across the *E. coli* strains to evaluate their capability for modulating energy metabolism and investigating whether this was able to enhance antibiotic efficacy against the resistant strain

6.2.1 Bedaquiline shows inconsistent synergy with meropenem in targeting meropenem-resistant *E. coli*

Bedaquiline, an FDA approved drug, targets bacterial ATP synthase, a critical enzyme in oxidative phosphorylation.[510] By impairing ATP production, bedaquiline can disrupt energy metabolism, an essential process for bacterial survival. While primarily used for treating drug-resistant Mycobacterium tuberculosis, its mechanism of action suggests its broader potential for targeting energy metabolism as a therapeutic strategy against antibiotic-resistant bacteria. [99,102]

The rationale for exploring bedaquiline in this study stemmed from the recognition of energy metabolism as a metabolic vulnerability in resistant *E. coli* strains.[58] Previous results identified metabolites including sedoheptulose 1-phosphate (linked to pentose phosphate pathway), glucose-1-phosphate (linked to glycolysis), and galactose metabolism, pentose phosphate pathway, and fructose and mannose metabolism, which are all associated with energy production, could be exploited as vulnerabilities in antibiotic resistant strains. [154,330,344] Despite its well-characterised efficacy against Mycobacterium tuberculosis, the effects of bedaquiline on meropenem-resistant *E. coli* strain, specifically those harbouring the NDM-7 gene, remained

unexplored. Here the impact of bedaquiline, both as standalone treatment and in combination with meropenem, was investigated to determine its potential for influencing carbapenem resistance.

The hypothesis was proposed that bedaquiline would disrupt energy metabolism in the meropenem-resistant strain (R) and therefore potentially enhance meropenem treatment efficacy. Experiments to investigate this hypothesis were conducted exclusively on the meropenem-resistant strain (R) to uncover whether targeting bacterial energy generation provided synergistic therapeutic benefits. Focusing on the resistant strain allowed for an assessment of energy metabolism as a specific resistance target.

6.2.1.1 Bedaquiline combined with meropenem provide synergistic antimicrobial effects

A checkerboard assay (**Figure 6.15**) was conducted in a 96-well microplate format to test combinations of bedaquiline (1 to 32 μg/mL) and meropenem (0.25 to 256 μg/mL) on a meropenem-resistant *E. coli* strain. Rows represented serial dilutions of meropenem, while columns represented serial dilutions of bedaquiline, enabling a matrix-based evaluation of potential synergistic effects. Wells containing 0 μg/mL meropenem tested the effect of bedaquiline alone, while wells with 0 μg/mL bedaquiline tested the effect of meropenem alone. Cells were inoculated at an initial OD_{600} of 0.01 and bacterial growth was measured after 24 hours of incubation using optical density at 600 nm (OD_{600}), providing a quantitative assessment of bacterial viability under each condition. The exposure time and concentration ranges were consistent with those used in earlier inhibitor checkerboard assays, allowing for direct comparison across experiments. The precipitation of bedaquiline at high concentrations likely affected OD_{600} readings slightly, but it did not alter the overall growth trends or conclusions.

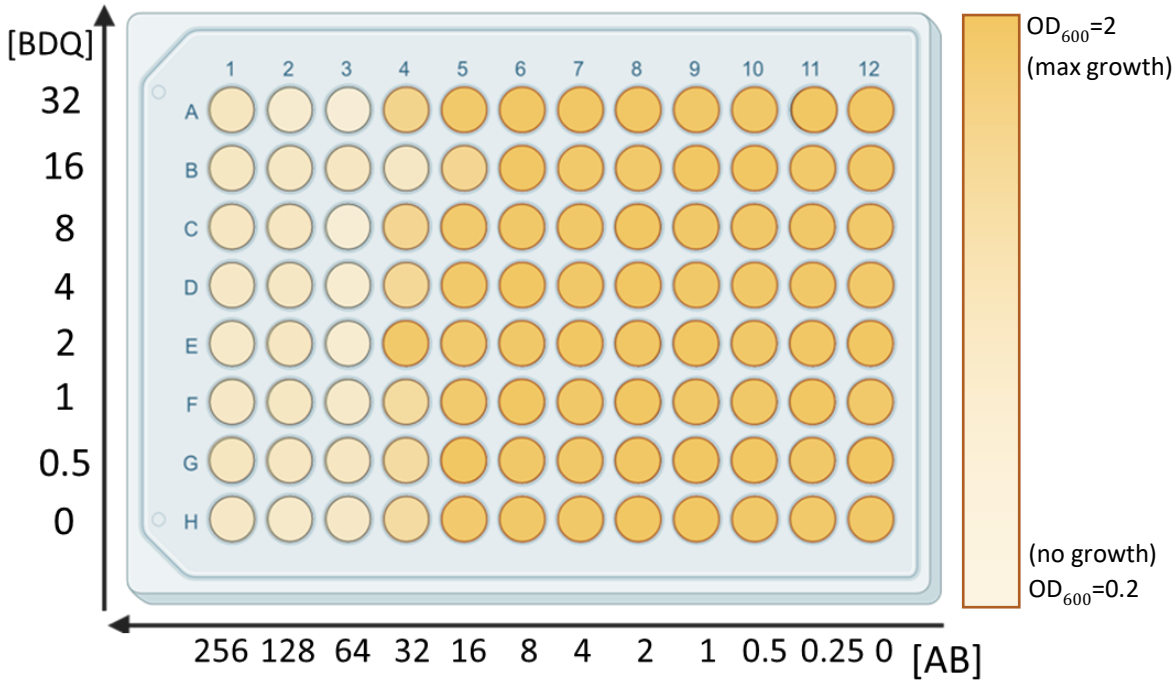

Figure 6.15 A checkerboard assay evaluating the synergistic effects of meropenem (rows) and bedaquiline (columns) on a meropenem-resistant* E. coli *strain. *Rows represent serial dilutions of meropenem, with concentrations ranging from 256 µg/mL to 0 µg/mL. Columns represent serial dilutions of bedaquiline, with concentrations ranging from 32 µg/mL to 0 µg/mL. Colour intensity indicates bacterial growth, with lighter wells representing greater growth inhibition.*

Figure 6.15 indicates that bedaquiline alone does not inhibit growth across any of the tested concentration. Meropenem alone completely inhibited growth at 64 µg/mL and higher, confirming its inhibitory effect at these concentrations. When bedaquiline was combined with meropenem, the inhibitory effect of meropenem was not significantly enhanced across most concentration combinations. A potential synergistic effect was noted at the combination of 16 µg/mL meropenem and 32 µg/mL bedaquiline, as evidenced by reduced bacterial growth compared to either compound alone. However, this trend was not consistent, and bacterial growth re-emerged at higher concentrations, such as 32 µg/mL bedaquiline combined with 32 µg/mL meropenem.

The initial checkerboard assay, which tested bedaquiline concentrations up to 32 µg/mL, showed limited and inconsistent growth inhibition and suggested only marginal synergy when combined with meropenem. However, higher bedaquiline concentrations might exert greater metabolic stress or enhance the inhibitory effects of meropenem. To explore this possibility, a second checkerboard assay (**Figure 6.16**) was conducted with increased bedaquiline

concentrations, ranging from 1 to 64 µg/mL, while maintaining the serial dilutions of meropenem (0.25 to 256 µg/mL). The experiment aimed to evaluate whether higher bedaquiline concentrations improve its standalone efficacy or enhanced its interaction with meropenem.

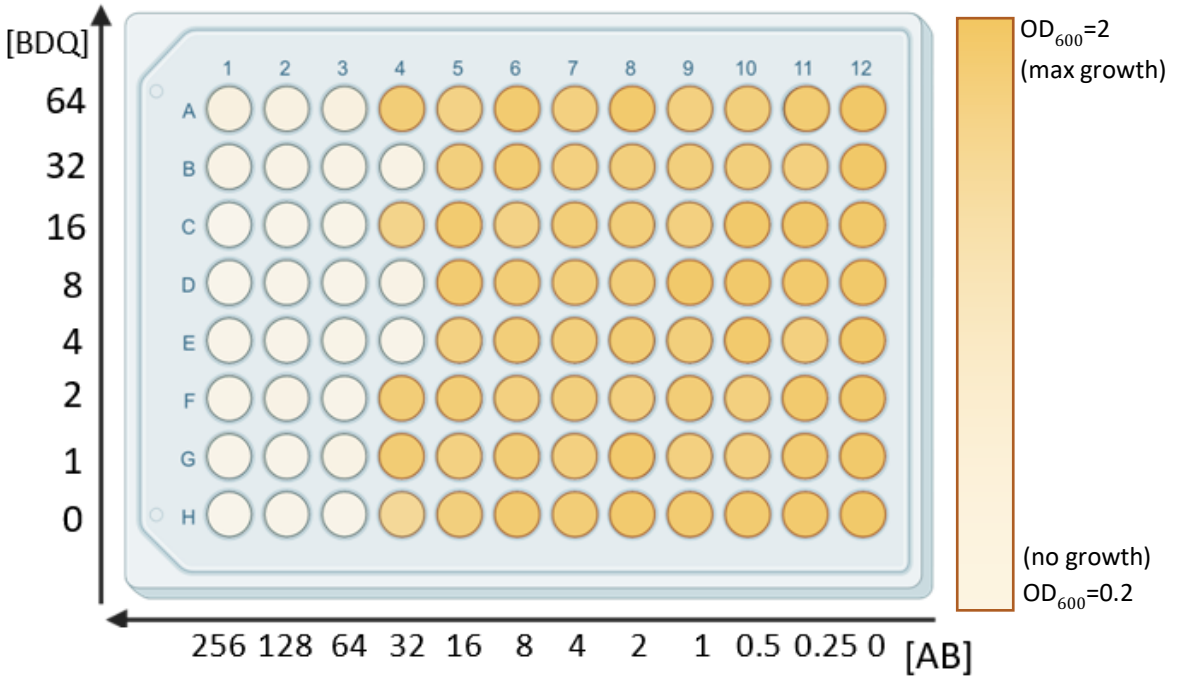

***Figure 6.16 Checkerboard assay evaluating the effects of higher bedaquiline concentrations combined with meropenem on meropenem-resistant* E. coli**. *A checkerboard assay displaying the effects of bedaquiline (columns, 64 to 1 µg/mL) and meropenem (rows, 256 to 0.25 µg/mL) on bacterial growth after 24 hours of incubation. Wells containing 0 µg/mL meropenem tested bedaquiline alone, while wells containing 0 µg/mL bedaquiline tested meropenem alone. Colour intensity correlates with bacterial growth, with lighter wells indicating greater growth inhibition.*

When combined with bedaquiline, meropenem showed evidence of increased bacterial susceptibility at specific concentrations. For instance, the combination of 32 µg/mL meropenem with 32 µg/mL, 8 µg/mL, and 4 µg/mL bedaquiline resulted in reduced bacterial growth compared to either drug alone. However, this effect was inconsistent, as bacterial growth re-emerged at other combinations, particularly at 32 µg/mL meropenem with 16 µg/mL, and 64 µg/mL bedaquiline concentrations.

These findings differ from the previous checkerboard assay (**Figure 6.15**), where similar combinations showed limited or no enhancement in bacterial susceptibility. The inconsistencies observed between the two assays may reflect experimental variability or differences in how bacterial cells respond to bedaquiline. The re-emergence of bacterial

growth at certain combinations could indicate a concentration-dependent threshold, beyond which the interaction between the two drugs becomes less effective or is influenced by additional factors, such as stability and solubility of bedaquiline, and metabolic compensation mechanisms.

The results suggested a potential synergistic interaction between bedaquiline and meropenem at specific concentration combinations, but the inconsistent effects of bedaquiline complicated definitive conclusions. One possible reason for the inconsistency was that inhibitory effect of bedaquiline on *E. coli* may vary depending on factors such as physiological state of the bacterial population.[511] Alternatively, the high concentrations of bedaquiline may exert stress that elicits variable bacterial responses, such as adaptive resistance mechanisms or heterogeneous metabolic activity within the population.

6.2.1.1.1 Conclusion

The results from both checkerboard assays indicated that bedaquiline alone did not reliably inhibit *E. coli* growth up to 64 μg/mL. When combined with meropenem, there was evidence of a potential synergistic effect at specific concentrations, such as 32 μg/mL meropenem with 32 μg/mL bedaquiline. However, this enhancement was inconsistent across assays and experimental conditions, with variability in bacterial responses. The observed inconsistencies could be attributed to factors such as physiological heterogeneity in bacterial populations, differences in the solubility or bioavailability of bedaquiline, or potential interference in OD_{600} measurements due to physical properties of the compound.[512] The findings suggested that while bedaquiline may modestly enhance meropenem activity in certain conditions, how this works in *E. coli* remain unclear.

Future studies should evaluate alternative experimental designs, such as pre-incubation with bedaquiline to allow metabolic adaptation, varying exposure times to assess time-dependent effects, or testing additional concentration ranges. Comparing responses in resistant and non-resistant strains could provide further insight into how resistance mechanisms influence drug synergy.

These findings also underscore the challenges of targeting bacterial energy metabolism as a therapeutic strategy. While bedaquiline serves as a proof-of-concept for this approach, the inconsistent results of its synergy with meropenem highlight the importance of identifying compound synergies. Exploring alternative inhibitors of energy metabolism or optimizing combinations with meropenem may uncover more reliable therapeutic options for resistant bacterial strains.

6.2.2 Exploration of 2-deoxy-D-glucose targeting glycolysis to combat antibiotic resistance

2-Deoxy-D-glucose (2-DG) is an inhibitor that disrupts bacterial energy metabolism by interfering with glycolysis, a critical pathway for ATP production and cellular viability.[513,514] Seahorse-based metabolic analyses (Chapter 5) and literature have demonstrated that 2-DG effectively suppresses bacterial metabolic function, suggesting its potential as a therapeutic agent.[94] However, its potential for synergistic interactions with antibiotics remains underexplored. To address this, the interaction between 2-DG and meropenem was investigated using a checkerboard assay to assess individual and combined effects on bacterial growth. The aim was to investigate whether glycolytic inhibition would contribute bacterial susceptibility meropenem.

6.2.2.1 Checkerboard assay reveals synergistic effects of 2-deoxy-D-glucose and meropenem against resistant E. coli

The concentrations used for 2-DG and meropenem ranged from to 0 μg/mL, to 32 μg/mL, consistent with previous experiments involving taniborbactam and bedaquiline. While differences in molecular weight result in variation in molar concentrations, maintaining consistency in mass-based concentrations provides a practical framework for comparison under identical experimental conditions.[515] However, it is acknowledged that binding affinity plays a crucial role in the efficacy of inhibitors and should be considered alongside concentration when evaluating their therapeutical potential. This strategy ensures a

standardized framework for comparing metabolic modulators and inhibitors, enabling a systematic exploration of therapeutic potential across different mechanisms of action.

The results of the checkerboards assay are presented in (**Figure 6.17**) each well represents a specific combination of 2-DG and meropenem concentrations, with transparency if colour indicating bacterial growth inhibition. The observed inhibition patterns revealed a concentration-dependent interaction between the two agents.

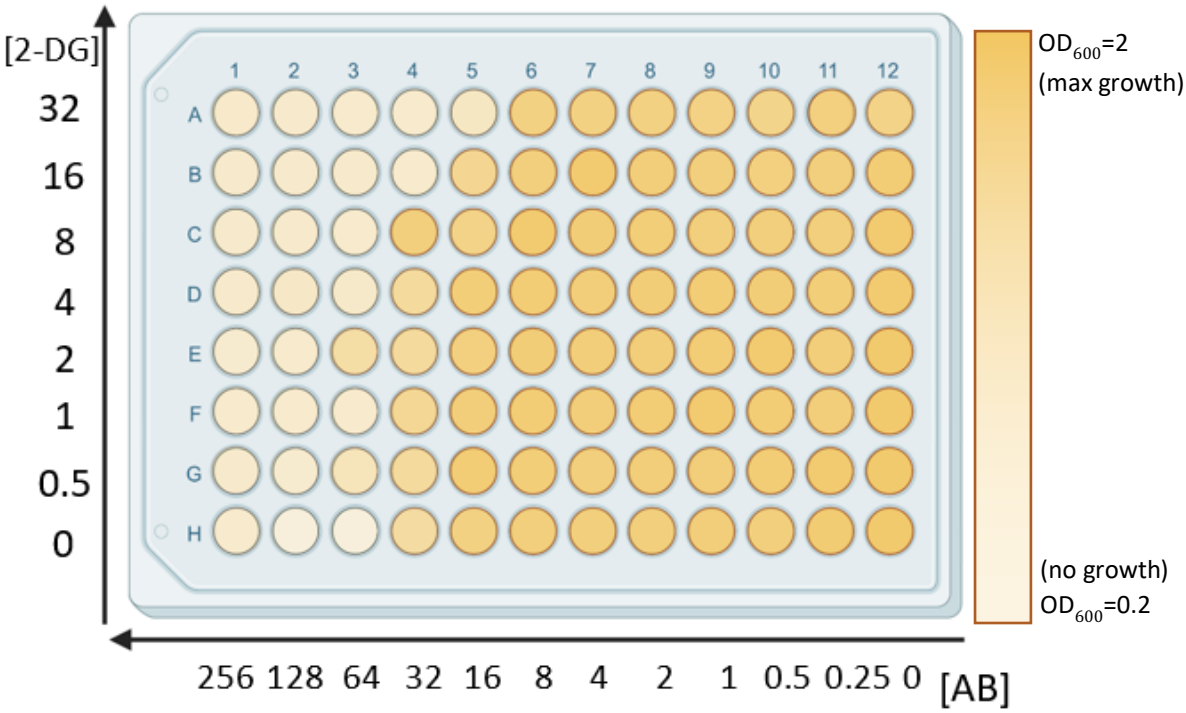

Figure 6.17 A checkerboard assay evaluating the interaction between meropenem ([AB], rows) and 2-DG ([2-DG], columns) against a meropenem-resistant E. coli strain. *Rows represent serial dilutions of meropenem, ranging from 256 µg/mL to 0 µg/mL, while columns represent serial dilutions of 2-DG, ranging from 32 µg/mL to 0 µg/mL. Colour intensity reflects bacterial growth, with lighter wells indicating greater growth inhibition and darker wells indicating higher bacterial growth.*

The results indicated that 2-DG alone, within the tested concentration range, did not inhibit bacterial growth. Meropenem alone showed complete inhibition at its MIC of 64 µg/mL. However, the combination of 2-DG and meropenem demonstrated enhanced bacterial growth inhibition. Specifically, from 16 µg/mL and above for 2-DG and meropenem (32 µg/mL meropenem with 16 µg/mL and 32 µg/mL 2-DG, 16 µg/mL meropenem with 32 µg/mL 2-DG), the MIC of meropenem is reduced suggesting that 2-DG enhanced the efficacy of meropenem. Notably, the combination of the two agents results in substantial inhibition compared to either agent alone, suggesting a synergistic effect.

By impairing glycolysis, 2-DG enhanced the efficacy of meropenem, even against resistant strains. Specifically, synergy was observed at concentrations of 32 μg/mL meropenem with 16 and 32 μg/mL 2-DG, and 16 μg/mL meropenem with 32 μg/mL 2-DG. These combinations inhibited bacterial growth at lower concentrations than meropenem alone at its MIC, underscoring potential of 2-DG to mitigate antibiotic resistance through metabolic disruption. While these results are promising, further investigations are needed to elucidate the precise mechanisms underlying this synergy. Key questions remain, including whether 2-DG affects bacterial energy reserves, interferes with metabolic compensation mechanisms, or indirectly influences pathways critical for survival under antibiotic stress. Additionally, evaluating effects of 2-DG in combination with meropenem in non-resistant strains and across a broader range of conditions would provide deeper insights into its mode of action and broader applicability.

Due to time constraints and resource availability, these additional analyses were beyond the scope of the current study. Future investigations could assess the clinical feasibility of incorporating 2-DG into combination therapy regimens. Exploring its effects in more complex bacterial models, such as biofilms or infection-relevant conditions, and investigating potential off-target effects may provide valuable insights into its safety and efficacy. These studies could help determine whether 2-DG has practical applications in mitigating antibiotic resistance and enhancing the therapeutic potential of existing antibiotics.

6.2.2.1.1 Conclusion

The checkerboard assay results showed a synergistic effect between 2-DG and meropenem against the resistant *E. coli* strain. The data indicated that while 2-DG alone does not affect bacterial growth, its combination with meropenem lowers the MIC of meropenem, highlighting its potential role in enhancing antibiotic efficacy. The synergistic interaction may come from documented ability of 2-DG to disrupt bacterial energy metabolism, sensitising the cells to meropenem.[516] These findings suggest further exploration of 2-DG as an adjuvant in combination therapy approaches to combat antibiotic resistance should be investigated.

6.2.3 Stimulating energy metabolism with glucose to alter antibiotic susceptibility in resistant *E. coli*

In contrast to strategies aimed at suppressing bacterial energy metabolism investigated above, an alternative approach was explored to try to enhance energy metabolism to potentiate antibiotic efficacy. Dormant or metabolically inactive bacterial cells often exhibit increased tolerance to antibiotics due to their reduced reliance on active metabolic processes.[517] Reactivating bacteria by stimulating energy metabolism has been proposed as a strategy to restore their susceptibility to antibiotics.[113,518]

Although meropenem-resistance strains are not necessarily dormant, the broader principle of increasing bacterial energy metabolism to influence antibiotic susceptibility was explored. Glucose, an important substrate in bacterial energy metabolism, was selected for its ability to stimulate pathways such as glycolysis and central carbon metabolism, which are critical for bacterial energy production.[519] Previous research has demonstrated the importance of central carbon metabolism in bacterial responses to antibiotics, providing a rationale for investigating whether stimulating metabolic activity with glucose could alter bacterial susceptibility.[335]

6.2.3.1 Seahorse analysis: Evaluating the impact of glucose supplementation on bacterial metabolism

In order to assess whether glucose supplementation could modulate bacterial metabolic activity in meropenem-resistant (R) and meropenem-susceptible (S) *E. coli* strains, the Seahorse metabolic analyser assay (investigated in Chapter 5) was employed to monitor OCR and ECAR, representing readouts for oxidative phosphorylation and glycolysis, respectively. By evaluating changes in OCR and ECAR, this experiment sought to determine whether glucose altered central metabolic pathways in bacteria, thereby enhancing bacterial energy metabolism, and whether strain-specific differences in energy metabolism were observed.

The metabolic activity of meropenem-susceptible (S) and meropenem-resistant (R) *E. coli* strains were both monitored under two conditions, with and without glucose supplementation. In this experiment, 56 µl of 2% glucose was added to 500 µl of the bacterial suspension to a

final concentration of 0.2%.[520] The susceptible strain (S) exhibited a substantial increase in both OCR and ECAR following glucose addition, reflecting enhanced oxidative phosphorylation and glycolytic activity. In contrast, the resistant strain (R) showed minimal changes in OCR and a modest but consistent increase in ECAR. Seahorse metabolic analysis revealed different responses between the susceptible and resistant strains upon glucose supplementation (**Figure 6.18**).

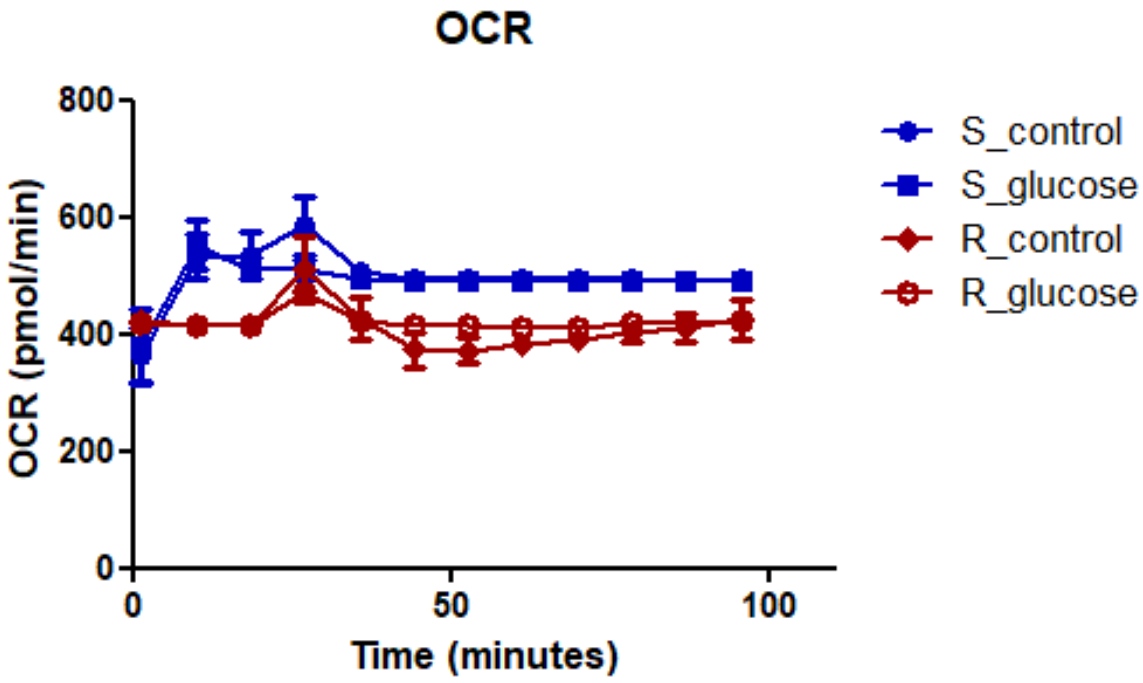

Figure 6.18 OCR in meropenem-susceptible and meropenem-resistant E. coli with and without glucose supplementation. *The graph depicts the OCR of meropenem-susceptible (S) and meropenem-resistant (R) E. coli strains over time, measured using a Seahorse Analyser. Glucose supplementation was performed by adding 56 µL of 2% glucose to 500 µL of bacterial suspension. Error bars represent the standard deviation of replicate measurements. Biological replicate n=5.*

In the susceptible strain, glucose addition caused a sharp initial increase in ECAR, which continued to rise, peaking at approximately 50 minutes, before gradually declining, as shown in **Figure 6.19**. The transient response indicates a temporary enhancement of glycolytic activity. Conversely, the resistant strain exhibited a similar initial rise in ECAR upon glucose supplementation, followed by a slight decrease, but with levels stabilizing and showing no further reduction throughout the observation period. These findings demonstrate that glucose supplementation activated glycolytic pathways in both strains, but with distinct temporal patterns that likely reflect differences in metabolic regulation and adaptive mechanisms between the susceptible and resistant strains.

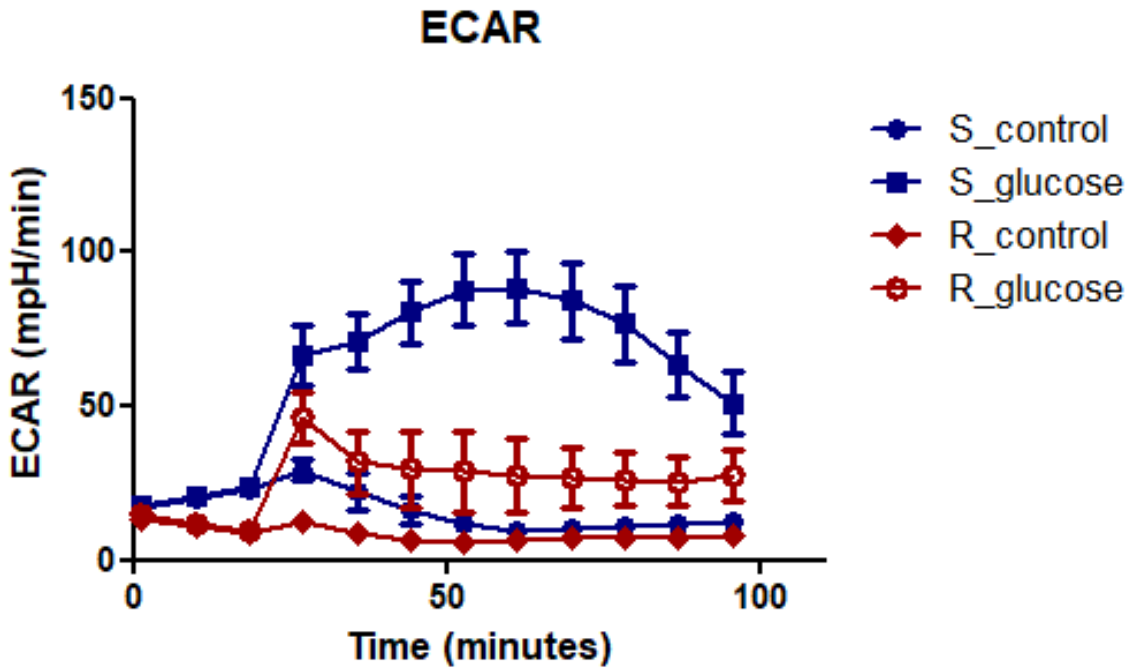

Figure 6.19 ECAR in meropenem-susceptible and meropenem-resistant E. coli with and without glucose supplementation. *The graph illustrates the ECAR of meropenem-susceptible (S) and meropenem-resistant (R) E. coli strains over time, measured using a Seahorse Analyser. Glucose supplementation was achieved by adding 56 µL of 2% glucose to 500 µL of bacterial suspension. Error bars represent the standard deviation of replicate measurements. Biological replicate n=5.*

The increase in ECAR in both strains following glucose supplementation demonstrates activation of glycolytic pathways, but the response differed between strains. In the susceptible strain (S), the transient spike and subsequent decline in ECAR suggest that the bacteria may have efficiently utilized glucose to fuel central carbon metabolism, with reduced activity as metabolic demands were met. In contrast, the sustained ECAR increase in the resistant strain (R) indicates prolonged glycolytic activity, potentially reflecting differences in metabolic regulation or energy demands between the two strains. These findings suggest that glucose can activate energy metabolism in both strains, although the dynamics of this activation differ.

6.2.3.2 Checkerboard assays: Evaluating the impact of glucose on meropenem efficacy

The experiment aimed to evaluate the impact of glucose supplementation on the efficacy of meropenem against meropenem-resistant *E. coli* strain. It was hypothesised that stimulating bacterial metabolism with glucose would alter antibiotic susceptibility, changing the MIC of meropenem and demonstrating synergy between glucose and antibiotic susceptibility. A checkerboard assay was conducted to systematically evaluate the interaction between glucose and meropenem across a range of concentrations.

The checkerboard assay combined serial dilutions of glucose (32 to 0 µg/mL, columns) with meropenem (256 to 0 µg/mL, rows). Bacterial growth was assessed after 24 hours of incubation, with growth inhibition visualized by changes in well opacity (**Figure 6.20**). The results showed that glucose supplementation did not reduce the MIC of meropenem; instead, it appeared to increase bacterial growth at higher concentrations of glucose. Notably, at 32 µg/mL glucose and 64 µg/mL meropenem, bacterial growth was observed, indicating that glucose enabled the resistant strain to tolerate inhibitory effects of meropenem.

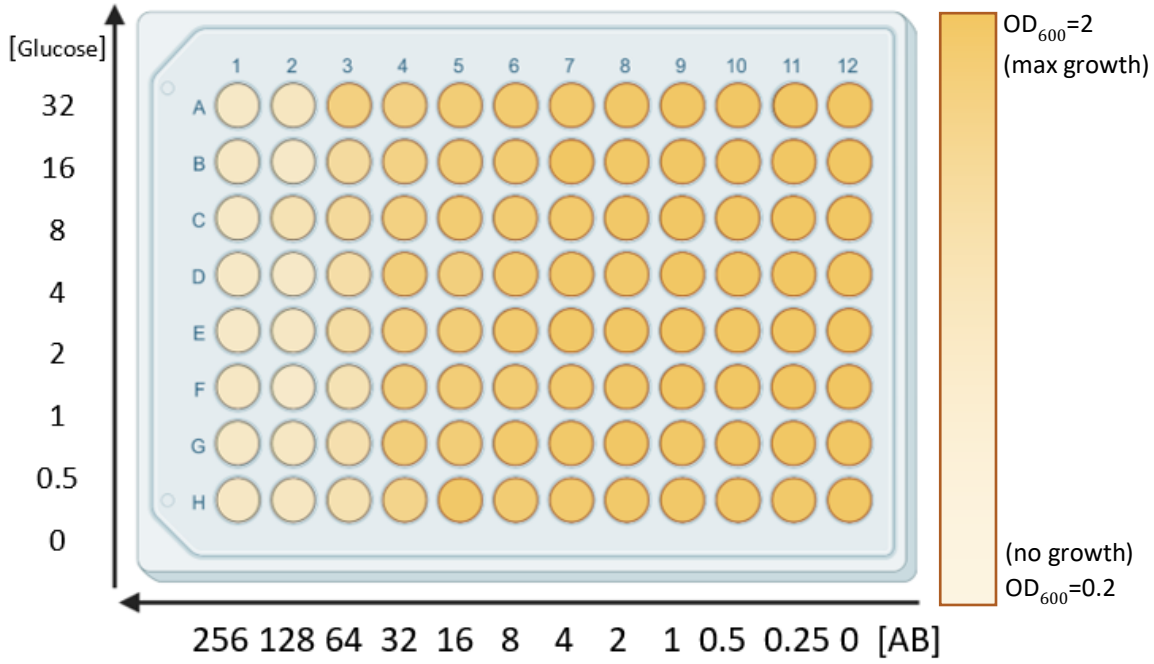

Figure 6.20 A checkerboard assay evaluating the interaction between glucose (columns) and meropenem (rows) against a meropenem-resistant E. coli strain. *Rows represent serial dilutions of meropenem, ranging from 256 µg/mL to 0 µg/mL, while columns represent serial dilutions of glucose, ranging from 64 µg/mL to 0 µg/mL. Colour intensity reflects bacterial growth, with lighter wells indicating greater inhibition of growth and darker wells indicating higher bacterial growth.*

The checkerboard assay indicated that glucose supplementation did not synergise with meropenem to more effectively kill resistant bacteria but rather increased the MIC of the antibiotic. The results suggested that glucose enhanced bacterial resistance to meropenem. These findings may reflect the ability of glucose to fuel metabolic processes that support bacterial survival under antibiotic stress, counteracting the inhibitory effects of meropenem.

The results provide important insights as they experimentally establish a relationship between bacterial metabolism and antibiotic efficacy, demonstrating that modulation of energy metabolism can directly impact meropenem activity. The experiment establishes a proof of

concept that altering bacterial energy metabolism can influence antibiotic susceptibility, offering a foundation for further research into the therapeutic potential of metabolic stimulation. Additionally, the results emphasize the dual potential of metabolic modulation, where stimulation of bacterial metabolism can either enhance antibiotic efficacy or, in some cases, contribute to increased resistance. Given the observation that altered energy metabolism impacts antibiotic activity, future experiments should explore whether reducing glucose availability further enhances meropenem susceptibility in the resistant strain.

6.3 Discussion and conclusion

This chapter has explored the potential of targeting bacterial energy metabolism as a combination therapy strategy to enhance the efficacy of antibiotics against resistant bacterial strains. By investigating the antimicrobial activity of meropenem alongside taniborbactam inhibitor, and metabolic modulators such as bedaquiline, 2-DG, and glucose, the results collectively provided new insights into the complex interplay between bacterial metabolism and antibiotic action. The findings highlighted the promise of metabolic modulation as a complementary therapeutic strategy, while also demonstrating the challenges associated with such a strategy.

Taniborbactam was shown to be an effective β-lactamase inhibitor, restoring meropenem efficacy by neutralising NDM-7-mediated resistance. Unlike metabolic modulators, the targeted function of taniborbactam did not induce significant metabolic changes in meropenem-resistant *E. coli* strains. The observations highlighted its value as a direct resistance-targeting agent; however, it also raises concerns about the potential for resistance to develop against such narrowly focused therapies, emphasising the importance of combining taniborbactam with complementary approaches to sustain its efficacy over time.[521-523]

The metabolic modulators investigated in this study focused on targeting bacterial energy pathways to evaluate their potential to complement antibiotic treatment. Bedaquiline, an ATP synthase inhibitor, is known to disrupt oxidative phosphorylation leading to impaired bacterial viability in TB. However, its effects in resistant *E. coli* were inconsistent, with variability

observed across concentration combinations in the checkerboard assay. While certain combinations, such as 16 μg/mL meropenem with 32 μg/mL bedaquiline, showed a reduction in bacterial growth, these effects were not reproducible across all conditions. The inconsistency may reflect strain-specific metabolic conditions or differences in the physiological state of the bacterial population, or the bedaquiline water solubility issue.[511] Despite these limitations, the findings demonstrate that bedaquiline may have the potential to enhance antibiotic activity under certain conditions, warranting further investigation into its mechanism of action and factors influencing its efficacy.

2-DG, a glycolysis inhibitor, showed more consistent results, enhancing meropenem efficacy by reducing the MIC of meropenem when combined. The checkerboard assay revealed clear synergy at specific concentration combinations, such as 32 μg/mL meropenem with 16 or 32 μg/mL 2-DG. The result demonstrates the potential of glycolytic inhibition as a therapeutic strategy to disrupt bacterial energy metabolism and sensitize resistant strains to antibiotics. However, the specific mechanisms driving this synergy, whether through depletion of ATP reserves, disruption of compensatory metabolic pathways, or other effects, remain unclear and require further exploration.

In contrast to these strategies aimed at suppressing bacterial energy metabolism, glucose supplementation was investigated for its potential to enhance metabolic activity and influence antibiotic susceptibility. Seahorse analysis revealed that glucose transiently increased glycolytic activity (ECAR) in the susceptible strain, while the resistant strain exhibited a more sustained ECAR response. These differences may reflect variations in metabolic regulation, with the resistant strain potentially activating adaptive mechanisms to maintain metabolic homeostasis. However, the checkerboard assay indicated that glucose supplementation did not synergize with meropenem; instead, it increased bacterial resistance, as evidenced by an increase in the MIC of meropenem in the presence of glucose. The finding suggested that metabolic stimulation may enhance bacterial survival under antibiotic stress, highlighting the complex interplay between metabolic activity and antibiotic efficacy.[495,524] The broader

implication of this result is that dietary or environmental factors influencing bacterial metabolism could impact therapeutic outcomes, emphasizing the importance of considering metabolic state of the host and pathogen when designing treatment strategies.[525,526]

Collectively, these findings establish that bacterial energy metabolism directly influences the efficacy of antibiotics, offering proof of concept for targeting metabolic pathways as a combination therapy strategy. The ability of taniborbactam to restore meropenem activity illustrates the value of targeting resistance mechanisms directly, while the experiments with bedaquiline and 2-DG demonstrate the potential of metabolic disruption to enhance antibiotic activity. However, the variability observed with bedaquiline and glucose highlights the complexity of bacterial metabolic regulation, suggesting that strain-specific factors and metabolic conditions substantially influence the efficacy of these approaches.

Future investigations may benefit from addressing several key areas to expand on the findings in this chapter. For example, to explore whether prolonged exposure to metabolic modulators or pre-treatment regimens enhances their impact on antibiotic efficacy. Additionally, validating these strategies in vivo is crucial to determine their therapeutic potential and safety in clinically relevant settings. Broader compound screening targeting other primary metabolic pathways, such as the TCA cycle or nucleotide biosynthesis, could identify more robust modulators for combination therapies by disrupting essential processes critical for bacterial survival, reducing the likelihood of resistance development, and enhancing the efficacy of existing antibiotics. Finally, in the longer term integrating metabolic modulators with antibiotics in clinically relevant combinations should be performed to optimise dosing regimens while minimising resistance development.

While taniborbactam demonstrated unparalleled efficacy in restoring antibiotic activity against resistant strains, the experiments with metabolic modulators such as bedaquiline, 2-DG, and glucose highlighted the potential of targeting bacterial energy metabolism as a complementary approach. These findings provide a foundation for future investigations into metabolic vulnerabilities as therapeutic targets, offering a pathway toward novel strategies to

overcome resistance and antibiotic tolerance. Although challenges remain, the results show the promise of combing metabolic modulation with conventional antibiotics help combat the growing threat of antimicrobial resistance.

Chapter 7 Thesis discussion and conclusions

7.1 Summary of findings and their implications

This thesis has explored the metabolic underpinnings of AMR in *E. coli*, with a focus on uncovering and investigating metabolic vulnerabilities that could provide novel therapeutic strategies. Through comprehensive investigations using metabolomics, live-cell analysis, and combination therapy approaches, the findings have provided new insights into the interplay between bacterial metabolism and antibiotic resistance, offering potential targets for novel therapeutic strategies. This chapter integrates the findings across the result chapters, discussing how they come together in contributing to knowledge in the field, and their implications for what future therapeutic strategies could be developed to address the challenges posed by AMR.

7.1.1 Metabolic adaptations underpinning resistance

The results presented in Chapter 3, after developing biological models and validating a metabolomics approach, demonstrated metabolic changes associated with the introduction of the pCR2.1 plasmid and the NDM-7 gene in *E. coli*. These findings demonstrated clearly that altered metabolism was linked directly to the presence of resistance. Functional analysis predicted alterations in nucleotide metabolism, amino acid biosynthesis, and central carbon metabolism, including glycolysis and the TCA cycle. Pathways, essential for energy production and biomass synthesis, were notably affected, likely reflecting an energy and resource cost imposed by resistance. Specifically, elevated levels of fructose 6-phosphate and sedoheptulose 1-phosphate in resistant strains highlighted the reprogramming of glycolytic and pentose phosphate pathways, while changes in nucleotide biosynthesis intermediates such as dCTP suggested a significant metabolic burden on cell cycle and/or signalling. Additionally, the observed metabolic changes emphasised that resistant cells may acquire a metabolic burden associated with plasmid-borne resistance. Pathways related to nucleotide biosynthesis, sugar metabolism, and oxidative stress management were identified as potential therapeutic

targets to counteract this metabolic burden. It is recommended that future strategies should include targeting these pathways initially by enzyme inhibition, such as blocking specific steps in nucleotide biosynthesis or oxidative phosphorylation, to undermine the fitness of resistant strains under subsequent antibiotic pressure. The findings therefore set the stage for further investigation into metabolic vulnerabilities that could inform the development of targeted interventions against AMR.

7.1.2 Metabolic changes in wild-type and meropenem-susceptible strain vs. stability and vulnerabilities in meropenem-resistant *E. coli*

In Chapter 4, the metabolic responses of wild-type, meropenem-susceptible, and meropenem-resistant strains to meropenem exposure were investigated. The wild-type and meropenem-susceptible strains exhibited extensive metabolic reprogramming under sub-lethal concentrations of meropenem. Metabolic pathways including nucleotide metabolism, glycerophospholipid metabolism, and peptidoglycan biosynthesis were impacted, revealing intense response as part of the cost of meropenem exposure.

In contrast, the meropenem-resistant strain displayed much less metabolic change in terms of altered profiles between treated and untreated conditions at sub-lethal doses. The stability attributed to the effective hydrolysis of meropenem by the presence of the NDM-7 enzyme, a metallo-β-lactamase that deactivates the antibiotic by cleaving its β-lactam ring. Comparisons between the meropenem-susceptible and meropenem-resistant strains indicated differences in pathways such as histidine metabolism, pyrimidine metabolism, O-antigen nucleotide sugar biosynthesis, peptidoglycan biosynthesis, polyketide sugar unit biosynthesis, and amino sugar and nucleotide sugar metabolism. These findings reflect distinct metabolic adaptations in the resistant strain that may support its survival under antibiotic exposure.

At MIC concentrations of the antibiotic (16 μg/mL), the meropenem-resistant strain exhibited notable changes in pathways related to oxidative stress management, energy homeostasis, and nucleotide biosynthesis. Functional analysis revealed significant alterations in pathways including purine metabolism, chlorocyclohexane and chlorobenzene degradation,

phenylalanine, tyrosine, and tryptophan biosynthesis, biosynthesis of siderophore group nonribosomal peptides, and novobiocin biosynthesis.

These findings show that while the meropenem-resistant strain maintains metabolic stability at sub-lethal does, MIC conditions imposed substantial physiological stress, manifesting in changes in energy homeostasis and oxidative stress management.

7.1.3 Challenges and insights in the analysis of energy metabolism in meropenem-susceptible and meropenem-resistant *E. coli*: Adapting mammalian-centric tools for bacterial systems

Chapter 5 pursued the findings from untargeted metabolomics experiments that revealed energy metabolism changes in the resistant compared to non-resistant strains. To support and extend this observation, global changes in energy metabolism were investigated across the *E. coli* strains using independent assays by employing live cell metabolism analysis using a Seahorse XF Analyser and ATP production quantification using the BacTiter-Glo™ bioluminometric cell viability assays. These independent methodologies confirmed bioenergetic differences between meropenem-susceptible and meropenem-resistant *E. coli* strains via oxygen consumption, extracellular acidification and ATP measurements but highlighted major methodological challenges in translating the various assays developed for mammalian systems involving ETC and mitochondrial inhibitors. For example, the Seahorse XF Analyser was employed to measure OCR and ECAR, providing a real-time assessment of oxidative phosphorylation and glycolytic activity in live bacterial cells. However, inhibitors such as oligomycin, rotenone, and antimycin A, commonly used in eukaryotic systems, showed limited effectiveness in bacterial cells, presumably due to branched ETC and metabolic flexibility in *E. coli*. These limitations hindered the ability of Seahorse assay to fully inhibit bacterial ETC components and accurately capture glycolytic compensatory responses.

Optimisation efforts focused on modifying cell adhesion protocols, seeding densities, and normalisation techniques to accommodate bacterial physiology. Despite these improvements, substantial limitations remained. Some strain-specific differences were observed, such as an

elevated baseline OCR in the meropenem-resistant strain, which reflected higher oxidative activity. Every assay result emphasised the need for the development of bacterial-specific inhibitors and protocols to study bacteria bioenergetics more effectively using the Seahorse system.

The BacTiter-Glo™ ATP assay provided complementary insights by quantifying differences in ATP levels under defined conditions. Resistant strains consistently demonstrated lower ATP levels, even under antibiotic exposure. However, the interpretation of the result was Challenging.

Key challenges identified during these experiments included the inherit differences in bacterial and mammalian bioenergetics, the structural diversity of bacterial ETC components, and the limited application of mammalian derived inhibitors. Future studies should prioritise the development of bacterial-specific inhibitors, recalibration of assay parameters such as P/O ratios, and incorporation of complementary techniques like metabolomics and direct measurement of fermentation by-produce to achieve a comprehensive understanding of bacterial energy metabolism.

In summary, while the Seahorse XF Analyser provided valuable baseline data on OCR and ECAR and highlighted strain-specific metabolic activity, the current form of the various assays developed to investigate energy metabolism in eukaryotic systems does not translate easily to prokaryotes and requires extensive development work. The BacTiter-Glo™ cell viability assay demonstrated high reliability in quantifying ATP levels and emphasised potential difference in ATP production between strains. However, the assay only captures the overall energetic status at a single time point rather than capturing dynamic changes in energy metabolism. Together, the results from this chapter provided the groundwork for future adaptation of real-time metabolic analysis tools for bacterial systems, offering potential to uncover metabolic vulnerabilities and inform novel therapeutic strategies targeting energy metabolism in AMR.

7.1.4 Targeting bacterial energy metabolism: Exploring taniborbactam, metabolic modulators, and nutrient influences in combating carbapenem resistance.

Having established energy metabolism as a potential target, Chapter 6 reports experiments designed to explore modulating bacterial energy metabolism as a combination therapy strategy. Untargeted metabolomics was employed to investigate the effect of taniborbactam (a novel metalloβlactamase inhibitor), both alone and in combination with, meropenem, with the aim of altering antibiotic susceptibility in ways that could be targeted therapeutically. Taniborbactam, effectively restored meropenem activity by neutralising NDM-7 mediated resistance without inducing significant metabolic changes. No specific metabolic pathways were linked to the increased susceptibility associated with taniborbactam treatment; however, these findings validate taniborbactam as a highly potent carbapenem resistance-targeting agent, demonstrating its potential for combatting metallo-β-lactamase-driven antimicrobial resistance effectively.

The investigation of potential metabolic modulators, including bedaquiline and 2-DG, revealed variable synergy with meropenem for inhibiting the growth of the meropenem-resistant *E. coli* strain. The effect of bedaquiline appeared to depend on experimental conditions, potentially influenced by factors such as bacterial metabolic states, environmental conditions, or its physiochemical properties. As a hydrophobic compound, bedaquiline has poor solubility in aqueous media, may have contributed to inconsistencies that were observed in its effects, highlighting the importance of optimised handling protocols. In contrast, 2-DG consistently reduced the MIC of meropenem by targeting glycolysis, disrupting energy metabolism, and weakening bacterial AMR. These findings suggest that while bedaquiline may have context-dependent applications, 2-DG holds promise as a candidate for combination therapy due to the reproducible effects observed with meropenem.

Further experiments showed that an increase in glucose concentration correlated with a higher MIC for meropenem, demonstrating a positive relationship between glucose levels and enhanced resistance. This observation suggested that elevated glucose availability enhanced

bacterial metabolic capacity, potentially supporting resistance mechanisms by providing additional energy and resources for cellular processes such as efflux pump activity, cell wall biosynthesis, or stress response pathways. These findings emphasise the dual nature of metabolic modulation as a complementary therapeutic approach, offering the potential for use to enhance antibiotic activity but recognises challenges to be overcome.

The relationship between glucose levels and resistance highlights the broader influence of metabolic state and nutrient availability on bacterial adaptation and antibiotic efficacy. In a clinical context, hyperglycaemia or high dietary glucose intake could potentially impact treatment outcomes by inadvertently supporting bacterial resistance for example. Conversely, controlling host metabolic states or modulating nutrient environments may enhance the effectiveness of some antibiotics.

Further research is needed to explore the interplay between diet, host metabolic conditions, and bacterial resistance. Nevertheless, the findings presented support the idea of personalised therapeutic strategies that integrate metabolic modulation, such as dietary interventions or targeted metabolic inhibitors, as having potential for providing new avenues to improve antibiotic efficacy and combat AMR.

7.2 Addressing objectives

The objectives of this thesis outlined in the introduction, centred around exploring the metabolic costs of resistance, the interplay between genetic and metabolic adaptations, and determining strategies for targeting these in the context of the need for innovative therapeutic strategies to overcome AMR. Results from untargeted metabolomics, and complementary approaches, established specific changes in metabolism linked to both resistance and antibiotic treatment. Metabolic pathway analysis provided functional insights into the way in which the *E. coli* strains responded to resistance and treatment, and thereby offered areas of metabolism as potential therapeutic targets. These functional changes were found to affect multiple areas of cell function centred on nucleotide metabolism, oxidative stress management and energy metabolism. Further studies revealed that modulating energy metabolism in resistant strains,

using a range of inhibitors and dietary supplementation, altered MICs alongside antibiotic treatment.

The investigation of co-therapy strategies further addressed the challenge of enhancing antibiotic efficacy. By exploring metabolic modulators in combination with antibiotics, results from these experiments offered a proof of concept for disrupting metabolic resilience to enhance antibiotic efficacy and a way to address the challenge of limited therapeutic options available in many cases. Targeting these as metabolic vulnerabilities offers a potential avenue for therapeutic testing, potentially enabling the disruption of metabolic stability and the restoration of antibiotic susceptibility. Testing these in depth was beyond the scope of this thesis but is a recommended future direction.

In addressing these objectives, it is also important to reflect on the limitations of the experimental model used. This study employed the use of a single lab-adapted strain with one high-copy number plasmid which does not fully represent the genotypic and phenotypic diversity found in clinical pathogenic *E. coli*. Alternative strains or the use of different plasmids with varied replication origins and copy numbers, may show distinct metabolic adaptations and could be explored in future work to validate and extend these findings.

Nonetheless, the model used in this thesis provides a controlled and reproducible framework for systematically dissecting the metabolic consequences of resistance gene carriage and antibiotic exposure. The consistency of the observed metabolic changes, particularly in nucleotide metabolism, oxidative stress management, and energy homeostasis, suggests these pathways may represent metabolic vulnerabilities worth investigating across *E. coli* strains. These findings lay the foundation for translational studies in clinically relevant backgrounds and emphasise the importance of accounting for metabolic cost and plasticity in the development of resistance-targeting therapies.

7.3 Broader implications for the field

This study contributes to the field of AMR research by providing a detailed metabolic perspective that complements existing genetic and proteomic insights. The genetic insights

include the use of the NDM-7 gene, carried on the pCR2.1 plasmid, which confers resistance by encoding the metallo-β-lactamase enzyme. Proteomic insights highlight the role of this enzyme, NDM-7, in hydrolysing carbapenems and driving resistance in the *E. coli* DH5α strain. The metabolomics findings presented bridge critical gaps in understanding how resistant strains sustain viability under antibiotic pressure, emphasising the role of metabolism as an important factor in whole organism resistance mechanisms. By focusing on metabolic pathways, this research highlighted opportunities to exploit bacterial vulnerabilities for therapeutic gain.

The insights gained from studying bacterial metabolism extended beyond their immediate relevance to AMR and provide actionable strategies for combating resistance. Understanding how metabolism supports resistance mechanisms can guide the design of next-generation antibiotics and combination therapies targeting key metabolic vulnerabilities. Based on the findings, glycolysis and the pentose phosphate pathway emerge as promising targets, as they are essential for energy production and nucleotide biosynthesis required to sustain resistance mechanisms. For example, inhibitors such as 2-DG, which disrupt glycolysis, could be used to weaken bacterial resilience and enhance the efficacy of existing antibiotics.

In addition, targeting the bacterial ETC could further impair energy metabolism, undermining resistance. Drugs such as bedaquiline, which inhibit ATP synthase in some bacteria, demonstrate the feasibility of this approach. The rationale for focusing on the ETC lies in its critical role in maintaining energy homeostasis under stress conditions, including antibiotic exposure. A key principle behind the potential efficacy of this approach was highlighted by the results in Chapter 6 which showed that the structural specificity of enzymes involved in bacterial and mammalian ETCs are very different, providing potential to target one without compromising the other. Studies have also explored other ETC inhibitors, such as phenothiazines, which could be considered for further development.[527]

Modulating the metabolic environment could offer complementary strategies. Depleting glucose or shifting bacterial metabolism toward less efficient energy substrates might reduce the metabolic capacity required for resistance. Conversely, the selective enhancement of

alternative substrates in combination with inhibitors of key pathways could be used to amplify metabolic disruption. Such approaches would benefit from tailoring to the specific metabolic state of the infection, guided by diagnostic tools.

The identification of metabolic biomarkers through studies like these could also enhance diagnostic precision, enabling the rapid detection of resistant infections and facilitating personalised treatment strategies.[528] For example, biomarkers associated with pathways like nucleotide biosynthesis or oxidative stress responses could provide real-time insight into bacterial susceptibility. Furthermore, studying bacterial responses to antibiotics across diverse environmental conditions, such as varying nutrient levels or host metabolic states, may be used to inform strategies for optimising antibiotic use in various clinical settings. These insights collectively support the development of metabolic-targeted therapies and diagnostic tools to advance the fight against AMR in both hospital and community settings.

7.4 Future directions

To build on the findings of this thesis, future research should aim to validate the identified metabolic targets and pathways in vivo or in other clinically relevant models. This validation is critical for translating the metabolic insights from this thesis into practical therapeutic applications. Specifically, pathways such as glycolysis, the pentose phosphate pathway, and nucleotide biosynthesis should be further validated as targets for disrupting bacterial resistance mechanisms. For instance, purine biosynthesis inhibitors like mycophenolic acid may disrupt nucleotide metabolism and reduce bacterial fitness under antibiotic exposure.

Validation experiments could also explore the role of plasmid-specific resistance mechanisms by utilising plasmids that lack β-lactam resistance genes, such as those conferring resistance to other antibiotic classes, to confirm whether the metabolic adaptations observed are universal or specific to β-lactam resistance. Such experiments would provide context-specific insights into the metabolic costs and vulnerabilities associated with resistance mechanisms. Developing bacterial-specific tools, such as adapting live-cell analysis tools like the Seahorse XF Analyser, would better capture bacterial metabolic dynamics. Temporal dynamics of

metabolic responses should be explored by conducting studies that capture the progression of metabolic changes under prolonged antibiotic exposure, revealing critical intervention points. Expanding compound screening to identify more robust metabolic modulators targeting other primary metabolic pathways such as the TCA cycle lipid metabolism, or additional enzymes involved in nucleotide biosynthesis, would provide additional therapeutic candidates. For example, TCA cycle inhibitor such as fluoroacetate may offer novel therapeutic options for disrupting energy metabolism in resistant strains.

Integrating metabolomics with transcriptomics and proteomics in a multi-omics approach would also provide a more comprehensive understanding of resistance mechanisms. The multi-omics approach could be used to reveal how changes at the transcriptional or proteomic level align with metabolic changes, offering new insights into how resistance mechanisms are maintained and suggesting additional targets for intervention. Such approaches could also uncover metabolic biomarkers for precise diagnostics, enabling tailored treatments based on the metabolic profile of the infection.

In summary, the findings from this thesis emphasise the importance of targeting bacterial metabolism in the fight against AMR. Future work should focus on validating key pathways, refining analytical tools for a bacterial-specific applications, and expanding therapeutic strategies to include metabolic modulators as part of a broader, multi-faced approach to combat resistance.

7.5 Concluding remarks

This thesis advances our understanding of the metabolic basis of AMR in, providing new knowledge on how resistant *E. coli* strains adapt and survive under antibiotic pressure. By uncovering metabolic vulnerabilities and exploring co-therapy strategies, this work contributes to the development of innovative approaches to combat resistance. The findings underscore the importance of integrating metabolic insights into AMR research, offering a pathway toward novel therapeutic solutions that align with global efforts to address the growing threat of antimicrobial resistance.

Chapter 8 References

1 Ahmed, S. K., Hussein, S., Qurbani, K., Ibrahim, R. H., Fareeq, A., Mahmood, K. A. & Mohamed, M. G. Antimicrobial resistance: Impacts, challenges, and future prospects. *Journal of Medicine, Surgery, and Public Health* **2**, 100081 (2024). https://doi.org/https://doi.org/10.1016/j.glmedi.2024.100081

2 Salam, M. A., Al-Amin, M. Y., Salam, M. T., Pawar, J. S., Akhter, N., Rabaan, A. A. & Alqumber, M. A. A. Antimicrobial Resistance: A Growing Serious Threat for Global Public Health. *Healthcare (Basel)* **11** (2023). https://doi.org/10.3390/healthcare11131946

3 Tang, K. W. K., Millar, B. C. & Moore, J. E. Antimicrobial Resistance (AMR). *Br J Biomed Sci* **80**, 11387 (2023). https://doi.org/10.3389/bjbs.2023.11387

4 Prestinaci, F., Pezzotti, P. & Pantosti, A. Antimicrobial resistance: a global multifaceted phenomenon. *Pathog Glob Health* **109**, 309-318 (2015). https://doi.org/10.1179/2047773215y.0000000030

5 Dadgostar, P. Antimicrobial Resistance: Implications and Costs. *Infect Drug Resist* **12**, 3903-3910 (2019). https://doi.org/10.2147/idr.S234610

6 Ho, C. S., Wong, C. T. H., Aung, T. T., Lakshminarayanan, R., Mehta, J. S., Rauz, S., McNally, A., Kintses, B., Peacock, S. J., de la Fuente-Nunez, C., Hancock, R. E. W. & Ting, D. S. J. Antimicrobial resistance: a concise update. *The Lancet Microbe*, 100947 (2024). https://doi.org/https://doi.org/10.1016/j.lanmic.2024.07.010

7 Mancuso, G., Midiri, A., Gerace, E. & Biondo, C. Bacterial Antibiotic Resistance: The Most Critical Pathogens. *Pathogens* **10** (2021). https://doi.org/10.3390/pathogens10101310

8 Iskandar, K., Murugaiyan, J., Hammoudi Halat, D., Hage, S. E., Chibabhai, V., Adukkadukkam, S., Roques, C., Molinier, L., Salameh, P. & Van Dongen, M. Antibiotic Discovery and Resistance: The Chase and the Race. *Antibiotics (Basel)* **11** (2022). https://doi.org/10.3390/antibiotics11020182

9 Naghavi, M., Vollset, S. E., Ikuta, K. S., Swetschinski, L. R., Gray, A. P., Wool, E. E., Robles Aguilar, G., Mestrovic, T., Smith, G., Han, C., Hsu, R. L., Chalek, J., Araki, D. T., Chung, E., Raggi, C., Gershberg Hayoon, A., Davis Weaver, N., Lindstedt, P. A., Smith, A. E., Altay, U., Bhattacharjee, N. V., Giannakis, K., Fell, F., McManigal, B., Ekapirat, N., Mendes, J. A., Runghien, T., Srimokla, O., Abdelkader, A., Abd-Elsalam, S., Aboagye, R. G., Abolhassani, H., Abualruz, H., Abubakar, U., Abukhadijah, H. J., Aburuz, S., Abu-Zaid, A., Achalapong, S., Addo, I. Y., Adekanmbi, V., Adeyeoluwa, T. E., Adnani, Q. E. S., Adzigbli, L. A., Afzal, M. S., Afzal, S., Agodi, A., Ahlstrom, A. J., Ahmad, A., Ahmad, S., Ahmad, T., Ahmadi, A., Ahmed, A., Ahmed, H., Ahmed, I., Ahmed, M., Ahmed, S., Ahmed, S. A., Akkaif, M. A., Al Awaidy, S., Al Thaher, Y., Alalalmeh, S. O., AlBataineh, M. T., Aldhaleei, W. A., Al-Gheethi, A. A. S., Alhaji, N. B., Ali, A., Ali, L., Ali, S. S., Ali, W., Allel, K., Al-Marwani, S., Alrawashdeh, A., Altaf, A., Al-Tammemi, A. B., Al-Tawfiq, J. A., Alzoubi, K. H., Al-Zyoud, W. A., Amos, B., Amuasi, J. H., Ancuceanu, R., Andrews, J. R., Anil, A., Anuoluwa, I. A., Anvari, S., Anyasodor, A. E., Apostol, G. L. C., Arabloo, J., Arafat, M., Aravkin, A. Y., Areda, D., Aremu, A., Artamonov, A. A., Ashley, E. A., Asika, M. O., Athari, S. S., Atout, M. M. d. W., Awoke, T., Azadnajafabad, S., Azam, J. M., Aziz, S., Azzam, A. Y., Babaei, M., Babin, F.-X., Badar, M., Baig, A. A., Bajcetic, M., Baker, S., Bardhan, M., Barqawi, H. J., Basharat, Z., Basiru, A., Bastard, M., Basu, S., Bayleyegn, N. S., Belete, M. A., Bello, O. O., Beloukas, A., Berkley, J. A., Bhagavathula, A. S., Bhaskar, S., Bhuyan, S. S., Bielicki, J. A., Briko, N. I., Brown, C. S., Browne, A. J., Buonsenso, D., Bustanji, Y., Carvalheiro, C. G., Castañeda-Orjuela, C. A., Cenderadewi, M., Chadwick, J., Chakraborty, S., Chandika, R. M., Chandy, S., Chansamouth, V., Chattu, V. K., Chaudhary, A. A., Ching, P. R., Chopra, H., Chowdhury, F. R., Chu, D.-T., Chutiyami, M., Cruz-Martins, N., da Silva, A. G., Dadras, O., Dai, X., Darcho, S. D., Das, S., De la Hoz, F. P., Dekker, D. M., Dhama, K., Diaz, D., Dickson, B. F. R., Djorie, S. G., Dodangeh, M., Dohare, S., Dokova, K. G., Doshi, O. P., Dowou, R. K., Dsouza, H. L., Dunachie, S. J., Dziedzic, A. M., Eckmanns, T., Ed-Dra, A., Eftekharimehrabad, A., Ekundayo, T. C., El Sayed, I., Elhadi, M., El-Huneidi, W., Elias, C., Ellis, S. J., Elsheikh, R., Elsohaby, I., Eltaha, C., Eshrati, B., Eslami, M., Eyre, D. W., Fadaka, A. O., Fagbamigbe, A. F., Fahim, A., Fakhri-Demeshghieh, A., Fasina, F. O., Fasina, M. M., Fatehizadeh, A., Feasey, N. A., Feizkhah, A., Fekadu, G., Fischer, F., Fitriana, I., Forrest, K. M., Fortuna Rodrigues, C., Fuller, J. E., Gadanya, M. A., Gajdács, M., Gandhi, A. P., Garcia-Gallo, E. E., Garrett, D. O., Gautam, R. K., Gebregergis, M. W., Gebrehiwot, M., Gebremeskel, T. G., Geffers, C., Georgalis, L., Ghazy, R. M., Golechha, M., Golinelli, D., Gordon, M., Gulati, S., Gupta, R. D., Gupta, S., Gupta, V. K., Habteyohannes, A. D., Haller, S., Harapan, H., Harrison, M. L., Hasaballah, A. I., Hasan, I., Hasan, R. S., Hasani, H., Haselbeck, A. H., Hasnain, M. S., Hassan, I. I., Hassan, S., Hassan Zadeh Tabatabaei, M. S., Hayat, K., He, J., Hegazi, O. E., Heidari, M., Hezam, K., Holla, R., Holm, M., Hopkins, H., Hossain, M. M., Hosseinzadeh, M., Hostiuc, S., Hussein, N. R., Huy, L. D., Ibáñez-Prada, E. D., Ikiroma, A., Ilic, I. M., Islam, S. M. S., Ismail, F., Ismail, N. E., Iwu, C. D., Iwu-Jaja, C. J., Jafarzadeh, A., Jaiteh, F., Jalilzadeh Yengejeh, R., Jamora, R. D. G., Javidnia, J., Jawaid, T., Jenney, A. W. J., Jeon, H. J., Jokar, M., Jomehzadeh, N., Joo, T., Joseph, N., Kamal, Z., Kanmodi, K. K., Kantar, R. S., Kapisi, J. A., Karaye, I. M., Khader, Y. S., Khajuria, H., Khalid, N., Khamesipour, F., Khan, A., Khan, M. J., Khan, M. T., Khanal, V., Khidri, F. F., Khubchandani, J., Khusuwan, S., Kim, M. S., Kisa, A., Korshunov, V. A., Krapp, F., Krumkamp, R., Kuddus, M., Kulimbet, M., Kumar, D., Kumaran, E. A. P., Kuttikkattu, A., Kyu, H. H., Landires, I., Lawal, B. K., Le, T. T. T., Lederer, I. M., Lee, M., Lee, S. W., Lepape, A., Lerango, T. L., Ligade, V. S., Lim, C., Lim, S. S., Limenh, L. W., Liu, C., Liu, X., Liu, X., Loftus, M. J., M Amin, H. I., Maass, K. L., Maharaj, S. B., Mahmoud, M. A., Maikanti-Charalampous, P., Makram, O. M., Malhotra, K., Malik, A. A., Mandilara, G. D., Marks, F., Martinez-Guerra, B. A., Martorell, M., Masoumi-Asl, H., Mathioudakis, A. G., May, J., McHugh, T. A., Meiring, J., Meles, H. N., Melese, A., Melese, E. B., Minervini, G., Mohamed, N. S., Mohammed, S., Mohan, S., Mokdad, A. H., Monasta, L., Moodi Ghalibaf, A., Moore, C. E.,

Moradi, Y., Mossialos, E., Mougin, V., Mukoro, G. D., Mulita, F., Muller-Pebody, B., Murillo-Zamora, E., Musa, S., Musicha, P., Musila, L. A., Muthupandian, S., Nagarajan, A. J., Naghavi, P., Nainu, F., Nair, T. S., Najmuldeen, H. H. R., Natto, Z. S., Nauman, J., Nayak, B. P., Nchanji, G. T., Ndishimye, P., Negoi, I., Negoi, R. I., Nejadghaderi, S. A., Nguyen, Q. P., Noman, E. A., Nwakanma, D. C., O'Brien, S., Ochoa, T. J., Odetokun, I. A., Ogundijo, O. A., Ojo-Akosile, T. R., Okeke, S. R., Okonji, O. C., Olagunju, A. T., Olivas-Martinez, A., Olorukooba, A. A., Olwoch, P., Onyedibe, K. I., Ortiz-Brizuela, E., Osuolale, O., Ounchanum, P., Oyeyemi, O. T., P A, M. P., Paredes, J. L., Parikh, R. R., Patel, J., Patil, S., Pawar, S., Peleg, A. Y., Peprah, P., Perdigão, J., Perrone, C., Petcu, I.-R., Phommasone, K., Piracha, Z. Z., Poddighe, D., Pollard, A. J., Poluru, R., Ponce-De-Leon, A., Puvvula, J., Qamar, F. N., Qasim, N. H., Rafai, C. D., Raghav, P., Rahbarnia, L., Rahim, F., Rahimi-Movaghar, V., Rahman, M., Rahman, M. A., Ramadan, H., Ramasamy, S. K., Ramesh, P. S., Ramteke, P. W., Rana, R. K., Rani, U., Rashidi, M.-M., Rathish, D., Rattanavong, S., Rawaf, S., Redwan, E. M. M., Reyes, L. F., Roberts, T., Robotham, J. V., Rosenthal, V. D., Ross, A. G., Roy, N., Rudd, K. E., Sabet, C. J., Saddik, B. A., Saeb, M. R., Saeed, U., Saeedi Moghaddam, S., Saengchan, W., Safaei, M., Saghazadeh, A., Saheb Sharif-Askari, N., Sahebkar, A., Sahoo, S. S., Sahu, M., Saki, M., Salam, N., Saleem, Z., Saleh, M. A., Samodra, Y. L., Samy, A. M., Saravanan, A., Satpathy, M., Schumacher, A. E., Sedighi, M., Seekaew, S., Shafie, M., Shah, P. A., Shahid, S., Shahwan, M. J., Shakoor, S., Shalev, N., Shamim, M. A., Shamshirgaran, M. A., Shamsi, A., Sharifan, A., Shastry, R. P., Shetty, M., Shittu, A., Shrestha, S., Siddig, E. E., Sideroglou, T., Sifuentes-Osornio, J., Silva, L. M. L. R., Simões, E. A. F., Simpson, A. J. H., Singh, A., Singh, S., Sinto, R., Soliman, S. S. M., Soraneh, S., Stoesser, N., Stoeva, T. Z., Swain, C. K., Szarpak, L., T Y, S. S., Tabatabai, S., Tabche, C., Taha, Z. M.-A., Tan, K.-K., Tasak, N., Tat, N. Y., Thaiprakong, A., Thangaraju, P., Tigoi, C. C., Tiwari, K., Tovani-Palone, M. R., Tran, T. H., Tumurkhuu, M., Turner, P., Udoakang, A. J., Udoh, A., Ullah, N., Ullah, S., Vaithinathan, A. G., Valenti, M., Vos, T., Vu, H. T. L., Waheed, Y., Walker, A. S., Walson, J. L., Wangrangsimakul, T., Weerakoon, K. G., Wertheim, H. F. L., Williams, P. C. M., Wolde, A. A., Wozniak, T. M., Wu, F., Wu, Z., Yadav, M. K. K., Yaghoubi, S., Yahaya, Z. S., Yarahmadi, A., Yezli, S., Yismaw, Y. E., Yon, D. K., Yuan, C.-W., Yusuf, H., Zakham, F., Zamagni, G., Zhang, H., Zhang, Z.-J., Zielińska, M., Zumla, A., Zyoud, S. e. H. H., Zyoud, S. H., Hay, S. I., Stergachis, A., Sartorius, B., Cooper, B. S., Dolecek, C. & Murray, C. J. L. Global burden of bacterial antimicrobial resistance 1990-2021: a systematic analysis with forecasts to 2050. *The Lancet* **404**, 1199-1226 (2024). https://doi.org/10.1016/S0140-6736(24)01867-1

10 de Kraker, M. E., Stewardson, A. J. & Harbarth, S. Will 10 Million People Die a Year due to Antimicrobial Resistance by 2050? *PLoS Med* **13**, e1002184 (2016). https://doi.org/10.1371/journal.pmed.1002184

11 Poudel, A. N., Zhu, S., Cooper, N., Little, P., Tarrant, C., Hickman, M. & Yao, G. The economic burden of antibiotic resistance: A systematic review and meta-analysis. *PLoS One* **18**, e0285170 (2023). https://doi.org/10.1371/journal.pone.0285170

12 Michaelis, C. & Grohmann, E. Horizontal Gene Transfer of Antibiotic Resistance Genes in Biofilms. *Antibiotics (Basel)* **12** (2023). https://doi.org/10.3390/antibiotics12020328

13 Reygaert, W. C. An overview of the antimicrobial resistance mechanisms of bacteria. *AIMS Microbiol* **4**, 482-501 (2018). https://doi.org/10.3934/microbiol.2018.3.482

14 Munita, J. M. & Arias, C. A. Mechanisms of Antibiotic Resistance. *Microbiol Spectr* **4** (2016). https://doi.org/10.1128/microbiolspec.VMBF-0016-2015

15 Bello, A. & Dingle, T. C. What's That Resistance Mechanism? Understanding Genetic Determinants of Gram-Negative Bacterial Resistance. *Clinical Microbiology Newsletter* **40**, 165-174 (2018). https://doi.org/https://doi.org/10.1016/j.clinmicnews.2018.10.001

16 Vinayamohan, P. G., Pellissery, A. J. & Venkitanarayanan, K. Role of horizontal gene transfer in the dissemination of antimicrobial resistance in food animal production. *Current Opinion in Food Science* **47**, 100882 (2022). https://doi.org/https://doi.org/10.1016/j.cofs.2022.100882

17 Di Lodovico, S., Fasciana, T., Di Giulio, M., Cellini, L., Giammanco, A., Rossolini, G. M. & Antonelli, A. Spread of Multidrug-Resistant Microorganisms. *Antibiotics (Basel)* **11** (2022). https://doi.org/10.3390/antibiotics11070832

18 Iovleva, A. & Doi, Y. Carbapenem-Resistant Enterobacteriaceae. *Clin Lab Med* **37**, 303-315 (2017). https://doi.org/10.1016/j.cll.2017.01.005

19 Larsson, D. G. J. & Flach, C.-F. Antibiotic resistance in the environment. *Nature Reviews Microbiology* **20**, 257-269 (2022). https://doi.org/10.1038/s41579-021-00649-x

20 Davies, J. & Davies, D. Origins and evolution of antibiotic resistance. *Microbiol Mol Biol Rev* **74**, 417-433 (2010). https://doi.org/10.1128/mmbr.00016-10

21 Dawan, J. & Ahn, J. Bacterial Stress Responses as Potential Targets in Overcoming Antibiotic Resistance. *Microorganisms* **10** (2022). https://doi.org/10.3390/microorganisms10071385

22 Kok, M., Maton, L., van der Peet, M., Hankemeier, T. & van Hasselt, J. G. C. Unraveling antimicrobial resistance using metabolomics. *Drug Discovery Today* **27**, 1774-1783 (2022). https://doi.org/https://doi.org/10.1016/j.drudis.2022.03.015

23 De Angelis, G., Del Giacomo, P., Posteraro, B., Sanguinetti, M. & Tumbarello, M. Molecular Mechanisms, Epidemiology, and Clinical Importance of β-Lactam Resistance in *Enterobacteriaceae*. *Int J Mol Sci* **21** (2020). https://doi.org/10.3390/ijms21145090

24 Narendrakumar, L., Chakraborty, M., Kumari, S., Paul, D. & Das, B. β-Lactam potentiators to re-sensitize resistant pathogens: Discovery, development, clinical use and the way forward. *Front Microbiol* **13**, 1092556 (2022). https://doi.org/10.3389/fmicb.2022.1092556

25 Bush, K. & Bradford, P. A. β-Lactams and β-Lactamase Inhibitors: An Overview. *Cold Spring Harbor perspectives in medicine* **6**, a025247-a025247 (2016). https://doi.org/10.1101/cshperspect.a025247

26 Meletis, G. Carbapenem resistance: overview of the problem and future perspectives. *Ther Adv Infect Dis* **3**, 15-21 (2016). https://doi.org/10.1177/2049936115621709

27 Sheu, C. C., Chang, Y. T., Lin, S. Y., Chen, Y. H. & Hsueh, P. R. Infections Caused by Carbapenem-Resistant *Enterobacteriaceae*: An Update on Therapeutic Options. *Front Microbiol* **10**, 80 (2019). https://doi.org/10.3389/fmicb.2019.00080

28 Boyd, S. E., Livermore, D. M., Hooper, D. C. & Hope, W. W. Metallo-β-Lactamases: Structure, Function, Epidemiology, Treatment Options, and the Development Pipeline. *Antimicrob Agents Chemother* **64** (2020). https://doi.org/10.1128/aac.00397-20

29 Palacios, A. R., Rossi, M. A., Mahler, G. S. & Vila, A. J. Metallo-β-Lactamase Inhibitors Inspired on Snapshots from the Catalytic Mechanism. *Biomolecules* **10** (2020). https://doi.org/10.3390/biom10060854

30 Palacios, A. R., Mojica, M. F., Giannini, E., Taracila, M. A., Bethel, C. R., Alzari, P. M., Otero, L. H., Klinke, S., Llarrull, L. I., Bonomo, R. A. & Vila, A. J. The Reaction Mechanism of Metallo-β-Lactamases Is Tuned by the Conformation of an Active-Site Mobile Loop. *Antimicrob Agents Chemother* **63** (2019). https://doi.org/10.1128/aac.01754-18

31 Bahr, G., González, L. J. & Vila, A. J. Metallo-β-lactamases in the Age of Multidrug Resistance: From Structure and Mechanism to Evolution, Dissemination, and Inhibitor Design. *Chem Rev* **121**, 7957-8094 (2021). https://doi.org/10.1021/acs.chemrev.1c00138

32 Krco, S., Davis, S. J., Joshi, P., Wilson, L. A., Monteiro Pedroso, M., Douw, A., Schofield, C. J., Hugenholtz, P., Schenk, G. & Morris, M. T. Structure, function, and evolution of metallo-β-lactamases from the B3 subgroup-emerging targets to combat antibiotic resistance. *Front Chem* **11**, 1196073 (2023). https://doi.org/10.3389/fchem.2023.1196073

33 Meini, M. R., Llarrull, L. I. & Vila, A. J. Overcoming differences: The catalytic mechanism of metallo-β-lactamases. *FEBS Lett* **589**, 3419-3432 (2015). https://doi.org/10.1016/j.febslet.2015.08.015

34 Palzkill, T. Metallo-β-lactamase structure and function. *Ann N Y Acad Sci* **1277**, 91-104 (2013). https://doi.org/10.1111/j.1749-6632.2012.06796.x

35 Zhou, R., Fang, X., Zhang, J., Zheng, X., Shangguan, S., Chen, S., Shen, Y., Liu, Z., Li, J., Zhang, R., Shen, J., Walsh, T. R. & Wang, Y. Impact of carbapenem resistance on mortality in patients infected with *Enterobacteriaceae*: a systematic review and meta-analysis. *BMJ Open* **11**, e054971 (2021). https://doi.org/10.1136/bmjopen-2021-054971

36 Ghahramani, A., Naghadian Moghaddam, M. M., Kianparsa, J. & Ahmadi, M. H. Overall status of carbapenem resistance among clinical isolates of *Acinetobacter baumannii*: a systematic review and meta-analysis. *Journal of Antimicrobial Chemotherapy* **79**, 3264-3280 (2024). https://doi.org/10.1093/jac/dkae358

37 Wu, W., Feng, Y., Tang, G., Qiao, F., McNally, A. & Zong, Z. NDM Metallo-β-Lactamases and Their Bacterial Producers in Health Care Settings. *Clin Microbiol Rev* **32** (2019). https://doi.org/10.1128/cmr.00115-18

38 Partridge, S. R., Kwong, S. M., Firth, N. & Jensen, S. O. Mobile Genetic Elements Associated with Antimicrobial Resistance. *Clin Microbiol Rev* **31** (2018). https://doi.org/10.1128/cmr.00088-17

39 Bennett, P. M. Plasmid encoded antibiotic resistance: acquisition and transfer of antibiotic resistance genes in bacteria. *Br J Pharmacol* **153 Suppl 1**, S347-357 (2008). https://doi.org/10.1038/sj.bjp.0707607

40 Emamalipour, M., Seidi, K., Zununi Vahed, S., Jahanban-Esfahlan, A., Jaymand, M., Majdi, H., Amoozgar, Z., Chitkushev, L. T., Javaheri, T., Jahanban-Esfahlan, R. & Zare, P. Horizontal Gene Transfer: From Evolutionary Flexibility to Disease Progression. *Front Cell Dev Biol* **8**, 229 (2020). https://doi.org/10.3389/fcell.2020.00229

41 Mojica, M. F., Rossi, M.-A., Vila, A. J. & Bonomo, R. A. The urgent need for metallo-β-lactamase inhibitors: an unattended global threat. *The Lancet Infectious Diseases* **22**, e28-e34 (2022). https://doi.org/https://doi.org/10.1016/S1473-3099(20)30868-9

42 Bahr, G., Vitor-Horen, L., Bethel, C. R., Bonomo, R. A., González, L. J. & Vila, A. J. Clinical Evolution of New Delhi Metallo-β-Lactamase (NDM) Optimizes Resistance under Zn(II) Deprivation. *Antimicrob Agents Chemother* **62** (2018). https://doi.org/10.1128/aac.01849-17

43 Yuan, W., Xu, J., Guo, L., Chen, Y., Gu, J., Zhang, H., Yang, C., Yang, Q., Deng, S., Zhang, L., Deng, Q., Wang, Z., Ling, B. & Deng, D. Clinical Risk Factors and Microbiological and Intestinal Characteristics of Carbapenemase-Producing *Enterobacteriaceae* Colonization and Subsequent Infection. *Microbiol Spectr* **10**, e0190621 (2022). https://doi.org/10.1128/spectrum.01906-21

44 Perry, E. K., Meirelles, L. A. & Newman, D. K. From the soil to the clinic: the impact of microbial secondary metabolites on antibiotic tolerance and resistance. *Nat Rev Microbiol* **20**, 129-142 (2022). https://doi.org/10.1038/s41579-021-00620-w

45 Stokes, J. M., Lopatkin, A. J., Lobritz, M. A. & Collins, J. J. Bacterial Metabolism and Antibiotic Efficacy. *Cell Metabolism* **30**, 251-259 (2019). https://doi.org/https://doi.org/10.1016/j.cmet.2019.06.009

46 Muteeb, G., Rehman, M. T., Shahwan, M. & Aatif, M. Origin of Antibiotics and Antibiotic Resistance, and Their Impacts on Drug Development: A Narrative Review. *Pharmaceuticals (Basel)* **16** (2023). https://doi.org/10.3390/ph16111615

47 Banerjee, S., Nandy, S. K. & Chakraborti, S. in *Oxidative Stress in Microbial Diseases* (eds Sajal Chakraborti, Tapati Chakraborti, Dhrubajyoti Chattopadhyay, & Chandrima Shaha) 111-124 (Springer Singapore, 2019).

48 Qi, W., Jonker, M. J., Teichmann, L., Wortel, M. & ter Kuile, B. H. The influence of oxygen and oxidative stress on de novo acquisition of antibiotic resistance in *E. coli* and *Lactobacillus lactis*. *BMC Microbiology* **23**, 279 (2023). https://doi.org/10.1186/s12866-023-03031-4

49 Hutton, C. A., Perugini, M. A. & Gerrard, J. A. Inhibition of lysine biosynthesis: an evolving antibiotic strategy. *Molecular BioSystems* **3**, 458-465 (2007). https://doi.org/10.1039/B705624A

50 Ye, D., Sun, J., Jiang, R., Chang, J., Liu, Y., Wu, X., Li, L., Luo, Y., Wang, J., Guo, K. & Yang, Z. β-lactam antibiotics induce metabolic perturbations linked to ROS generation leads to bacterial impairment. *Front Microbiol* **15**, 1514825 (2024). https://doi.org/10.3389/fmicb.2024.1514825

51 Mourenza, Á., Gil, J. A., Mateos, L. M. & Letek, M. Oxidative Stress-Generating Antimicrobials, a Novel Strategy to Overcome Antibacterial Resistance. *Antioxidants (Basel)* **9** (2020). https://doi.org/10.3390/antiox9050361

52 Cabral, D. J., Wurster, J. I. & Belenky, P. Antibiotic Persistence as a Metabolic Adaptation: Stress, Metabolism, the Host, and New Directions. *Pharmaceuticals* **11**, 14 (2018).

53 Vestergaard, M., Bald, D. & Ingmer, H. Targeting the ATP synthase in bacterial and fungal pathogens: beyond *Mycobacterium tuberculosis*. *Journal of Global Antimicrobial Resistance* **29**, 29-41 (2022). https://doi.org/https://doi.org/10.1016/j.jgar.2022.01.026

54 Kant, S., Till, J. K. A., Liu, L., Margolis, A., Uppalapati, S., Kim, J.-S. & Vazquez-Torres, A. Gre factors help Salmonella adapt to oxidative stress by improving transcription elongation and fidelity of metabolic genes. *PLOS Biology* **21**, e3002051 (2023). https://doi.org/10.1371/journal.pbio.3002051

55 Guan, N., Li, J., Shin, H.-d., Du, G., Chen, J. & Liu, L. Microbial response to environmental stresses: from fundamental mechanisms to practical applications. *Applied Microbiology and Biotechnology* **101**, 3991-4008 (2017). https://doi.org/10.1007/s00253-017-8264-y

56 Yang, Y., Wu, Y., Sun, X.-D. & Zhang, Y. in *Oxidative Stress: Human Diseases and Medicine* (eds Canhua Huang & Yuanyuan Zhang) 213-235 (Springer Singapore, 2021).

57 Wolfe, A. J. Glycolysis for Microbiome Generation. *Microbiol Spectr* **3** (2015). https://doi.org/10.1128/microbiolspec.MBP-0014-2014

58 Martínez, J. L. & Rojo, F. Metabolic regulation of antibiotic resistance. *FEMS Microbiology Reviews* **35**, 768-789 (2011). https://doi.org/10.1111/j.1574-6976.2011.00282.x

59 Zampieri, M., Enke, T., Chubukov, V., Ricci, V., Piddock, L. & Sauer, U. Metabolic constraints on the evolution of antibiotic resistance. *Mol Syst Biol* **13**, 917 (2017). https://doi.org/10.15252/msb.20167028

60 Lobritz, M. A., Belenky, P., Porter, C. B. M., Gutierrez, A., Yang, J. H., Schwarz, E. G., Dwyer, D. J., Khalil, A. S. & Collins, J. J. Antibiotic efficacy is linked to bacterial cellular respiration. *Proceedings of the National Academy of Sciences* **112**, 8173 LP-8180 (2015). https://doi.org/10.1073/pnas.1509743112

61 Varela, M. F., Stephen, J., Lekshmi, M., Ojha, M., Wenzel, N., Sanford, L. M., Hernandez, A. J., Parvathi, A. & Kumar, S. H. Bacterial Resistance to Antimicrobial Agents. *Antibiotics* **10**, 593 (2021).

62 Urban-Chmiel, R., Marek, A., Stępień-Pyśniak, D., Wieczorek, K., Dec, M., Nowaczek, A. & Osek, J. Antibiotic Resistance in Bacteria-A Review. *Antibiotics (Basel)* **11** (2022). https://doi.org/10.3390/antibiotics11081079

63 Huang, L., Wu, C., Gao, H., Xu, C., Dai, M., Huang, L., Hao, H., Wang, X. & Cheng, G. Bacterial Multidrug Efflux Pumps at the Frontline of Antimicrobial Resistance: An Overview. *Antibiotics* **11**, 520 (2022).

64 Azeem, K., Fatima, S., Ali, A., Ubaid, A., Husain, F. M. & Abid, M. Biochemistry of Bacterial Biofilm: Insights into Antibiotic Resistance Mechanisms and Therapeutic Intervention. *Life* **15**, 49 (2025).

65 Keller, M., Han, X. & Dörr, T. Disrupting Central Carbon Metabolism Increases β-Lactam Antibiotic Susceptibility in Vibrio cholerae. *Journal of Bacteriology* **205**, e00476-00422 (2023). https://doi.org/doi:10.1128/jb.00476-22

66 Halawa, E. M., Fadel, M., Al-Rabia, M. W., Behairy, A., Nouh, N. A., Abdo, M., Olga, R., Fericean, L., Atwa, A. M., El-Nablaway, M. & Abdeen, A. Antibiotic action and resistance: updated review of mechanisms, spread, influencing factors, and alternative approaches for combating resistance. *Front Pharmacol* **14**, 1305294 (2023). https://doi.org/10.3389/fphar.2023.1305294

67 Reygaert, W. C. An overview of the antimicrobial resistance mechanisms of bacteria. *AIMS microbiology* **4**, 482-501 (2018). https://doi.org/10.3934/microbiol.2018.3.482

68 Wright, G. D. Molecular mechanisms of antibiotic resistance. *Chem. Commun.* **47**, 4055-4061 (2011). https://doi.org/10.1039/C0CC05111J

69 Zeng, X. & Lin, J. Beta-lactamase induction and cell wall metabolism in Gram-negative bacteria. *Frontiers in microbiology* **4**, 128 (2013). https://doi.org/10.3389/fmicb.2013.00128

70 Acosta, I. C. & Alonzo, F., 3rd. The Intersection between Bacterial Metabolism and Innate Immunity. *J Innate Immun* **15**, 782-803 (2023). https://doi.org/10.1159/000534872

71 Kim, S. Y., Park, C., Jang, H.-J., Kim, B.-o., Bae, H.-W., Chung, I.-Y., Kim, E. S. & Cho, Y.-H. Antibacterial strategies inspired by the oxidative stress and response networks. *Journal of Microbiology* **57**, 203-212 (2019). https://doi.org/10.1007/s12275-019-8711-9

72 Gupta, A. & Imlay, J. A. How a natural antibiotic uses oxidative stress to kill oxidant-resistant bacteria. *Proceedings of the National Academy of Sciences* **120**, e2312110120 (2023). https://doi.org/doi:10.1073/pnas.2312110120

73 Zampieri, M., Zimmermann, M., Claassen, M. & Sauer, U. Nontargeted Metabolomics Reveals the Multilevel Response to Antibiotic Perturbations. *Cell Reports* **19**, 1214-1228 (2017). https://doi.org/10.1016/j.celrep.2017.04.002

74 Zheng, E. J., Andrews, I. W., Grote, A. T., Manson, A. L., Alcantar, M. A., Earl, A. M. & Collins, J. J. Modulating the evolutionary trajectory of tolerance using antibiotics with different metabolic dependencies. *Nature Communications* **13**, 2525 (2022). https://doi.org/10.1038/s41467-022-30272-0

75 Kratz, J. C. & Banerjee, S. Gene expression tradeoffs determine bacterial survival and adaptation to antibiotic stress. *bioRxiv* (2024). https://doi.org/10.1101/2024.01.20.576495

76 Thorfinnsdottir, L. B., Bø, G. H., Booth, J. A. & Bruheim, P. Survival of *Escherichia coli* after high-antibiotic stress is dependent on both the pregrown physiological state and incubation conditions. *Front Microbiol* **14**, 1149978 (2023). https://doi.org/10.3389/fmicb.2023.1149978

77 Batchelder, J. I., Taylor, A. J. & Mok, W. W. K. Metabolites augment oxidative stress to sensitize antibiotic-tolerant *Staphylococcus aureus* to fluoroquinolones. *mBio* **15**, e02714-02724 (2024). https://doi.org/doi:10.1128/mbio.02714-24

78 Seixas, A. F., Quendera, A. P., Sousa, J. P., Silva, A. F. Q., Arraiano, C. M. & Andrade, J. M. Bacterial Response to Oxidative Stress and RNA Oxidation. *Front Genet* **12**, 821535 (2021). https://doi.org/10.3389/fgene.2021.821535

79 Shin, B., Park, C. & Park, W. Stress responses linked to antimicrobial resistance in *Acinetobacter* species. *Applied Microbiology and Biotechnology* **104**, 1423-1435 (2020). https://doi.org/10.1007/s00253-019-10317-z

80 Qi, W., Jonker, M. J., de Leeuw, W., Brul, S. & ter Kuile, B. H. Reactive oxygen species accelerate *de novo* acquisition of antibiotic resistance in *E. coli*. *iScience* **26** (2023). https://doi.org/10.1016/j.isci.2023.108373

81 Mandon, K., Nazaret, F., Farajzadeh, D., Alloing, G. & Frendo, P. Redox Regulation in Diazotrophic Bacteria in Interaction with Plants. *Antioxidants* **10**, 880 (2021). https://doi.org/10.3390/antiox10060880

82 Kracke, F., Vassilev, I. & Krömer, J. O. Microbial electron transport and energy conservation – the foundation for optimizing bioelectrochemical systems. *Frontiers in Microbiology* **6** (2015). https://doi.org/10.3389/fmicb.2015.00575

83 Wangsanut, T. & Pongpom, M. The Role of the Glutathione System in Stress Adaptation, Morphogenesis and Virulence of Pathogenic Fungi. *International Journal of Molecular Sciences* **23**, 10645 (2022).

84 Li, H., Zhou, X., Huang, Y., Liao, B., Cheng, L. & Ren, B. Reactive Oxygen Species in Pathogen Clearance: The Killing Mechanisms, the Adaption Response, and the Side Effects. *Frontiers in Microbiology* **11** (2021). https://doi.org/10.3389/fmicb.2020.622534

85 Yi, X., Feng, M., He, F., Xiao, Z., Wang, Y., Wang, S. & Yao, H. Multi-omics analysis explores the impact of ofloxacin pressure on the metabolic state in *Escherichia coli*. *Journal of Global Antimicrobial Resistance* **39**, 59-68 (2024). https://doi.org/https://doi.org/10.1016/j.jgar.2024.07.020

86 Kim, D., Bhat, A., Kim, S. K., Lee, S. & Ryu, C. M. Small RNA-modulated anaerobic respiration allows bacteria to survive under antibiotic stress conditions. *Front Cell Infect Microbiol* **14**, 1287557 (2024). https://doi.org/10.3389/fcimb.2024.1287557

87 MacDermott-Opeskin, H. I., Gupta, V. & O'Mara, M. L. Lipid-mediated antimicrobial resistance: a phantom menace or a new hope? *Biophysical Reviews* **14**, 145-162 (2022). https://doi.org/10.1007/s12551-021-00912-8

88 Lee, T. H., Charchar, P., Separovic, F., Reid, G. E., Yarovsky, I. & Aguilar, M. I. The intricate link between membrane lipid structure and composition and membrane structural properties in bacterial membranes. *Chem Sci* **15**, 3408-3427 (2024). https://doi.org/10.1039/d3sc04523d

89 Elbediwi, M. & Rolff, J. Metabolic pathways and antimicrobial peptide resistance in bacteria. *Journal of Antimicrobial Chemotherapy* **79**, 1473-1483 (2024). https://doi.org/10.1093/jac/dkae128

90 Gadar, K. & McCarthy, R. R. Using next generation antimicrobials to target the mechanisms of infection. *npj Antimicrobials and Resistance* **1**, 11 (2023). https://doi.org/10.1038/s44259-023-00011-6

91 Belete, T. M. Novel targets to develop new antibacterial agents and novel alternatives to antibacterial agents. *Human Microbiome Journal* **11**, 100052 (2019). https://doi.org/https://doi.org/10.1016/j.humic.2019.01.001

92 Estrada, A., Wright, D. L. & Anderson, A. C. Antibacterial Antifolates: From Development through Resistance to the Next Generation. *Cold Spring Harb Perspect Med* **6** (2016). https://doi.org/10.1101/cshperspect.a028324

93 Baran, A., Kwiatkowska, A. & Potocki, L. Antibiotics and Bacterial Resistance—A Short Story of an Endless Arms Race. *International Journal of Molecular Sciences* **24**, 5777 (2023).

94 Murima, P., McKinney, John D. & Pethe, K. Targeting Bacterial Central Metabolism for Drug Development. *Chemistry & Biology* **21**, 1423-1432 (2014). https://doi.org/https://doi.org/10.1016/j.chembiol.2014.08.020

95 Fiorillo, M., Lamb, R., Tanowitz, H. B., Cappello, A. R., Martinez-Outschoorn, U. E., Sotgia, F. & Lisanti, M. P. Bedaquiline, an FDA-approved antibiotic, inhibits mitochondrial function and potently blocks the proliferative expansion of stem-like cancer cells (CSCs). *Aging (Albany NY)* **8**, 1593-1607 (2016). https://doi.org/10.18632/aging.100983

96 Field, S. K. Bedaquiline for the treatment of multidrug-resistant tuberculosis: great promise or disappointment? *Ther Adv Chronic Dis* **6**, 170-184 (2015). https://doi.org/10.1177/2040622315582325

97 Baquero, F., Martínez, J. L., V, F. L., Rodríguez-Beltrán, J., Galán, J. C., San Millán, A., Cantón, R. & Coque, T. M. Evolutionary Pathways and Trajectories in Antibiotic Resistance. *Clin Microbiol Rev* **34**, e0005019 (2021). https://doi.org/10.1128/cmr.00050-19

98 Mackenzie, J. S., Lamprecht, D. A., Asmal, R., Adamson, J. H., Borah, K., Beste, D. J. V., Lee, B. S., Pethe, K., Rousseau, S., Krieger, I., Sacchettini, J. C., Glasgow, J. N. & Steyn, A. J. C. Bedaquiline reprograms central metabolism to reveal glycolytic vulnerability in *Mycobacterium tuberculosis*. *Nature Communications* **11**, 6092 (2020). https://doi.org/10.1038/s41467-020-19959-4

99 Lee, B. S., Kalia, N. P., Jin, X. E. F., Hasenoehrl, E. J., Berney, M. & Pethe, K. Inhibitors of energy metabolism interfere with antibiotic-induced death in mycobacteria. *J Biol Chem* **294**, 1936-1943 (2019). https://doi.org/10.1074/jbc.RA118.005732

100 Seung, K. J., Keshavjee, S. & Rich, M. L. Multidrug-Resistant Tuberculosis and Extensively Drug-Resistant Tuberculosis. *Cold Spring Harb Perspect Med* **5**, a017863 (2015). https://doi.org/10.1101/cshperspect.a017863

101 Jang, J. G. & Chung, J. H. Diagnosis and treatment of multidrug-resistant tuberculosis. *Yeungnam Univ J Med* **37**, 277-285 (2020). https://doi.org/10.12701/yujm.2020.00626

102 Sarathy, J. P., Gruber, G. & Dick, T. Re-Understanding the Mechanisms of Action of the Anti-Mycobacterial Drug Bedaquiline. *Antibiotics (Basel)* **8** (2019). https://doi.org/10.3390/antibiotics8040261

103 Zhang, B., Watts, K. M., Hodge, D., Kemp, L. M., Hunstad, D. A., Hicks, L. M. & Odom, A. R. A second target of the antimalarial and antibacterial agent fosmidomycin revealed by cellular metabolic profiling. *Biochemistry* **50**, 3570-3577 (2011). https://doi.org/10.1021/bi200113y

104 Umeda, T., Tanaka, N., Kusakabe, Y., Nakanishi, M., Kitade, Y. & Nakamura, K. T. Molecular basis of fosmidomycin's action on the human malaria parasite *Plasmodium falciparum*. *Sci Rep* **1**, 9 (2011). https://doi.org/10.1038/srep00009

105 Perez-Gil, J., Behrendorff, J., Douw, A. & Vickers, C. E. The methylerythritol phosphate pathway as an oxidative stress sense and response system. *Nature Communications* **15**, 5303 (2024). https://doi.org/10.1038/s41467-024-49483-8

106 Gräwert, T., Groll, M., Rohdich, F., Bacher, A. & Eisenreich, W. Biochemistry of the non-mevalonate isoprenoid pathway. *Cell Mol Life Sci* **68**, 3797-3814 (2011). https://doi.org/10.1007/s00018-011-0753-z

107 Guggisberg, A. M., Amthor, R. E. & Odom, A. R. Isoprenoid biosynthesis in *Plasmodium falciparum*. *Eukaryot Cell* **13**, 1348-1359 (2014). https://doi.org/10.1128/ec.00160-14

108 Knak, T., Abdullaziz, M. A., Höfmann, S., Alves Avelar, L. A., Klein, S., Martin, M., Fischer, M., Tanaka, N. & Kurz, T. Over 40 Years of Fosmidomycin Drug Research: A Comprehensive Review and Future Opportunities. *Pharmaceuticals* **15**, 1553 (2022).

109 Piselli, C. & Benz, R. Fosmidomycin transport through the phosphate-specific porins OprO and OprP of *Pseudomonas aeruginosa*. *Mol Microbiol* **116**, 97-108 (2021). https://doi.org/10.1111/mmi.14693

110 Armstrong, C. M., Meyers, D. J., Imlay, L. S., Freel Meyers, C. & Odom, A. R. Resistance to the antimicrobial agent fosmidomycin and an FR900098 prodrug through mutations in the deoxyxylulose phosphate reductoisomerase gene (*dxr*). *Antimicrob Agents Chemother* **59**, 5511-5519 (2015). https://doi.org/10.1128/aac.00602-15

111 Belenky, P., Ye, J. D., Porter, C. B., Cohen, N. R., Lobritz, M. A., Ferrante, T., Jain, S., Korry, B. J., Schwarz, E. G., Walker, G. C. & Collins, J. J. Bactericidal Antibiotics Induce Toxic Metabolic Perturbations that Lead to Cellular Damage. *Cell Rep* **13**, 968-980 (2015). https://doi.org/10.1016/j.celrep.2015.09.059

112 Cabral, D. J., Penumutchu, S., Reinhart, E. M., Zhang, C., Korry, B. J., Wurster, J. I., Nilson, R., Guang, A., Sano, W. H., Rowan-Nash, A. D., Li, H. & Belenky, P. Microbial Metabolism Modulates Antibiotic Susceptibility within the Murine Gut Microbiome. *Cell Metabolism* **30**, 800-823.e807 (2019). https://doi.org/10.1016/j.cmet.2019.08.020

113 Liu, Y., Yang, K., Zhang, H., Jia, Y. & Wang, Z. Combating Antibiotic Tolerance Through Activating Bacterial Metabolism. *Front Microbiol* **11**, 577564 (2020). https://doi.org/10.3389/fmicb.2020.577564

114 Goossens, S. N., Sampson, S. L. & Van Rie, A. Mechanisms of Drug-Induced Tolerance in *Mycobacterium tuberculosis*. *Clin Microbiol Rev* **34** (2020). https://doi.org/10.1128/cmr.00141-20

115 Ying, L., Zhu, H., Shoji, S. & Fredrick, K. Roles of specific aminoglycoside-ribosome interactions in the inhibition of translation. *Rna* **25**, 247-254 (2019). https://doi.org/10.1261/rna.068460.118

116 Blount, Z. D. The unexhausted potential of *E. coli*. *eLife* **4**, e05826 (2015). https://doi.org/10.7554/eLife.05826

117 Pontrelli, S., Chiu, T.-Y., Lan, E. I., Chen, F. Y. H., Chang, P. & Liao, J. C. *Escherichia coli* as a host for metabolic engineering. *Metabolic Engineering* **50**, 16-46 (2018). https://doi.org/https://doi.org/10.1016/j.ymben.2018.04.008

118 Ruiz, N. & Silhavy, T. J. How *Escherichia coli* Became the Flagship Bacterium of Molecular Biology. *Journal of Bacteriology* **204**, e00230-00222 (2022). https://doi.org/doi:10.1128/jb.00230-22

119 Tuttle, A. R., Trahan, N. D. & Son, M. S. Growth and Maintenance of *Escherichia coli* Laboratory Strains. *Curr Protoc* **1**, e20 (2021). https://doi.org/10.1002/cpz1.20

120 Adamczyk, P. A. & Reed, J. L. *Escherichia coli* as a model organism for systems metabolic engineering. *Current Opinion in Systems Biology* **6**, 80-88 (2017). https://doi.org/https://doi.org/10.1016/j.coisb.2017.11.001

121 Fakruddin, M., Mohammad Mazumdar, R., Bin Mannan, K. S., Chowdhury, A. & Hossain, M. N. Critical Factors Affecting the Success of Cloning, Expression, and Mass Production of Enzymes by Recombinant *E. coli*. *ISRN Biotechnol* **2013**, 590587 (2013). https://doi.org/10.5402/2013/590587

122 Aminian-Dehkordi, J., Rahimi, S., Golzar-Ahmadi, M., Singh, A., Lopez, J., Ledesma-Amaro, R. & Mijakovic, I. Synthetic biology tools for environmental protection. *Biotechnology Advances* **68**, 108239 (2023). https://doi.org/https://doi.org/10.1016/j.biotechadv.2023.108239

123 Pokharel, P., Dhakal, S. & Dozois, C. M. The Diversity of *Escherichia coli* Pathotypes and Vaccination Strategies against This Versatile Bacterial Pathogen. *Microorganisms* **11**, 344 (2023).

124 Russo, T. A. & Johnson, J. R. Medical and economic impact of extraintestinal infections due to *Escherichia coli*: focus on an increasingly important endemic problem. *Microbes and Infection* **5**, 449-456 (2003). https://doi.org/https://doi.org/10.1016/S1286-4579(03)00049-2

125 Terlizzi, M. E., Gribaudo, G. & Maffei, M. E. UroPathogenic *Escherichia coli* (UPEC) Infections: Virulence Factors, Bladder Responses, Antibiotic, and Non-antibiotic Antimicrobial Strategies. *Front Microbiol* **8**, 1566 (2017). https://doi.org/10.3389/fmicb.2017.01566

126 Zou, Z., Potter, R. F., McCoy, W. H. t., Wildenthal, J. A., Katumba, G. L., Mucha, P. J., Dantas, G. & Henderson, J. P. *E. coli* catheter-associated urinary tract infections are associated with distinctive virulence and biofilm gene determinants. *JCI Insight* **8** (2023). https://doi.org/10.1172/jci.insight.161461

127 Daga, A. P., Koga, V. L., Soncini, J. G. M., de Matos, C. M., Perugini, M. R. E., Pelisson, M., Kobayashi, R. K. T. & Vespero, E. C. *Escherichia coli* Bloodstream Infections in Patients at a University Hospital: Virulence Factors and Clinical Characteristics. *Front Cell Infect Microbiol* **9**, 191 (2019). https://doi.org/10.3389/fcimb.2019.00191

128 Pakbin, B., Brück, W. M. & Rossen, J. W. A. Virulence Factors of Enteric Pathogenic *Escherichia coli*: A Review. *Int J Mol Sci* **22** (2021). https://doi.org/10.3390/ijms22189922

129 Wozniak, T. M., Dyda, A. & Lee, X. The Increased Length of Hospital Stay and Mortality Associated With Community-Associated Infections in Australia. *Open Forum Infect Dis* **9**, ofac133 (2022). https://doi.org/10.1093/ofid/ofac133

130 Husna, A., Rahman, M. M., Badruzzaman, A. T. M., Sikder, M. H., Islam, M. R., Rahman, M. T., Alam, J. & Ashour, H. M. Extended-Spectrum β-Lactamases (ESBL): Challenges and Opportunities. *Biomedicines* **11** (2023). https://doi.org/10.3390/biomedicines11112937

131 Kaper, J. B., Nataro, J. P. & Mobley, H. L. T. Pathogenic *Escherichia coli*. *Nature Reviews Microbiology* **2**, 123-140 (2004). https://doi.org/10.1038/nrmicro818

132 Carrilero, L., Dunn, S. J., Moran, R. A., McNally, A. & Brockhurst, M. A. Evolutionary Responses to Acquiring a Multidrug Resistance Plasmid Are Dominated by Metabolic Functions across Diverse *Escherichia coli* Lineages. *mSystems* **8**, e0071322 (2023). https://doi.org/10.1128/msystems.00713-22

133 Pearcy, N., Hu, Y., Baker, M., Maciel-Guerra, A., Xue, N., Wang, W., Kaler, J., Peng, Z., Li, F. & Dottorini, T. Genome-Scale Metabolic Models and Machine Learning Reveal Genetic Determinants of Antibiotic Resistance in *Escherichia coli* and Unravel the Underlying Metabolic Adaptation Mechanisms. *mSystems* **6**, e0091320 (2021). https://doi.org/10.1128/mSystems.00913-20

134 San Millan, A. Evolution of Plasmid-Mediated Antibiotic Resistance in the Clinical Context. *Trends in Microbiology* **26**, 978-985 (2018). https://doi.org/10.1016/j.tim.2018.06.007

135 İncir, İ. & Kaplan, Ö. *Escherichia coli* in the production of biopharmaceuticals. *Biotechnology and Applied Biochemistry* (2024). https://doi.org/https://doi.org/10.1002/bab.2664

136 Katz, L., Chen, Y. Y., Gonzalez, R., Peterson, T. C., Zhao, H. & Baltz, R. H. Synthetic biology advances and applications in the biotechnology industry: a perspective. *Journal of Industrial Microbiology and Biotechnology* **45**, 449-461 (2018). https://doi.org/10.1007/s10295-018-2056-y

137 Snaith, A. E., Dunn, S. J., Moran, R. A., Newton, P. N., Dance, D. A. B., Davong, V., Kuenzli, E., Kantele, A., Corander, J. & McNally, A. The highly diverse plasmid population found in *Escherichia coli* colonizing travellers to Laos and its role in antimicrobial resistance gene carriage. *Microb Genom* **9** (2023). https://doi.org/10.1099/mgen.0.001000

138 Carattoli, A. Plasmids and the spread of resistance. *International Journal of Medical Microbiology* **303**, 298-304 (2013). https://doi.org/https://doi.org/10.1016/j.ijmm.2013.02.001

139 Tao, S., Chen, H., Li, N., Wang, T. & Liang, W. The Spread of Antibiotic Resistance Genes In Vivo Model. *Can J Infect Dis Med Microbiol* **2022**, 3348695 (2022). https://doi.org/10.1155/2022/3348695

140 Khan, A. U., Maryam, L. & Zarrilli, R. Structure, Genetics and Worldwide Spread of New Delhi Metallo-β-lactamase (NDM): a threat to public health. *BMC Microbiology* **17**, 101 (2017). https://doi.org/10.1186/s12866-017-1012-8

141 San Millan, A. & MacLean, R. C. Fitness Costs of Plasmids: a Limit to Plasmid Transmission. *Microbiol Spectr* **5** (2017). https://doi.org/10.1128/microbiolspec.MTBP-0016-2017

142 Händel, N., Schuurmans, J. M., Brul, S. & ter Kuile, B. H. Compensation of the metabolic costs of antibiotic resistance by physiological adaptation in *Escherichia coli*. *Antimicrob Agents Chemother* **57**, 3752-3762 (2013). https://doi.org/10.1128/aac.02096-12

143 Negeri, A. A., Mamo, H., Gahlot, D. K., Gurung, J. M., Seyoum, E. T. & Francis, M. S. Characterization of plasmids carrying bla(CTX-M) genes among extra-intestinal *Escherichia coli* clinical isolates in Ethiopia. *Sci Rep* **13**, 8595 (2023). https://doi.org/10.1038/s41598-023-35402-2

144 Ibekwe, A., Durso, L., Ducey, T. F., Oladeinde, A., Jackson, C. R., Frye, J. G., Dungan, R., Moorman, T., Brooks, J. P., Obayiuwana, A., Karathia, H., Fanelli, B. & Hasan, N. Diversity of Plasmids and Genes Encoding Resistance to Extended-Spectrum β-Lactamase in *Escherichia coli* from Different Animal Sources. *Microorganisms* **9** (2021). https://doi.org/10.3390/microorganisms9051057

145 Ma, J., Song, X., Li, M., Yu, Z., Cheng, W., Yu, Z., Zhang, W., Zhang, Y., Shen, A., Sun, H. & Li, L. Global spread of carbapenem-resistant *Enterobacteriaceae*: Epidemiological features, resistance mechanisms, detection and therapy. *Microbiological Research* **266**, 127249 (2023). https://doi.org/https://doi.org/10.1016/j.micres.2022.127249

146 Budia-Silva, M., Kostyanev, T., Ayala-Montaño, S., Bravo-Ferrer Acosta, J., Garcia-Castillo, M., Cantón, R., Goossens, H., Rodriguez-Baño, J., Grundmann, H. & Reuter, S. International and regional spread of carbapenem-resistant *Klebsiella pneumoniae* in Europe. *Nature Communications* **15**, 5092 (2024). https://doi.org/10.1038/s41467-024-49349-z

147 Porse, A., Schønning, K., Munck, C. & Sommer, M. O. Survival and Evolution of a Large Multidrug Resistance Plasmid in New Clinical Bacterial Hosts. *Mol Biol Evol* **33**, 2860-2873 (2016). https://doi.org/10.1093/molbev/msw163

148 Wein, T., Hülter, N. F., Mizrahi, I. & Dagan, T. Emergence of plasmid stability under non-selective conditions maintains antibiotic resistance. *Nature Communications* **10**, 2595 (2019). https://doi.org/10.1038/s41467-019-10600-7

149 Yang, J., Wu, R., Xia, Q., Yu, J., Yi, L. X., Huang, Y., Deng, M., He, W. Y., Bai, Y., Lv, L., Burrus, V., Wang, C. & Liu, J. H. The evolution of infectious transmission promotes the persistence of mcr-1 plasmids. *mBio* **14**, e0044223 (2023). https://doi.org/10.1128/mbio.00442-23

150 Clish, C. B. Metabolomics: an emerging but powerful tool for precision medicine. *Cold Spring Harb Mol Case Stud* **1**, a000588 (2015). https://doi.org/10.1101/mcs.a000588

151 Qiu, S., Cai, Y., Yao, H., Lin, C., Xie, Y., Tang, S. & Zhang, A. Small molecule metabolites: discovery of biomarkers and therapeutic targets. *Signal Transduction and Targeted Therapy* **8**, 132 (2023). https://doi.org/10.1038/s41392-023-01399-3

152 Wang, H. & de Carvalho, L. P. S. Metabolomic profiling reveals bacterial metabolic adaptation strategies and new metabolites. *Current Opinion in Chemical Biology* **74**, 102287 (2023). https://doi.org/https://doi.org/10.1016/j.cbpa.2023.102287

153 Goodacre, R., Vaidyanathan, S., Dunn, W. B., Harrigan, G. G. & Kell, D. B. Metabolomics by numbers: acquiring and understanding global metabolite data. *Trends in Biotechnology* **22**, 245-252 (2004). https://doi.org/https://doi.org/10.1016/j.tibtech.2004.03.007

154 Venkataraman, R., Nakedi, K., Akhade, A. S. & Soni, V. in *Antimicrobial Resistance: Factors to Findings: Omics and Systems Biology Approaches* (eds Vijay Soni & Ajay Suresh Akhade) 151-177 (Springer International Publishing, 2024).

155 Soni, V., Wang, Z. & Singh, V. Editorial: Bacterial metabolomics approach towards antimicrobials and resistance. *Front Microbiol* **14**, 1222594 (2023). https://doi.org/10.3389/fmicb.2023.1222594

156 Zhang, X.-w., Li, Q.-h., Xu, Z.-d. & Dou, J.-j. Mass spectrometry-based metabolomics in health and medical science: a systematic review. *RSC Advances* **10**, 3092-3104 (2020). https://doi.org/10.1039/C9RA08985C

157 Bingol, K. Recent Advances in Targeted and Untargeted Metabolomics by NMR and MS/NMR Methods. *High-Throughput* **7**, 9 (2018).

158 Ahmed, S., Shams, S., Trivedi, D., Lima, C., McGalliard, R., Parry, C. M., Carrol, E. D., Muhamadali, H. & Goodacre, R. Metabolic response of *Klebsiella oxytoca* to ciprofloxacin exposure: a metabolomics approach. *Metabolomics* **21**, 8 (2024). https://doi.org/10.1007/s11306-024-02206-y

159 Tang, J. Microbial metabolomics. *Curr Genomics* **12**, 391-403 (2011). https://doi.org/10.2174/138920211797248619

160 Thukral, M., Allen, A. E. & Petras, D. Progress and challenges in exploring aquatic microbial communities using non-targeted metabolomics. *The ISME Journal* **17**, 2147-2159 (2023). https://doi.org/10.1038/s41396-023-01532-8

161 Liu, R., Bao, Z. X., Zhao, P. J. & Li, G. H. Advances in the Study of Metabolomics and Metabolites in Some Species Interactions. *Molecules* **26** (2021). https://doi.org/10.3390/molecules26113311

162 Pan, Y., Cheng, J.-H. & Sun, D.-W. Metabolomic analyses on microbial primary and secondary oxidative stress responses. *Comprehensive Reviews in Food Science and Food Safety* **20**, 5675-5697 (2021). https://doi.org/https://doi.org/10.1111/1541-4337.12835

163 Eoh, H., Liu, R., Lim, J., Lee, J. J. & Sell, P. Central carbon metabolism remodeling as a mechanism to develop drug tolerance and drug resistance in *Mycobacterium tuberculosis*. *Front Cell Infect Microbiol* **12**, 958240 (2022). https://doi.org/10.3389/fcimb.2022.958240

164 Wang, H., Fan, M., Liu, S., Qu, M., Hou, X., Hou, J., Xu, Y., Shang, X., Liu, C., He, M., Gao, J., Chen, J. & Li, X. Redox homeostasis of one-carbon metabolism-dependent reprogramming is critical for RCC progression under exogenous serine/glycine-deprived conditions. *BMC Cancer* **24**, 1515 (2024). https://doi.org/10.1186/s12885-024-13304-4

165 Wu, Z., Liang, X., Li, M., Ma, M., Zheng, Q., Li, D., An, T. & Wang, G. Advances in the optimization of central carbon metabolism in metabolic engineering. *Microbial Cell Factories* **22**, 76 (2023). https://doi.org/10.1186/s12934-023-02090-6

166 Fortuin, S. & Soares, N. C. The Integration of Proteomics and Metabolomics Data Paving the Way for a Better Understanding of the Mechanisms Underlying Microbial Acquired Drug Resistance. *Front Med (Lausanne)* **9**, 849838 (2022). https://doi.org/10.3389/fmed.2022.849838

167 Derewacz, D. K., Goodwin, C. R., McNees, C. R., McLean, J. A. & Bachmann, B. O. Antimicrobial drug resistance affects broad changes in metabolomic phenotype in addition to secondary metabolism. *Proceedings of the National Academy of Sciences of the United States of America* **110**, 2336-2341 (2013). https://doi.org/10.1073/pnas.1218524110

168 Li, X. Z., Plésiat, P. & Nikaido, H. The challenge of efflux-mediated antibiotic resistance in Gram-negative bacteria. *Clin Microbiol Rev* **28**, 337-418 (2015). https://doi.org/10.1128/cmr.00117-14

169 Alonso-Vásquez, T., Fondi, M. & Perrin, E. Understanding Antimicrobial Resistance Using Genome-Scale Metabolic Modeling. *Antibiotics (Basel)* **12** (2023). https://doi.org/10.3390/antibiotics12050896

170 Gonzalez-Covarrubias, V., Martínez-Martínez, E. & Del Bosque-Plata, L. The Potential of Metabolomics in Biomedical Applications. *Metabolites* **12** (2022). https://doi.org/10.3390/metabo12020194

171 Marchev, A. S., Vasileva, L. V., Amirova, K. M., Savova, M. S., Balcheva-Sivenova, Z. P. & Georgiev, M. I. Metabolomics and health: from nutritional crops and plant-based pharmaceuticals to profiling of human biofluids. *Cellular and Molecular Life Sciences* **78**, 6487-6503 (2021). https://doi.org/10.1007/s00018-021-03918-3

172 Commisso, M., Strazzer, P., Toffali, K., Stocchero, M. & Guzzo, F. UNTARGETED METABOLOMICS: AN EMERGING APPROACH TO DETERMINE THE COMPOSITION OF HERBAL PRODUCTS. *Computational and Structural Biotechnology Journal* **4**, e201301007 (2013). https://doi.org/https://doi.org/10.5936/csbj.201301007

173 Johnson, C. H., Ivanisevic, J. & Siuzdak, G. Metabolomics: beyond biomarkers and towards mechanisms. *Nat Rev Mol Cell Biol* **17**, 451-459 (2016). https://doi.org/10.1038/nrm.2016.25

174 Johnson, C. H. & Gonzalez, F. J. Challenges and opportunities of metabolomics. *J Cell Physiol* **227**, 2975-2981 (2012). https://doi.org/10.1002/jcp.24002

175 Rampler, E., Abiead, Y. E., Schoeny, H., Rusz, M., Hildebrand, F., Fitz, V. & Koellensperger, G. Recurrent Topics in Mass Spectrometry-Based Metabolomics and Lipidomics—Standardization, Coverage, and Throughput. *Analytical Chemistry* **93**, 519-545 (2021). https://doi.org/10.1021/acs.analchem.0c04698

176 Rinschen, M. M., Ivanisevic, J., Giera, M. & Siuzdak, G. Identification of bioactive metabolites using activity metabolomics. *Nat Rev Mol Cell Biol* **20**, 353-367 (2019). https://doi.org/10.1038/s41580-019-0108-4

177 Ghafari, N. & Sleno, L. Challenges and recent advances in quantitative mass spectrometry-based metabolomics. *Analytical Science Advances* **5**, e2400007 (2024). https://doi.org/https://doi.org/10.1002/ansa.202400007

178 Roberts, L. D., Souza, A. L., Gerszten, R. E. & Clish, C. B. Targeted metabolomics. *Curr Protoc Mol Biol* **Chapter 30**, Unit 30.32.31-24 (2012). https://doi.org/10.1002/0471142727.mb3002s98

179 Rêgo, A. M., Alves da Silva, D., Ferreira, N. V., de Pina, L. C., Evaristo, J. A. M., Caprini Evaristo, G. P., Nogueira, F. C. S., Ochs, S. M., Amaral, J. J., Ferreira, R. B. R. & Antunes, L. C. M. Metabolic profiles of multidrug resistant and extensively drug resistant *Mycobacterium tuberculosis* unveiled by metabolomics. *Tuberculosis* **126**, 102043 (2021). https://doi.org/https://doi.org/10.1016/j.tube.2020.102043

180 Wen, Z., Liu, M., Rui, D., Liao, X., Su, R., Tang, Z., Wen, Z. & Ling, Z. The Metabolome of Carbapenem-Resistant *Klebsiella pneumoniae* Infection in Plasma. *Dis Markers* **2021**, 7155772 (2021). https://doi.org/10.1155/2021/7155772

181 Mielko, K. A., Jabłoński, S. J., Pruss, Ł., Milczewska, J., Sands, D., Łukaszewicz, M. & Młynarz, P. Metabolomics Comparison of Drug-Resistant and Drug-Susceptible *Pseudomonas aeruginosa* Strain (Intra- and Extracellular Analysis). *Int J Mol Sci* **22** (2021). https://doi.org/10.3390/ijms221910820

182 Rihacek, M., Kosaristanova, L., Fialova, T., Rypar, T., Sterbova, D. S., Adam, V., Zurek, L. & Cihalova, K. Metabolic adaptations of *Escherichia coli* to extended zinc exposure: insights into tricarboxylic acid cycle and trehalose synthesis. *BMC Microbiology* **24**, 384 (2024). https://doi.org/10.1186/s12866-024-03463-6

183 Chen, Y. T., Yang, K. X., Dai, Z. Y., Yi, H., Peng, X. X., Li, H. & Chen, Z. G. Repressed Central Carbon Metabolism and Its Effect on Related Metabolic Pathways in Cefoperazone/Sulbactam-Resistant *Pseudomonas aeruginosa*. *Front Microbiol* **13**, 847634 (2022). https://doi.org/10.3389/fmicb.2022.847634

184 Tran, D. T. & Dahlin, A. in *Antimicrobial Resistance: Factors to Findings: Omics and Systems Biology Approaches* (eds Vijay Soni & Ajay Suresh Akhade) 275-294 (Springer International Publishing, 2024).

185 Molina-Mora, J. A. & García, F. Molecular Determinants of Antibiotic Resistance in the Costa Rican *Pseudomonas aeruginosa* AG1 by a Multi-omics Approach: A Review of 10 Years of Study. *Phenomics* **1**, 129-142 (2021). https://doi.org/10.1007/s43657-021-00016-z

186 Pang, H. & Hu, Z. Metabolomics in drug research and development: The recent advances in technologies and applications. *Acta Pharmaceutica Sinica B* **13**, 3238-3251 (2023). https://doi.org/https://doi.org/10.1016/j.apsb.2023.05.021

187 Francine, P. Systems Biology: New Insight into Antibiotic Resistance. *Microorganisms* **10** (2022). https://doi.org/10.3390/microorganisms10122362

188 Barderas, M. G., Laborde, C. M., Posada, M., de la Cuesta, F., Zubiri, I., Vivanco, F. & Alvarez-Llamas, G. Metabolomic profiling for identification of novel potential biomarkers in cardiovascular diseases. *J Biomed Biotechnol* **2011**, 790132 (2011). https://doi.org/10.1155/2011/790132

189 Tsouka, S. & Masoodi, M. Metabolic Pathway Analysis: Advantages and Pitfalls for the Functional Interpretation of Metabolomics and Lipidomics Data. *Biomolecules* **13** (2023). https://doi.org/10.3390/biom13020244

190 Xavier, J. C., Gerhards, R. E., Wimmer, J. L. E., Brueckner, J., Tria, F. D. K. & Martin, W. F. The metabolic network of the last bacterial common ancestor. *Communications Biology* **4**, 413 (2021). https://doi.org/10.1038/s42003-021-01918-4

191 Wang, Y., Wondisford, F. E., Song, C., Zhang, T. & Su, X. Metabolic Flux Analysis-Linking Isotope Labeling and Metabolic Fluxes. *Metabolites* **10** (2020). https://doi.org/10.3390/metabo10110447

192 Emwas, A. H., Roy, R., McKay, R. T., Tenori, L., Saccenti, E., Gowda, G. A. N., Raftery, D., Alahmari, F., Jaremko, L., Jaremko, M. & Wishart, D. S. NMR Spectroscopy for Metabolomics Research. *Metabolites* **9** (2019). https://doi.org/10.3390/metabo9070123

193 Alseekh, S., Aharoni, A., Brotman, Y., Contrepois, K., D'Auria, J., Ewald, J., J, C. E., Fraser, P. D., Giavalisco, P., Hall, R. D., Heinemann, M., Link, H., Luo, J., Neumann, S., Nielsen, J., Perez de Souza, L., Saito, K., Sauer, U., Schroeder, F. C., Schuster, S., Siuzdak, G., Skirycz, A., Sumner, L. W., Snyder, M. P., Tang, H., Tohge, T., Wang, Y., Wen, W., Wu, S., Xu, G., Zamboni, N. & Fernie, A. R. Mass spectrometry-based metabolomics: a guide for annotation, quantification and best reporting practices. *Nat Methods* **18**, 747-756 (2021). https://doi.org/10.1038/s41592-021-01197-1

194 Fiehn, O. Metabolomics by Gas Chromatography-Mass Spectrometry: Combined Targeted and Untargeted Profiling. *Curr Protoc Mol Biol* **114**, 30.34.31-30.34.32 (2016). https://doi.org/10.1002/0471142727.mb3004s114

195 Berg, M., Vanaerschot, M., Jankevics, A., Cuypers, B., Breitling, R. & Dujardin, J.-C. LC-MS metabolomics from study design to data-analysis – using a versatile pathogen as a test case. *Computational and Structural Biotechnology Journal* **4**, e201301002 (2013). https://doi.org/https://doi.org/10.5936/csbj.201301002

196 Gowda, G. A., Zhang, S., Gu, H., Asiago, V., Shanaiah, N. & Raftery, D. Metabolomics-based methods for early disease diagnostics. *Expert Rev Mol Diagn* **8**, 617-633 (2008). https://doi.org/10.1586/14737159.8.5.617

197 Dai, X. & Shen, L. Advances and Trends in Omics Technology Development. *Front Med (Lausanne)* **9**, 911861 (2022). https://doi.org/10.3389/fmed.2022.911861

198 Caprioli, R. M. Imaging mass spectrometry: enabling a new age of discovery in biology and medicine through molecular microscopy. *J Am Soc Mass Spectrom* **26**, 850-852 (2015). https://doi.org/10.1007/s13361-015-1108-z

199 Stasulli, N. M. & Shank, E. A. Profiling the metabolic signals involved in chemical communication between microbes using imaging mass spectrometry. *FEMS Microbiol Rev* **40**, 807-813 (2016). https://doi.org/10.1093/femsre/fuw032

200 Rivera, E. S., Weiss, A., Migas, L. G., Freiberg, J. A., Djambazova, K. V., Neumann, E. K., Van de Plas, R., Spraggins, J. M., Skaar, E. P. & Caprioli, R. M. Imaging mass spectrometry reveals complex lipid distributions across *Staphylococcus aureus* biofilm layers. *J Mass Spectrom Adv Clin Lab* **26**, 36-46 (2022). https://doi.org/10.1016/j.jmsacl.2022.09.003

201 McCullagh, J. & Probert, F. New analytical methods focusing on polar metabolite analysis in mass spectrometry and NMR-based metabolomics. *Curr Opin Chem Biol* **80**, 102466 (2024). https://doi.org/10.1016/j.cbpa.2024.102466

202 Sun, Y., Saito, K., Iiji, R. & Saito, Y. Application of Ion Chromatography Coupled with Mass Spectrometry for Human Serum and Urine Metabolomics. *SLAS Discov* **24**, 778-786 (2019). https://doi.org/10.1177/2472555219850082

203 Delou, J. M. A., Souza, A. S. O., Souza, L. C. M. & Borges, H. L. Highlights in Resistance Mechanism Pathways for Combination Therapy. *Cells* **8** (2019). https://doi.org/10.3390/cells8091013

204 Sun, Y., Saito, K., Iiji, R. & Saito, Y. Application of Ion Chromatography Coupled with Mass Spectrometry for Human Serum and Urine Metabolomics. *SLAS Discovery* **24**, 778-786 (2019). https://doi.org/https://doi.org/10.1177/2472555219850082

205 Walsby-Tickle, J., Gannon, J., Hvinden, I., Bardella, C., Abboud, M. I., Nazeer, A., Hauton, D., Pires, E., Cadoux-Hudson, T., Schofield, C. J. & McCullagh, J. S. O. Anion-exchange chromatography mass spectrometry provides extensive coverage of primary metabolic pathways revealing altered metabolism in IDH1 mutant cells. *Communications Biology* **3**, 247 (2020). https://doi.org/10.1038/s42003-020-0957-6

206 Ngere, J. B., Ebrahimi, K. H., Williams, R., Pires, E., Walsby-Tickle, J. & McCullagh, J. S. O. Ion-Exchange Chromatography Coupled to Mass Spectrometry in Life Science, Environmental, and Medical Research. *Analytical Chemistry* **95**, 152-166 (2023). https://doi.org/10.1021/acs.analchem.2c04298

207 Petrova, B., Maynard, A. G., Wang, P. & Kanarek, N. Regulatory mechanisms of one-carbon metabolism enzymes. *J Biol Chem* **299**, 105457 (2023). https://doi.org/10.1016/j.jbc.2023.105457

208 Ji, E. H., Lee, J. & Hu, S. in *Cancer Metabolomics: Methods and Applications* (ed Shen Hu) 149-159 (Springer International Publishing, 2021).

209 Harrieder, E.-M., Kretschmer, F., Böcker, S. & Witting, M. Current state-of-the-art of separation methods used in LC-MS based metabolomics and lipidomics. *Journal of Chromatography B* **1188**, 123069 (2022). https://doi.org/https://doi.org/10.1016/j.jchromb.2021.123069

210 Hvinden, I. *Exploring metabolic vulnerability and therapeutic potential in cancers with isocitrate dehydrogenase mutations*, University of Oxford, (2022).

211 Pan, Z. & Raftery, D. Comparing and combining NMR spectroscopy and mass spectrometry in metabolomics. *Analytical and Bioanalytical Chemistry* **387**, 525-527 (2007). https://doi.org/10.1007/s00216-006-0687-8

212 Son, A., Kim, W., Park, J., Park, Y., Lee, W., Lee, S. & Kim, H. Mass Spectrometry Advancements and Applications for Biomarker Discovery, Diagnostic Innovations, and Personalized Medicine. *Int J Mol Sci* **25** (2024). https://doi.org/10.3390/ijms25189880

213 Bruggink, C. & Jensen, D. Combining ion chromatography with mass spectrometry and inductively coupled plasma-mass spectrometry: Annual review 2020. *Analytical Science Advances* **2**, 238-249 (2021). https://doi.org/https://doi.org/10.1002/ansa.202000120

214 Vranakis, I., Goniotakis, I., Psaroulaki, A., Sandalakis, V., Tselentis, Y., Gevaert, K. & Tsiotis, G. Proteome studies of bacterial antibiotic resistance mechanisms. *Journal of Proteomics* **97**, 88-99 (2014). https://doi.org/https://doi.org/10.1016/j.jprot.2013.10.027

215 Wen, X., Cao, J., Mi, J., Huang, J., Liang, J., Wang, Y., Ma, B., Zou, Y., Liao, X., Liang, J. B. & Wu, Y. Metabonomics reveals an alleviation of fitness cost in resistant *E. coli* competing against susceptible *E. coli* at sub-MIC doxycycline. *Journal of Hazardous Materials* **405**, 124215 (2021). https://doi.org/https://doi.org/10.1016/j.jhazmat.2020.124215

216 Mohd Kamal, K., Mahamad Maifiah, M. H., Abdul Rahim, N., Hashim, Y. Z. H., Abdullah Sani, M. S. & Azizan, K. A. Bacterial Metabolomics: Sample Preparation Methods. *Biochem Res Int* **2022**, 9186536 (2022). https://doi.org/10.1155/2022/9186536

217 Morales-Durán, N., León-Buitimea, A. & Morones-Ramírez, J. R. Unraveling resistance mechanisms in combination therapy: A comprehensive review of recent advances and future directions. *Heliyon* **10**, e27984 (2024). https://doi.org/10.1016/j.heliyon.2024.e27984

218 Yamin, D., Uskoković, V., Wakil, A. M., Goni, M. D., Shamsuddin, S. H., Mustafa, F. H., Alfouzan, W. A., Alissa, M., Alshengeti, A., Almaghrabi, R. H., Fares, M. A. A., Garout, M., Al Kaabi, N. A., Alshehri, A. A., Ali, H. M., Rabaan, A. A., Aldubisi, F. A., Yean, C. Y. & Yusof, N. Y. Current and Future Technologies for the Detection of Antibiotic-Resistant Bacteria. *Diagnostics (Basel)* **13** (2023). https://doi.org/10.3390/diagnostics13203246

219 Sengupta, S., Chattopadhyay, M. K. & Grossart, H. P. The multifaceted roles of antibiotics and antibiotic resistance in nature. *Front Microbiol* **4**, 47 (2013). https://doi.org/10.3389/fmicb.2013.00047

220 Lee, C. R., Lee, J. H., Park, K. S., Jeong, B. C. & Lee, S. H. Quantitative proteomic view associated with resistance to clinically important antibiotics in Gram-positive bacteria: a systematic review. *Front Microbiol* **6**, 828 (2015). https://doi.org/10.3389/fmicb.2015.00828

221 Bobate, S., Mahalle, S., Dafale, N. A. & Bajaj, A. Emergence of environmental antibiotic resistance: Mechanism, monitoring and management. *Environmental Advances* **13**, 100409 (2023). https://doi.org/https://doi.org/10.1016/j.envadv.2023.100409

222 Hornsey, M., Phee, L. & Wareham, D. W. A novel variant, NDM-5, of the New Delhi metallo-β-lactamase in a multidrug-resistant *Escherichia coli* ST648 isolate recovered from a patient in the United Kingdom. *Antimicrob Agents Chemother* **55**, 5952-5954 (2011). https://doi.org/10.1128/aac.05108-11

223 Elbing, K. & Brent, R. Media preparation and bacteriological tools. *Curr Protoc Mol Biol* **Chapter 1**, Unit 1.1 (2002). https://doi.org/10.1002/0471142727.mb0101s59

224 Hanahan, D. Studies on transformation of *Escherichia coli* with plasmids. *Journal of Molecular Biology* **166**, 557-580 (1983). https://doi.org/https://doi.org/10.1016/S0022-2836(83)80284-8

225 Green, M. R. & Sambrook, J. Cloning and transformation with plasmid vectors. *Cold Spring Harbor protocols* **2021**, 420-436 (2021). https://doi.org/10.1101/pdb.top101170

226 Krishnamurthi, V. R., Niyonshuti, I. I., Chen, J. & Wang, Y. A new analysis method for evaluating bacterial growth with microplate readers. *PLOS ONE* **16**, e0245205 (2021). https://doi.org/10.1371/journal.pone.0245205

227 Bren, A., Hart, Y., Dekel, E., Koster, D. & Alon, U. The last generation of bacterial growth in limiting nutrient. *BMC Systems Biology* **7**, 27 (2013). https://doi.org/10.1186/1752-0509-7-27

228 Campos, A. I. & Zampieri, M. Metabolomics-Driven Exploration of the Chemical Drug Space to Predict Combination Antimicrobial Therapies. *Molecular Cell* **74**, 1291-1303 e1296 (2019). https://doi.org/10.1016/j.molcel.2019.04.001

229 Maifiah, M. H. M., Creek, D. J., Nation, R. L., Forrest, A., Tsuji, B. T., Velkov, T. & Li, J. Untargeted metabolomics analysis reveals key pathways responsible for the synergistic killing of colistin and doripenem combination against *Acinetobacter baumannii*. *Scientific Reports* **7**, 45527-45527 (2017). https://doi.org/10.1038/srep45527

230 Feliu, J. X. & Villaverde, A. An optimized ultrasonication protocol for bacterial cell disruption and recovery of β-galactosidase fusion proteins. *Biotechnology Techniques* **8**, 509-514 (1994). https://doi.org/10.1007/BF00222845

231 Bradford, M. M. A rapid and sensitive method for the quantitation of microgram quantities of protein utilizing the principle of protein-dye binding. *Analytical biochemistry* **72**, 248-254 (1976). https://doi.org/10.1016/0003-2697(76)90527-3

232 Griffiths Robert, I., Whiteley Andrew, S., O'Donnell Anthony, G. & Bailey Mark, J. Rapid Method for Coextraction of DNA and RNA from Natural Environments for Analysis of Ribosomal DNA- and rRNA-Based Microbial Community Composition. *Applied and Environmental Microbiology* **66**, 5488-5491 (2000). https://doi.org/10.1128/AEM.66.12.5488-5491.2000

233 García-Alegría, A. M., Anduro-Corona, I., Pérez-Martínez, C. J., Guadalupe Corella-Madueño, M. A., Rascón-Durán, M. L. & Astiazaran-Garcia, H. Quantification of DNA through the NanoDrop Spectrophotometer: Methodological Validation Using Standard Reference Material and Sprague Dawley Rat and Human DNA. *Int J Anal Chem* **2020**, 8896738 (2020). https://doi.org/10.1155/2020/8896738

234 Horai, H., Arita, M. & Nishioka, T. in *2008 International Conference on BioMedical Engineering and Informatics.* 853-857.

235 Miyamoto, S., Abe, R., Endo, Y. & Takeshita, J.-i. *Ward method of hierarchical clustering for non-Euclidean similarity measures*. (2015).

236 Sønderholm, M., Bjarnsholt, T., Alhede, M., Kolpen, M., Jensen, P. Ø., Kühl, M. & Kragh, K. N. The Consequences of Being in an Infectious Biofilm: Microenvironmental Conditions Governing Antibiotic Tolerance. *International Journal of Molecular Sciences* **18**, 2688 (2017).

237 Uruén, C., Chopo-Escuin, G., Tommassen, J., Mainar-Jaime, R. C. & Arenas, J. Biofilms as Promoters of Bacterial Antibiotic Resistance and Tolerance. *Antibiotics* **10**, 3 (2021).

238 Walters, M. C., Roe, F., Bugnicourt, A., Franklin, M. J. & Stewart, P. S. Contributions of Antibiotic Penetration, Oxygen Limitation, and Low Metabolic Activity to Tolerance of *Pseudomonas aeruginosa* Biofilms to Ciprofloxacin and Tobramycin. *Antimicrobial Agents and Chemotherapy* **47**, 317-323 (2003). https://doi.org/doi:10.1128/aac.47.1.317-323.2003

239 Pontes, M. H. & Groisman, E. A. A Physiological Basis for Nonheritable Antibiotic Resistance. *mBio* **11**, 10.1128/mbio.00817-00820 (2020). https://doi.org/doi:10.1128/mbio.00817-20

240 Mancini, L. & Pilizota, T. Environmental conditions define the energetics of bacterial dormancy and its antibiotic susceptibility. *bioRxiv*, 2020.2006.2018.160226 (2022). https://doi.org/10.1101/2020.06.18.160226

241 Rasouly, A., Shamovsky, Y., Epshtein, V., Tam, K., Vasilyev, N., Hao, Z., Quarta, G., Pani, B., Li, L., Vallin, C., Shamovsky, I., Krishnamurthy, S., Shtilerman, A., Vantine, S., Torres, V. J. & Nudler, E. Analysing the fitness cost of antibiotic resistance to identify targets for combination antimicrobials. *Nature Microbiology* **6**, 1410-1423 (2021). https://doi.org/10.1038/s41564-021-00973-1

242 Wu, J., Dong, X., Zhang, L., Lin, Y. & Yang, K. Reversing Antibiotic Resistance Caused by Mobile Resistance Genes of High Fitness Cost. *mSphere* **6**, 10.1128/msphere.00356-00321 (2021). https://doi.org/doi:10.1128/msphere.00356-21

243 Andersson, D. I. & Levin, B. R. The biological cost of antibiotic resistance. *Current Opinion in Microbiology* **2**, 489-493 (1999). https://doi.org/https://doi.org/10.1016/S1369-5274(99)00005-3

244 Baquero, F. & Martínez, J.-L. Interventions on Metabolism: Making Antibiotic-Susceptible Bacteria. *mBio* **8**, 10.1128/mbio.01950-01917 (2017). https://doi.org/doi:10.1128/mbio.01950-17

245 Hye Hyun, C., Gye Cheol, K. & Semi, K. Distribution of *Pseudomonas*-Derived Cephalosporinase and Metallo-β-Lactamases in Carbapenem-Resistant *Pseudomonas aeruginosa* Isolates from Korea. *J. Microbiol. Biotechnol.* **25**, 1154-1162 (2015). https://doi.org/10.4014/jmb.1503.03065

246 Lisa, M.-N., Palacios, A. R., Aitha, M., González, M. M., Moreno, D. M., Crowder, M. W., Bonomo, R. A., Spencer, J., Tierney, D. L., Llarrull, L. I. & Vila, A. J. A general reaction mechanism for carbapenem hydrolysis by mononuclear and binuclear metallo-β-lactamases. *Nature Communications* **8**, 538 (2017). https://doi.org/10.1038/s41467-017-00601-9

247 Gil-Gil, T., Corona, F., Martínez, J. L. & Bernardini, A. The inactivation of enzymes belonging to the central carbon metabolism, a novel mechanism of developing antibiotic resistance. *bioRxiv*, 823013 (2019). https://doi.org/10.1101/823013

248 Derewacz, D. K., Goodwin, C. R., McNees, C. R., McLean, J. A. & Bachmann, B. O. Antimicrobial drug resistance affects broad changes in metabolomic phenotype in addition to secondary metabolism. *Proceedings of the National Academy of Sciences* **110**, 2336-2341 (2013). https://doi.org/doi:10.1073/pnas.1218524110

249 Martínez, J. L., Baquero, F. & Andersson, D. I. Predicting antibiotic resistance. *Nat Rev Microbiol* **5**, 958-965 (2007). https://doi.org/10.1038/nrmicro1796

250 Blount, Z. D. The unexhausted potential of E. coli. *Elife* **4** (2015). https://doi.org/10.7554/eLife.05826

251 Bock, A. & Sawers, G. *Escherichia coli* and *Salmonella*: Cellular and molecular biology, 2nd edition. *Fermentation*, 262-282 (1996).

252 Saha, D. & Bal, M. Transformation and expression of a staphylococcal plasmid in *Escherichia coli*. *FEMS Microbiology Letters* **109**, 279-282 (1993). https://doi.org/10.1111/j.1574-6968.1993.tb06181.x

253 He, K., Li, W., Zhao, B., Xu, H., Pan, Y., He, D., Hu, G., Wu, H. & Yuan, L. Spreading Advantages of Coresident Plasmids bla_{CTX-M}-Bearing IncFII and *mcr-1*-Bearing IncI2 in *Escherichia coli*. *Microbiology Spectrum* **10**, e01706-01721 (2022). https://doi.org/doi:10.1128/spectrum.01706-21

254 Laufs, R. & Kleimann, F. Antibiotic resistance factors and other plasmids in bacterial isolates from hospitalized patients. *Zentralbl Bakteriol Orig A* **240**, 503-516 (1978).

255 Lee, H. & Ko, K. S. Effect of multiple, compatible plasmids on the fitness of the bacterial host by inducing transcriptional changes. *Journal of Antimicrobial Chemotherapy* **76**, 2528-2537 (2021). https://doi.org/10.1093/jac/dkab240

256 Göttig, S., Hamprecht, A. G., Christ, S., Kempf, V. A. J. & Wichelhaus, T. A. Detection of NDM-7 in Germany, a new variant of the New Delhi metallo-β-lactamase with increased carbapenemase activity. *Journal of Antimicrobial Chemotherapy* **68**, 1737-1740 (2013). https://doi.org/10.1093/jac/dkt088

257 Shao, C., Hao, Y., Wang, Y., Jiang, M. & Jin, Y. Genotypic and Phenotypic Characterization of bla (NDM-7)-Harboring IncX3 Plasmid in a ST11 *Klebsiella pneumoniae* Isolated From a Pediatric Patient in China. *Front Microbiol* **11**, 576823 (2020). https://doi.org/10.3389/fmicb.2020.576823

258 Liu, L., Zhao, M., Tang, Y., Shen, A., Yang, X., Yao, L. & Tian, D. Dissemination of clinical Escherichia coli strains harboring mcr-1, blaNDM−7 and siderophore-producing plasmids in a Chinese hospital. *Antimicrobial Resistance & Infection Control* **13**, 66 (2024). https://doi.org/10.1186/s13756-024-01423-3

259 Calderaro, A., Buttrini, M., Piergianni, M., Montecchini, S., Martinelli, M., Covan, S., Piccolo, G., Medici, M. C., Arcangeletti, M. C., Chezzi, C. & De Conto, F. Evaluation of a modified meropenem hydrolysis assay on a large cohort of KPC and VIM carbapenemase-producing *Enterobacteriaceae*. *PLoS One* **12**, e0174908 (2017). https://doi.org/10.1371/journal.pone.0174908

260 Makena, A., Brem, J., Pfeffer, I., Geffen, R. E. J., Wilkins, S. E., Tarhonskaya, H., Flashman, E., Phee, L. M., Wareham, D. W. & Schofield, C. J. Biochemical characterization of New Delhi metallo-β-lactamase variants reveals differences in protein stability. *The Journal of antimicrobial chemotherapy* **70**, 463-469 (2015). https://doi.org/10.1093/jac/dku403

261 Makena, A., Brem, J., Pfeffer, I., Geffen, R. E. J., Wilkins, S. E., Tarhonskaya, H., Flashman, E., Phee, L. M., Wareham, D. W. & Schofield, C. J. Biochemical characterization of New Delhi metallo-β-lactamase variants reveals differences in protein stability. *Journal of Antimicrobial Chemotherapy* **70**, 463-469 (2014). https://doi.org/10.1093/jac/dku403

262 Farhat, N. & Khan, A. U. Inhibitors against New Delhi metallo-betalactamase-1 (NDM-1) and its variants endemic in Indian settings along with the laboratory functional gain mutant of NDM-1. *European Journal of Clinical Microbiology & Infectious Diseases* (2024). https://doi.org/10.1007/s10096-024-04761-7

263 Livermore, D. M. & Woodford, N. Carbapenemases: a problem in waiting? *Curr Opin Microbiol* **3**, 489-495 (2000). https://doi.org/10.1016/s1369-5274(00)00128-4

264 Green, M. R. & Sambrook, J. Cloning Polymerase Chain Reaction (PCR) Products: TA Cloning. *Cold Spring Harb Protoc* **2021** (2021). https://doi.org/10.1101/pdb.prot101303

265 Garforth, S. J. & Sayers, J. R. Structure-Specific DNA Binding by Bacteriophage T5 5′→3′ Exonuclease. *Nucleic Acids Research* **25**, 3801-3807 (1997). https://doi.org/10.1093/nar/25.19.3801

266 Yao, S., Hart, D. J. & An, Y. Recent advances in universal TA cloning methods for use in function studies. *Protein Eng Des Sel* **29**, 551-556 (2016). https://doi.org/10.1093/protein/gzw047

267 Nora, L. C., Westmann, C. A., Martins-Santana, L., Alves, L. F., Monteiro, L. M. O., Guazzaroni, M. E. & Silva-Rocha, R. The art of vector engineering: towards the construction of next-generation genetic tools. *Microb Biotechnol* **12**, 125-147 (2019). https://doi.org/10.1111/1751-7915.13318

268 Froger, A. & Hall, J. E. Transformation of Plasmid DNA into *E. coli* Using the Heat Shock Method. *JoVE*, e253 (2007). https://doi.org/doi:10.3791/253

269 Deylami, J., Sin Chng, S. & Hou Yong, E. Towards Understanding Antibiotic Permeation Across The Gram-Negative Bacteria Outer Membrane. *Biophysical Journal* **120**, 44a (2021). https://doi.org/https://doi.org/10.1016/j.bpj.2020.11.513

270 Tsuchido, T., Katsui, N., Takeuchi, A., Takano, M. & Shibasaki, I. Destruction of the outer membrane permeability barrier of *Escherichia coli* by heat treatment. *Applied and Environmental Microbiology* **50**, 298-303 (1985). https://doi.org/doi:10.1128/aem.50.2.298-303.1985

271 Vafaee, Y., Staniek, A., Mancheno-Solano, M. & Warzecha, H. A Modular Cloning Toolbox for the Generation of Chloroplast Transformation Vectors. *PLOS ONE* **9**, e110222 (2014). https://doi.org/10.1371/journal.pone.0110222

272 Birnboim, H. C. & Doly, J. A rapid alkaline extraction procedure for screening recombinant plasmid DNA. *Nucleic Acids Res* **7**, 1513-1523 (1979). https://doi.org/10.1093/nar/7.6.1513

273 Tipu, H. N. & Shabbir, A. Evolution of DNA sequencing. *J Coll Physicians Surg Pak* **25**, 210-215 (2015).

274 Slatko, B. E., Albright, L. M., Tabor, S. & Ju, J. DNA Sequencing by the Dideoxy Method. *Current Protocols in Molecular Biology* **47**, 7.4A.1-7.4A.39 (1999). https://doi.org/https://doi.org/10.1002/0471142727.mb0704as47

275 Messing, J. in *Methods in Enzymology* Vol. 101 20-78 (Academic Press, 1983).

276 Kuhn, R., Böllmann, J., Krahl, K., Bryant, I. M. & Martienssen, M. Data on DNA gel sample load, gel electrophoresis, PCR and cost analysis. *Data in Brief* **16**, 732-751 (2018). https://doi.org/https://doi.org/10.1016/j.dib.2017.11.082

277 Cuzon, G., Bonnin, R. A. & Nordmann, P. First Identification of Novel NDM Carbapenemase, NDM-7, in *Escherichia coli* in France. *PLOS ONE* **8**, e61322 (2013). https://doi.org/10.1371/journal.pone.0061322

278 Roux, K. H. Optimization and troubleshooting in PCR. *Cold Spring Harb Protoc* **2009**, pdb.ip66 (2009). https://doi.org/10.1101/pdb.ip66

279 Diederich, L., Roth, A. & Messer, W. A versatile plasmid vector system for the regulated expression of genes in *Escherichia coli*. *Biotechniques* **16**, 916-923 (1994).

280 Arrolla, L., Kanigiri, D. S., Mohammed, A. & Kona, V. S. K. Plasmids for Efficient Production of Recombinant Proteins in *E. coli*. *International Journal of Indigenous Herbs and Drugs* **8**, 7-13 (2023). https://doi.org/10.46956/ijihd.v8i4.469

281 Millan, A. S., Santos-Lopez, A., Ortega-Huedo, R., Bernabe-Balas, C., Kennedy, S. P. & Gonzalez-Zorn, B. Small-Plasmid-Mediated Antibiotic Resistance Is Enhanced by Increases in Plasmid Copy Number and Bacterial Fitness. *Antimicrobial Agents and Chemotherapy* **59**, 3335-3341 (2015). https://doi.org/doi:10.1128/aac.00235-15

282 Zwanzig, M. & Berger, U. Self-organisation and persistence of antibiotic resistance in evolving plasmid communities. *bioRxiv*, 2020.2009.2015.297721 (2020). https://doi.org/10.1101/2020.09.15.297721

283 Turner, P. E., Williams, E. S. C. P., Okeke, C., Cooper, V. S., Duffy, S. & Wertz, J. E. Antibiotic resistance correlates with transmission in plasmid evolution. *Evolution* **68**, 3368-3380 (2014). https://doi.org/10.1111/evo.12537

284 Gómez-Sanz, E., Kadlec, K., Feßler, A. T., Zarazaga, M., Torres, C. & Schwarz, S. Novel *erm*(T)-Carrying Multiresistance Plasmids from Porcine and Human Isolates of Methicillin-Resistant *Staphylococcus aureus* ST398 That Also Harbor Cadmium and Copper Resistance Determinants. *Antimicrobial Agents and Chemotherapy* **57**, 3275-3282 (2013). https://doi.org/doi:10.1128/aac.00171-13

285 Lucic, A., Malla, T. R., Calvopiña, K., Tooke, C. L., Brem, J., McDonough, M. A., Spencer, J. & Schofield, C. J. Studies on the Reactions of Biapenem with VIM Metallo β-Lactamases and the Serine β-Lactamase KPC-2. *Antibiotics* **11**, 396 (2022).

286 Krause, K. M., Serio, A. W., Kane, T. R. & Connolly, L. E. Aminoglycosides: An Overview. *Cold Spring Harb Perspect Med* **6** (2016). https://doi.org/10.1101/cshperspect.a027029

287 Jae-Woo, A. Rv3168 Phosphotransferase Activity Mediates Kanamycin Resistance in *Mycobacterium tuberculosis*. *J. Microbiol. Biotechnol.* **23**, 1529-1535 (2013). https://doi.org/10.4014/jmb.1306.06048

288 Zaunbrecher, M. A., Sikes, R. D., Metchock, B., Shinnick, T. M. & Posey, J. E. Overexpression of the chromosomally encoded aminoglycoside acetyltransferase *eis* confers kanamycin resistance in *Mycobacterium tuberculosis*. *Proceedings of the National Academy of Sciences* **106**, 20004-20009 (2009). https://doi.org/doi:10.1073/pnas.0907925106

289 Khulaif, M. J. & Al-Charrakh, A. H. Detection of Class 1 Integron and Antibiotic Resistance of β-Lactamase-Producing *Escherichia coli* Isolated from Four Hospitals in Babylon, Iraq. *Medical Journal of Babylon* **20**, 375-382 (2023). https://doi.org/10.4103/mjbl.Mjbl_155_23

290 Salahuddin, P., Kumar, A. & Khan, A. U. Structure, Function of Serine and Metallo-β-lactamases and their Inhibitors. *Curr Protein Pept Sci* **19**, 130-144 (2018). https://doi.org/10.2174/0929866524666170724160623

291 Iacoviello, M. P. & Rubin, S. A. Sterile Preparation of Antibiotic-Selective LB Agar Plates Using a Microwave Oven. *BioTechniques* **30**, 963-965 (2001). https://doi.org/10.2144/01305bm08

292 Zhong, F., Xu, M., Metz, P., Ghosh-Dastidar, P. & Zhu, J. A quantitative metabolomics study of bacterial metabolites in different domains. *Analytica Chimica Acta* **1037**, 237-244 (2018). https://doi.org/10.1016/j.aca.2018.02.046

293 Chaudhuri, M., Ak, P. & Pal, A. ISOLATION OF POTENTIAL ANTIMICROBIAL METABOLITE FROM ENDOPHYTIC *BACILLUS AMYLOLIQUEFACIENS* DL06 OF CARNIVOROUS PLANT *DROSERA BURMANNII VAHL*. *Asian Journal of Pharmaceutical and Clinical Research* **14**, 163-170 (2021). https://doi.org/10.22159/ajpcr.2021.v14i1.40187

294 Zhou, B., Xiao, J. F., Tuli, L. & Ressom, H. W. LC-MS-based metabolomics. *Mol Biosyst* **8**, 470-481 (2012). https://doi.org/10.1039/c1mb05350g

295 Cajka, T. & Fiehn, O. Toward Merging Untargeted and Targeted Methods in Mass Spectrometry-Based Metabolomics and Lipidomics. *Analytical Chemistry* **88**, 524-545 (2016). https://doi.org/10.1021/acs.analchem.5b04491

296 Bouhifd, M., Hartung, T., Hogberg, H. T., Kleensang, A. & Zhao, L. Review: toxicometabolomics. *J Appl Toxicol* **33**, 1365-1383 (2013). https://doi.org/10.1002/jat.2874

297 Shehadul Islam, M., Aryasomayajula, A. & Selvaganapathy, P. R. A Review on Macroscale and Microscale Cell Lysis Methods. *Micromachines (Basel)* **8** (2017).

298 Zhao, F., Wang, Z. & Huang, H. Physical Cell Disruption Technologies for Intracellular Compound Extraction from Microorganisms. *Processes* **12**, 2059 (2024).

299 Mapar, M., Rydzak, T., Groves, R. A. & Lewis, I. A. Biomarker enrichment medium: A defined medium for metabolomic analysis of microbial pathogens. *Frontiers in Microbiology* **13** (2022). https://doi.org/10.3389/fmicb.2022.957158

300 Pinu, F. R. & Villas-Boas, S. G. Extracellular Microbial Metabolomics: The State of the Art. *Metabolites* **7**, 43 (2017).

301 Neidhardt, F. C., Bloch, P. L. & Smith, D. F. Culture medium for *enterobacteria*. *J Bacteriol* **119**, 736-747 (1974). https://doi.org/10.1128/jb.119.3.736-747.1974

302 Zampieri, M., Hörl, M., Hotz, F., Müller, N. F. & Sauer, U. Regulatory mechanisms underlying coordination of amino acid and glucose catabolism in *Escherichia coli*. *Nature Communications* **10**, 3354 (2019). https://doi.org/10.1038/s41467-019-11331-5

303 Faijes, M., Mars, A. E. & Smid, E. J. Comparison of quenching and extraction methodologies for metabolome analysis of *Lactobacillus plantarum*. *Microbial Cell Factories* **6**, 27 (2007). https://doi.org/10.1186/1475-2859-6-27

304 Mohd Kamal, K., Mahamad Maifiah, M. H., Abdul Rahim, N., Hashim, Y. Z. H.-Y., Abdullah Sani, M. S. & Azizan, K. A. Bacterial Metabolomics: Sample Preparation Methods. *Biochemistry Research International* **2022**, 9186536 (2022). https://doi.org/https://doi.org/10.1155/2022/9186536

305 Prasad Maharjan, R. & Ferenci, T. Global metabolite analysis: the influence of extraction methodology on metabolome profiles of Escherichia coli. *Analytical Biochemistry* **313**, 145-154 (2003). https://doi.org/https://doi.org/10.1016/S0003-2697(02)00536-5

306 Wong, F., Stokes, J. M., Cervantes, B., Penkov, S., Friedrichs, J., Renner, L. D. & Collins, J. J. Cytoplasmic condensation induced by membrane damage is associated with antibiotic lethality. *Nature Communications* **12**, 2321 (2021). https://doi.org/10.1038/s41467-021-22485-6

307 Canelas, A. B., Ras, C., ten Pierick, A., van Dam, J. C., Heijnen, J. J. & van Gulik, W. M. Leakage-free rapid quenching technique for yeast metabolomics. *Metabolomics* **4**, 226-239 (2008). https://doi.org/10.1007/s11306-008-0116-4

308 Winder, C. L., Dunn, W. B., Schuler, S., Broadhurst, D., Jarvis, R., Stephens, G. M. & Goodacre, R. Global Metabolic Profiling of Escherichia coli Cultures: an Evaluation of Methods for Quenching and Extraction of Intracellular Metabolites. *Analytical Chemistry* **80**, 2939-2948 (2008). https://doi.org/10.1021/ac7023409

309 Bhatia, R. P., Kirit, H. A., Predeus, A. V. & Bollback, J. P. Transcriptomic profiling of *Escherichia coli* K-12 in response to a compendium of stressors. *Scientific Reports* **12**, 8788 (2022). https://doi.org/10.1038/s41598-022-12463-3

310 Olivier, I. & Loots, D. T. A comparison of two extraction methods for differentiating and characterising various *Mycobacterium* species and *Pseudomonas aeruginosa* using GC-MS metabolomics. *Afr J Microbiol Res* **6**, 3159-3172 (2012).

311 Pinu, F. R., Villas-Boas, S. G. & Aggio, R. Analysis of Intracellular Metabolites from Microorganisms: Quenching and Extraction Protocols. *Metabolites* **7**, 53 (2017).

312 Macedo, A. N., Faccio, A. T., Fukuji, T. S., Canuto, G. A. B. & Tavares, M. F. M. in *Separation Techniques Applied to Omics Sciences: From Principles to Relevant Applications* (ed Ana Valéria Colnaghi Simionato) 215-242 (Springer International Publishing, 2021).

313 Prasannan, C. B., Jaiswal, D., Davis, R. & Wangikar, P. P. An improved method for extraction of polar and charged metabolites from cyanobacteria. *PLOS ONE* **13**, e0204273 (2018). https://doi.org/10.1371/journal.pone.0204273

314 Amato, S. M., Fazen, C. H., Henry, T. C., Mok, W. W., Orman, M. A., Sandvik, E. L., Volzing, K. G. & Brynildsen, M. P. The role of metabolism in bacterial persistence. *Frontiers in Microbiology* **5**, 70 (2014). https://doi.org/10.3389/fmicb.2014.00070

315 Fuchs, T. M., Eisenreich, W., Heesemann, J. & Goebel, W. Metabolic adaptation of human pathogenic and related nonpathogenic bacteria to extra- and intracellular habitats. *FEMS Microbiology Reviews* **36**, 435-462 (2012). https://doi.org/10.1111/j.1574-6976.2011.00301.x

316 Aminov, R. Metabolomics in antimicrobial drug discovery. *Expert Opinion on Drug Discovery* **17**, 1047-1059 (2022). https://doi.org/10.1080/17460441.2022.2113774

317 Alonso-Vásquez, T., Fondi, M. & Perrin, E. Understanding Antimicrobial Resistance Using Genome-Scale Metabolic Modeling. *Antibiotics* **12**, 896 (2023). https://doi.org/10.3390/antibiotics12050896

318 Schrimpe-Rutledge, A. C., Codreanu, S. G., Sherrod, S. D. & McLean, J. A. Untargeted Metabolomics Strategies-Challenges and Emerging Directions. *J Am Soc Mass Spectrom* **27**, 1897-1905 (2016). https://doi.org/10.1007/s13361-016-1469-y

319 Sumner, L. W., Amberg, A., Barrett, D., Beale, M. H., Beger, R., Daykin, C. A., Fan, T. W., Fiehn, O., Goodacre, R., Griffin, J. L., Hankemeier, T., Hardy, N., Harnly, J., Higashi, R., Kopka, J., Lane, A. N., Lindon, J. C., Marriott, P., Nicholls, A. W., Reily, M. D., Thaden, J. J. & Viant, M. R. Proposed minimum reporting standards for chemical analysis Chemical Analysis Working Group (CAWG) Metabolomics Standards Initiative (MSI). *Metabolomics* **3**, 211-221 (2007). https://doi.org/10.1007/s11306-007-0082-2

320 Li, S., Park, Y., Duraisingham, S., Strobel, F. H., Khan, N., Soltow, Q. A., Jones, D. P. & Pulendran, B. Predicting network activity from high throughput metabolomics. *PLoS Comput Biol* **9**, e1003123 (2013). https://doi.org/10.1371/journal.pcbi.1003123

321 Beloborodova, N. V. & Fedotcheva, N. I. Influence of the Microbial Metabolite Acetyl Phosphate on Mitochondrial Functions Under Conditions of Exogenous Acetylation and Alkalization. *Metabolites* **14**, 703 (2024).

322 Duarte, N. C., Becker, S. A., Jamshidi, N., Thiele, I., Mo, M. L., Vo, T. D., Srivas, R. & Palsson, B. Ø. Global reconstruction of the human metabolic network based on genomic and bibliomic data. *Proceedings of the National Academy of Sciences* **104**, 1777-1782 (2007). https://doi.org/doi:10.1073/pnas.0610772104

323 Pang, Z., Chong, J., Zhou, G., de Lima Morais, D. A., Chang, L., Barrette, M., Gauthier, C., Jacques, P.-É., Li, S. & Xia, J. MetaboAnalyst 5.0: narrowing the gap between raw spectra and functional insights. *Nucleic Acids Research* **49**, W388-W396 (2021). https://doi.org/10.1093/nar/gkab382

324 Ma, H., Sorokin, A., Mazein, A., Selkov, A., Selkov, E., Demin, O. & Goryanin, I. The Edinburgh human metabolic network reconstruction and its functional analysis. *Mol Syst Biol* **3**, 135 (2007). https://doi.org/10.1038/msb4100177

325 Li, S., Pozhitkov, A., Ryan, R. A., Manning, C. S., Brown-Peterson, N. & Brouwer, M. Constructing a fish metabolic network model. *Genome Biology* **11**, R115 (2010). https://doi.org/10.1186/gb-2010-11-11-r115

326 Hung, K. S., Hsiao, C. C., Pai, T. W., Hu, C. H., Tzou, W. S., Wang, W. D. & Chen, Y. R. Functional enrichment analysis based on long noncoding RNA associations. *BMC Syst Biol* **12**, 45 (2018). https://doi.org/10.1186/s12918-018-0571-0

327 Kanehisa, M., Goto, S., Hattori, M., Aoki-Kinoshita, K. F., Itoh, M., Kawashima, S., Katayama, T., Araki, M. & Hirakawa, M. From genomics to chemical genomics: new developments in KEGG. *Nucleic Acids Res* **34**, D354-357 (2006). https://doi.org/10.1093/nar/gkj102

328 Calvo, J. M., Stevens, C. M., Kalyanpur, M. G. & Umbarger, H. E. The Absolute Configuration of α-carboxyisocaproic Acid (3-Isopropylmalic Acid), an Intermediate in Leucine Biosynthesis*. *Biochemistry* **3**, 2024-2027 (1964). https://doi.org/10.1021/bi00900a043

329 Howell, D. M., Graupner, M., Xu, H. & White, R. H. Identification of enzymes homologous to isocitrate dehydrogenase that are involved in coenzyme B and leucine biosynthesis in methanoarchaea. *J Bacteriol* **182**, 5013-5016 (2000). https://doi.org/10.1128/jb.182.17.5013-5016.2000

330 TeSlaa, T., Ralser, M., Fan, J. & Rabinowitz, J. D. The pentose phosphate pathway in health and disease. *Nature Metabolism* **5**, 1275-1289 (2023). https://doi.org/10.1038/s42255-023-00863-2

331 Edward H Rowsell; Smith, J. M. A. W. B. L. T. CheA, CheW, and CheY Are Required for Chemotaxis to Oxygen and Sugars of the Phosphotransferase System in *Escherichia coli*. *JOURNAL OF BACTERIOLOGY* **177**, 6011-6014 (1995).

332 Rodríguez, M., Good, T. A., Wales, M. E., Hua, J. P. & Wild, J. R. Modeling allosteric regulation of de novo pyrimidine biosynthesis in *Escherichia coli*. *Journal of Theoretical Biology* **234**, 299-310 (2005). https://doi.org/https://doi.org/10.1016/j.jtbi.2004.11.023

333 Kohanski, M. A., Dwyer, D. J. & Collins, J. J. How antibiotics kill bacteria: from targets to networks. *Nature Reviews Microbiology* **8**, 423-435 (2010). https://doi.org/10.1038/nrmicro2333

334 Wong, F., Stokes, J. M., Bening, S. C., Vidoudez, C., Trauger, S. A. & Collins, J. J. Reactive metabolic byproducts contribute to antibiotic lethality under anaerobic conditions. *Molecular Cell* **82**, 3499-3512.e3410 (2022). https://doi.org/https://doi.org/10.1016/j.molcel.2022.07.009

335 Stokes, J. M., Lopatkin, A. J., Lobritz, M. A. & Collins, J. J. Bacterial Metabolism and Antibiotic Efficacy. *Cell Metab* **30**, 251-259 (2019). https://doi.org/10.1016/j.cmet.2019.06.009

336 Andrews, J. M. Determination of minimum inhibitory concentrations. *Journal of Antimicrobial Chemotherapy* **48**, 5-16 (2001). https://doi.org/10.1093/jac/48.suppl_1.5

337 Tunçer, S. & Gurbanov, R. Non-growth inhibitory doses of dimethyl sulfoxide alter gene expression and epigenetic pattern of bacteria. *Applied Microbiology and Biotechnology* **107**, 299-312 (2023). https://doi.org/10.1007/s00253-022-12296-0

338 Administration, U. S. F. a. D. (U.S. Food and Drug Administration, 2008).

339 Hombach, M., Bloemberg, G. V. & Böttger, E. C. Effects of clinical breakpoint changes in CLSI guidelines 2010/2011 and EUCAST guidelines 2011 on antibiotic susceptibility test reporting of Gram-negative bacilli. *Journal of Antimicrobial Chemotherapy* **67**, 622-632 (2011). https://doi.org/10.1093/jac/dkr524

340 Ho, P.-L., Lai, E. L., Chow, K.-H. & Cheng, V. C. C. Effect of applying the new CLSI imipenem susceptibility breakpoints for *Enterobacteriaceae* in Hong Kong. *Journal of Antimicrobial Chemotherapy* **66**, 2671-2673 (2011). https://doi.org/10.1093/jac/dkr325

341 Donovan, G. T., Norton, J. P., Bower, J. M. & Mulvey, M. A. Adenylate cyclase and the cyclic AMP receptor protein modulate stress resistance and virulence capacity of uropathogenic *Escherichia coli*. *Infect Immun* **81**, 249-258 (2013). https://doi.org/10.1128/iai.00796-12

342 Molina-Quiroz, R. C., Silva-Valenzuela, C., Brewster, J., Castro-Nallar, E., Levy, S. B. & Camilli, A. Cyclic AMP Regulates Bacterial Persistence through Repression of the Oxidative Stress Response and SOS-Dependent DNA Repair in Uropathogenic *Escherichia coli*. *mBio* **9**, 10.1128/mbio.02144-02117 (2018). https://doi.org/doi:10.1128/mbio.02144-17

343 Sivaraman, J., Sauvé, V., Matte, A. & Cygler, M. Crystal Structure of *Escherichia coli* Glucose-1-Phosphate Thymidylyltransferase (RffH) Complexed with dTTP and Mg^{2+}. *Journal of Biological Chemistry* **277**, 44214-44219 (2002). https://doi.org/10.1074/jbc.M206932200

344 Hollinshead, W. D., Rodriguez, S., Martin, H. G., Wang, G., Baidoo, E. E. K., Sale, K. L., Keasling, J. D., Mukhopadhyay, A. & Tang, Y. J. Examining *Escherichia coli* glycolytic pathways, catabolite repression, and metabolite channeling using Δpfk mutants. *Biotechnology for Biofuels* **9**, 212 (2016). https://doi.org/10.1186/s13068-016-0630-y

345 Remus, B. S., Jacewicz, A. & Shuman, S. Structure and mechanism of *E. coli* RNA 2',3'-cyclic phosphodiesterase. *Rna* **20**, 1697-1705 (2014). https://doi.org/10.1261/rna.046797.114

346 Collard, F., Stroobant, V., Lamosa, P., Kapanda, C. N., Lambert, D. M., Muccioli, G. G., Poupaert, J. H., Opperdoes, F. & Van Schaftingen, E. Molecular Identification of N-Acetylaspartylglutamate Synthase and β-Citrylglutamate Synthase*. *Journal of Biological Chemistry* **285**, 29826-29833 (2010). https://doi.org/10.1074/jbc.M110.152629

347 Howell, D. M., Graupner, M., Xu, H. & White, R. H. Identification of Enzymes Homologous to Isocitrate Dehydrogenase That Are Involved in Coenzyme B and Leucine Biosynthesis in Methanoarchaea. *Journal of Bacteriology* **182**, 5013-5016 (2000). https://doi.org/doi:10.1128/jb.182.17.5013-5016.2000

348 Zhao, J., Chen, K., Palsson, B. O. & Yang, L. StressME: Unified computing framework of *Escherichia coli* metabolism, gene expression, and stress responses. *PLoS Comput Biol* **20**, e1011865 (2024). https://doi.org/10.1371/journal.pcbi.1011865

349 Roufou, S., Griffin, S., Katsini, L., Polańska, M., Van Impe, J. F. M., Alexiou, P. & Valdramidis, V. P. Identification of genes used by *Escherichia coli* to mitigate climatic stress conditions. *Gene Reports* **36**, 101998 (2024). https://doi.org/https://doi.org/10.1016/j.genrep.2024.101998

350 Zhang, Z., Wei, M., Jia, B. & Yuan, Y. Recent Advances in Antimicrobial Resistance: Insights from *Escherichia coli* as a Model Organism. *Microorganisms* **13**, 51 (2025).

351 San Millan, A. & MacLean, R. C. Fitness Costs of Plasmids: a Limit to Plasmid Transmission. *Microbiology Spectrum* **5**, 10.1128/microbiolspec.mtbp-0016-2017 (2017). https://doi.org/doi:10.1128/microbiolspec.mtbp-0016-2017

352 Jozefczuk, S., Klie, S., Catchpole, G., Szymanski, J., Cuadros-Inostroza, A., Steinhauser, D., Selbig, J. & Willmitzer, L. Metabolomic and transcriptomic stress response of *Escherichia coli*. *Mol Syst Biol* **6**, 364 (2010). https://doi.org/10.1038/msb.2010.18

353 Duggal, Y., Kurasz, J. E., Fontaine, B. M., Marotta, N. J., Chauhan, S. S., Karls, A. C. & Weinert, E. E. Cellular Effects of 2',3'-Cyclic Nucleotide Monophosphates in Gram-Negative Bacteria. *J Bacteriol* **204**, e0020821 (2022). https://doi.org/10.1128/jb.00208-21

354 Dion, M. Z., Leiske, D., Sharma, V. K., Zuch de Zafra, C. L. & Salisbury, C. M. Mitigation of Oxidation in Therapeutic Antibody Formulations: a Biochemical Efficacy and Safety Evaluation of N-Acetyl-Tryptophan and L-Methionine. *Pharmaceutical Research* **35**, 222 (2018). https://doi.org/10.1007/s11095-018-2467-5

355 Verrier, E. R. & Langevin, C. Cyclic Guanosine Monophosphate-Adenosine Monophosphate Synthase (cGAS), a Multifaceted Platform of Intracellular DNA Sensing. *Front Immunol* **12**, 637399 (2021). https://doi.org/10.3389/fimmu.2021.637399

356 Sohlenkamp, C. & Geiger, O. Bacterial membrane lipids: diversity in structures and pathways. *FEMS Microbiology Reviews* **40**, 133-159 (2015). https://doi.org/10.1093/femsre/fuv008

357 Geiger, O., Sohlenkamp, C. & López-Lara, I. M. in *Biogenesis of Fatty Acids, Lipids and Membranes* (ed Otto Geiger) 87-107 (Springer International Publishing, 2019).

358 Percudani, R. & Peracchi, A. A genomic overview of pyridoxal-phosphate-dependent enzymes. *EMBO Rep* **4**, 850-854 (2003). https://doi.org/10.1038/sj.embor.embor914

359 Mooney, S., Leuendorf, J.-E., Hendrickson, C. & Hellmann, H. Vitamin B6: A Long Known Compound of Surprising Complexity. *Molecules* **14**, 329-351 (2009).

360 Shane, B. Folate and Vitamin B12 Metabolism: Overview and Interaction with Riboflavin, Vitamin B6, and Polymorphisms. *Food and Nutrition Bulletin* **29**, S5-S16 (2008). https://doi.org/10.1177/15648265080292s103

361 Poole, K. Bacterial stress responses as determinants of antimicrobial resistance. *Journal of Antimicrobial Chemotherapy* **67**, 2069-2089 (2012). https://doi.org/10.1093/jac/dks196

362 Bekker, M., Kramer, G., Hartog, A. F., Wagner, M. J., de Koster, C. G., Hellingwerf, K. J. & Teixeira de Mattos, M. J. Changes in the redox state and composition of the quinone pool of *Escherichia coli* during aerobic batch-culture growth. *Microbiology* **153**, 1974-1980 (2007). https://doi.org/https://doi.org/10.1099/mic.0.2007/006098-0

363 Dalebroux, Z. D. Cues from the Membrane: Bacterial Glycerophospholipids. *Journal of Bacteriology* **199**, 10.1128/jb.00136-00117 (2017). https://doi.org/doi:10.1128/jb.00136-17

364 Cavas, L. & Kirkiz, I. Characterization of siderophores from *Escherichia coli* strains through genome mining tools: an antiSMASH study. *AMB Express* **12**, 74 (2022). https://doi.org/10.1186/s13568-022-01421-x

365 Xie, B., Wei, X., Wan, C., Zhao, W., Song, R., Xin, S. & Song, K. Exploring the Biological Pathways of Siderophores and Their Multidisciplinary Applications: A Comprehensive Review. *Molecules* **29**, 2318 (2024).

366 Schalk, I. J. Bacterial siderophores: diversity, uptake pathways and applications. *Nature Reviews Microbiology* (2024). https://doi.org/10.1038/s41579-024-01090-6

367 Kwon, S. J., Boer, A. L. d., Petri, R. & Schmidt-Dannert, C. High-Level Production of Porphyrins in Metabolically Engineered *Escherichia coli*: Systematic Extension of a Pathway Assembled from Overexpressed Genes Involved in Heme Biosynthesis. *Applied and Environmental Microbiology* **69**, 4875-4883 (2003). https://doi.org/doi:10.1128/AEM.69.8.4875-4883.2003

368 Min Ju, L., Hye-Jung, K., Ju-Young, L., An Sung, K., Soo Youn, J. & Sang Hyeon, K. Effect of Gene Amplifications in Porphyrin Pathway on Heme Biosynthesis in a Recombinant *Escherichia coli*. *J. Microbiol. Biotechnol.* **23**, 668-673 (2013). https://doi.org/10.4014/jmb.1302.02022

369 Thunell, S. Porphyrins, porphyrin metabolism and porphyrias. I. Update. *Scandinavian Journal of Clinical and Laboratory Investigation* **60**, 509-540 (2000). https://doi.org/10.1080/003655100448310

370 Javor, G. T. Thiol-stimulated secretion of riboflavin and porphyrins by *Escherichia coli*. *FEMS Microbiology Letters* **27**, 243-245 (1985). https://doi.org/10.1111/j.1574-6968.1985.tb00675.x

371 Vasilakou, E., van Loosdrecht, M. C. M. & Wahl, S. A. *Escherichia coli* metabolism under short-term repetitive substrate dynamics: adaptation and trade-offs. *Microbial Cell Factories* **19**, 116 (2020). https://doi.org/10.1186/s12934-020-01379-0

372 Reaves, M. L., Young, B. D., Hosios, A. M., Xu, Y. F. & Rabinowitz, J. D. Pyrimidine homeostasis is accomplished by directed overflow metabolism. *Nature* **500**, 237-241 (2013). https://doi.org/10.1038/nature12445

373 Winkler, M. E. & Ramos-Montañez, S. Biosynthesis of Histidine. *EcoSal Plus* **3** (2009). https://doi.org/10.1128/ecosalplus.3.6.1.9

374 Lu, C.-D. Pathways and regulation of bacterial arginine metabolism and perspectives for obtaining arginine overproducing strains. *Applied Microbiology and Biotechnology* **70**, 261-272 (2006). https://doi.org/10.1007/s00253-005-0308-z

375 Charlier, D. & Bervoets, I. Regulation of arginine biosynthesis, catabolism and transport in *Escherichia coli*. *Amino Acids* **51**, 1103-1127 (2019). https://doi.org/10.1007/s00726-019-02757-8

376 Helbig, K., Bleuel, C., Krauss, G. J. & Nies, D. H. Glutathione and Transition-Metal Homeostasis in *Escherichia coli*. *Journal of Bacteriology* **190**, 5431-5438 (2008). https://doi.org/doi:10.1128/jb.00271-08

377 Guan, X. Glutathione and glutathione disulfide – their biomedical and pharmaceutical applications. *Medicinal Chemistry Research* **32**, 1972-1994 (2023). https://doi.org/10.1007/s00044-023-03116-9

378 Páez, P. L., Becerra, M. C. & Albesa, I. Effect of the association of reduced glutathione and ciprofloxacin on the antimicrobial activity in *Staphylococcus aureus*. *FEMS Microbiology Letters* **303**, 101-105 (2010). https://doi.org/10.1111/j.1574-6968.2009.01867.x

379 Kohanski, M. A., Dwyer, D. J., Hayete, B., Lawrence, C. A. & Collins, J. J. A Common Mechanism of Cellular Death Induced by Bactericidal Antibiotics. *Cell* **130**, 797-810 (2007). https://doi.org/https://doi.org/10.1016/j.cell.2007.06.049

380 Islam, N., Kazi, M. I., Kang, K. N., Biboy, J., Gray, J., Ahmed, F., Schargel, R. D., Boutte, C. C., Dörr, T., Vollmer, W. & Boll, J. M. Peptidoglycan Recycling Promotes Outer Membrane Integrity and Carbapenem Tolerance in *Acinetobacter baumannii*. *mBio* **13**, e01001-01022 (2022). https://doi.org/doi:10.1128/mbio.01001-22

381 Garde, S., Chodisetti, P. K. & Reddy, M. Peptidoglycan: Structure, Synthesis, and Regulation. *EcoSal Plus* **9** (2021). https://doi.org/doi:10.1128/ecosalplus.ESP-0010-2020

382 Zeng, X. & Lin, J. Beta-lactamase induction and cell wall metabolism in Gram-negative bacteria. *Front Microbiol* **4**, 128 (2013). https://doi.org/10.3389/fmicb.2013.00128

383 Cho, T. H. S., Murray, C., Malpica, R., Margain-Quevedo, R., Thede, G. L., Lu, J., Edwards, R. A., Glover, J. N. M. & Raivio, T. L. The sensor of the bacterial histidine kinase CpxA is a novel dimer of extracytoplasmic Per-ARNT-Sim domains. *J Biol Chem* **300**, 107265 (2024). https://doi.org/10.1016/j.jbc.2024.107265

384 Winkler Malcolm, E. & Ramos-Montañez, S. Biosynthesis of Histidine. *EcoSal Plus* **3**, 10.1128/ecosalplus.1123.1126.1121.1129 (2009). https://doi.org/10.1128/ecosalplus.3.6.1.9

385 Turnbough, C. L., Jr. & Switzer, R. L. Regulation of pyrimidine biosynthetic gene expression in bacteria: repression without repressors. *Microbiol Mol Biol Rev* **72**, 266-300, table of contents (2008). https://doi.org/10.1128/mmbr.00001-08

386 Samuel, G. & Reeves, P. Biosynthesis of O-antigens: genes and pathways involved in nucleotide sugar precursor synthesis and O-antigen assembly. *Carbohydr Res* **338**, 2503-2519 (2003). https://doi.org/10.1016/j.carres.2003.07.009

387 Morè, N., Martorana, A. M., Biboy, J., Otten, C., Winkle, M., Serrano, C. K. G., Montón Silva, A., Atkinson, L., Yau, H., Breukink, E., den Blaauwen, T., Vollmer, W. & Polissi, A. Peptidoglycan Remodeling Enables *Escherichia coli* To Survive Severe Outer Membrane Assembly Defect. *mBio* **10** (2019). https://doi.org/10.1128/mBio.02729-18

388 Peirú, S., Rodríguez, E., Menzella, H. G., Carney, J. R. & Gramajo, H. Metabolically engineered *Escherichia coli* for efficient production of glycosylated natural products. *Microb Biotechnol* **1**, 476-486 (2008). https://doi.org/10.1111/j.1751-7915.2008.00046.x

389 Liu, Y., LaBonte, S., Brake, C., LaFayette, C., Rosebrock, A. P., Caudy, A. A. & Straight, P. D. (eLife Sciences Publications, Ltd, 2024).

390 Marconi, D., Ranfley, H., Menck, C. F. M., Ferreira, C. P. & Câmara, N. O. S. Interface of DNA Repair and Metabolism. *Current Tissue Microenvironment Reports* **1**, 209-220 (2020). https://doi.org/10.1007/s43152-020-00018-5

391 Cummings, M., Breitling, R. & Takano, E. Steps towards the synthetic biology of polyketide biosynthesis. *FEMS Microbiology Letters* **351**, 116-125 (2014). https://doi.org/10.1111/1574-6968.12365

392 Miyanaga, A. Structure and function of polyketide biosynthetic enzymes: various strategies for production of structurally diverse polyketides. *Bioscience, Biotechnology, and Biochemistry* **81**, 2227-2236 (2017). https://doi.org/10.1080/09168451.2017.1391687

393 Annunziato, G. Strategies to Overcome Antimicrobial Resistance (AMR) Making Use of Non-Essential Target Inhibitors: A Review. *Int J Mol Sci* **20** (2019). https://doi.org/10.3390/ijms20235844

394 Raetz, C. R. H. & Kennedy, E. P. Function of Cytidine Diphosphate-Diglyceride and Deoxycytidine Diphosphate-Diglyceride in the Biogenesis of Membrane Lipids in *Escherichia coli*. *Journal of Biological Chemistry* **248**, 1098-1105 (1973). https://doi.org/https://doi.org/10.1016/S0021-9258(19)44376-7

395 Wang, D., Qi, J., Han, W., Gao, J. M. & Horsman, G. P. Kanamycin-induced production of 2',3'-cyclic AMP in *Escherichia coli*. *Biochem Biophys Res Commun* **527**, 854-860 (2020). https://doi.org/10.1016/j.bbrc.2020.04.144

396 Krol, E., Werel, L., Essen, L. O. & Becker, A. Structural and functional diversity of bacterial cyclic nucleotide perception by CRP proteins. *microLife* **4** (2023). https://doi.org/10.1093/femsml/uqad024

397 Łyżeń, R., Gawron, G., Kadziński, L. & Banecki, B. GSH Protects the *Escherichia coli* Cells from High Concentrations of Thymoquinone. *Molecules* **27** (2022). https://doi.org/10.3390/molecules27082546

398 Venkat, S., Chen, H., Stahman, A., Hudson, D., McGuire, P., Gan, Q. & Fan, C. Characterizing Lysine Acetylation of Isocitrate Dehydrogenase in *Escherichia coli*. *J Mol Biol* **430**, 1901-1911 (2018). https://doi.org/10.1016/j.jmb.2018.04.031

399 Cabrera, R., Baez, M., Pereira, H. M., Caniuguir, A., Garratt, R. C. & Babul, J. The crystal complex of phosphofructokinase-2 of *Escherichia coli* with fructose-6-phosphate: kinetic and structural analysis of the allosteric ATP inhibition. *J Biol Chem* **286**, 5774-5783 (2011). https://doi.org/10.1074/jbc.M110.163162

400 Fraser, H. I., Kvaratskhelia, M. & White, M. F. The two analogous phosphoglycerate mutases of *Escherichia coli*. *FEBS Lett* **455**, 344-348 (1999). https://doi.org/10.1016/s0014-5793(99)00910-2

401 Khan, M. S., Gargiulo, S. & Soumillion, P. Promiscuous activity of 3-isopropylmalate dehydrogenase produced at physiological level affords *Escherichia coli* growth on d-malate. *FEBS Lett* **594**, 2421-2430 (2020). https://doi.org/10.1002/1873-3468.13814

402 Usuda, Y. & Kurahashi, O. Effects of deregulation of methionine biosynthesis on methionine excretion in *Escherichia coli*. *Appl Environ Microbiol* **71**, 3228-3234 (2005). https://doi.org/10.1128/aem.71.6.3228-3234.2005

403 Léon, M., Dondon, J., Labouesse, J., Grunberg-Manago, M. & Buckingham, R. H. Recognition of tRNA Trp by initiation factors from *Escherichia coli*. *Eur J Biochem* **98**, 149-154 (1979). https://doi.org/10.1111/j.1432-1033.1979.tb13171.x

404 Krishna, R. V., Krishnaswamy, P. R. & Rao, D. R. Enzymic synthesis of N-acetyl-L-phenylalanine in *Escherichia coli* K12. *Biochem J* **124**, 905-913 (1971). https://doi.org/10.1042/bj1240905

405 Dubreuil, M. M., Morgens, D. W., Okumoto, K., Honsho, M., Contrepois, K., Lee-McMullen, B., Traber, G. M., Sood, R. S., Dixon, S. J., Snyder, M. P., Fujiki, Y. & Bassik, M. C. Systematic Identification of Regulators of Oxidative Stress Reveals Non-canonical Roles for Peroxisomal Import and the Pentose Phosphate Pathway. *Cell Reports* **30**, 1417-1433.e1417 (2020). https://doi.org/https://doi.org/10.1016/j.celrep.2020.01.013

406 Bonney, R. J. & Weinfeld, H. Regulation of thymidine metabolism in *Escherichia coli* K-12: studies on the inducer and the coordinateness of induction of the enzymes. *J Bacteriol* **106**, 812-818 (1971). https://doi.org/10.1128/jb.106.3.812-818.1971

407 Hubbard, B. K., Koch, M., Palmer, D. R., Babbitt, P. C. & Gerlt, J. A. Evolution of enzymatic activities in the enolase superfamily: characterization of the (D)-glucarate/galactarate catabolic pathway in *Escherichia coli*. *Biochemistry* **37**, 14369-14375 (1998). https://doi.org/10.1021/bi981124f

408 Walker, M. C. & van der Donk, W. A. The many roles of glutamate in metabolism. *Journal of Industrial Microbiology and Biotechnology* **43**, 419-430 (2016). https://doi.org/10.1007/s10295-015-1665-y

409 Bratek, E., Ziembowicz, A. & Salinska, E. N-Acetylaspartylglutamate (NAAG) Pretreatment Reduces Hypoxic-Ischemic Brain Damage and Oxidative Stress in Neonatal Rats. *Antioxidants* **9**, 877 (2020).

410 Van Acker, H., Gielis, J., Acke, M., Cools, F., Cos, P. & Coenye, T. The Role of Reactive Oxygen Species in Antibiotic-Induced Cell Death in *Burkholderia cepacia* Complex Bacteria. *PLoS One* **11**, e0159837 (2016). https://doi.org/10.1371/journal.pone.0159837

411 de Silva, A. O. & Fraenkel, D. G. The 6-phosphogluconate dehydrogenase reaction in *Escherichia coli*. *Journal of Biological Chemistry* **254**, 10237-10242 (1979). https://doi.org/10.1016/S0021-9258(19)86699-1

412 Marín, M., Pérez-Pantoja, D., Donoso, R., Wray, V., González, B. & Pieper Dietmar, H. Modified 3-Oxoadipate Pathway for the Biodegradation of Methylaromatics in *Pseudomonas reinekei* MT1. *Journal of Bacteriology* **192**, 1543-1552 (2010). https://doi.org/10.1128/jb.01208-09

413 Park Chan, B., Lee Sun, B. & Ryu Dewey, D. Y. l-Pyroglutamate Spontaneously Formed from l-Glutamate Inhibits Growth of the Hyperthermophilic Archaeon *Sulfolobus solfataricus*. *Applied and Environmental Microbiology* **67**, 3650-3654 (2001). https://doi.org/10.1128/AEM.67.8.3650-3654.2001

414 Conway, T. & Cohen Paul, S. Commensal and Pathogenic *Escherichia coli* Metabolism in the Gut. *Microbiology Spectrum* **3**, 10.1128/microbiolspec.mbp-0006-2014 (2015). https://doi.org/10.1128/microbiolspec.mbp-0006-2014

415 Mainprize, I. L., Bean, J. D., Bouwman, C., Kimber, M. S. & Whitfield, C. The UDP-glucose dehydrogenase of *Escherichia coli* K-12 displays substrate inhibition by NAD that is relieved by nucleotide triphosphates. *J Biol Chem* **288**, 23064-23074 (2013). https://doi.org/10.1074/jbc.M113.486613

416 Hayakawa, H., Kumura, K. & Sekiguchi, M. Role of uracil-DNA glycosylase in the repair of deaminated cytosine residues of DNA in *Escherichia coli*. *J Biochem* **84**, 1155-1164 (1978). https://doi.org/10.1093/oxfordjournals.jbchem.a132231

417 Alikhanian, S. I., Iljina, T. S., Kaliaeva, E. S., Kameneva, S. V. & Sukhodolec, V. V. Mutants of *Escherichia coli* K12 Lacking Thymine. *Nature* **206**, 848-849 (1965). https://doi.org/10.1038/206848a0

418 Garde, S., Chodisetti Pavan, K. & Reddy, M. Peptidoglycan: Structure, Synthesis, and Regulation. *EcoSal Plus* **9** (2021). https://doi.org/10.1128/ecosalplus.ESP-0010-2020

419 Samsonov, V. V., Kuznetsova, A. A., Rostova, J. G., Samsonova, S. A., Ziyatdinov, M. K. & Kiriukhin, M. Y. Revealing a New Family of D-2-Hydroxyglutarate Dehydrogenases in *Escherichia coli* and *Pantoea ananatis* Encoded by *ydiJ*. *Microorganisms* **10** (2022). https://doi.org/10.3390/microorganisms10091766

420 Müller-Santos, M., Koskimäki, J. J., Alves, L. P. S., de Souza, E. M., Jendrossek, D. & Pirttilä, A. M. The protective role of PHB and its degradation products against stress situations in bacteria. *FEMS Microbiology Reviews* **45** (2020). https://doi.org/10.1093/femsre/fuaa058

421 Soria, S., Carreón-Rodríguez, O. E., de Anda, R., Flores, N., Escalante, A. & Bolívar, F. Transcriptional and Metabolic Response of a Strain of Escherichia coli PTS− to a Perturbation of the Energetic Level by Modification of [ATP]/[ADP] Ratio. *BioTech* **13**, 10 (2024).

422 Njenga, R., Boele, J., Öztürk, Y. & Koch, H.-G. Coping with stress: How bacteria fine-tune protein synthesis and protein transport. *Journal of Biological Chemistry* **299** (2023). https://doi.org/10.1016/j.jbc.2023.105163

423 Pezo, V., Hassan, C., Louis, D., Sargueil, B., Herdewijn, P. & Marlière, P. Metabolic Recruitment and Directed Evolution of Nucleoside Triphosphate Uptake in *Escherichia coli*. *ACS Synth Biol* **7**, 1565-1572 (2018). https://doi.org/10.1021/acssynbio.8b00048

424 Warner, D. F., Evans, J. C. & Mizrahi, V. Nucleotide Metabolism and DNA Replication. *Microbiology Spectrum* **2**, 10.1128/microbiolspec.mgm1122-0001-2013 (2014). https://doi.org/doi:10.1128/microbiolspec.mgm2-0001-2013

425 Puja, H., Mislin, G. L. A. & Rigouin, C. Engineering Siderophore Biosynthesis and Regulation Pathways to Increase Diversity and Availability. *Biomolecules* **13** (2023). https://doi.org/10.3390/biom13060959

426 Rodriguez, A., Martnez, J. A., Flores, N., Escalante, A., Gosset, G. & Bolivar, F. Engineering *Escherichia coli* to overproduce aromatic amino acids and derived compounds. *Microbial Cell Factories* **13**, 126 (2014). https://doi.org/10.1186/s12934-014-0126-z

427 Shende, V. V., Bauman, K. D. & Moore, B. S. The shikimate pathway: gateway to metabolic diversity. *Natural Product Reports* **41**, 604-648 (2024). https://doi.org/10.1039/D3NP00037K

428 Dangel, V., Eustáquio, A. S., Gust, B. & Heide, L. novE and novG act as positive regulators of novobiocin biosynthesis. *Archives of Microbiology* **190**, 509-519 (2008). https://doi.org/10.1007/s00203-008-0396-0

429 Xiang, Y., Xiong, J.-X., Xie, Z.-F., Huang, D., Song, Q., Wu, J., Yan, D. & Chao, H.-J. The XylR/NtrC-type regulator CbsR positively regulates upstream pathway of chlorobenzene degradation in *Pandoraea pnomenusa*. *Journal of Applied Microbiology* **134** (2023). https://doi.org/10.1093/jambio/lxad064

430 Leonard, P. G., Satani, N., Maxwell, D., Lin, Y. H., Hammoudi, N., Peng, Z., Pisaneschi, F., Link, T. M., Lee, G. R. t., Sun, D., Prasad, B. A. B., Di Francesco, M. E., Czako, B., Asara, J. M., Wang, Y. A., Bornmann, W., DePinho, R. A. & Muller, F. L. SF2312 is a natural phosphonate inhibitor of enolase. *Nat Chem Biol* **12**, 1053-1058 (2016). https://doi.org/10.1038/nchembio.2195

431 Vaishampayan, A. & Grohmann, E. Antimicrobials Functioning through ROS-Mediated Mechanisms: Current Insights. *Microorganisms* **10** (2021). https://doi.org/10.3390/microorganisms10010061

432 Barb, A. W., McClerren, A. L., Snehelatha, K., Reynolds, C. M., Zhou, P. & Raetz, C. R. Inhibition of lipid A biosynthesis as the primary mechanism of CHIR-090 antibiotic activity in *Escherichia coli*. *Biochemistry* **46**, 3793-3802 (2007). https://doi.org/10.1021/bi6025165

433 Frlan, R., Hrast, M. & Gobec, S. Inhibition of MurA Enzyme from *Escherichia coli* by Flavonoids and Their Synthetic Analogues. *ACS Omega* **8**, 33006-33016 (2023). https://doi.org/10.1021/acsomega.3c04813

434 Dwyer, D. J., Belenky, P. A., Yang, J. H., MacDonald, I. C., Martell, J. D., Takahashi, N., Chan, C. T., Lobritz, M. A., Braff, D., Schwarz, E. G., Ye, J. D., Pati, M., Vercruysse, M., Ralifo, P. S., Allison, K. R., Khalil, A. S., Ting, A. Y., Walker, G. C. & Collins, J. J. Antibiotics induce redox-related physiological alterations as part of their lethality. *Proc Natl Acad Sci U S A* **111**, E2100-2109 (2014). https://doi.org/10.1073/pnas.1401876111

435 Mempin, R., Tran, H., Chen, C., Gong, H., Kim Ho, K. & Lu, S. Release of extracellular ATP by bacteria during growth. *BMC Microbiology* **13**, 301 (2013). https://doi.org/10.1186/1471-2180-13-301

436 Desousa, B. R., Kim, K. K., Jones, A. E., Ball, A. B., Hsieh, W. Y., Swain, P., Morrow, D. H., Brownstein, A. J., Ferrick, D. A., Shirihai, O. S., Neilson, A., Nathanson, D. A., Rogers, G. W., Dranka, B. P., Murphy, A. N., Affourtit, C., Bensinger, S. J., Stiles, L., Romero, N. & Divakaruni, A. S. Calculation of ATP production rates using the Seahorse XF Analyzer. *EMBO reports* **24**, e56380 (2023). https://doi.org/https://doi.org/10.15252/embr.202256380

437 Sharma, P. & Puduvalli, V. K. Protocol for real-time assessment of mitochondrial and glycolytic ATP production in patient-derived glioma stem-like cells. *STAR Protocols* **5**, 103159 (2024). https://doi.org/https://doi.org/10.1016/j.xpro.2024.103159

438 Yoo, I., Ahn, I., Lee, J. & Lee, N. Extracellular flux assay (Seahorse assay): Diverse applications in metabolic research across biological disciplines. *Molecules and Cells* **47**, 100095 (2024). https://doi.org/https://doi.org/10.1016/j.mocell.2024.100095

439 Perlin, D. S., Latchney, L. R. & Senior, A. E. Inhibition of *Escherichia coli* H+-ATPase by venturicidin, oligomycin and ossamycin. *Biochim Biophys Acta* **807**, 238-244 (1985). https://doi.org/10.1016/0005-2728(85)90254-3

440 Marquis, R. E. Nature of the Bactericidal Action of Antimycin A for *Bacillus megaterium*. *J Bacteriol* **89**, 1453-1459 (1965). https://doi.org/10.1128/jb.89.6.1453-1459.1965

441 Francis, R., Singh, P. K., Singh, S., Giri, S. & Kumar, A. Glycolytic inhibitor 2-deoxyglucose suppresses inflammatory response in innate immune cells and experimental staphylococcal endophthalmitis. *Exp Eye Res* **197**, 108079 (2020). https://doi.org/10.1016/j.exer.2020.108079

442 Guo, H., Suzuki, T. & Rubinstein, J. L. Structure of a bacterial ATP synthase. *eLife* **8**, e43128 (2019). https://doi.org/10.7554/eLife.43128

443 Millard, P., Smallbone, K. & Mendes, P. Metabolic regulation is sufficient for global and robust coordination of glucose uptake, catabolism, energy production and growth in *Escherichia coli*. *PLOS Computational Biology* **13**, e1005396 (2017). https://doi.org/10.1371/journal.pcbi.1005396

444 Magalon, A. & Alberge, F. Distribution and dynamics of OXPHOS complexes in the bacterial cytoplasmic membrane. *Biochimica et Biophysica Acta (BBA) - Bioenergetics* **1857**, 198-213 (2016). https://doi.org/https://doi.org/10.1016/j.bbabio.2015.10.015

445 Price, C. E. & Driessen, A. J. M. Biogenesis of membrane bound respiratory complexes in *Escherichia coli*. *Biochimica et Biophysica Acta (BBA) - Molecular Cell Research* **1803**, 748-766 (2010). https://doi.org/https://doi.org/10.1016/j.bbamcr.2010.01.019

446 Williams, C. F. in *Encyclopedia of Infection and Immunity* (ed Nima Rezaei) 363-376 (Elsevier, 2022).

447 Schmidt, C. A., Fisher-Wellman, K. H. & Neufer, P. D. From OCR and ECAR to energy: Perspectives on the design and interpretation of bioenergetics studies. *J Biol Chem* **297**, 101140 (2021). https://doi.org/10.1016/j.jbc.2021.101140

448 Wyatt, C. N. & Buckler, K. J. The effect of mitochondrial inhibitors on membrane currents in isolated neonatal rat carotid body type I cells. *J Physiol* **556**, 175-191 (2004). https://doi.org/10.1113/jphysiol.2003.058131

449 Heinz, S., Freyberger, A., Lawrenz, B., Schladt, L., Schmuck, G. & Ellinger-Ziegelbauer, H. Mechanistic Investigations of the Mitochondrial Complex I Inhibitor Rotenone in the Context of Pharmacological and Safety Evaluation. *Scientific Reports* **7**, 45465 (2017). https://doi.org/10.1038/srep45465

450 Alteri Christopher, J., Himpsl Stephanie, D., Shea Allyson, E. & Mobley Harry, L. T. Flexible Metabolism and Suppression of Latent Enzymes Are Important for *Escherichia coli* Adaptation to Diverse Environments within the Host. *Journal of Bacteriology* **201**, 10.1128/jb.00181-00119 (2019). https://doi.org/10.1128/jb.00181-19

451 San Román, M., Cancela, H. & Acerenza, L. Source and regulation of flux variability in *Escherichia coli*. *BMC Systems Biology* **8**, 67 (2014). https://doi.org/10.1186/1752-0509-8-67

452 Yoo, I., Ahn, I., Lee, J. & Lee, N. Extracellular flux assay (Seahorse assay): Diverse applications in metabolic research across biological disciplines. *Mol Cells* **47**, 100095 (2024). https://doi.org/10.1016/j.mocell.2024.100095

453 Liu, T., Wen, Z., Shao, L., Cui, Y., Tang, X., Miao, H., Shi, J., Jiang, L., Feng, S., Zhao, Y., Zhang, H., Liang, Q., Chen, D., Zhang, Y. & Wang, C. ATF4 knockdown in macrophage impairs glycolysis and mediates immune tolerance by targeting HK2 and HIF-1α ubiquitination in sepsis. *Clinical Immunology* **254**, 109698 (2023). https://doi.org/https://doi.org/10.1016/j.clim.2023.109698

454 Chou, F. J., Liu, Y., Lang, F. & Yang, C. D-2-Hydroxyglutarate in Glioma Biology. *Cells* **10** (2021). https://doi.org/10.3390/cells10092345

455 Ye, D., Guan, K. L. & Xiong, Y. Metabolism, Activity, and Targeting of D- and L-2-Hydroxyglutarates. *Trends Cancer* **4**, 151-165 (2018). https://doi.org/10.1016/j.trecan.2017.12.005

456 Zheng, M., Pan, M., Zhang, W., Lin, H., Wu, S., Lu, C., Tang, S., Liu, D. & Cai, J. Poly(α-l-lysine)-based nanomaterials for versatile biomedical applications: Current advances and perspectives. *Bioactive Materials* **6**, 1878-1909 (2021). https://doi.org/https://doi.org/10.1016/j.bioactmat.2020.12.001

457 Lobritz, M. A., Belenky, P., Porter, C. B. M., Gutierrez, A., Yang, J. H., Schwarz, E. G., Dwyer, D. J., Khalil, A. S. & Collins, J. J. Antibiotic efficacy is linked to bacterial cellular respiration. *Proceedings of the National Academy of Sciences* **112**, 8173-8180 (2015). https://doi.org/doi:10.1073/pnas.1509743112

458 Colville, K., Tompkins, N., Rutenberg, A. D. & Jericho, M. H. Effects of poly(L-lysine) substrates on attached *Escherichia coli* bacteria. *Langmuir* **26**, 2639-2644 (2010). https://doi.org/10.1021/la902826n

459 Technologies, A. Technical overview: Measuring mitochondrial respiration and glycolysis in live cells using the XFe24 Analyzer. (Santa Clara, CA, 2017).

460 Tahernia, M., Plotkin-Kaye, E., Mohammadifar, M., Gao, Y., Oefelein, M. R., Cook, L. C. & Choi, S. Characterization of Electrogenic Gut Bacteria. *ACS Omega* **5**, 29439-29446 (2020). https://doi.org/10.1021/acsomega.0c04362

461 Garimella, S. S. S., Rachakonda, S. V., Pratapa, S. S., Mannem, G. D. & Mahidhara, G. From cells to power cells: harnessing bacterial electron transport for microbial fuel cells (MFCs). *Annals of Microbiology* **74**, 19 (2024). https://doi.org/10.1186/s13213-024-01761-y

462 Urbana-Champaign, U. o. I. Hoechst Stains. (2005).

463 Kluza, J., Peugnet, V., Daunou, B., Laine, W., Kervoaze, G., Rémy, G., Loyens, A., Maboudou, P., Fovez, Q., Grangette, C., Wolowczuk, I., Gosset, P., Garçon, G., Marchetti, P., Pinet, F., Pichavant, M. & Dubois-Deruy, E. A New Strategy to Preserve and Assess Oxygen Consumption in Murine Tissues. *Int J Mol Sci* **23** (2021). https://doi.org/10.3390/ijms23010109

464 Jahreis, K., Pimentel-Schmitt, E. F., Brückner, R. & Titgemeyer, F. Ins and outs of glucose transport systems in eubacteria. *FEMS Microbiology Reviews* **32**, 891-907 (2008). https://doi.org/10.1111/j.1574-6976.2008.00125.x

465 Ruan, H., Yu, H. & Xu, J. The glucose uptake systems in *Corynebacterium glutamicum*: a review. *World Journal of Microbiology and Biotechnology* **36**, 126 (2020). https://doi.org/10.1007/s11274-020-02898-z

466 Matsuno-Yagi, A. & Hatefi, Y. Ubiquinol-Cytochrome *c* Oxidoreductase: THE REDOX REACTIONS OF THE BIS-HEME CYTOCHROME *b* IN UBIQUINONE-SUFFICIENT AND UBIQUINONE-DEFICIENT SYSTEMS. *Journal of Biological Chemistry* **271**, 6164-6171 (1996). https://doi.org/10.1074/jbc.271.11.6164

467 Cruz-Pulido, Y. E., LoMascolo, N. J., May, D., Hatahet, J., Thomas, C. E., Chu, A. K. W., Stacey, S. P., Villanueva Guzman, M. d. M., Aubert, G. & Mounce, B. C. Polyamines mediate cellular energetics and lipid metabolism through mitochondrial respiration to facilitate virus replication. *PLOS Pathogens* **20**, e1012711 (2024). https://doi.org/10.1371/journal.ppat.1012711

468 Childers, G. & Harry, G. J. in *Experimental Neurotoxicology Methods* (eds Jordi Llorens & Marta Barenys) 305-324 (Springer US, 2021).

469 Calhoun, M. W., Oden, K. L., Gennis, R. B., de Mattos, M. J. & Neijssel, O. M. Energetic efficiency of Escherichia coli: effects of mutations in components of the aerobic respiratory chain. *J Bacteriol* **175**, 3020-3025 (1993). https://doi.org/10.1128/jb.175.10.3020-3025.1993

470 Unden, G. & Dünnwald, P. The Aerobic and Anaerobic Respiratory Chain of *Escherichia coli* and *Salmonella enterica*: Enzymes and Energetics. *EcoSal Plus* **3**, 10.1128/ecosalplus.1123.1122.1122 (2008). https://doi.org/doi:10.1128/ecosalplus.3.2.2

471 Calhoun, M. W., Oden, K. L., Gennis, R. B., Mattos, M. J. d. & Neijssel, O. M. Energetic efficiency of *Escherichia coli*: effects of mutations in components of the aerobic respiratory chain. *Journal of Bacteriology* **175**, 3020-3025 (1993). https://doi.org/doi:10.1128/jb.175.10.3020-3025.1993

472 Steinsiek, S., Stagge, S. & Bettenbrock, K. Analysis of *Escherichia coli* Mutants with a Linear Respiratory Chain. *PLOS ONE* **9**, e87307 (2014). https://doi.org/10.1371/journal.pone.0087307

473 Forkink, M., Basit, F., Teixeira, J., Swarts, H. G., Koopman, W. J. H. & Willems, P. Complex I and complex III inhibition specifically increase cytosolic hydrogen peroxide levels without inducing oxidative stress in HEK293 cells. *Redox Biol* **6**, 607-616 (2015). https://doi.org/10.1016/j.redox.2015.09.003

474 Rotsaert, F. A., Ding, M. G. & Trumpower, B. L. Differential efficacy of inhibition of mitochondrial and bacterial cytochrome bc1 complexes by center N inhibitors antimycin, ilicicolin H and funiculosin. *Biochim Biophys Acta* **1777**, 211-219 (2008). https://doi.org/10.1016/j.bbabio.2007.10.011

475 Schneider, D., Pohl, T., Walter, J., Dörner, K., Kohlstädt, M., Berger, A., Spehr, V. & Friedrich, T. Assembly of the *Escherichia coli* NADH:ubiquinone oxidoreductase (complex I). *Biochim Biophys Acta* **1777**, 735-739 (2008). https://doi.org/10.1016/j.bbabio.2008.03.003

476 Brown, A. N., Anderson, M. T., Bachman, M. A. & Mobley, H. L. T. The ArcAB Two-Component System: Function in Metabolism, Redox Control, and Infection. *Microbiol Mol Biol Rev* **86**, e0011021 (2022). https://doi.org/10.1128/mmbr.00110-21

477 Wu, J., Li, Y., Cai, Z. & Jin, Y. Pyruvate-associated acid resistance in bacteria. *Appl Environ Microbiol* **80**, 4108-4113 (2014). https://doi.org/10.1128/aem.01001-14

478 Luo, Q., Ding, N., Liu, Y., Zhang, H., Fang, Y. & Yin, L. Metabolic Engineering of Microorganisms to Produce Pyruvate and Derived Compounds. *Molecules* **28** (2023). https://doi.org/10.3390/molecules28031418

479 Gawryluk, R. M. R., Chisholm, K. A., Pinto, D. M. & Gray, M. W. Composition of the mitochondrial electron transport chain in Acanthamoeba castellanii: Structural and evolutionary insights. *Biochimica et Biophysica Acta (BBA) - Bioenergetics* **1817**, 2027-2037 (2012). https://doi.org/https://doi.org/10.1016/j.bbabio.2012.06.005

480 Vik, S. B. ATP Synthesis by Oxidative Phosphorylation. *EcoSal Plus* **2**, 10.1128/ecosalplus.1123.1122.1123 (2007). https://doi.org/doi:10.1128/ecosalplus.3.2.3

481 Liu, S., Zhao, J., Guo, Y., Ma, X., Sun, C., Cai, M., Chi, Y. & Xu, K. Application of ATP-based bioluminescence technology in bacterial detection: a review. *Analyst* **148**, 3452-3459 (2023). https://doi.org/10.1039/D3AN00576C

482 Cheung, C. H. P., Alorabi, M., Hamilton, F., Takebayashi, Y., Mounsey, O., Heesom, K. J., Williams, P. B., Williams, O. M., Albur, M., MacGowan, A. P. & Avison, M. B. Trade-Offs between Antibacterial Resistance and Fitness Cost in the Production of Metallo-β-Lactamases by Enteric Bacteria Manifest as Sporadic Emergence of Carbapenem Resistance in a Clinical Setting. *Antimicrob Agents Chemother* **65**, e0241220 (2021). https://doi.org/10.1128/aac.02412-20

483 Lodhiya, T., Palande, A., Veeram, A., Larrouy-Maumus, G., Beste, D. J. V. & Mukherjee, R. (eLife Sciences Publications, Ltd, 2024).

484 Akhova, A. V. & Tkachenko, A. G. ATP/ADP alteration as a sign of the oxidative stress development in *Escherichia coli* cells under antibiotic treatment. *FEMS Microbiology Letters* **353**, 69-76 (2014). https://doi.org/10.1111/1574-6968.12405

485 Peetermans, A., Foulquié-Moreno, M. R. & Thevelein, J. M. Mechanisms underlying lactic acid tolerance and its influence on lactic acid production in *Saccharomyces cerevisiae*. *Microb Cell* **8**, 111-130 (2021). https://doi.org/10.15698/mic2021.06.751

486 Deng, Y., Beahm, D. R., Ionov, S. & Sarpeshkar, R. Measuring and modeling energy and power consumption in living microbial cells with a synthetic ATP reporter. *BMC Biology* **19**, 101 (2021). https://doi.org/10.1186/s12915-021-01023-2

487 Chinemerem Nwobodo, D., Ugwu, M. C., Oliseloke Anie, C., Al-Ouqaili, M. T. S., Chinedu Ikem, J., Victor Chigozie, U. & Saki, M. Antibiotic resistance: The challenges and some emerging strategies for tackling a global menace. *J Clin Lab Anal* **36**, e24655 (2022). https://doi.org/10.1002/jcla.24655

488 Murugaiyan, J., Kumar, P. A., Rao, G. S., Iskandar, K., Hawser, S., Hays, J. P., Mohsen, Y., Adukkadukkam, S., Awuah, W. A., Jose, R. A. M., Sylvia, N., Nansubuga, E. P., Tilocca, B., Roncada, P., Roson-Calero, N., Moreno-Morales, J., Amin, R., Kumar, B. K., Kumar, A., Toufik, A. R., Zaw, T. N., Akinwotu, O. O., Satyaseela, M. P. & van Dongen, M. B. M. Progress in Alternative Strategies to Combat Antimicrobial Resistance: Focus on Antibiotics. *Antibiotics (Basel)* **11** (2022). https://doi.org/10.3390/antibiotics11020200

489 Alaoui Mdarhri, H., Benmessaoud, R., Yacoubi, H., Seffar, L., Guennouni Assimi, H., Hamam, M., Boussettine, R., Filali-Ansari, N., Lahlou, F. A., Diawara, I., Ennaji, M. M. & Kettani-Halabi, M. Alternatives Therapeutic Approaches to Conventional Antibiotics: Advantages, Limitations and Potential Application in Medicine. *Antibiotics (Basel)* **11** (2022). https://doi.org/10.3390/antibiotics11121826

490 Si, Z., Pethe, K. & Chan-Park, M. B. Chemical Basis of Combination Therapy to Combat Antibiotic Resistance. *JACS Au* **3**, 276-292 (2023). https://doi.org/10.1021/jacsau.2c00532

491 Larkins-Ford, J. & Aldridge, B. B. Advances in the design of combination therapies for the treatment of tuberculosis. *Expert Opin Drug Discov* **18**, 83-97 (2023). https://doi.org/10.1080/17460441.2023.2157811

492 Hawas, S., Verderosa, A. D. & Totsika, M. Combination Therapies for Biofilm Inhibition and Eradication: A Comparative Review of Laboratory and Preclinical Studies. *Front Cell Infect Microbiol* **12**, 850030 (2022). https://doi.org/10.3389/fcimb.2022.850030

493 Lai, C., Ma, Z., Zhang, J., Wang, J., Wang, J., Wu, Z. & Luo, Y. Efficiency of combination therapy versus monotherapy for the treatment of infections due to carbapenem-resistant Gram-negative bacteria: a systematic review and meta-analysis. *Systematic Reviews* **13**, 309 (2024). https://doi.org/10.1186/s13643-024-02695-x

494 Rose, W., Fantl, M., Geriak, M., Nizet, V. & Sakoulas, G. Current Paradigms of Combination Therapy in Methicillin-Resistant *Staphylococcus aureus* (MRSA) Bacteremia: Does it Work, Which Combination, and For Which Patients? *Clin Infect Dis* **73**, 2353-2360 (2021). https://doi.org/10.1093/cid/ciab452

495 Liu, Y., Li, R., Xiao, X. & Wang, Z. Bacterial metabolism-inspired molecules to modulate antibiotic efficacy. *Journal of Antimicrobial Chemotherapy* **74**, 3409-3417 (2019). https://doi.org/10.1093/jac/dkz230

496 Papp-Wallace, K. M., Endimiani, A., Taracila, M. A. & Bonomo, R. A. Carbapenems: past, present, and future. *Antimicrob Agents Chemother* **55**, 4943-4960 (2011). https://doi.org/10.1128/aac.00296-11

497 Bush, K. & Bradford, P. A. β-Lactams and β-Lactamase Inhibitors: An Overview. *Cold Spring Harb Perspect Med* **6** (2016). https://doi.org/10.1101/cshperspect.a025247

498 Piccirilli, A., Segatore, B., Brisdelli, F., Amicosante, G. & Perilli, M. Potent inhibitory activity of taniborbactam towards NDM-1 and NDM-1^{Q119X} mutants, and in vitro activity of cefepime/taniborbactam against MBLs producing *Enterobacterales*. *International Journal of Antimicrobial Agents* **57**, 106228 (2021). https://doi.org/https://doi.org/10.1016/j.ijantimicag.2020.106228

499 Hamrick, J. C., Docquier, J.-D., Uehara, T., Myers, C. L., Six, D. A., Chatwin, C. L., John, K. J., Vernacchio, S. F., Cusick, S. M., Trout, R. E. L., Pozzi, C., Luca, F. D., Benvenuti, M., Mangani, S., Liu, B., Jackson, R. W., Moeck, G., Xerri, L., Burns, C. J., Pevear, D. C. & Daigle, D. M. VNRX-5133 (Taniborbactam), a Broad-Spectrum Inhibitor of Serine- and Metallo-β-Lactamases, Restores Activity of Cefepime in *Enterobacterales* and *Pseudomonas aeruginosa*. *Antimicrobial Agents and Chemotherapy* **64**, 10.1128/aac.01963-01919 (2020). https://doi.org/doi:10.1128/aac.01963-19

500 Wang, X., Zhao, C., Wang, Q., Wang, Z., Liang, X., Zhang, F., Zhang, Y., Meng, H., Chen, H., Li, S., Zhou, C., Li, H. & Wang, H. In vitro activity of the novel β-lactamase inhibitor taniborbactam (VNRX-5133), in combination with cefepime or meropenem, against MDR Gram-negative bacterial isolates from China. *Journal of Antimicrobial Chemotherapy* **75**, 1850-1858 (2020). https://doi.org/10.1093/jac/dkaa053

501 Black, C., Al Mahmud, H., Howle, V., Wilson, S., Smith, A. C. & Wakeman, C. A. Development of a Polymicrobial Checkerboard Assay as a Tool for Determining Combinatorial Antibiotic Effectiveness in Polymicrobial Communities. *Antibiotics (Basel)* **12** (2023). https://doi.org/10.3390/antibiotics12071207

502 (International Union of Pure and Applied Chemistry (IUPAC), 2019).

503 Nicolau, D. P. Carbapenems: a potent class of antibiotics. *Expert Opin Pharmacother* **9**, 23-37 (2008). https://doi.org/10.1517/14656566.9.1.23

504 Maldonado, R. F., Sá-Correia, I. & Valvano, M. A. Lipopolysaccharide modification in Gram-negative bacteria during chronic infection. *FEMS Microbiology Reviews* **40**, 480-493 (2016). https://doi.org/10.1093/femsre/fuw007

505 Herald, F. & Burgos, R. M. Clinical Evaluation of Meropenem-Vaborbactam Combination for the Treatment of Urinary Tract Infection: Evidence to Date. *Infect Drug Resist* **16**, 555-568 (2023). https://doi.org/10.2147/idr.S187360

506 Arer, V. & Kar, D. Biochemical exploration of β-lactamase inhibitors. *Front Genet* **13**, 1060736 (2022). https://doi.org/10.3389/fgene.2022.1060736

507 Pajak, B., Siwiak, E., Sołtyka, M., Priebe, A., Zieliński, R., Fokt, I., Ziemniak, M., Jaśkiewicz, A., Borowski, R., Domoradzki, T. & Priebe, W. 2-Deoxy-d-Glucose and Its Analogs: From Diagnostic to Therapeutic Agents. *Int J Mol Sci* **21** (2019). https://doi.org/10.3390/ijms21010234

508 Wijayasinghe, Y. S., Bhansali, M. P., Borkar, M. R., Chaturbhuj, G. U., Muntean, B. S., Viola, R. E. & Bhansali, P. R. A Comprehensive Biological and Synthetic Perspective on 2-Deoxy-d-Glucose (2-DG), A Sweet Molecule with Therapeutic and Diagnostic Potentials. *J Med Chem* **65**, 3706-3728 (2022). https://doi.org/10.1021/acs.jmedchem.1c01737

509 Carreón-Rodríguez, O. E., Gosset, G., Escalante, A. & Bolívar, F. Glucose Transport in Escherichia coli: From Basics to Transport Engineering. *Microorganisms* **11** (2023). https://doi.org/10.3390/microorganisms11061588

510 Krah, A., Grüber, G. & Bond, P. J. Binding properties of the anti-TB drugs bedaquiline and TBAJ-876 to a mycobacterial F-ATP synthase. *Curr Res Struct Biol* **4**, 278-284 (2022). https://doi.org/10.1016/j.crstbi.2022.09.001

511 Khoshnood, S., Goudarzi, M., Taki, E., Darbandi, A., Kouhsari, E., Heidary, M., Motahar, M., Moradi, M. & Bazyar, H. Bedaquiline: Current status and future perspectives. *Journal of Global Antimicrobial Resistance* **25**, 48-59 (2021). https://doi.org/https://doi.org/10.1016/j.jgar.2021.02.017

512 Ajayi, T. O., Poka, M. S. & Witika, B. A. Formulation and optimisation of bedaquiline nanoemulsions for the potential treatment of multi drug resistant tuberculosis in paediatrics using quality by design. *Scientific Reports* **14**, 31891 (2024). https://doi.org/10.1038/s41598-024-83408-1

513 Pająk, B., Zieliński, R., Manning, J. T., Matejin, S., Paessler, S., Fokt, I., Emmett, M. R. & Priebe, W. The Antiviral Effects of 2-Deoxy-D-glucose (2-DG), a Dual D-Glucose and D-Mannose Mimetic, against SARS-CoV-2 and Other Highly Pathogenic Viruses. *Molecules* **27** (2022). https://doi.org/10.3390/molecules27185928

514 Singh, R., Gupta, V., Kumar, A. & Singh, K. 2-Deoxy-D-Glucose: A Novel Pharmacological Agent for Killing Hypoxic Tumor Cells, Oxygen Dependence-Lowering in Covid-19, and Other Pharmacological Activities. *Adv Pharmacol Pharm Sci* **2023**, 9993386 (2023). https://doi.org/10.1155/2023/9993386

515 Tan, M. T. & Fang, H.-B. in *Contemporary Experimental Design, Multivariate Analysis and Data Mining: Festschrift in Honour of Professor Kai-Tai Fang* (eds Jianqing Fan & Jianxin Pan) 127-144 (Springer International Publishing, 2020).

516 Xi, H., Kurtoglu, M. & Lampidis, T. J. The wonders of 2-deoxy-d-glucose. *IUBMB Life* **66**, 110-121 (2014). https://doi.org/https://doi.org/10.1002/iub.1251

517 Wood, T. K., Knabel, S. J. & Kwan, B. W. Bacterial persister cell formation and dormancy. *Appl Environ Microbiol* **79**, 7116-7121 (2013). https://doi.org/10.1128/aem.02636-13

518 Stojowska-Swędrzyńska, K., Kuczyńska-Wiśnik, D. & Laskowska, E. New Strategies to Kill Metabolically-Dormant Cells Directly Bypassing the Need for Active Cellular Processes. *Antibiotics (Basel)* **12** (2023). https://doi.org/10.3390/antibiotics12061044

519 Schink, S. J., Christodoulou, D., Mukherjee, A., Athaide, E., Brunner, V., Fuhrer, T., Bradshaw, G. A., Sauer, U. & Basan, M. Glycolysis/gluconeogenesis specialization in microbes is driven by biochemical constraints of flux sensing. *Mol Syst Biol* **18**, e10704 (2022). https://doi.org/10.15252/msb.202110704

520 Thomson, M., Liu, Y., Nunta, K., Cheyne, A., Fernandes, N., Williams, R., Garza-Garcia, A. & Larrouy-Maumus, G. Expression of a novel mycobacterial phosphodiesterase successfully lowers cAMP levels resulting in reduced tolerance to cell wall-targeting antimicrobials. *J Biol Chem* **298**, 102151 (2022). https://doi.org/10.1016/j.jbc.2022.102151

521 Woods, R. J. & Read, A. F. Combination antimicrobial therapy to manage resistance. *Evolution, Medicine, and Public Health* **11**, 185-186 (2023). https://doi.org/10.1093/emph/eoad005

522 Wang, N., Luo, J., Deng, F., Huang, Y. & Zhou, H. Antibiotic Combination Therapy: A Strategy to Overcome Bacterial Resistance to Aminoglycoside Antibiotics. *Front Pharmacol* **13**, 839808 (2022). https://doi.org/10.3389/fphar.2022.839808

523 Alm, R. A. & Lahiri, S. D. Narrow-Spectrum Antibacterial Agents—Benefits and Challenges. *Antibiotics* **9**, 418 (2020).

524 Amato, S. M., Fazen, C. H., Henry, T. C., Mok, W. W., Orman, M. A., Sandvik, E. L., Volzing, K. G. & Brynildsen, M. P. The role of metabolism in bacterial persistence. *Front Microbiol* **5**, 70 (2014). https://doi.org/10.3389/fmicb.2014.00070

525 Oliver, A., Xue, Z., Villanueva, Y. T., Durbin-Johnson, B., Alkan, Z., Taft, D. H., Liu, J., Korf, I., Laugero, K. D., Stephensen, C. B., Mills, D. A., Kable, M. E. & Lemay, D. G. Association of Diet and Antimicrobial Resistance in Healthy U.S. Adults. *mBio* **13**, e00101-00122 (2022). https://doi.org/doi:10.1128/mbio.00101-22

526 Theophilus, R. J. & Taft, D. H. Antimicrobial Resistance Genes (ARGs), the Gut Microbiome, and Infant Nutrition. *Nutrients* **15**, 3177 (2023).

527 Dastidar, S. G., Kristiansen, J. E., Molnar, J. & Amaral, L. Role of Phenothiazines and Structurally Similar Compounds of Plant Origin in the Fight against Infections by Drug Resistant Bacteria. *Antibiotics (Basel)* **2**, 58-72 (2013). https://doi.org/10.3390/antibiotics2010058

528 Guha, P., Dutta, S., Murti, K., Charan, J. K., Pandey, K., Ravichandiran, V. & Dhingra, S. The integration of omics: A promising approach to personalized tuberculosis treatment. *Medicine in Omics* **12**, 100033 (2024). https://doi.org/https://doi.org/10.1016/j.meomic.2024.100033

Appendix

Appendix I

This appendix includes the metabolite database used for AEC-MS analyses and CFU data. These resources were used throughout the thesis to support metabolomic and bacterial studies.

***Table Appendix I.I Metabolite database for AEC-MS analysis**. The database contained compound ID, description, neutral mass, retention time (min), and formula. The database was used within Progenesis QI to aid metabolic identification. The databases were established by members of the McCullagh group.*

Compound ID	Description	Neutral Mass	Retention time (min)	Formula
HMDB0012141	(R)-2,3-Dihydroxy-3-methylbutanoate (new)	134.0579	5.23	C5H10O4
HMDB0060320	(Z)-But-1-ene-1,2,4-tricarboxylate (new)	188.0321	16.88	C7H8O6
HMDB0013674	1,2,3-Trihydroxybenzene/Pyrogallol	126.03224	23.21	C6H6O3
HMDB0000957	1,2-Dihydroxybenzene	110.03678	25.92	C6H6O2
HMDB0013593	1,4 dihydrotheritol	154.01222	14.86	C4H10O2S2
HMDB0001213	1-Deoxy-D-xylulose 5-phosphate	214.02424	10.32	C5H11O7P
1-Hydroxy-2-methyl-2-butenyl 4-pyrophosphate	1-Hydroxy-2-methyl-2-butenyl 4-pyrophosphate	262.00074	16.68	C5H12O8P2
HMDB0243941	1-Methyl indole	131.07405	28.33	C9H9N
1-Methyl-1H-indole-3-carboxamide	1-Methyl-1H-indole-3-carboxamide	174.07986	33.86	C10H10N2O
HMDB0000001	1-Methylhistidine	169.08513	12.89	C7H11N3O2
HMDB0001369	1-Pyrroline hydroxycarboxylic acid	129.04259	4.48	C5H7NO3
HMDB0001301	1-Pyrroline-5-carboxylic acid	113.04768	9.37	C5H7NO2
HMDB0002006	2,3-Diaminopropionic acid	104.05913	11.75	C3H8N2O2
HMDB0001294	2,3-Diphosphoglyceric acid	265.95927	22.21	C3H8O10P2
HMDB0000152	2,5-Dihydroxybenzoic acid	154.02661	32.16	C7H6O4
2-amino-5-hydroxybenzoic acid	2-amino-5-hydroxybenzoic acid	153.04314	33.19	C7H7NO3
HMDB0001123	2-Aminobenzoic acid/Anthranilic acid	137.04768	25.09	C7H7NO2
HMDB0001906	2-Aminoisobutyric acid	103.06333	9.92	C4H9NO2
HMDB0032059	2-Bromophenol	171.95293	9.03	C6H5BrO
2-butyl-3-ureido-succinate	2-butyl-3-ureido-succinate	232.10592	11.98	C9H16N2O5
HMDB0304060	2-C-Methyl-D-erythritol-2,4-cyclopyrophosphate	277.9962	15.28	C5H12O9P2
HMDB0304061	2-C-Methylerythritol 4-phosphate	214.02424	9.88	C5H13O7P
HMDB0000617	2-Furoate (new)	112.016	9.48	C5H4O3
HMDB0000317	2-hydroxy-3-methylvaleric acid (new)	132.0786	7.22	C6H12O3
2-Hydroxy-4-phenylbutanoic acid	2-Hydroxy-4-phenylbutanoic acid	180.07919	14.39	C10H12O3
HMDB0000008	2-Hydroxybutyric acid	104.04734	5.41	C4H8O3
HMDB0059655	2-Hydroxyglutarate	148.03717	10.9	C5H8O5
HMDB0001624	2-hydroxyhexanoic acid (new)	132.0786	11.55	C6H12O3
HMDB0000402	2-Isopropylmalic acid	176.06847	12.32	C7H12O5
HMDB0000005	2-Ketobutyric acid	102.03169	7.86	C4H6O3
HMDB0000379	2-Methylcitric acid	206.0432	16.09	C7H10O7
HMDB0000208	2-Oxoglutaric acid	146.02152	12.85	C5H6O5
HMDB0000362	2-Phosphoglyceric acid	185.99294	16.34	C3H7O7P
HMDB0000397	2-Pyrocatechuic acid	154.02661	33.01	C7H6O4
HMDB0002039	2-Pyrrolidinone	85.05331	13.37	C4H7NO
HMDB0002441	3,3 Dimethyl glutarate	160.07356	11.41	C7H12O4
HMDB0012153	3,4,Dihydroxybenzylamine	139.06388	13.52	C7H9NO2
HMDB0001336	3,4-dihydroxyphenyl acetic acid	168.04226	22.6	C8H8O4
HMDB0003911	3-Aminoisobutanoic acid	103.06333	10.32	C4H9NO2
HMDB0003540	3'-AMP	347.06254	13.43	C10H14N5O7P
HMDB0012710	3-Dehydroquinate	190.04774	5.51	C7H10O6
HMDB0001376	3-deoxy-2-keto-6-phosphogluconic acid	258.01407	15.93	C6H11O9P
3-Ethylmalate	3-Ethylmalate (new)	162.0528	10.85	C6H10O5
HMDB0001476	3-Hydroxyanthranilic acid	153.04314	26.46	C7H7NO3

HMDB0002466	3-Hydroxybenzoic acid	138.03224	22.66	C7H6O3
HMDB0000357	3-Hydroxybutyric acid	104.04734	5.36	C4H8O3
HMDB0000023	3-Hydroxyisobutyric acid	104.04734	5.04	C4H8O3
HMDB0000754	3-Hydroxyisovaleric acid	118.06354	5.34	C5H10O3
HMDB0000355	3-Hydroxymethylglutarate	162.05282	10.76	C6H10O5
HMDB0013188	3-Hydroxypicolinic acid	139.02694	18.07	C6H5NO3
HMDB0005784	3-Hydroxytyrosol	154.06299	15.76	C8H10O3
HMDB0012156	3-isopropylmalic acid (new)	176.0685	11.52	C7H12O5
HMDB0059969	3-methoxyphenylacetic acid	166.06299	10.04	C9H10O3
HMDB0000491	3-Methyl-2-oxovaleric acid	130.06299	10.67	C6H10O3
HMDB0001904	3-Nitrotyrosine	226.05897	8.77	C9H10N2O5
HMDB0013701	3-Oxoglutarate (new)	174.0528	11.48	C7H10O5
HMDB0000807	3-Phosphoglyceric acid	185.99294	15.84	C3H7O7P
HMDB0061881	4-Acetylbutyrate	130.06354	5.09	C6H10O3
HMDB0060466	4-Hydroxy-2-oxoglutarate	162.01644		C5H6O6
HMDB0000291	4-Hydroxy-3-methoxymandelic acid	198.05282	15.77	C9H10O5
HMDB0000500	4-Hydroxybenzoic acid	138.03169	18.86	C7H6O3
HMDB0000710	4-Hydroxybutyric acid	104.04734	10.65	C4H8O3
HMDB0244973	4-hydroxyphenyl glycine/Oxfenicine	167.05824	18.59	C8H9NO3
4-Hydroxyphenylbutyric acid	4-Hydroxyphenylbutyric acid	179.07137	17.51	C10H12O3
HMDB0000707	4-Hydroxyphenylpyruvic acid	180.04226	27.88	C9H8O4
HMDB0000725	4-Hydroxyproline	131.05824	9.68	C5H9NO3
4-Hydroxypyrrolidinone	4-Hydroxypyrrolidinone	101.04768	2.94	C4H7NO2
HMDB0001101	4-Methoxybenzoic acid (new)	152.0473	16.4	C8H8O3
HMDB0000695	4-methyl-2-oxovaleric acid (ketoleucine) (new)	130.06299	9.99	C6H10O3
4-Methyl-2-ureido-pentanoic acid/Carbamoyl isoleucine	4-Methyl-2-ureido-pentanoic acid/Carbamoyl isoleucine	174.10099	6.36	C7H14N2O3
HMDB0000873	4-Methylcatechol	124.05298	29.91	C7H8O2
HMDB0036619	5,7-Dihydroxyflavone (Chrysin)	254.05846	4.33	C15H10O4
HMDB0001149	5-Aminolevulinic acid	131.05879	3.89	C5H9NO3
5-Formyl-dCTP	5-Formyl-dCTP	494.98505	20.45	C10H16N3O14P3
HMDB0000525	5-Hydroxyhexanoic acid	132.07919	6.83	C6H12O3
HMDB0000763	5-Hydroxyindoleacetic acid	191.05824	26.83	C10H9NO3
HMDB0246808	5-Hydroxymethyl-2'-deoxyuridine	258.085	6.48	C10H14N2O6
5-Hydroxy-methyl-dCTP	5-Hydroxy-methyl-dCTP	497.00016	19.4	C10H18N3O14P3
HMDB0004096	5-Methoxyindoleacetate	205.07389	29.66	C11H11NO3
5-Methyl-dCTP	5-Methyl-dCTP	481.00525	18.96	C10H18N3O13P3
HMDB0038804	6-hydroxy-2,5,7,8-tetramethylchromane-2-carboxylic acid (Trolox)	250.12051	29.39	C14H18O4
HMDB0001316	6-Phosphogluconic acid	276.02463	15.18	C6H13O10P
HMDB0001127	6-phosphonoglucono-lactone	258.01462	11.52	C6H11O9P
HMDB0003333	8-Hydroxy-deoxyguanosine	283.09167	19.83	C10H13N5O5
HMDB0011615	8-Oxo-dGTP	522.99011	19.78	C10H16N5O14P3
HMDB0036093	Abscisic acid (new)	264.1362	11.85	C15H20O4
HMDB0000042	Acetic acid	60.02113	3.85	C2H4O2
HMDB0000060	Acetoacetate	102.03169	5.14	C4H6O3
HMDB0001484	Acetoacetyl-CoA	851.13634	33.1	C25H40N7O18P3S
HMDB0001206	Acetyl-CoA	809.12577	7.59	C23H38N7O17P3S
HMDB0001890	Acetylcysteine	163.03031	11.56	C5H9NO3S
HMDB0247933	Acetylenedicarboxylic acid (new)	113.9953	17.1	C4H2O4
HMDB0000532	Acetylglycine	117.04259	4.07	C4H7NO3
HMDB0001494	Acetylphosphate	139.98801	12.66	C2H5O5P
HMDB0000034	Adenine	135.0545	15.32	C5H5N5
HMDB0011616	Adenosine 2',3'-cyclic phosphate	329.05197	9.41	C10H12N5O6P

HMDB0001341	Adenosine diphosphate	427.02941	19.79	C10H15N5O10P2
HMDB0000045	Adenosine monophosphate (AMP)	347.06308	13.84	C10H14N5O7P
HMDB0000538	Adenosine triphosphate (ATP)	506.99575	24.53	C10H16N5O13P3
HMDB0001332	Adenylsuccinate	463.07404	23.15	C14H18N5O11P
HMDB0012882	Adipate semialdehyde	130.06299	11.34	C6H10O3
HMDB0000508	Adonitol (ribitol)	152.06847	2.86	C5H12O5
HMDB0006557	ADP Glucose	589.08224	14.3	C16H25N5O15P2
HMDB0001517	AICAR (new)	338.06275	12.55	C9H15N4O8P
HMDB0000462	Allantoin	158.04454	5.95	C4H6N4O3
HMDB0001151	Allose	180.06339	3.04	C6H12O6
HMDB0000650	Alpha-aminobutyrate	103.06333	10.32	C4H9NO2
HMDB0002166	Alpha-aminoisobutyrate	103.06333	10.06	C4H9NO2
HMDB0000019	alpha-Ketoisovaleric acid (new)	116.04734	7.7	C5H8O3
HMDB0035030	Amygdalin (new)	457.1584	4.92	C20H27NO11
HMDB0000539	Arabinonic acid	166.04774	4.9	C5H10O6
HMDB0000646	Arabinose	150.05282	3.06	C5H10O5
HMDB0029942	Arabinose	150.05282	3.06	C5H10O5
HMDB0000568	Arabitol	152.06847	2.71	C5H12O5
HMDB0000044	Ascorbate	176.03209	12.36	C6H8O6
HMDB0000191	Aspartate	133.03751	11.78	C4H7NO4
Benzoyl-L-citrulline methyl ester	Benzoyl-L-citrulline methyl ester	293.1381	11.17	C14H19N3O4
HMDB0000056	Beta-Alanine	89.04768	4.73	C3H7NO2
HMDB0013220	Beta-Citryl-L-glutamic acid	321.0696	20.62	C11H15NO10
Butyl ureidosuccinic acid	Butyl ureidosuccinic acid	232.10647	10.61	C9H16N2O5
HMDB0000039	Butyric acid	88.05243	6.32	C4H8O2
HMDB0001964	Caffeic acid (new)	180.0423	29.38	C9H8O4
HMDB0001847	Caffeine	194.08092		C8H10N4O2
HMDB0000535	Caproic acid/Hexanoic acid	116.08428	8.58	C6H12O2
HMDB0001096	Carbamoyl phosphate	140.98271	15.06	CH4NO5P
HMDB0000033	Carnosine	225.09931	3.93	C9H14N4O3
HMDB0001564	CDP-ethanolamine (new)	446.06038	9.6	C11H20N4O11P2
HMDB0003164	Chlorogenic acid	354.09563		C16H18O9
HMDB0011621	Cinnamoylglycine	205.07334	20.81	C11H11NO3
HMDB0000393	cis,cis-Muconate (new)	142.0266	12.83	C6H6O4
HMDB0000072	cis-Aconitic acid	174.01644	18.12	C6H6O6
HMDB0001413	Citicoline (new)	488.10787	3.71	C14H26N4O11P2
HMDB0000634	Citraconic acid	130.02661	11.96	C5H6O4
HMDB0000426	Citramalic acid	148.03717	10.75	C5H8O5
HMDB0000094	Citric acid	192.027	16.91	C6H8O7
HMDB0000904	Citrulline	175.09569	4.12	C6H13N3O3
HMDB0015020	Clomifene	405.18594	16.22	C26H28ClNO
HMDB0001423	Coenzyme A	767.11521	25.32	C21H36N7O16P3S
HMDB0000058	Cyclic AMP	329.05252	15.1	C10H12N5O6P
HMDB0001314	Cyclic GMP	345.04743	24.09	C10H12N5O7P
HMDB0060150	Cysteamine	77.02992	9.87	C2H7NS
HMDB0002757	Cysteic acid	169.00449	12.19	C3H7NO5S
HMDB0000574	Cysteine	121.01975	15.66	C3H7NO2S
HMDB0000089	Cytidine	243.08607	8.48	C9H13N3O5
HMDB0001546	Cytidine diphosphate	403.01763	16.34	C9H15N3O11P2
HMDB0000095	Cytidine monophosphate	323.05185	11.78	C9H14N3O8P
HMDB0001176	Cytidine monophosphate N-acetylneuraminic acid	614.14727	9.79	C20H31N4O16P
HMDB0000082	Cytidine triphosphate	482.98451	21.06	C9H16N3O14P3

HMDB0000630	Cytosine	111.04326	5.52	C4H5N3O
HMDB0001508	dADP	411.0345	18.27	C10H15N5O9P2
HMDB0000905	dAMP	331.06817	12.88	C10H14N5O6P
HMDB0001245	dCDP	387.02327	30.12	C9H15N3O10P2
HMDB0001202	dCMP	307.05694	10.06	C9H14N3O7P
HMDB0000998	dCTP	466.9896	19.55	C9H16N3O13P3
Dehydrocholic acid	Dehydrocholic acid	401.23335		C24H34O5
HMDB0000101	Deoxyadenosine	251.10184	12.14	C10H13N5O3
HMDB0001532	Deoxyadenosine triphosphate	491.00083	24.33	C10H16N5O12P3
HMDB0000014	Deoxycytidine	227.09115	4.69	C9H13N3O4
HMDB0000085	deoxyguanosine	283.09222	4.08	C10H13N5O4
HMDB0001031	Deoxyribose 5-phosphate	214.02424	11.06	C5H11O7P
HMDB0246094	Deoxythymidine	225.08808	7.67	C10H14N2O4
HMDB0000012	Deoxyuridine	228.07462	7.62	C9H12N2O5
HMDB0062739	D-erythro-3-Methylmalate (new)	148.0372	10.68	C5H8O5
HMDB0000960	dGDP	427.02941	24.67	C10H15N5O10P2
HMDB0001044	dGMP	347.06308	20.57	C10H14N5O7P
HMDB0001440	dGTP	506.9952	29.43	C10H16N5O13P3
Diaminocyclohexane-N,N,N′,N′-tetraacetic acid (DCTA)	Diaminocyclohexane-N,N,N′,N′-tetraacetic acid (DCTA)	345.13034	8.92	C14H22N2O8
HMDB0014724	Diclofenac	295.01614	1.22	C14H11Cl2NO2
HMDB0003349	Dihydroorotic acid	158.03276	11.63	C5H6N2O4
HMDB0000076	Dihydrouracil	114.04238	13.43	C4H6N2O2
HMDB0001882	Dihydroxyacetone	90.03169	4.74	C3H6O3
HMDB0001473	Dihydroxyacetone phosphate (new)	169.998	11.36	C3H7O6P
HMDB0000181	Dihydroxyphenylalanine (L-DOPA)	197.06881	32.44	C9H11NO4
HMDB0031257	Dimethyl fumarate	144.04226	13.16	C6H8O4
HMDB0001120	Dimethylallyl pyrophosphate	246.00583	18.73	C5H12O7P2
HMDB0000092	Dimethylglycine	103.06333	10.15	C4H9NO2
HMDB0006555	dIMP	332.05219	18.99	C10H13N4O7P
DL-Threo-beta-Hydroxyaspartic acid	DL-Threo-beta-Hydroxyaspartic acid	148.02515	10.43	C4H7NO5
HMDB0000073	Dopamine	153.07898	19.68	C8H11NO2
HMDB0001328	dTDP-D-glucose	564.07576	17.06	C16H26N2O16P2
HMDB0001000	dUDP	388.00728	19.6	C9H14N2O11P2
HMDB0001409	dUMP	308.04095	17.1	C9H13N2O8P
HMDB0001191	dUTP	467.97361	25.45	C9H15N2O14P3
HMDB0015109	EDTA	292.09067	10.83	C10H16N2O8
HMDB0000900	Ergocalciferol	396.33867	4.21	C28H44O
HMDB0000878	Ergosterol	396.33867	1.13	C28H44O
HMDB0001321	Erythrose 4-phosphate	200.00859	12.91	C4H9O7P
Ethionine	Ethionine	163.06725	33.54	C6H13NO2S
HMDB0000622	Ethylmalonic acid	132.04226	11.62	C5H8O4
HMDB0001248	FAD	785.15713	28.12	C27H33N9O15P2
HMDB0000954	Ferulic acid	194.05791	27.02	C10H10O4
HMDB0001520	Flavin Mononucleotide (unconfirmed)	456.10461		C17H21N4O9P
HMDB0014684	Fluorouracil	130.01786	13.57	C4H3FN2O2
HMDB0014615	Fluoxetine	309.1346	21.52	C17H18F3NO
HMDB0000660	Fructose	180.06339	3.06	C6H12O6
HMDB0001058	Fructose 1,6-bisphosphate	339.99605	20.44	C6H14O12P2
HMDB0001047	Fructose 2,6 diphosphate	339.99605	17.52	C6H14O12P2
HMDB0000124	Fructose 6-phosphate	260.02972	11.88	C6H13O9P

HMDB0000134	Fumarate	116.01096	13.63	C4H4O4
HMDB0000639	Galactaric acid (mucic acid)	210.03757	10.94	C6H10O8
HMDB0000143	Galactose	180.06339	3.02	C6H12O6
HMDB0000645	Galactose 1-phosphate	260.02972	9.39	C6H13O9P
Galactose-6-phosphate	Galactose-6-phosphate	260.02917	11.77	C6H13O9P
HMDB0002545	Galacturonic acid (new)	194.0427	6.51	C6H10O7
HMDB0005807	Gallic acid (new)	170.0215	29.59	C7H6O5
HMDB0013233	Gamma-delta-Dioxovaleric acid	130.02661	10.65	C5H6O4
HMDB0003559	Gibberellin A3	346.14164	12.68	C19H22O6
HMDB0000625	Gluconate	196.0583	4.67	C6H12O7
HMDB0000150	Gluconolactone	178.04774	4.71	C6H10O6
HMDB0001514	Glucosamine	179.07937	11.58	C6H13NO5
HMDB0001254	Glucosamine 6-phosphate	259.0457	13.18	C6H14NO8P
HMDB0000122	Glucose	180.06339	3.43	C6H12O6
HMDB0001586	Glucose 1-phosphate	260.02972	9.66	C6H13O9P
HMDB0001401	Glucose 6-phosphate	260.02972	12.38	C6H13O9P
HMDB0000127	Glucuronic acid	194.04265	8.27	C6H10O7
HMDB0000620	Glutaconic acid	130.02661	12.69	C5H6O4
HMDB0000148	Glutamic acid	147.05316	14.79	C5H9NO4
HMDB0000641	Glutamine	146.06914	11.67	C5H10N2O3
HMDB0001049	Glutamylcysteine	250.06289	16.61	C8H14N2O5S
HMDB0000661	Glutaric acid	132.04226	10.87	C5H8O4
HMDB0001339	Glutaryl CoA	881.1469	19.81	C26H42N7O19P3S
HMDB0000125	Glutathione (GSH)	307.08381	15.16	C10H17N3O6S
HMDB0001112	Glyceraldehyde 3-phosphate	169.99802	11.73	C3H7O6P
HMDB0000139	Glyceric acid	106.02661	5.23	C3H6O4
HMDB0000131	Glycerol	92.04734	2.86	C3H8O3
HMDB0000126	Glycerol 3-phosphate	172.01367	9.79	C3H9O6P
HMDB0003344	Glycoaldehyde	60.02113	7.52	C2H4O2
HMDB0000115	Glycolic acid (new)	76.016	4.74	C2H4O3
HMDB0000119	Glyoxylic acid	74.00039	8.05	C2H2O3
HMDB0000370	Glyphosate/2-Amino-3-phosphonopropionic acid	169.01456	14.56	C3H8NO5P
HMDB0000133	Guanosine	283.09167	22.22	C10H13N5O5
HMDB0001201	Guanosine diphosphate (GDP)	443.02378	27.56	C10H15N5O11P2
HMDB0001397	Guanosine monophosphate	363.058	22.22	C10H14N5O8P
HMDB0001273	Guanosine triphosphate	522.99066	30.62	C10H16N5O14P3
HMDB0003466	Gulono-1,4-lactone (new)	178.0477	4.37	C6H10O6
HMDB0012326	Gulose	180.06339	3.05	C6H12O6
HMDB0030311	Harmine	212.09551		C13H12N2O
HMDB0005782	Hesperitin	302.07849	28.5	C16H14O6
HMDB0000714	Hippuric acid	179.05824	11.63	C9H9NO3
HMDB0000870	Histamine	111.0802	7.08	C5H9N3
Homarine	Homarine	137.04768	11.66	C7H7NO2
HMDB0000130	Homogentisic acid	168.04226	17.49	C8H8O4
HMDB0000118	Homovanillic acid	182.05791	17.21	C9H10O4
HMDB0001212	Hydantoin-5-propionic acid	172.04786	11.4	C6H8N2O4
HMDB0000764	Hydrocinnamic acid	150.06863	15.63	C9H10O2
HMDB0000528	Hydroorotic acid	158.03276	10.36	C5H6N2O4
HMDB0001855	Hydroxy-indole acetic acid	177.07898	26.62	C10H11NO2
HMDB0062640	Hydroxy-isobutyric acid	103.04007	4.46	C4H7O3
HMDB0126088	Hydroxy-isobutyric acid	104.04734	4.46	C4H8O3
HMDB0002207	Hydroxyisoheptanoic acid	146.09484	9.74	C7H14O3
HMDB0000732	Hydroxykynurenine	224.08026	13.91	C10H12N2O4
Hydroxy-methyl-dUTP	Hydroxy-methyl-dUTP	497.98418	20.48	C10H17N2O15P3
HMDB0000711	Hydroxyoctanoic acid	160.11049	7.52	C8H16O3

HMDB0000700	Hydroxypropionic acid	90.03224	4.88	C3H6O3
HMDB0001352	Hydroxypyruvic acid	104.01096	11.64	C3H4O4
HMDB0000965	Hypotaurine	109.01975	14.89	C2H7NO2S
HMDB0000157	Hypoxanthine	136.03851	21.34	C5H4N4O
HMDB0011140	Hypusine	233.17449	9.42	C10H23N3O3
HMDB0003335	IDP	428.01343	26.55	C10H14N4O11P2
HMDB0001190	Indole-3-acetaldehyde	159.06841	27.44	C10H9NO
HMDB0000671	Indole-3-lactic acid	205.07389	27.23	C11H11NO3
HMDB0000197	Indoleacetic acid	175.06333	28.43	C10H9NO2
HMDB0000195	Inosine	268.08077	5.6	C10H12N4O5
HMDB0000175	Inosine monophosphate	348.0471	21.97	C10H13N4O8P
HMDB0000189	Inosine triphosphate	507.97976	30.13	C10H15N4O14P3
HMDB0001143	Inositol 1,3,4-trisphosphate	419.96238	25.85	C6H15O15P3
HMDB0000193	Isocitrate	192.027	17.55	C6H8O7
HMDB0001347	Isopentenyl pyrophosphate	246.00583	18.45	C5H12O7P2
HMDB0000718	Isovaleric Acid	102.06863	9.43	C5H10O2
HMDB0000678	Isovalerylglycine	159.08954	6.07	C7H13NO3
HMDB0002092	Itaconic acid	130.02661	12.13	C5H6O4
HMDB0032797	Jasmonic acid	210.12559	12.22	C12H18O3
HMDB0032923	Kojic acid	142.02661	8.81	C6H6O4
HMDB0000715	Kynurenic acid	189.04259	27.57	C10H7NO3
HMDB0000684	Kynurenine	208.08479	8.81	C10H12N2O3
HMDB0000190	Lactic acid	90.03169	5.05	C3H6O3
HMDB0000186	Lactose	342.11676	3.04	C12H22O11
HMDB0062180	Lactoyl-isoleucine	203.11631	7.02	C9H17NO4
HMDB0240656	Lanthionine	208.05233	33	C6H12N2O4S
HMDB0004823	Lanthionine ketimine	189.01013	30.82	C6H7NO4S
HMDB0000624	Leucic acid	132.07919	7.51	C6H12O3
HMDB0254310	Maleamate (new)	115.0269	5.61	C4H5NO3
HMDB0000176	Maleic acid	116.01096	12.43	C4H4O4
HMDB0000744	Malic acid (new)	134.0215	10	C4H6O5
HMDB0002928	Malitol	344.13186	3.08	C12H24O11
HMDB0006112	Malondialdehyde	72.02113	8.86	C3H4O2
HMDB0000691	Malonic acid (new)	104.011	11.08	C3H4O4
HMDB0060486	Manelonitrile	133.05276	29.49	C8H7NO
HMDB0000765	Mannitol	182.07904	2.76	C6H14O6
HMDB0000169	Mannose	180.06339	3.14	C6H12O6
HMDB0001078	Mannose 6-phosphate	260.02972	12.73	C6H13O9P
HMDB0001892	Menadione	172.05298	11.43	C11H8O2
HMDB0000749	Mesaconic acid	130.02661	12.51	C5H6O4
HMDB0002005	Methionine sulfoxide	165.04596		C5H11NO3S
HMDB0029965	Methyl beta-D-glucopyranoside	194.07904	2.74	C7H14O6
HMDB0001167	Methyl glyoxal/Pyruvaldehyde	72.02168	4.89	C3H4O2
HMDB0032617	Methyl phenylacetate	150.06863	14.11	C9H10O2
Methyl-3-hydroxybenzoic acid	Methyl-3-hydroxybenzoic acid	152.04789	28.57	C8H8O3
HMDB0004815	Methyl-4-hydroxybenzoic acid	152.04789	32.63	C8H8O3
HMDB0000752	Methylglutaric acid	146.05791	10.73	C6H10O4
HMDB0006471	Methylisocitric acid	206.04265	15.82	C7H10O7
HMDB0032572	Methylparaben	152.04734	17.77	C8H8O3
HMDB0000227	Mevalonic acid	148.07356	15.14	C6H12O4
HMDB0001343	Mevalonic acid-5P	228.03989	14.84	C6H13O7P
Mildronate	Mildronate	146.10498	1.2	C6H4N2O2
HMDB0000211	Myoinositol	180.06339	2.81	C6H12O6
HMDB0003502	Myo-inositol hexakisphosphate/Phytic Acid	659.86192	24.31	C6H18O24P6
HMDB0039002	Mytilin A	332.12251	3.67	C13H20N2O8
HMDB0033442	Mytilin B	346.13816	3.5	C14H22N2O8
HMDB0033816	Mytilitol	194.07959	2.58	C7H14O6

N-Acetyl cytosine	N-Acetyl cytosine	153.05437	8.13	C6H7N3O2
HMDB0003357	N-Acetyl ornithine	174.10044	8.73	C7H14N2O3
HMDB0094701	N-Acetyl proline	157.07444	4.42	C7H11NO3
HMDB0000812	N-Acetyl-aspartate	175.04807	10.03	C6H9NO5
HMDB0001067	N-Acetylaspartylglutamic acid	304.09067	14.4	C11H16N2O8
HMDB0000215	N-Acetyl-D-glucosamine	221.08994	3.02	C8H15NO6
HMDB0001062	N-Acetyl-D-Glucosamine 6-Phosphate	301.05627	12.41	C8H16NO9P
HMDB0001121	N-Acetyl-D-mannosamine 6-phosphate (ManNac-6-P)	301.05627	12.11	C8H16NO9P
HMDB0001367	N-acetyl-glucosamine-1-phosphate	301.05627	11.66	C8H16NO9P
HMDB0001138	N-Acetylglutamate	189.06427	9.84	C7H11NO5
HMDB0000766	N-Acetyl-L-alanine	131.05824	4.23	C5H9NO3
HMDB0006488	N-Acetyl-L-glutamate 5-semialdehyde	173.06881	13.97	C7H11NO4
HMDB0006456	N-Acetyl-L-glutamyl 5-phosphate	269.03005		C7H12NO8P
HMDB0011745	N-Acetyl-L-methionine	191.06161	5.91	C7H13NO3S
HMDB0000512	N-Acetyl-L-phenylalanine	207.08954	8.89	C11H13NO3
HMDB0001129	N-Acetylmannosamine (ManNac)	221.08994	5.39	C8H15NO6
HMDB0006268	N-Acetylneuraminate 9-phosphate	389.07231	13.98	C11H20NO12P
HMDB0000230	N-acetylneuraminic acid (new)	309.106	4.63	C11H19NO9
HMDB0013713	N-Acetyltryptophan	246.10044	18.41	C13H14N2O3
HMDB0011757	N-Acetylvaline	159.08954	4.83	C7H13NO3
HMDB0000902	NAD+	664.11695	9.94	C21H28N7O14P2
HMDB0001487	NADH	665.12477	17	C21H29N7O14P2
HMDB0000217	NADP+	744.08328	16.43	C21H29N7O17P3
HMDB0000221	NADPH	745.0911	21.37	C21H30N7O17P3
HMDB0002670	Naringenin	272.06902		C15H12O5
HMDB0013287	Ne,Ne dimethyllysine	174.13683	3.79	C8H18N2O2
N-Formyl-DL-ethionine	N-Formyl-DL-ethionine	191.06216	7.53	C7H13NO3S
HMDB0001200	N-Formylkynurenine	236.08026	22.44	C11H12N2O4
HMDB0001015	N-Formyl-methionine	177.04596	6.73	C6H11NO3S
HMDB0001406	Nicotinamide	122.04801	24.05	C6H6N2O
HMDB0341363	Nicotinic Acid N-Oxide	139.02694	5.94	C6H5NO3
HMDB0002393	N-Methyl-D-aspartic acid	147.05316	10.06	C5H9NO4
HMDB0011717	Nonate	188.10541	13.85	C9H16O4
HMDB0013716	Norvaline	117.07953	33.46	C5H11NO2
HMDB0255221	N-Oxalylglycine	147.0168	12.59	C4H5NO5
HMDB0003011	O-Acetylserine	147.05316	4.36	C5H9NO4
HMDB0000482	Octanoic acid	144.11503	19.95	C8H16O2
HMDB0001721	O-Phosphoserine (new)	185.00892	13.7	C3H8NO6P
HMDB0005765	Ophthalmic Acid	289.12793	8.51	C11H19N3O6
HMDB0000226	Orotic acid	156.01711	16.58	C5H4N2O4
HMDB0000788	Orotidine	288.05882	16.11	C10H12N2O8
HMDB0000218	Orotidylic acid/OMP	368.02624	9.67	C10H13N2O11P
HMDB0000223	Oxalacetic acid	132.00587	10.3	C4H4O5
HMDB0002329	Oxalic acid	89.99531	13.4	C2H2O4
HMDB0000225	Oxoadipic acid	160.03717	13.08	C6H8O5
HMDB0001865	Oxovaleric Acid	116.04789	7.56	C5H8O3
HMDB0014733	Oxytetracylcine	460.14818	29.58	C22H24N2O9
HMDB0240389	Pantoic acid (new)	148.0736	5.56	C6H12O4
HMDB0000210	Pantothenic acid	219.11067	5	C9H17NO5
HMDB0062802	Parabanic Acid/Oxalylyurea	114.00599	8.17	C3H2N2O3
HMDB0002035	p-Coumaric acid	164.04734	29.16	C9H8O3
HMDB0015050	Phenformin	241.10997	14.07	C10H16ClN5
HMDB0040733	Phenylacetic Acid	136.05298	13.28	C8H8O2
HMDB0000821	Phenylacetylglycine/Phenaceturic acid	193.07444	9.23	C10H11NO3

HMDB0000205	Phenylpyruvic acid	164.04734	30.55	C9H8O3
HMDB0001511	Phosphocreatine	211.03636	8.56	C4H10N3O5P
HMDB0000263	Phosphoenolpyruvic acid	167.98237	17.96	C3H5O6P
HMDB0000816	Phosphoglycolic acid	155.98237	16.32	C2H5O6P
HMDB0000280	Phosphoribosyl pyrophosphate (PRPP)	389.95181	22.27	C5H13O14P3
HMDB0002107	Phthalate (new)	166.0266	16.51	C8H6O4
HMDB0000020	p-Hydroxyphenylacetic acid	152.04789	16.97	C8H8O3
HMDB0000774	Pregnenolone sulfate	396.19759	21.87	C21H32O5S
HMDB0012283	Prephenic Acid	226.04774	11.47	C10H10O6
HMDB0015169	Procainamide	235.16846	21.97	C13H21N3O
HMDB0000237	Propionic acid	74.03733	5.69	C3H6O2
HMDB0001275	Propionyl-CoA	823.14197	10.52	C24H40N7O17P3S
HMDB0000783	Propionyl-glycine	131.05824	4.27	C5H9NO3
HMDB0001856	Protocatechuic acid	154.02661	25.29	C7H6O4
HMDB0001491	Pyridoxal 5'-phosphate	247.02457	21.74	C8H10NO6P
HMDB0001431	Pyridoxamine	168.08988	6.71	C8H12N2O2
HMDB0000267	Pyroglutamic acid	129.04314	4.49	C5H7NO3
HMDB0000243	Pyruvic acid	88.01604	6.8	C3H4O3
HMDB0005794	Quercetin	302.0421	28.65	C15H10O7
HMDB0003072	Quinic acid	192.06339	4.74	C7H12O6
HMDB0000232	Quinolinic acid	167.02186	13.74	C7H5NO4
Quisqualic acid	Quisqualic acid	189.03912	14.33	C5H7N3O5
HMDB0003213	Raffinose	504.16904	2.8	C18H32O16
HMDB0001852	Retinoic acid	300.20948	8.39	C20H28O2
HMDB0000244	Riboflavin	376.13828	24.51	C17H20N4O6
HMDB0000283	Ribose	150.05282	3.17	C5H10O5
HMDB0001548	Ribose 5-phosphate	230.01915	13.19	C5H11O8P
HMDB0000621	Ribulose	150.05282	3.51	C5H10O5
HMDB0011688	Ribulose 1,5,diphosphate	309.98603	19.79	C5H12O11P2
HMDB0000618	Ribulose 5-phosphate	230.01915	9.67	C5H11O8P
HMDB0000663	Saccharic acid	210.03757	12.05	C6H10O8
HMDB0000279	Saccharopine	276.13214	13.56	C11H20N2O6
HMDB0001185	S-adenosyl methionine	399.14506	8.71	C15H23N6O5S
HMDB0001895	Salicylic acid	138.03224	32.17	C7H6O3
HMDB0006088	Scyllitol	180.06339	2.67	C6H12O6
HMDB0000792	Sebacic acid	202.12051	18.3	C10H18O4
HMDB0060274	Sedoheptulose 1,7-bisphosphate	370.00661	19.08	C7H16O13P2
HMDB0060509	Sedoheptulose 1-phosphate	290.04028	10.74	C7H15O10P
HMDB0001068	Sedoheptulose 7-phosphate	290.04028	13.21	C7H15O10P
HMDB0003070	Shikimic acid	174.05282	5.13	C7H10O5
HMDB0032616	Sinapic acid	224.06847	25.12	C11H12O5
HMDB0000247	Sorbitol	182.07904	2.77	C6H14O6
HMDB0005831	Sorbitol-6-phosphate	262.04537	9.23	C6H15O9P
HMDB0001266	Sorbose	180.06339	3.06	C6H12O6
HMDB0006797	Sorbose 1-phosphate	260.02917	11.96	C6H13O9P
HMDB0000254	Succinic acid	118.02661	11.11	C4H6O4
HMDB0001259	Succinic semialdehyde (new)	102.03169	5.37	C4H6O3
HMDB0255868	Succinyl-Homoserine	219.074	9.41	C8H13NO6
HMDB0002085	Syringic acid	198.05282	17.5	C9H10O5
HMDB0029416	Targinine	188.12787	33.55	C7H16N4O2
HMDB0000956	Tartaric acid (new)	150.0164	11.04	C4H6O6
HMDB0000251	Taurine	125.01466	5.14	C2H7NO3S
HMDB0001274	TDP	402.02293	21.72	C10H16N2O11P2
HMDB0000234	Testosterone	288.20948	27.34	C19H28O2
HMDB0003193	Testosterone glucuronide	464.24047	8.06	C25H36O8
HMDB0002833	Testosterone sulfate	368.16629	18.09	C19H28O5S
HMDB0014897	Tetracycline	444.15272	20.98	C22H24N2O8

HMDB0002825	Theobromine	180.06418	17.74	C7H8N4O2
HMDB0029178	Thialysine	164.0625	33.42	C5H12N2O2S
HMDB0002666	Thiamine monophosphate	344.07026		C12H17N4O4PS
HMDB0001372	Thiamine pyrophosphate	425.04497	25.64	C12H19N4O7P2S
HMDB0004136	Threitol	122.05791	2.78	C4H10O4
HMDB0001227	Thymidine 5'-phosphate (TMP)	322.0566	16.77	C10H15N2O8P
HMDB0001342	Thymidine triphosphate	481.98926	25.42	C10H17N2O14P3
HMDB0000262	Thymine	126.04293	9.9	C5H6N2O2
HMDB0015256	Tolbutamide	270.10436	15.08	C12H18N2O3S
HMDB0029635	Toluate (new)	136.0524	20.64	C8H8O2
trans-2,3-epoxysuccinic acid	trans-2,3-epoxysuccinic acid (new)	132.0059	12.02	C4H4O5
HMDB0000930	trans-cinnamic acid (new)	148.05243	24.51	C9H8O2
HMDB0062562	Trans-urocanate	137.03565	18.19	C6H5N2O2
HMDB0062590	Tropic acid (new)	166.063	9.33	C9H10O3
HMDB0000303	Tryptamine	160.1006		C10H12N2
HMDB0004284	Tyrosol	138.06808	17.77	C8H10O2
HMDB0000302	UDP-galactose	566.05502	18	C15H24N2O17P2
HMDB0000935	UDP-glucoronate	580.03428	24.31	C15H22N2O18P2
HMDB0000286	UDP-glucose	566.05502	18.4	C15H24N2O17P2
HMDB0013112	UDP-N-acetyl-D-mannosamine (unconfirmed)	607.08157		C17H27N3O17P2
HMDB0000300	Uracil	112.02728	8.92	C4H4N2O2
HMDB0000026	Ureidopropionic acid	132.05404	4.46	C4H8N2O3
HMDB0000828	Ureidosuccinic acid (N-carbamoyl-L-aspartic acid)	176.04332	10.86	C5H8N2O5
HMDB0000289	Uric acid	168.02834	19.45	C5H4N4O3
HMDB0000296	Uridine	244.06954	9.04	C9H12N2O6
HMDB0000295	Uridine 5'-diphosphate	404.0022	23.85	C9H14N2O12P2
HMDB0000288	Uridine 5'-monophosphate	324.03587	18.6	C9H13N2O9P
HMDB0000290	Uridine diphosphate-N-acetylglucosamine	607.08157	17.77	C17H27N3O17P2
HMDB0000285	Uridine triphosphate	483.96853	27.32	C9H15N2O15P3
HMDB0000892	Valeric Acid	102.06863	9.65	C5H10O2
HMDB0012308	Vanillin	152.04789		C8H8O3
HMDB0001554	Xanthylic acid	364.04256	20.7	C10H13N4O9P
HMDB0002917	Xylitol	152.06847	2.79	C5H12O5
HMDB0001644	Xylulose	150.05282	3.64	C5H10O5
HMDB0000868	Xylulose 5-phosphate	230.01915	13.16	C5H11O8P
HMDB0015464	Yohimbine	354.19489	26.07	C21H26N2O3

Table Appendix I.II Bacterial growth data over time showing OD600, CFU/mL, and log10(CFU/mL). *OD600 represents the optical density, reflecting the total biomass of the culture. CFU/mL indicates the number of viable cells capable of forming colonies, while log10(CFU/mL) is the logarithmic transformation of CFU/mL values to illustrate changes in viability on a logarithmic scale. Measurements were taken at specified time intervals to monitor the growth dynamics of the bacterial culture.*

Time (h)	OD_{600}	CFU/mL	Log10(CFU/mL)
0	0.057	21000000	7.322219
1	0.065	57000000	7.755875
2	0.145	203000000	8.307496
3	0.257	250000000	8.39794
4	0.531	318000000	8.502427
5	0.64	427000000	8.630428
6	0.877	544000000	8.735599
8	1.128	544000000	8.735599
10	1.242	174000000	8.240549

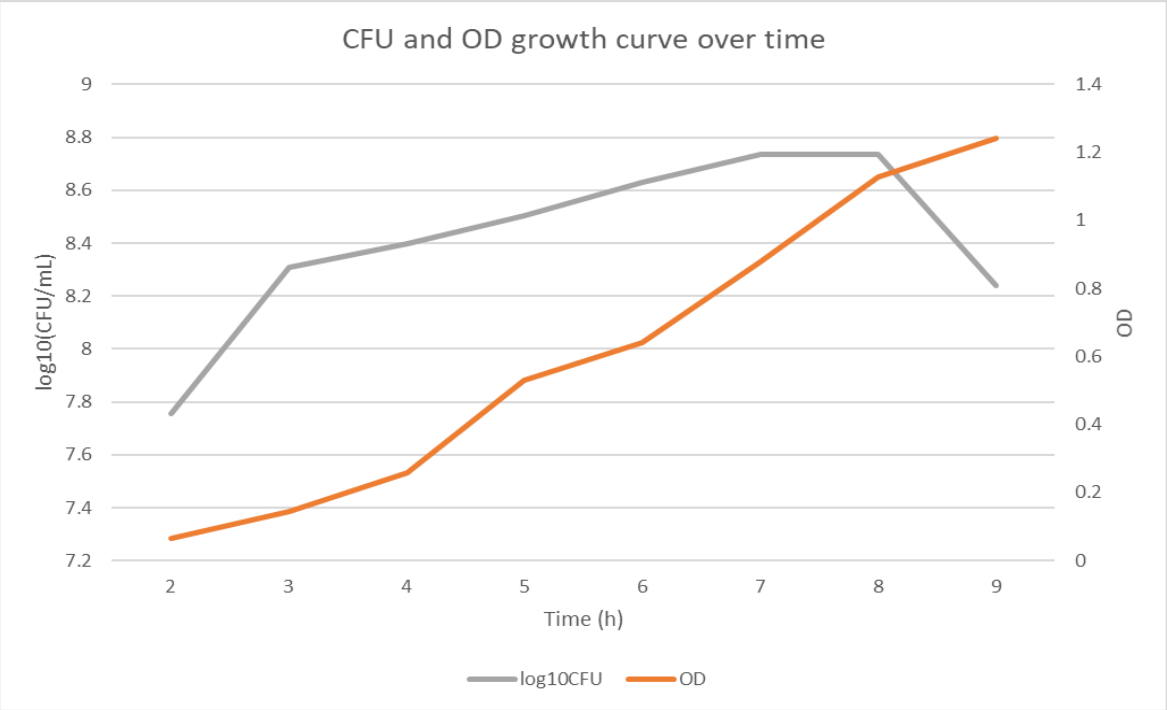

Figure I.I Growth curve showing the relationship between OD_{600} and log10(CFU/mL) over time. *The orange line represents the OD600, reflecting the total biomass of the culture, including viable and non-viable cells. The grey line represents log10(CFU/mL), indicating the number of viable cells capable of forming colonies. Both metrics were measured at regular intervals, illustrating the growth dynamics of the bacterial culture. Differences in trends between OD_{600} and log10(CFU/mL) highlight potential variations in viability relative to biomass over time.*

Appendix II

This appendix provides supplementary data supporting the metabolomics analyses presented in Chapters 3 and 4.

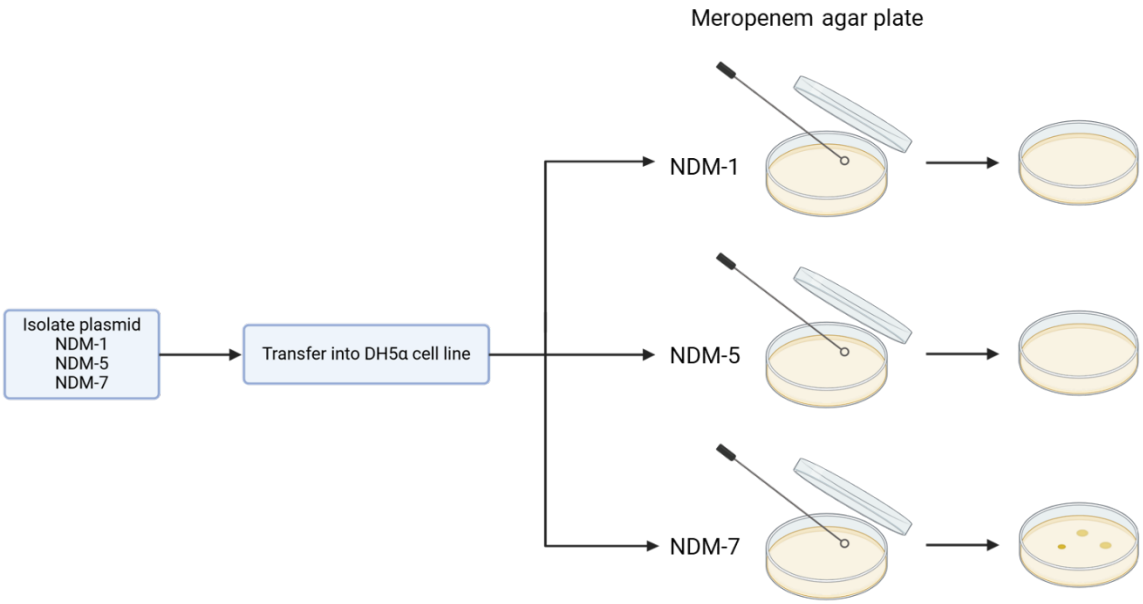

***Figure II.I Stability of NDM-1, NDM-5, and NDM-7 in* E. coli.** *Plasmids containing NDM-1, NDM-5, and NDM-7 were isolated and transformed into DH5α cells. The transformed cells were plated on meropenem-containing agar plates to assess their ability to grow under meropenem exposure. Only cells harbouring the NDM-7 plasmid consistently grew, indicating that NDM-1 and NDM-5 were unstable under these conditions.*

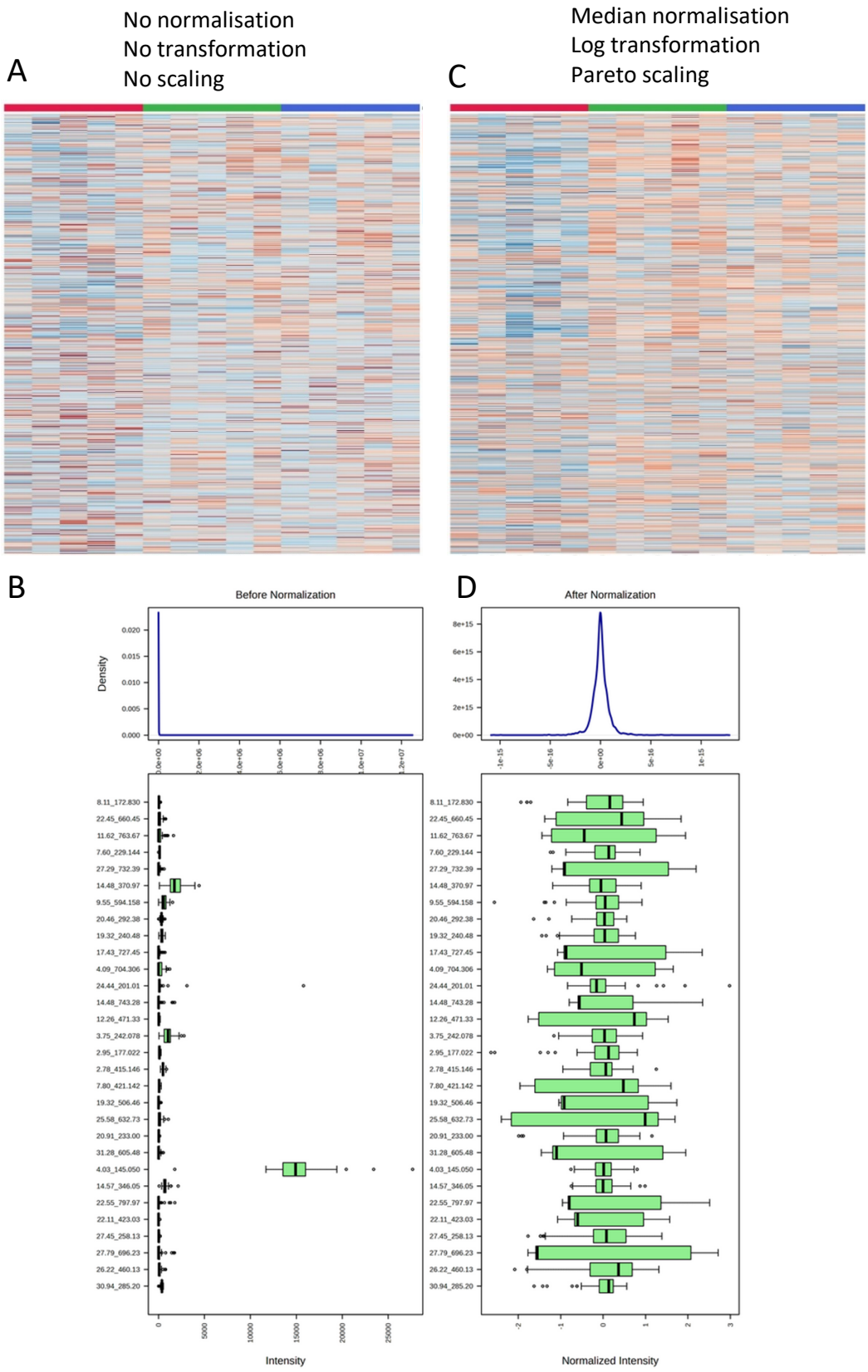

Figure II.II Data normalization and transformation for metabolic profiling. *(A, C) Heatmaps showing the raw (A) and normalized (C) intensities of metabolites across all samples, illustrating improved consistency after normalization. (B, D) Kernel density plots of feature intensities distribution before (B) and after (D) normalization, normal distribution after scaling and transformation, making it suitable for multivariate analysis.*

Table Appendix II.I List of metabolites significantly altered in abundance between the wild-type, meropenem-susceptible, and meropenem-resistant strains. Statistical significance was determined using one-way ANOVA (p < 0.05, FDR corrected). *The table includes the F-value, raw p-value, -log10(p) transformation, and FDR-adjusted p-value for each metabolite. Pairwise comparisons (Fisher's LSD post-hoc test) indicate the specific strain comparisons (E_0, S_0, and R_00 where significant differences were observed.*

Name	f.value	p.value	-LOG10(p)	FDR	Fisher's LSD
3-isopropylmalic acid (new)	146.53	3.70E-09	8.4313	4.78E-07	E_0 - R_0; E_0 - S_0; S_0 - R_0
Fructose 6-phosphate	124.28	9.54E-09	8.0204	6.15E-07	R_0 - E_0; S_0 - E_0; S_0 - R_0
Guanosine diphosphate (GDP)	98.386	3.61E-08	7.443	1.22E-06	R_0 - E_0; S_0 - E_0
Glucose 1-phosphate	97.542	3.79E-08	7.4218	1.22E-06	R_0 - E_0; S_0 - E_0; R_0 - S_0
Galactaric acid (mucic acid)	69.475	2.52E-07	6.5979	6.51E-06	E_0 - R_0; E_0 - S_0; S_0 - R_0
dCTP	66.479	3.22E-07	6.4924	6.92E-06	R_0 - E_0; S_0 - E_0
Hippuric acid	61.235	5.05E-07	6.2967	9.18E-06	E_0 - R_0; E_0 - S_0; S_0 - R_0
Uracil	59.905	5.69E-07	6.2446	9.18E-06	E_0 - R_0; E_0 - S_0
Sorbitol-6-phosphate	51.892	1.24E-06	5.9068	1.73E-05	R_0 - E_0; S_0 - E_0; R_0 - S_0
Cyclic AMP	51.161	1.34E-06	5.8737	1.73E-05	E_0 - R_0; S_0 - E_0; S_0 - R_0
Sedoheptulose 1-phosphate	48.875	1.71E-06	5.7673	2.00E-05	R_0 - E_0; S_0 - E_0; R_0 - S_0
Cytidine monophosphate	45.707	2.44E-06	5.6124	2.62E-05	R_0 - E_0; S_0 - E_0
Cytidine triphosphate	44.743	2.73E-06	5.5633	2.71E-05	R_0 - E_0; S_0 - E_0
N-Acetyl-L-phenylalanine	43.601	3.13E-06	5.5041	2.79E-05	E_0 - R_0; E_0 - S_0; S_0 - R_0
Thymine	43.303	3.25E-06	5.4884	2.79E-05	E_0 - R_0; E_0 - S_0
N-Acetyltryptophan	38.172	6.28E-06	5.202	5.06E-05	E_0 - R_0; E_0 - S_0; S_0 - R_0
Isocitrate	36.336	8.10E-06	5.0913	6.15E-05	E_0 - R_0; E_0 - S_0; S_0 - R_0
Adenine	34.949	9.90E-06	5.0045	6.82E-05	R_0 - E_0; S_0 - E_0; R_0 - S_0
Uridine 5'-diphosphate	34.843	1.01E-05	4.9978	6.82E-05	R_0 - E_0; S_0 - E_0; R_0 - S_0
Salicylic acid	32.131	1.52E-05	4.8188	9.79E-05	E_0 - R_0; E_0 - S_0; S_0 - R_0
dGDP	31.491	1.68E-05	4.7747	0.000102	R_0 - E_0; S_0 - E_0
N-acetylneuraminic acid (new)	31.273	1.74E-05	4.7594	0.000102	R_0 - E_0; S_0 - E_0
Glucuronic acid	30.85	1.86E-05	4.7297	0.000105	E_0 - R_0; E_0 - S_0
Succinyl-Homoserine	28.928	2.57E-05	4.5901	0.000136	R_0 - E_0; S_0 - E_0; R_0 - S_0
Maleamate (new)	28.789	2.63E-05	4.5797	0.000136	R_0 - E_0; S_0 - E_0
AICAR (new)	27.934	3.06E-05	4.5149	0.000152	R_0 - E_0; S_0 - E_0
Thymidine triphosphate	27.455	3.33E-05	4.4778	0.000159	R_0 - E_0; S_0 - E_0; R_0 - S_0
N-Acetylvaline	26.907	3.67E-05	4.4349	0.000169	E_0 - R_0; E_0 - S_0
N-Acetyl-L-methionine	24.728	5.54E-05	4.2563	0.000247	E_0 - R_0; E_0 - S_0
4-methyl-2-oxovaleric acid (ketoleucine) (new)	24.021	6.37E-05	4.1956	0.000274	E_0 - R_0; E_0 - S_0
Adenosine 2',3'-cyclic phosphate	19.731	0.000161	3.7938	0.00065	E_0 - R_0; S_0 - R_0
Thymidine 5'-phosphate (TMP)	19.718	0.000161	3.7925	0.00065	R_0 - E_0; S_0 - E_0
Aspartate	18.896	0.000196	3.7078	0.000766	R_0 - E_0; S_0 - E_0
N-Acetylaspartylglutamic acid	18.691	0.000206	3.6863	0.000767	E_0 - R_0; S_0 - R_0
2-Isopropylmalic acid	18.649	0.000208	3.6819	0.000767	R_0 - E_0; S_0 - E_0
TDP	18.512	0.000215	3.6674	0.000771	R_0 - E_0; S_0 - E_0
Glycolic acid (new)	17.019	0.000314	3.5036	0.001093	R_0 - E_0; S_0 - E_0; R_0 - S_0
Glutathione (GSH)	16.795	0.000333	3.4781	0.001129	R_0 - E_0; S_0 - E_0
Gluconolactone	16.142	0.000396	3.4024	0.00131	R_0 - E_0; R_0 - S_0

Pyroglutamic acid	15.715	0.000445	3.3517	0.001435	R_0 - E_0; S_0 - E_0
UDP-galactose	14.899	0.00056	3.2518	0.001762	R_0 - E_0; S_0 - E_0
Ribulose 5-phosphate	14.667	0.000599	3.2227	0.001797	E_0 - R_0; E_0 - S_0
Oxoadipic acid	14.666	0.000599	3.2226	0.001797	E_0 - R_0; E_0 - S_0
Mannitol	14.135	0.0007	3.1548	0.002053	R_0 - E_0; S_0 - E_0
3-Methyl-2-oxovaleric acid	13.538	0.000839	3.0763	0.002405	R_0 - E_0; S_0 - E_0
Fructose 2,6 diphosphate	13.024	0.000984	3.0069	0.00276	S_0 - E_0; S_0 - R_0
2,3-Diphosphoglyceric acid	12.704	0.00109	2.9627	0.002991	S_0 - E_0; S_0 - R_0
Uridine 5'-monophosphate	11.792	0.001471	2.8324	0.003953	R_0 - E_0; S_0 - E_0
Glutaconic acid	11.622	0.001558	2.8074	0.004102	R_0 - E_0; S_0 - E_0
Methylisocitric acid	10.644	0.002194	2.6587	0.005661	E_0 - R_0; S_0 - R_0
Glucose	10.174	0.002606	2.584	0.006592	R_0 - E_0; S_0 - E_0
3-methoxyphenylacetic acid	10.076	0.002703	2.5682	0.006706	E_0 - R_0; E_0 - S_0
Acetoacetate	9.8662	0.002925	2.5339	0.007118	R_0 - E_0; S_0 - E_0
(R)-2,3-Dihydroxy-3-methylbutanoate (new)	9.2877	0.003655	2.4371	0.008731	R_0 - E_0; S_0 - E_0
Adenosine monophosphate (AMP)	8.7245	0.004578	2.3393	0.010737	S_0 - E_0; S_0 - R_0
Adenosine diphosphate	8.0977	0.005943	2.226	0.01369	S_0 - E_0; S_0 - R_0
2-hydroxy-3-methylvaleric acid (new)	7.525	0.007622	2.1179	0.01725	R_0 - E_0; S_0 - E_0
6-phosphonoglucono-lactone	7.3532	0.00823	2.0846	0.018012	R_0 - E_0; S_0 - E_0
Ribulose 1,5,diphosphate	7.351	0.008238	2.0842	0.018012	R_0 - E_0; S_0 - E_0
3-Hydroxyisovaleric acid	7.2401	0.008661	2.0624	0.018451	R_0 - E_0; S_0 - E_0
4-Acetylbutyrate	7.2239	0.008725	2.0592	0.018451	R_0 - E_0; S_0 - E_0
Methylglutaric acid	7.0488	0.009451	2.0245	0.019664	R_0 - E_0; S_0 - E_0
2-Phosphoglyceric acid	7.0124	0.009611	2.0172	0.01968	R_0 - E_0; S_0 - E_0
Nonate	6.9569	0.009861	2.0061	0.019876	R_0 - E_0; S_0 - E_0
Succinic acid	6.4857	0.012315	1.9096	0.024441	R_0 - E_0
N-Acetyl-L-alanine	6.2628	0.01372	1.8626	0.026817	E_0 - R_0
Cytidine diphosphate	6.2184	0.014022	1.8532	0.026998	R_0 - E_0; S_0 - E_0
Dimethyl fumarate	6.1072	0.014813	1.8294	0.028101	S_0 - E_0
Glutaric acid	5.981	0.015774	1.8021	0.029491	R_0 - E_0; S_0 - E_0
Ureidopropionic acid	5.8732	0.016653	1.7785	0.030275	R_0 - E_0; S_0 - E_0
Butyric acid	5.872	0.016663	1.7782	0.030275	S_0 - E_0
3-Phosphoglyceric acid	5.817	0.017134	1.7661	0.030699	R_0 - E_0; S_0 - E_0
3,3 Dimethyl glutarate	5.7698	0.017551	1.7557	0.031014	R_0 - E_0; S_0 - E_0
Shikimic acid	5.6857	0.018322	1.737	0.031934	R_0 - E_0; S_0 - E_0
Methyl beta-D-glucopyranoside	5.66	0.018566	1.7313	0.031934	R_0 - E_0; S_0 - E_0
Hydrocinnamic acid	5.5919	0.01923	1.716	0.03264	R_0 - E_0; S_0 - E_0
3-Hydroxymethylglutarate	5.5319	0.019838	1.7025	0.033235	R_0 - E_0; S_0 - E_0
2-Ketobutyric acid	5.3071	0.022325	1.6512	0.036923	S_0 - E_0
N-Acetylglutamate	5.2354	0.023194	1.6346	0.037874	E_0 - R_0
Kojic acid	5.0941	0.025024	1.6016	0.040351	R_0 - E_0
Pantoic acid (new)	5.0005	0.026329	1.5796	0.041932	E_0 - S_0; R_0 - S_0

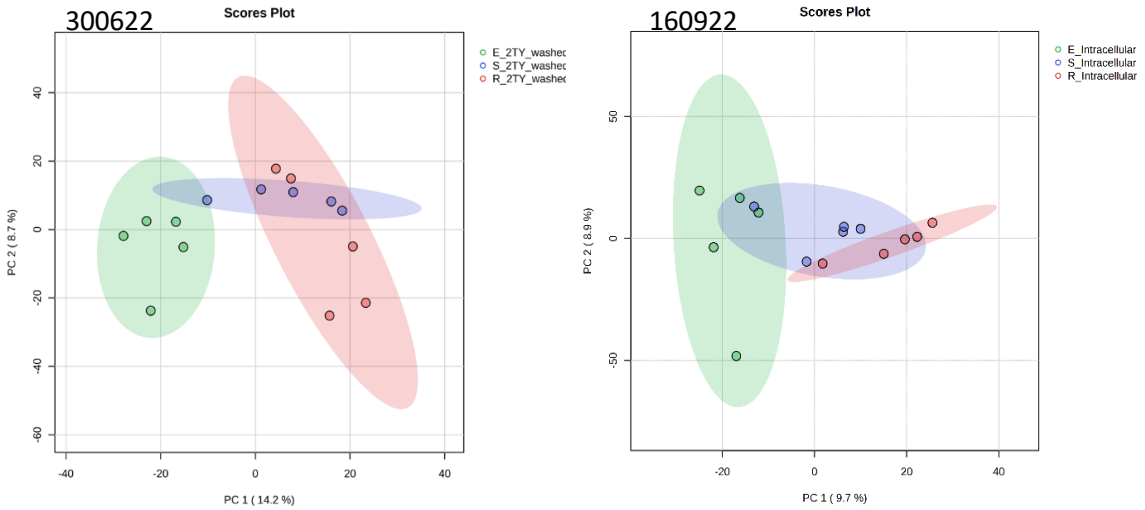

Figure II.III PCA of metabolic profiles from repeated experiments. *PCA scores plots show the clustering of metabolic profiles for* E. coli *strains (E, S, and R) under identical experimental conditions in two separate experimental repeats. (A) PCA plot of experiment from 300622 metabolites showing distinct clustering for E and R strains, with S positioned in between, consistent with the trends observed in the primary dataset. (B) PCA plot of experiment from 160922 demonstrating similar reproducibility in clustering patterns between experimental batches. These results confirm the reproducibility of observed trends under the same experimental conditions.*

***Table Appendix II.II Attempt to identify compound features based on retention time and* m/z.** *Possible metabolites were suggested using database searches from HMDB, METLIN, and ECMDB. The table includes information on whether predicted MS/MS spectra were available for these features and whether experimental MS/MS data matched the predicted spectra. Many features either lacked predicted MS/MS spectra or showed no matches to experimental MS/MS data, highlighting challenges in definitive metabolite identification. Top 10 most significantly altered compound features between E, S, and R strain.*

Compound-feature (RT_*m/z*)	Possible metabolite	Database source	Predicted MS/MS available?	MS/MS Match?
9.48_729.6900	Diglyceride or diacylglycerol (+364 other possibility)	HMDB	No	No
12.53_319.0960	4-[(1,3-Dithian-2-yl)methyl]-4-(ethoxycarbonyl)hexanoate	METLIN	No	No
16.89_351.1274	Amylose	ECMDB	Yes	No
20.99_319.0960	320 possibilities	HMDB		
4.46_305.0881	Pirimiphos-methyl	METLIN/HMDB	No	No
13.81_223.7514	Phosphorus dibromide chloride	METLIN	No	No
3.39_569.2583	Dipiperamide E (+218)	HMDB	Yes	No
3.30_240.1354	N/A			
7.80_226.0622	N/A			
22.20_371.5388	N/A			

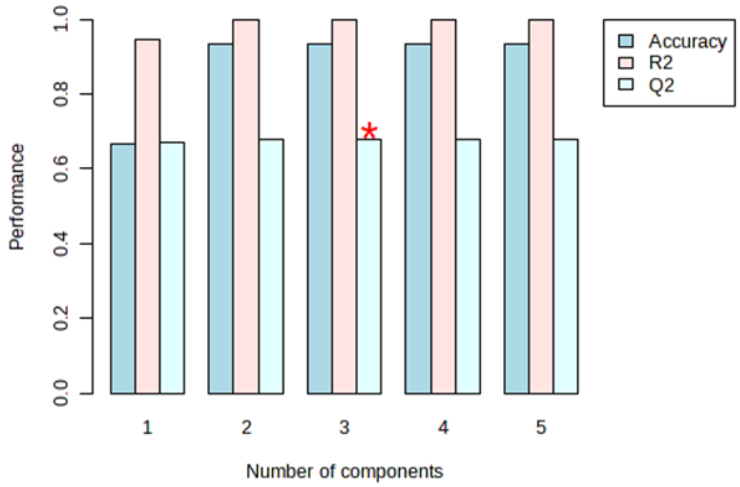

Figure II.IV Performance metrics for PLS-DA model across wild-type (E), meropenem-susceptible (S), meropenem-resistant (R) strains. *The plot illustrates accuracy (blue), R2 (pink), and Q2 (light blue) values for each component. An asterisk (*) marks the optimal number of components (3), where the balance between explained variance (R2) and predictive power (Q2) is maximized. The results highlight potential concerns with overfitting, as the Q2 values are consistently lower compared to R2, suggesting limited predictive power despite high accuracy and explained variance.*

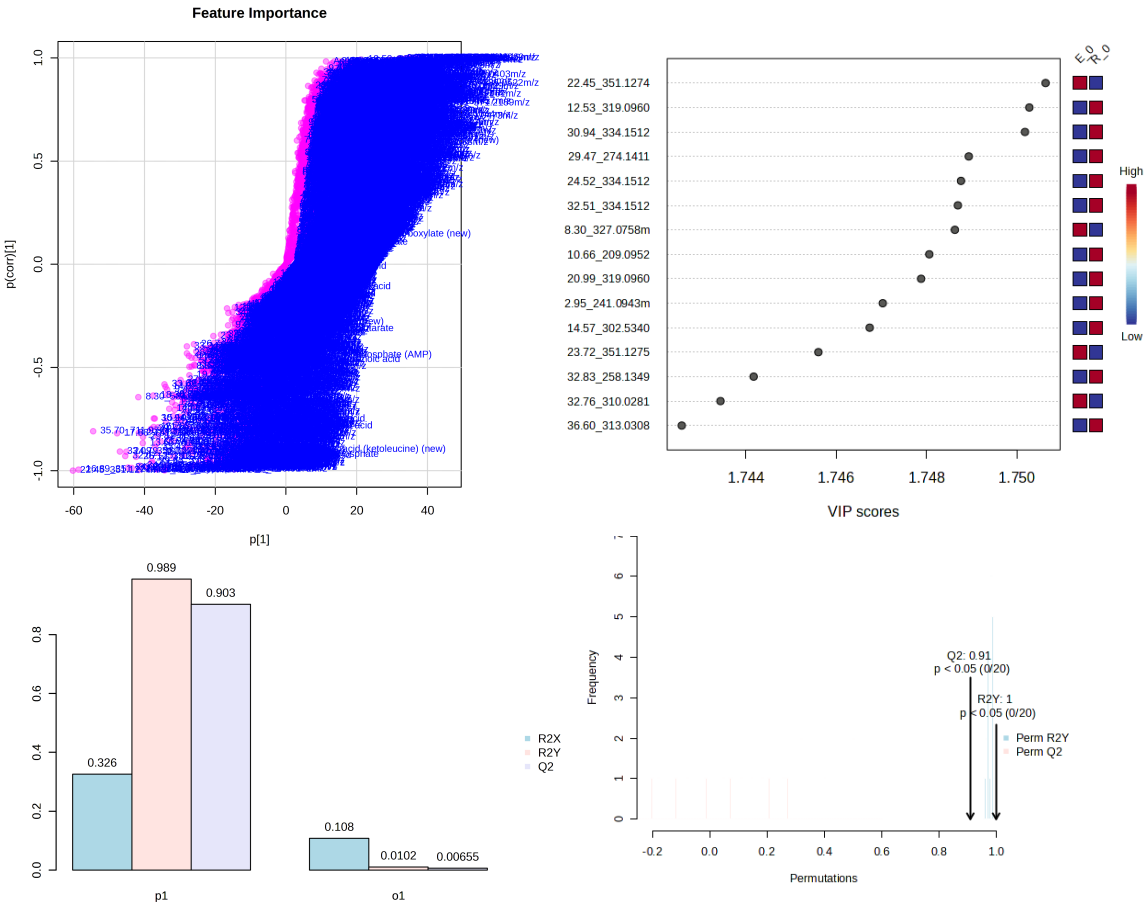

Figure II.V OPLS-DA analysis for E vs. S strains. *The feature importance plot (top-left) displays the contribution of each compound feature to the model, with significant metabolites highlighted. The VIP scores plot (top-right) ranks the most important metabolites contributing to group separation. The model validation metrics (bottom-left) show high R2Y (0.999) and Q2 (0.91) values, indicating a strong model fit and predictive ability. The permutation test results (bottom-right) confirm that the observed Q2 and R2Y values are significantly higher than those obtained from 20 permutations ($p < 0.05$, 0/20 permutations), verifying the model's statistical significance. These results demonstrate that the observed separation between E and S strains is robust and not due to random chance.*

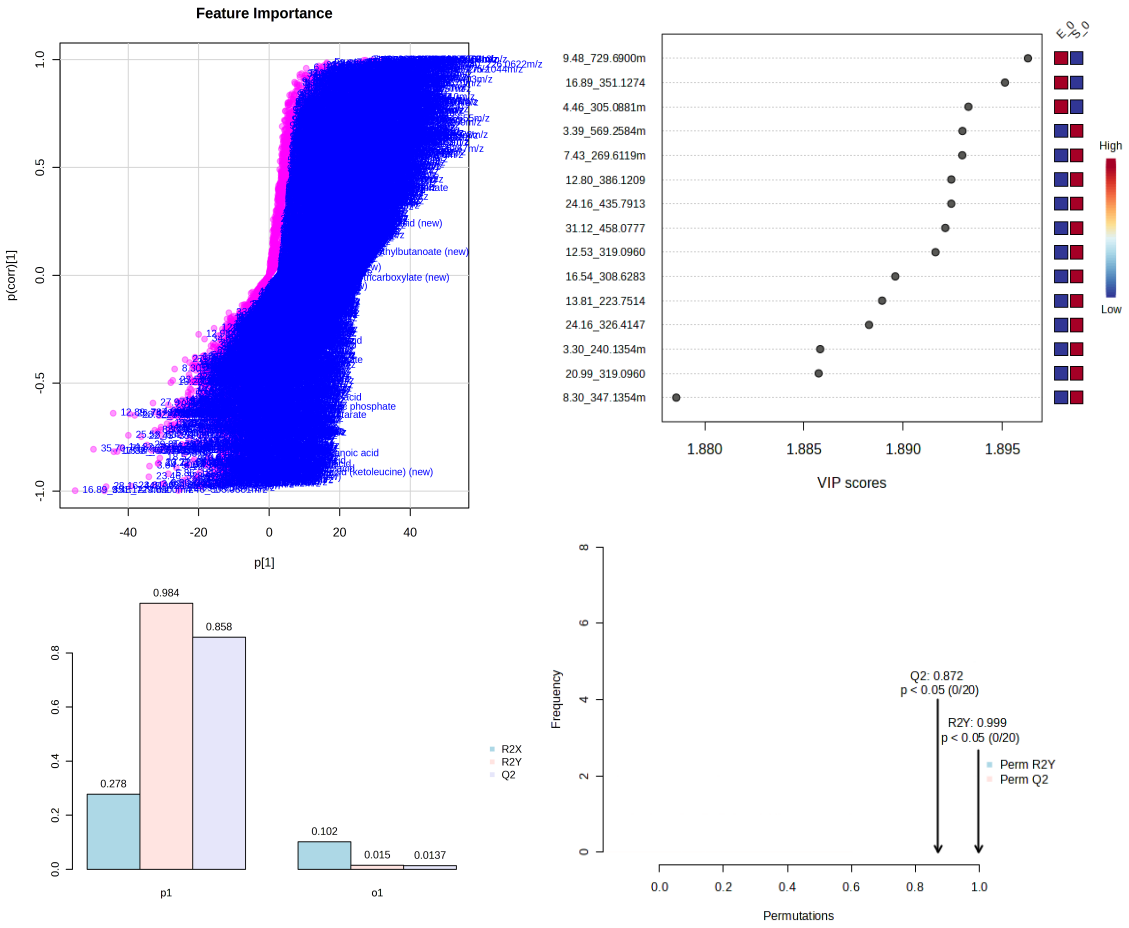

Figure II.VI OPLS-DA analysis for E vs. R strains. *The feature importance plot (top-left) highlights the contribution of individual metabolites to the separation between E and R strains, with key compound feature labelled. The VIP scores plot (top-right) ranks the most important metabolites contributing to group separation. The model validation metrics (bottom-left) show R2Y = 0.999 and Q2 = 0.872, indicating a strong model fit and predictive power. The permutation test results (bottom-right) confirm the statistical significance of the model, with observed Q2 and R2Y values significantly higher than those obtained from 20 permutations (p < 0.05, 0/20 permutations). These results validate the robustness of the model in distinguishing between E and R strains while indicating potential concerns regarding overfitting.*

Table Appendix II.III Attempt to identify compound features significantly altered between S and R strains under 4 µg/ml meropenem*. Features were identified based on retention time (RT) and m/z values. Possible metabolites were suggested using database searches from HMDB. The table includes information on whether predicted MS/MS spectra were available for these features and whether experimental MS/MS data matched the predicted spectra. Many features lacked predicted MS/MS spectra or showed no matches to experimental MS/MS data, underscoring the challenges in definitive metabolite identification.*

Compound-feature (RT_*m/z*)	Possible metabolite	Database source	Predicted MS/MS available?	MS/MS Match?
7.96_162.9579	N/A	HMDB	No	No
30.94_373.1328	1,1'-Bis(2-hydroxy-3-methylcarbazole)	HMDB	Yes	No
4.52_714.4621	N/A	HMDB	Yes	No
4.46_269.0701	N,N'-Bis(g-glutamyl)-3,3'-(1,2-propylenedithio)dialanine	HMDB	Yes	No
4.46_305.0881	Starch acetate	HMDB	No	No
3.59_225.0518	3-Nitrotyrosine	HMDB	No	No
10.75_602.2020	N-[(1R)-1-[3-(4-Ethoxyphenyl)-4-oxopyrido[2,3-d]pyrimidin-2-yl]ethyl]-N-(pyridine-3-ylmethyl)-2-[4-(trifluoromethoxy)phenyl]acetamide (blood?)	HMDB	Yes	No
18.24_338.5447	UCP-N-acetylmuraminate	HMDB	No	No
8.02_204.9674	Etidronic acid	HMDB	Yes	No
8.02_202.9705	Acetazolamide	HMDB	Yes	No

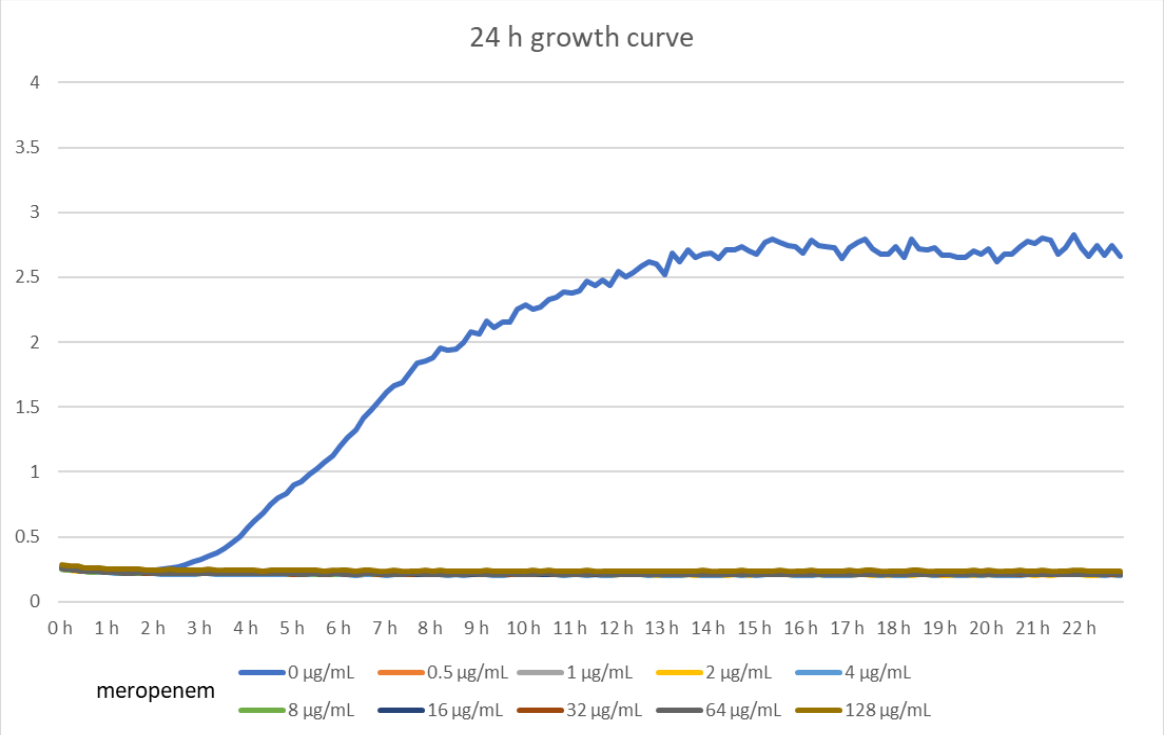

Figure II.VII 24-hour growth curve of* E. coli *wild-type strain in the presence of various concentration of meropenem. *The OD600 was measured every 10 minutes for over a 24-hour period. The concentrations of meropenem tested were 0, 0.25, 0.5, 1, 2, 4, 8, 16, 32, 64, 128, 256 µg/mL, as indicated in the legend.*

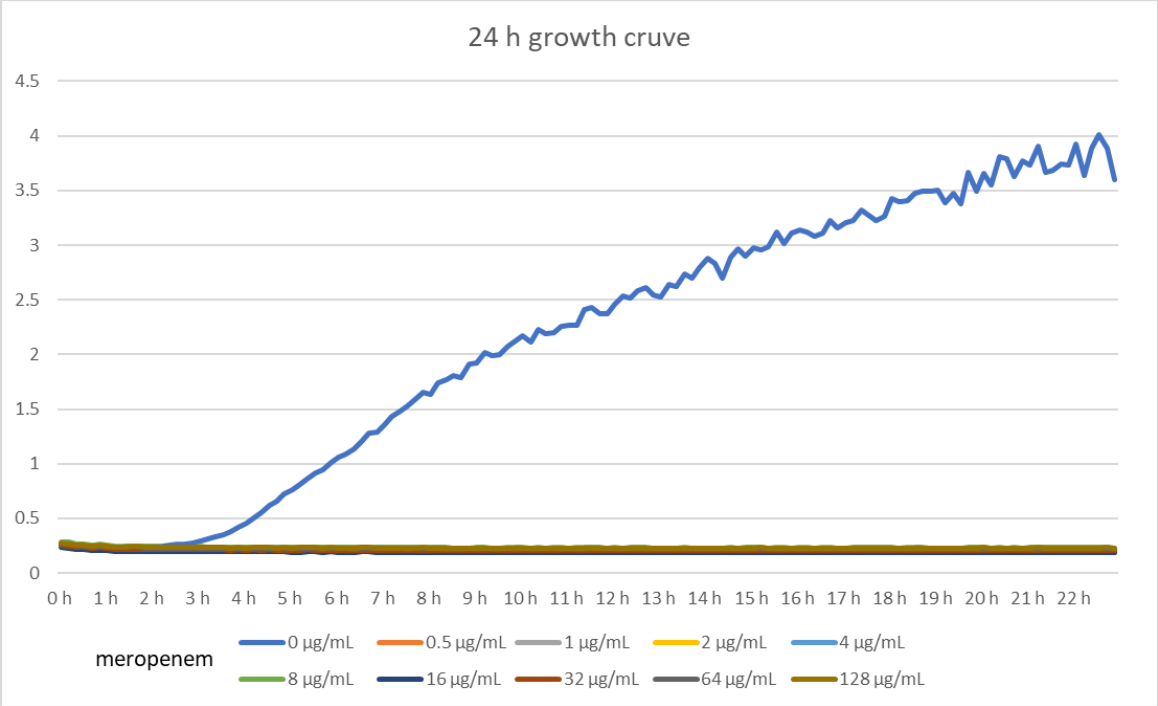

Figure II.VIII 24-hour growth curve of* E. coli *meropenem-susceptible strain in the presence of various concentration of meropenem. *The OD600 was measured every 10 minutes for over a 24-hour period. The concentrations of meropenem tested were 0, 0.25, 0.5, 1, 2, 4, 8, 16, 32, 64, 128, 256 µg/mL, as indicated in the legend.*

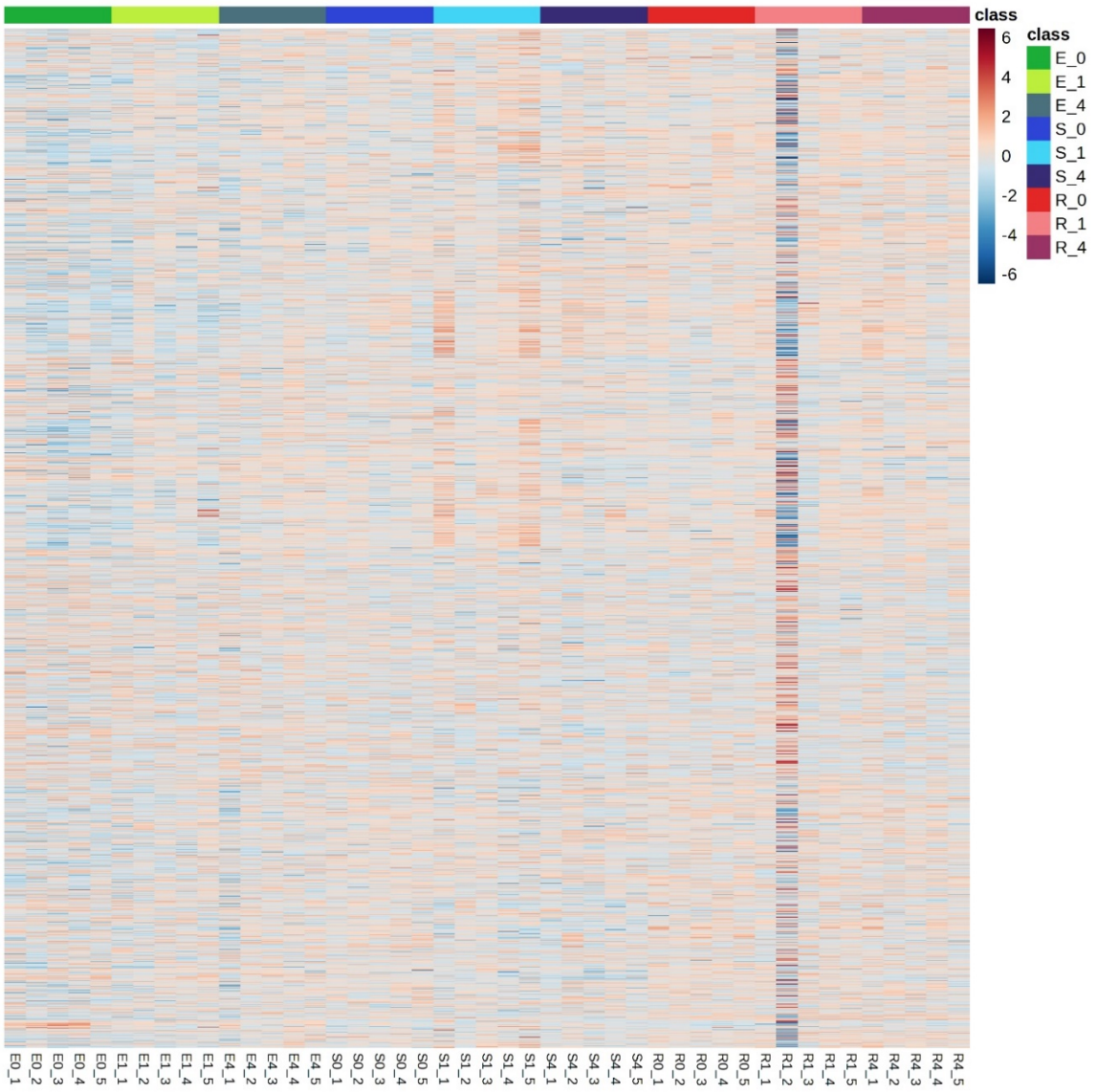

Figure II.IX Unclustered heatmap of normalized metabolite abundances across* E. coli *strains and treatment conditions. *The heatmap displays metabolite abundance profiles across wild-type (*E*), meropenem-susceptible (*S*), and meropenem-resistant (*R*) strains under different treatment conditions (0 µg/mL, 1 µg/mL, and 4 µg/mL meropenem exposure). Rows represent individual metabolites, while columns correspond to biological replicates for each condition. Metabolite abundances are scaled (z-scores) and visualized using a gradient from blue (low abundance) to red (high abundance). The colour-coded bar at the top indicates different strains and treatment groups.*

Figure II.X PCA scores plot of metabolomic profiles across* E. coli *strains and treatment conditions. *The PCA plot visualizes the distribution of metabolite profiles in wild-type (*E*), susceptible (*S*), and resistant (*R*) strains under different treatment conditions (0 µg/mL, 1 µg/mL. and 4 µg/mL meropenem exposure). Each point represents an individual biological replicate, with ellipses indicating 95% confidence intervals for each group. Principal component 1 (PC1) and principal component 2 (PC2) explain 9.7% and 5.0% of the variance, respectively.*

Appendix III

This appendix provides supplementary data supporting the Seahorse Analyser data for Chapter 5.

Appendix III.I Pilot study using XF Glycolysis Stress Test to investigate glycolytic function in *E. coli*

To explore the feasibility of live bacterial cell analysis using the Seahorse XF system, the XF Glycolysis Stress Test was chosen as a pilot assay to investigate glycolytic function in *E. coli* strains with and without meropenem exposure. The assay aimed to determine glycolytic capacity and reserve through sequential injections of glucose, oligomycin, and 2-DG, providing a dynamic assessment of cellular energy metabolism. The study employed the standard assay designed for eukaryotic cells to evaluate its relevance for bacterial systems and the effectiveness of the pharmacological interventions used therein.

III.I.I Experimental Design and Workflow

Cells were grown overnight and subcultures to an optical density (OD) of 0.3 before being diluted to an OD of 0.02.[434] A volume of 250 µl was spun down and fresh media was added to a final volume of 500 µl for the assay. The Glycolysis Stress Test medium was prepared according to XF Glycolysis Stress Test Assay guidelines (2.6.3.1). The assay began with cells in the glycolysis stress test medium devoid of glucose or pyruvate, creating a substrate-limited environment. This condition allowed the establishment of a baseline measurements for ECAR and OCR, representing non-glycolytic acidification and basal oxygen consumption.

For each strain, cells were divided into two groups, one group had an extra meropenem injection before the injection of glucose, while the other group received only the assay compounds without additional meropenem. This setup allowed a direct comparison of metabolic responses with and without antibiotic.

All samples were injected with glucose to stimulate glycolysis. The increased glycolytic flux was intended to enhance the production of pyruvate, ATP, NADH, water and protons. Pyruvate, depending on cellular conditions, could be metabolised via two primary routes: conversion to acetyl-CoA for entry into the TCA cycle, supporting OXPHOS through the bacterial ETC. The increased proton export associated with these metabolic processes expected to elevate ECAR, representing glycolytic activity.

Subsequently, oligomycin was injected as an ATP synthase inhibitor, blocking proton re-entry through ATP synthase and inhibiting oxidative phosphorylation. This forced cells to rely entirely on glycolysis for ATP production. In *E. coli*, this inhibition is expected to lead to an accumulation of acetyl-CoA and enhanced proton export through glycolytic pathways, further increasing ECAR. The ECAR during this phase represented the maximal glycolytic capacity of the cells, highlighting their ability to compensate for inhibited oxidative metabolism.

The final step involved the injection of 2-DG, a glucose analogue that inhibit glycolysis by competitively blocking glucose phosphorylation via glucokinase, preventing glucose-6-phosphate entry into glycolysis, halting glycolytic acidification. The resulting ECAR reflected non-glycolytic acidification, arising from processes such as CO_2 hydration or basal proton export. By subtracting this value from earlier measurements, key parameters such as glycolytic activity and reserve capacity were quantified.

Two basic measurements made in the Seahorse assay: 1) extracellular acidification and 2) oxygen levels. When combined with the effect of the pharmacological interventions which manipulated energy metabolism in eukaryotic cells, and changes in these levels over time, these data are used to interpret non-glycolytic acidification, glycolysis rate, glycolytic capacity, and glycolytic reserve. Non-glycolytic acidification was determined as the lowest ECAR after 2-DG injection, representing acidification not attributed to glycolysis. Glycolysis was calculated as the difference between maximal ECAR after glucose injection and the non-glycolytic acidification rate. Glycolytic capacity was determined as the maximal ECAR achieved after oligomycin injection minus the non-glycolytic acidification rate, reflecting the ability of cells to enhance glycolytic flux when oxidative pathways were inhibited. Glycolytic reserve was defined as the difference between glycolytic capacity and glycolysis, indicating the ability of cells to meet increased energy demands through glycolysis.

III.I.II Results

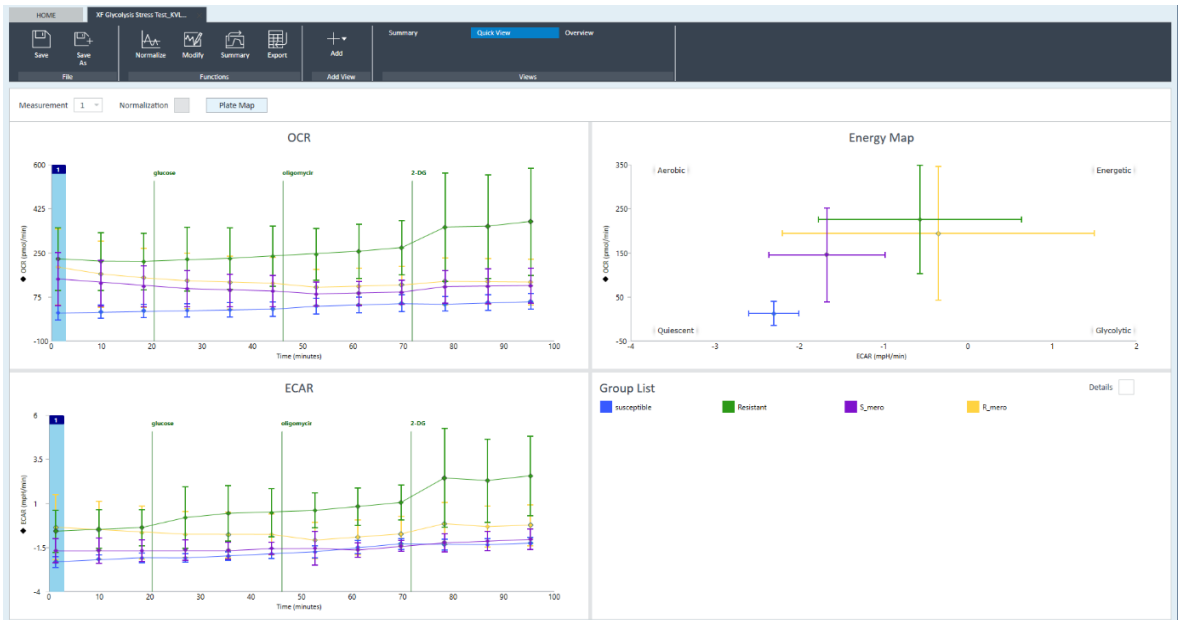

Figure III.I Overview of XF Glycolysis Stress Test pilot experiment. *The top left panel shows the oxygen consumption rate (OCR) over time for meropenem-susceptible (blue) and meropenem-resistant (green) E. coli strains under sequential injections of glucose, oligomycin, and 2-DG. Planned additions of meropenem (purple -susceptible, and yellow- resistant) was incomplete due to errors in assay protocol. The bottom left panel displays the extracellular acidification rate (ECAR) for the same strains over the course of the assay. The right panel presents an energy map derived from the OCR and ECAR data, categorising the metabolic profiles of the strains into aerobic, energetic, glycolytic, or quiescent states. Error bars represent standard deviations from three technical replicates.*

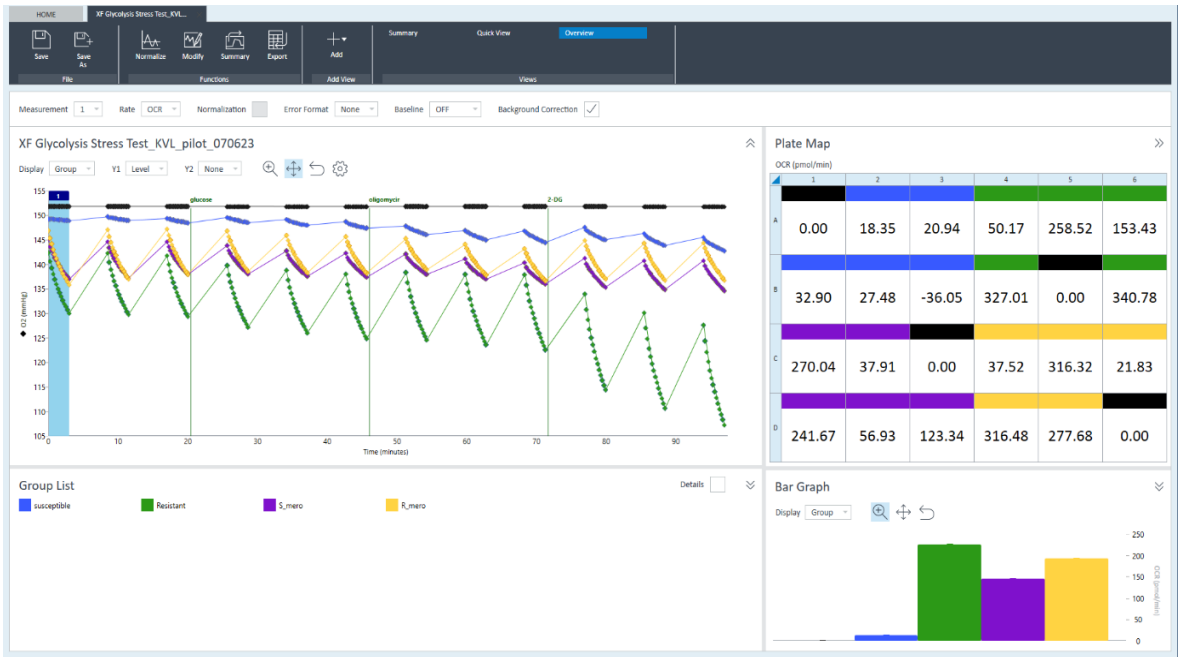

Figure III.II Detailed OCR Results from XF Glycolysis Stress Test for E. coli Strains*. Oxygen consumption rate (OCR) measurements for meropenem-susceptible (blue) and meropenem-resistant (green) E. coli strains under the XF Glycolysis Stress Test. The sequential injections of glucose, oligomycin, and 2-deoxy-D-glucose (2-DG) are marked along the timeline, capturing basal respiration, ATP-linked respiration, and non-ETC-related respiration. The plate map on the right shows OCR values for individual wells at the end of the assay, highlighting variability in respiration rates across the experimental groups. The bar graph presents the average OCR for each condition, indicating differences between the strains. High variability in OCR values indicates potential issues with cell adhesion to the plate and assay conditions.*

III.I.III Discussion

The pilot study underscored significant limitations in using the XF Glycolysis Stress Test for bacterial systems. The experimental outcomes deviated significantly from what would be expected in eukaryotic systems due to procedural errors, including incorrect injection sequences and incomplete data acquisition in certain groups. For instance, in the meropenem-treated susceptible strain (S_mero), the final injection delivered oligomycin instead of 2-DG, compromising ECAR interpretation and obscuring glycolytic responses. Substantial variability in OCR values, including abnormally low or negative readings in some wells were linked to inadequate cell adhesion and uneven cell distribution. Similar variability in ECAR data further supported these findings. For non-adherent *E. coli* cells, the absence of proper plate coating, such as poly-L-lysine, contributed to cell detachment during the assay. Detached cells reduced the reliability of metabolic measurements, leading to diminished OCR and ECAR values and increased variability across replicates. Additionally, the rapid oxygen consumption by *E. coli* created hypoxic conditions within the assay chamber, further complicating OCR measurements and reducing the robustness of the data.

Moreover, the design of the Glycolysis Stress Test assumes that glycolytic acidification primarily reflects lactate production, a pathway dominant in mammalian cells. However, in *E. coli*, extracellular acidification is primarily driven by proton export and the production of fermentation by-products such as acetate and formate, rather than lactate. This metabolic distinction rendered the assay unsuitable for accurately quantifying glycolytic activity in *E. coli*, as the underlying assumptions did not align with the bacterial physiology.

These findings revealed the need to transition from the Glycolysis Stress Test to the XF Glycolysis Rate Assay for future studies. The Glycolysis Rate Assay accounts for non-glycolytic contributions to acidification, offering a more accurate and nuanced assessment of glycolytic activity in bacterial systems. By distinguishing glycolysis-specific acidification from other sources, the Glycolysis Rate Assay addresses the limitations observed in the pilot study and provides a more reliable framework for investigating glycolytic dynamics in *E. coli*.

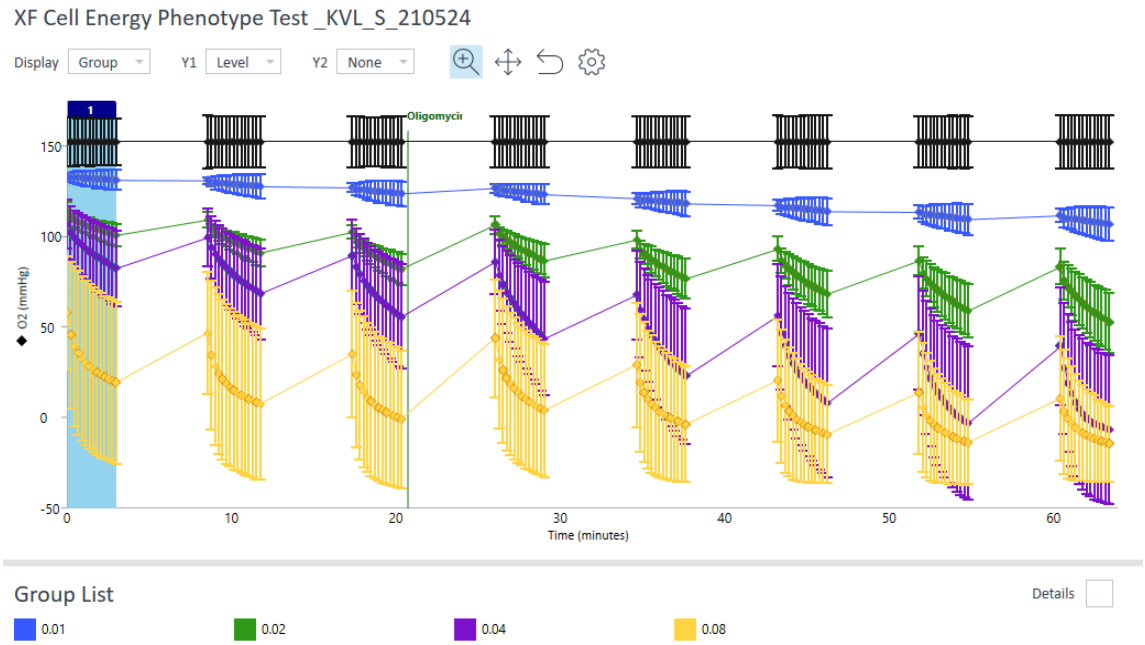

Figure III.III Oxygen levels during the XF Cell Phenotype Test for meropenem-susceptible (E. coli) at varying seeding densities. *Oxygen levels (mmHg) were monitored throughout the Seahorse XF Cell Energy Phenotype Test for cells seeded at OD 0.01 (blue), 0.02 (green), 0.04 (purple), and 0.08 (yellow). The periodic dips correspond to measurement and mixing cycles, with the injection of oligomycin indicated in green. Oxygen depletion was observed at higher densities, particularly at OD 0.08, where levels consistently dropped below the hypoxia threshold (35 mmHg) during later time points. These data were used to assess oxygen availability across different seeding conditions and inform the selection of optimal densities for Seahorse assays. Error bars represent standard deviations from biological replicates (n=5).*

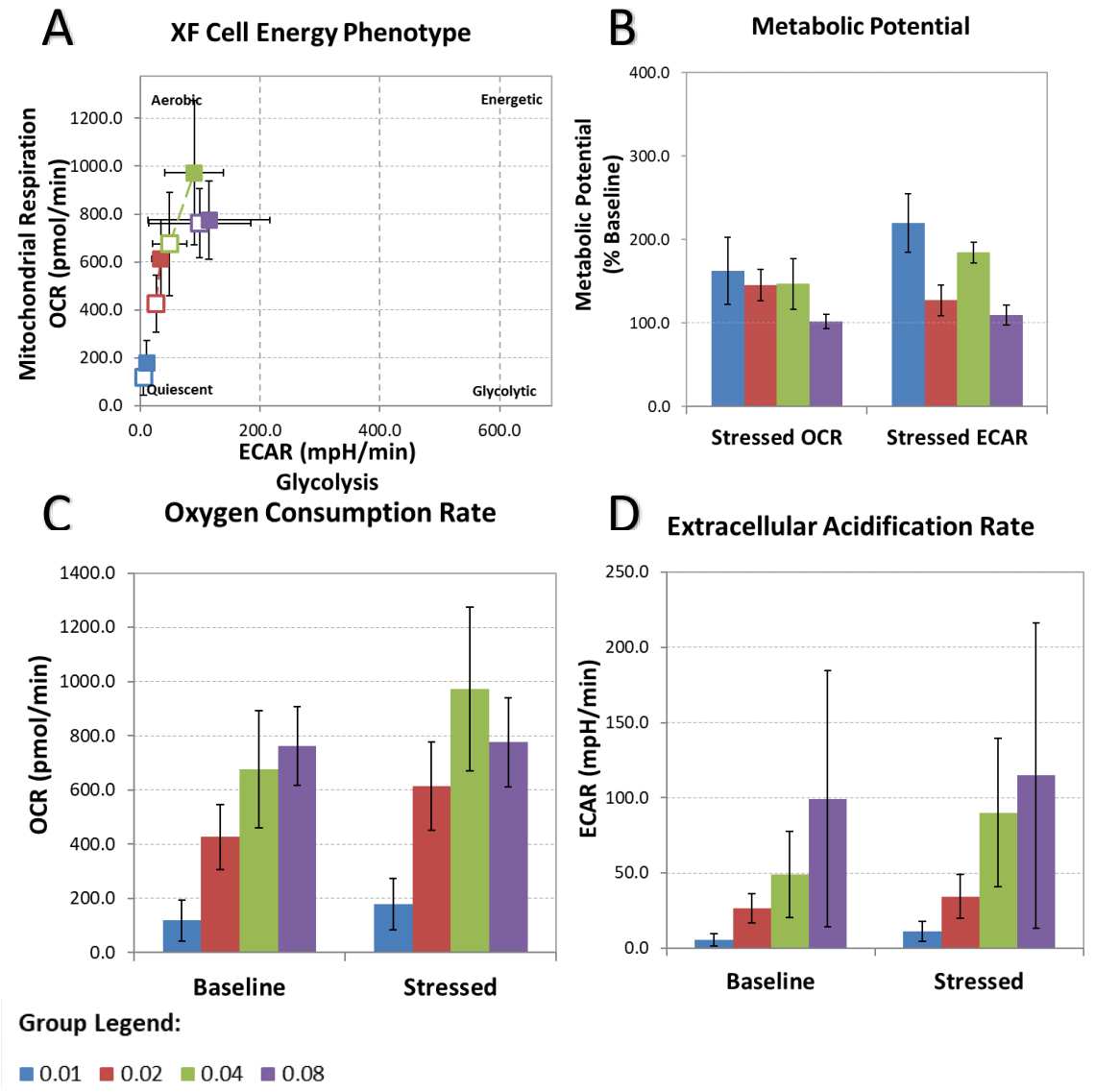

Figure III. IV Seahorse XF Cell Energy Phenotype Test Report for the meropenem-susceptible (S)* E. coli *strain. *The data show A) XF cell energy phenotype, B) metabolic potential, C) oxygen consumption rate (OCR), and D) extracellular acidification rate (ECAR) under basal and stressed conditions across seeding densities (OD 0.01, 0.02, 0.04, and 0.08). Group legend colours correspond to OD densities: blue (0.01), red (0.02), green (0.04), and purple (0.08). Error bars represent standard deviation across replicates (n=5).*

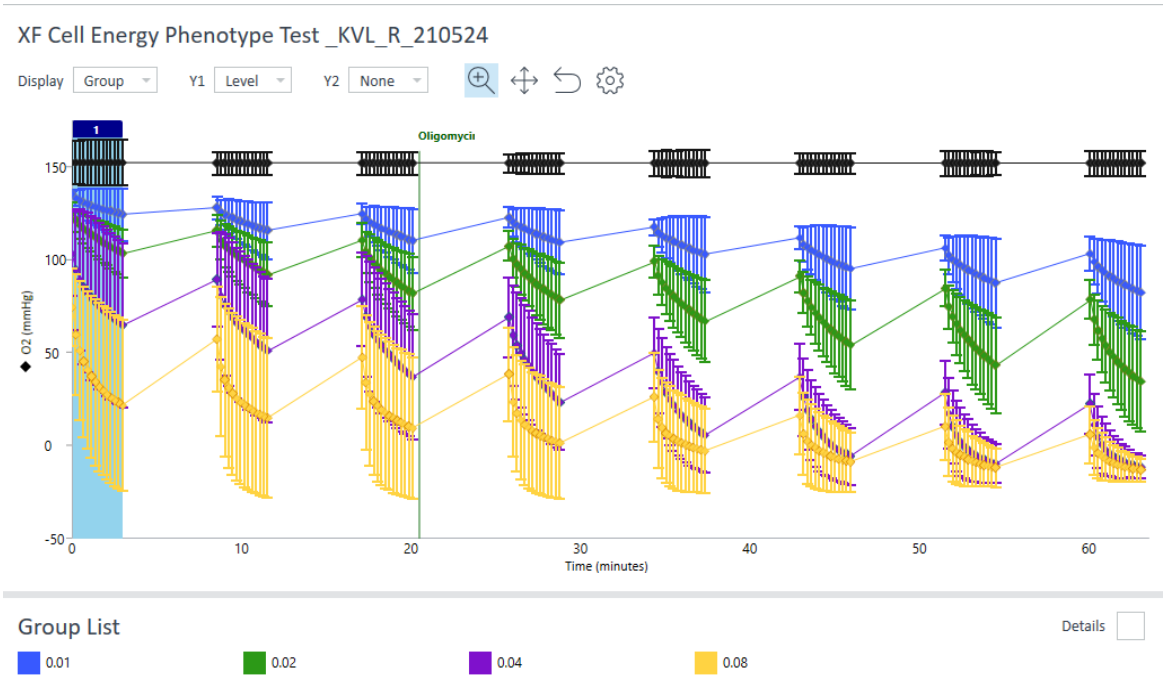

Figure III.V Oxygen levels during the XF Cell Energy Phenotype Test for meropenem-resistant (*E. coli*) at varying seeding densities. *Oxygen levels (mmHg) were monitored throughout the Seahorse XF Cell Energy Phenotype Test for the meropenem-resistant (*E. coli*) strain at OD 0.01 (blue), 0.02 (green), 0.04 (purple), and 0.08 (yellow). The periodic declines correspond to measurement and mixing cycles, with the oligomycin injection indicated in green. Oxygen depletion was most pronounced at OD 0.08, where levels consistently dropped below the hypoxia threshold (35 mmHg) as the assay progressed. These data highlight the impact of cell density on oxygen availability and were used to determine optimal seeding conditions for Seahorse assays. Error bars represent standard deviation from biological replicates (n=5).*

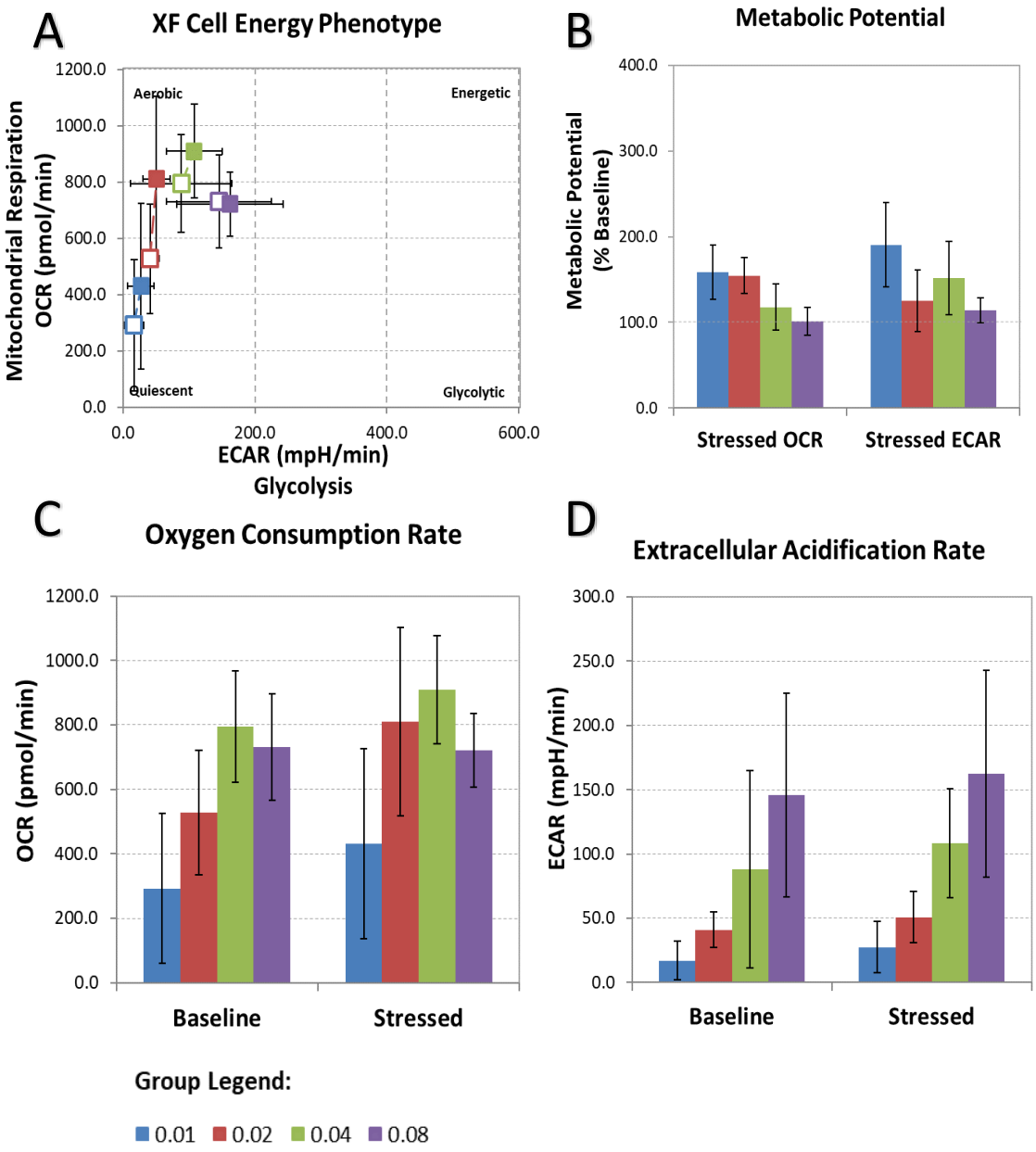

Figure III.VI Seahorse XF Cell Energy Phenotype Test Report for the meropenem-resistant (R)* E. coli *strain. *The data display A) XF cell energy phenotype, B) metabolic potential, C) oxygen consumption rate (OCR), and D) extracellular acidification rate (ECAR) under basal and stressed conditions across seeding densities (OD 0.01, 0.02, 0.04, and 0.08). Group legend colours correspond to OD densities: blue (0.01), red (0.02), green (0.04), and purple (0.08). Error bars represent standard deviations across replicates.*

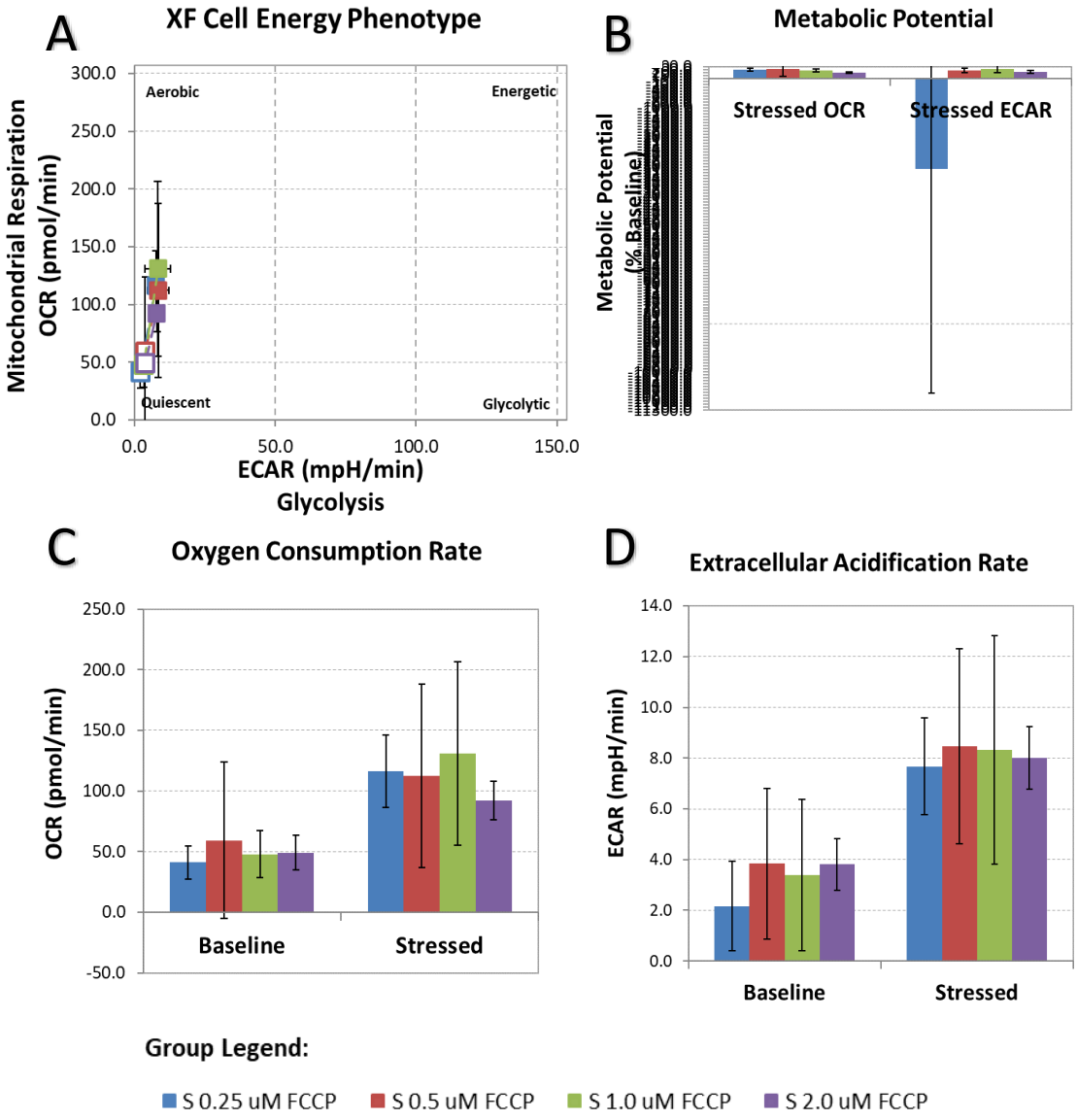

Figure III.VII Seahorse XF Cell Energy Phenotype Test Report for the meropenem-susceptible (S)* E. coli *strains at varying FCCP concentrations (0.25 µM, 0.5 µM, 1.0 µM, 2.0 µM). *The metabolic phenotype is categorized into aerobic, energetic, glycolytic, and quiescent states based on OCR and ECAR measurements. The data display A) XF cell energy phenotype, B) metabolic potential, C) OCR, and D) extracellular acidification rate (ECAR) under basal and stressed conditions across FCCP concentration (0.25, 0.5, 1.0, and 2.0 µM). Group legend colours correspond to FCCP concentrations: blue (0.25), red (0.5), green (1.0), and purple (2.0). Error bars represent standard deviations across replicates.*

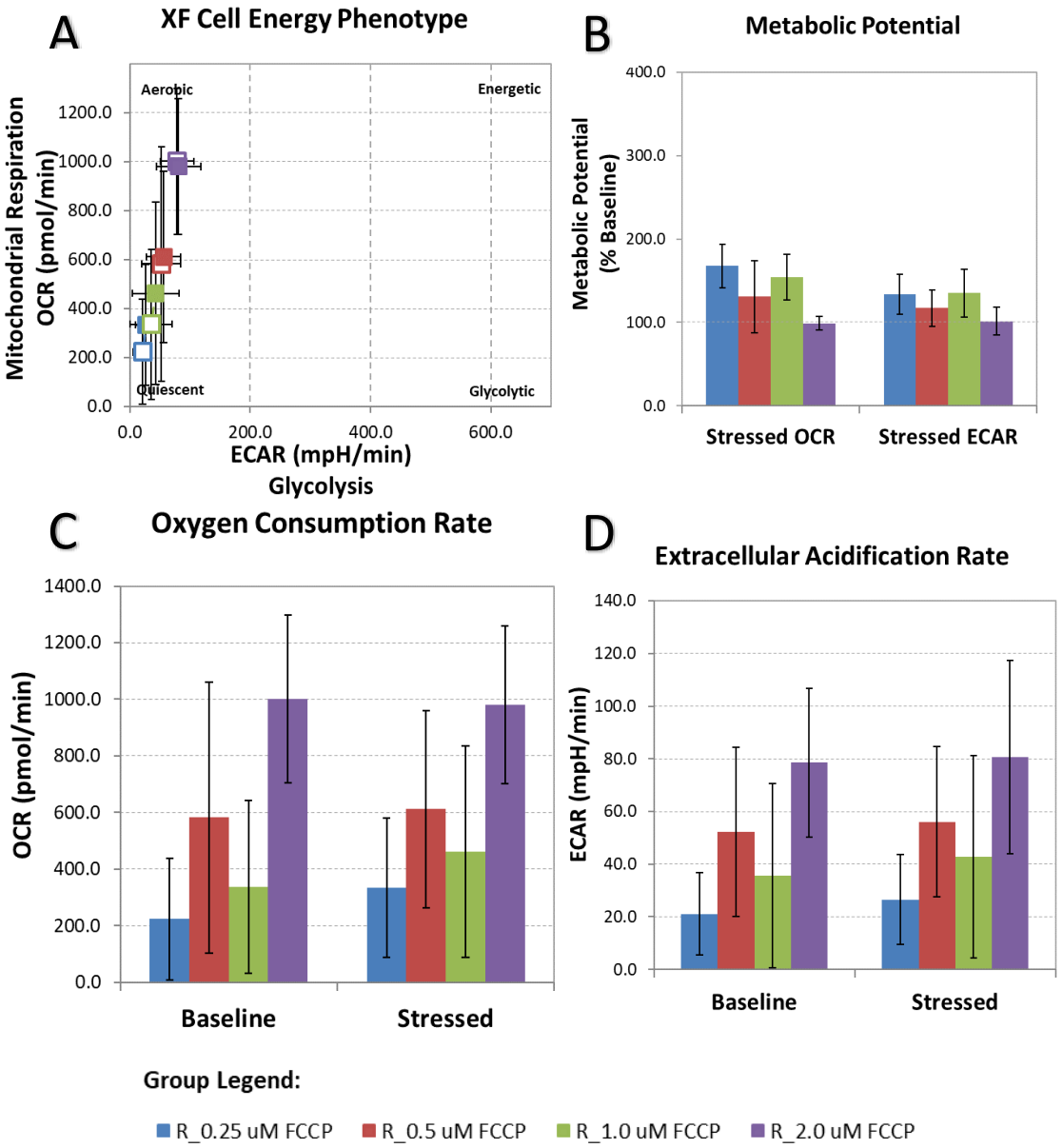

Figure III.VIII Energy map of meropenem-resistant (R)* E. coli *strains at varying FCCP concentrations (0.25 µM, 0.5 µM, 1.0 µM, 2.0 µM). *The metabolic phenotype is categorized into aerobic, energetic, glycolytic, and quiescent states based on OCR and ECAR measurements. The data display A) XF cell energy phenotype, B) metabolic potential, C) oxygen consumption rate (OCR), and D) extracellular acidification rate (ECAR) under basal and stressed conditions across FCCP concentration (0.25, 0.5, 1.0, and 2.0 µM). Group legend colours correspond to FCCP concentrations: blue (0.25), red (0.5), green (1.0), and purple (2.0). Error bars represent standard deviations across replicates.*

Appendix III.II Buffer factor calculation

The BF is a measure of the medium's buffering capacity, defined as the amount of acid (or base) required to induce a unit change in pH. It is calculated using the formula:

$$BF = \frac{\Delta C}{\Delta pH}$$

ΔC = total concentration of titrant (HCl) added in mM

ΔpH = change in pH resulting from titration

Linear regression was performed on pH response data for HCl-treated wells where media titrated with HCl and control wells where an equivalent volume of 2TY medium added instead of HCL, providing a baseline of pH variation in the absence of acid titration.

Regression equations:

Control: $pH = 0.0159x + 6.6536$

This equation confirms that background fluctuations in pH are minimal, validating that pH shifts in the experimental wells are due to HCl titration rather than dilution effects.

HCl-treated wells: $pH = -0.1828x + 6.6193$

The slope (-0.1828) represents the rate of pH change per unit of added HCl concentration.

Since BF is based on the buffering effect of the medium, only the HCl-treated condition is used for the calculation.

The total amount of HCl added per well was determined as follows:

Initial well volume = 525 µL

HCl stock concentration = mM

Injection volume per addition = 75 µL

Total number of injections = 3

Total volume of HCl added = 75 µL × 3 = 225 µL

Using dilution principles, the total concentration of HCl in the well is:

$$C_{total} = \frac{(225\ \mu L\ \times 5\ mM)}{(525\ \mu L + 225\ \mu L)} = \frac{1125\ nmol}{750\ \mu L}\ 1.5\ mM$$

The change in pH (ΔpH) is calculated by substituting x = 1.5 mM into the HCl-treated regression equation:

Initial pH (before HCl addition): $pH_{initial} = 6.6193$

Final pH (after 1.5 mM HCl addition): $pH_{final} = (-0.1828\ \times 1.5) + 6.6193 = 6.3451$

Change in pH: $\Delta pH = 6.6193 - 6.3451 = 0.3324$

$$BF = \frac{1.5\ mM}{0.3324} = 5.0339 mM/pH$$

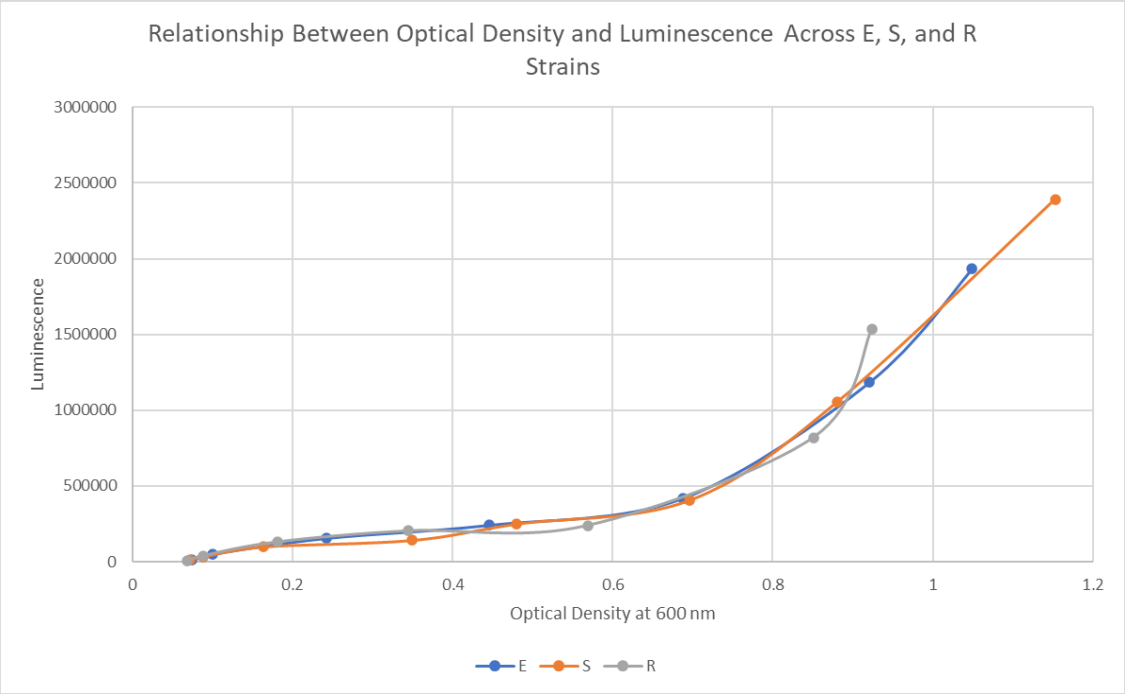

Figure III.IX The concentration curve illustrates the relationship between optical density (OD) and luminescence as measured by BacTiter-Glo™ for E (wild-type), S (susceptible), and R (resistant) strains. *Luminescence reflects metabolic activity corresponding to bacterial growth.*

Appendix IV

This appendix presents data from the exploration of alternative compounds for potential combination therapy with meropenem.

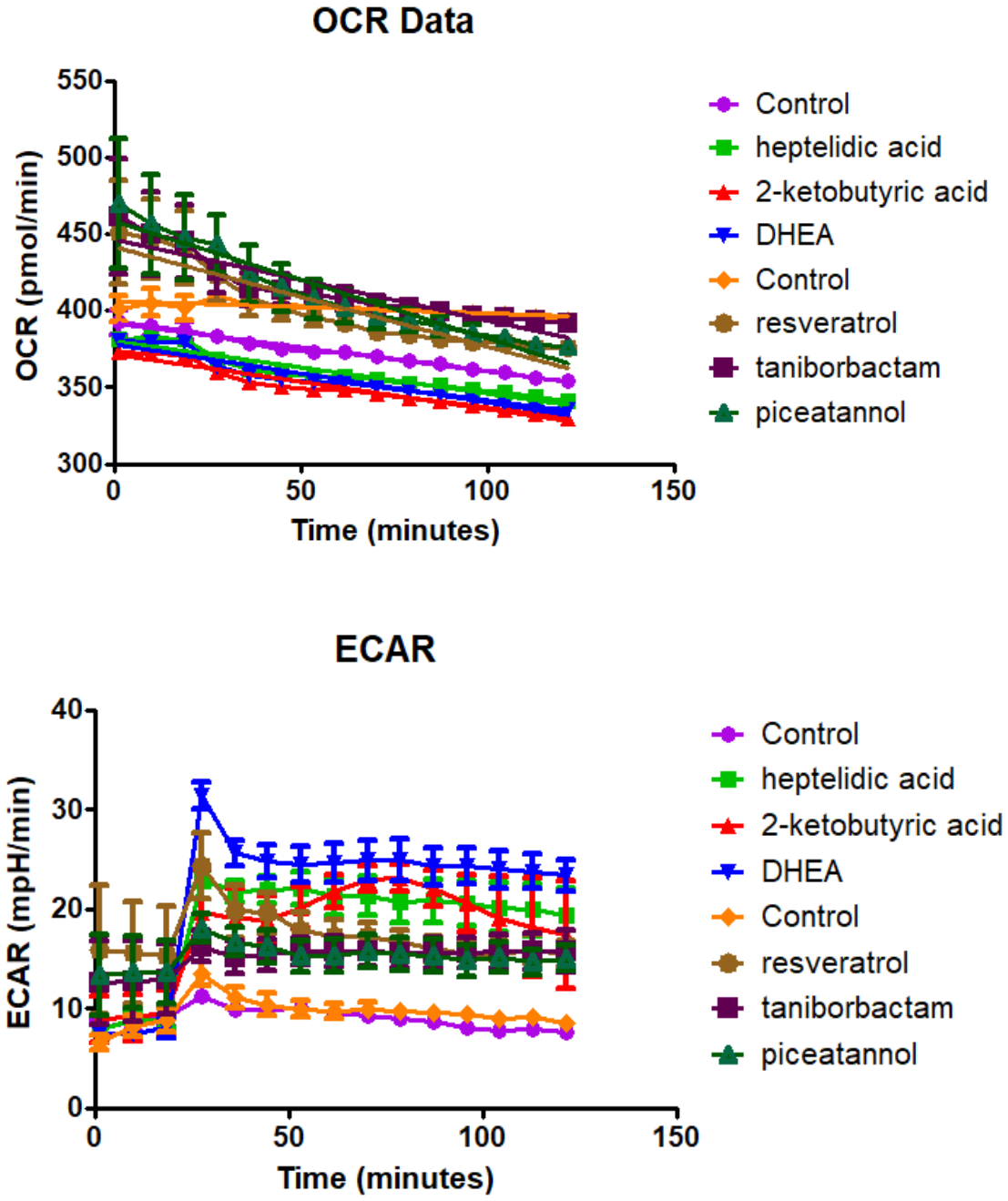

Figure IV.I Impact of compounds on OCR and ECAR in meropenem-resistant E. coli strain. *OCR (top panel) and ECAR (bottom panel) were measured over time using a Seahorse XFe24 Analyzer after the addition of 100 µM of different compounds to a meropenem-resistant E. coli strain. The compounds tested included heptelidic acid, 2-ketobutyric acid, DHEA, resveratrol, taniborbactam, and piceatannol, alongside control conditions. Error bars represent the standard error of the mean (SEM) for each condition. Significant changes in OCR or ECAR may indicate metabolic disruptions caused by the compounds.*